Seismically-Induced Rock-Slope Failure: Numerical Investigations using the Bonded Particle Model

Lorne Arnold

A dissertation
submitted in partial fulfillment of the
requirements for the degree of

Doctor of Philosophy

University of Washington

2016

Reading Committee:

Joseph Wartman, Chair

Pedro Arduino

Steven Kramer

Program Authorized to Offer Degree:
Civil and Environmental Engineering

University of Washington

Abstract

Seismically-Induced Rock-Slope Failure: Numerical Investigations using the Bonded Particle Model

Lorne Arnold

Chair of the Supervisory Committee:
Professor Joseph Wartman
Civil and Environmental Engineering

Seismically-induced rock-slope failures have caused the deaths of tens of thousands of people and economic losses in the billions over the last century. They are among the most common, dangerous, and still today, least understood of all seismic hazards. This research aims to further the understanding of seismically-induced rock-slope failure by studying the initiation and growth of fractures in rock-slopes during seismic loading. The Bonded Particle Model, which is commonly used in the static simulation of complex rock mechanics applications, is extended for use in fully-dynamic 2-dimensional simulation of rock-slopes. Using this model, the influence of ground motion characteristics and structural geology on the behavior and performance of rock-slopes during earthquakes is explored. The results show that dynamic stresses that develop within rock-slopes make the face of the slope particularly susceptible to damage. As damage accumulates in rock-slopes during dynamic loading, slopes can soften and become more sensitive to lower frequency input. Loading amplitude and frequency have a substantial impact on the seismic performance of rock-slopes, and this impact is highly dependent on the internal geologic structure of the rock-slope. The model results are consistent with observations of several historical earthquake-induced rock-slope failure events, and provide insight into the fundamental mechanisms behind seismically-induced rock-slope failures.

TABLE OF CONTENTS

LIST OF FIGURES

LIST OF TABLES

ACKNOWLEDGMENTS

I am grateful to my wife, Morgan, who has provided years of understanding support and encouragement as I worked countless nights and weekends on this research.

Several people have contributed to the work contained in this document and provided invaluable guidance to me along the way. I am grateful to have been a part of the NEESROCK project team and am indebted to Joe Wartman (principal investigator) for bringing me on board, guiding and encouraging me through the research process, and exposing me to national and international collaborative research. I am also grateful for the guidance and insights of David Keefer and Mary MacLaughlin, also principal investigators of the NEESROCK project. In addition to the principal investigator, I owe a debt of gratitude to Chris Massey (GNS Science) for support, data, and insights on the modeling of case-histories from the Port Hills of New Zealand, which comprise an important part of this work. I am grateful to Alison Duvall for serving as the graduate school representative on my committee and providing helpful questions and insights into the potential geomorphological implications of this work. Several of my fellow graduate students at the University of Washington contributed to this research either directly or indirectly, particularly, Kermit Applegate, Jake Dafni, and Matt Gibson. Shannon Smith and Sara Adams, graduates of Montana Tech also contributed to this research and are gratefully acknowledged. I am also grateful to Steve Kramer for diverting my interests from structural to geotechnical engineering, and to Pedro Arduino for showing me that I am capable of learning things that I previously thought were reserved for 'smart people.'

DEDICATION

To my wife, who married me when I had one year of school left. . . seven years ago.

Chapter 1

INTRODUCTION AND PROJECT GOALS

1.1 Introduction

In May 1970, a M_w7.9 earthquake hit Ancash, a coastal region of Peru located north of the capital city of Lima. The event triggered a massive rock-slope failure that buried the city of Yungay, killing over 25,000 people [1, 2]. Before and after aerial images of the city are shown in Figure 1.1. In 2008, rock-slope failures were a major feature of the M_w 7.9 Wenchuan earthquake. These failures were collectively responsible for an estimated 20,000 fatalities [3] and for the creation of 256 landslide debris dams that forced massive post-earthquake evacuations [4]. Worldwide, seismically induced rock-slope failures have been responsible for approximately 30% of the most significant landslide catastrophes of the past century [5]. They are among the most common, dangerous, and still today, least understood of all seismic hazards [6].

More recently, a M_w6.3 earthquake struck the Canterbury region of New Zealand triggering several rock-slope failures resulting in at least five fatalities and extensive property damage [7]. Figures 1.2,1.3, and 1.4 show some of the impacts of the seismically induced rock-slope failures in New Zealand. In addition to the immediate effects of the rock-slope failures, the newly realized hazard required a dramatic rezoning effort affecting thousands of local residences and businesses. The effort to quantify the risk of future seismogenic rock-slope failures is still ongoing. Key questions in that process include: 1) To what extent did the Canterbury earthquake sequence damage and weaken rock-slopes in the region making them further susceptible to failure? 2) What failure mechanisms can be expected in future seismic events? 3) What volume of material is at risk of future destabilization? The ability to understand the mechanical behavior of the rock-slope mass, joints, and fractures during dynamic loading is a crucial part of answering these question.

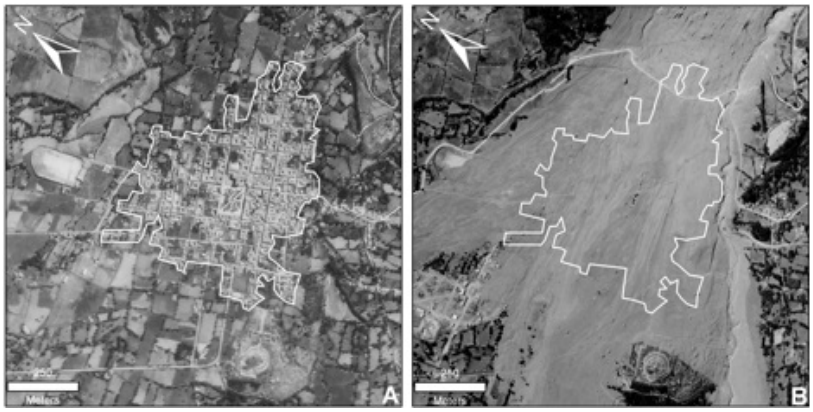

Figure 1.1: The city of Yungay, Peru before (left) and after (right) the May 1970 landslide. The outline of the city is shown in white.

Figure 1.2: Large rock fall in Sumner, New Zealand (rock fall fatality reported at the building site left) [photo credit: GNS Science]

Figure 1.3: Rock and debris falls on 50m high cliff behind houses in Sumner, New Zealand [photo credit: GNS Science]

Figure 1.4: Large rock and debris falls on the 60m high cliff face behind Redcliffs School in Redcliffs, New Zealand [photo credit: GNS Science]

1.2 Project Goals

This dissertation is part of the *Seismically-Induced Rock-slope Failure: Mechanisms and Prediction* project (hereafter NEESROCK), which is led by Dr. Joseph Wartman (University of Washington), Dr. Mary MacLaughlin (Montana Tech), and Dr. David Keefer (University of Maine). NEESROCK aims to substantially advance the fundamental understanding of the rock-slope failure process under seismic conditions. The resulting improved knowledge will drive the development of improved rock-slope failure assessment guidelines, analysis procedures, and predictive tools.

This work is a subset of the larger NEESROCK project. It aims to further the understanding of seismically-induced rock-slope failure by focusing on the initiation and growth of fractures in rock-slopes during seismic loading. Failure mechanisms for rock-slopes that do not require initiation or growth of new fractures (toppling, sliding, and slumping, e.g.) are outside of the scope of this study. Even under the umbrella of seismically-induced fracture in rock-slopes, there are several aspects of the event that are not being considered here. For example, upon fracture, sections of the slope may become structurally independent of the rest of the slope and become part of a different rock slope failure mechanism (e.g., a block slide). Once a rock-slope fails, large volumes of disrupted material are displaced and runout. Runout distance and crushing of landslide debris are also not within the scope of this work.

The role of fractures in rock-slope stability and rock-slope dynamics will primarily be investigated with the use of numerical experiments on simplified rock-slopes. Numerical modeling will be done with the commercially available program Particle Flow Code (PFC). The models will be verified by comparison to existing literature on rock mechanics behavior and modeling, dynamic physical experiments on artificial rock, and case-histories involving seismically-induced rock-slope failure events.

Specific questions to be addressed in this work include:

1. What is the role of input ground motion characteristics, particularly frequency content and amplitude, on the initiation of fracture in rock-slopes during seismic events?

2. What is the role of joint structure (orientation, spacing, and persistence) on rock-slope dynamics?

3. What is the role of joint structure on dynamic rock-slope stability?

4. Which slope and input motion parameters influence the consequences of seismically-induced rock-slope failure events (e.g., the displaced volume of the failure event)?

5. To what extent, if any, does earthquake shaking fracture and thus condition slopes for subsequent failure under non-seismic conditions?

6. For a range of common geologic conditions, how do dynamic rock-slope failures initiate and progress? Do failures occur as a single event or in a staged, episodic manner?

1.3 Project Approach

The approach used to answer the questions above involves the development of a numerical model that can be used to model rock fracture under dynamic conditions. The development of the numerical model includes the expansion of the use of a tool (the Bonded Particle Model) that is commonly used to study rock mechanics under static conditions to be used under dynamic conditions. A tool that can capture fundamental rock behavior, including the transmission of dynamic stresses, provides the necessary framework for answering the project questions.

1.4 Dissertation Outline

The next chapter presents a review of the current state of knowledge on selected topics relating to this research. These topics include the state of the practice for evaluation of seismic rock-slope stability and numerical modeling of rock.

The following chapter will describe the development of a dynamic Bonded Particle Model

Chapters 4, 5 and 6 will present the work done with the developed model that aims to address the questions raised in the NEESROCK project. Chapter 4 is divided into two parts. Part I of Chapter 4 will present the simulation of two case-histories of seismically-induced rock-slope failure in the Port Hills of New Zealand during the Canterbury Earthquake Se-

quence. The purpose of this modeling effort was twofold –first, the case-histories presented an excellent opportunity to verify the ability of the developed model to capture realistic dynamic rock-slope behavior at sites that have been extremely well-characterized. Second, verified models of realistic rock-slopes provide the framework for a study of different ground motion characteristics and structural geologic features on dynamic rock-slope behavior. Part II of Chapter 4 will present results related to the variation of ground motion and structural geology for one of the Port Hills sites from developed for the case-studies. Although significant insight is gained through the modeling presented in Chapter 4, the complexity of natural slopes involving multiple geologic layers and pre-existing discontinuities sets a limit on the understanding that can be gained and then applied to general rock-slopes.

Chapter 5 presents simulations on homogeneous (i.e., without structural geologic features) rock slopes with various dynamic inputs. This is essentially a parametric study where the characteristics of the input motions are the varied parameters. The results of Chapter 5 provide a more generally applicable understanding of the mechanics of rock-slope failure because of the simplicity of the slope configuration.

Chapter 6 presents simulations of a parametric study on the effects of discontinuities on the dynamic behavior and performance of rock-slopes. The influence of discontinuities on the natural frequency, pseudostatic stability, and the dynamic stability of rock-slopes are explored.

Chapter 7 provides a summary of the conclusions of this research, including thoughts on future research related to the furthering of the work presented here.

Chapter 2

LITERATURE REVIEW

In this chapter, an overview of selected topics relating to this research will be described. These topics include the state of the practice for evaluating the susceptibility of rock-slopes to seismically-induced failure, descriptions of different known failure modes in rock-slopes, and numerical methods of rock mechanics and rock-slope analysis. Where appropriate, the literature review section will point readers to critical or relevant references for further reading. Additionally, background on specific topics related to more detailed aspects of the work will be addressed throughout the dissertation.

Some topics related to this research required more in-depth discussion and have been summarized previously for the NEESROCK project group. A selection of these topics are attached as standalone appendices to this document. Fracture mechanics, for example, is a critical topic in understanding mechanisms relating to the kinds of rock-slope failure this research will focus on. An overview of linear elastic fracture mechanics is presented in Appendix A. The dynamic behavior of an elastic cantilever beam was also an important topic. The formulation of an analytical solution for its behavior is shown in Appendix B.

2.1 Rock-Slope Failure Modes

In nature, rock-slopes experience many different failure modes based on their geometry, strength, internal structure, and loading conditions, among other factors. Goodman and Kieffer (2000) provide a thorough discussion of common failure modes and highlight the characteristics that distinguish one from another [8]. Of particular interest to this research, which will focus on rock-slope failures involving fracture of rock material, are modes involving rock fracturing. Figure 2.1 shows examples from Goodman and Kieffer (2000) of rock-slope failures involving rock bridge cracking in tension, rock bridge cracking in compression and shear, and slide base rupture. Aydan (2013) also provide examples of rock-slope

failures involving intact rock with an emphasis on modes induced by earthquakes [9]. Shear failure, bending failure, and flexural toppling failure are identified as common seismically-induced rock-slope failure modes involving fracture of intact rock. These failure modes are illustrated in Figure 2.2.

The modes of failure illustrated here represent a wide range of mechanisms where failure surfaces develop entirely through the rupture of intact rock, or by the joining of existing discontinuities by rupture of a rock bridge. Stead and Wolter (2015) provide a critical review of rock-slope failure mechanisms emphasizing the role of structural geology on the determination of rock-slope failure modes [10]. Terzaghi (1962) and Eberhardt (2003), among others, have noted that the effect of structural geology on rock-slope stability varies with the nature and extent of discontinuities, overall slope geometry, and intact rock mass engineering properties [11], [12]. The ability to identify the mechanisms that enable movement of the rock-slope mass is an important component of assessing the stability of rock-slopes.

2.2 Landslides Caused by Earthquakes

Earthquakes are known to be a major cause of landslides of all kinds, and earthquake-induced landslides have been documented from as early as the 4th Century B.C. [Seed (1968) and Keefer (1984)]. Keefer (1984) performed a survey of 40 historical worldwide earthquakes and the resulting landslides. Table 2.1 presents a summary of the abundance of different seismically-induced landslide types with associated depths of failure. The types of earthquake-induced landslides involving rock-slopes can be broadly categorized into two groups –deep and shallow rock-slope failures. Note that other categorizations, based on internal disruption of the failure mass, for example, are possible. In general, shallow rock-slope failures tend to involve a high degree of internal disruption and deep failures tend to involve slight or moderate internal disruption. Rock avalanches, which are an uncommon, but extremely hazardous failure mode are an exception because they are characterized by both deep failure surfaces and high internal disruption. Concerning shallow, disrupted landslides and deep, coherent landslides in rock, Keefer notes:

> Rock falls [and] rock slides... are initiated by the weakest shaking. In partic-

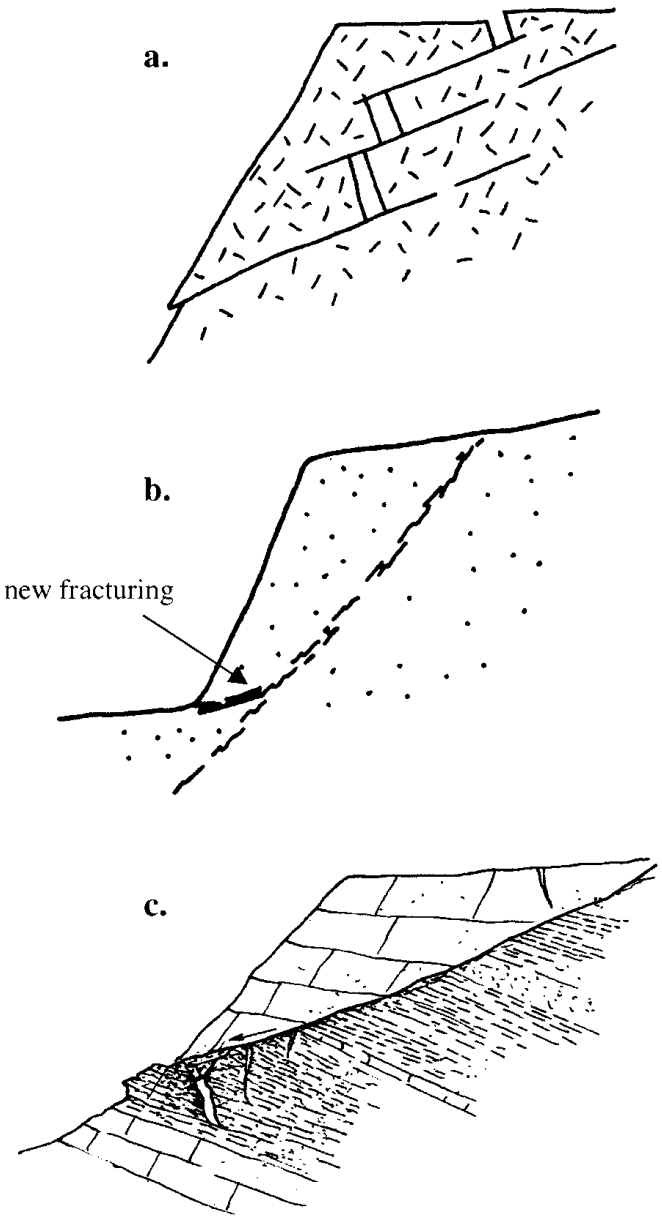

Figure 2.1: Failure modes involving rock fracturing from Goodman and Kieffer (2000): (a) rock bridge cracking in tension, (b) rock bridge failure in compression, and (c) slide base rupture.

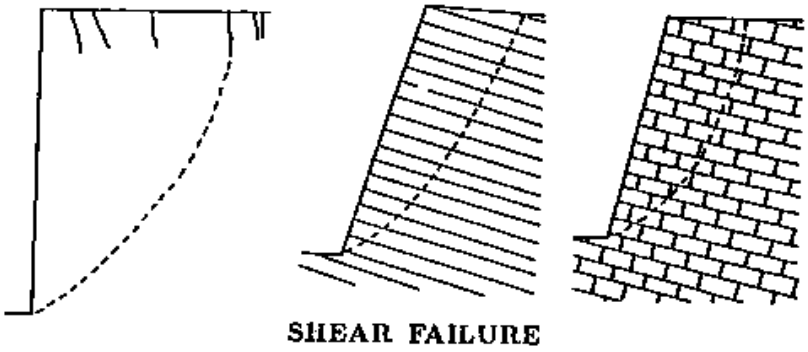

(a)

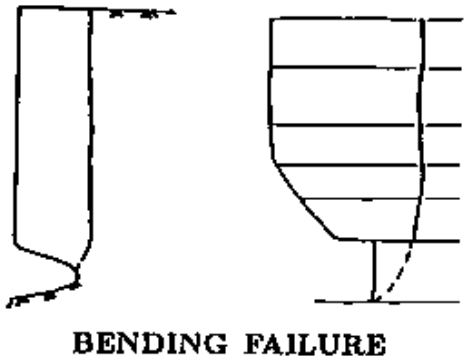

(b)

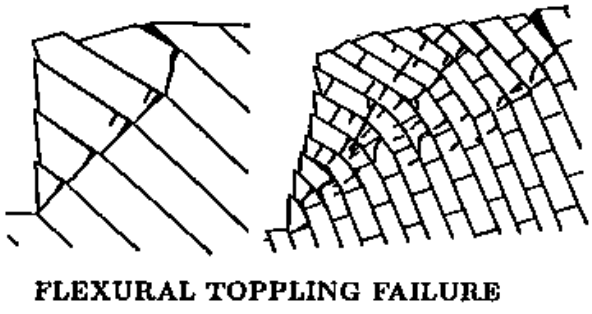

(c)

Figure 2.2: Failure modes involving rock fracturing from Aydan (2013): (a) shear failure, (b) bending failure, and (c) flexural toppling failure.

> ular, these shallow, highly disrupted landslides from steep slopes are probably susceptible to the short-duration, high-frequency shaking characteristic of small earthquakes. Coherent, generally deep-seated landslides are initiated by stronger and probably longer-duration shaking.

Since 1984, several seismically-induced rock-slope failures have been observed and documented [Sepulveda et al. (2005), Xu et al. (2009), Kveldsvik et al. (2009), Topal et al. (2012), and Huang et al. (2013) and Massey et al. (2016), among others]. The documented seismic failures were observed to impact the built and natural environments in several ways including the creating of landslide dams, destruction of roads and buildings and loss of life [**?**, 4, 13–16]. Some of the most recent and well-documented seismically-induced rock-slope failures occurred as a result of the Canterbury Earthquake Sequence (CES) in the Port Hills region of New Zealand in 2010 and 2011.

Massey et al. (2014, 2016) assessed and documented multiple rock-slope failures in the Port Hills of New Zealand during the CES [17], [16]. Shallow rock falls (also called 'debris avalanche' and 'cliff-collapse' by Massey et al.) dominated the response of steep-rock slopes during the CES, and the partial development of deep-seated rock slumps was inferred from the displacement profile at the cliff top. In addition to the types of failures induced by the earthquakes, Massey et al. describe earthquake-induced damage to the portion of the slopes left standing, made evident by the development of new cracks and dilation of existing cracks at cliff faces (see Figure 2.3).

Table 2.1: Types of landslides caused by earthquakes with abundance of the landslide types from 40 historical earthquakes and associated depths as reported by Keefer (1984).

Abundance	**Landslide type**	**Depth**[1]	**Internal disruption**[2]
Very Abundant	Rock falls	shallow	High or very high
>100,000	Disrupted soil slides	shallow	High
	Rock slides	shallow	High
Abundant	Soil lateral spreads	variable	Moderate to high
10,000 to 100,000	Soil slumps	deep	Slight or moderate
	Soil block slides	deep	Slight or moderate
	Soil avalanches	shallow	Very high
Moderately Common	Soil falls	shallow	High or very high
1,000 to 10,000	Rapid soil flows	shallow	Very high
	Rock slumps	deep	Slight or moderate
Uncommon	Subaqueous landslides	variable	High or very high
100 to 1,000	Soil earth flows	variable	Slight
	Rock block slides	deep	Slight or moderate
	Rock avalanches	deep	Very high

1. Depth: "shallow" signifies thickness generally <3 m; "deep" signifies depth generally >3 m.

2. Internal disruption: "slight" signifies landslide consists of one or a few coherent blocks; "moderate" signifies several coherent blocks; "high" signifies numerous small blocks and individual soil grains and rock fragments; "very high" signifies nearly complete disaggregation into individual soil grains or small rock fragments.

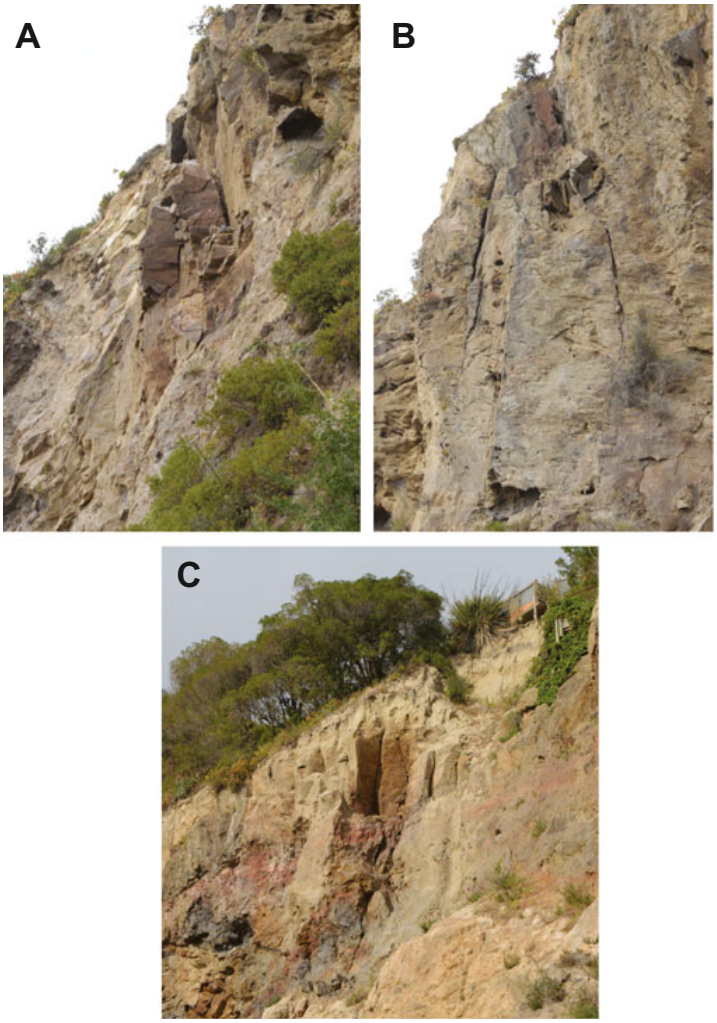

Figure 2.3: Seismically-induced damage to rock-slope cliff faces in the Port Hills region of New Zealand from Massey et al. (2016).

2.3 Methods of Evaluating Seismic Stability of Rock-Slopes

The current state of the practice for evaluating the stability of rock-slopes under seismic loading is generally limited to either (1) empirical methods, which produce qualitative results, (2) pseudostatic methods resulting in a factor of safety, or (3) sliding block analysis methods, which provide an estimate of the co-seismic displacement of the slope.

2.3.1 Emperical Methods for Seismic Rock-Slope Stability Assessment

Two of the most popular empirical methods are those of Keefer (1993) [18] and Harp and Noble (1993) [19]. Keefer's method is based on a decision tree that includes several rock mass characteristics that influence stability (see Figure 2.4). The decision tree, which is based on empirical data from 60 different slope units in 24 separate earthquakes, accounts for eight slope characteristics: height, inclination, the degree of weathering, strength of induration, openness of fissures, spacing of fissures, vegetation, and moisture conditions. The results of Keefer's method are qualitative descriptors giving five possible levels of susceptibility to failure ranging from 'low' to 'extremely high'.

Harp and Noble (1993) provide a method for determining the susceptibility of a rock-slope to seismically-induced failure based on the rock mass quality, or Q. Rock mass quality is calculated based on the fracture spacing in the rock mass, the roughness and frictional characteristics of the joint walls or filling materials, the total in situ stress, and the water pressure in the slope system [20]. This method also produces qualitative descriptors ranging from 'highly susceptible' to 'mostly stable' in four levels of susceptibility. Another recently developed evaluation system, the Comprehensive Areal Model of Earthquake-Induced Landslides (CAMEL), uses fuzzy logic systems and geographic information systems to screen for different levels of hazard on a regional scale [21].

While these methods provide a good starting point, they do not account for the dynamic behavior of the rock-slope itself, which will play a crucial role in the development of internal forces. Several important ground motion characteristics (frequency content, duration, etc.) are also not accounted for.

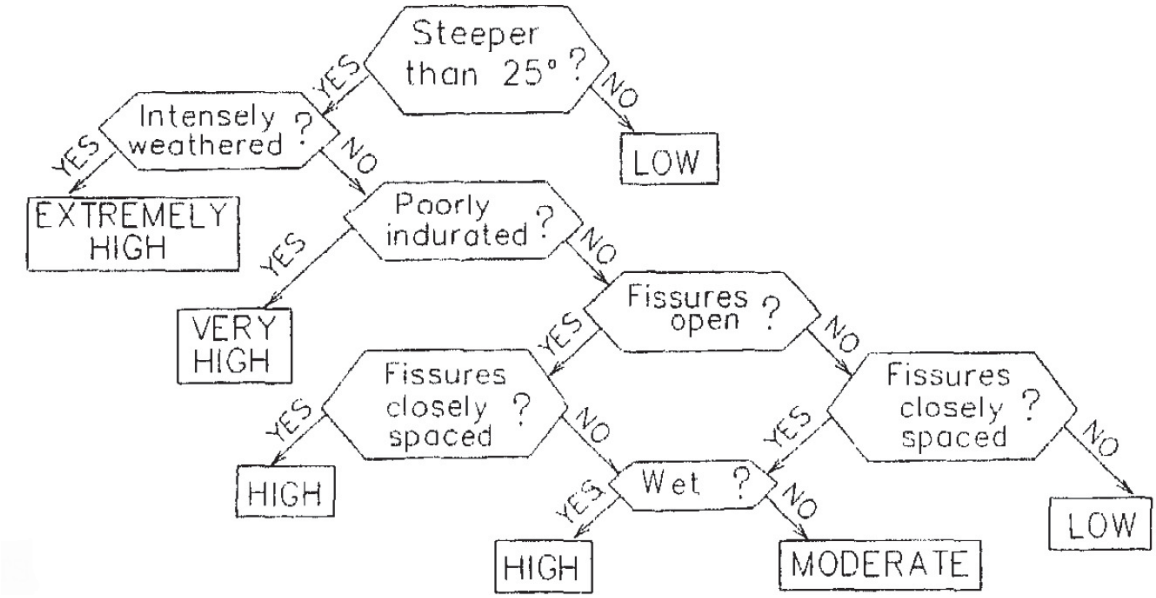

Figure 2.4: Decision tree for susceptibility of rock-slopes to earthquake-induced failure by Keefer (1993)

2.3.2 Pseudostatic Methods for Seismic Rock-Slope Stability Assessment

Pseudostatic methods of analysis simulate the inertial effects of dynamic loads by the application of a constant horizontal acceleration. The use of pseudostatic methods is commonly applied to limit equilibrium simulations, but can also be used in numerical analyses. The result of a pseudostatic analysis is generally either a factor of safety against a certain level of horizontal acceleration, or the horizontal acceleration required to initiate yield, k_y.

Although pseudostatic analyses have been used for nearly a century and is commonly used in practice today, it has serious fundamental limitations. The complex dynamic effects of ground motion waves and their interaction on soil or rock slopes are lost with this approach, which reduces all these effects to a single parameter [22].

2.3.3 Sliding Block Methods for Seismic Rock-Slope Stability Assessment

Newmark (1965) proposed a method for analyzing the behavior of dams and embankments by treating them as rigid masses that slide on inclined planes [23]. Although originally

developed for evaluation of dams and embankments, sliding block analysis has become one of the most common methods for assessing the impact of earthquakes on slopes, including rock-slopes [24], [25], [26]. The inputs for a Newmark analysis are the horizontal acceleration yield coefficient, k_y, and an acceleration time history. The method estimates displacements by integrating the parts of the acceleration time history that exceed k_y, then integrating that portion of the signal again to yield the cumulative displacement of the rigid block. Multiple variations of the rigid sliding block analysis, including the decoupled and coupled methods, have been proposed over the years and are also widely used. A 'coupled' variation of the sliding block analysis considers the dynamic response of the slope. The following explanation of coupled sliding block displacement is taken from the SLAMMER (Seismic LAndslide Movement Modeled using Earthquake Records) user guide [27]:

> Coupled analysis models the interaction of sliding/limited shear stresses on the dynamic response of the sliding mass. In SLAMMER, the dynamic response of the sliding mass is computed using a one-dimensional, modal analysis in the time domain (Rathje and Bray, 1999). The sliding mass is defined by its height, shear-wave velocity, and damping ratio; the shear-wave velocity below the sliding mass is also specified (this can be conservatively taken as rock). The modal analysis has a rigid base, but the effects of a visco-elastic base are modeled through additional damping that is assigned based on the Vs of the base and the Vs of the sliding mass (Lee, 2004). The dynamic response can be modeled as linear elastic or equivalent linear. Coupled analysis is considered the most rigorous and yields the most accurate estimates of displacement for deeper landslides in softer material.

Although sliding block methods yield displacements as output, Bray and Travasarou (2007) suggest that this output is appropriately viewed as an index of seismic performance [28].

One of the flaws in sliding block analyses for use with rock-slopes is that the internal disruption of the rock mass with co-seismic displacement is not captured. Stead et al. (2006) presented numerical simulations of the development of the internal disruption that can accompany the sliding of a rock-slope failure mass [29] (see Figure 2.5).

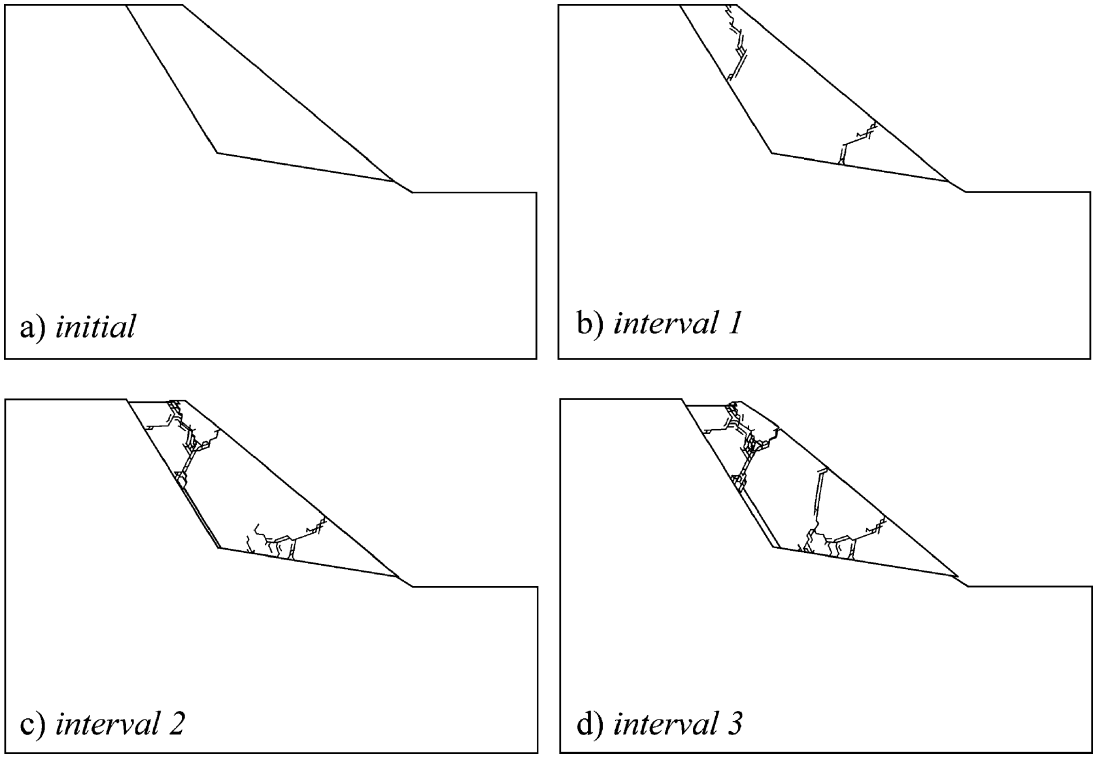

Figure 2.5: Illustration of internal disruption with rock mass sliding from a numerical simulation presented by Stead et al. (2006).

2.4 Numerical Modeling of Rock

The limitations of the commonly used slope stability analysis methods described above have lead to the development and use of numerical techniques for the evaluation of rock-slope stability. In the numerical investigation of the mechanical behavior of rock, two basic classes of methods are typically employed: continuum and discontinuum methods [30].

Continuum methods, such as the finite element method (FEM), finite difference method (FDM), and the boundary element method (BEM), approximate what is assumed to be a continuous system with infinite degrees of freedom by discretizing the system into one with finite degrees of freedom. In rock mechanics, continuum methods involve interpretation and homogenization of an inherently heterogeneous system into elements whose constitutive behavior is intended to incorporate the influence of the fractures and flaws not explicitly represented. Plastic softening and damage models are common tools for capturing localization and failure within continuum models [31]. Explicit representation of fractures with hybrid continuum-discontinuum is also possible [32, 33].

Discontinuum methods approximate the mechanical behavior of a body with independent elements that interact with each other at points of contact. Several discontinuum methods exist under the umbrella of the 'discrete element method', defined by Cundall and Hart (1992) as any method that (1) allows finite displacements and rotations of discrete bodies, including detachment, and (2) automatically recognizes new contacts as part of the calculation process [34]. Discontinuous deformation analysis (DDA) and the distinct element method (DEM) are both discrete element methods.

The kind of numerical model used is to some extent dictated by the subject of the study. Rock masses come in a variety of configurations that may require a particular model type or may be appropriately modeled by multiple available modeling methods.

A detailed explanation of modern modeling approaches in rock engineering can be found in *A review of techniques, advances, and outstanding issues in numerical modelling for rock mechanics and rock engineering* by L. Jing, 2003 [32]. Jing also presents general guidelines for where different models types are typically used. Considerations for model type include the relative scale of the model and the discontinuities in the rock mass, the

expected failure mechanism(s), if any, and the level of uncertainty in the model components. Jing summarizes:

> There are no clear-cut advantages or shortcomings when considering continuum or discrete models for simulating fractured rocks. Continuum models often include a limited number of explicitly represented fractures of usually larger scales, and the blocks in the discrete models are treated as continuum bodies with standard discretization meshes. The main difference is:
>
> - whether contacts between the blocks (particles) remain unchanged (continuum approach) or need to be continuously updated using contact mechanics principles (discrete approach), and
> - whether the fractures are permitted to have large-scale displacement/movement, including rotation and complete detachment (discrete approach).
>
> Since the main effects of the fractures are mostly concentrated near excavated surfaces, the discrete approach is more appropriate for near-field representations and the equivalent continuum approach is more efficient for far-field regions. Hybrid models are therefore the natural product of combinations of the two.

Since Jing's 2003 publication, the bonded-particle model (BPM), which was introduced by Potyondy and Cundall (2004) and is a further subset of DEM [35], has become a widely used tool in rock modeling. Figures 2.6 and 2.7 illustrate the formulation of the BPM and its behavior from Cho (2007) [36]. When combined with a discrete fracture network (DFN), the BPM becomes a synthetic rock mass (SRM) that can be used to model a rock mass with pre-defined joints as well as the ability for new joints to form through the fracturing of intact material either by the creation of new fractures or the propagation of existing fractures [37]. Figure 2.8 illustrates the inclusion of fractures in BPM using the smooth joint contact model developed by Mas Ivars et al. (2011).

The same principles for models selection apply to scope and scale, but with BPM, a finer scale is possible than with traditional (blockly) DEM, however, new challenges are introduced. For example, a material's fracture toughness (i.e., its resistance to fracturing)

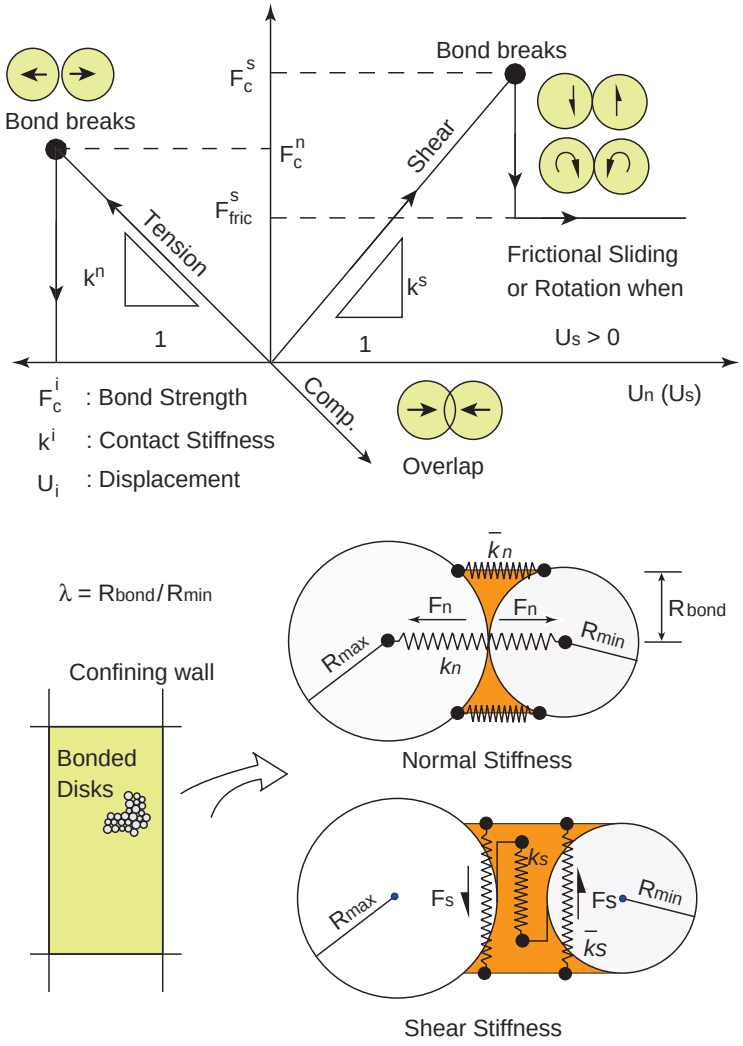

Figure 2.6: Microparameters and the illustration of yielding process for bonding. Note that the compressive stiffness in the figure is the same as the tensile stiffness, which is not the case for a parallel-bonded model. This constitutive behavior is possible for a contact-bonded material. [Figure from Cho 2007]

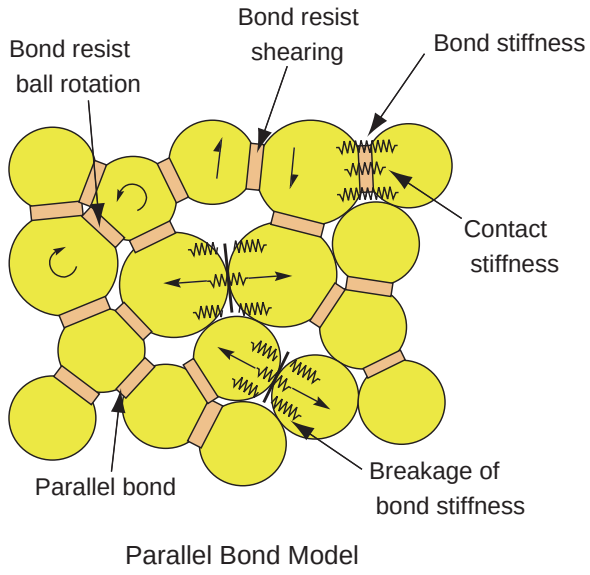

Figure 2.7: Illustration of the parallel-bond model in PFC [Figure from Cho 2007]

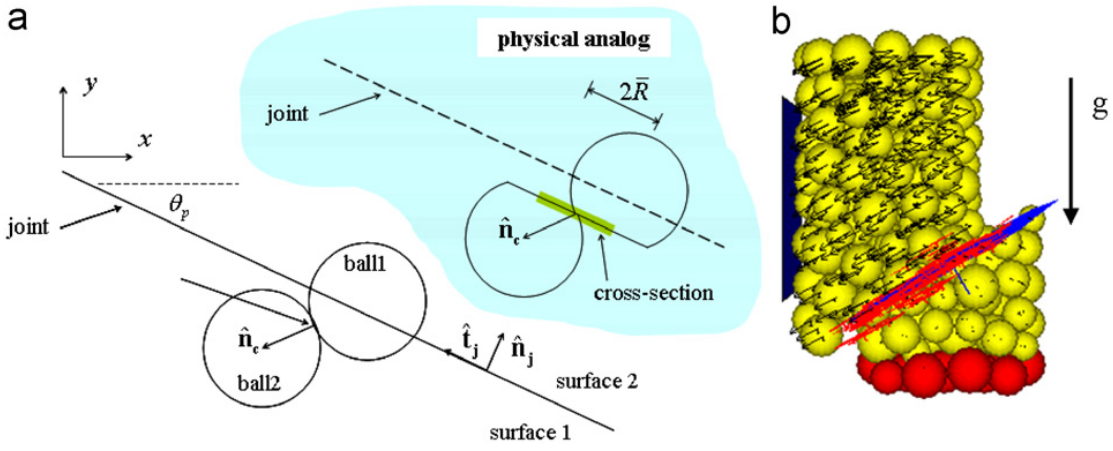

Figure 2.8: Effective joint geometry (a) and example of sliding in a specimen with an angled, frictionless smooth joint plane (b) from Mas Ivars et al. (2011) [38].

is dependent on an internal length scale related to the size of micromechanical flaws (see Appendix A for further explanation). Potyondy and Cundall explain that, in DEM, this internal length scale is directly dependent on particle size. For this reason, the particle sizes in the model cannot be adjusted without changing the material's resistance to fracture.

While the equations describing the particles and contacts comprising the BPM are simple, the system as a whole is capable of displaying several complex behaviors observed in rock. Examples in the literature show several rock types that have been successfully modeled with BPM such as granite [39], chalk [40], and sandstone [41]. A list of complex rock behaviors BPM has been shown to replicate is provided by Potyondy and Cundall (2004) and is reproduced here without revision [35]:

1. Continuously non-linear stressstrain response, with ultimate yield, followed by softening or hardening.
2. Behavior that changes in character, according to stress state; for example, crack patterns are quite different in the tensile, unconfined- and confined-compressive regimes.
3. Memory of previous stress or strain excursions, in both magnitude and direction. This behavior is commonly expressed in terms of moving yield surfaces, or evolving anisotropic damage tensors.
4. Dilatancy that depends on history, mean stress and initial state.
5. Hysteresis at all levels of cyclic loading/unloading; cyclic energy dissipation is strongly dependent on cyclic amplitude.
6. Transition from brittle to ductile shear response as the mean stress is increased.
7. Dependence of incremental stiffness on mean stress and history.
8. Induced anisotropy of stiffness and strength with stress and strain path.
9. Non-linear envelope of strength.
10. Spontaneous appearance of microcracks and localized macrofractures.
11. Spontaneous emission of acoustic energy.

Several researchers have used the BPM to study rock-slope stability under static conditions, including Wang et al. (2003), Lorig et al. (2009), and Camones et al. (2013). Figure 2.9 shows examples of the use of BPM in rock-slope stability analysis from Stead and Wolter (2015).

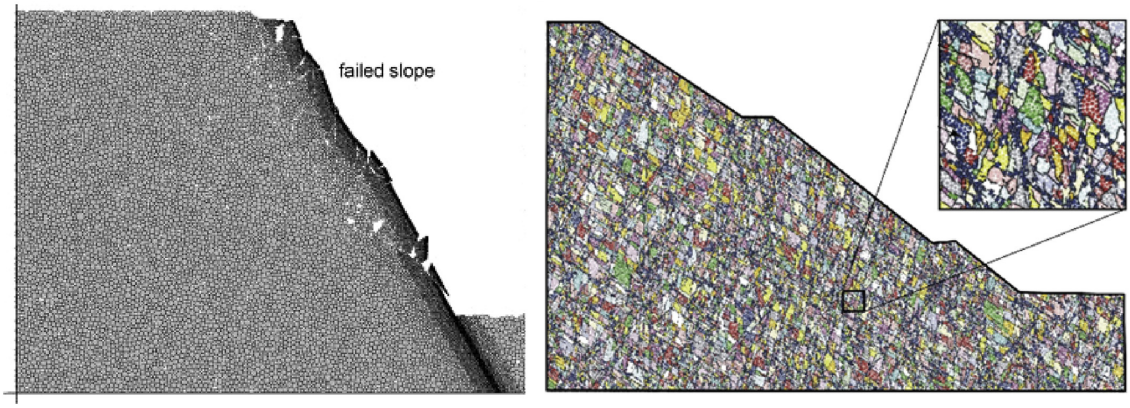

Figure 2.9: Examples of the use of the bonded particle model in rock-slope stability from Stead and Wolter (2015). An unjointed BPM rock-slope from Wang et al. (2003) is shown on the left. A jointed BPM from Lorig et al. (2009) using smooth joints is shown on the right.

The bonded particle model has been selected for use in this project because of their well-demonstrated ability to model complex, rock-like behavior and the relatively simple mathematical framework used to solve them. BPM is not commonly used in dynamic simulations, however, it has been shown to be capable of accurately modeling some dynamic behavior such as p-wave propagation [42, 43] and wave scattering [44]. Hazzard and Young (2004) demonstrated that the dynamic behavior of a DEM model at the micromechanical level is important even for seemingly static simulations [45]. Damping, they argue, is not a free parameter that exclusively influences global dynamic model behavior. It also has a measurable influence on model strength. This is particularly important for the calibration of a model that will be used in dynamic simulations because it suggests that the dynamic calibration parameters and the strength parameters cannot be decoupled.

Chapter 3

MODEL DEVELOPMENT

3.1 Development of a Discrete Element Model in PFC2D

The development of a BPM requires the selection of the appropriate microparameters to match a desired macro-level behavior through a calibration process [35]. Microparameters that can be used to achieve calibration include particle size and size distribution, particle normal and shear stiffness, bond normal and shear stiffness, bond normal and shear strength, and viscous damping. In addition to these mechanical microparameters, local damping and the calculation timestep can be adjusted to influence the results, particularly in dynamic simulations.

The Itasca program Particle Flow Code 2D (PFC2D) was used for this research [46]. Advanced control of PFC2D is possible with the use of Itasca's FISH programing language [47]. FISH is an embedded language that allows users to define variables and functions to build, control, or plot elements of simulations. Several FISH routines were written to develop the models presented in this dissertation. Examples of the code used are included in Appendix E.

Local and viscous damping are the only two forms of damping explicitly available in PFC2D. Material damping in the form of interparticle friction also acts on DEM models in PFC2D. Local and viscous damping are further explained in Section 3.2.2. Each input parameter can be thought of as a knob that can be turned to make adjustments to the model behavior. The calibration process, then, is the process of finding the best setting for each knob to produce a model behavior similar to a specified set of target macro-properties from a physical material. The combination of microparameters to produce a calibrated model is not necessarily unique. The 'proper' combination may be controlled by the type of simulations being performed or the key behaviors being investigated. The potential number of acceptable combinations is not infinite. For example, the size of specimens to be tested

may require a certain particle size, for which there may only be one set of stiffnesses to produce the proper modulus. Unconfined compressive strength, tensile strength, Young's Modulus and Poisson's ratio are all common calibration metrics [30, 48, 49].

Researchers have used various methods such as trial-and-error, experimental design and optimization [48], and dimensional analysis [30] to find the ideal set of microparameters. For the calibration of this model, a set of initial microparameters was selected based on reported values of similar models, as found in publications on BPM. The microparameters were systematically varied in a range suggested by a review of existing BPM literature to find the relationships between input microproperties and emergent macroproperties.

The intended use of the BPM in the current study includes simulation of failure of rock-slope systems under seismic conditions, so the calibration metrics need to include dynamic parameters. Rock-slopes, particularly those with sub vertical joint dips, experience and often fail in flexure [50], so the behavior of the model under flexural loading is also of interest. Current use of BPM has been largely in the realm of static or pseudo-static simulations where the true dynamic response of a system subjected to a dynamic load is not considered. Additionally, although the use of the parallel-bond is common with the BPM, its effect on the flexural modulus of a system is not addressed in the literature. This effect turns out to be dramatic and cannot be neglected in dynamic simulations. The definition of boundary conditions, another critical topic for dynamic simulations, has been loosely addressed in the literature to date, but a complete framework for modeling seismic loading with BPM has not been demonstrated.

This chapter will describe the calibration of the BPM to static strength and stiffness properties and then address the several topics related to the dynamic behavior: Calculation timestep, the parallel-bond, damping, wave transmission and reflection, and boundary conditions.

3.1.1 Calibration Test Models

Models of three typical laboratory tests used for BPM calibration were developed – unconfined compressive strength (UCS), Brazilian tensile strength (BT), and single-edge notched

beam (SENB). Figure 3.1 shows the models as built in PFC. Additionally, a large-scale cantilever beam was developed for dynamic calibration of the model to compare to experimental results from a centrifuge test. The centrifuge experimental setup is described in Appendix C.

Laboratory Scale DEM Models

The bonded particle models used in these simulations were created using a randomized placement scheme for a set of particles with sizes uniformly distributed between r = 1-mm and r = 2-mm, where r is the particle radius. The distribution of sizes allows for a non-uniform packing matrix that can be changed with the random seed used in PFC. This allows several versions of the same model to be created with unique particle arrangements, which is analogous to casting multiple models of the same concrete mix, or testing multiple samples from the same intact rock material. Particles are placed within a set of walls of the same area as the cross section of the physical test and are confined to atmospheric pressure by gradually changing the radius of the particles. Once the stress state is set, the particles are bonded with parallel bonds, the confining walls are deleted, and the model is allowed to come to equilibrium.

The specific laboratory tests are described as follows:

1. **UCS Model:** This sample contained approximately 2,500 particles and 6,400 contacts. It was loaded by placing it between two walls, holding the upper wall fixed, and slowly raising the lower wall to induce a compressive load. See Figure 3.1a.

2. **BT Model:** This sample contained approximately 2,500 particles and 6,400 contacts. It was loaded with slightly curved walls to help stabilize the disk. The walls were controlled in the same way as the UCS test was. See Figure 3.1b.

3. **SENB Model:** This sample contained approximately 1,200 particles and 3,000 contacts. The three-point loading on the beam was applied with large particles (r = 2-cm). As in the physical experiments, the purpose of this test is to determine the model's fracture toughness. See Figure 3.1c.

The results of several simulations on the calibration models described above are shown in Figures 3.2 through 3.6. The calibration results confirm the trends expected based on published calibration data, particularly from Fakhimi and Villegas [30], who provide dimensional charts for BPM calibration relationships. BPM elastic modulus increases linearly with increasing bond normal stiffness (see Figure 3.2). Compressive and tensile strengths increase linearly with increasing bond normal strength (see Figures 3.3 and 3.5). Compressive strength decreases slightly with increasing bond normal stiffness (see Figure 3.4). The fracture toughness for 50 different SENB models with tensile strength of approximately 5 MPa is shown in Figure 3.6. More randomized versions of the SENB model were run due to the uncertainty in the fracture toughness result. The UCS and BT values of a BPM model are fairly well understood, but the fracture toughness remains a challenging parameter to model well. Potyondy and Cundall (2006) proposed the following relationship between BPM tensile strength (σ_t) and fracture toughness (K_{Ic}):

$$K_{Ic} = 2/3\sigma_t\sqrt{\pi\alpha R} \tag{3.1}$$

where R is the average particle radius, and α is a dimensionless factor that increases with increased packing irregularity [35].

Centrifuge Scale DEM Model

The bonded particle model used in these simulations is created using a randomized placement scheme for a set of particles with sizes uniformly distributed between r = 2-cm and r = 4-cm, where r is the particle radius. Particles are placed within a set of walls that created a 4.12-m by 1.00-m area and are confined to a specified stress state by gradually changing the radius of the particles. Once the stress state is set, the particles are bonded with parallel bonds, the walls are deleted, and the model is allowed to come to equilibrium. The final model has approximately 1200 particles and 2200 bonds. A strip of particles at the base of the model is converted into a *clump* of particles approximately 0.12-m thick. In PFC2D, a *clump* is a group of particles that act as a rigid body. During the calculation cycle, the equations of motion for contacts internal to the clump are skipped, and the particles within

the clump remain at a fixed distance from each other [51]. The rigid clump formed at the base of the beam acts as a unit, leaving a 4-m by 1-m cantilever beam to simulate the centrifuge model. This base unit is given the velocity time history to provide the dynamic input to the model.

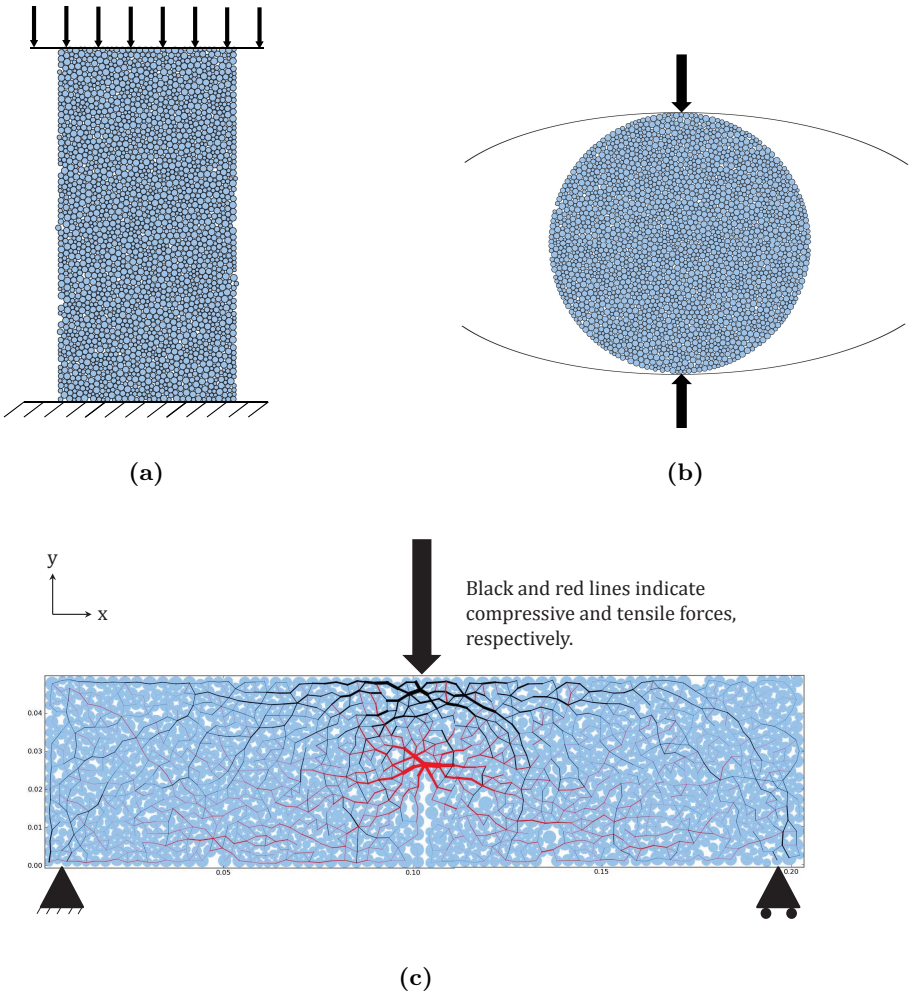

Figure 3.1: Laboratory Scale DEM Models for (a) the UCS test, (b) the BT test, and (c) the SENB test. The thickness of the red and black lines in (c) indicate the magnitude of the interparticle forces.

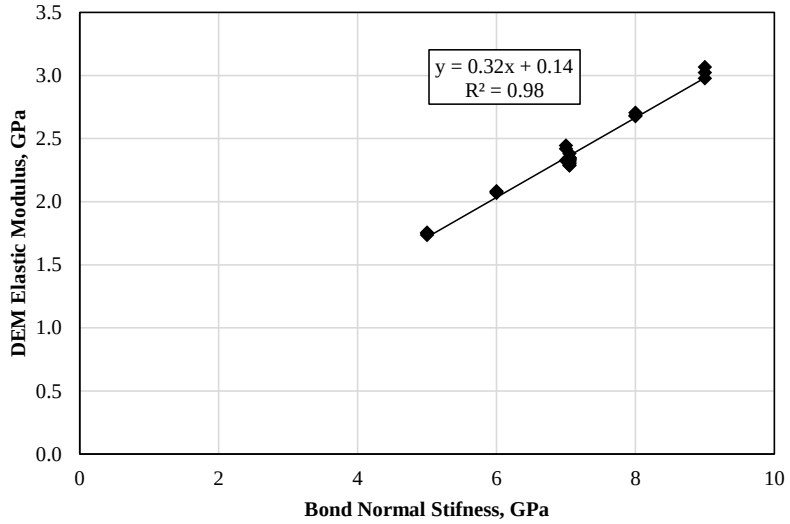

Figure 3.2: Relationship between elastic modulus in a DEM model and bond normal stiffness.

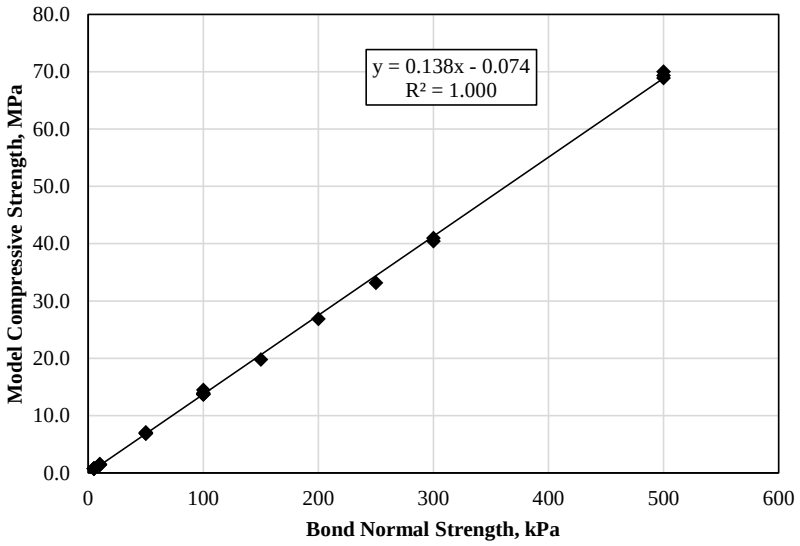

Figure 3.3: Relationship between compressive strength in a DEM model and bond normal strength.

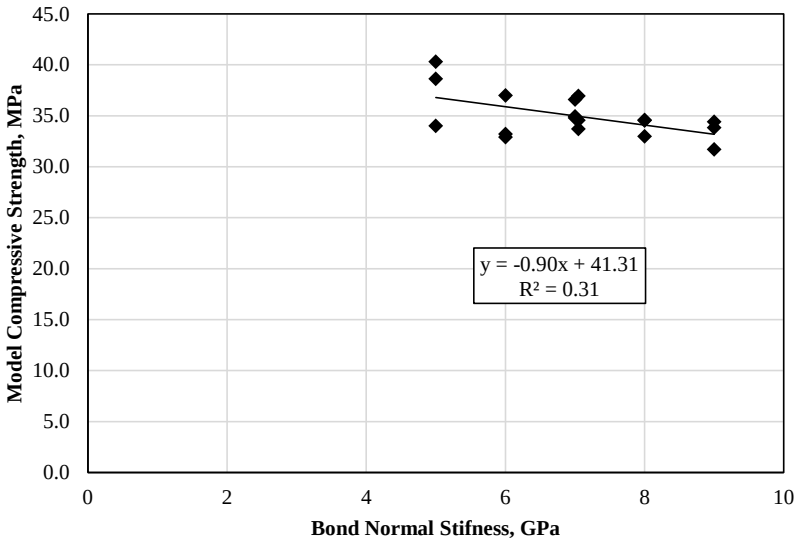

Figure 3.4: Relationship between compressive strength in a DEM model and bond normal stiffness. There is a slight, linear relationship of decreasing strength with increasing bond stiffness.

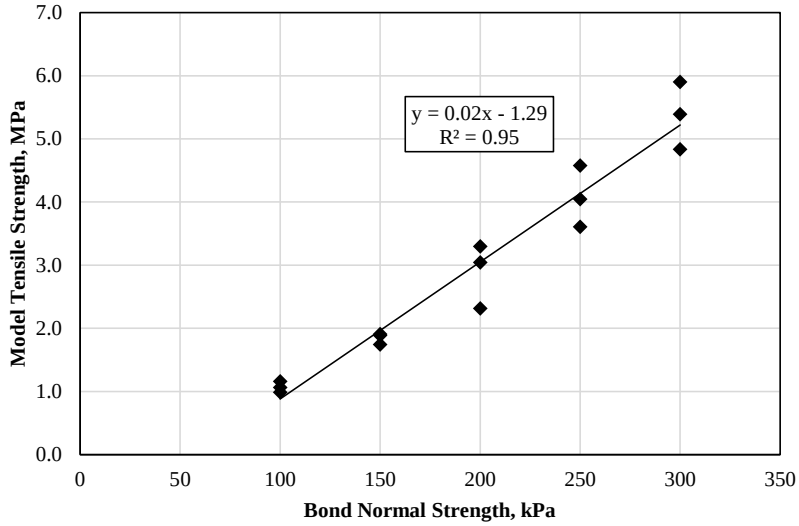

Figure 3.5: Relationship between tensile strength in a DEM model and bond normal strength.

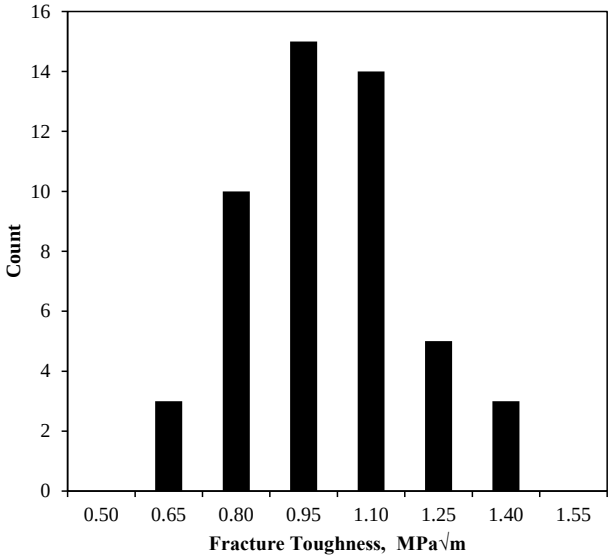

Figure 3.6: The distribution of fracture toughness from single-edge notched beam tests for a single set of BPM microproperties with random particle arrangement. For the 50 samples tested the results are distributed about a mean of 1.07 MPa-m$^{0.5}$ with a standard deviation of 0.18 MPa-m$^{0.5}$.

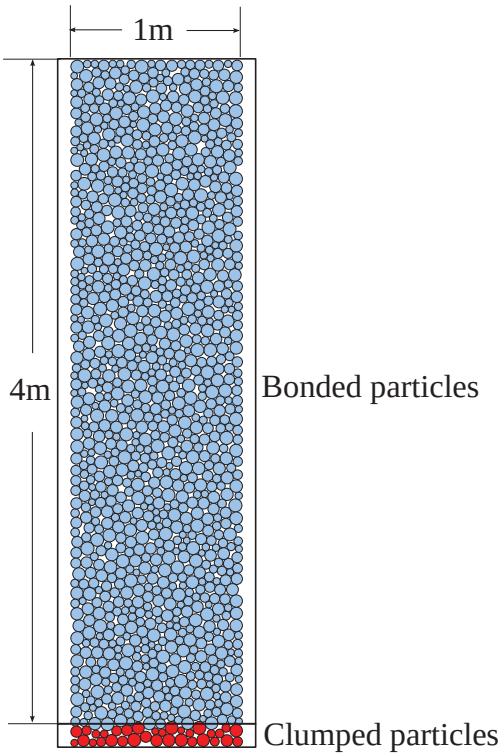

Figure 3.7: PFC beam model

3.1.2 Timestep in the DEM model

The selection of an appropriate integration timestep is crucial to producing quality results in any dynamic simulation. The smaller the timestep, the more accurate the integration will be, and the longer the simulation will take. The ideal timestep, therefore, is as large as possible while still providing a sufficient solution. Whether or not a solution is "sufficient" is somewhat subjective and depends on the specific simulation and its application. For the calibration tests in this project, the solution is considered sufficient when the key behaviors of the model converge to a consistent value.

By default, PFC selects a timestep sufficiently small that, during a single timestep, disturbances cannot propagate further from any particle than its immediate neighbors [52]. This calculation is based on the masses of the individual particles and the interparticle contact stiffnesses. Since the particles themselves are rigid, their size only affects the timestep in that it affects the mass. Because PFC is primarily used for non-dynamic simulations in practice, research, and in the PFC manual, the default selected timestep given by PFC requires some investigation. To accomplish this, the effect of the timestep on three dynamic results (natural frequency, max Fourier amplitude, and average intensity) on PFC simulations was tested. Beams as in Figure 3.15b were subjected to a frequency sweep motion. Ten beam assemblies, made unique by the use of a different random seed, were tested at nine different timesteps ranging from 100% to 25% of the default PFC timestep. The results of these simulations are shown in Figure 3.8. Note that the results shown in these figures are normalized by the solution each sample converged to, which are normally distributed about some mean. The models appear to converge in each case by 50% of the default PFC simulation.

Like the calculation timestep, particle resolution is also an important model parameter that affects the quality of the simulations and the time it takes to run them. Considerations related to the particle resolution are described in Appendix D.

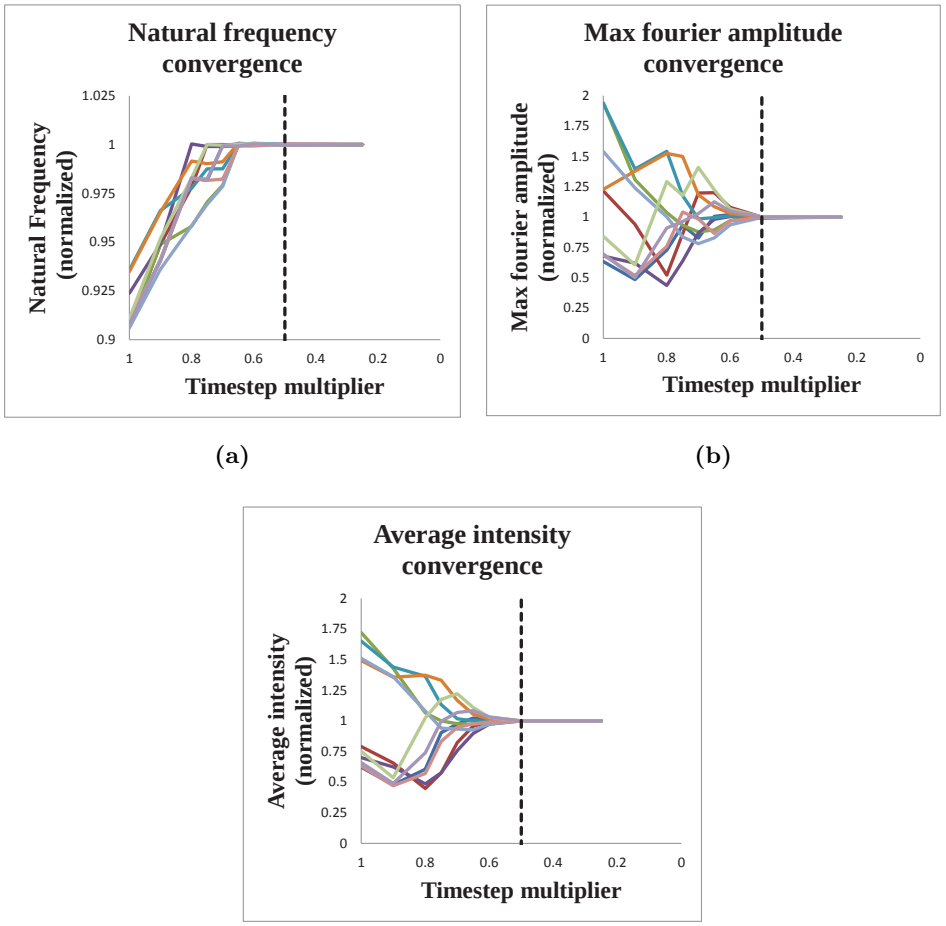

Figure 3.8: Convergence of dynamic parameters with integration timestep: (a) Natural frequency, (b) maximum Fourier amplitude, and (c) average intensity.

3.2 Dynamics of a Bonded Particle Model of a Cantilever Beam

This section will address the dynamics of a BPM model of a cantilever beam. An evaluation of the flexual behavior of a BPM assembly with parallel bonds, selection of damping parameters, and model verification through comparison with analytical and experimental results will be discussed

3.2.1 Flexure in the Bonded Particle Model

The flexural behavior of a BPM assembly with parallel bonds will be discussed. Flexural behavior is an important part of dynamic simulations, particularly when steep rock-slopes with columnar joints will be investigated, however, the behavior of a BPM assembly in flexure is not addressed in the literature. A prediction of flexural behavior in BPM using a simple analogy was successfully developed and will be presented in the following sections.

The Parallel-Bond Model

In Discrete Element Models (DEM), a parallel bond acts as a spring between two particles with a finite strength and stiffness. As the name indicates, it acts in parallel with the spring representing the stiffness of the contact between the two particles [35]. There are several differences between the parallel bond spring and the contact spring, but if we look at a simple 1-D case, one difference is particularly significant: The parallel bond spring is active in both tension and compression, while the contact spring is only active in compression. Figure 3.9 shows simple 1-D spring models for a contact with a parallel bond. When loaded in compression, the system resists the load with a compressive stiffness, K_C. When loaded in tension, the system resists the load with a tensile stiffness, K_T. This introduces an inherent *double elasticity* into the material, meaning that the material has a modulus in tension, E_t, and a modulus in compression, E_c, that are unequal. Double elasticity is common in cemented granular materials and the elasticity ratio ($R_E = E_c/E_t$) in rock can range from 1 to 10 [53].

Based on the ratio, r_k of contact stiffness to parallel bond stiffness, the system can be described with Equations 3.2 through 3.4.

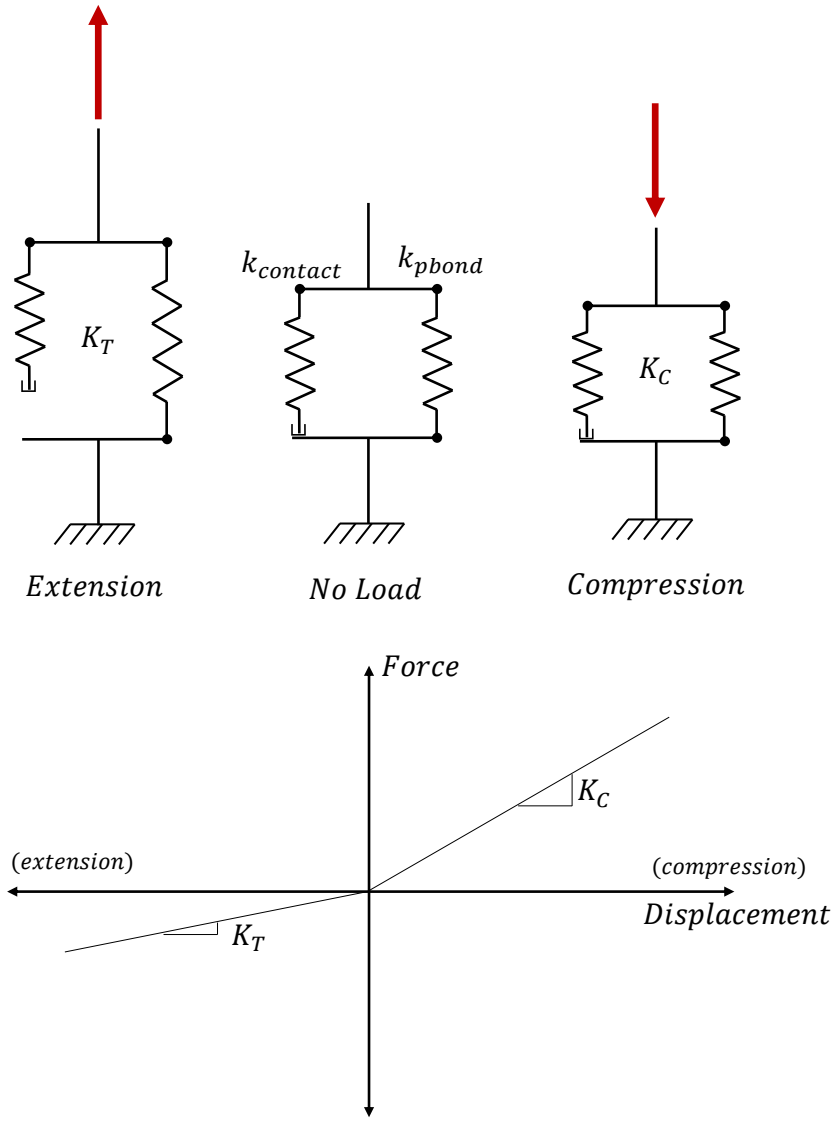

Figure 3.9: A 1-D parallel bond model. When the system is extended from its neutral position, the contact spring is inactive, and the stiffness is equal to the stiffness of the bond ($K_T = k_{pbond}$). In comrpression both contact and bond springs are active ($K_C = k_{contact} + k_{pbond}$).

$$k_{contact} = r_k k_{pbond} \tag{3.2}$$

$$K_C = k_{contact} + k_{pbond} \tag{3.3}$$

$$K_T = k_{pbond} \tag{3.4}$$

A Simple Beam System

In this section, a simple beam system is used as an analogy to the cantilever beam shown in Figure 3.15b. Note that inertial terms are not considered in this analysis as the analogy is not intended to predict dynamic behavior, rather, it is intended to provide a link between the elastic flexural behavior of the beam and the BPM microproperties.

When parallel bonds are used in DEM to model a system subjected to flexural loads, both K_C and K_T will resist loading in the system. A simplified DEM system with two parallel bonded contacts, 1 and 2, is shown in Figure 3.10 to illustrate how the double elastic nature of the material will affect its behavior in flexure. The system is shown with no applied load (on the left) and with an applied moment (on the right). Two square, rigid blocks are connected by a pair of parallel bonded contacts. The lower block is fixed and a point, O, is at the centroid of the upper block. The two contacts are evenly spaced at a distance $w/4$ from the centerline, where w is the width of the beam.

When a counterclockwise moment is applied to the system at point O, the rotation of the upper block is resisted by the contacts–contact 1 in compression and contact 2 in tension. Since the contacts have different stiffnesses, contact 1 deforms less than contact 2 and the upper block rotates off-center. Point B shows the position of the pivot point where the base of the upper block does not change position.

B marks the point in the beam that divides between zones of tension and compression. This is, by definition, the 'neutral axis' of the flexed system. In a mono-elastic beam, where stiffness is uniform, the neutral axis will always stay on the centerline of the beam. Unlike a

mono-elastic beam, a double elastic beam will have a flexual modulus, E_{flex}, that is between its tensile and compressive moduli.

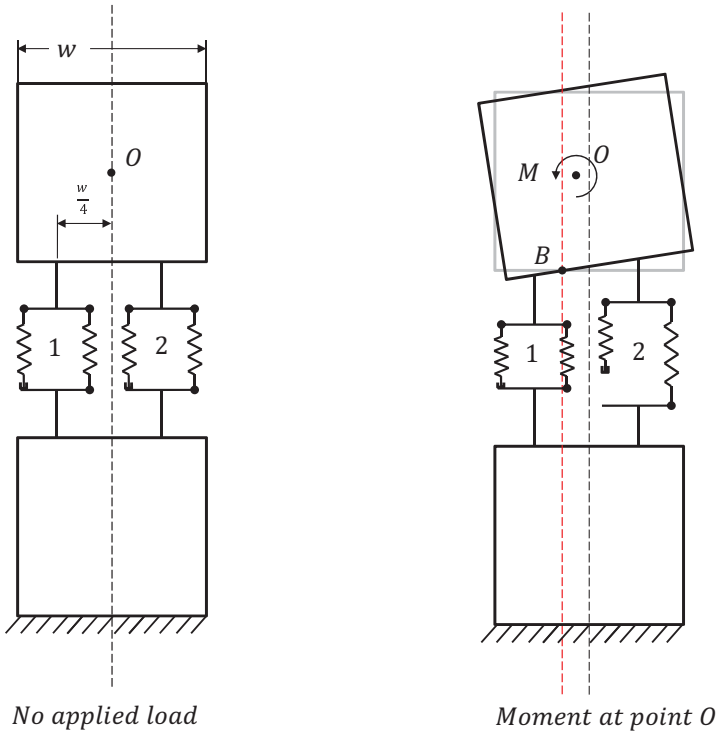

Figure 3.10: A simple beam system with two parallel bonds

Equilibrium

To solve this system, its load-deformation behavior must be fully described. The information for defining the system's equilibrium is shown in Figure 3.11. Summation of the moments and forces on the upper block yields Equations 3.5 through 3.7.

$$\sum M_o = 0 = M + F_1(-d_1) - F_2 d_2 \tag{3.5}$$

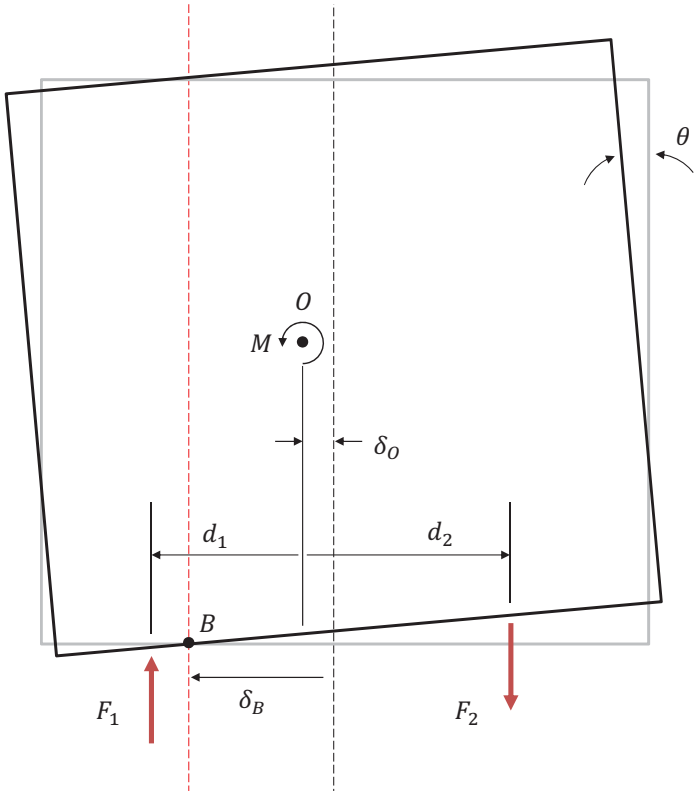

Figure 3.11: Free body diagram for equilibrium equations

$$\sum F_x = 0 \tag{3.6}$$

$$\sum F_y = 0 = F_1 - F_2 \tag{3.7}$$

Kinematics

The kinematics (motion) of the upper block can be described by Equations 3.8 through 3.12 and Figure 3.12.

$$\Delta y = y_2 - y_1 \tag{3.8}$$

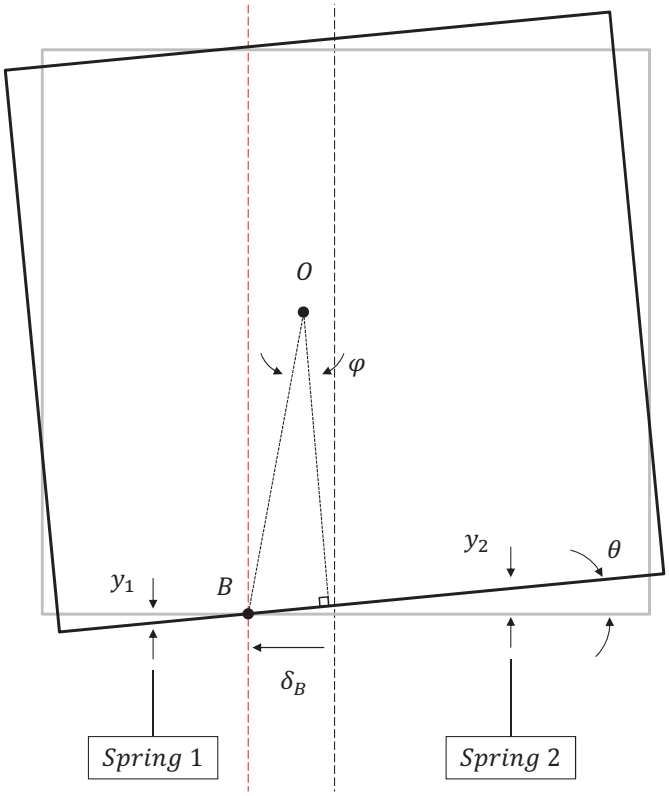

Figure 3.12: Kinematic behavior for the parallel bond beam

$$d_1 = \frac{w}{4} - \delta_O \tag{3.9}$$

$$d_2 = \frac{w}{4} + \delta_O \tag{3.10}$$

$$\delta_B = \frac{w}{4}\left(1 - \frac{2y_1}{y_2 - y_1}\right) = \frac{\frac{w}{4} r_k}{2 + r_k} \tag{3.11}$$

$$\delta_O = \frac{w}{2} \sin\theta \left(1 + \tan^{-1}\phi \tan^{-1}\theta\right) \tag{3.12}$$

Constitutive Behavior

The constitutive (force-displacement) behavior of the upper block is described by Equations 3.13 and 3.14.

$$F_1 = y_1 K_C \tag{3.13}$$

$$F_2 = y_2 K_T \tag{3.14}$$

Solution

Combining the equations for equilibrium, kinematic and constitutive behavior provides a solution for the behavior of the beam system under moment loading at point O (Equation 3.15).

$$M = -k_{pbond}(1 + r_k) y_1 \frac{w}{2} \tag{3.15}$$

Effective Flexural Stiffness

As shown in Figure 3.10, a beam with different stiffness in tension and compression, like one modeled with a parallel bonded DEM, will have an off-centered neutral axis. Figure 3.13 shows mono-elastic (having the same stiffness in tension and compression) beams that could be expected to behave similarly to the DEM beam. A mono-elastic beam with the same width as the original DEM beam would have a stiffness E_{Flex}, which is the effective flexural stiffness of a beam with two stiffnesses, E_C and E_T.

E_{Flex} can be related to E_t and E_C as follows:

$$E_{Flex} = E_T w'_T = E_C w'_C \tag{3.16}$$

Since it is the microproperties ($k_{contact}$ and k_{pbond}) that are specified in DEM, it is useful to define E_{Flex} in terms of the ratio between the microstiffnesses, r_k, and the compressive stiffness, E_C, which is what is typically measured in a laboratory.

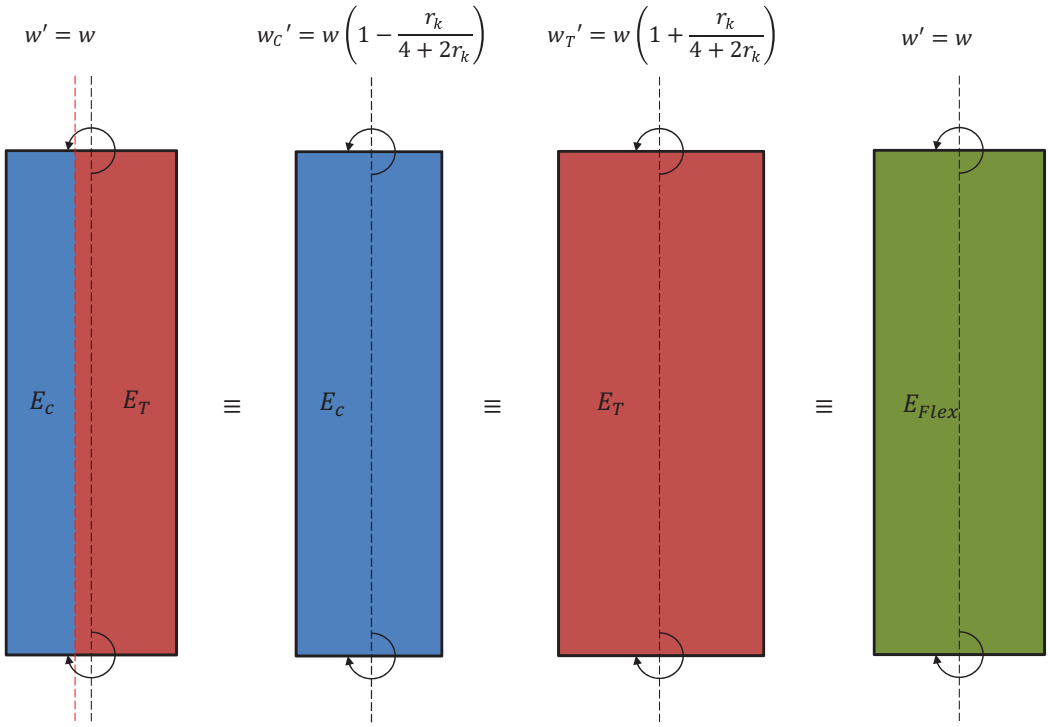

Figure 3.13: Effective flexural stiffness for traditional beams

$$E_{Flex} = \left(1 + \frac{r_k}{4 + 2r_k}\right) E_C \tag{3.17}$$

A real discrete element model is made up of many bonded contacts, and each contact has its own orientation. Contacts also have a set of shear springs, unlike the simple 1-D models shown previously. The added complexity of a full DEM creates a slightly different behavior than the one modeled in Figure 3.10. The primary difference is due to the change in orientation of the springs. When all the springs are aligned in the direction of loading (as in the simplified model), there is no Poisson effect (lateral strain due to an axial load). In a DEM simulation, the Poisson effect is observed, and the Poisson forces are resisted by the tensile strength and stiffness of the bonds. a that the global compressive modulus E_C

is dependent on k_{pbond} and is therefore also a function of r_k.

When the data from the DEM simulations are normalized by their global compressive moduli as measured in a non-destructive UCS simulation, the agreement with equation 3.17 is very good (see Figure 3.14). This relationship can guide the selection of microparameters for a discrete element model that will be subjected to tensile and compressive loading.

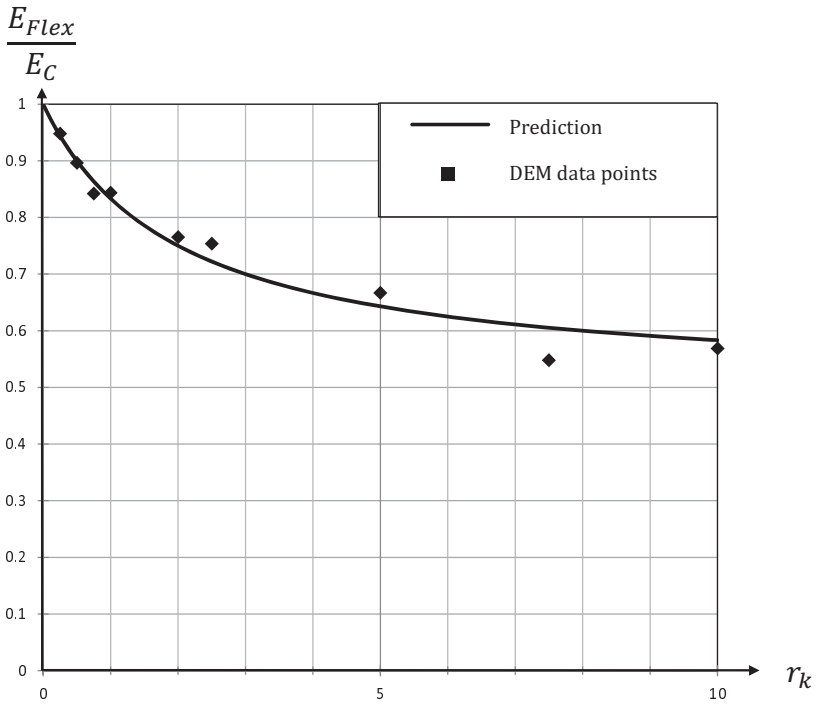

Figure 3.14: Normalized effective flexural modulus vs. contact to parallel bond stiffness ratio

3.2.2 Damping the Discrete Element Model

The following sections will present an overview of viscous and local damping in the Bonded Particle Model.

Viscous Damping

Viscous damping in PFC is implemented with viscous dashpots that act in parallel with existing contacts and bonds [54]. The dashpot introduces a viscous damping force, F_v^d, at the contact in proportion to the relative velocity between the particles and opposes their relative motion:

$$F_v^d = \xi_v c^{crit} |V| \tag{3.18}$$

The viscous damping ratio, ξ_v, is the ratio between the damping applied by PFC2D and the critical damping constant of the interparticle contact. The critical damping constant, c^{crit}, is defined as follows:

$$c^{crit} = 2m\omega_n = 2\sqrt{mk} \tag{3.19}$$

where m is the effective mass of the two particles at the contact, ω_n is the natural frequency of the particle-contact system in radians per second, and k is the contact stiffness. Effective mass is given by

$$m = \frac{m_1 m_2}{m_1 + m_2} \tag{3.20}$$

where m_1 and m_1 are the respective masses of the two particles at the contact. The effect of viscous damping, therefore, varies linearly with relative velocity and is frequency dependent.

The natural frequency of particle-contact systems in the model will be orders of magnitude higher than the natural frequency of the system itself, so the effect of the viscous dashpot on the global response of the model may be minimal.

Local Damping

Local damping is achieved by adding a local damping force, F_l^d, into the equation of motion for each particle [54]. The modified equations of motion have the form:

$$F + F_l^d = MA \tag{3.21}$$

where F, M, and A are the unbalanced force, mass and acceleration of the particle, respectively. The magnitude of F_l^d is determined by :

$$F_l^d = -\alpha|F|sign(V) \tag{3.22}$$

where α is the local damping constant and V is the velocity of the particle. For small levels of damping, α can be related to a local damping ratio, ξ_l, by $\xi_l = \alpha/\pi$. The inclusion of the damping force into the equation of motion effectively changes the apparent mass of the particle. There is no physical analogue to the local damping mechanism; rather it is a purely numerical technique to suck energy out of the system and allow the model to reach equilibrium more quickly. Unlike viscous damping, local damping is independent of frequency and opposes acceleration rather than velocity. Another important distinction between local and viscous damping is that local damping opposes the motion of each particle with respect to a global frame of reference rather than the relative motion between particles.

3.2.3 Simulations of a Study on Damping in BPM

As mentioned in Section 2.4, there is a significant gap in the literature regarding the role of damping in DEM modeling. In order to determine how viscous and local damping directly affect the model's behavior, those variables were isolated and tested on beams (as described in section 3.1.1) and at the particle level on a single pair of bonded particles. The microparameters in the two-particle system are identical to those in the beam model except that rather than a distribution of particle sizes, the two particles in the single bond system have radii equal to the average particle radius in the beam. Both models are shown in Figure 3.15.

Damping Study on the Two-Particle Model

The particle-scale damping behavior in PFC was tested in 3 degrees of freedom: relative displacements in normal, shear and rotational directions. An initial static load was applied to the upper particle while the lower particle was held fixed. The upper particle was held fixed in all degrees except the one being tested. The initial load was released, and the

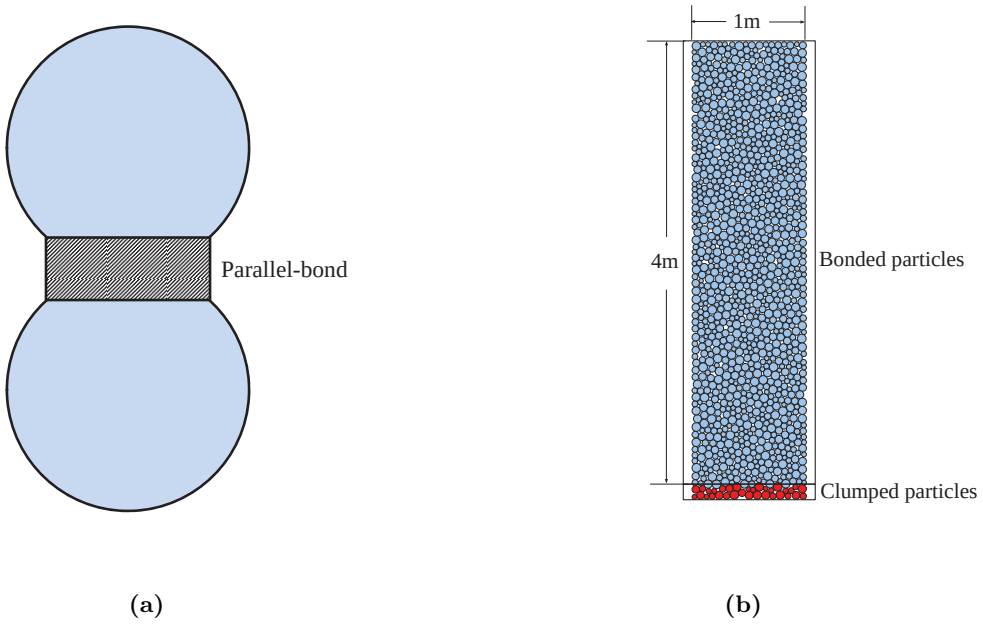

Figure 3.15: Damping study models: (a) A two-particle system with a parallel bond and (b) a BPM cantilever beam model.

system was allowed to oscillate in free vibration. The logarithmic decay damping (ξ), natural frequency (f_n), and maximum Fourier amplitude ($c_{n,max}$) were all used to judge the effects of damping.

The viscous damping ratio was varied from 0 to 1.0 and the local damping ratio was varied from 0.015 to 0.22 (ratios are reported in decimals, not percents). The default local damping ratio for fully static simulations is 0.22, so the dynamic test was not extended beyond that point.

Damping Study on the Beam Model

The beam model was tested with four dynamic motions: one frequency sweep with a peak acceleration of 0.2 g and three impulse motions with peak accelerations of about 0.01, 0.02, and 0.1 g. The logarithmic decay damping (ξ), natural frequency (f_n), and maximum Fourier amplitude ($c_{n,max}$) were all used to judge the effects of damping.

The viscous damping ratio was varied from 0 to 1 and the local damping ratio was varied from 0.015 to 0.07. The range of local damping ratios is smaller for the beams because the behavior at larger values becomes increasingly unrealistic and hard to interpret.

3.2.4 Results of the Damping Study

Viscous Damping Effects on the Two-Particle System

Figure 3.16 presents the effects of viscous damping on the two-particle system. Only the normal displacement shows any damping at all because the shear and rotational displacements do not directly load the contact; they only load the parallel-bond. As mentioned above, the dashpots act in parallel to the contact, not the bond. The increase in the measured normal damping ratio is roughly linear with increased viscous damping ratio, but shows lower measured values than input values. This is also due to the fact that the dashpots only act when there is a non-zero force at the contact. As the particle oscillates, the system goes back and forth between tension and compression. The contact force is only non-zero when the system is in compression, so the motion in tension is completely undamped.

Similar to the measured damping ratio, the natural frequency of the two-particle system is only affected by the viscous damping ratio in with respect to normal displacement. The differences in initial natural frequency in normal and shear displacement oscillations for these simulations are expected because the normal stiffness of the bond is higher than the shear stiffness. The rotational frequency is slightly lower than the normal frequency because it does not load the contact in compression. Compressive loading in the normal direction provides some additional stiffness due to the particle stiffness. The viscous damper has little effect on natural frequency until it reaches high damping values ($\xi_v = 0.8$). This decrease in rotational frequency starting at $\xi_v = 0.8$ is not entirely expected. The rotational motion should not induce any viscous force and normal and shear degrees of freedom were restricted during the rotational tests. Still, there is some slight normal and shear displacement locally at the contact, and only the translational normal and shear degrees of freedom were restricted, not local normal and shear displacements at the particle edges (which would also restrict rotation).

Maximum Fourier amplitude decreases exponentially with increased viscous damping for movement in the normal direction. Again, the slight effect of viscous damping on rotation above $\xi_v = 0.8$ is observed for maximum Fourier amplitude

Local Damping Effects on the Two-Particle System

Figure 3.17) presents the effects of local damping on the two-particle system. Local damping, which acts at on the particle mass to resist its movement relative to the global reference frame, affects all degrees of freedom. The measured damping ratio increases roughly linearly with increased local damping. A fair amount of scatter in the trend related to the timestep of the program output used to analyze the results. For comparison, a dashed line representing the theoretical one to one relationship between local and measured damping is shown on Figure 3.17a. The measured damping ratios generally fall on, or slightly above this line. Increased local damping has a slight decreasing effect on the natural frequency of the system. The maximum Fourier amplitude of the system decreases exponentially with increasing local damping ratio.

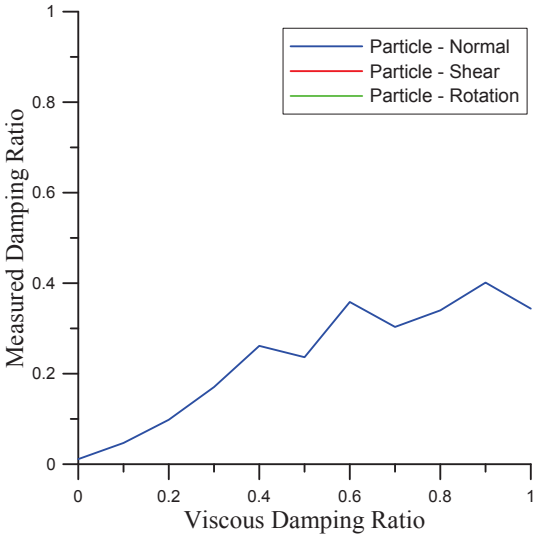

(a) Measured damping ratio in the two-particle system with change in PFC viscous damping ratio

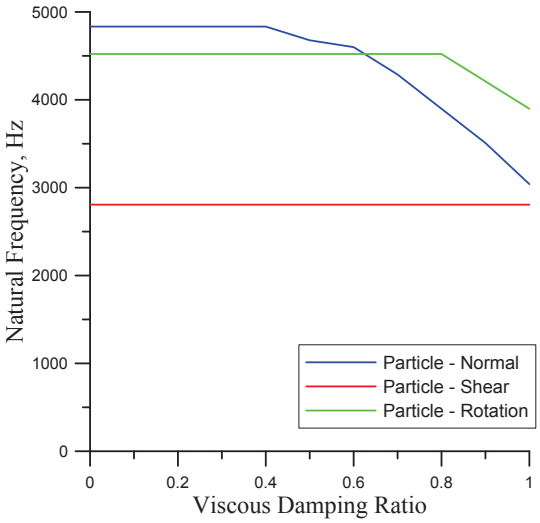

(b) Natural frequency of the two particle system with change in PFC viscous damping ratio

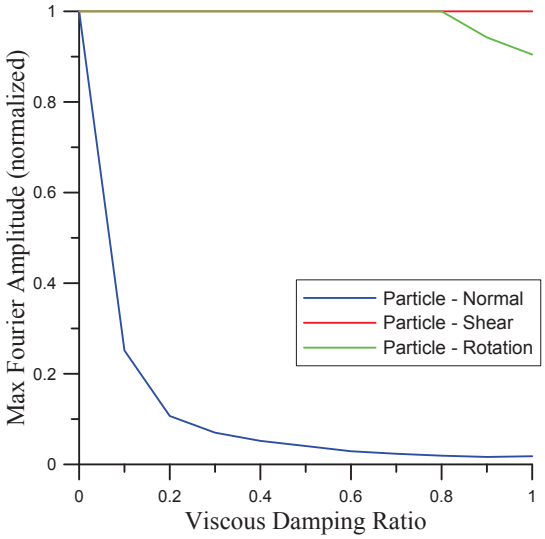

(c) Normalized maximum Fourier amplitude in the two-particle system with change in PFC viscous damping ratio

Figure 3.16: Viscous damping effects at on the two-particle system for normal, shear, and rotational degrees of freedom. Viscous damping, which acts at the contacts between particles only has a significant effect on the dynamics of the normal degree of freedom.

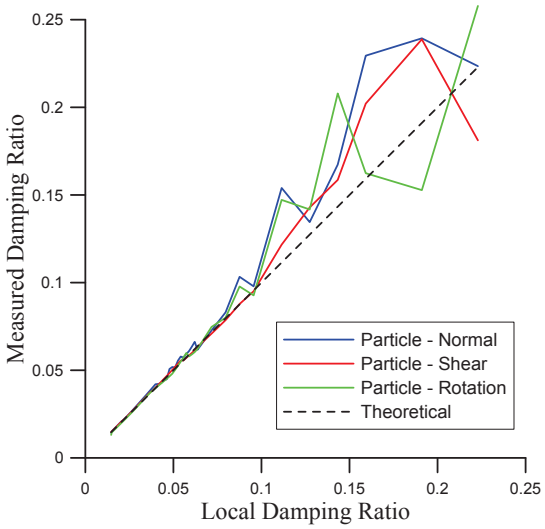

(a) Measured damping ratio in the two-particle system with change in PFC local damping ratio

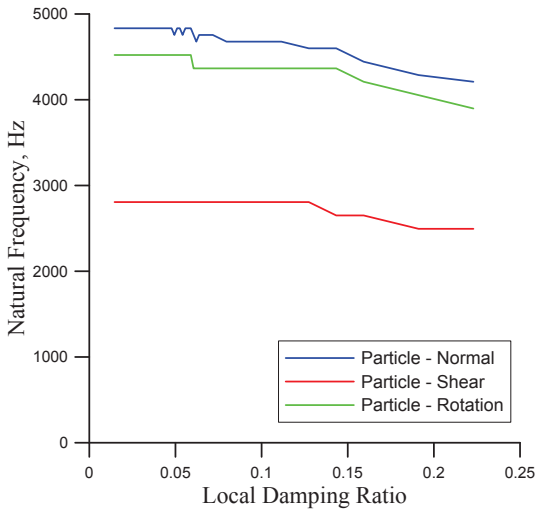

(b) Natural frequency of the two particle system with change in PFC local damping ratio

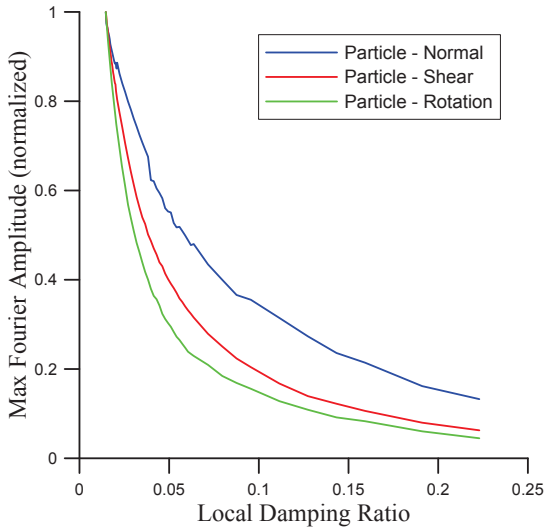

(c) Normalized maximum Fourier amplitude in the two-particle system with change in PFC local damping ratio

Figure 3.17: Local damping effects at on the two-particle system for normal, shear, and rotational degrees of freedom. Local damping, which acts at on the particle mass to resist its movement relative to the global reference frame, affects all degrees of freedom.

Viscous Damping Effects on the Cantilever Beam Model

Figure 3.18 presents the effects of viscous damping on the cantilever beam system The measured logarithmic decay damping ratio appears to decrease slightly with increased viscous damping. The change is very small, as expected, because the natural frequency of the beam is about $1/400^{th}$ of the target frequency of the dashpots. However, the trend is in the opposite direction of what is expected –an increase in applied damping should not result in a decrease in measured damping.

The natural frequency measurement from the frequency sweep responds slightly to the viscous damping ratio. The natural frequency measured from the pulse input simulations showed no change with change in viscous damping The frequency sweep simulations also have a slightly higher average natural frequency than the pulses. This is possibly explained by the difference in frequency content in the input motions.

The max Fourier amplitude increases slightly with increased damping. Similar to the effect on measured dampoing ration, this result is counterintuitive and indicates that viscous damping is affecting the model in unexpected and unexplained ways. It is interesting, though, that these two unexplained behaviors are measured in both the time domain (damping) and the frequency domain (maximum Fourier amplitude) and are consistent with each other.

Local Damping Effects on the Cantilever Beam Model

Figure 3.19a presents the effects of viscous dampoing on the cantilever beam system. The measured damping ratio increases with increased local damping ratio for the pulse simulations. An interesting feature of these results is that the damping effect increases much more at lower amplitude impulses. In all cases, and at all levels of damping, the measured damping falls above the theoretical one to one relationship between local and measured damping as shown in Figure 3.19a.

The natural frequency of the beam does not change with local damping ratio for the pulse simulations, where the natural frequency is assessed due to the behavior of the model in free vibration. The natural frequency measured due to the beam's response to the frequency

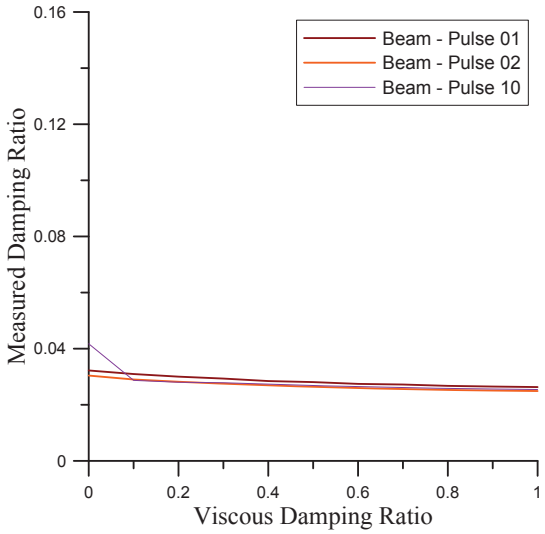

(a) Measured damping ratio in the cantilever beam system with change in viscous damping.

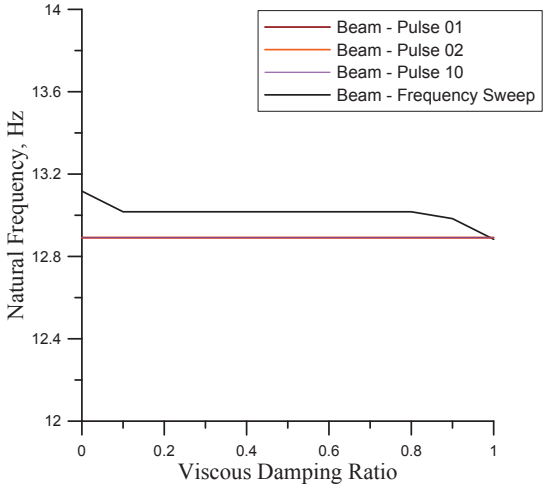

(b) Natural frequency of the cantilever beam system with change in viscous damping.

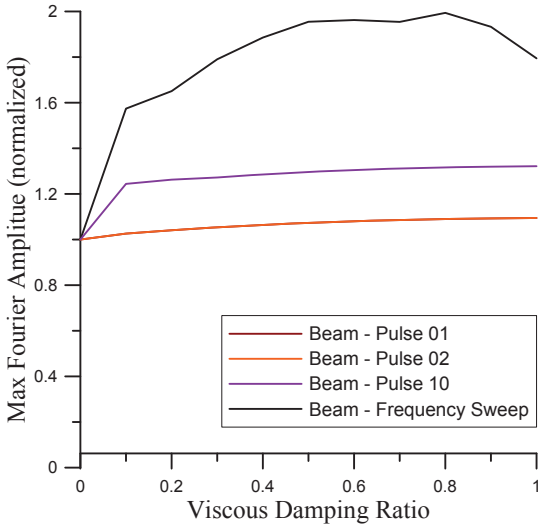

(c) Normalized maximum Fourier amplitude in the cantilever beam system with change in viscous damping.

Figure 3.18: Viscous damping effects on the cantilever beam model for pulse and frequency sweep loading. Viscous damping, which acts at the contacts between particles that make up the beam, has a slight effect on the behavior of the beam and the trends in the results are not well understood. Pulse motions, 'Pulse 01', 'Pulse 02', and 'Pulse 10' have peak accelerations of 0.01, 0.02, and 0.1 g, respectively. The frequency sweep motion has a peak acceleration of 0.2 g.

sweep decreases slightly with increasing local damping for local damping ratios above 0.04.

Maximum Fourier amplitude decreases exponentially with increased local damping. This effect is relatively weaker in the frequency sweep response of the beam. This is understood to be because the frequency sweep simulation involves continuous loading throughout the simulation, whereas, the pulse motion simulations involve a single event followed by free vibration.

Conclusions (on the Damping Study)

At the particle level, viscous damping as implemented in PFC2D has some undesirable features, namely that it only resists motion in the normal degree of freedom, and only when the contact between the particles are in compression. For simulations that involve dynamic flexure, contacts and bonds go through cycles of tensile and compressive loading, and the lack of damping while in tension could be a serious problem. At the beam level, viscous damping has some strange effects that remain unexplained. Even if the effects could be explained, the range of the effects is extremely limited by the fact that the contact's natural frequency is so much higher than the system's.

Local damping appears to be a much more promising tool. At the particle level, its effects are very reasonable, and the behavior of the beam model with local damping seem reasonable overall. The frequency independence of local damping is also evident in the similarity between the effects at small and large scales.

Moving forward with this research, local damping will be used as the primary tool used to set the damping response of the model.

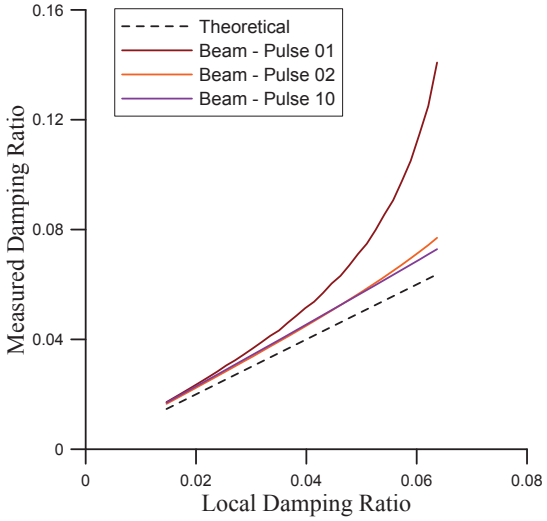

(a) Measured damping ratio in the cantilever beam model with change in local damping ratio

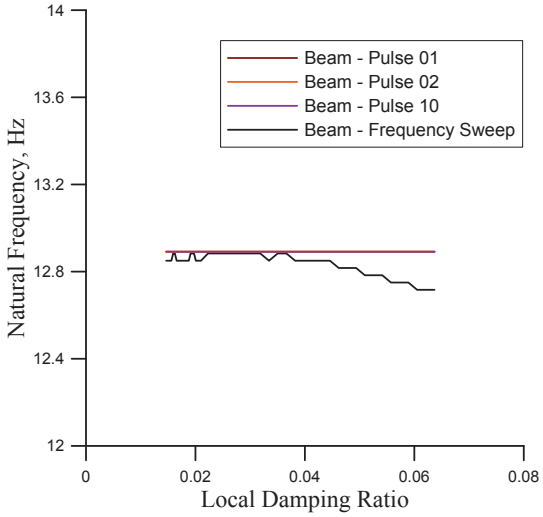

(b) Natural frequency of the cantilever beam model with change in local damping ratio

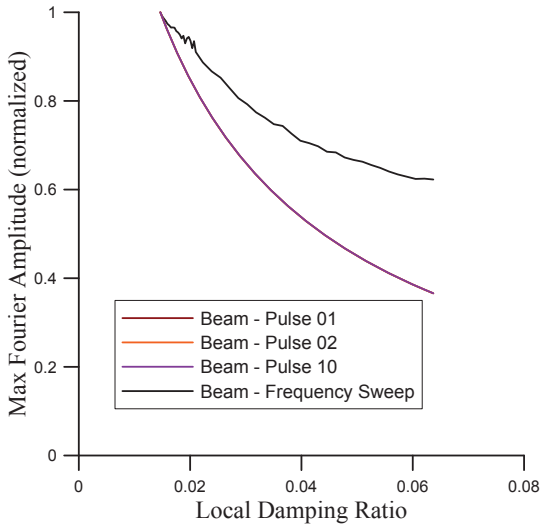

(c) Normalized maximum Fourier amplitude in the cantilever beam model with change in local damping ratio

Figure 3.19: Local damping effects on the cantilever beam system for pulse and frequency sweep loading. Local Damping, which acts on the particle masses and resists motion relative to the global reference frame has a clear and reasonable effect on the behavior of the beam. Pulse motions, 'Pulse 01', 'Pulse 02', and 'Pulse 10' have peak accelerations of 0.01, 0.02, and 0.1 g, respectively. The frequency sweep motion has a peak acceleration of 0.2 g.

3.2.5 Verification of the BPM Dynamic Cantilever Beam Behavior

A graphical comparison of three models of a cantilever beam, (i) a physical model tested in a centrifuge, (ii) an analytical solution for cantilever beam vibration, and (iii) the PFC cantilever beam model, is shown in Figure 3.20. The physical beam model and its testing in a centrifuge is described in Appendix C. The analytical solution for the vibration of a cantilever beam is described in Appendix B. Figures 3.20a through 3.20c show the models' displacement response in the time domain. Figure 3.20d is in the frequency domain.

The shape of the ground motion, including the variation if frequency can be seen in Figure 3.20a. The motion begins at a low frequency and gradually increases in frequency while decreasing in amplitude. Figure 3.20b shows a portion of the low frequency motion. In this figure, the analytical and BPM responses appear to be similar in magnitude and frequency content. However, neither model captures the low-frequency amplification observed in the experimental response. At higher frequencies, however, the analytical solution and the BPM response meet and exceed the experimental response (Figure 3.20c).

The frequency domain responses in Figure 3.20d show that although the predominant frequencies of each model are similar, the level of amplification and the bandwidth of amplification are different. The experimental results have a fairly low amplification over a wide bandwidth while the analytical and BPM results have higher peaks and more narrow bandwidths.

The three models (experimental, analytical, and numerical) show reasonable agreement in the areas examined. This shows that with proper selection of key microparameters (r_k, ξ_v, and ξ_l), a bonded particle model is capable of replicating some aspects of the dynamic behavior of rock-like material. However, both the numerical and analytical simulations are unable to fully capture the damping behavior and the peak acceleration response behavior simultaneously. This may be because the ARM is not a perfectly linear elastic material and that the ability to measure its response is limited.

The BPM and the analytical solution agree more closely with each other than either does with the experimental results. This indicates that the BPM is doing a good job at capturing the fundamental dynamic behavior of the beam insofar as it behaves ideally. The ability

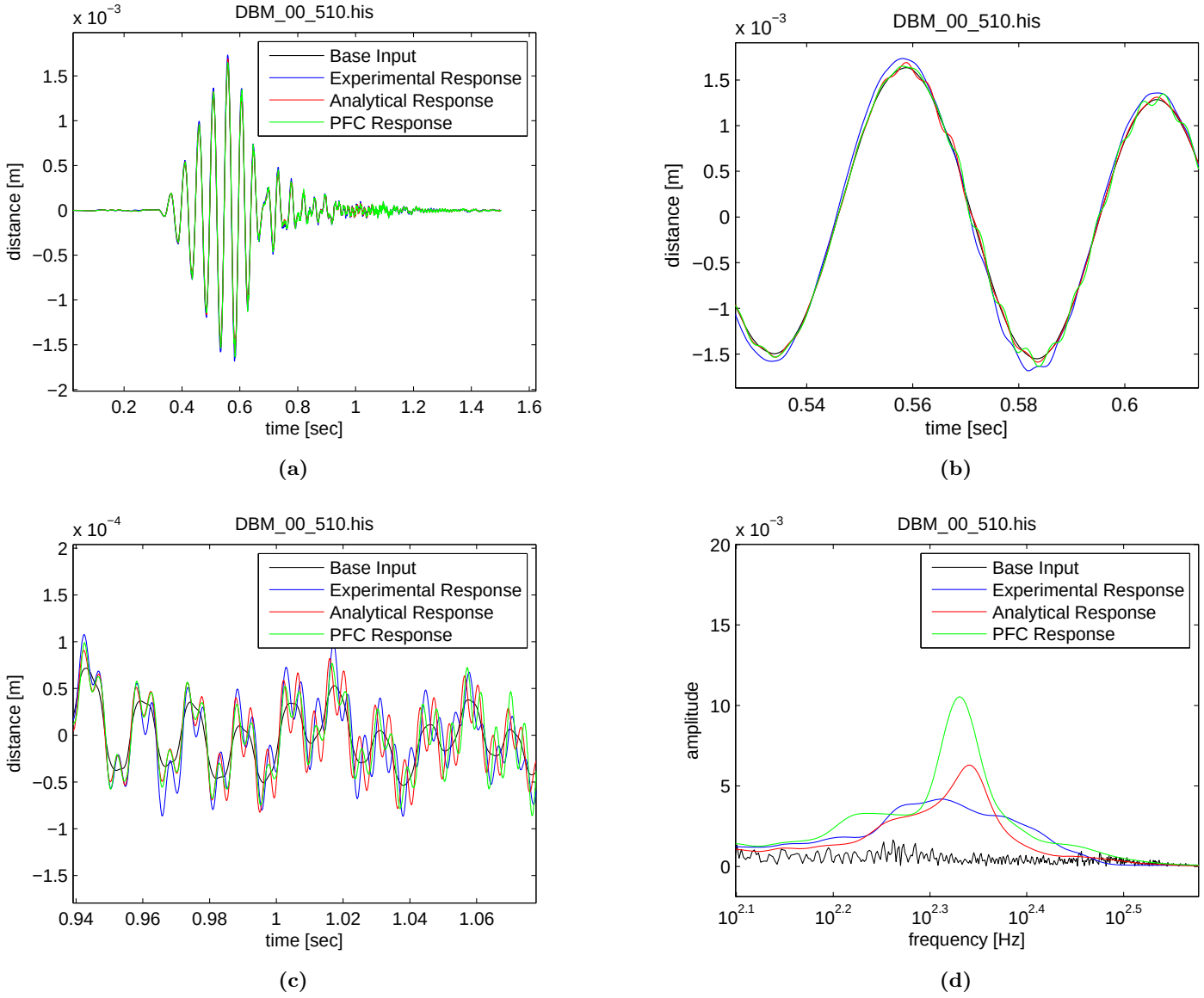

Figure 3.20: Comparision of experimental, analytical, and BPM behavior of the dynamic response of a cantilever beam: (a) The full displacement time-history of a frequency sweep, (b) a zoomed-in view of the a portion of the response between 0.53 and 0.61 seconds, (c) a zoomed-in view of the portion of the response between 0.94 and 1.07 seconds, and (d) the Fourier amplitude around the natural frequency of the beam.

to match the dynamic behavior of the physical beam more closely may require the use of more parameters than are currently available in PFC2D. Additional methods of damping, in particular, should be explored.

At its current level of calibration, the model can provide a dynamic response very similar to the single rock column. Expansion of the model's dynamic capability will involve comparison of the BPM in more general configurations to experimental results on similar models. Future research will involve verification of the calibration with more dynamic tests of this sort and, ultimately, models that experience failure due to dynamic loading.

3.3 Boundary Conditions

Numerical simulations of geologic phenomena are generally truncated in scope to a zone of interest that is much smaller than the tectonic-scale geologic setting that the area of interest exists in. The portion of the setting not explicitly modeled is approximated by the behavior of an artificial boundary. In static simulations, fixed artificial boundaries can be used without much reduction in accuracy. In dynamic simulations, fixed boundaries simulate an interface with an infinitely stiff material that absorbs no wave energy and therefore traps energy in the model by reflecting it back into the model domain. This can be an appropriate approximation in certain cases –for a very soft soil on stiff bedrock, or for modeling a centrifuge experiment, for example. But in geologic settings without a sharp change in stiffness, energy that ought to leave the model domain gets trapped inside it and can have a significant influence on the model behavior.

Artificial Boundary Methods

A number of methods exist for creating artificial boundaries to absorb wave energy from within the model. Engquist and Majda showed that it is possible to absorb waves at a boundary by using a hierarchy of local boundary conditions that approximate a zero reflection wave equation solution [55]. Cundall et al. presented a practical solution to the boundary reflection problem by the superposition of two separate boundary value problems. A constant-velocity and a constant-stress solution are summed incrementally at the boundaries. This requires equations of motion to be evaluated once at every point within

the model and twice at the model boundaries [56]. Generating reflection coefficients as an expression of a linear combination of wave fields approaching the boundary at different timesteps is another method that can produce an absorbing numerical boundary [57]. The Perfectly-Matched Layer concept, introduced by Berenger for the absorption of electromagnetic waves, has been extended to other applications including geologic media [58, 59].

One of the simplest and most popular methods was developed by Lysmer and Kuhlemeyer and presented in *Finite Dynamic Model for Infinite Media* (1969) [60]. They showed that a viscous stress-controlled boundary can be defined by

$$\sigma = \rho V_P \dot{w} \tag{3.23}$$

and

$$\tau = \rho V_S \dot{u} \tag{3.24}$$

where σ and τ are the respective normal and shear stresses at the boundary, ρ is the material density, V_P and V_S are the material p-wave and s-wave speeds, and $\dot{w}$ and $\dot{u}$ are the normal and tangential boundary velocities. According to their numerical simulations, this type of boundary can be 98.5% effective in absorbing p-waves and 95% effective in absorbing s-waves. The absorption is nearly perfect for waves whose angle of incidence is greater than 30 degrees.

Explored Alternatives

Several alternatives were considered for creating boundary controls in the BPM in this study. In addition to the methods described above, simply extending the model domain and increasing the damping and/or decreasing stiffness in the extended material was considered. Initially, the models were flat ground models with periodic lateral boundaries to simulate an infinite width geologic layers. After an initial consideration of several boundary types, three types of models were built for comparison: 1) a rigid-base model, 2) an extended boundary model, and 3) a viscous boundary model. The viscous boundary model was ultimately selected as the best approach for dynamic modeling in PFC.

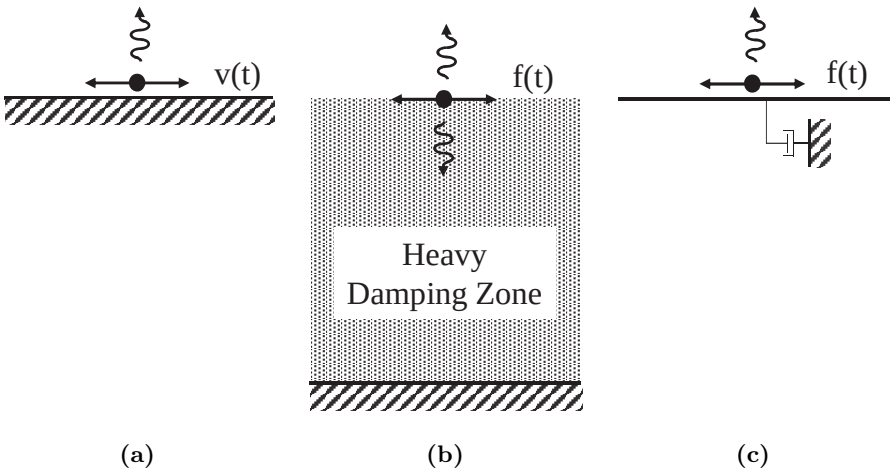

Figure 3.21: Dynamic input and boundary conditions for three types of models: (a) A rigid base model with velocity input, (b) a heavy damping zone model with force input at the center of the model, and (c) a viscous boundary model with force input –dampers on the base absorb the energy from the force input and reflected waves from the surface.

The rigid base model, shown in Figure 3.21a, has a base of velocity-controlled particles that sends a velocity time history up into the model. Because the velocity is prescribed, the base is not allowed to respond with displacement to waves reflected back from the free surface, so it behaves as a rigid base and reflects all downward wave energy back into the model (see Figure 3.22).

The extended boundary model was built several times with a variety of stiffness and damping profiles to create a 'heavy damping zone'. The purpose of the 'heavy damping zone' was to receive downward propagating waves that reflected from the surface or were part of the dynamic input from the time history input location. Unlike the rigid base model, the ground motion in this case is prescribed as a force time history. Equation 3.24 shows the

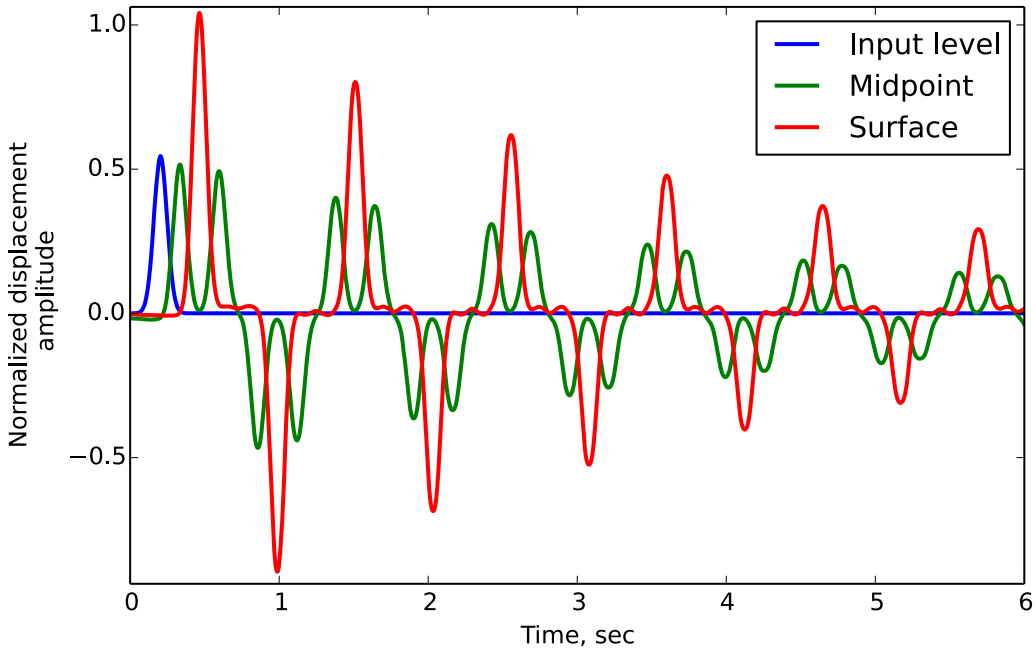

Figure 3.22: Pulse transmission and reflection in the rigid boundary model from a single pulse. No energy is absorbed at the boundary so the pulse bounces back and forth between the base and the surface. Damping only occurs as a result of material damping as the wave travels.

relationship between tangential particle velocity and shear stress with respect to material density and shear wave velocity. The corresponding force is simply the shear stress times the tributary area of the individual particle being controlled. Because half of the input energy will travel up and half will travel down, the stress amplitude must be increased by a factor of two from Equation 3.24 resulting in the following equation for direct application of force to a particle:

$$f_i(t) = 2\rho V_s t d_i v_i(t) \tag{3.25}$$

where t is the thickness of the model and d_i is the diameter of particle i. Clearly this approach requires a larger model than a user-controlled boundary approach. However, it was explored to determine whether the additional model size required would be more or

less computationally intensive than direct control of the model boundary through repeated execution of user-defined FISH functions. This method was found to be inefficient and did a poor job of absorbing reflected waves (see Figure 3.23).

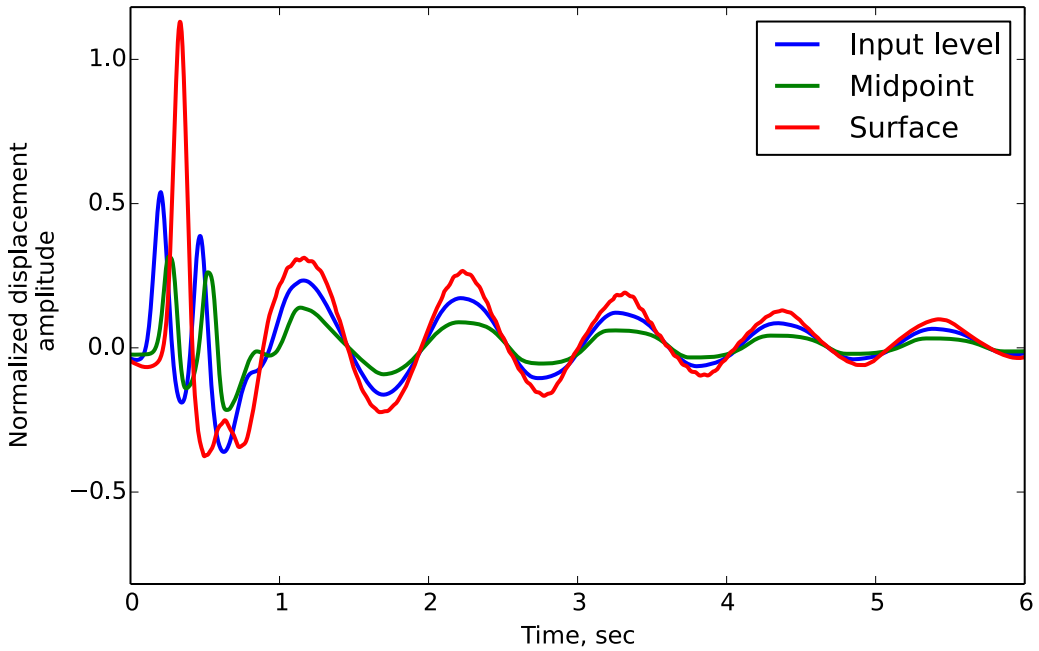

Figure 3.23: Pulse transmission and reflection in the 'Heavy Damping Zone' model. The absorption of the reflected wave is improved over the rigid base model, however the waveform is distorted and still affecting the model after several cycles.

The viscous boundary model (shown in Figure 3.21c) is the method presented by Lysmer and Kuhlemeyer and was ultimately determined to be the best of the explored alternatives. The ground motion is applied as a force time history as described in Equation 3.25, but the downward propagating wave is absorbed by a damping function simulating a viscous damper between each particle and the global reference frame. The damping function:

$$F_{damp} = -c_s v_i \tag{3.26}$$

where c_s is the shear-direction viscous damping coefficient, and v_i is the velocity of particle

i. The viscous damping coefficient is determined by:

$$c_s = 2d_i t \rho V_s \tag{3.27}$$

The damping force, F_{damp}, is calculated for each boundary particle at every calculation cycle. The dashpot coefficients are calculated at the beginning of the simulation and stored in a linked-list memory structure. The list includes all boundary particles and their respective damping coefficients and static equilibrium forces. This method proved to be more computationally efficient than the heavy damping zone model and also performed very well. Mild signal distortions were observed, but the reflected surface wave was successfully absorbed (see Figure 3.24).

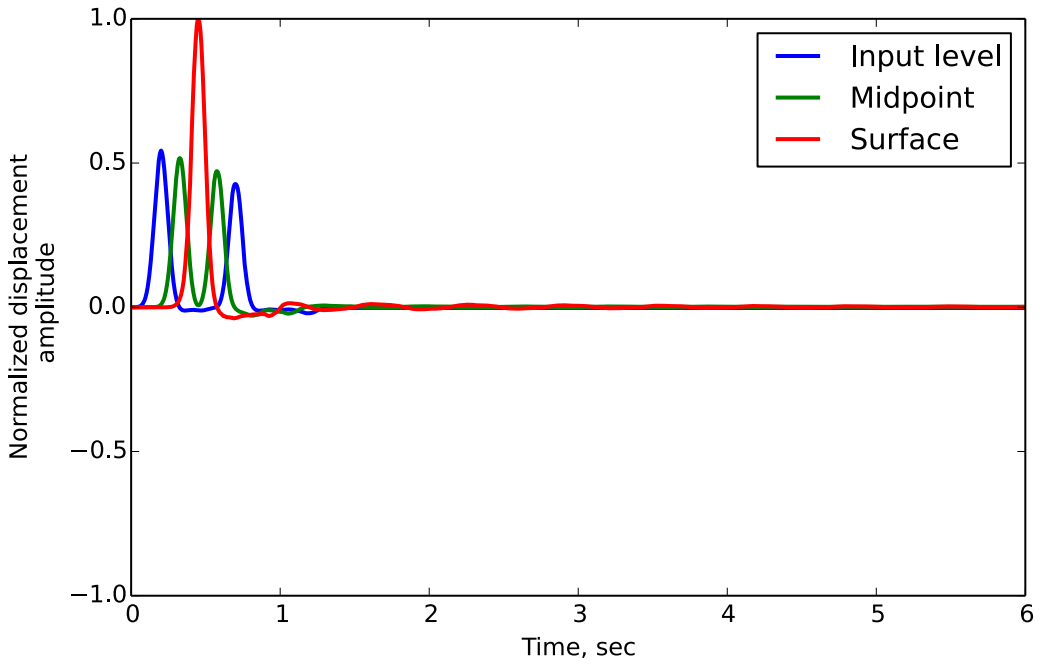

Figure 3.24: Pulse transmission and reflection in the viscous boundary model. The viscous boundary absorbs the pulse reflected back from the surface well. Only mild signal distortion is observed.

Although these initial alternatives were flat-ground models with periodic boundaries, periodic boundaries are only appropriate for modeling specific situations. A flat-ground,

infinite width model is an ideal scenario for periodic boundaries. A flat-ground model with a discrete feature, like a two-sided slope, may be modeled with periodic boundaries, however, the model will repeat itself and simulate several two-sided slopes periodically in space. This may or may not be acceptable depending on the width of the model within the periodic space and the level of interference from the repeated feature. Modeling a one-sided slope is not acceptable because the ground surface is not the same elevation on either side of the model. A visual explanation of periodic boundary behavior in these situations is given in figures 3.25a–3.25b. The final models are built with enforced free-field conditions at the lateral boundaries as show in Figure 3.26, which is taken from the FLAC manual on Dynamic Analysis [61].

3.3.1 The Pseudo-Periodic Boundary

To achieve the boundary conditions as seen in Figure 3.26, the free-field response must be calculated in columns for each side of the model. The free-field response can be most easily calculated with periodic boundary conditions, however, due to a limitation of PFC2D, periodic space must be used on the entire model domain or none of it. The free-field response columns then, must be created without explicitly using the periodic space feature in PFC. This limitation necessitated the development of 'pseudo-periodic' boundaries using clump logic. The development of the boundary conditions presented here has been published in the Proceedings of the 4th Itasca Symposium on Applied Numerical Modeling [62].

In PFC, 'clump' refers to group of particles which are slaved together and behave as a rigid body. Internal contacts between clumped particles are skipped during the calculation cycle. Clumps are typically used to create a bonded-particle model with irregular grain shapes. Cho et al. have shown this to be an effective technique for capturing several rock-like behaviors, e.g. a more accurate post-peak friction angle [36]. It is not necessary, however, that particles in a clump be in contact with each other or even in the same vicinity. The rules that create the clump logic in PFC are very similar to the slave-controller laws for a periodic boundary, so it is possible to use clump logic to create a nearly periodic boundary condition.

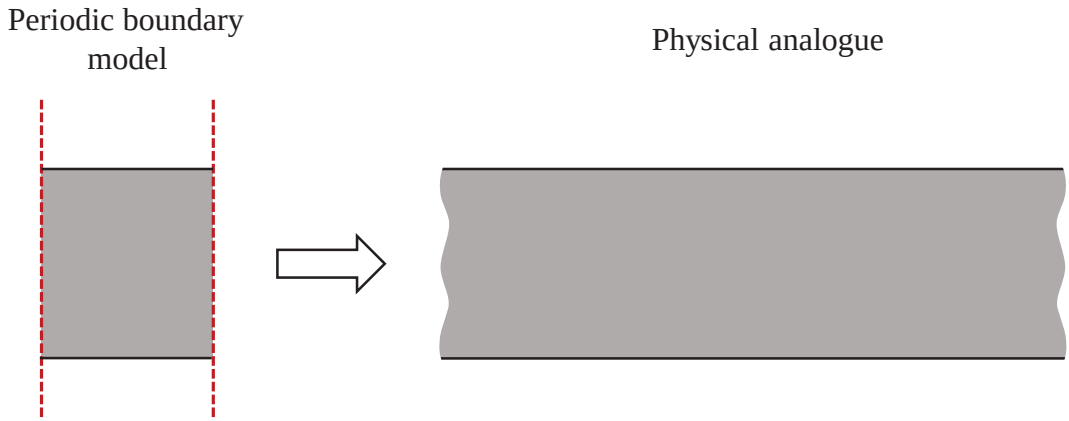

(a) Periodic boundary and its physical analogue for a flat-ground model. A flat-ground model is ideal for infinite width representation with periodic boundaries.

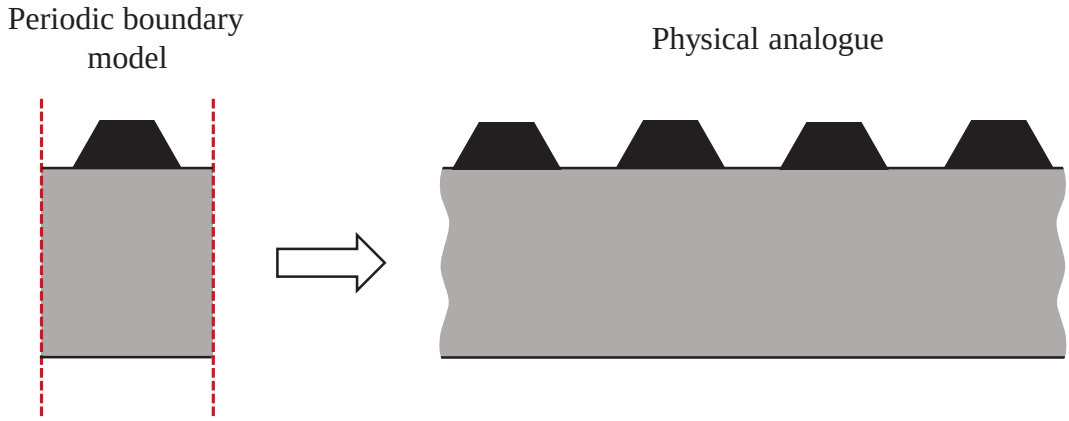

(b) Periodic boundary and its physical analogue for a two-sided slope model. A model with a discrete feature, like a two-sided slope, may be acceptable if the repeated features are sufficiently far apart that they do not interfere with one another.

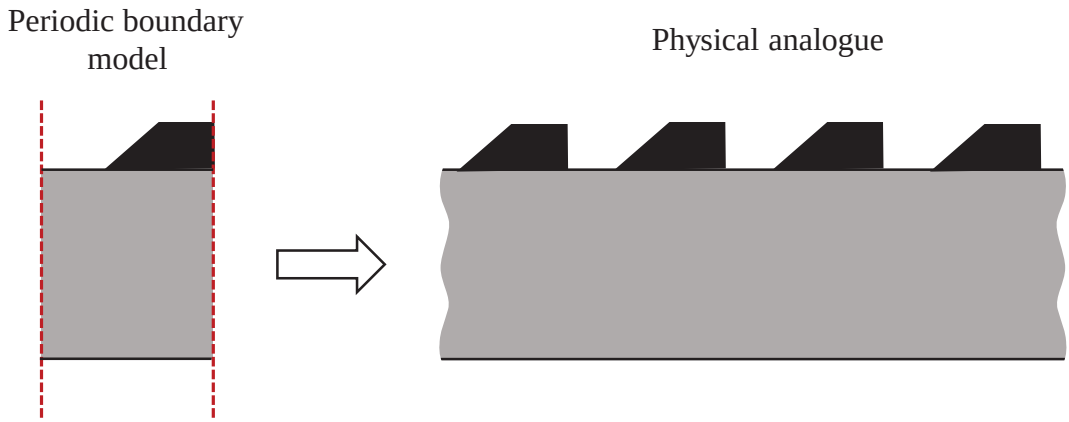

(c) Periodic boundary and its physical analogue for a one-sided slope model. A model with a one-sided slope is cannot be modeled with periodic boundaries. The physical analogue does not match the intended model.

Figure 3.25: Periodic boundary models and their physical analogues for different model geometries.

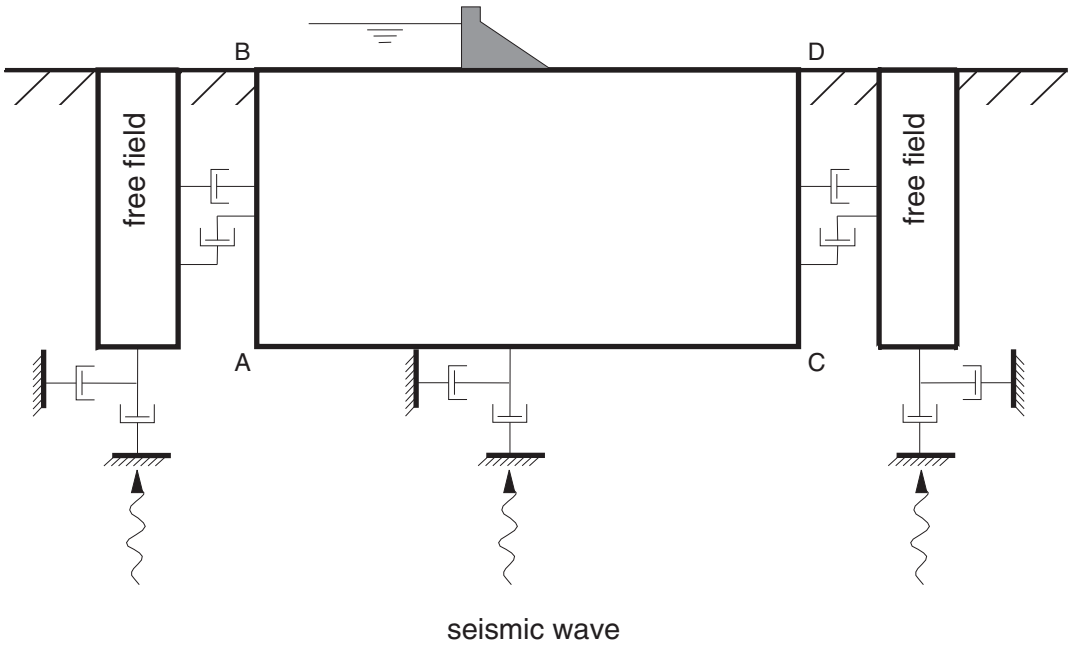

Figure 3.26: Model for seismic analysis of surface structures with free-field lateral boundary conditions and a quiet base from the FLAC manual.

By bounding a bonded particle model with a series of two-particle clumps –one on either side of the model, the forces on each side of the model are directly transmitted to the opposite side. In a periodic model, one of the boundary particles is a controller and its counterpart on the opposite side is a slave. Controllers exchange information with their slaves during calculation cycles to behave as a single particle [63]. In equation 3.28, the controller particle will be assigned the subscript'1' and the slave will be '2'. The slave particle has the same motion as the controller particle in every degree of freedom, so:

$$dx_1 = dx_2 \ , \ dy_1 = dy_2 \ , \ \theta_1 = \theta_2 \tag{3.28}$$

Unlike in a periodic space, the two particles in the clump are required to have the same motion with respect to θ, but not with respect to x and y. However, the distance between the two particles must remain the same and they are not allowed to rotate with respect to

each other, so:

$$\sqrt{(dx_2 - dx_1)^2 + (dy_2 - dy_1)^2} = 0 \ , \ \theta_1 = \theta_2 \ , \ \phi_{12} = 0 \tag{3.29}$$

where ϕ_{12} is the relative rotation of the two particles with respect to each other.

By imposing the additional constraint that $\theta_1 = \theta_2 = 0$, the two-particle clump is not also restricted to $dx_1 = dx_2$ and $dy_1 = dy_2$ thereby creating a 'pseudo-periodic' boundary.

Figure 3.27 shows the pseudo-periodic model with its infinite repetition effect. The two main differences between the pseudo-periodic and true periodic boundaries are (1) the pseudo-periodic boundary particles are completely restricted from rotating, and (2) the pseudo-periodic boundary particles are identical in size. The second difference is imposed to simplify the model generation process. It results in an infinitely repeating model with irregular particle size and packing except for thin columns of two particle pairs spaced at the width of the pseudo-periodic boundary. A comparison between the s-wave and p-wave transmission behavior of the pseudo-periodic and true periodic boundary models showed no difference between the two boundary conditions for flat ground models, so pseudo-periodic boundaries are considered a valid tool for creating free-field response columns.

3.3.2 Particle control in PFC

In PFC, particles may be directly controlled with user-written FISH functions. FISH provides the user with the ability to prescribe a particles velocity or apply a force (or moment). To control more than one particle at a time, groups of particles can be converted into clumps. Using a viscous damping function on a clumped boundary would be an efficient way to absorb plane waves. However, any wave front that was not perfectly plane and met the boundary with a 90-degree angle of incidence would need a boundary capable of differential displacement, which clumps do not allow. It is necessary, then, to control the boundary particles individually.

To control the boundary particle subset of the particle model efficiently, the memory addresses of the boundary particles as well as variables needed in their control are stored in a linked-list data structure. When the model is built, a variable ('Boundary Head') is

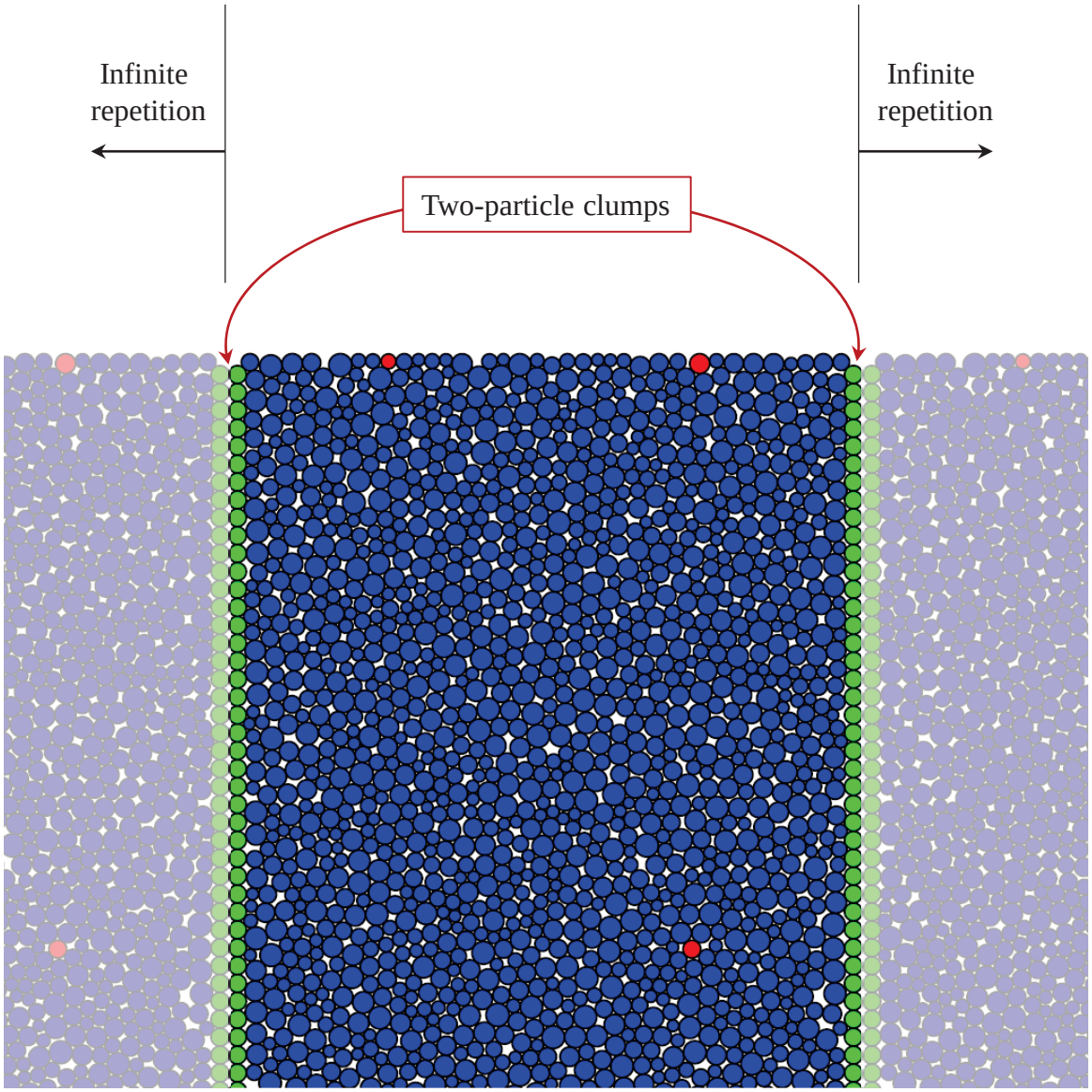

Figure 3.27: Pseudo-periodic boundary conditions with clumps. The model is bounded by two particle clumps which are restricted from rotating. An infinite repetition effect, similar to a true periodic boundary, is created.

created to point to the head of the linked-list, and the list is populated. The boundary control functions, which must be executed on each boundary particle at each timestep, are run within a loop that traverses the boundary linked-list. Figure 3.28 illustrates the

linked-list data structure used to control the boundary.

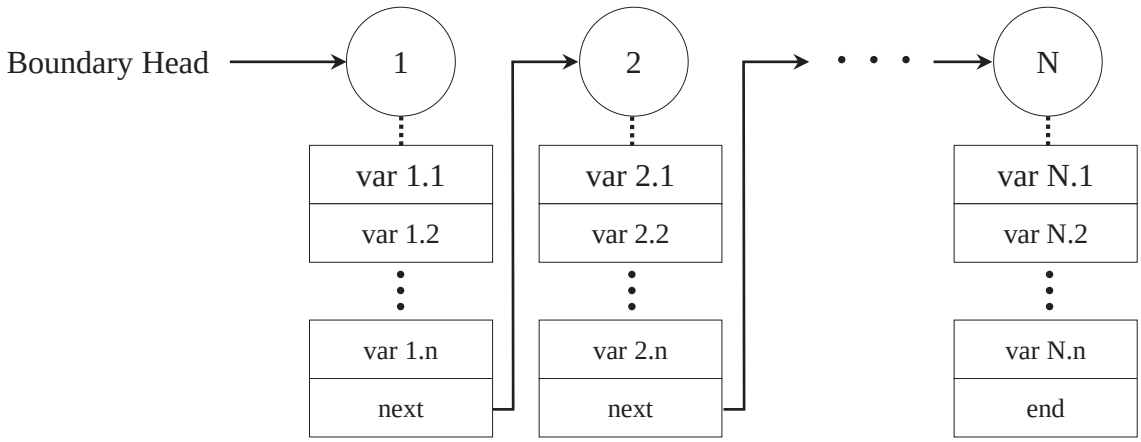

Figure 3.28: Linked-list data structure for N boundary particles. The 'Boundary Head' variable points to the first boundary particle in the list. The memory associated with each particle contains variables used in the user-defined control functions. The last memory slot points to the next particle in the list. When particle N is reached, the list terminates.

To create the viscous boundary control, the wave speed of the BPM must be known. Like all other macroproperties, wave speed is controlled by microproperties in BPM. For the given bond to particle stiffness ratio needed for flexural behavior, and a given shear to normal stiffness ratio, V_s and V_p can be determined as a function of normal particle stiffness. Results of measured s-wave and p-wave speeds are shown in Figure 3.29 with equations for V_s and V_p. Since particle stiffness is directly proportional to modulus, and wave speed is proportional to the square root of modulus, the BPM results are consistent with elastic wave theory in the tested range.

3.3.3 Base boundary control

On the base boundary, viscous dampers were used in the x-direction only. It is possible to include y-direction dampers, but the model tends to drift and rotate due to numerical force imbalances. A purely translational drift would be acceptable because the trend could be easily removed from the data and the gravitation field orientation with respect to the

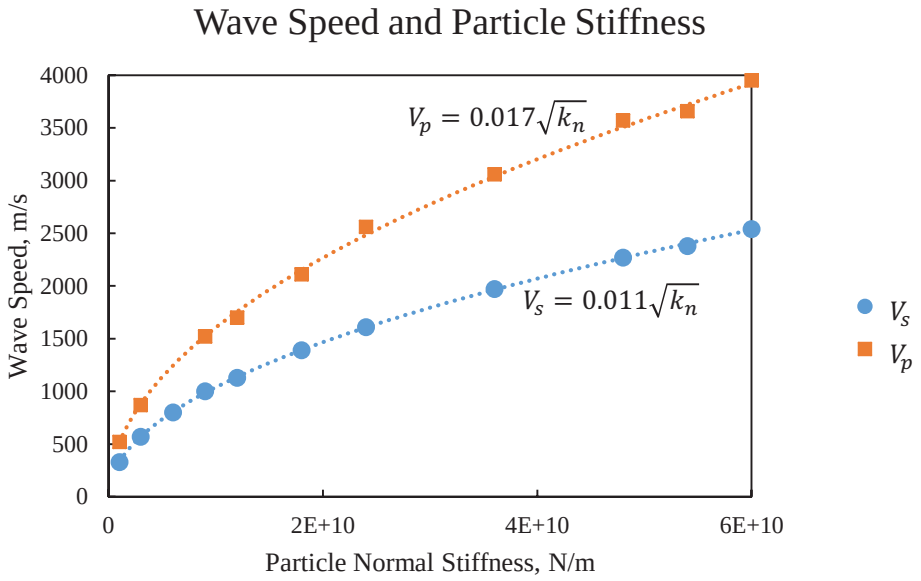

Figure 3.29: Wave speed and particle stiffness functions based on a fit of BPM tests. The functions are used to create the viscous boundary parameters.

model would remain unchanged. Rotational drift, however, is not easy to correct for and also changes the effective gravitational direction in the model, so it is unacceptable. Not allowing displacement in the y-direction avoids this problem. It also means that the model cannot accept vertical ground motion input.

3.3.4 Lateral boundary control

The lateral boundary conditions are different from the base in two respects: 1) both horizontal and vertical motion is allowed and damped, and 2) the dampers resist velocity with respect to the free-field site response rather than the global reference frame.

Vertical motion may be considered in the lateral dashpots because the fixity at the base prevents the model from drifting in the y-direction. It is desirable to be able to absorb the vertical components of reflected waves at the lateral boundary even when plane shear waves are used as input because reflections from the surface (when not perfectly flat) will result in non-plane and non-horizontal wave fronts.

The damping of the lateral boundary particles is more involved than the base because of the link between the main model and the free-field response columns. Each lateral particle has an associated and unique free-field response particle that provides the free-field velocity at its given position in the geologic layer. The damping force is proportional to the difference in velocity between the lateral boundary particle and its free-field reference particle.

$$F_{damp} = -c(v_p - v_{ref}) \tag{3.30}$$

This is similar to connecting the main model to the free-field with a dashpot with a coefficient c, except that the damping force is only applied to the boundary particles on the main model. There is no effect on the free-field response column from anything that happens in the main model.

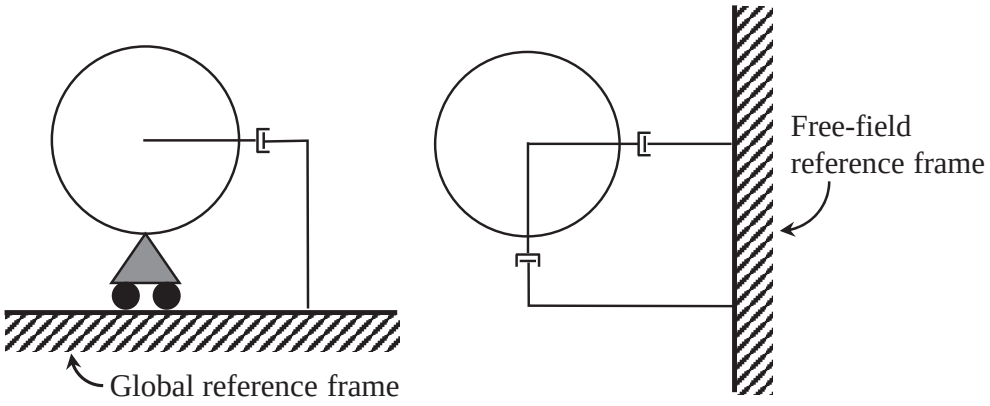

(a) Base particle boundary conditions. **(b)** Lateral particle boundary conditions.

Figure 3.30: Base particle motion is fixed in the vertical direction and attached to the global reference frame by a viscous dashpot (a). Lateral particle motion is damped in vertical an horizontal directions by attachment to the free-field reference frame (b).

One of the advantages of using explicitly modeled free-field boundary conditions (as opposed to periodic boundaries) is the ability to have non-uniform boundary heights, which may be required to model some situations (e.g. a cliff at the edge of a plateau). Figure 3.31 shows how the introduced boundary scheme can be used to create such a geometry by

cutting a slope in the model and through one of the free-field response columns. Caution must be taken when cutting the model by deleting particles. Any user-defined linked-list in the model will be broken if particles in the list are deleted. A list-preserving function of some sort should be used to avoid this.

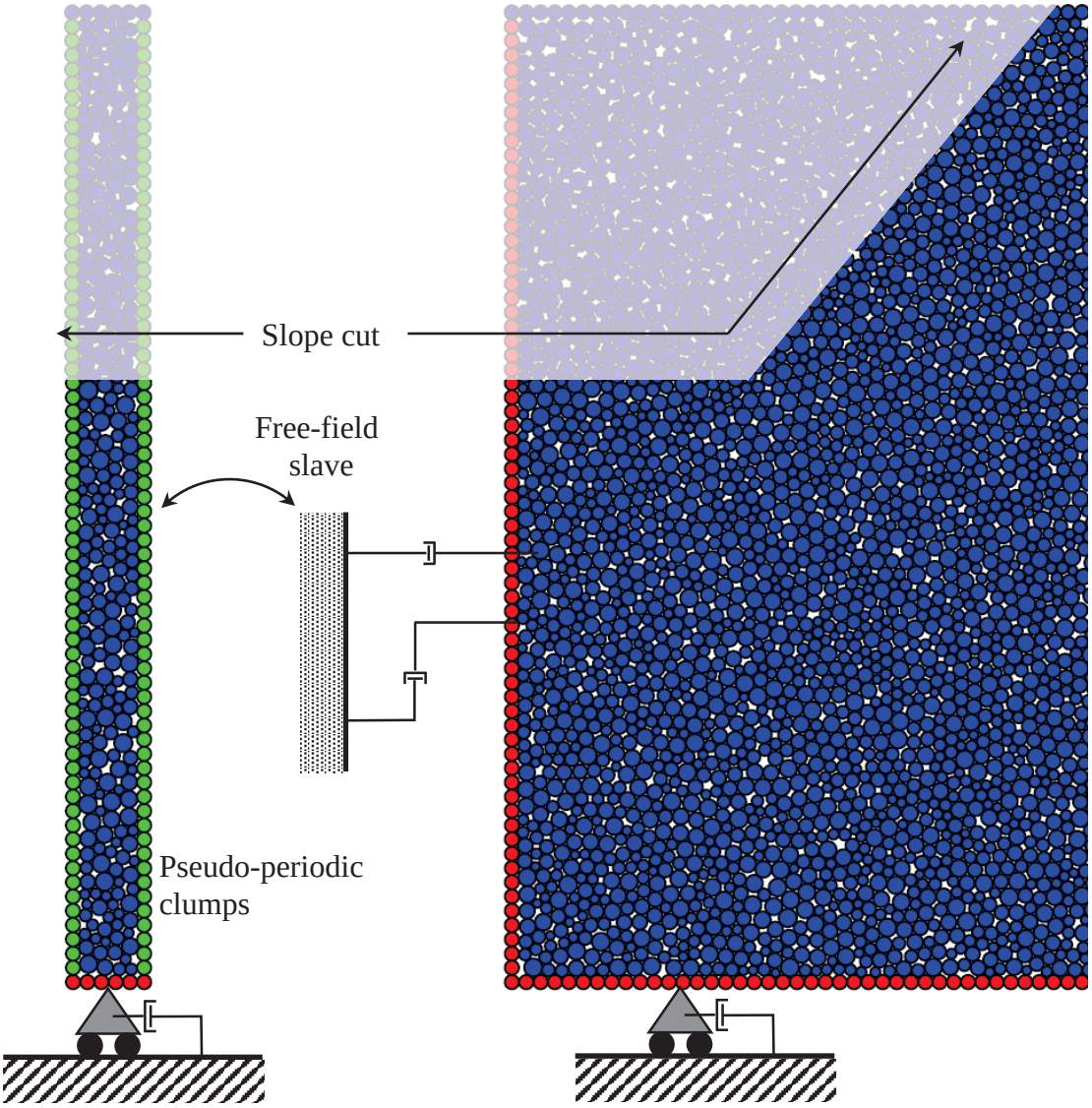

Figure 3.31: Model for dynamic simulations in PFC. One side of the model domain is shown with the connection between the main model and the free-field column. This approach allows for one-sided slopes to be cut into the model while preserving the free-field boundary control.

3.3.5 Results and comparison with other boundary conditions

The viscous boundary condition and the free-field response columns with pseudo-periodic boundaries appear to work very well and are fairly efficient. To further confirm the ability of BPM to transmit and reflect waves appropriately, layers are introduced, and more complex wave motions are sent through the model. Three shear wave velocity profiles (shown in Figure 3.32) were subjected to pulse motions to accomplish this. Profile 1, which has uniform V_s, was also subjected to an earthquake motion.

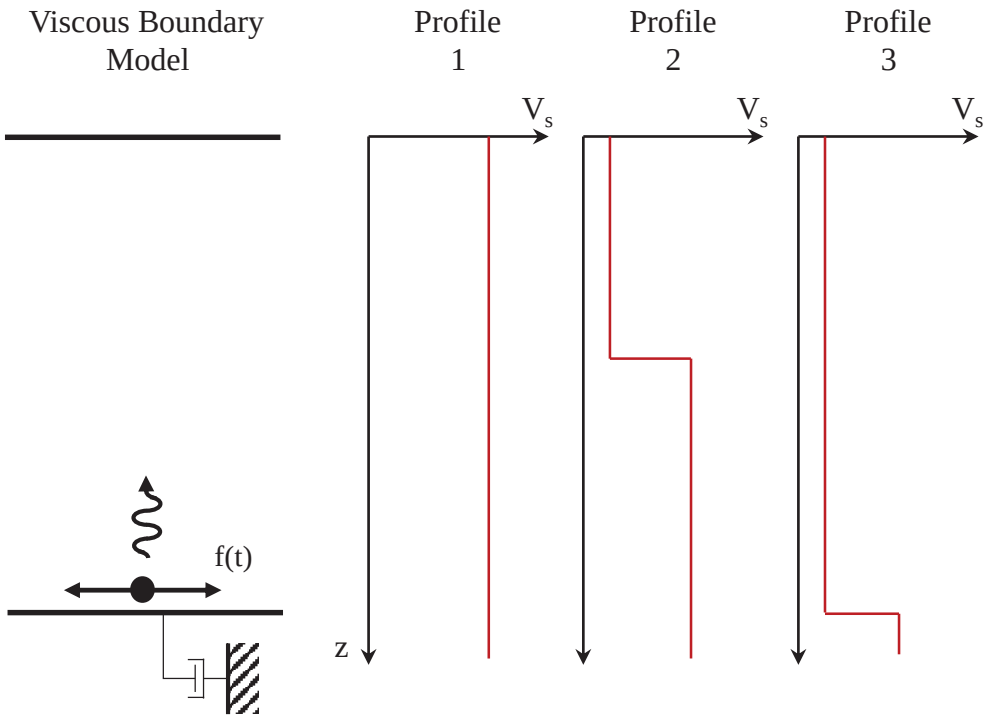

Figure 3.32: The viscous boundary model and three shear wave velocity profiles used to test the ability of BPM and the viscous base to transmit, reflect, and absorb seismic waves. Profile 1 is uniform and stiff. Profile 2 has two layers of equal height - soft on top of stiff. Profile 3 is uniformly soft with a stiff damper.

To determine the validity of the BPM results, they were compared to an analytical solution for elastic one-dimensional ground response in the same profiles. The formulation of the analytical solution is taken from Section 7.2.1 of *Geotechnical Earthquake Engineering*

(Kramer, 1996) on the Linear Approach to One-Dimensional Ground Response Analysis.

The pulse transmission and absorption in Profile 1 demonstrates at a very basic level the particulate DEM's ability to transmit shear waves from the viscous base, to the free surface, and back. As expected, the displacement amplitude doubles at the surface and is reflected back as a pulse of the same displacement polarity. The comparison with the analytical solution in Figure 3.33 shows that the model is capturing consistent wave speeds and amplitudes with elastic wave theory. Figure 3.34 shows that when a more complex wave form in introduced, the model continues to replicate elastic wave behavior with a high degree of accuracy. These figures present a comparison of model displacement to expected displacement. Displacement time-histories are used for comparison because individually monitored particles in BPM tend to have very small, local vibrations that obscure trends in acceleration and velocity time-histories, particularly for inputs of small amplitude.

Profile 2 tests the model's ability to transmit and reflect waves at an impedance contrast within the model. In this case, the model showed some minimal wave scattering but had good agreement with the analytical results (Figure 3.35).

In Profile 3, the impedance contrast is at the viscous boundary rather than within the model. Although this profile is similar to Profile 2, the implementation of the impedance contrast is fundamentally different because it is handled by the user-defined boundary condition rather than the automatic DEM calculations. Figure 3.36 compares the DEM result for Profile 3 with the analytical solution and shows that the user-defined boundary can handle the impedance contrast well.

These comparisons provide some confidence that PFC and these unique boundary conditions can be used to simulate elastic ground response analysis in a variety of geologic settings for general ground motions.

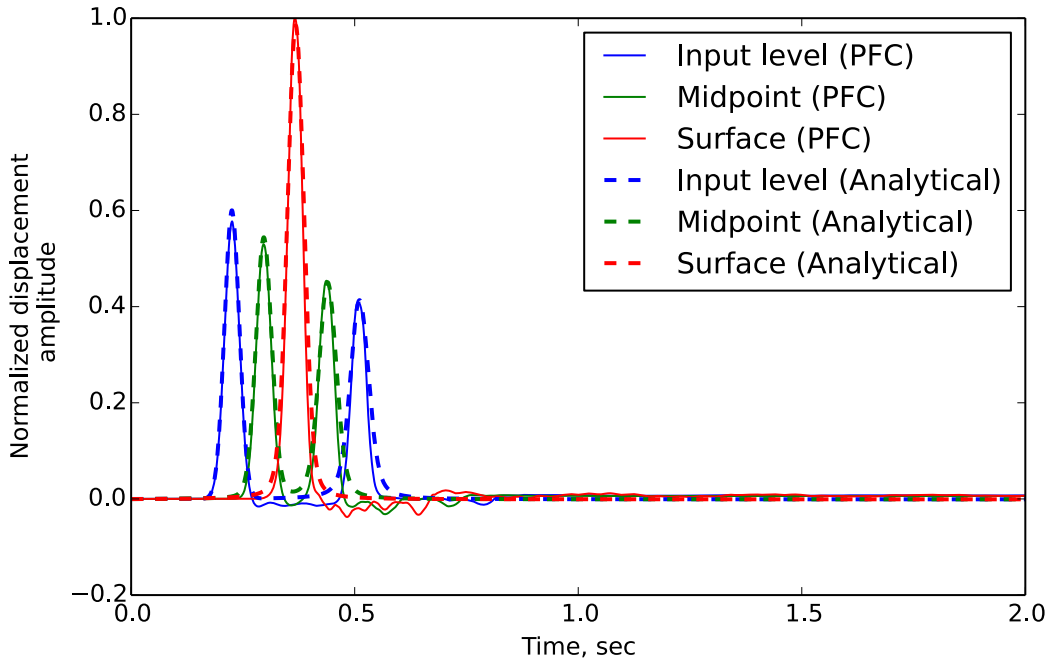

Figure 3.33: Comparison of the PFC and analytical responses to a single pulse in Profile 1. The initial pulse comes in at the base of the model and is slightly damped as it travels through the midpoint and to the surface. At the free surface, the displacement amplitude is doubled, and the pulse is reflected back down. Upon reaching the input level again, the wave is absorbed by the viscous base. The PFC and analytical solutions match well in wave speed and amplitude.

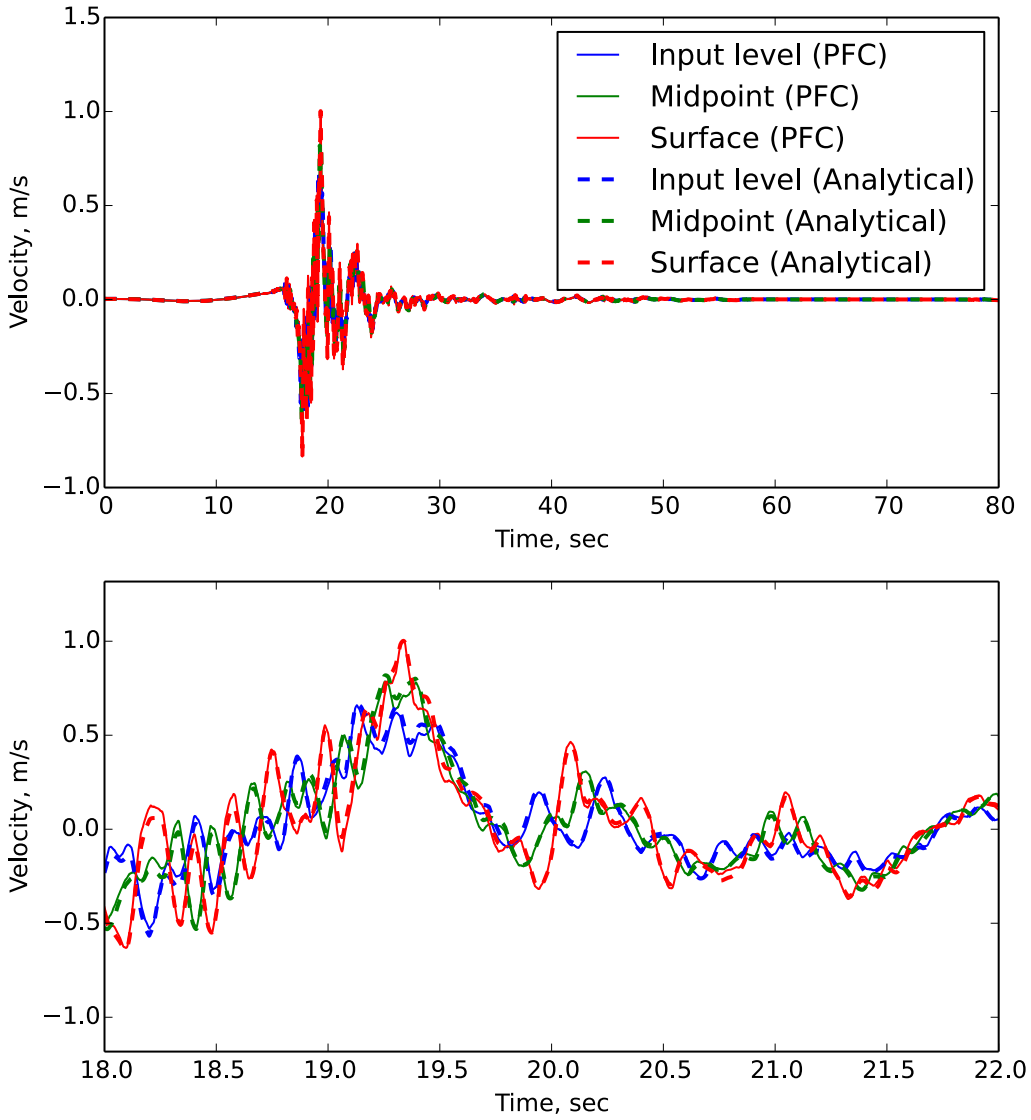

Figure 3.34: PFC and analytical response comparison for an earthquake motion in Profile 1. The motion is derived from the February 22nd, 2011 Canterbury event. The lower figure shows that there is a high level of agreement between the two solutions in a selection of the response between 18 and 22 seconds.

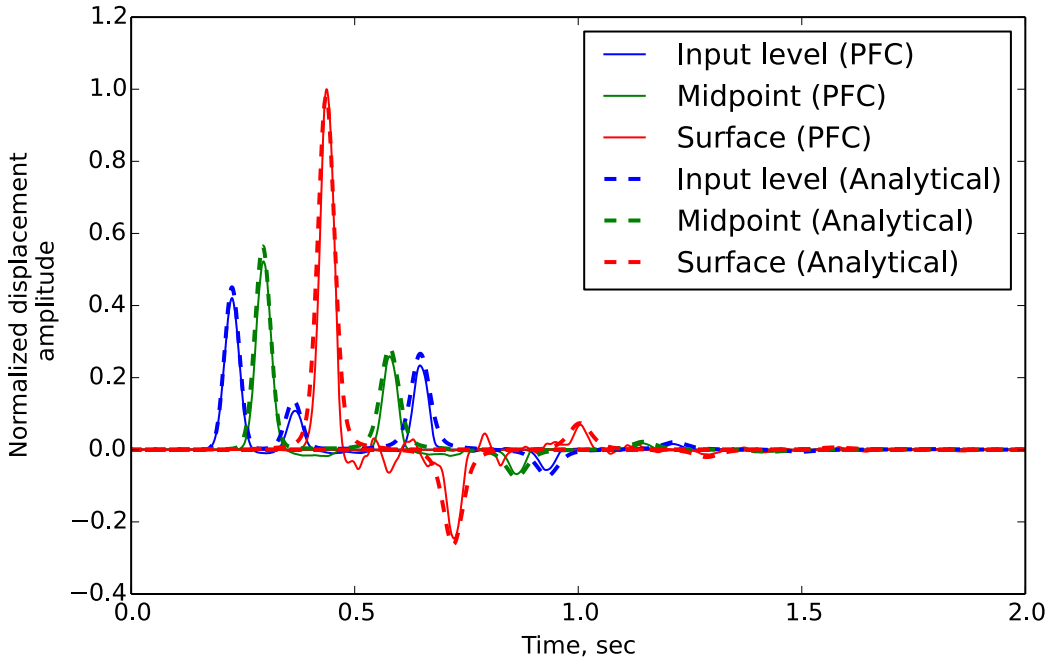

Figure 3.35: Comparison of the PFC and analytical responses to a single pulse in Profile 2. In this profile, when the pulse reaches the midpoint, part of the pulse is reflected back due to impedance contrast. Some noise can be seen in the surface signal of the PFC response. However, the agreement between the two solutions is good in both arrival time and amplitude.

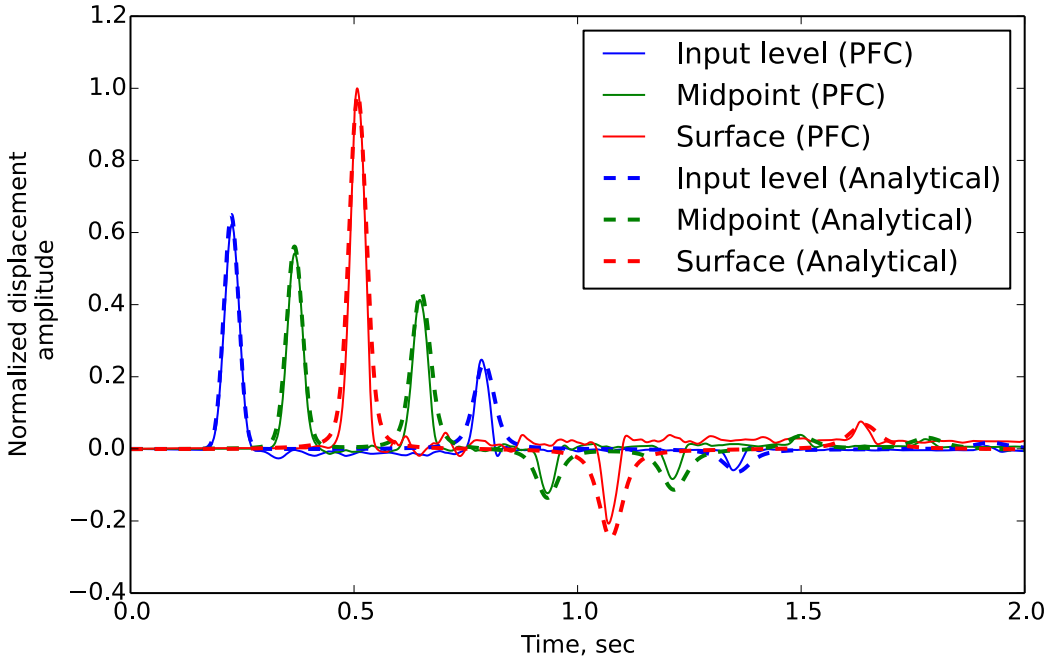

Figure 3.36: Comparison of the PFC and analytical responses to a single pulse in Profile 3. The pulse travels up to the surface and back and is then reflected in part and absorbed in part by the stiff viscous boundary. In this softer material, the analytical solution shows the shape of the pulse widening as it travels, while the PFC response does not. There is good agreement in wave response time and peak amplitude.

3.4 Wave Behavior in Steep Slopes with the Bonded Particle Model

When the ground surface is sloped, the particle motion of incident SH-waves is not parallel to the ground surface. For the case of a steep rock-slope, the inclination of the ground surface relative to the particle motion can be at or very near 90 degrees, essentially producing a discontinuous ground surface. This causes the creation of surface waves P-waves and Rayleigh waves that travel up the slope face [64]. Rayleigh waves are by evanescent by nature, meaning that their amplitude decreases exponentially with depth from the surface. In the case of a rock-slope, which can transmit tensile waves as well as compressive waves, these surface waves can result in volumetric expansion close to the slope face. Behind the slope, the incident SH-wave continues to propagate up to the top of the cliff, so the shear stresses induced by the incident SH-wave, the Rayleigh waves at the surface and cliff face, and the P-wave can potentially combine to create a critical stress state. The volumetric expansion can be particularly damaging because, although intact rock can transmit tensile stresses, the tensile strength of rock is much lower than its compressive strength, particularly at a slope face where the rock has been weathered. The reflection of the SH-wave off the cliff top surface can also interact with the slope face to create surface waves.

3.4.1 Modeling Wave Behavior in Steep Rock-Slopes in PFC

Knowing that (1) the BPM model developed so far can transmit and reflect waves properly according to wave theory, (2) the BPM model boundary conditions are sufficient to absorb 95 percent of reflected wave energy when angles of incidence are less than 30 degrees, models to test the behavior of waves in arbitrary geometries can be conducted.

It is worth noting that BPM or any other discrete element code is not the ideal tool for simply modeling elastic wave behavior. The key feature of any DEM code is the ability for elements to spontaneously detach from and contact each other. In an elastic simulation, does not occur so the benefit of DEM over continuum analysis methods is lost. However, the ultimate goal of the model being developed is to simulate the extension and initiation of fractures due to dynamic loads and so the elastic behavior of the BPM model is critical. The elastic simulations and their results presented here are simply tools to provide

a better understanding of the dynamic rock-slope failure mechanisms. A full, quantitative characterization of the behavior of waves in steep slopes would require a different modeling technique and is outside of the scope of this research. The simulation presented below is more qualitative in nature, however, it does illustrate the dynamically induces stresses that are fundamental to the rock-slope failures described in later chapters.

3.4.2 A Simple Pulse Simulation

A simple way to visualize the behavior of a wave in a steep rock-slope is with a single pulse.

The slope used to test the wave is made of a uniform BPM with Vs = 750 m/s and Vp = 1150 m/s. For the elastic simulation, frictional sliding between particles and bond breakage was not allowed, and no fracture network was introduced to the model. The extents of the model were 320 meters wide and 160 meters tall with an 80 degree slope 80 meters in height cut out.

3.4.3 Pulse Simulation Results

The dynamic stresses induced in the uniform slope can be seen in Figure 3.37. The figure shows the magnitude of the change in the first invariant of the stress tensor due to the application of a shear pulse wavelet to the system. The first invariant of the stress tensor is directly related to the magnitude of volumetric stresses in the material.

At t = 0.55s, the pulse is just encountering the toe of the slope and localized compression at the toe can be seen. Two bands, corresponding to the two peaks in velocity time history of the pulse can also be seen here. These two bands correspond to the points of peak shear stress in the wavelet. The shear stress zones are visible in the volumetric stress plot because locally, discrete particles in the shear zones will experience some dilation (either expansive or contractive) due to the random packing structure. Although the shear zones are visible in the figures below, the net volumetric stresses in any given area of shear is zero. At T = 0.75s and T = 0.81s, local concentrations of volumetric expansion can be clearly observed near the slope face. Volumetric expansion can be extremely destructive in rock, even at moderate magnitudes due to the relatively low tensile strength of fractured rock masses and

their stress-dependent shear strength. The color scale in the figures is set such that the hot and cold maximums correspond to a percentage of the nominal shear stress of the applied pulse. The magnitude of the volumetric expansion at the slope face is approximately equal to 40 percent of the shear stress of the applied pulse.

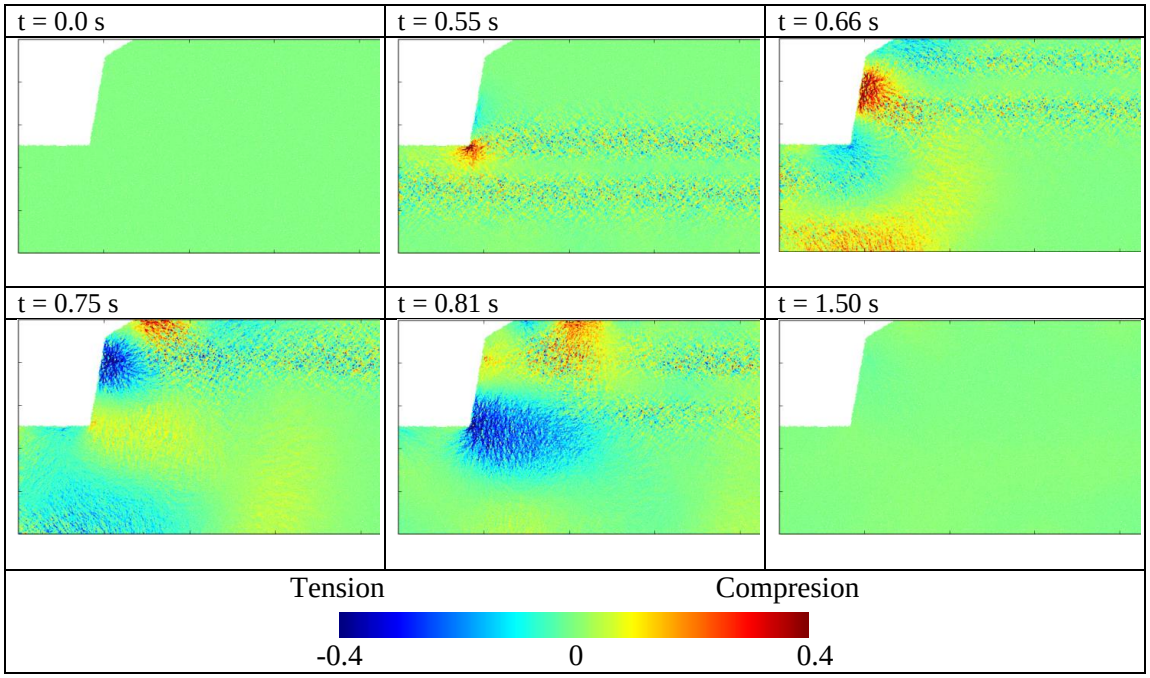

Figure 3.37: Change in first stress tensor invariant (volumetric stresses) in a rock-slope induced by an upward propagating shear pulse. The extremes of the colormap correspond to a stress magnitude equal to 0.4 times the amplitude of the input shear wave stress. Blue indicates tension. Red indicates compresion.

3.5 Conclusions

This chapter presents the BPM framework used in this research. The strength parameters of the bonded particle model, as well as its dynamic behavior, is presented. A rational approach to the selection of micro stiffness parameters based on the inherent double elasticity of a parallel-bonded BPM assembly is described and verified.

The ability of the BPM model to accurately capture the dynamic flexural behavior

of a cantilever beam and wave transmission, reflection, and absorption is verified with analytical solutions and experimental data. A pseudo-periodic boundary using clump logic is developed and implemented to create free-field response columns for boundary control. These boundary conditions provide the ability to model dynamic input in simple rock-slope configurations in a well-established 2-D dynamic analysis framework.

A demonstration of the model behavior through the transmission of a dynamic pulse provides verification that the model is capturing the theoretical behavior of wage interaction on steep slope geometries. The demonstration also shows the development of potentially damaging stresses concentrated near the slope face, which may provide some insight into the behavior of steep rock-slopes under strong ground motions.

The developed model provides the necessary numerical framework to investigate the behavior of rock-slopes during seismic events.

Chapter 4

NEW ZEALAND CASE STUDIES

4.1 Introduction

In 2010 and 2011, a series of four major earthquakes occurred in the Canterbury region of New Zealand [65]. These earthquakes, which are known as the Canterbury Earthquake Sequence (CES), were large magnitude (M_w 5.9 or greater) as shown in Table 4.1. The peak ground accelerations (PGAs) listed in Table 4.1 are as recorded by the Lyttelton Port Company (LPCC) station, which is essentially a rock outcrop motion [66].

Table 4.1: Major events of the Canterbury Earthquake Sequence as reported by Bradely et al, 2014 [66]

Date	**Magnitude**	**PGA (LPCC)**
Sept. 4, 2010	7.1	0.29 g
Feb. 22, 2010	6.2	0.92 g
June 13, 2010	6.0	0.64 g
Dec. 23, 2010	5.9	0.44 g

During the Canterbury Earthquake sequence, rock-slope failures resulted in loss of life and significant loss of inhabitable property in the Christchurch region of New Zealand [67], [68], [17]. Damage to rock-slopes during these events, was characterized by two key features: (1) cliff-collapse, where a relatively shallow failure of intact or partially intact rock along the cliff face fails (also referred to as 'debris avalanche' [69] or 'rock fall' [70]), and (2) cliff top displacement, where the portion of the slope mass that did not collapse experiences some incremental movement toward the cliff face [71]. In the field, cliff top displacement was made evident by cracking of the ground behind the slope crest [69], [71].

The effects of strong ground motion at several rock-slopes in the Port Hills were well documented and characterized. These case histories provide an excellent opportunity to verify the ability of the bonded particle model (BPM) to capture not only the fundamental mechanical behavior of rock (as has been well-documented), but also the dynamic behavior of fracturing rock masses using the newly-developed boundary condition scheme presented in the previous chapter.

This chapter is divided into two parts. Part I will present the dynamic BPM models subjected to the February 22, 2011 earthquake and compare the results to the field behaviors of the sites, as well as results from the more traditional modeling approaches described above. The BPM model results presented in Part I were published as part of the Proceedings of the 6th International Conference on Earthquake Geotechnical Engineering [72]. Part II will present the results further testing of one the modeled sites under different loading conditions and structural characteristics.

PART I: MODELING A CANTERBURY EARTHQUAKE SEQUENCE EVENT

4.2 New Zealand Sites

Cross-sections from two sites from the Port Hills area in New Zealand, Redcliffs and Richmond Hill, were selected for modeling. These sites were selected because (i) both cliff collapse (as shown in Figure 4.1) and cliff top displacement were observed following strong ground motion, (ii) the sites have relatively two-dimensional cliff face sections, and (iii) they have been well characterized by field and laboratory testing. The field and laboratory characterization were performed by GNS Science (GNS), a research and consulting center (http://www.gns.cri.nz/).

(a) **(b)**

Figure 4.1: Cliff collapse at Richmond Hill (a) and Redcliffs (b) sites after the February 22, 2011 earthquake.[photo credit:GNS Science]

The sections of the two cliff sites discussed here are composed primarily of a loess and fill mantle over rock. The rock in the slopes is composed of 1) columnar jointed basalt lava and breccia, 2) epiclastics, 3) Trachy basalt breccia, and 4) Trachy basalt lava. A) Loess and fill covered with vegetation,

The engineering geological descriptions of the units at as reported by GNS [71] are listed below.

- **Loess and fill** – The loess mantling the cliff top at Richmond Hill Road is similar to other areas of the Port Hills. It is a relatively cohesive silt-dominated soil with only minor clay mineral content and the strength of loess is largely controlled by the soil-moisture content. The loess in the main zone of cracking at the cliff top is unsaturated and relatively strong where exposed. Similarly, the thin layer of loess/volcanic colluvium sometimes present above the bedrock and at the base of the loess does not appear particularly weak or wet. The thickness of the loess, inferred from drillhole records and field mapping, varies between 7 m at the slope crest to less than a metre near the cliff edge, where it pinches out against bedrock.

- **Columnar jointed basalt lava** – Dark greenish grey to black, unweathered to moderately weathered, sometimes vesicular, Basalt, very strong with variably developed columnar joints, widely to very widely spaced (1.5'5 m), typically giving large to very large block sizes that are columnar in shape. Columnar joints are often radial to flow margins, and lavas have gradational contacts with lava breccia at their upper and side margins. Joint faces are generally rough to very rough, stepped or irregular, commonly manganese oxide or calcite coated, and only rarely have clay or silt fill. Individual flows form lensoidal bodies throughout the cliffs, ranging from 0.5 to 2'4 m thick. Columnar jointing is well expressed where flows are thick, and gives way to thin, platy flow orientated jointing where flows are thin.

- **Basalt lava breccia** – Slightly weathered to highly weathered, light grey to dark grey when slightly weathered to orange or red-brown when highly weathered, massive, brecciated Basaltic Lava Fragments, moderately strong to strong (but varies to weak or very weak when highly or completely weathered), with very widely spaced irregular discontinuities. At all sites basaltic lavas have flowed within thick carapaces of brecciated lava, with the breccia often exceeding the thickness of its source lava (brecciated units may be 2 to ¿10 m thick.). Breccias are poorly graded, angular lava fragments with a fine to coarse matrix supporting unsorted cobbles, blocks and often 1'5 m diameter megablocks of broken lava. Breccia fragments are often more vesicular

and scoriaceous than the source lava, and prone to weathering due to high porosity. Bedding is massive, poorly jointed, with lower boundaries gradational with the source lava and upper boundaries roughly planar. Weathering expression is cavernous and spheroidal, of fine and coarse blocks respectively, and in some cases development of cliff parallel exfoliation joints/cracks. Freshly exposed breccia faces show extensive interstitial clay weathering and deposition of clay within vesicles and between clasts.

- **Epiclastics** – Moderately to highly weathered or oxidised brown to red-brown or yellow-brown thinly bedded Tuff or Tuffaceous Sandstone, intercalated with or grading into fine to coarse pebbly Lapilli Tuffs or Gravelly Sandstone and conglomerate, with occasional cobble-sized blocks and bombs of basalt, moderately strong to weak, very weak to extremely weak when highly weathered. Rarely jointed, prone to cracking on exposed surfaces and easily eroded. Bedding is thin (0.1'2 m) and discontinuous, disrupted by overlying lavas. In all sites, these layers of red-oxidised pyroclastic and epiclastic paleosol material are found between lava flows and breccias, usually at the top of the preceeding lava breccia, and oxidised/baked by the overlying lava flow. The thinly bedded ash and lapilli, with occasional blocks and bombs, is discontinuous due to re-working by water-driven epiclastic processes or re-working by overlying lava flows. The pyroclastic material exposed in the cliffs is often vegetated or a focus for fluid flow, being relatively impermeable compared to the overlying jointed lavas and porous breccias. Contacts are often gradational into lava breccia or lahar/debris-flow depsoits.

- **Trachy basalt breccia** – Slightly weathered to highly weathered, dark grey when fresh, weathering to pale tan, yellow or mauve patches with spheroidal and cavernous weathering structures; massive and unsorted brecciated trachy basalt Lava fragments, moderately strong to extremely weak and the highly weathered material appears stronger than the slightly weathered material. The breccia can change rapidly from being clast-supported to matrix-supported. The trachy basalt Lava on Wakefield Avenue has flowed within a thick upper and lower carapace of autobrecciated

lava, up to 4'5 m thick below the main lava, and up to 10 m thick above it, with gradational contacts between the lava and its breccia. Massive and poorly jointed, but with extensive leaching and clayey alteration present in upper parts below top contact with overlying tuffs and basalt lavas, and at lower contact below the lava at South Wakefield Avenue. Weathering expression is cavernous and spheroidal, with extensive clayey alteration and oxidation of clasts in some locations (South Wakefield Avenue). Freshly exposed faces by Wakefield Avenue Croquet Club show interstitial clay deposition and shrinkage cracks on exposure, and examples of polished slickensides (Iron and manganese oxide stained slickensides have been observed in blocks of lava breccia that have fallen from the Wakefield Avenue slope face during the 2010/11 Canterbury earthquakes).

- **Trachy basalt lava** – Unweathered to moderately weathered, pinkish brown to grey brown when fresh, flowbanded trachy basalt, very strong, with pronounced anastomosing flow parallel banding and joints that are closely spaced (approximately 0.1'0.25 m spacing), typically giving large to very large block sizes that are tabular shaped. Columnar joints are either very poorly developed or absent. Lower contact with its own breccia is often sharp, upper contact is gradational into autobreccia.

The complete assessment of the two sites can be found in the GNS Science reports on risk assessment for the two sites: *Canterbury Earthquakes 2010/11 Port Hills Slope Stability: Debris avalanche risk assessment for Richmond Hill* [71] and *Canterbury Earthquakes 2010/11 Port Hills Slope Stability: Risk assessment for Redcliffs* [69]).

4.2.1 Richmond Hill

The Richmond Hill site is located on a volcanic spur with a very steep cliff face on one side and a fairly gentle (30 degrees) slope on the other. The cliff itself is about 50 to 60 meters high and 540 meters long with a slope angle between 50 degrees and 90 degrees. A wide section of the cliff face can be characterized by three main geologic units. From top to bottom they are: A) Loess and fill covered with vegetation, B) Columnar jointed basalt

lava and breccia, C) Epiclastics, and D) Trachy basalt lava.

Figure 4.2 shows a section of the Richmond Hill cliff face with its geologic units.

Figure 4.2: From *Canterbury Earthquakes 2010/11 Port Hills Slope Stability: Debris avalanche risk assessment for Richmond Hill* [71]: Geologic units at the Richmond Hill cliff face. A) Loess and fill covered by vegitation, B) Blocky columnar jointed basalt lava and breccia, C) Epiclastics, and D) Trachy basalt lava breccia.

Observed Seismically-Induced Failure

Descriptions of the effects of the CES events on the Redcliffs slope as presented by GNS in [71] are listed below:

- **September 4, 2010 earthquake**: No 2010 displacement of the cliff top has been reported to GNS Science. Approximately 40 m^3 of debris is estimated to have fallen from the cliff face (M. Yetton, personal communication 2011 [*Note: personal communication with GNS Science staff*]).

- **February 22, 2011 earthquakes**: Some cracking at the cliff top (in loess) was reported to the Port Hills Geotechnical Group (PHGG) consultants following this earthquake. These cracks were assessed at the time as being superficial, and of little significance to the stability of the cliff. During this earthquake approximately 5,260 ('1,000) m^3 of rock fell from the slope (Table 3), onto residential and commercial properties at the bottom of the slope, killing one person who was working immediately below the cliff. In some locations, the cliff edge receded up to 3 m. Many cracks were visible in the cliff face after these events (Massey et al., 2012a).

- **June 13, 2011 earthquake**: The mapped crack distributions (in loess) at the cliff top were mainly generated by the 13 June 2011 earthquake. These include those related to the loess slump... Horizontal permanent displacement of the cliff top in response to this earthquake (inferred from analysis of geodetic surveys and measuring of crack apertures) varied between 200 and 800 mm towards the east, with vertical displacements of 200'400 mm. During this earthquake, about 10,120 ('1,050) m^3 of rock fell off the cliff, some onto dwellings and other buildings at the bottom, which were unoccupied following the 22 February 2011 earthquake. The cliff edge receded by up to 5 m in some locations (Massey et al., 2012a) and many more cracks appeared on the cliff face.

- **December 23, 2011 earthquake**: Monitored survey marks at the cliff top indicate horizontal displacements relative to the adjacent land of about 80 mm to the east and

vertical displacement of 50 mm downward. Re-survey of crack apertures ' by PHGG consultants ' showed further opening of existing cracks. During this earthquake about 1,400 ('130) m^3 fell from the cliff, on to unoccupied dwellings at the bottom.

Table 4.2 summarizes the estimates of volume loss due to cliff collapse and of cliff top displacements at Richmond Hill made by GNS for each major earthquake in the sequence. The February 22, 2011 event triggered the first massive volume loss and will be the focus of the modeling effort presented in the chapter. Table 4.3 shows the approximate depths of failure during the February event by geologic unit as inferred from Lidar change models [17].

Table 4.2: Estimated volume loss and cliff top displacement at Richmond Hill during the Canterbury Earthquake Sequence [71]. Cliff top displacement includes both horizontal and vertical displacement.

Date	**Approximate Volume Loss (m^3)**	**Cliff Top Displacement (meters)**
Sept. 4, 2010	40	None
Feb. 22, 2011	5,260 ± 1,000	Small (not measured)
June 13, 2011	10,120 ± 1,050	0.2 to 0.8
Dec. 23, 2011	1,400 ± 130	0.05 to 0.08

Table 4.3: Estimated Depths of Failure at Richmond Hill During the Feburary 22, 2011 Event by Geologic Unit [71].

Geologic Unit	**Depth of Failure (meters)**
Basalt Lava and Breccia	up to 3
Trachyte Lava Breccia	up to 6
Trachyte Lava	0

In some areas along the cliff face, overhanging geometry was created where a section of the Trachyte Lava Breccia experienced failure and volume loss and the stronger Basalt Lava

above did not. Where the Basalt Lava layer is columnar, dilation of the vertical joints was observed very near the cliff face. The cracks at these dilated joints were observed to extend down into the Trachyte Lava Breccia. Figure 4.3 shows this failure mechanism clearly and provides strong evidence for a shallow cliff-collapse mechanism caused by the development of tensile cracks due to dilation of pre-existing joints very close to the cliff face.

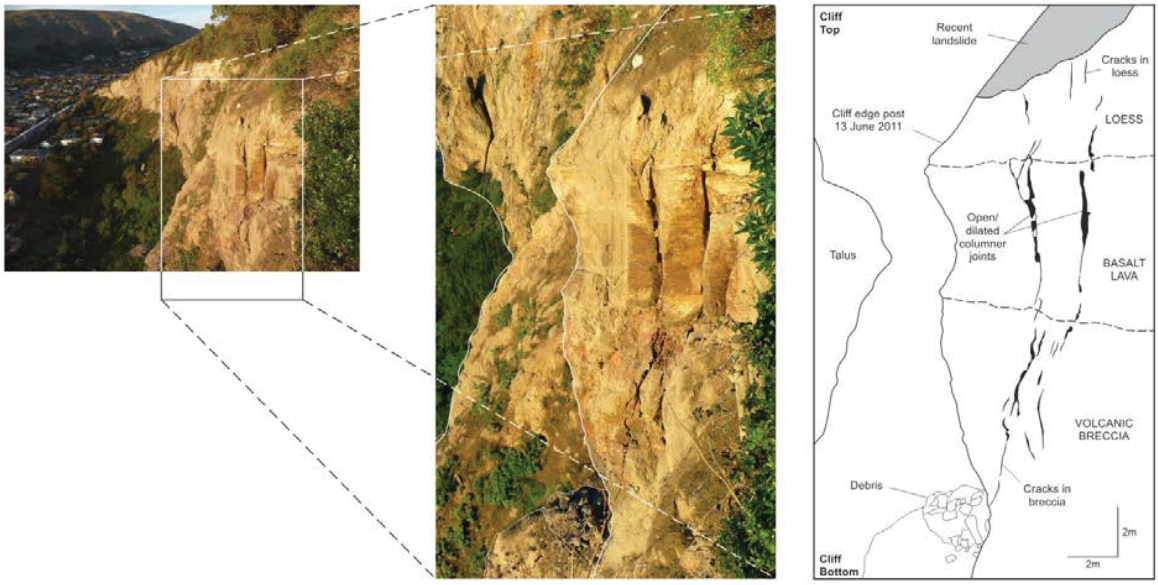

Figure 4.3: From [71]: Cracks observed at the Richmond Hill cliff face. Pre-existing columnar joints have dilated and extended down into the breccia below and up into the loess above.

4.2.2 Redcliffs

The Redcliffs site is a 70- to 80-meter high cliff with a slope angle between 50 and 80 degrees. The majority of the cliff face can be characterized by four main geologic units. From top to bottom they are: A) Basalt lava breccia, B) Columnar jointed basalt lava and breccia, C) Epiclastics, and D) a second layer of basalt lava breccia. Figure 4.4 show a section of the Redcliffs cliff face with its geologic units. As with the Richmond Hill site, a thin layer of loess and vegetation sits above the rock.

Figure 4.4: From *Canterbury Earthquakes 2010/11 Port Hills Slope Stability: Risk assessment for Redcliffs* [69]: Geologic units at the Redcliffs cliff face: A) Basalt lava breccia, B) Columnar jointed basalt lava and breccia, C) Epiclastics, and D) a second layer of basalt lava breccia.

Observed Seismically-Induced Failure

Descriptions of the effects of the CES events on the Redcliffs slope as presented by GNS in [71] are listed below:

- **September 4, 2010 earthquake**: no mapped displacement of the cliff face or cracking of the cliff top was identified; about 60 m^3 of debris fell from the cliff face.

- **February 22, 2011 earthquakes**: The cracks, mainly in loess at the cliff crest. . . were mainly generated on 22 February 2011 by one or more earthquakes that occurred on this day. Permanent total displacement of the area, inferred from the results of mapping of cracks and measurement of their apertures was between 0.03 and 1.7 m. Surveying of cadastral marks, was carried out by GNS Science to allow before and after (the 2010/11 Canterbury earthquakes) measurements to be made. Many of the identified cadastral survey marks were outside the main areas of inferred movement. The displacements of the two survey marks, only marginally within the inferred areas of movement, were about 0.2'0.3 m, and represent lower bound estimates of the total displacement during the earthquakes. During these earthquakes approximately 23,900 ('6,600) m^3 of rock fell from the slope, onto residential and commercial properties at the toe of the slope, killing two people. In some locations the cliff edge receded up to six metres. Many cracks were visible in the cliff face after these events (Massey et al., 2012a). The area behind the rockfall bund, constructed behind the Redcliffs School hall, was completely filled in by debris, and is now incorporated in the debris.

- **June 13, 2011 earthquake**: Some new cracks, and the reactivation (further opening) of existing cracks, were recorded (in loess) at the cliff crest following these earthquakes. Horizontal permanent displacement of the cliff crest in response to these earthquakes (inferred from crack apertures) ranged between 0.2 and 0.7 m; vertical displacements were not measured. During this earthquake, about 11,800 ('3,500) m^3 of rock fell from the cliff, some onto dwellings and other buildings at the cliff toe, which were unoccupied following the 22 February 2011 earthquake. The cliff edge locally receded

by up to seven metres (Massey et al., 2012a) and many more cracks appeared on the cliff face.

- **December 23, 2011 earthquake**: During this earthquake about 1,180 ('130) m^3 fell from the cliff, on to unoccupied dwellings at the cliff toe.

Varying levels of failure at the Redcliffs site for the CES events are summarized in Table 4.2. As with the Richmond Hill site, the February 22, 2011 event triggered the first massive volume loss (and the greatest volume loss at this site) and will be the focus of the modeling efforts for this site. Table 4.3 summarizes the approximate depths of failure at Redcliffs caused by the February event by geologic unit.

Table 4.4: Estimated volume loss and cliff top displacement at Redcliffs during the Canterbury Earthquake Sequence [69]. Cliff top displacement includes both horizontal and vertical displacement.

Date	**Approximate Volume Loss (m^3)**	**Cliff Top Displacement (meters)**
Sept. 4, 2010	60	None
Feb. 22, 2011	23,900 ± 6,600	2 to 3
June 13, 2011	11,800 ± 3,500	0.2 to 0.8
Dec. 23, 2011	1,180 ± 130	None

Table 4.5: Estimated Depths of Failure at Redcliffs During the Feburary 22, 2011 Event by Geologic Unit [69].

Geologic Unit	**Depth of Failure (meters)**
Basalt Lava and Breccia	up to 6
Trachyte Lava Breccia	up to 6
Trachyte Lava	up to 6
Trachyte Lava	0 (covered by talus)

The post-earthquake cliff face at Redcliffs had distinct benched geometries in some areas. These benched geometries (observable in Figure 4.1b) generally occur around the Basalt lava breccia and columnar basalt lava and breccia interface and the columnar basalt lava and breccia and epiclastics interface.

4.3 GNS Site Characterization and Modeling

GNS developed engineering geology cross-sections for multiple locations along these two slopes. Layering and strength parameters were assigned based on lab tests on samples from drillhole cores and fallen boulders and from other published testing results for materials in the Port Hills area. Rock mass strength parameters were derived from the lab tests and the geologic strength index (GSI) based on the crock core characteristics after Hoek (1999) [73]. GNS developed at least two estimates of the rock mass strength parameters that they termed the 'average' estimate and the reasonable 'lower' estimate. The average estimates were generally derived from the samples taken from drill cores. The lower estimates were generally derived from the samples taken from fallen boulders, indicating the degree of weathering at the cliff face. Tables 4.6 and 4.7 show the average and lower bound estimates for the engineering properties of each layer at the sites.

GNS performed static stability analysis using both the limit equilibrium and finite element methods, and dynamic stability analysis using the decoupled method after Makdisi and Seed (1977) [74]. A two-dimensional site response analysis was performed to determine the peak acceleration experienced by the slope under different seismic events.

The failure surfaces of the static limit equilibrium modeling for Richmond Hill are shown in Figure 4.5. The model shows a fairly deep failure surface that cuts through the upper Basalt Lava and Breccia and Trachyte Basalt Breccia layers. The lower Trachy Basalt Lava layer is significantly stronger and showed no significant failure. The minimum calculated static factor of safety for the slope using the lower estimate strength parameters under dry ground conditions was 1.5. Using the finite element method and the same strength parameters, the minimum calculated factor of safety was 1.6. The dynamic stability analysis results for Richmond Hill are shown in Figure 4.6. To produce any significant displacement of the failure masses using the decoupled method, the lower estimates of strength had to be

Table 4.6: Average estimates for engineering properties of intact materials at the Richmond Hill (RH) and Redcliffs (RC) sites. The average estimate properties generally represent the intact rock strength of the majority of the slope (where not affected by weathering). Rock property symbols: σ_c is unconfined compressive strength, σ_t is tensite strength, E is the elastic modulus, V_s is the shear wave velocity, and ρ is the density.

Layer	$\boldsymbol{\sigma_c}$**[MPa]**	$\boldsymbol{\sigma_t}$**[MPa]**	**E [GPa]**	**Vs [m/s]**	$\boldsymbol{\rho}$ **[kg/m^3]**
Columnar Basalt Lava (RH)	55	5.7	12.0	1500	2800
Trachyte Lava Breccia (RH)	5.0	0.7	3.8	1500	2200
Trachyte Lava Breccia (RH)	150	10.5	13.0	2300	2600
Upper Breccia (RC)	1.7	0.3	0.2	800	1800
Columnar Basalt Lava (RC)	200	12.0	8.5	1700	2800
Epiclastics (RC)	4.7	0.5	0.3	1000	1900
Lower Breccia (RC)	2.7	0.4	0.5	700	1900

Table 4.7: Lower bound estimates for engineering properties of intact materials at the Richmond Hill (RH) and Redcliffs (RC) sites. The lower bound estimates generally represent the weathered rock condition close to the cliff face. Rock property symbols: σ_c is unconfined compressive strength, σ_t is tensite strength, E is the elastic modulus, V_s is the shear wave velocity, and ρ is the density.

Layer	$\boldsymbol{\sigma_c}$**[MPa]**	$\boldsymbol{\sigma_t}$**[MPa]**	**E [GPa]**	**Vs [m/s]**	ρ **[kg/m^3]**
Columnar Basalt Lava (RH)	20	5.7	10.0	1400	2800
Trachyte Lava Breccia (RH)	3.0	0.7	1.0	800	2200
Trachyte Lava Breccia (RH)	101	10.5	10.0	2000	2600
Upper Breccia (RC)	1.3	0.2	0.1	600	1800
Columnar Basalt Lava (RC)	150	10.0	3.4	1100	2800
Epiclastics (RC)	3.7	0.4	0.3	1000	1900
Lower Breccia (RC)	1.8	0.3	0.4	600	1900

used.

The same analyses were performed on a representative cross-section from the Redcliffs site. The failure surfaces of the static limit equilibrium results for the Redcliffs model are shown in Figure 4.7. Under static, dry ground conditions, using the lower estimate strength parameters the calculated factor of safety for this cross-section of the slope was 1.1 using the limit equilibrium method and 1.0 using the finite element method. Models of the dynamic stability analyses are shown in Figures 4.8 and 4.9. In this case, both the average and lower estimates of strength parameters resulted in some displacement. Table 4.8 summarizes the GNS results for the cross-sections at Richmond Hill and Redcliffs that were the basis of the BPM models developed for this study.

Table 4.8: Summary of select results from the GNS modeling of Richmond Hill and Redcliffs sites.

Layer	**Limit Equilibrium FS**	**Finite Element FS**	**Maximum Co-seismic Displacement [meters]**
Richmond Hill (lower strength)	2.0	1.6	0.5
Redcliffs (average strength)	1.7	–	0.6
Redcliffs (lower strength)	1.1	–	1.7

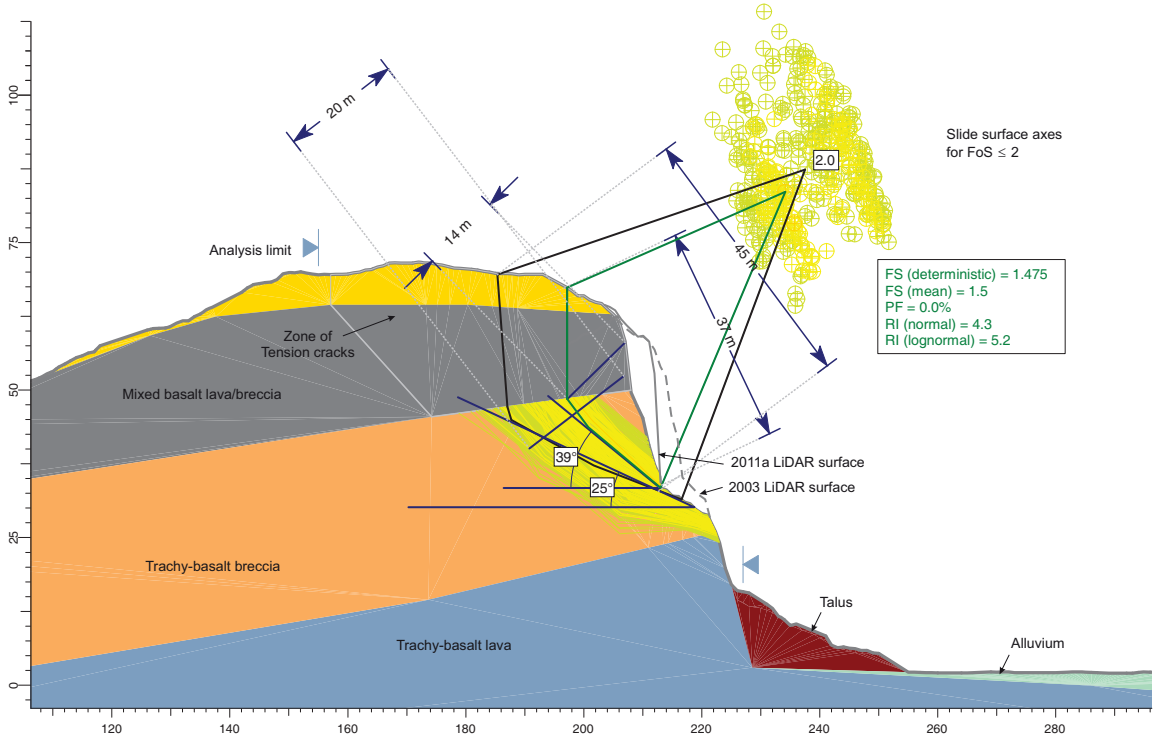

Figure 4.5: GNS model: Richmond Hill static stability analysis with the limit equilibrium method using the lower estimate of material properties.

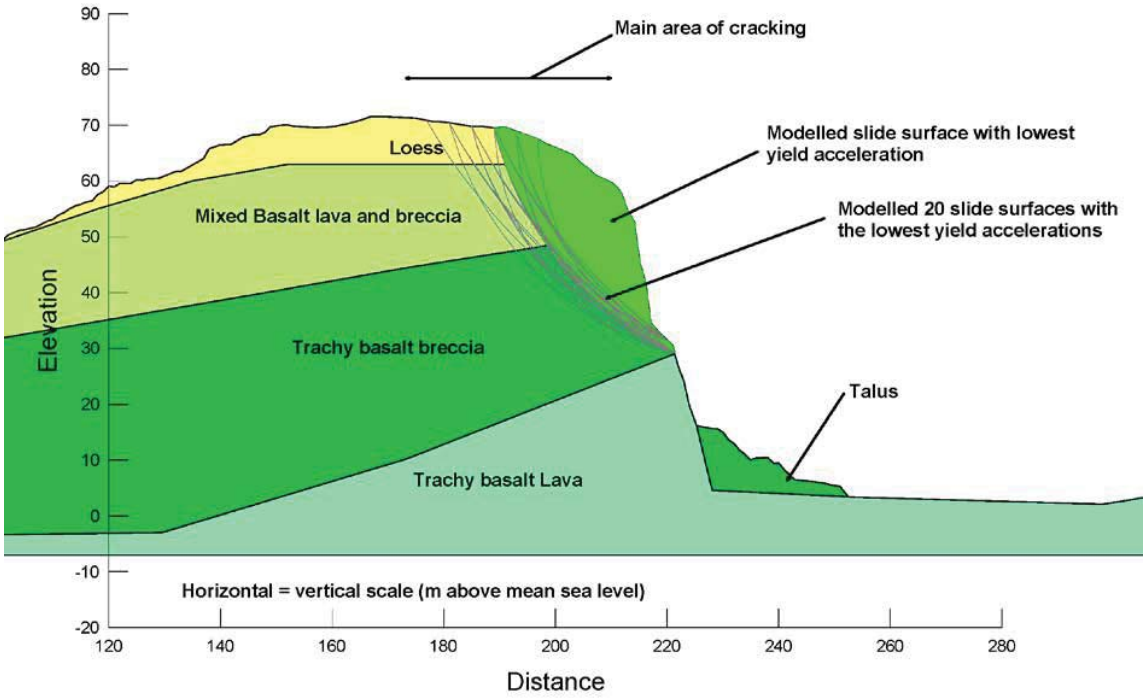

Figure 4.6: GNS model: Richmond Hill dynamic stability model used for estimating with the decoupled method using the lower estimate of material properties.

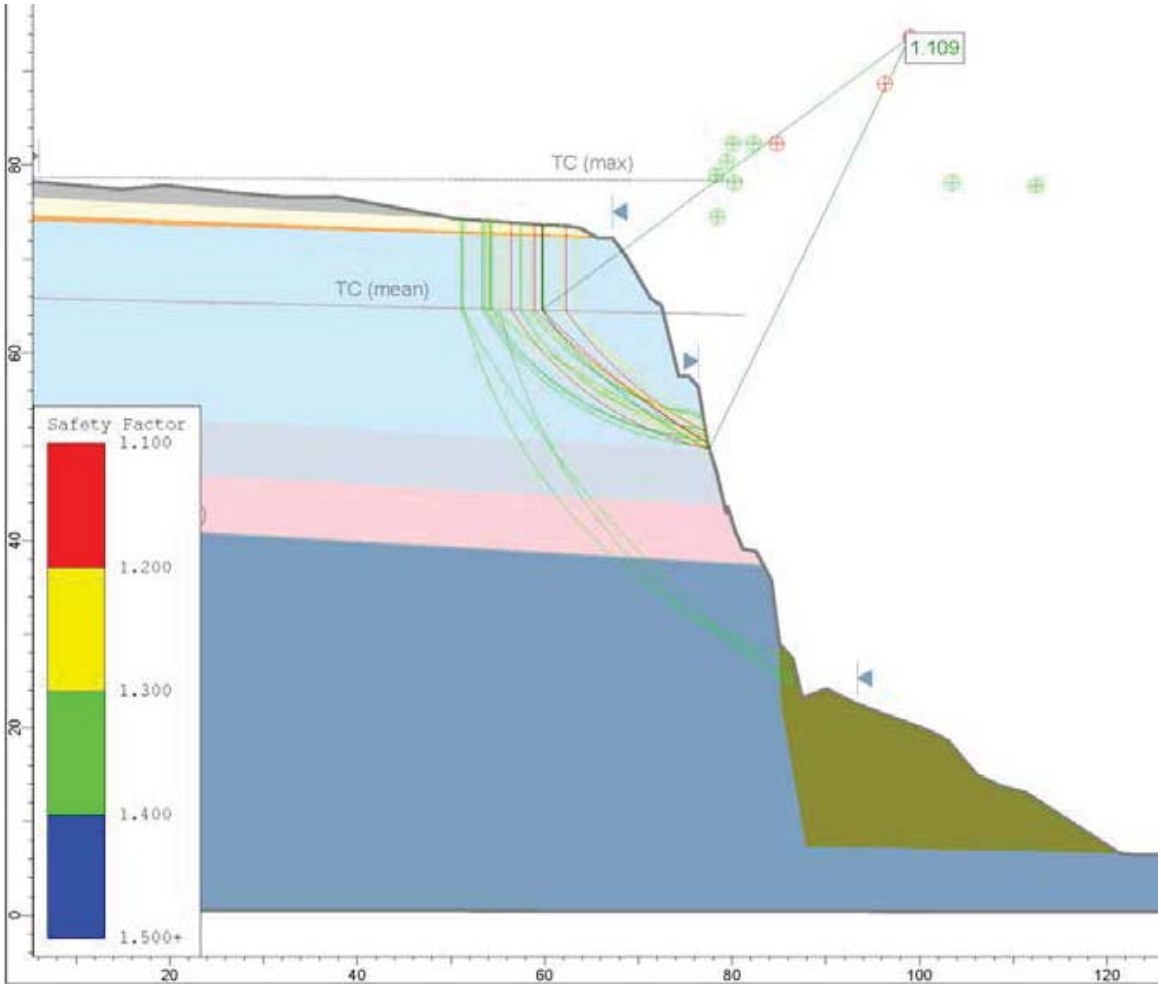

Figure 4.7: GNS model: Redcliffs static stability analysis with the limit equilibrium method using the lower estimate of material properties.

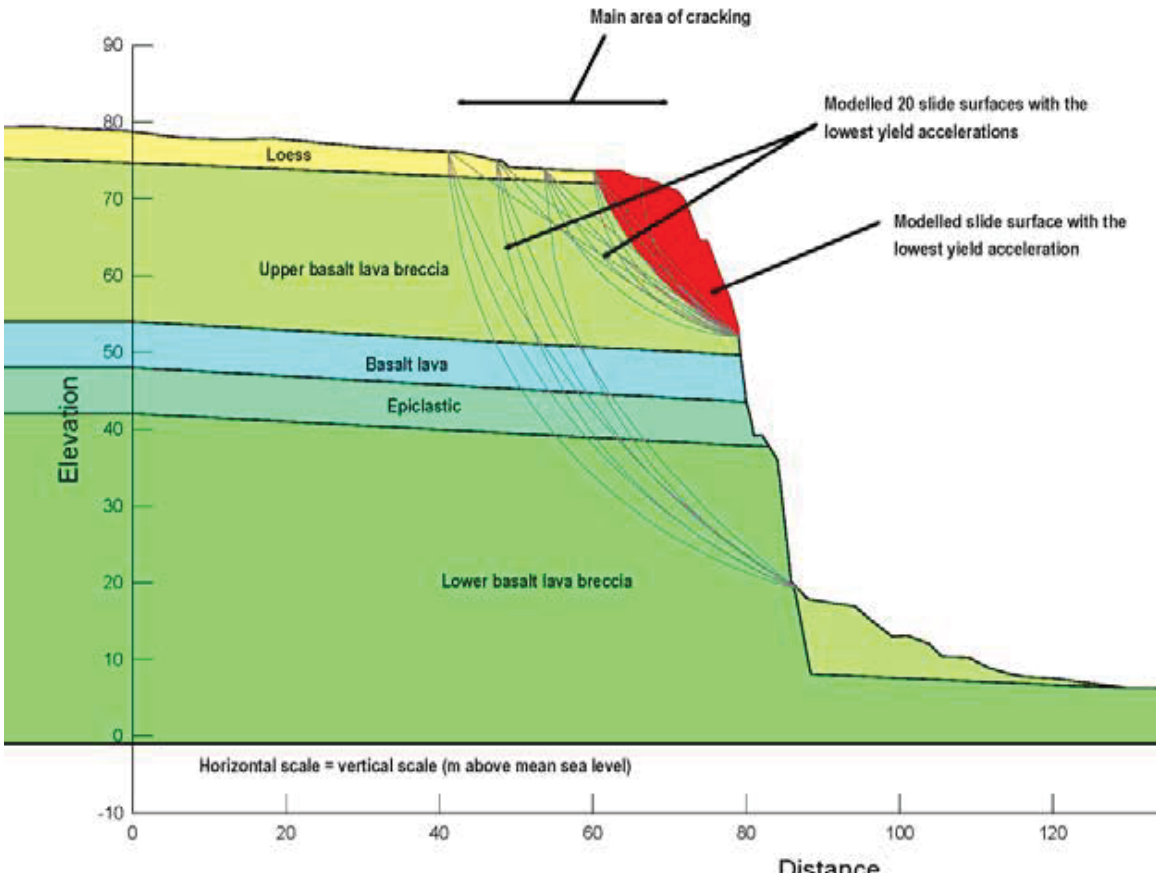

Figure 4.8: GNS model: Redcliffs dynamic stability model used for estimating with the decoupled method using the average estimate of material properties.

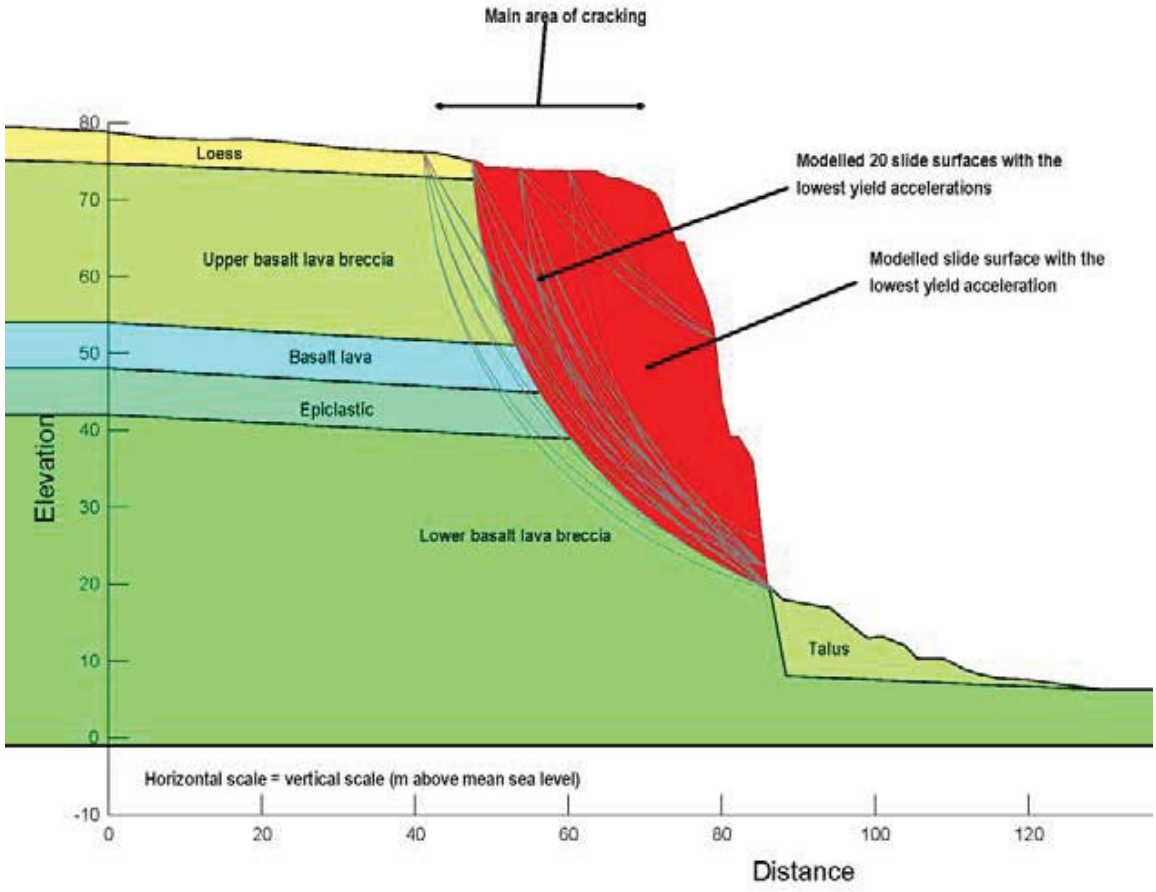

Figure 4.9: GNS model: Redcliffs dynamic stability model used for estimating with the decoupled method using the lower estimate of material properties.

Discussion of the GNS model results

Based on the results of these models, GNS concluded that the models showed:

- Good correlation between the locations and shape of the slide surfaces derived from the limit equilibrium and finite element static stability modeling and those from the dynamic modeling.

- Good correlation with the inferred coseismic displacements from the June and February events when the lower strength property estimates were used. At the Redcliffs site, the average strength properties showed good correlation with the lower estimate of cliff-top displacement.

- Relatively deep failure surfaces that correspond to permanent cliff displacements, but not shallow cliff collapses.

The GNS models were able to capture the magnitude of cliff top displacement using the simplified Makdisi and Seed procedure. In the case of the Richmond Hill site, the target magnitude of displacement in the model was only achieved by using the lower bound material properties throughout the entire model. Although the displacement magnitudes in the models matched their targets, the models only provide a single displacement value for the entire cliff, as opposed to a distribution of displacements as observed in the field.

The methods used were unable to predict or even suggest a failure mode similar to the cliff-collapse that was observed in the field and responsible for the majority of the damage associated with the sites.

4.4 Modeling the Port Hills sites with the Bonded Particle Model

The following sections will present the BPM model developed to simulate the seismically-induced rock-slope failures at the two selected Port Hills sites. The purpose of the models is to:

1. Verify the ability of the dynamic BPM model to replicate realistic dynamic rock-slope behavior with a particular focus on cliff-collapse.

2. Determine the extent to which BPM is better or worse than traditional methods for seismic rock-slope evaluation as a predictive tool.

3. Provide insight into the observed behaviors of rock-slopes during the CES by identifying the mechanisms of failure that contributed to the behaviors.

The approach used in developing the site-specific BPM models was to characterize the sites, run simulations on the models, and observe how closely the model matched the field behavior. The parameters presented here were not altered following this comparison to achieve the best possible match in behavior. Any similarities and differences between the model and field behaviors then, provide an indication of how well the BPM models could have predicted the performance of the site slopes prior to the CES. The final model results to not represent the limit of how well BPM could theoretically capture the slope behavior because no updates to the models were made following the initial comparisons in an attempt to capture the field behavior more closely.

4.5 BPM Model Details

Site-specific models for the Richmond Hill and Redcliffs sites were built and evaluated in PFC at two levels of resolution. Initially, lower resolution models with an average particle radius of 0.9 meters were developed. Several of levels of geologic detail are included in the models. These include the geologic layering, strength reduction near the face of the slope due to weathering, and pre-existing fractures. Each of these levels of detail was incorporated into the model sequentially - first the layering, then the weathering, and then the fractures. By running the simulations at each stage of development, the influence of each can be better identified. Higher resolution models with an average particle radius of 0.45 meters were developed later to assess the extent to which the particle resolution is affecting the results.

The behavior of the models at different levels of resolution will be different in several ways [75]. The higher resolution models will have an increased number of contacts to approximate a stress field with. They may also be weaker, even for the same calibrated strength, due to an increased number of locations for damage to occur in a randomized

assembly [35]. Additionally, the influence of pre-existing joints will be different due to the relative change in distance from the pre-existing joint tips to the nearest bond. These differences will be discussed in more detail in Section 4.11.

The majority of the slope was given the average engineering properties, and the face of the slope was given the lower estimate properties in a discrete 'weathered' zone (see Tables 4.6 and 4.7). From the face of the slope to the edge of the weathered zone (20 meters in width), the strength properties were increased with the square root of the distance from the face so that 20 meters into the slope face, the engineering properties matched the average values (See Figure 4.10). The result is a fairly shallow zone of reduction in strength properties that represent a realistic estimate of the strength close to the slope face.

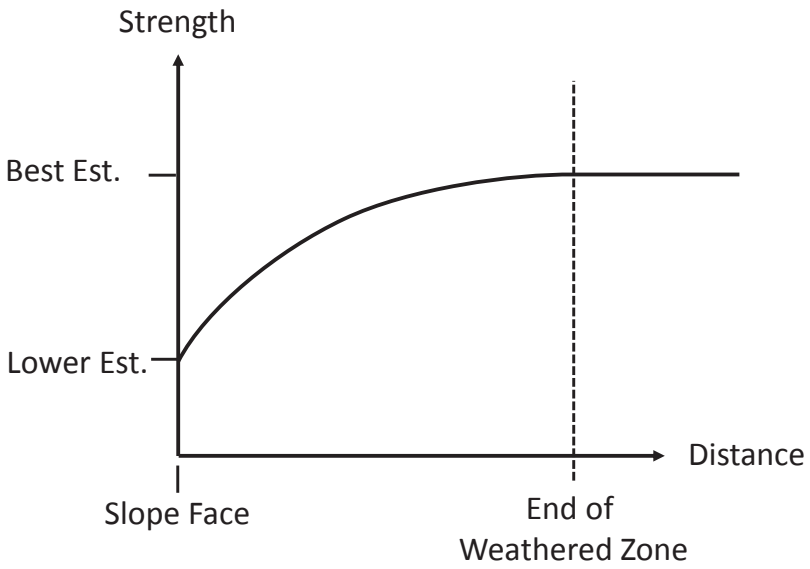

Figure 4.10: Weathering pattern used in the Richmond Hill and Redcliffs PFC models. At the face of the slope, the lower bound rock-mass strength was used to simulate a weathered condition. The rock-mass strength increases with the square root of the distance from the slope face. At the end of the weathered zone, the rock-mass strength matches the rest of the slope. The weathered zone width is 20 meters in the two slope models.

Other than the columnar basalt layers, the natural fractures in the rock-slopes as observed from rock cores were very irregular. An approximation of fracture frequency and

extent based on drilled borings was made and applied to the BPM using the smooth-joint contact method developed by Mas Ivars et al. (2011) [38]. The columnar basalt layers at both sites were given a 3-meter joint spacing and 20-meter joint lengths with a vertical orientation and 5-meter rock bridge lengths. At both sites, the columnar basalt layers in the field were observed to be heterogeneous and also contain inclusions of unstructured breccia. The BPM models, however, assume that the entire layer is made up of columnar basalt. The 3 meter spacing in the columnar basalt layers is wider than what was observed in the field. However, 3 meters was determined to be the minimum allowable spacing for the given size of particles used in the model. All other layers were given a 20-meter joint spacing and 10 to 20-meter joint lengths with random orientation.

The resulting fracture network is fairly simple and the regular spacing and length of the discontinuities are not very realistic. However, the purpose is to introduce random discontinuities in the rock slope where points of high stress intensity may be created during dynamic loading. Building a more randomized fracture network in two dimensions can easily result in kinematically independent blocks, which are not realistic. Even with the overly-structured fractured pattern, the behavior of the four random models will show whether or not the particular arrangement of any given model is producing a result that is strongly controlled by the specific fracture network structure.

Two features of the slopes that were not believed to have a strong impact on the slope behavior were not incorporated into the models - the loess at the top of the slope and the talus piles at the toe. The loess (a lightly cemented, wind-deposited sediment) is very soft and weak and, therefore, not able to contribute much to the overall stability of the slope. Additionally, PFC is not well-suited to model a thin layer of this material at the resolutions being used here. The talus piles that cover the toes of the slopes were not included for similar reasons. While the talus piles may have some global stabilizing effect, their primary impact is likely in restraining material loss from cliff-collapse in the lower portion of the cliff that they cover. At both sites, the talus piles (before the CES) covered the majority of the lowest geologic unit of the slopes (about 20 percent of the cliff face at Richmond Hill, and up to 40 percent of the cliff face at Redcliffs). In terms of impacts, cliff-collapse in the range of the talus pile is negligible compared to the higher sections of the cliff face due to

the lower potential energy.

For the two site-specific model geometries, four unique models of each site at each level of resolution were generated (eight models total per site). At each level of resolution, the models vary only by the randomized packing of the particles and the randomized orientations of the non-columnar joints. By evaluating multiple models with unique particle arrangements but which are otherwise identical, the sensitivity of the model result to the particle structure and fracture orientations can be evaluated.

Tables 4.9 and 4.10 show the BPM microproperties used to replicate the average and lower estimate strength properties for each geologic unit for the two sites. In addition to the microproperties shown in Tables 4.9 and 4.10 all layers have the following characteristics in common: the interparticle and bond shear stiffnesses were equal to 57 percent of the normal stiffnesses, and the bond shear strength was equal to the bond normal strength and, the particle stiffness is 0.1 times the bond stiffness. The interparticle friction coefficient is 0.6.

Figures 4.11 through 4.16 show several examples of the high and low resolution models for the sites. Figures 4.11 and 4.12 show the overall slope and layer geometry (taken from the low-resolution models). Figures 4.13 and 4.14 show the area surrounding the slope face in the low-resolution models with the joint sets visible. In the low-resolution models, the columnar joints are so tightly spaced relative to the particle size, that nearly every particle in the layer is touching a joint. This is not an ideal configuration for modeling damage to the basalt columns, however, because the intact basalt strength is so high, the columns are expected to behave elastically — only breaking at the connections to the rock mass above and below. Figures 4.15 and 4.16 show the area surrounding the slope face in the high-resolution models with the joint sets visible.

Table 4.9: BPM microproperties for the average material estimates for the Richmond Hill (RH) and Redcliffs (RC) sites. Property symbols: $k_{n(bond)}$ is the normal stiffness of the bond, N_{bond} is the normal (tensile) strength of the bond, and $\rho_{particle}$ is the particle density.

Layer	$\boldsymbol{k_{n(bond)}}$ **[N/m^2]**	$\boldsymbol{N_{bond}}$ **[N/m^2]**	$\boldsymbol{\rho_{particle}}$ **[kg/m^3]**
Columnar Basalt Lava (RH)	1.86E+10	5.50E+05	3192
Trachyte Lava Breccia (RH)	1.86E+10	5.00E+04	2508
Trachyte Lava Breccia (RH)	4.37E+10	1.60E+06	2964
Upper Breccia (RC)	5.29E+09	1.70E+04	2052
Columnar Basalt Lava (RC)	2.39E+10	1.00E+06	3192
Epiclastics (RC)	8.26E+09	4.70E+04	2166
Lower Breccia (RC)	4.05E+09	2.70E+04	2166

Table 4.10: BPM microproperties for the lower bound material estimates for the Richmond Hill (RH) and Redcliffs (RC) sites. Property symbols: $k_{n(bond)}$ is the normal stiffness of the bond, N_{bond} is the normal (tensile) strength of the bond, and $\rho_{particle}$ is the particle density.

Layer	$\boldsymbol{k_{n(bond)}}$ **[N/m^2]**	$\boldsymbol{N_{bond}}$ **[N/m^2]**	$\boldsymbol{\rho_{particle}}$ **[kg/m^3]**
Columnar Basalt Lava (RH)	1.86E+10	2.75E+05	3192
Trachyte Lava Breccia (RH)	1.86E+10	2.50E+04	2508
Trachyte Lava Breccia (RH)	4.37E+10	8.00E+05	2964
Upper Breccia (RC)	5.29E+09	8.50E+03	2052
Columnar Basalt Lava (RC)	2.39E+10	5.00E+05	3192
Epiclastics (RC)	8.26E+09	2.35E+04	2166
Lower Breccia (RC)	4.05E+09	1.35E+04	2166

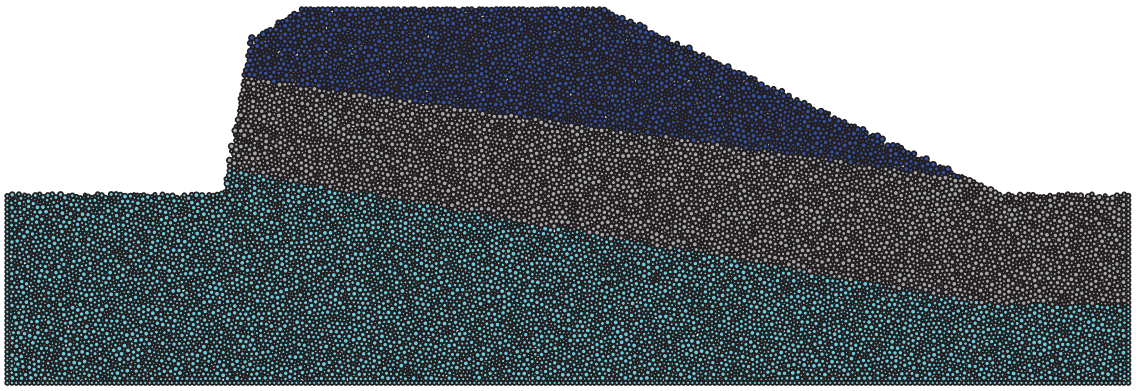

Figure 4.11: Full model extents of the Richmond Hill model. The coloring of the particles in the model indicates the geologic layer: Blue – Columnar Basalt Lava, Gray – Trachyte Basalt Breccia, Cyan – Trachyte Basalt Lava. The lower-resolution BPM is shown. For reference, the height of the slope is 60 meters.

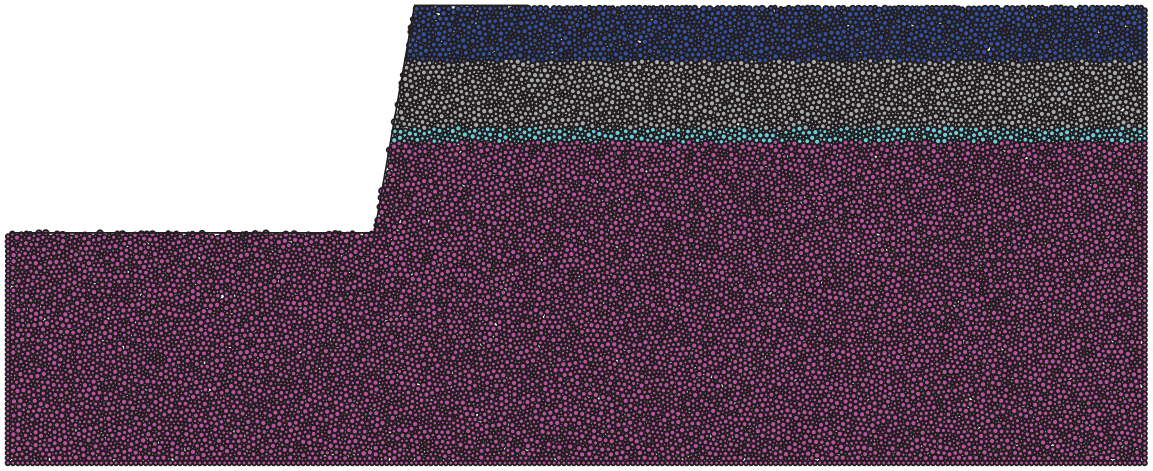

Figure 4.12: Full model extents of the Redcliffs. The coloring of the particles in the model indicates the geologic layer: Blue – Upper Breccia, Gray – Columnar Basalt Lava, Cyan – Epiclastics, Magenta – Lower Breccia .The lower-resolution BPM is shown. For reference, the height of the slope is 80 meters.

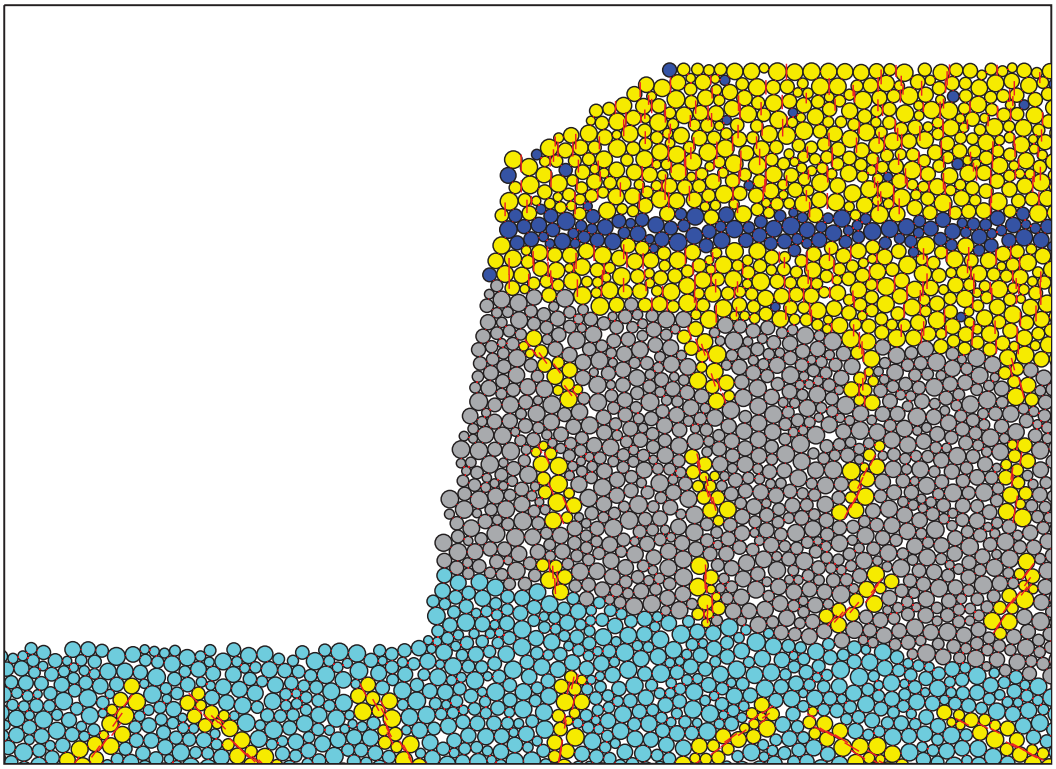

Figure 4.13: A zoomed in view of a low-resolution Richmond Hill slope model. Thin red lines in the model indicate where a smooth-joint contact model has been applied to create a joint. Particles adjacent to the joints have been colored yellow. For reference, the height of the slope is 60 meters.

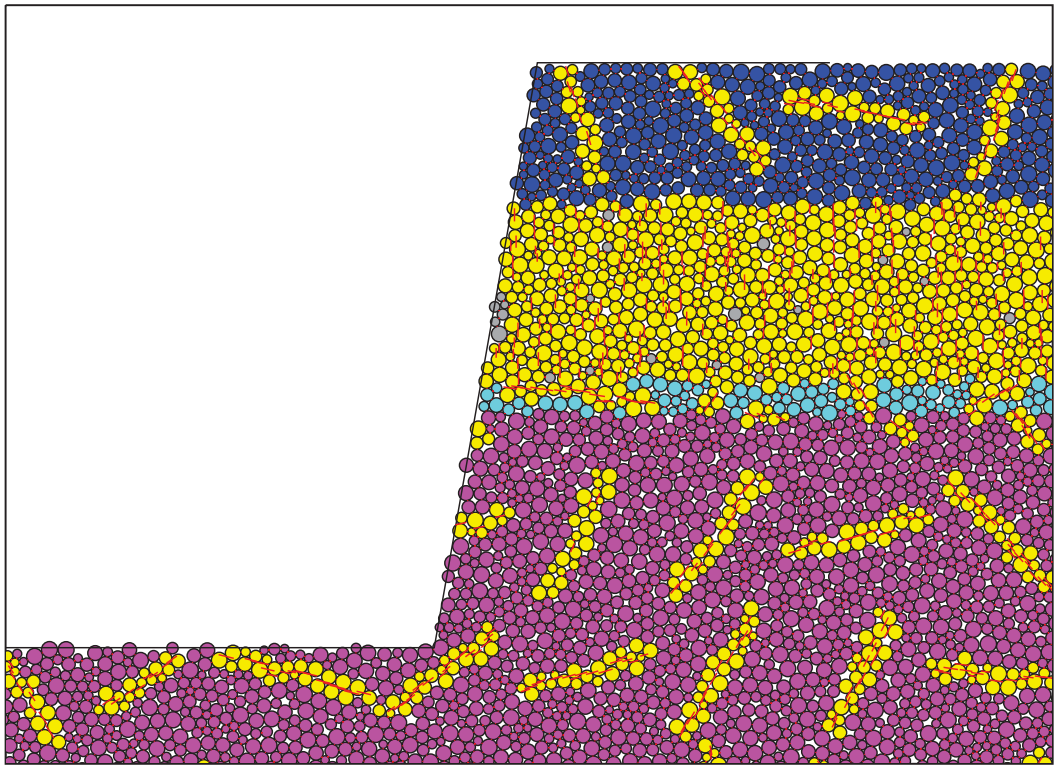

Figure 4.14: A zoomed in view of a low-resolution Redcliffs slope model. Thin red lines in the model indicate where a smooth-joint contact model has been applied to create a joint. Particles adjacent to the joints have been colored yellow. For reference, the hight of the slope is 80 meters.

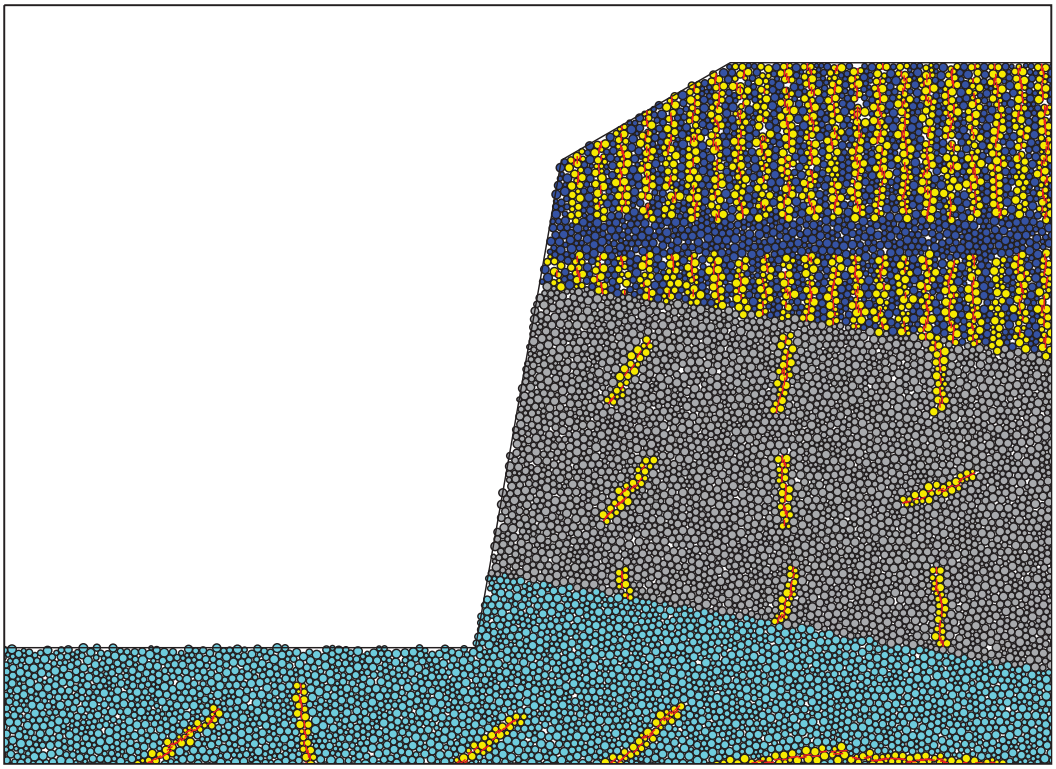

Figure 4.15: A zoomed in view of a high-resolution Richmond Hill slope model. Thin red lines in the model indicate where a smooth-joint contact model has been applied to create a joint. Particles adjacent to the joints have been colored yellow. For reference, the height of the slope is 60 meters.

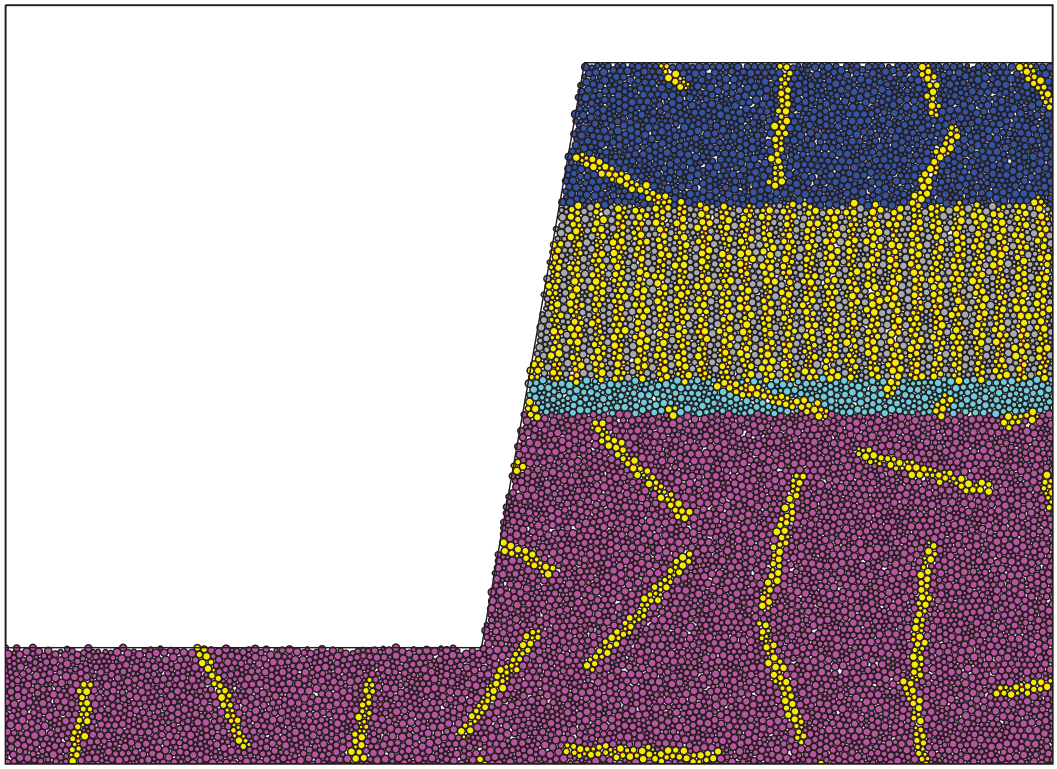

Figure 4.16: A zoomed in view of a high-resolution Redcliffs slope model. Thin red lines in the model indicate where a smooth-joint contact model has been applied to create a joint. Particles adjacent to the joints have been colored yellow. For reference, the height of the slope is 80 meters.

4.5.1 Ground Motions

The two site models were both subjected to the M_w 6.2 February 22nd, 2011 strong ground motion which was the first event in the CES to trigger significant cliff-collapse at both sites. The horizontal components of the Lyttelton Port Company (LPCC) station recording were used as inputs. Bradley and Cubrinovski (2011) consider the LPCC station site to behave as a rock outcrop site [76]. Houette et al. (2012) note that there is some question as to the behavior of the subsurface, particularly at very shallow depths at LPCC [77]. Wood et al. (2011) present SASW measurements for LPCC taken about 300 meters from the recording station that show uniform shear wave velocity of 1500 m/s below 7 meters from the ground surface [78]. For use in this case-history study, the LPCC station recordings are assumed to represent rock outcrop motions on a uniform site and converted to bedrock motions using the wave transfer function presented in the previous chapter. When applied to the two slopes, the horizontal components of the LPCC recording were used to find the ground motion acting perpendicular to the cliff faces of each slope. Figure 4.17 shows the acceleration and velocity time histories used for each model.

The LPCC station sits on a weak rock site (Site Class B) and is within 5.25 km of the two rock-slopes. According to the LPCC station recording, this earthquake had a peak horizontal acceleration of 0.92g and peak spectral frequency of around 5 Hz (Bradley et al., 2014).

4.6 Results

The following sections describe the results of simulations over the evolution of the model as it grew to incorporate more geologic detail. There are three stages to the model evolution: (1) Models with geologic layers, but no weathering and no jointing, (2) Models with layers and weathering, but no jointing, and (3) Models with layers, weathering and jointing. Initially, only the lower resolution models were generated, so these stages only apply to the lower resolution versions of the Redcliffs and Richmond Hill models. The higher resolution models were generated after the full development of the lower resolution models and incorporate layering, weathering, and jointing.

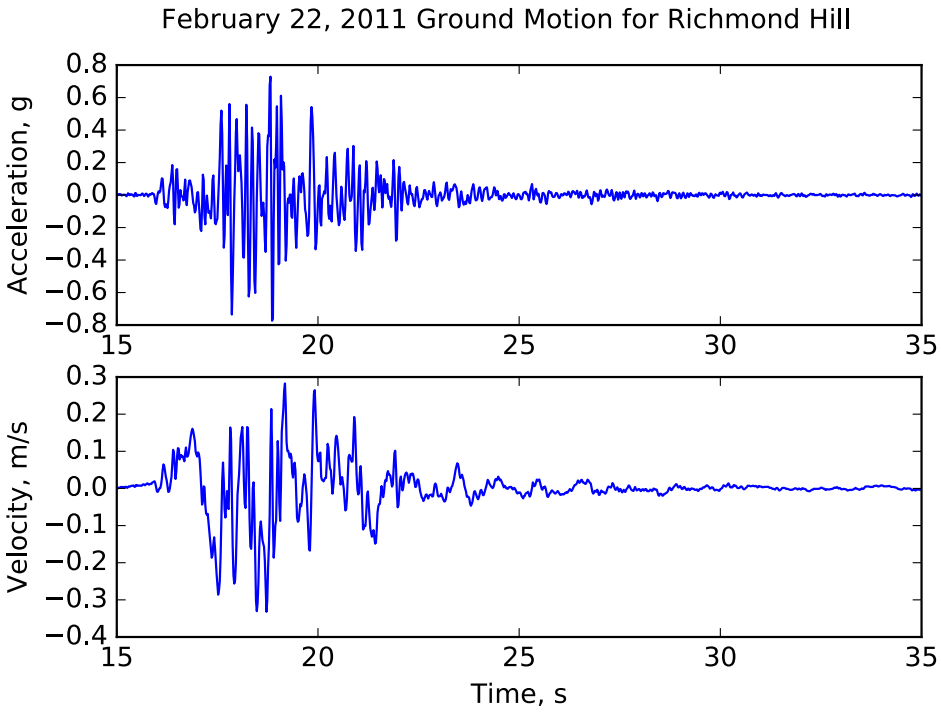

(a)

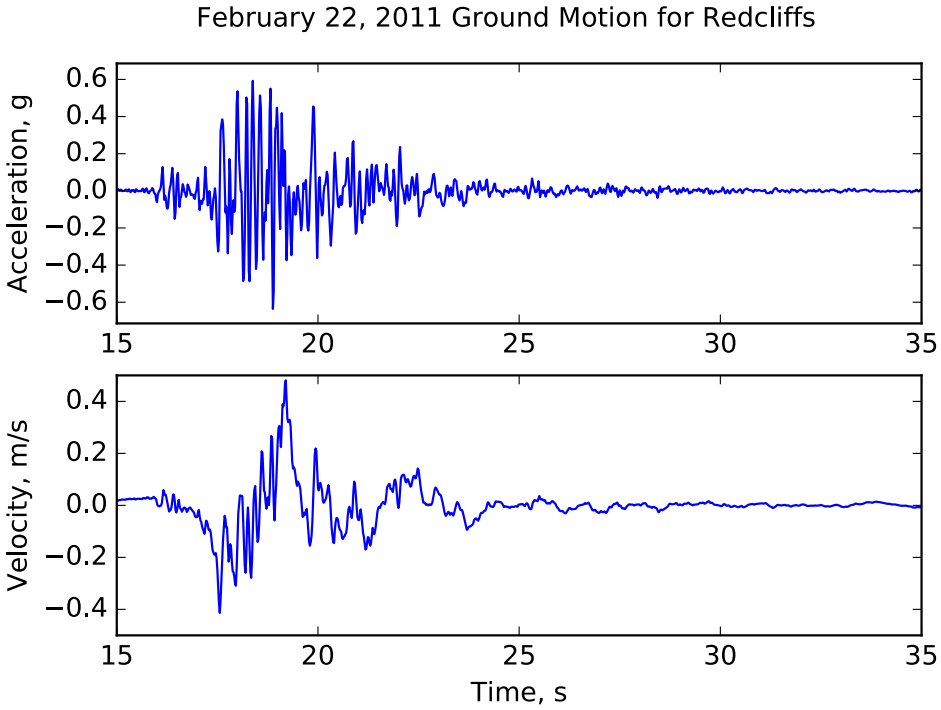

(b)

Figure 4.17: Acceleration and velocity time histories for the Richmond Hill site (a) and the Redcliffs site (b) derived from the LPCC station February 22, 2011 ground motion recording.

4.6.1 Unweathered, Unjointed Behavior

When subjected to the February 22, 2011 strong ground motion, the unweathered, unjointed models for Redcliffs and Richmond Hill experienced no failure. Four unique models of each site were tested. The models are made unique by changing the random seed, which affects the particle arrangements.

4.6.2 Weathered, Unjointed Behavior

When subjected to the February 22, 2011 strong ground motion, the weathered, unjointed models for Redcliffs (4 unique models) experienced no failure. Three of the Richmond Hill experienced no failure, and one experienced a minor failure at the slope face in the Trachye Lava Breccia layer where a single layer of particles detached from the face of the slope.

4.6.3 Completed Model Behavior (Weathered and Jointed)

Failure Mechanisms and Modes at Richmond Hill

In all simulations, at both levels of resolution, the models experience similar failure mechanisms, which lead to the primary failure mode — cliff-collapse. The primary observed failure mechanisms were:

1. Dilation and extension of the columnar basalt joints into the intact rock material immediately above and below.

2. Tensile rupture of the trachyte lava breccia near the cliff face.

3. Scattered damage at the interface between the trachyte lava breccia and the columnar basalt above.

These failure mechanisms (particularly numbers 1 and 2) combined to create an extremely unstable zone of heavily damaged rock near the cliff face, leading to cliff-collapse.

Failure Mechanisms and Modes at Redcliffs

In all simulations, at both levels of resolution, the models experienced similar failure mechanisms, which led to the primary failure mode — cliff-collapse. The primary observed failure mechanisms were:

1. Dilation and extension of the columnar basalt joints into the intact rock material immediately above and below.

2. Tensile rupture of the trachyte lava breccia near the cliff face.

3. Tensile failure of the upper breccia layer at the crest of the slope.

4. Scattered damage in the form of tensile and shear wing cracks at the tips of pre-existing fractures in the lower breccia layer.

5. Scattered damage at the interface between the columnar basalt and the breccia above.

These failure mechanisms (particularly numbers 1, 2, and 3) combined to create an extremely unstable zone of heavily damaged rock near the cliff face, leading to cliff-collapse.

Cliff-Collapse in the Low-Resolution Models

When subjected to the February 22, 2011 strong ground motion, the weathered, jointed low-resolution models for Redcliffs (4 unique models) and Richmond Hill (4 unique models) all experienced failure. The resulting depth of failure for the low-resolution Richmond Hill and Redcliffs models are shown in Tables 4.11 and 4.12, respectively. In general, the results from both sites tend to over-estimate the depth of failure when compared to the field observations.

At Richmond Hill, the average of the four unique models overestimated the depth of cliff collapse by a factor of 4.5 in the Basalt Lava and Breccia layer and by a factor of 1.4 in the Trachyte Basalt Breccia Layer. The lower Trachyte Lava experienced no failure either in the field or the models. Three of the four low-resolution models at this site overestimated the

Table 4.11: Richmond Hill low-resolution results. Depth of material loss in meters by layer for each unique model (A, B, C, and D) compared with the range of material loss observed in the field. The models are made unique by changing the random seed, which affects the particle arrangements, and random joint orientations. The average model results overestimate the depth of material loss in all layers by a factor of 1.4 to 4.5.

Layer	**Depth of Material Loss [meters]**					
	A	**B**	**C**	**D**	**Average**	**Field Observations**
1 - Basalt Lava Breccia	10	1	15	10	9	up to 3
2 - Trachyte Lava Breccia	8	5	10	9	8	up to 6
3 - Trachyte Lava	0	0	0	0	0	0

Table 4.12: Redcliffs low-resolution results. Depth of material loss in meters by layer for each unique model (A, B, C, and D) compared with the range of material loss observed in the field. The models are made unique by changing the random seed, which affects the particle arrangements, and random joint orientations. The average model results overestimate the depth of material loss in all layers by factors of three to five.

Layer	**Depth of Material Loss [meters]**					
	A	**B**	**C**	**D**	**Average**	**Field Observations**
1 - Upper Breccia	25	30	30	40	31	up to 6
2 - Basalt Lava	18	20	25	30	23	up to 6
3 - Epiclastics	18	18	18	25	20	up to 6
4 - Lower Breccia	10	12	12	15	12	covered by talus

depth of failure. One of the models had a slightly lower depth of failure than was observed in the field. Figure 4.18 shows the four low-resolution Richmond Hill cliff faces post-failure.

Although the damage is overestimated in general, some of the key features observed at Richmond Hill in the field are present in these results.

- The cliff face collapses leaving a steep post-failure cliff face.

- In some models, overhanging geometry is created by deeper failure in the Trachye Lava Breccia layer than in the Basalt Lava and Breccia layer above. Some of the joints in the upper layer have opened, but the material beneath has not completely failed, resulting in a precarious zone of dilated and damaged rock high on the cliff face (similar to the photograph shown in Figure 4.3).

At the Redcliffs site, the model results overestimated the depth of failure by a factor of about 3 to 5. Figure 4.19 shows the four low-resolution Redcliffs cliff faces post-failure. In some cases, the collapsed cliff face remains fairly high on the model due to the pile up of the basalt columns. This stacking is not realistic and is an artifact of the very high intact strength of the basalt columns, which makes them behave essentially as rigid blocks once they are independent of the slope.

As with the Richmond Hill site, the Redcliffs results, although they overestimate the depth of failure significantly, still capture some of the observed behaviors. Some of the key features observed at Redcliffs in the field and present in the model results include:

- The cliff faces collapsed, leaving a steep post-failure cliff face, where the cliff face is not covered by large talus piles.

- Relatively more material is lost from higher layers resulting in a benched post-failure geometry.

Cliff-Collapse in the High-Resolution Models

When subjected to the February 22, 2011 strong ground motion, the weathered, jointed high-resolution models for Redcliffs (4 unique models) and Richmond Hill (4 unique models) all

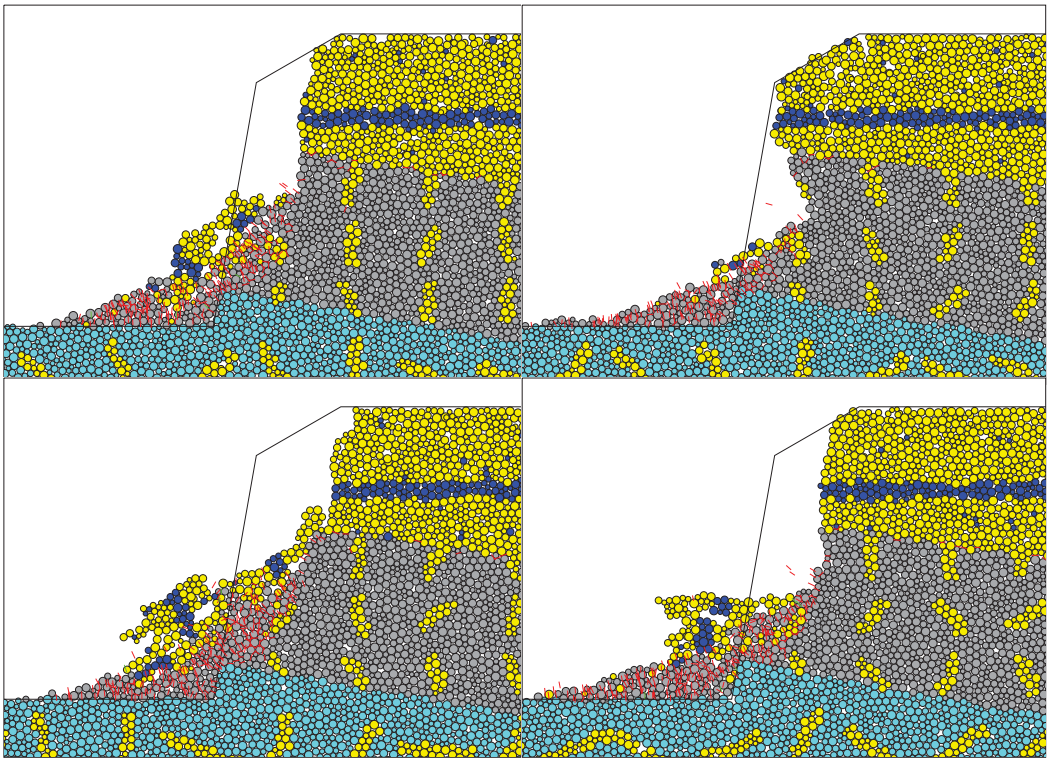

Figure 4.18: Post-shaking state of the four low-resolution models of Richmond Hill In these plots, the particle colors are unchanged from the previous figures (Figures 4.11 through 4.16), however, the red lines now indicate the failure of a parallel bond that has broken in tension. Green lines indicate a shear failure. For reference, the height of the each slope is 60 meters. The four models are identified as A, B, C, and D starting in the upper left and moving clockwise.

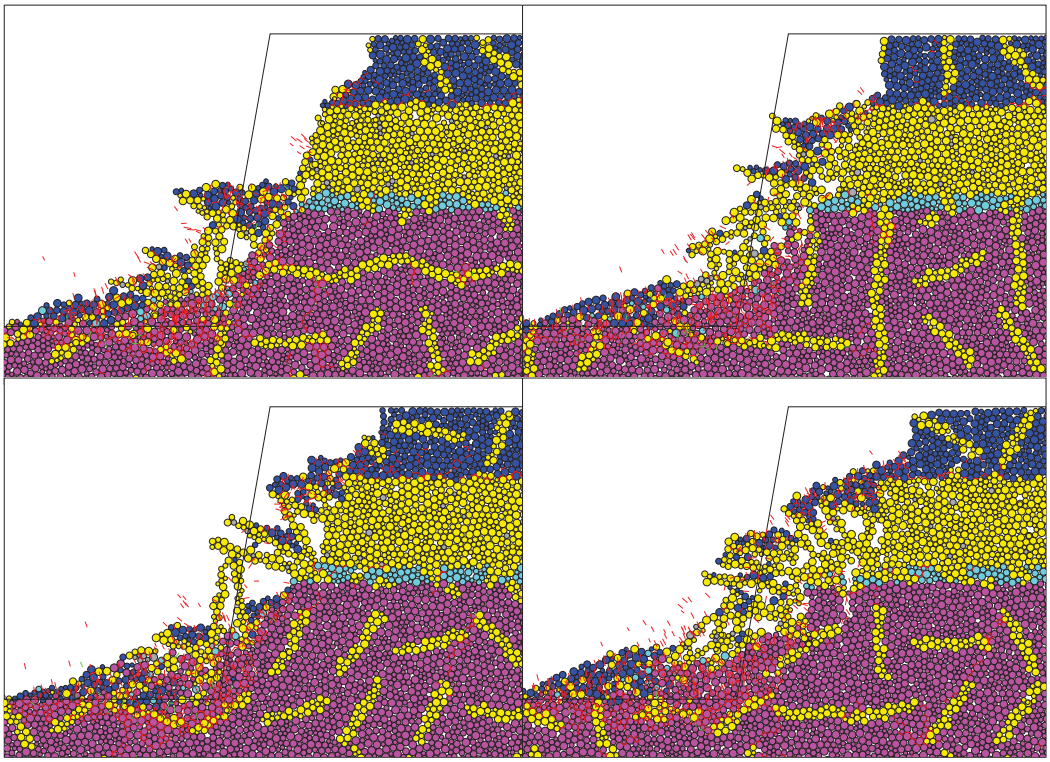

Figure 4.19: Post-shaking state of the four low-resolution models of Redcliffs. In these plots, the particle colors are unchanged from the previous figures (Figures 4.11 through 4.16), however, the red lines now indicate the failure of a parallel bond that has broken in tension. Green lines indicate a shear failure. For reference, the height of the each slope is 80 meters. The four models are identified as A, B, C, and D starting in the upper left and moving clockwise.

experienced failure. The resulting depth of failure for the low-resolution Richmond Hill and Redcliffs models are shown in Tables 4.13 and 4.14, respectively.

The high-resolution Richmond Hill results underestimate the depth of material loss when compared to the field behavior. Figure 4.20 shows the four high-resolution Richmond Hill cliff faces post-failure. The same features observed in common between the low-resolution results and the field behavior are also present in the high-resolution results.

The primary differences between the high- and low-resolution Richmond Hill models (other than the magnitude of material loss) are:

- Relatively little failure due to crack extension of the columnar basalt joints in the high-resolution models, and

- The tensile failures near the cliff face in the trachyte lava breccia occured entirely within the intact rock area, i.e., the pre-existing joints did not directly contribute to the cliff-collapse.

Both of these differences are consistent with the expected behaviors of a model with increased resolution mentioned in Section 4.5 — the intact rock mass strength is lower, and the resistance to crack extension is higher.

The high-resolution Redcliffs model depth of material loss results are generally very similar to the field observations. Figure 4.21 shows the four low-resolution Redcliffs cliff faces post-failure.

The same features observed in common between the low-resolution results and the field behavior are also present in the high-resolution results. The primary difference between the results at different levels of resolution is the magnitude of material loss.

Table 4.13: Richmond Hill high resolution results. Depth of material loss in meters by layer for each unique model (A, B, C, and D) compared with the range of material loss observed in the field. The models are made unique by changing the random seed, which affects the particle arrangements, and random joint orientations. The results for the high resolution versions of the Richmond Hill model underestimate the depth of material loss.

Layer	**Depth of Material Loss [meters]**					
	A	**B**	**C**	**D**	**Average**	**Field Observations**
1 - Basalt Lava Breccia	0	0	1	0	0.25	up to 3
2 - Trachyte Lava Breccia	1	4	2	2	2.25	up to 6
3 - Trachyte Lava	0	0	0	0	0	0

Table 4.14: Redcliffs high resolution results. Depth of material loss in meters by layer for each unique model (A, B, C, and D) compared with the range of material loss observed in the field. The models are made unique by changing the random seed, which affects the particle arrangements, and random joint orientations. The results for the high resolution versions of the Redcliffs model are comparable in magnitude to the observed field behavior.

Layer	**Depth of Material Loss [meters]**					
	A	**B**	**C**	**D**	**Average**	**Field Observations**
1 - Upper Breccia	10	10	12	8	10	up to 6
2 - Basalt Lava	6	4	6	5	6.5	up to 6
3 - Epiclastics	6	4	6	6	5.5	up to 6
4 - Lower Breccia	6	4	6	4	5	covered by talus

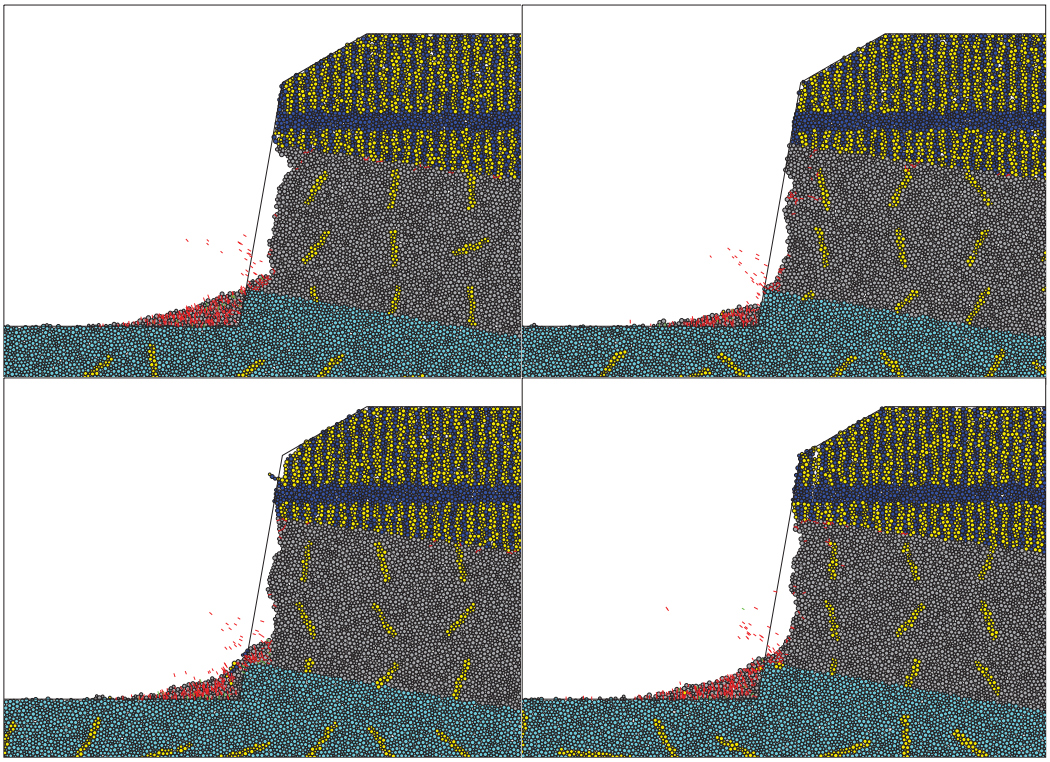

Figure 4.20: Post-shaking state of the four high-resolution models of Richmond Hill The red lines indicate the failure of a parallel bond that has broken in tension. Green lines indicate a shear failure. For reference, the height of the each slope is 60 meters. The four models are identified as A, B, C, and D starting in the upper left and moving clockwise.

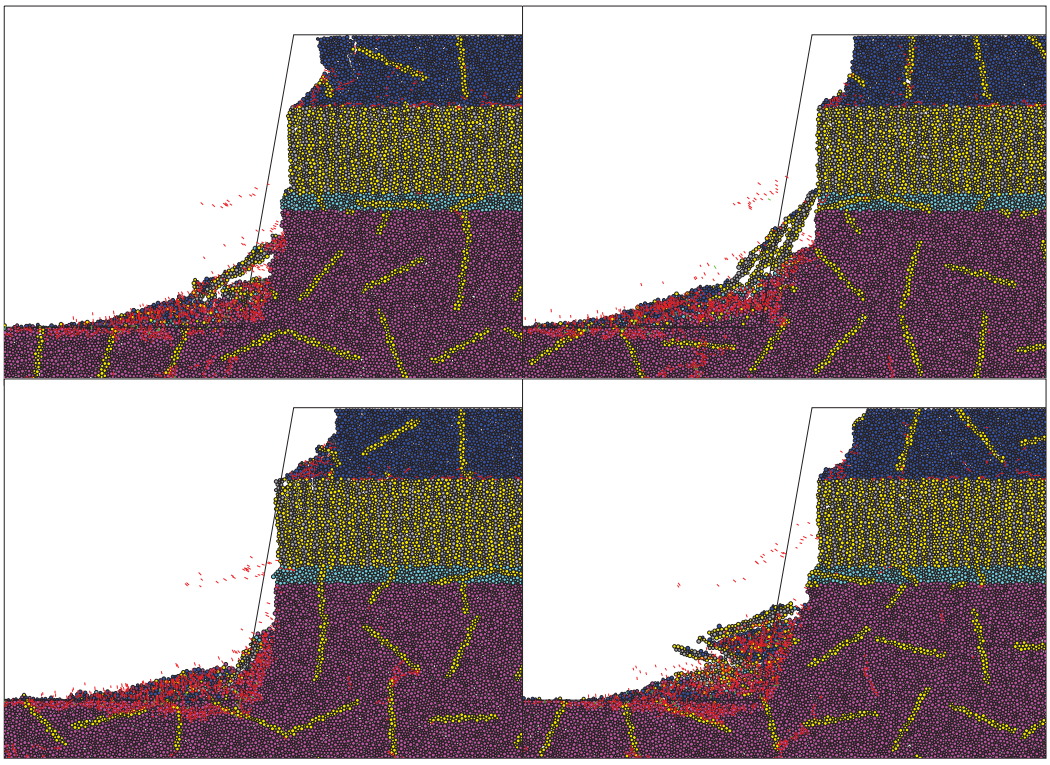

Figure 4.21: Post-shaking state of the four high-resolution models of Redcliffs. The red lines indicate the failure of a parallel bond that has broken in tension. Green lines indicate a shear failure. For reference, the height of the each slope is 80 meters. The four models are identified as A, B, C, and D starting in the upper left and moving clockwise.

4.6.4 Cliff Top Displacment

The PFC models (at either level of resolution) do not predict the cliff top displacement that were observed in the field at both sites. Figures 4.22 and 4.22 show the post-earthquake cliff top displacements for the Richmond Hill and Redcliffs models, respectively, at both levels of resolution. The PFC results are obtained by taking the average particle displacements from 20m wide, 10m deep bins along the top of the cliff. The results in Figures 4.22 and 4.23 essentially tell the same story: the BPM models are not capturing the cliff-top displacement well, and the high-resolution results are further removed from the field observations than the low-resolution results. In the low-resolution model results, the cliff top displacement is underestimated until about 40 meters from the original cliff edge. In the 40 meters closest to the original cliff edge, the displacements become large and erratic. This is due to the nearly-collapsed material displacements near to the cliff edge. In the higher resolution models, the model cliff top displacements are an order of magnitude smaller than the observed displacements and the low-resolution model displacements.

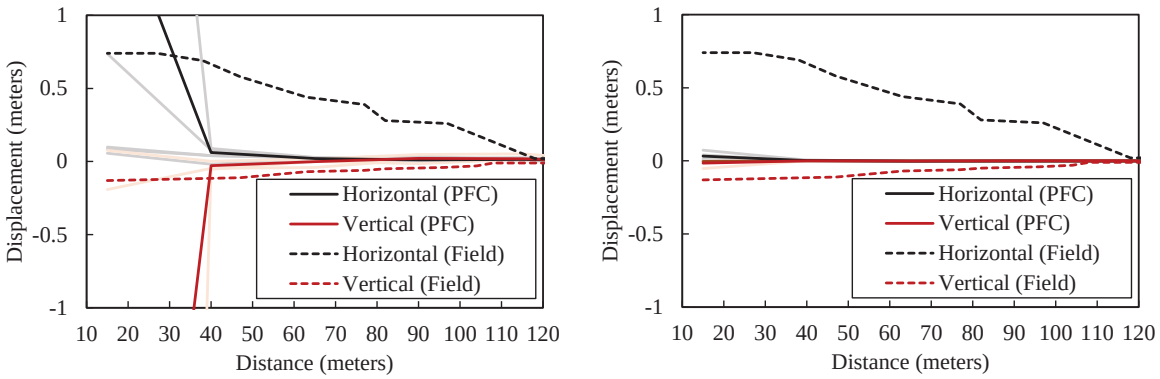

(a) Low resolution model

(b) High resolution model

Figure 4.22: Cliff-top displacement from PFC simulations of the Richmond Hill site compared with the measured displacements in the field. The results for individual simulations are lightly shaded and the average horizontal and vertical displacements are shown in black and red solid lines, respectively. The observed horizontal and vertical field displacements are shown in dashed black and red lines, respectively. The low resolution model results (4.22a) and the high resolution model results (4.22b) both show a different displacement pattern than the observed behavior.

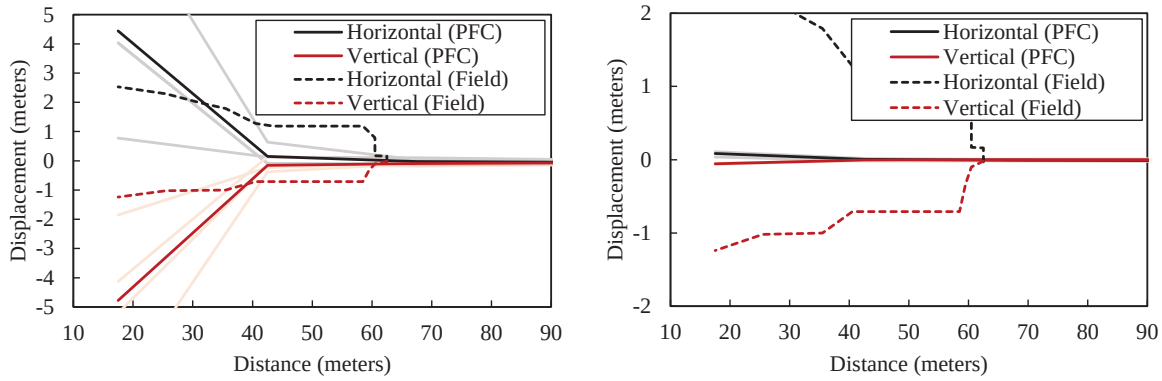

(a) Low resolution model

(b) High resolution model

Figure 4.23: Cliff-top displacement from PFC simulations of the Redcliffs site compared with the measured displacements in the field. The results for individual simulations are lightly shaded and the average horizontal and vertical displacements are shown in black and red solid lines, respectively. The observed horizontal and vertical field displacements are shown in dashed black and red lines, respectively. The low resolution model results (4.23a) and the high resolution model results (4.23b) both show a different displacement pattern than the observed behavior.

4.7 Discussion

4.7.1 Geologic Detail in the Models

The level of geologic detail in the models is a limiting factor on the ability of the model to replicate the field behavior. For example, the columnar zones are known not to be constant in a given layer. At the Richmond Hill site, the columnar jointing in the "Basalt Lava and Breccia" layer is limited in its lateral extents –only the Basalt Lava portion is columnar; the breccia is not. The two material types are intermixed within the layer, and the extent of each material type within the layer is unknown. So even in a cliff with a fairly two-dimensional profile, the internal geologic detail may be inherently three-dimensional. At the Redcliffs site, during one of the failure episodes, a columnar basalt section completely detached from the cliff-face, leaving a non-structured breccia exposed behind it. These known features are not incorporated into these BPM models. As a result, the columnar layers in models, which had very high intact rock strengths, may have over estimated the overall stability of the slopes, particularly in the Richmond Hill slope, where the columnar joints were non-continuous within the layer. This overestimation in strength is a likely cause for the models' inability to capture the cliff-top displacement observed in the field. A better match between the field and model behaviors would be possible by adjusting these properties, however, the goals of this modeling effort were to determine how well the BPM model could be used as a predictive tool, rather than to iterate material properties to find the closest possible match between model and field behavior.

Additionally, the configuration of the columnar joints on the Richmond Hill Models is not very realistic. Although the joints in this layer were non-continuous in the field, the perfectly horizontal zone of intact basalt between joints is not realistic and should have been modeled differently. As mentioned in Section 4.5, building a more realistic and randomized fracture network is difficult in two dimensions because it can easily create undesirable discrete rock blocks. The consistency of the results between the four randomized slopes within each slope set indicates that although the fracture network was very simple, the level of geologic detail in the models provides a reasonable approximation of some sections of the real slope in two dimensions.

4.7.2 Effects of Resolution on Cliff Collapse

Changing the resolution of a jointed BPM model can change the model's behavior, even when the calibrated strength and stiffness is the same. The changes in behavior observed in these two sites are 1) the intact rock material is more susceptible to damage in the higher-resolution models, and 2) the pre-existing joints have a smaller influence on the high-resolution models.

The apparent weakening of the intact rock mass at higher resolutions was made evident by the damage in the high-resolution Richmond Hill models. Most of the damage in these models was not associated with crack extension, and simply involved tensile rupture of intact rock material at the cliff face. In the low-resolution models, the pre-existing joints were directly responsible for most of the failure in the mode. When pre-existing joints were not present in the low-resolution models, only one of the four models experienced any failure at all.

The apparently reduced influence of pre-existing cracks at higher resolutions in the model is due to the difference in nominal and effective crack lengths at different model resolutions. The nominal crack length is the length within the model where bonds are deleted, and smooth-joint contacts are installed. The effective crack extends from the nominal crack tip to the nearest bond. The potential length of this effective extension ranges from zero to twice the particle radius. In these models, for a crack with a nominal length of 10 meters, whose ends are both contained within the model, the effective crack length could be as high as 13.6 meters in the low-resolution models and 11.8 meters in the high-resolution models. The higher effective crack length in the low-resolution models results in higher average stress intensity than the high-resolution models. Longer crack lengths and shorter crack bridges could result in up to a 20 percent increase in stress intensity in the low-resolution models, leading to more failures in crack extension.

Fakhimi and Garahbagh (2011) [79] discuss the idea of representative elemental volume (REV) in BPM with respect to particle resolution. The particle resolution needed to create an REV varies by the parameters of interest. For example, a relatively small REV is required to produce a consistent Young's modulus between randomized BPM samples. They note

that the crack initiation stresses require the largest REV to obtain consistent results. They further state that there may not be a single appropriate REV for consistent crack initiation stresses. This is a topic for future research.

For the current study, the model high and low resolutions are both considered to be appropriate because of the consistent model behavior at each level of resolution. The differences between the behavior of the two sets of models at different resolutions confirm that the REV for crack initiation has not been met .Although the ideal REV has not been met, as expected, the model results are consistent enough that probably either resolution could be made to replicate the field depth of failure given the proper joint properties.

4.7.3 Cliff-Top Displacement in BPM

The fact that the cliff top displacement results get worse (further from the observed field behavior) at higher resolutions indicate that the model is not capturing the physical mechanisms responsible for the cliff-top displacements observed at the sites. Capturing post-peak displacements in DEM can be challenging. When smaller displacements are observed at higher resolution models, it indicates that the displacements are due to the loss of stiffness at contacts where bonds have broken. The contact stiffness being much smaller than the bond stiffness, a broken bond results in an instantaneous local reduction in stiffness. The stiffness reduction is proportional to the particle radius, so lower resolution models accumulate more displacements than higher resolution models due to broken bonds.

BPM models are well-suited to model the evolution of cracks and the development of failure surfaces but are not well-suited to predict displacements along failure surface that are not pre-defined. The relatively large particle sizes and dense packing structure results in extremely dilative frictional behavior that essentially restricts sliding. Particles can sometimes more easily be sheared off than slide over one another. Sliding can then occur after several layers of particle get sheared off near the failure surface, creating a failure band, where particles are free to roll and slide relative to one another.

It is not entirely clear how much of the cliff top displacement that was observed in the field was due to slumping of the loess that tops the slops and how much is due to damage

to the rock-mass. GNS Science has concluded, however, that not all of the displacement can be attributed to the loess because the magnitude of vertical displacement along the cliff top is not consistent with the inclination of the interface between the loess and the rock below. This is one area where the simplified models are prohibiting a full representation of the actual behavior in the field.

There are a number of possibilities for why the observed cliff-top displacement was not captured in PFC. It could be that the discrete nature of the particulate BPM does not allow for the post-failure displacements at the resolution used in these models. It is also possible that a significant portion of the observed cliff-top displacement is a result of deformation in the loess on the top of the slope. The variability of the geologic layers in the actual slopes which may allow for more deformation than the over-simplified PFC cross sections may also contribute to this discrepancy. In all likelihood, all of these factors contribute to the difference between the observed and the modeled behavior.

4.8 Conclusions

The seismically-induced cliff collapse observed throughout the Port Hills area during the Canterbury Earthquake Sequence cannot be adequately evaluated with traditional rock-slope analysis methods because of the complex nature of joint structure, weathering, and dynamic stresses. Using a fully dynamic bonded particle model, the cliff-collapse at two Port Hills sites was successfully modeled. Several features of the rock-slope failures induced during the CES were captured by the model including:

1. a relatively shallow cliff-collapse failure mode,
2. different levels of material loss from different geologic units,
3. overhanging and benched geometries created on rock-slope faces, and
4. newly formed and/or dilated cracks near the post-failure cliff face.

The model results indicate that these collapses were due to a combination of weathering, fractures, and dynamic stress conversions near the slope face.The PFC model was unable to capture the cliff top displacement at the level of resolution used. This indicates that

although BPM is a powerful tool, it may only be appropriate for use as a supplement to, rather than a replacement for, traditional methods. The fact that the results from traditional methods employed by GNS were fairly successful where the BPM models were not, and vice versa, provides a strong argument for using multiple methods of evaluation

By observing the failure mechanisms that lead to the cliff-collapse in the models, we have an indication of the mechanisms that likely contributed to the field behavior. Based on the tensile stresses observed near the cliff face in the weathered zone, and the increases in damage due to extension of pre-existing fractures, it appears that a combination of dynamic stresses at the cliff face, weathering, and pre-existing fractures all contributed to the observed cliff-collapse in the Port Hills during the Canterbury Earthquake Sequence.

PART II: FURTHER TESTING THE REDCLIFFS SITE UNDER VARIED LOADING CONDITIONS

4.9 Further Testing of the Redcliffs Model

Having shown that the developed PFC model is capable of replicating some field behavior (cliff-collapse), and understanding that it was unable, at its current level of resolution and geologic, to replicate others (cliff top displacement), this section will present further analysis of the high-resolution Redcliffs site model and a variant of that model. The variant slope will have the same height and slope angle as the Redcliffs models, but with different internal features and material properties.

These additional simulations are designed to address the following questions:

- Is cliff-collapse a strictly short-duration feature? In other words, with long-duration ground motions, will a deeper failure surface develop leading to a massive runout scenario where the observed cliff-collapse would be erased?

- Since a combination of weathering and pre-existing fractures were responsible for cliff-collapse in the model, will the cliff stop collapsing after the weathered material has been shed from the slope, or will cliff-collapse continue?

- What effect does loading frequency have on the behavior of the slope in terms of failure modes and levels of damage within the slope?

- To what extent are the pre-existing fractures in the layers influencing the slope behavior? Certainly in the columnar basalt layer, which has an intact rock strength an order of magnitude larger than the other materials, the pre-existing joints are having a strong effect. But what about the weaker layers? Could they be approximated with layers with no pre-existing joints, but a reduced intact rock strength?

When using the developed model to address these questions, it is important to remember that the model has been unable to replicate cliff top displacement as observed in the

field. Since the observed cliff top displacement has been at least partially attributed to the development of some deep-seated failure, it's reasonable to assume that the model is under-representing the potential for deep-seated failure. Therefore, a lack of deep-seated failure in long-duration simulations is not a solid indication that Redcliffs will not develop such a failure mode in future seismic events. As stated above, the traditional methods used by GNS should be used in conjunction with the BPM model to make that kind of prediction. On the other hand, if the BPM model does show the development of a deep-seated failure surface, and the GNS models show the same thing, that would indicate that the observed cliff-collapse was a feature of short-duration loading.

4.10 Model Details

The models used to address the questions above are separated into two categories: Model Set A, and Model B. The two categories are described below:

- **Model Set A**: These models are unchanged from the high-resolution Redcliffs slope models presented in Section 4.5. There are four Redcliffs models in Model Set A, each made unique by varying the random seed, which affects particle arrangement and joint orientations. They contain four geologic layers, each with its own rock-mass strength, shear wave velocity, and pre-existing joint sets.

  The natural frequencies of the models in this set fall within a narrow range as shown in Table 4.15. Natural frequencies were determined by the frequency associated with the maximum Fourier amplitude of the acceleration response of the slope to a frequency sweep.

- **Model B**: This model is similar to the models in Model Set A, but the jointing in all layers except the columnar basalt have the joints removed. The intact rock strength in all layers except the columnar basalt layer was set to the lower bound estimates (roughly half of the average estimates) of the lower breccia layer. Based on the modeling performed by GNSm, using the lower bound estimates for strength without random joints is expected to result in a model that has roughly the same

stability as those in Model Set A. Only one version of Model B was generated because, without the random joints, the variation in behavior with random seed is expected to be minimal. The natural frequency of Model B is 1.4 Hz.

4.11 Ground Motion Details

A series of constant peak velocity (v_{max}) sine motions were run through the models described above. Frequencies of 0.5 Hz, 1 Hz, 2 Hz, 3 Hz, and 5 Hz were used. The tuning ratio –the ratio of the input signal frequency to the natural frequency of the slope– will be used to address the effects of frequency on the slopes. The v_{max} of the sine waves was held constant (after an initial ramping period of 1 second) at 0.78 m/s, which was roughly the v_{max} of the February 22, 2011 strong ground motion used on the Redcliffs slopes.

The ground motions were run for 20 seconds to allow for continued failure and multiple failure events.

The peak acceleration, a_{max}, of the sine motion suite varies with frequency as follows:

- 0.5 Hz loading: $a_{max} = 0.25$ g
- 1.0 Hz loading: $a_{max} = 0.5$ g
- 2.0 Hz loading: $a_{max} = 1.0$ g
- 3.0 Hz loading: $a_{max} = 1.5$ g
- 5.0 Hz loading: $a_{max} = 2.5$ g

Table 4.15: Natural frequency of models in Model Set A

Model Number	Natural Frequency, Hz
A.1	1.1
A.2	1.1
A.3	1.2
A.4	1.0

The reason that constant v_{max} motions were used (as opposed to constant a_{max}) is that, for the range of frequencies tested, the ranges of displacement with constant a_{max} motions would be unrealistically large. After the initiation of failure, high displacement motions can cause severe damage to the model, making the results meaningless within a few cycles of motion after failure. Also, because shear stresses induced by ground motion are directly proportional to particle velocity, and cliff-collapse appears to be closely related to dynamic stresses, a constant v_{max} motion suite is expected to provide the most appropriate points of comparison for these simulations. The BPM models are not significantly different than structural models in that they are an assembly of masses and springs of finite strength. Research by Song and Heaton [80] shows that PGV and PGD are better predictors of damage in structures than PGA.

4.12 Results

The following sections describe the results of the constant v_{max} sine motions on Model Set A and Model B.

4.12.1 Model Set A results

Failure Mechanisms and Modes in Model Set A

When subjected to the sine motions, all of the Model Set A models showed a similar failure behavior to the simulations of the Feb. 22, 2011 event. One additional failure mechanism (shown in **bold** below) was observed at some loading frequencies. The primary observed failure mechanisms were:

1. Scattered damage in the form of tensile and shear wing cracks at the tips of pre-existing fractures in the lower breccia layer.

2. Dilation of the columnar basalt joints resulting in damage in the rock layers immediately above and below.

3. Tensile failure of the upper breccia layer at the crest of the slope.

4. **Crushing of intact rock material at the toe of the slope (observed at some loading frequencies).**

Table 4.16 shows the failure mechanisms observed in the models for each loading frequency.

Table 4.16: Observed failure mechanisms in the Model Set A slopes under long-duration sine loading.

Loading Frequency	**Wing cracks in lower breccia**	**Dilation of basalt columns**	**Tensile failure in upper breccia**	**Crushing at the toe**
0.5 Hz	–	√	√	–
1 Hz	√	√	√	√
2 Hz	√	√	√	√
3 Hz	√	√	√	√
5 Hz	√	√	√	–

In all loading cased, the damage induced by strong ground motion results in cliff-collapse. With repeated cycles of shaking, some of the models experienced repeated failure. In some cases, however, the debris from the collapses created talus piles large enough to buttress the slope from further collapse. At all loading frequencies except for 5 Hz, the slopes experienced toppling of the basalt columns after the initial cliff-collapse.

Model A.3 Failure Sequence Example

Figure 4.24 shows the sequential failure of Model A.3 subjected to 20 seconds of strong shaking at 2 Hz.

Fracture initiates with crack extension and coalescence in the lower breccia and some damage at the interface between the upper breccia and the columnar basalt layer at t = 1.03s. The damage to in the upper breccia layer increases and is concentrated near the

crest. By t = 4.13s, rock has begun to fall from the crest, and some collapse at the cliff face near the toe is apparent. As damage continues to accrue in the model, the collapse of material at the cliff face deepens, and some of the columnar basalt joints collapse without the underlying support (t = 11.2s). The material at the crest has already fallen from the cliff at this point, and toppling of material behind the crest can be observed. At t = 20s, the damage of material in the lower breccia has progressed deeper into the slope, and another collapse of the columnar basalt material above has occurred.

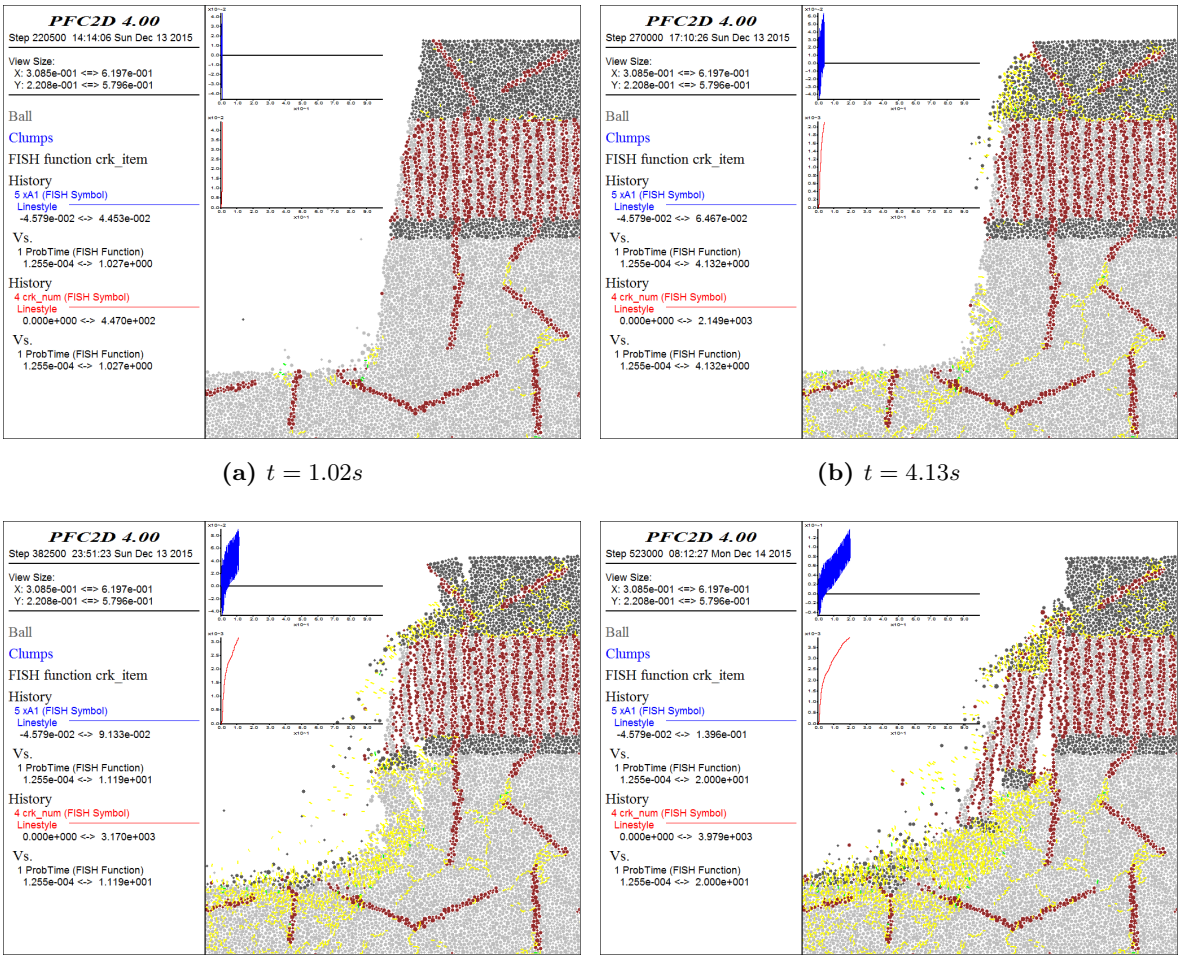

(a) $t = 1.02s$ **(b)** $t = 4.13s$

(c) $t = 11.2s$ **(d)** $t = 20.0s$

Figure 4.24: Failure sequence of Model A.3 subjected to 20 seconds of strong shaking at 2 Hz.

Cliff-collapse in Model Set A

All models showed the cliff-collapse failure mode, however, the depth of cliff-collapse was frequency dependent. Figures 4.25 through 4.29 show the Model Set A models after 20 seconds of strong shaking for the different loading frequencies applied to the slopes. The greatest depths of cliff-collapse occurred closest to the natural frequency of the slope, as shown in Figure 4.30, which shows the depth of failure for each model for each loading. In general, the four models show the same trend of reduced levels of damage above and below a tuning ratio of one indicating a strong influence from the dynamic response of the model. Model A.1 is an outlier in terms of the shape of the trend, which shows a plateau in the tuning ratio range of about one to three. This plateau is caused by the random placement of a pre-existing joint in the lower breccia layer in Model A.1. The crack that caused the plateau in the Model A.1 trend is pointed out as a "pre-existing crack of interest" in Figure 4.25. When the intact rock material near the tip of this crack was damaged by crushing at the toe of the slope, sliding along the crack was enabled, and a deep cliff-collapse was observed. As is evident by the shape of the plateau, the 1 Hz, 2 Hz, and 3 Hz motions resulted in damage which activated sliding along the crack, while the 0.5 Hz and 5 Hz motions did not. This is consistent with the loading frequencies that resulted in crushing at the toe as shown in Table 4.16.

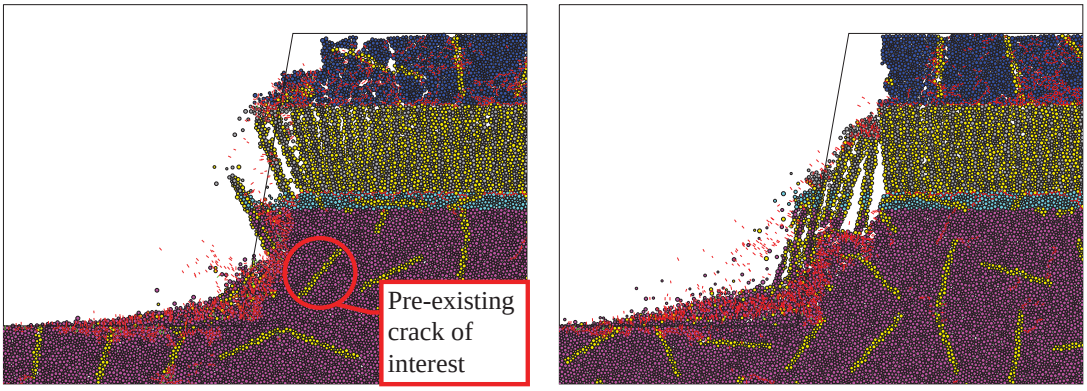

Model A.1

Model A.2

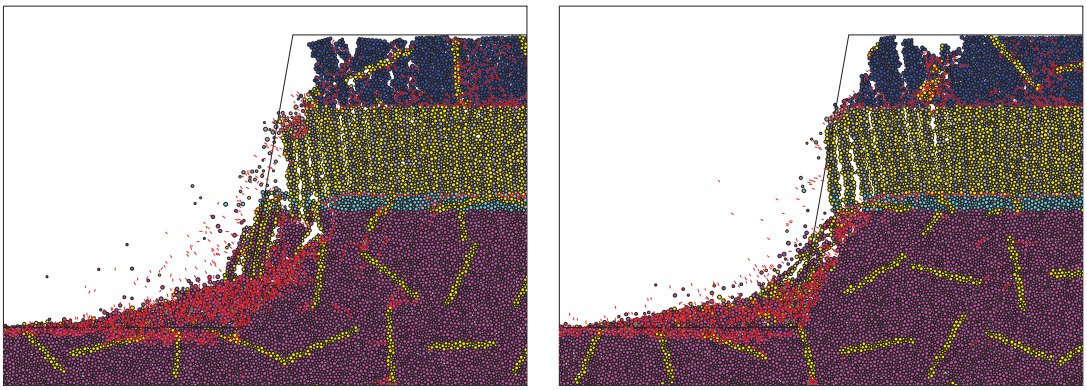

Model A.3

Model A.4

Figure 4.25: Post-shaking state of Model Set A after 20 seconds of strong shaking at 0.5 Hz. A crack of interest is called out on Model A.1. Sliding on this crack resulted in relatively deep failures at other loading frequencies. For reference, the height of the each slope is 80 meters.

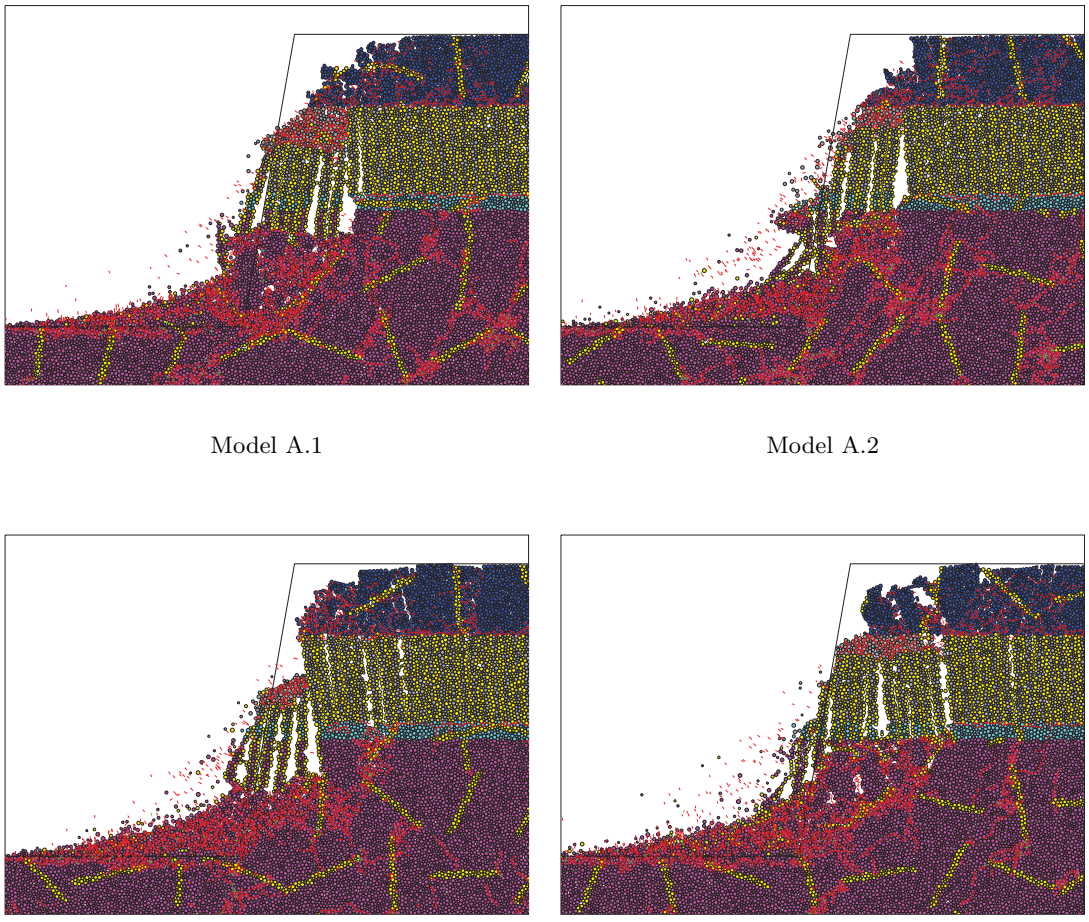

Model A.1 Model A.2

Model A.3 Model A.4

Figure 4.26: Post-shaking state of Model Set A after 20 seconds of strong shaking at 1 Hz. For reference, the height of the each slope is 80 meters.

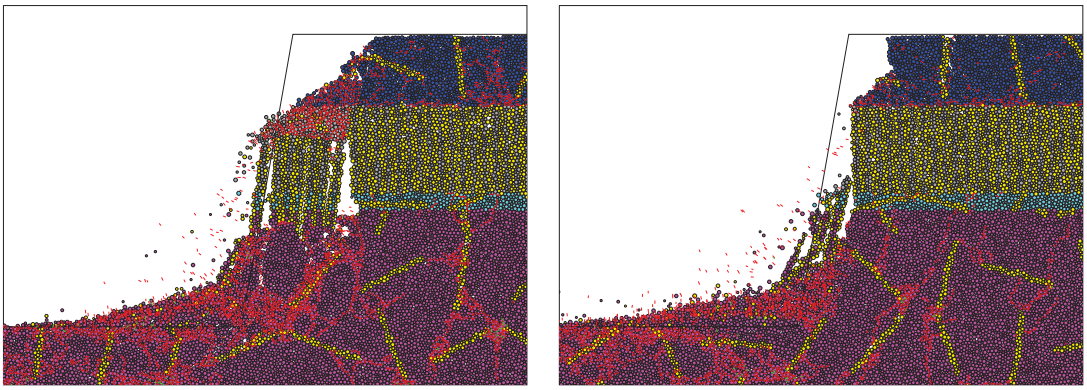

Model A.1

Model A.2

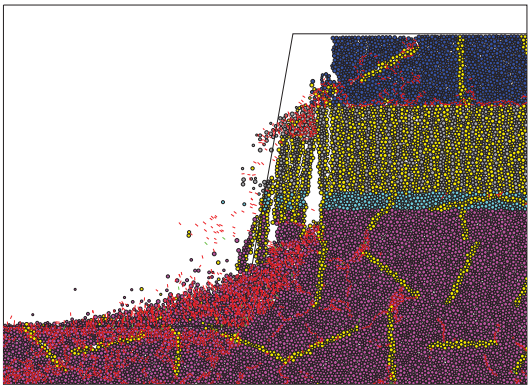

Model A.3

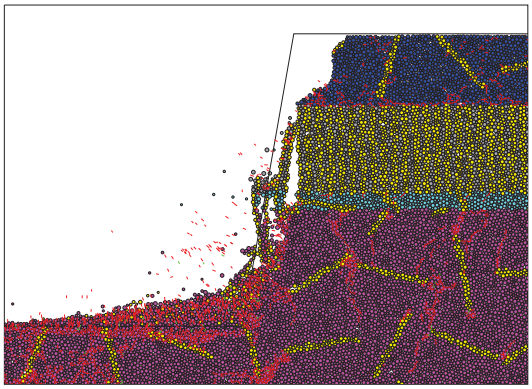

Model A.4

Figure 4.27: Post-shaking state of Model Set A after 20 seconds of strong shaking at 2 Hz. For reference, the height of the each slope is 80 meters.

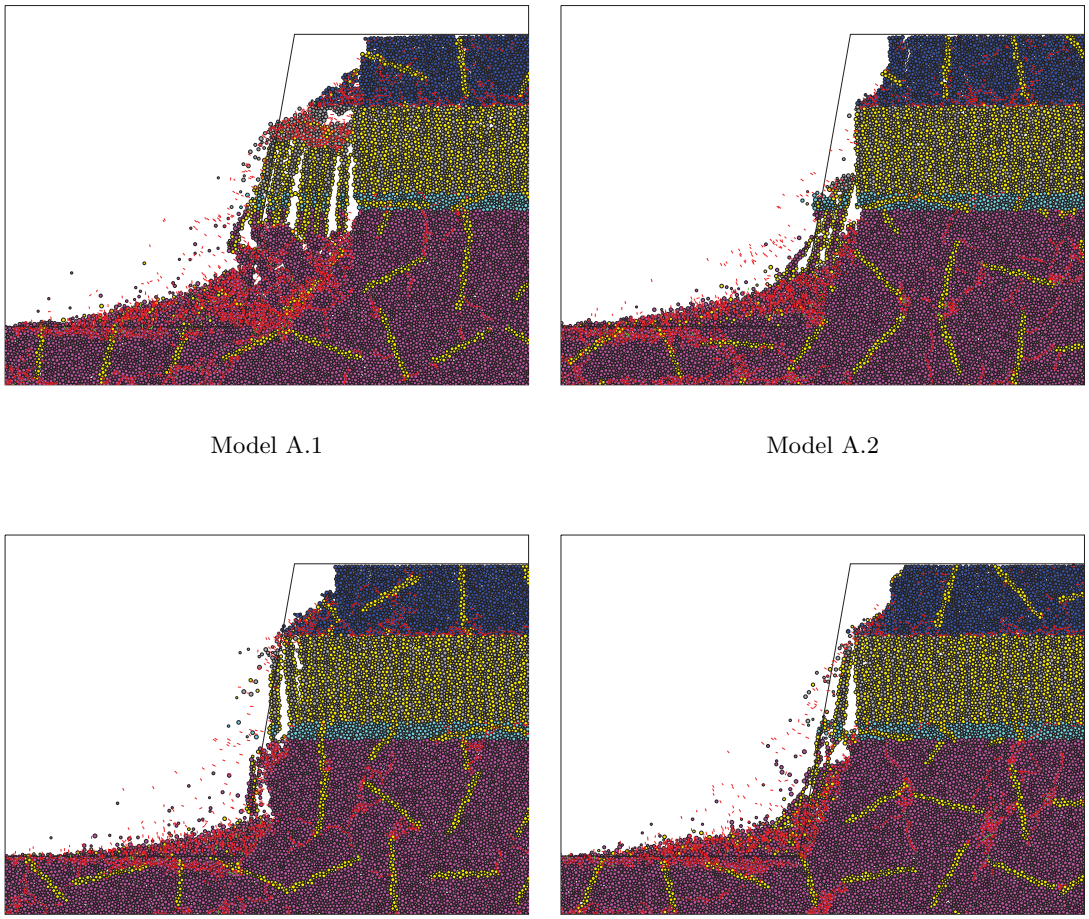

Model A.1 Model A.2

Model A.3 Model A.4

Figure 4.28: Post-shaking state of Model Set A after 20 seconds of strong shaking at 3 Hz. For reference, the height of the each slope is 80 meters.

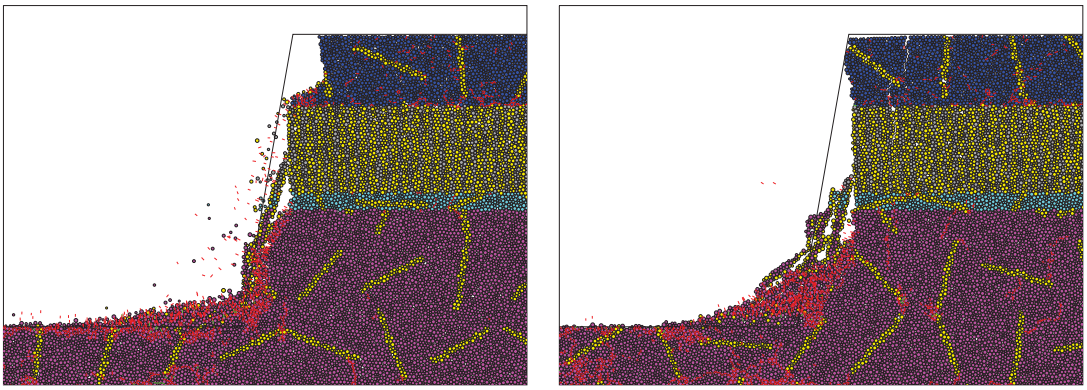

Model A.1

Model A.2

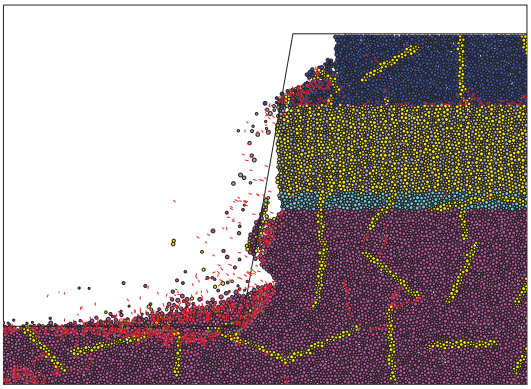

Model A.3

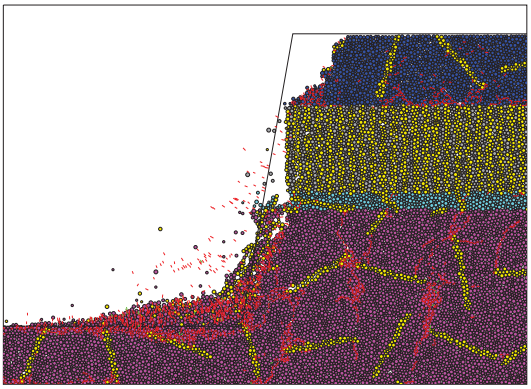

Model A.4

Figure 4.29: Post-shaking state of Model Set A after 20 seconds of strong shaking at 5 Hz. For reference, the height of the each slope is 80 meters.

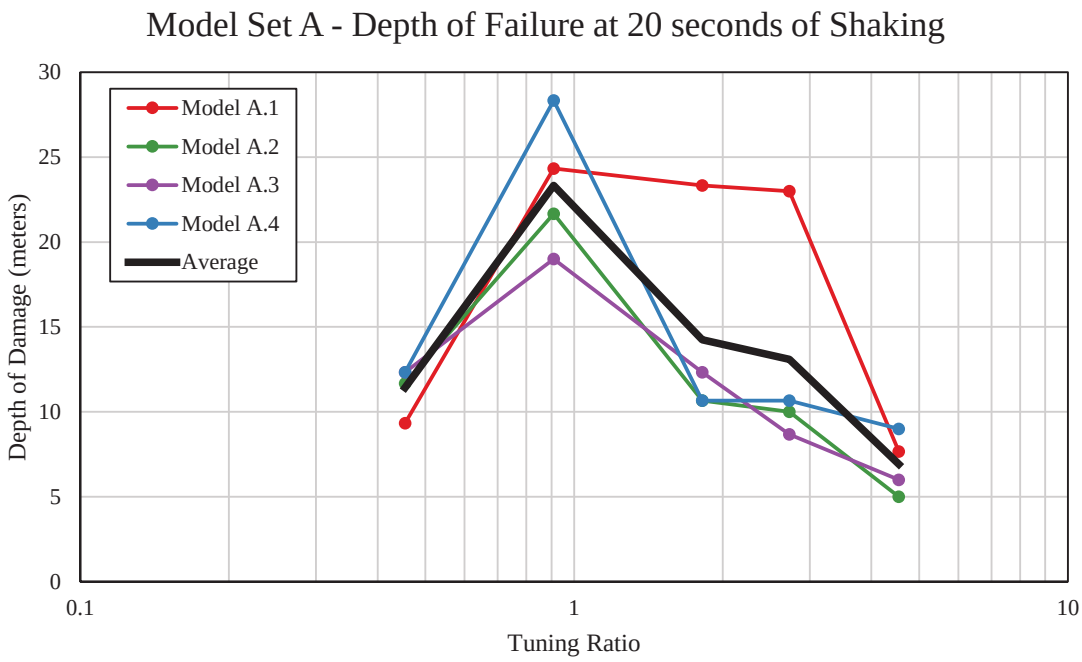

Figure 4.30: Depth of cliff-collapse failure in Model Set A (Redcliffs) with tuning ratio. The four models in the set follow the same general trend with the exception of Model A.1, where a pre-existing joint allowed deeper failure at higher tuning ratios.

Levels of damage in Model Set A

Another way to represent the damage in the in the models due to strong ground motion is the number of bonds broken in the model. Figure 4.31 shows the number of broken bonds for the four models in Model Set A with tuning ratio. The trend is similar to, but more smoothed than the depth of damage with tuning ratio trend shown in Figure 4.30. The plateau of failure depth in Model A.1 is visible as a slightly raised portion of the number of broken bonds in Model A.1 above a tuning ratio of one. The number of broken bonds has two main advantages as a damage index over the depth of damage. First, it includes the damage in the slope that did not result in a global, large-runout failure. Damage in the portion of the slope that remains standing after strong ground motion indicates the susceptibility of the slope to future failure and accelerated weathering. Second, it allows for general comparison between slopes that may not have the same failure mode, where a measured depth of cliff-collapse may have little or no meaning.

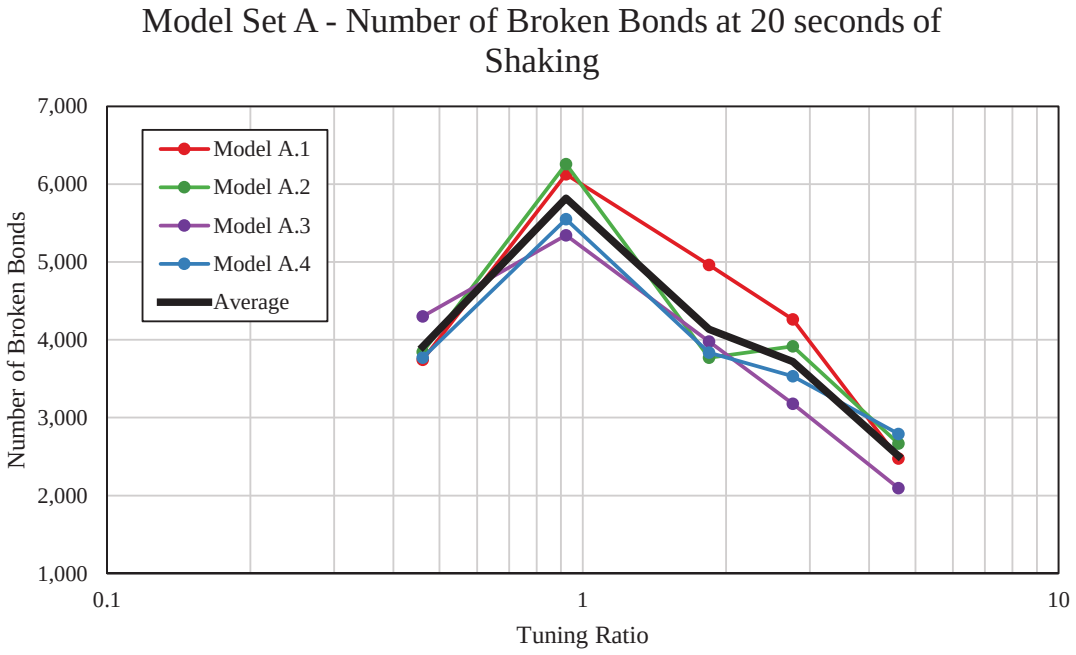

Figure 4.31: Number of broken bonds in Model Set A (Redcliffs) with tuning ratio. The four models in the set follow the same general trend with a well-defined peak at a tuning ratio of one.

4.12.2 Model B results

Failure Mechanisms and Modes in Model B

Model B experienced some different failure mechanisms than Model Set A when subjected to the sine motions. The observed failure mechanisms were:

1. Tensile failure of the upper breccia layer at the crest of the slope.
2. Flexural failure of basalt columns at the interface above and below the columnar basalt.
3. Crushing of intact rock material at the toe.
4. Wedge failure between the toe of the slope to the base of the columnar basalt.

Table 4.17 shows the failure mechanisms observed at each loading frequency.

Table 4.17: Observed failure mechanisms in Model B under long-duration sine loading.

Loading Frequency	**Tensile failure in upper breccia**	**Flexural failure of basalt columns**	**Crushing at the toe**	**Wedge failure**
0.5 Hz	√	√	–	–
1 Hz	√	√	–	–
2 Hz	√	–	√	–
3 Hz	√	–	√	√
5 Hz	√	–	√	√

Because of the different failure mechanisms observed in Model B, a true cliff-collapse mode was not observed in all the simulations. Cliff-collapse, resulting from loss of support in the lower portion of the slope due to the crushing of material and wedge failure near the toe, was observed in the 2 Hz, 3 Hz, and 5 Hz simulations. In the 0.5 Hz and 1 Hz loading

simulations, where the failures in the lower portion of the slope were not observed, toppling of the columnar basalt was the primary failure mode.

Levels of damage in Model B

The post-shaking condition of Model B is shown in Figure 4.32. The number of broken bonds in Model B under different tuning ratios is shown in Figure 4.33. The average trend of the Model Set A results is also shown for comparison. The figure shows nearly the opposite trend in damage with tuning ratio as the results from Model Set A.

These results are surprising initially. However, they are consistent with the observed failure mechanisms. Toppling, which is the primary mode of failure in the 0.5 Hz and 1 Hz simulations, is known to most sensitive to low-frequency input, regardless of natural frequency as described by Gibson (2015), and confirmed by further dynamic BPM results presented in Chapter 6. The wedge failures, which lead to cliff-collapse in the 2 Hz, 3 Hz, and 5 Hz simulations, occurred in the lower portion of the slope beneath the columnar basalt. Using the empirical slope frequency formula $f_n = \frac{V_s}{5H}$, setting H equal to the height of the lowest layer (33 meters), and setting V_s equal to the shear wave velocity of the lowest layer (700 $\frac{m}{s}$), the natural frequency of the layer were the wedge failure occurred is around 4.25 Hz.

The main failure mechanisms (those that caused the majority of the damage) were different across the range of frequencies in the sine motion suite. If the results are viewed in terms of their main failure mechanisms, the observed frequency-dependent behavior seems very reasonable. The primary failure mechanism in the 0.5 Hz and 1 Hz motions is the interface failures above and below the columnar basalt leading to toppling. The primary failure mechanism in the 2 Hz, 3 Hz, and 5 Hz motion are the crushing at the toe and the wedge failures in the lower portion of the slope, leading to cliff-collapse. The full extent of the excitation of the lower breccia layer was not studied, however, the damage trend for the 2 Hz, 3 Hz, and 5 Hz motions shown in Figure 4.33 indicates that the natural frequency of the layer where the main failure mechanism occurs, rather than the natural frequency of the entire slope may be driving the behavior.

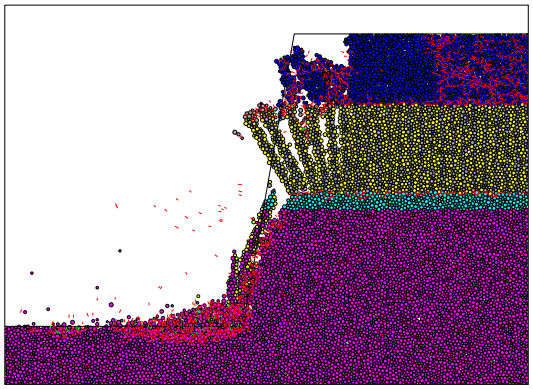

Loading Frequency: 0.5 Hz

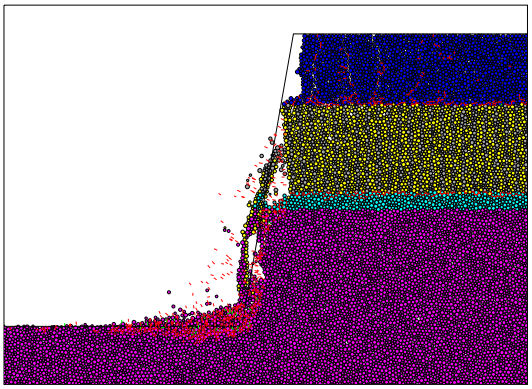

Loading Frequency: 1 Hz

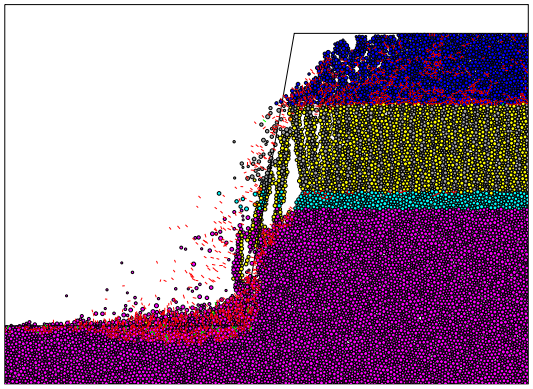

Loading Frequency: 2 Hz

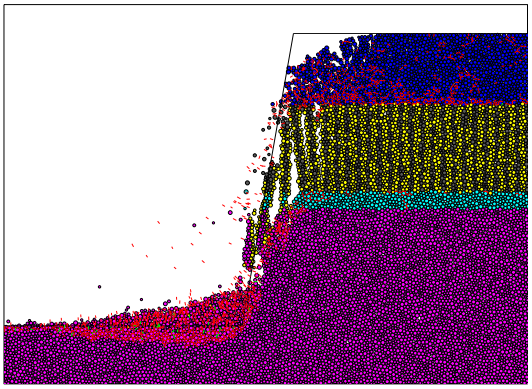

Loading Frequency: 3 Hz

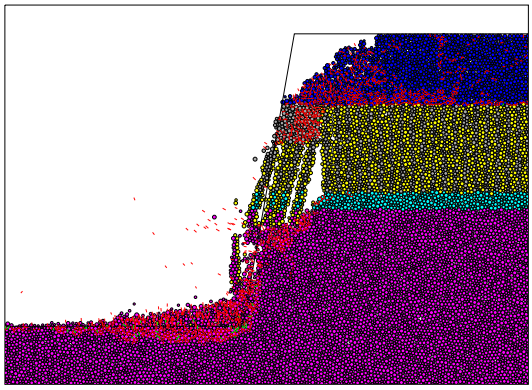

Loading Frequency: 5 Hz

Figure 4.32: Post-shaking state of Model B after 20 seconds of strong shaking at various loading frequencies. For reference, the height of the slope is 80 meters.

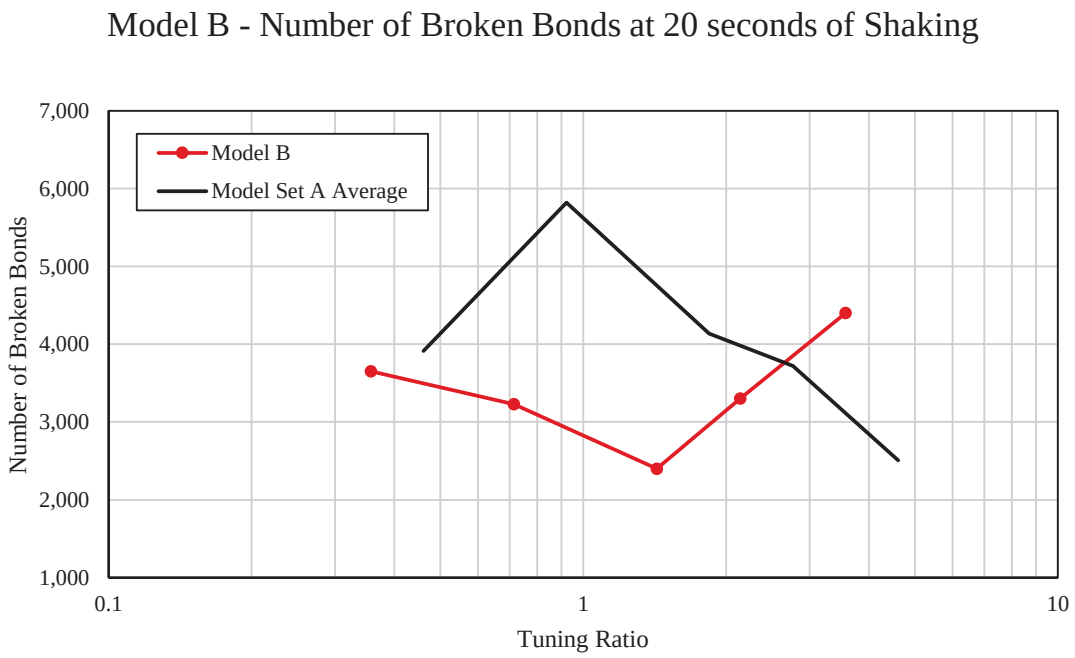

Figure 4.33: Number of broken bonds in Model B with tuning ratio. The model shows an opposite trend than Model Set A (Figure 4.31). The average trend from Model Set A is shown for reference.

The difference between the trends in the number of broken bonds with tuning ratio between Model B and Model Set A highlights how sensitive the dynamics response and failure of the system can be to the internal structure of the rock-slope. The "trend" in Figure 4.33 is not truly a trend at all because the failure mechanisms across the frequencies were not uniform. There are two trends, one for the flexural toppling controlled failures, which is consistent with expected trends in flexural toppling slopes, the other is the failure in the lower part of the slope, which is consistent with the natural frequency of the lower layer.

4.13 Redcliffs Study Discussion

The average number of broken bonds across all frequencies of loading in Model Set A (4000) and for Model B (3400) are similar, suggesting a similar order of magnitude of stability, as expected. At any given loading frequency, however, the damage in the slope may vary significantly. The random pre-existing joints present in Model Set A, and absent from Model B, have a significant, but non-uniform effect of the response of the slope.

The effect of loading frequency in Model Set A and Model B is strong. The fact that the trend in the two is so different is interesting in itself. This difference illustrates an important point: the behavior of a rock-slope to seismic loading is highly dependent on the failure mechanisms induced by the loading. And a single slope may exhibit different failure mechanisms at different loading frequencies, leading to a frequency-dependent behavior that deviates from expectations. The difference in behaviors between Model Set A and Model B also highlights the importance of the pre-existing fractures in the model behavior. In Model Set A, the pre-existing joints allow for more damage in the lower portion of the slope. The pre-existing joints and the induced damage have a lower stiffness than the intact rock and also have no tensile capacity. The resulting wave transmission is different enough from Model B to allow for different initial failure mechanisms.

Pre-existing joints also had a pronounced affect within the four randomized slopes in Model Set A. Model A.1 had a significantly different depth of damage that the other slopes in Model Set A due to a single random joint near to the toe of the slope. The strong influence of joints on rock-slope stability is well-known and this influence has been well-

studied under static conditions [11, 12, 50, 81]. The Model Set A results show that the influence of joints can also be frequency-dependent since sliding along the "pre-existing crack of interest" from figure 4.25 was activated only under loading the loading frequencies closed to the slope natural frequency.

None of the Model Set A simulations lead to a deep-seated failure of the slope. While this does not provide certainty that deep-seated failures are unlikely with future strong ground motions due to the previously noted model limitations, the behavior of the models does allow some conclusions to be drawn related to the nature of the cliff-collapse mode. Several of the cliff-collapse events extended deeper into the slope than the weathered zone, indicating that even after the weathered material has been removed from the slope, it is still susceptible to cliff-collapse. Future seismic events may be expected to continue to produce cliff-collapse in a similar manner to what was experienced in the past. Additional failure mechanisms and modes may also result from future seismic events.

4.14 Redcliffs Study Conclusions

Based on the results of the long-duration loading simulations, the following conclusions are made regarding the questions raised in Section 4.9.

- It appears that cliff-collapse is not a strictly short-duration feature. While other failure modes may (or may not) develop with continued strong ground motion, cliff-collapse appears to continue to occur in repeated cycles of strong ground motion.

- In several cases, the depth of cliff-collapse exceded the depth of weathering in the slopes. This indicates that, for the Redcliffs site, the slope is still susceptible to cliff-collapse after the weathered material has been "shed" from the slope face.

- The seismic performance of rock-slopes appears to be frequency-dependent, but not uniformly so. The nature of the frequency-dependence is strongly influenced by the particular failure mechanisms induced by the ground motion. When evaluating rock-slopes for potential seismic performance, then, the identification of potential failure mechanisms will be an important step.

- Although the similarity in behavior of four models with random joint sets indicates that the random joint pattern is not dictating the behavior of the slope, the dissimilarity in behavior when the random joints are removed, and the weathered properties are applied throughout the slope, suggests that the presence of the joints, regardless of their orientation, may dictate the behavior of the slope.

The importance of the initial failure mechanisms and the force and stress states that cause them has been highlighted here. Due to the pre-existing discontinuities in Model Set A and even in Model B, the stress states in the model are difficult to evaluate. The next chapter will deal with homogeneous rock-slopes. Without discontinuities and impedance contrasts, the approximate stress states can be more easily evaluated and provide further (and more quantitative) insight into the mechanisms of dynamic rock-slope behavior.

Chapter 5

THE RESPONSE OF HOMOGENEOUS ROCK-SLOPES TO STRONG GROUND MOTION

5.1 Introduction

The previous chapter demonstrated the dynamic BPM model's ability to capture some realistic seismically-induced behavior of rock-slopes for some specific sites with fairly complex geology. The models showed frequency-dependent damage behavior, but these dependencies were highly sensitive to the internal features of the rock-slope. In this chapter, the effects of strong ground motion and the frequency content of that motion on homogenous rock-slopes, i.e., with uniform geology and no pre-existing joints, will be evaluated. Because the slopes modeled in this chapter have no pre-existing joints, the wave transmission is simpler than in the models from the previous chapter. The relative uniformity of the rock-slope also allows for an approximation of the stresses over an area composed of several particles to be made. BPM, while capable of evaluating the dynamic response of a rock-slope and providing an approximation of the stress states in the model over time, is not the natural tool for such an evaluation. It is useful, however, to use BPM for these evaluations under non-destructive conditions and then look at the same model when damage is allowed to occur.

Several questions about the nature of rock-slope dynamics and rock-slope failure due to strong ground motion can be addressed with this homogeneous model. These questions include:

1. How does the level of amplification from harmonic input change with tuning ratio (TR) for a BPM rock-slope?

2. When subjected to harmonic input of different frequencies, what is the nature of the stress fields induced within the rock-slope.

3. What are the failure mechanisms observed in the rock-slope(s) and how are those

related to the dynamic response of the slope to strong ground motion?

4. Once failure is initiated, how does the failure progress throughout the slope with continued ground shaking?

5. How does rock-slope behavior as modeled with BPM compare the results of a more traditional sliding block analysis?

To answer these questions, a series of strong ground motion simulations were used to produce failure in the homogeneous slope models. Multiple non-destructive simulations ere also conducted to measure the dynamic behavior and characteristics of the model, as well as some non-dynamic simulations to asses the static and pseudostatic stability of the models.

5.2 Model Details

Two homogeneous rock-slope models were used to address the questions outlined above. These models are 80 meters tall and have a slope angle of 80 degrees. Figure 5.1 shows the full extents of the model and the approximate extents of the view frames used in subsequent figures, which are zoomed in on the slope for clarity. The full model domain is 280 meters wide and 160 meters tall. They are identical other than the strength of the bonds in the models. The names of the models – "587" and "591" – come from the sequential steps of model development, and are essentially arbitrary. Table 5.1 shows the microproperties of the two models. As with the high-resolution cliff models in the previous chapter, the average particle radius is 0.45 meters and is uniformly distributed over plus and minus 50 percent of the average. A local damping ratio of 2 percent was used in the simulations.

The models use the coupled free-field response columns on the lateral boundaries and have a quiet boundary at the base as described in Chapter 3. A "no crack boundary", where bonds are not allowed to break is offset 60 meters from the model extents to protect the boundary conditions.

The resulting macroproperties of the two models are shown in Table 5.2

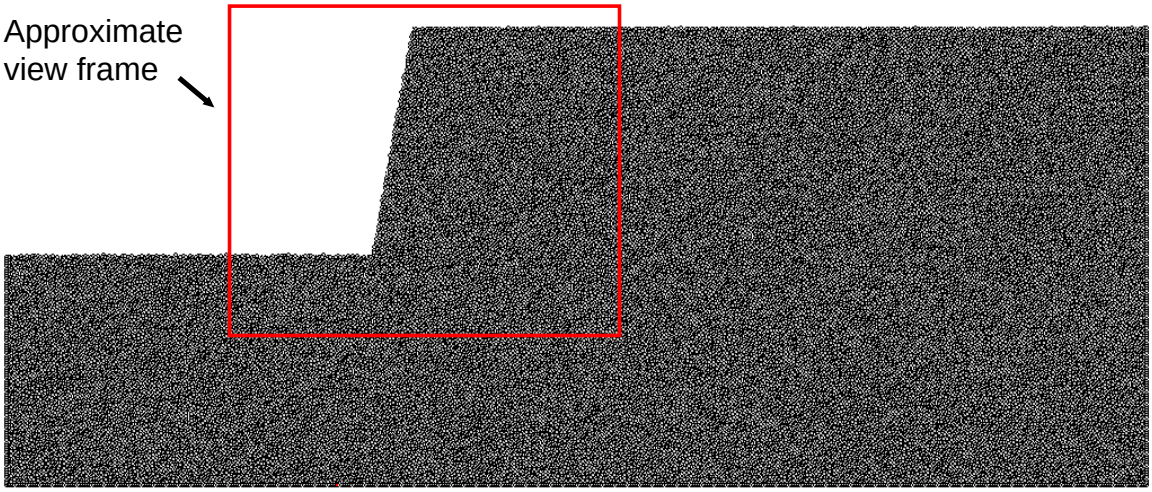

Figure 5.1: Full slope model extents (280 meters wide and 160 meters tall) with an approximate view frame shown. Subsequent slope model figures are zoomed in to the slope area for clarity.

Table 5.1: BPM microproperties for two homogeneous rock-slope models. Property symbols: $k_{n(bond)}$ is the normal stiffness of the bond, N_{bond} is the normal (tensile) strength of the bond, and $\rho_{particle}$ is the particle density.

Model ID	$\boldsymbol{k_{n(bond)}}$ **[N/m^2]**	$\boldsymbol{N_{bond}}$ **[N/m^2]**	$\boldsymbol{\rho_{particle}}$ **[kg/m^3]**
Model 587	1.2E+10	1.34E+04	2800
Model 591	1.2E+10	2.50E+04	2800

Table 5.2: Rock mass engineering properties for Models 587 and 591. Rock property symbols: σ_c is unconfined compressive strength, σ_t is tensite strength, E is the elastic modulus, V_s is the shear wave velocity, and ρ is the density.

Layer	$\boldsymbol{\sigma_c}$**[MPa]**	$\boldsymbol{\sigma_t}$**[MPa]**	**E [GPa]**	**Vs [m/s]**	$\boldsymbol{\rho}$ **[kg/m^3]**
Model 587	13.4	1.4	6.5	1200	1900
Model 591	25.0	3.0	6.5	1200	1900

5.3 Loading Details

The loading the the models were subjected to include:

- Static and pseudostatic loading,
- A non-destructive frequency sweep,
- A constant v_{max} harmonic motion suite (both destructive and non-destructive), and
- A suite of recorded strong ground motions.

The following sections describe the loading conditions.

5.3.1 Static and Pseudostatic Loading

The slopes were evaluated under static and pseudostatic loading to determine the static factor of safety and pseudostatic yield acceleration, k_y. Additionally, the shapes of failure surfaces under these loading conditions are of interest.

The static factor of safety is determined by a strength reduction method. The bond strength and interparticle friction coefficients are reduced by small increments until failure occurs. The original strength of the slope material is taken as the resisting capacity (RC) of the slope and the final strength, at the point of failure initiation is taken as the driving force (DF). The static factor of safety is taken as RC/DF.

The pseudostatic yield acceleration is determined by incrementally increasing the horizontal acceleration coefficient, k, on the slope model. Between incremental applications of k, the model is allowed to come to rest. During the time where the model comes to equilibrium, a high level of damping is used to prevent damage in the model due to the shock of instantaneous horizontal acceleration. The yield acceleration, k_y is taken as the horizontal acceleration applied to the model at the initiation of failure.

5.3.2 Frequency Sweep Loading

The purpose of the frequency sweep is to evaluate the natural frequency/frequencies of the slope model. The frequency sweep contains loading frequencies of 1 to 30 Hz and a constant

input acceleration of 0.01 g (after an initial ramping period at 1 Hz).

5.3.3 Harmonic Loading

A series of constant peak velocity (v_{max}) harmonic motions were run through the models. Frequencies of 0.5 Hz, 1 Hz, 2 Hz, 3 Hz, and 5 Hz were used. The v_{max} of the sine waves was held constant (after an initial ramping period of 1 second) at 0.78 m/s, which corresponds to a peak acceleration (a_{max}) of 1 g at a 2 Hz loading frequency.

The input accelerations of the sine motion suite varies with frequency as follows:

- 0.5 Hz loading: $a_{max} = 0.25$ g
- 1.0 Hz loading: $a_{max} = 0.5$ g
- 2.0 Hz loading: $a_{max} = 1.0$ g
- 3.0 Hz loading: $a_{max} = 1.5$ g
- 5.0 Hz loading: $a_{max} = 2.5$ g

This is the same harmonic motion suite used in Part II of Chapter 4.

5.3.4 Recorded Ground Motions

Four recorded earthquakes were used on the slope models. The main purpose of the earthquake simulations was to get a sense of the extent to which the insights gained through the harmonic motion suite apply to more complex ground motions with non-uniform frequency content. One of the earthquakes, the February 22, 2011 Christchurch event, was used twice, with the horizontal components used for the Richmond Hill and Redcliffs simulations. These components have slightly different frequency content.

The characteristic frequency, f, of a recorded ground motion can be evaluated in several ways. Rathje et al., 2004 [82], found that the mean period, T_m, provides a good scalar approximation of a ground motion's frequency content. In this study, f is taken as $1/T_m$. Note that the inverse of the mean period is not the same as the mean frequency, f_m.

Table 5.3 summarizes the recorded ground motions used on the model. Figures 5.2 through 5.6 present normalized Stockwell transforms of the earthquake motions. Stockwell transform plots show the relative amplitude of different frequencies at different points in time in the ground motion. This means of viewing a motion's frequency content goes to the opposite extreme of using a scalar value to characterize the entire signal. The Stockwell transform plots can provide helpful insight into understanding the nature of the ground motion; however, the inverse of the mean period will be used as the primary method of assessing the motions' frequency content.

Table 5.3: Recorded ground motions used on slope Models 587 and 591 and their characteristics

Event	a_{max}**[g]**	f**[Hz]**	**Scaled** a_{max}**[g]**	**Scaled** v_{max}**[m/s]**
Michoacan	0.12	1.0	0.44	0.78
Northridge	0.93	2.2	0.94, 0.62, 0.43, 0.31, 0.25, 0.18	0.78, 0.5, 0.35, 0.25, 0.2, 0.15
LomaPrieta (G1)	0.44	2.9	0.90, 0.58, 0.40, 0.29, 0.23, 0.17	0.78, 0.5, 0.35, 0.25, 0.2, 0.15
Redcliffs	0.63	3.7	1.0	0.78
Richmond Hill	0.78	4.5	1.82, 0.47, 0.35	0.78, 0.20, 0.15

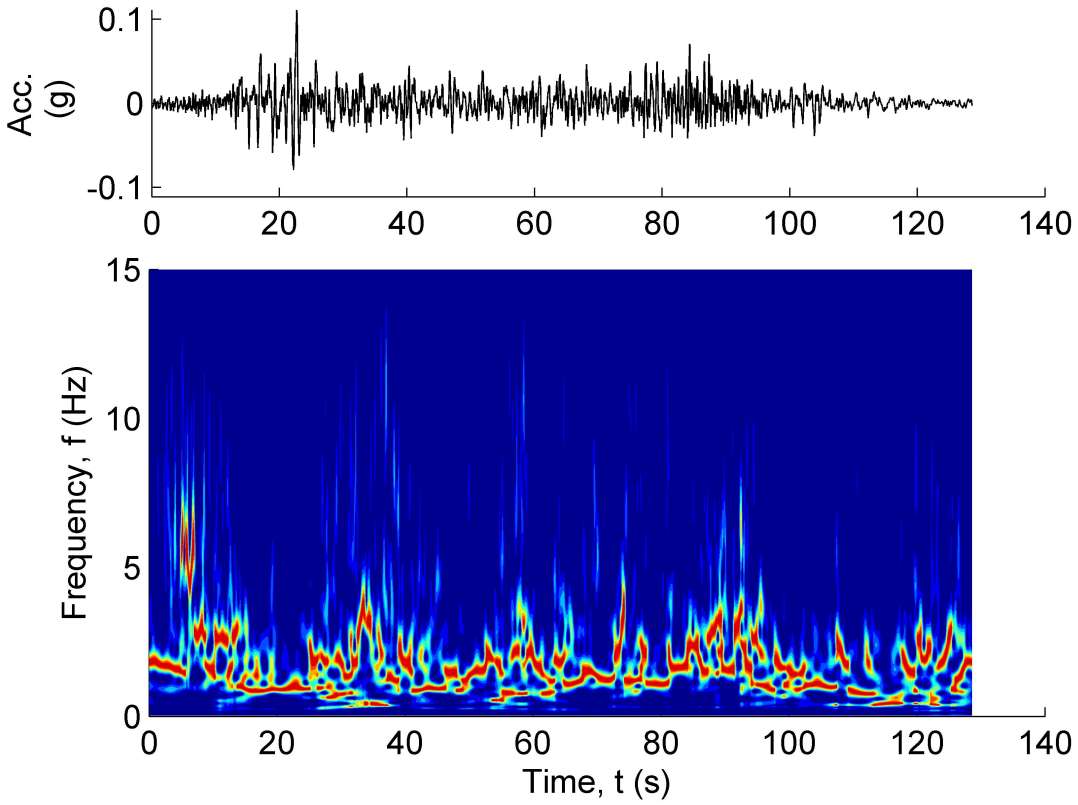

Figure 5.2: Normalized Stockwell transform for the Michoacan recorded ground motion. For any given time, red corresponds to the frequencies with the highest Fourier amplitudes at that point in time. Blue colors indicate lower amplitudes.

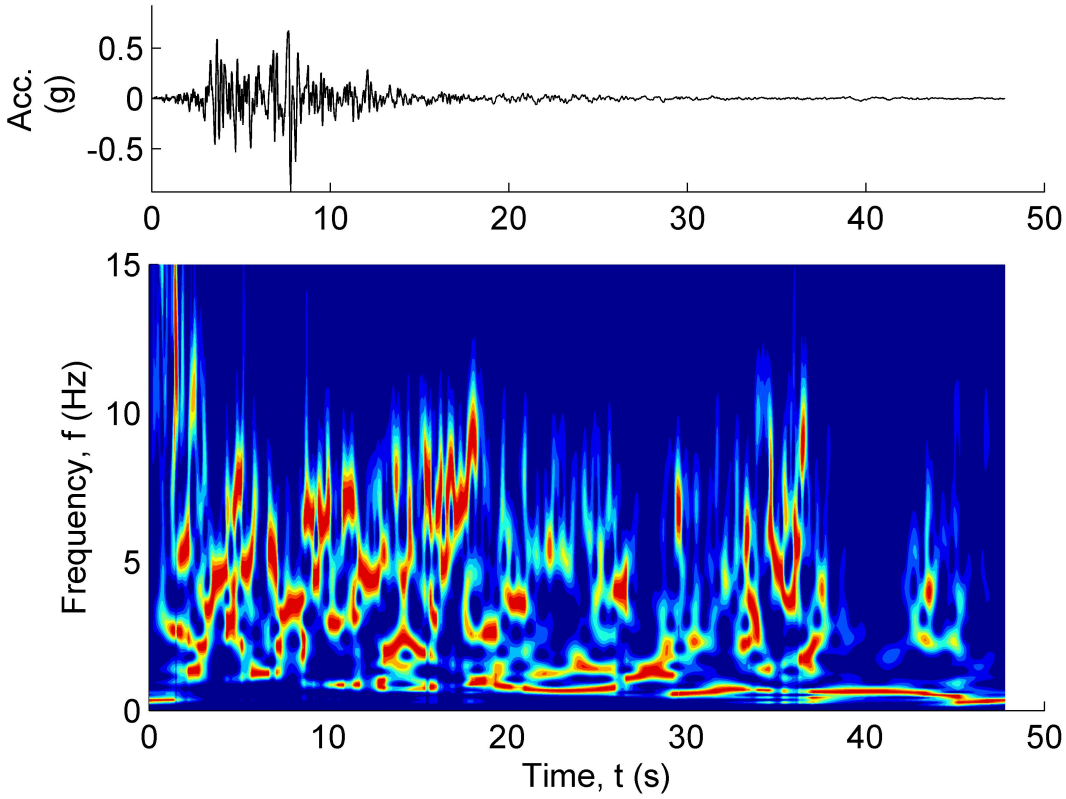

Figure 5.3: Normalized Stockwell transform for the Northridge recorded ground motion. For any given time, red corresponds to the frequencies with the highest Fourier amplitudes at that point in time. Blue colors indicate lower amplitudes.

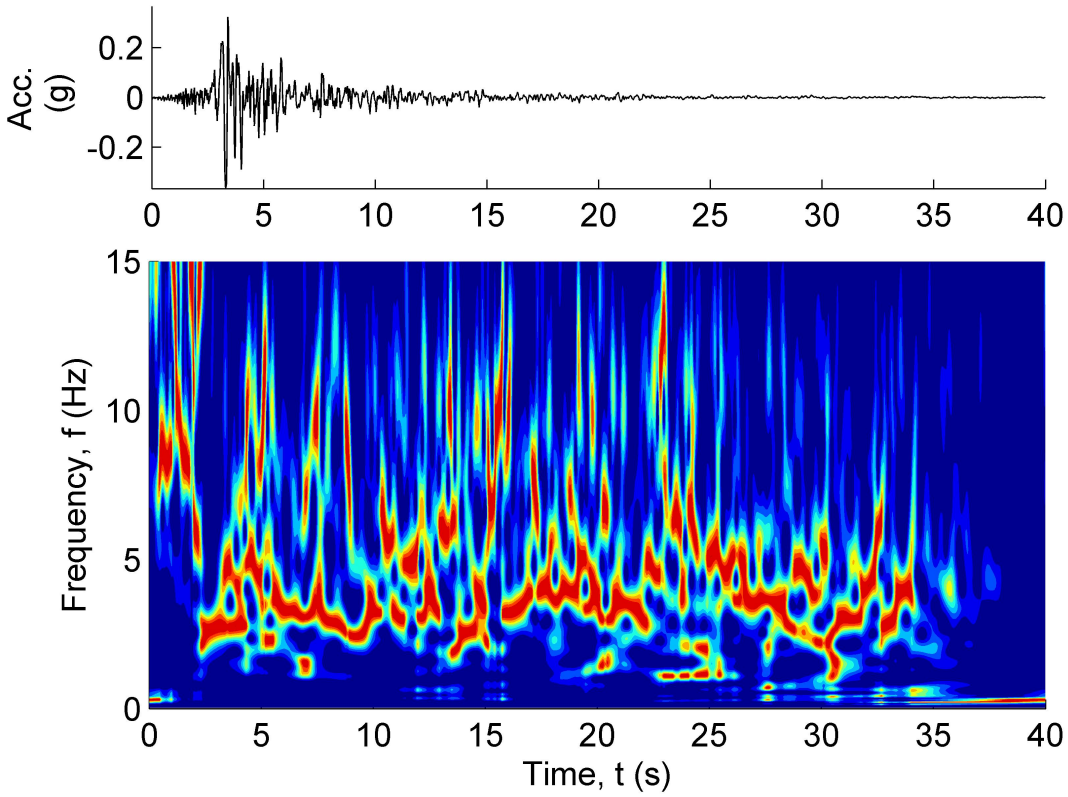

Figure 5.4: Normalized Stockwell transform for the Loma Prieta (g1) recorded ground motion. For any given time, red corresponds to the frequencies with the highest Fourier amplitudes at that point in time. Blue colors indicate lower amplitudes.

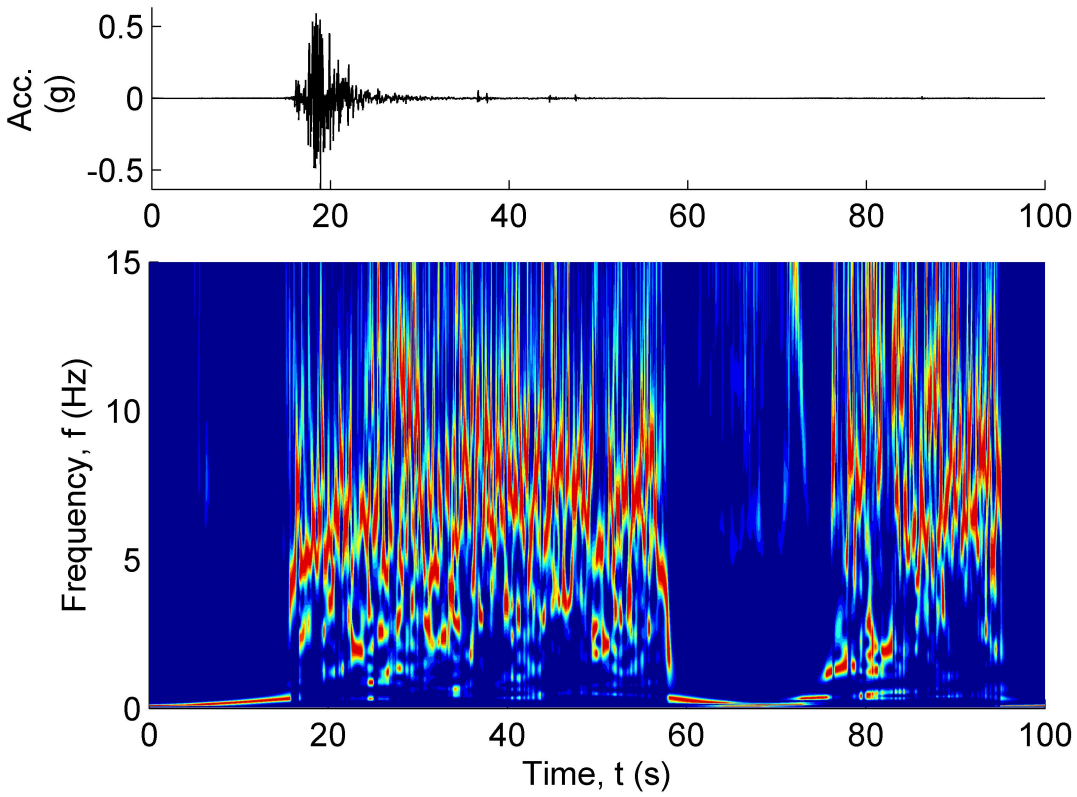

Figure 5.5: Normalized Stockwell transform for the Redcliffs recorded ground motion. For any given time, red corresponds to the frequencies with the highest Fourier amplitudes at that point in time. Blue colors indicate lower amplitudes.

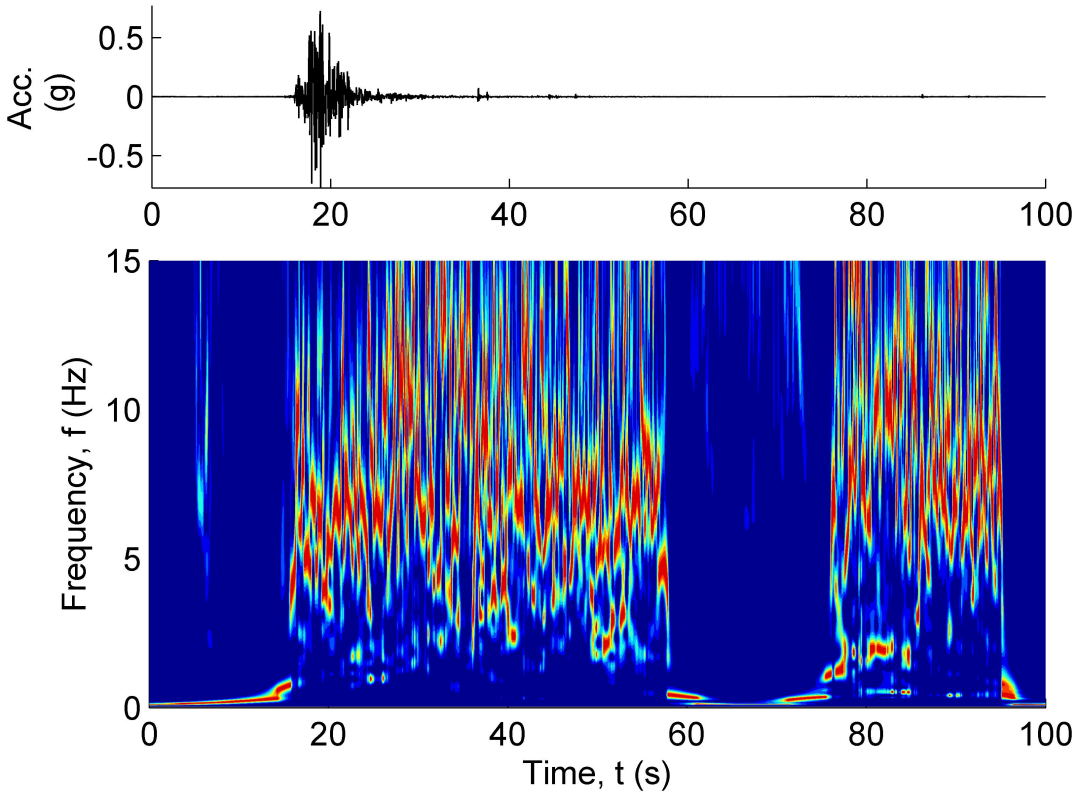

Figure 5.6: Normalized Stockwell transform for the Richmond Hill recorded ground motion. For any given time, red corresponds to the frequencies with the highest Fourier amplitudes at that point in time. Blue colors indicate lower amplitudes.

5.4 Results

This section will present the behavior of the models under the loading conditions described above.

5.4.1 Static and Pseudostatic Loading

Models 587 and 591 had a factor of safety against static failure of 1.9 and 3.5, respectively. The yield acceleration, k_y, of models 587 and 591 is 0.55 g and 1.15 g, respectively.

The extent of failure under static conditions for Models 587 and 591 are shown in Figures 5.7 and 5.8, respectively. Model 587 fails in a shallow wedge, initiating at the toe of the slope, resulting in fairly shallow failure surface with a steep back angle. Model 591 also fails at the toe, however, the material surrounding the toe is strong enough to support the cliff face without the toe material, and a precarious overhanging geometry is created.

The extent of failure under pseudostatic conditions for Models 587 and 591 are shown in Figures 5.9 and 5.10, respectively.

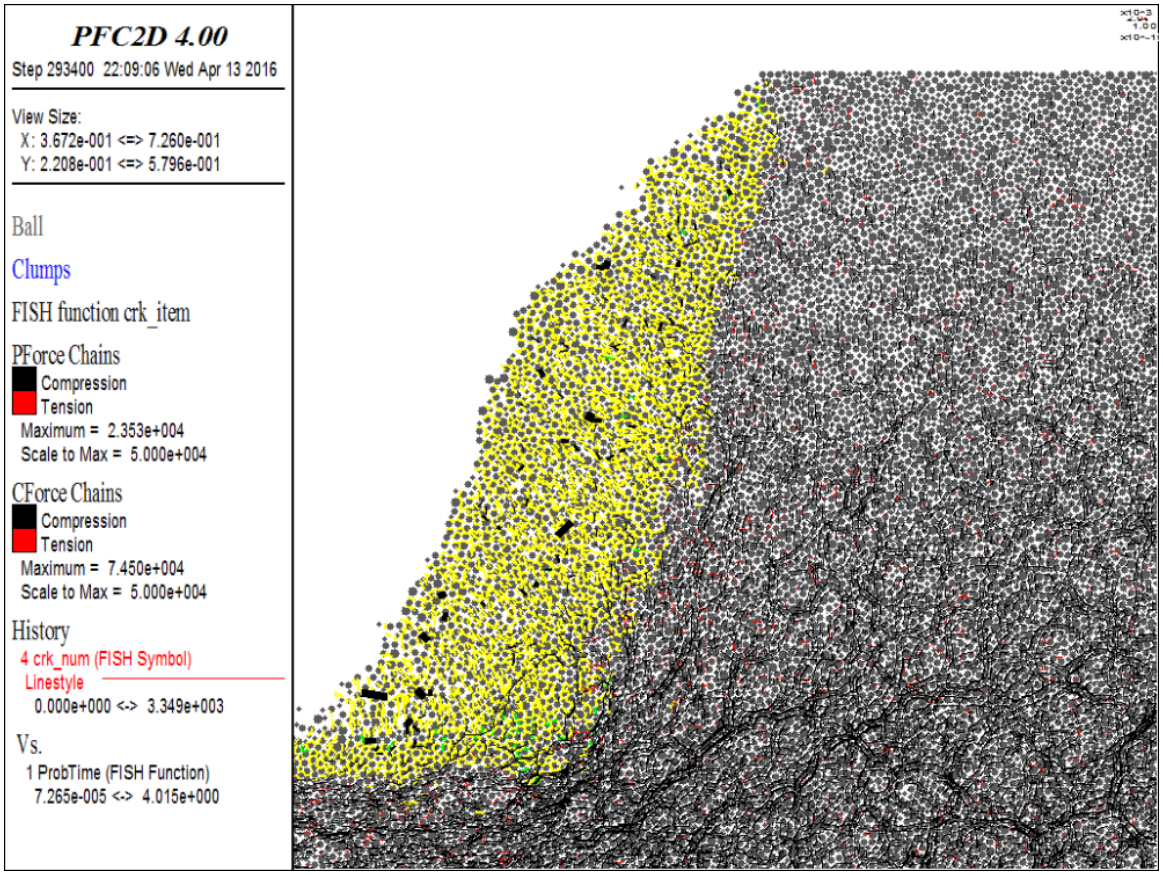

Figure 5.7: Static failure condition for Model 587 – FS = 1.9. Under static conditions, a shallow failure surface, initiating at the toe, and resulting in cliff-collapse develops. For reference, the slope height is 80 meters.

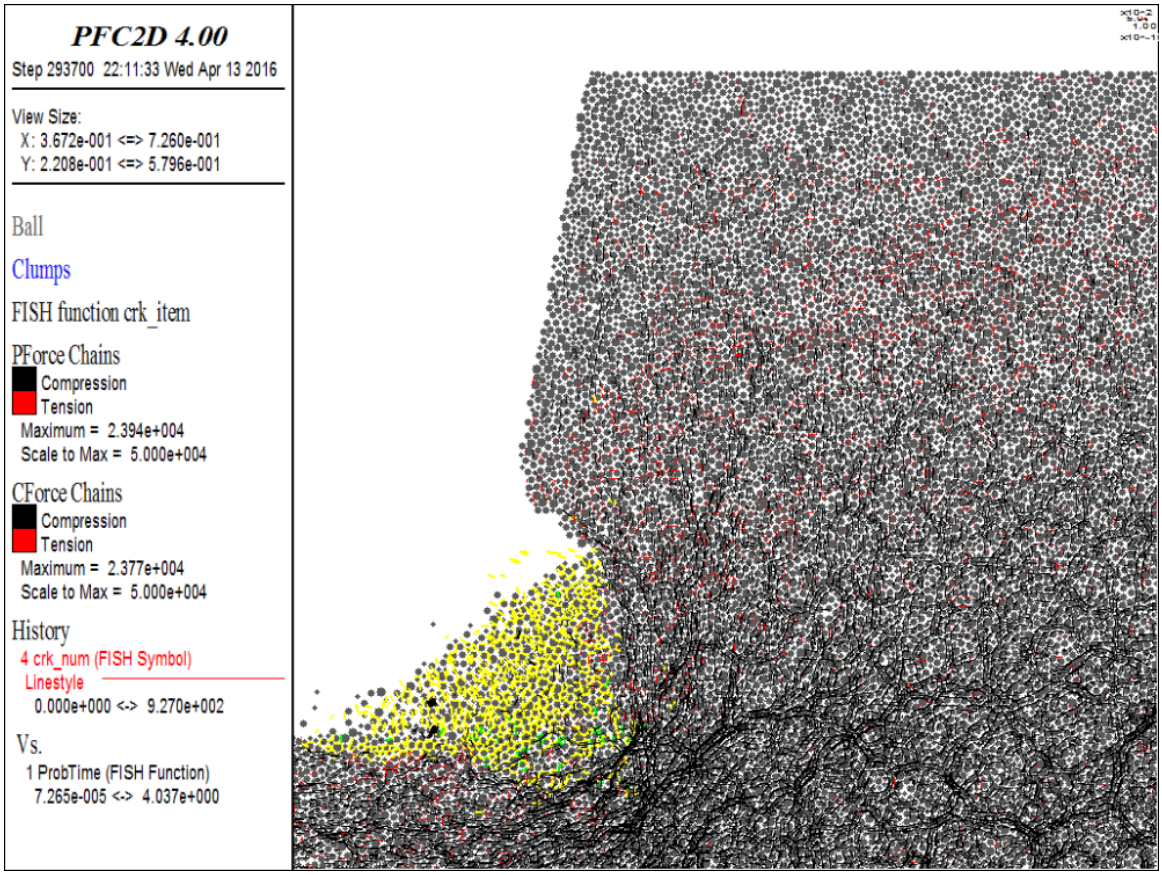

Figure 5.8: Static failure condition for Model 591 – FS = 3.5. Failure initiates at the toe, but the material above the toe is strong enough to support the cliff face without the toe material and a precarious overhanging geometry is created For reference, the slope height is 80 meters.

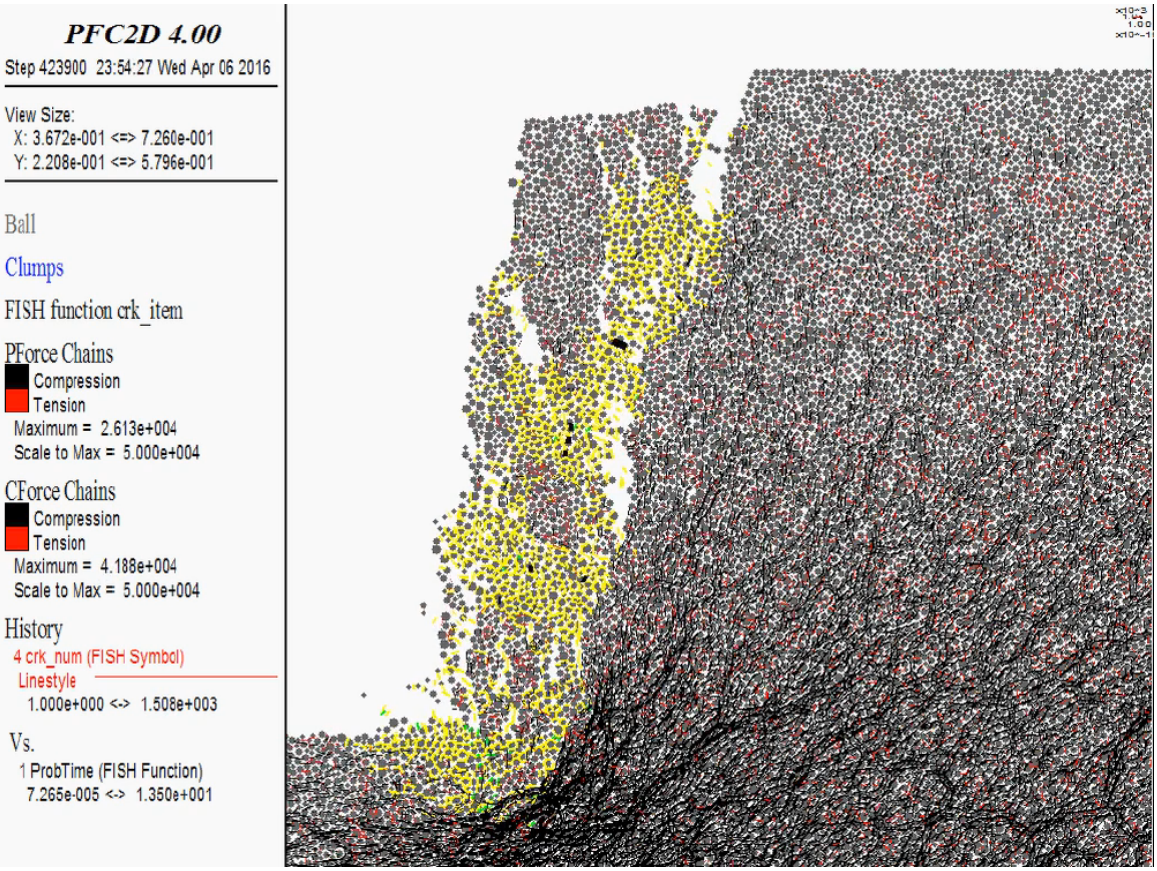

Figure 5.9: Pseudostatic failure condition for Model 587 – $k_y = 0.5g$. A shallow, cliff-collapse failure extending from the toe to the crest develops under pseudostatic loading. The extent of the failure surface is similar to the static failure condition. For reference, the slope height is 80 meters.

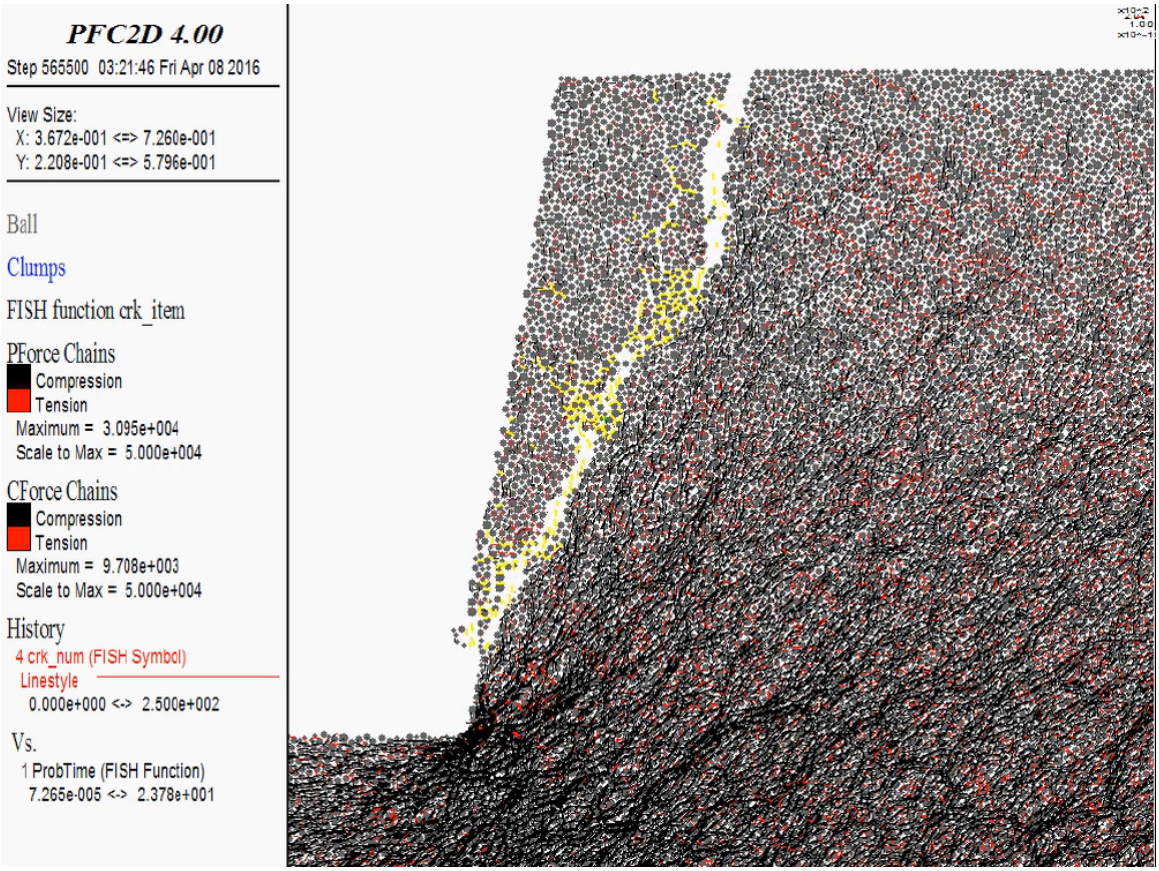

Figure 5.10: Pseudostatic failure condition for Model 591 – $k_y = 1.15g$. A wedge failure that removes a shallow portion of the cliff face develops under pseudostatic loading. The failure surface exits the slope face above the toe. For reference, the slope height is 80 meters.

5.4.2 Frequency Sweep Loading

Figure 5.11a shows a graphical legend for the response of the slope to the frequency sweep. The colors correspond to different elevations of monitored particles within the model. The line thicknesses correspond to proximity to the slope face. The thickest line is at the slope face and line width decreases with the monitored particle's distance from the slope face. Dashed lines indicate the monitored particle is in front of the cliff face and solid lines indicate the monitored particle is behind the cliff face.

Figure 5.11 shows the time and frequency domain responses of Models 587 and 591 to the frequency sweep using the legend shown if Figure 5.11a. Note that because the only difference between Models 587 and 591 are their interparticle bond strengths, Figure 5.11 represents the responses of both models.

At the first mode of vibration shown on Figure 5.11, which is at about 2.9 Hz, the slope responds to loading as a whole – amplification is present at the crest, midway down the slope, and some distance behind the crest as well. At the second mode of vibration (approximately 5 Hz), only amplification of the crest is evident. These observations are consistent with the behavior of a classic multiple degree of freedom system, where the first mode shape includes the entire body, and the vibration of subsequent modes involves less and less of the body acting as a whole.

The first mode, or the natural frequency, f_n, is also consistent with the empirical formula for the natural frequency of slopes $f_{n(emp)} = V_s/5H$ [83]. For Models 587 and 591,

$$f_{n(emp)} = \frac{1200\frac{m}{s}}{5 * 80m} = 3Hz \tag{5.1}$$

Although this formula does not provide an estimate for the second mode of vibration, the slope response indicates that no more than half of the slope height is being excited at the second mode. If the excited portion of the slope is thought of as its own slope, the boundary conditions are slightly different because there is no material restraining motion at the toe. This change in boundary condition would soften the second mode slope, so a relatively lower frequency can be expected. A reasonable conclusion for an estimate of the frequency of the second mode, then, might look like:

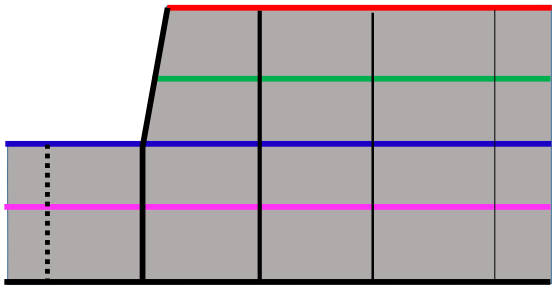

Graphical legend for monitored particles in BPM slopes. Line colors correspond to elevations and line widths and types correspond to position from the slope face.

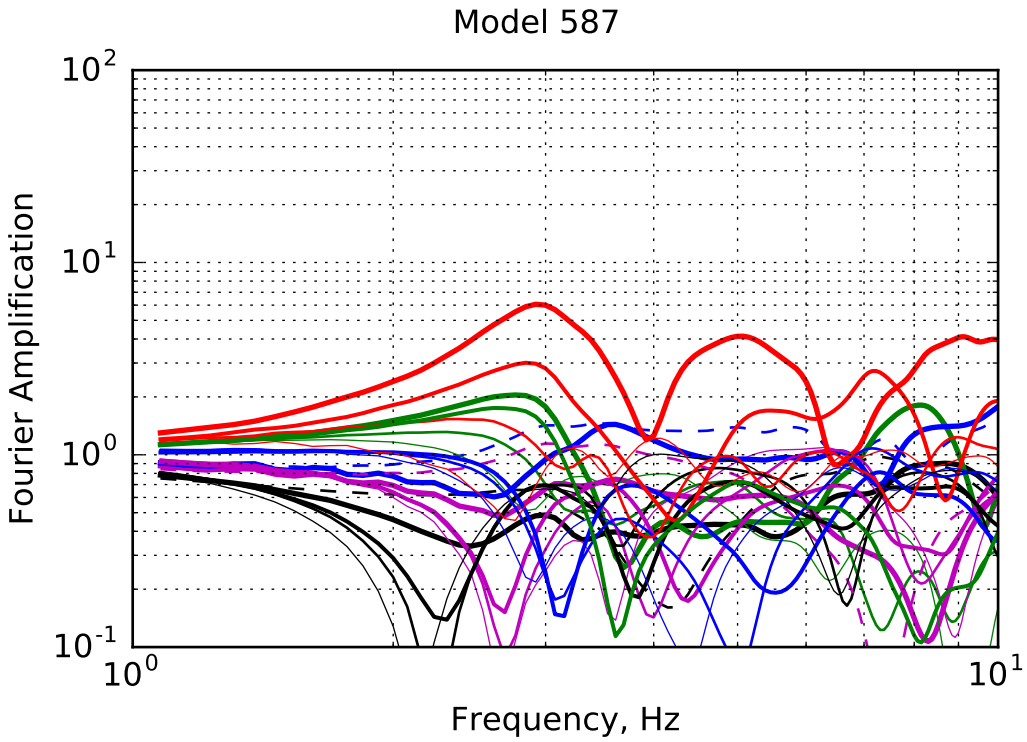

Figure 5.11: Frequency domain Fourier amplitude amplification of acceleration in Model 587/591 relative to base input from a frequency sweep. Because Models 587 and 591 vary only by strength, this response represents both models. The first mode of vibration is apparent at 2.9 Hz, where the acceleration amplification is strongest and affects multiple monitored points within the slope. The second mode, where only amplification closest to the crest is apparent, is at 5 Hz.

$$f_{II} \leq \frac{V_s}{5H/2} \tag{5.2}$$

which yields $f_{II} \leq 6$ for this slope, so the value of $f_{II} = 5$ interpreted from the FAS in Figure 5.11 appears to be very reasonable.

5.4.3 Non-Destructive Harmonic Loading

The response of the models subjected to harmonic loading can be visualized in a number of ways. Three types of visualization have been used here – velocity fields and time histories, force-chain fields, and stress fields – and are summarized below:

1. **Velocity Fields and Time-Histories** – The velocity field figures provide a helpful visualization for the motion of the particles throughout the slope. They are taken from outputs of the PFC2D program. The time history plots show the velocities measured in the model during first ten cycles of the motion. Input velocity, the velocity at the crest and several points throughout the slope are shown. Refer to Figure 5.12 for the legend relating the identifiers to the position within the model.

2. **Force-chain Field** – These figures show the magnitude of compressive (black) and tensile (red) interparticle and bond forces in the model. The distribution, orientation, and sign of force chains under non-destructive loading conditions provide insight into the response of the slope under different loading conditions and the potential initial behavior of the slope under destructive loading.

3. **Stress Fields** – These figures are generated by post-processing user-written PFC2D output files. The output used to generate the figures are the average approximate stress state of 9-meter by 9-meter square cells in the slope. Each cell has a single stress state, in the form of a 2-dimensional stress tensor, which is the average of the approximate stress state of each particle within the cell. The approximate stress state of a particle in BPM is given by:

$$\sigma_{ij}^{p} = \frac{1}{V^{p}} \sum_{N_c^p} \left(x_i^c - x_i^p\right) F_j^{(c,p)} \tag{5.3}$$

after Potyondy et al. (2004) [35]. σ_{ij}^{p} is the 2-dimensional stress tensor of the particle, V^p is the volume of the particle, N_c^p is the number of contacts on the particle, x_i^c and x_i^p are the positions of the contact and the particle, respectively, and $F_j^{(c,p)}$ is the force at the contact acting on the particle. The stress fields are presented using four plots. An example is shown in Figure 5.13. The two upper plots show the first principal stress magnitude ($|\sigma_1|$) on the left, and the second principal stress magnitude ($|\sigma_2|$) on the right, for each cell in the slope. Both figures have horizontal lines a H/10 and H/2 indicating where cell stress states have been extracted for further plotting on the lower two plots. The plot on the lower left shows the stresses along the two measurement lines in principal stress space. Two Hoek-Brown failure envelopes are plotted for Models 587 and 591. It is important to note that failure (i.e., the rupture of bonds) in BPM is not dictated by the stress state, but by interparticle forces. The stress state relative to the failure envelope provides an indication of the likelihood of failure, but does not control failure. The dashed line in this plot represents the volumetric stress axis, where $|\sigma_1| = |\sigma_2|$. The plot on the lower right shows the stresses along the same measurement lines with stress on the y-axis and distance on the x-axis. Note that the scale and position of the x-coordinates on the lower right figure do not line up with the figure(s) above. The x-axis on the bottom plot starts at the slope face near the bottom of the slope. The example in Figure 5.13 shows the stresses for the static condition of the slope.

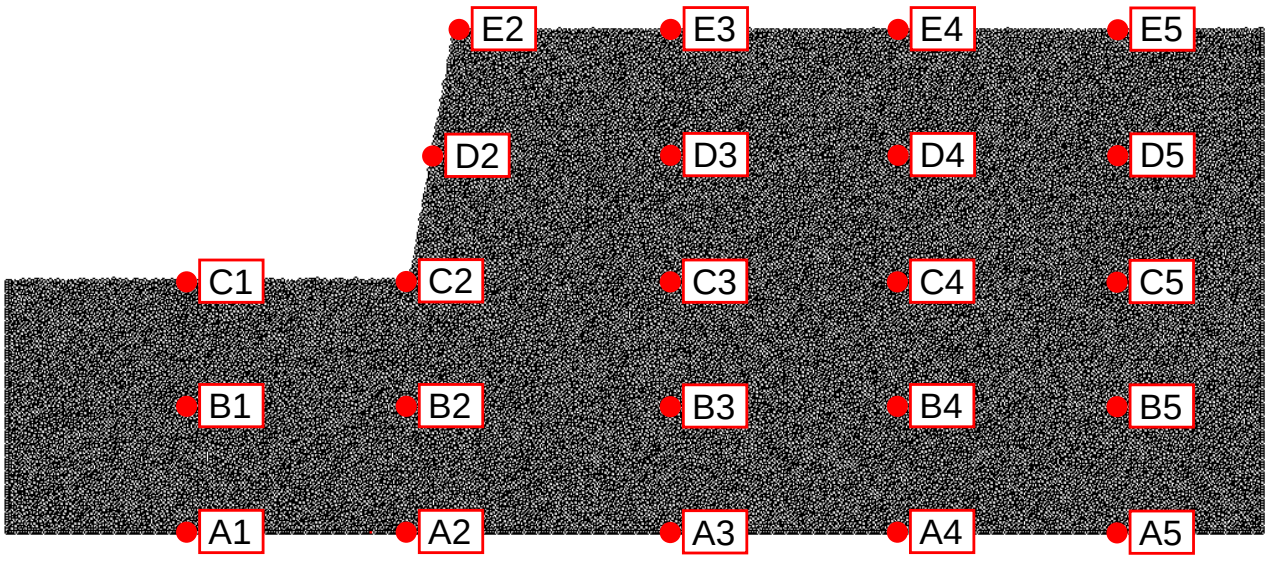

Figure 5.12: Legend of identifiers for monitored points in BPM slopes used in this study. The letters indicates the elevation in the model of the monitored point from 'A', at the base, to 'E' at the surface at the top of the slope. The numbers indicate the proximity to the slope face, with '2' being associated with the slope face and increasing numbers indicating increasing distance behind the slope face. For reference, the height of the entire model shown in 160 meters.

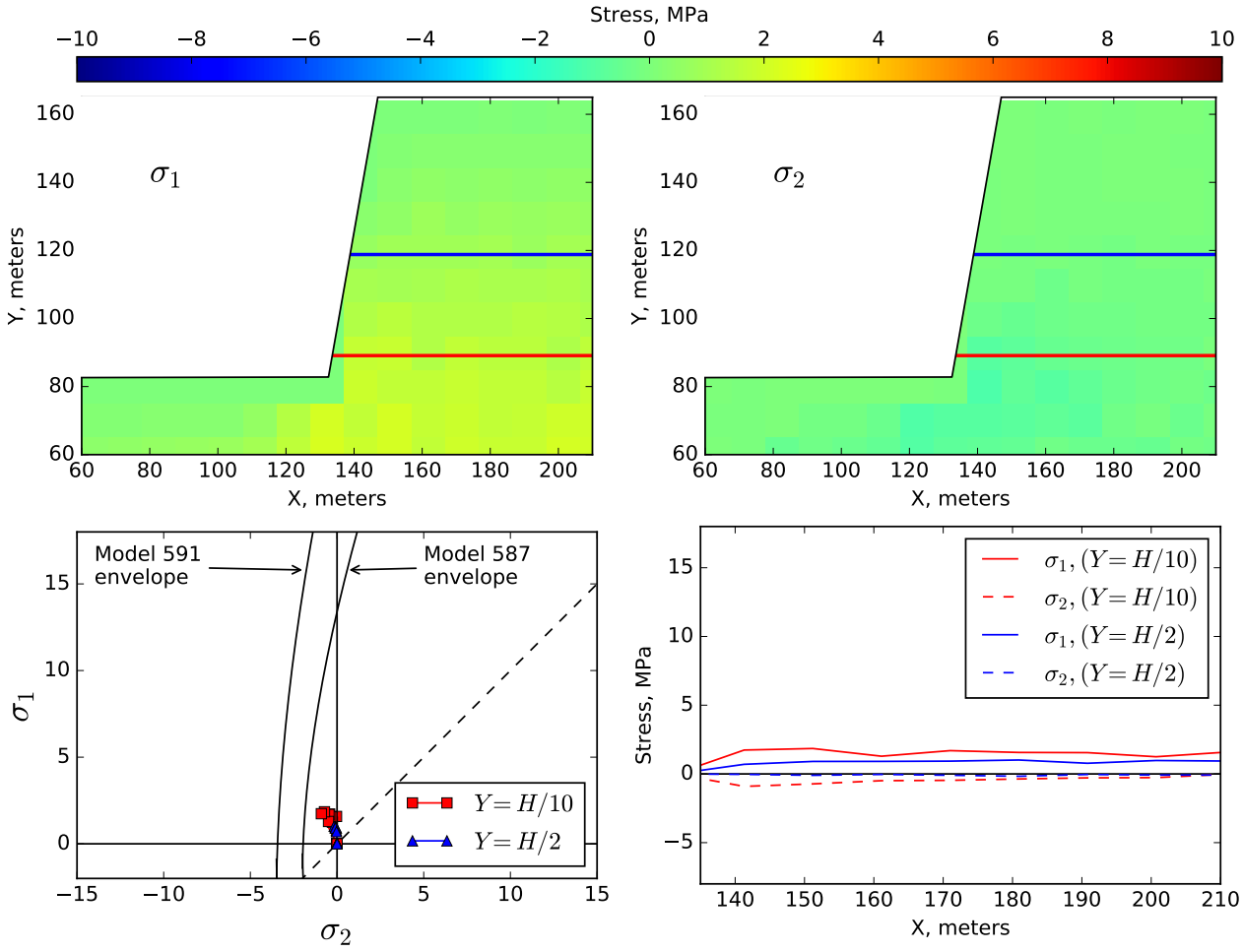

Figure 5.13: Example of a stress state plot for non-destructive loading conditions. The static stress conditions of the slope are shown. The approximate stress field is shown in four plots. The two upper plots show the first principal stress magnitude ($|\sigma_1|$) on the left, and the second principal stress magnitude ($|\sigma_2|$) on the right, for each cell in the slope. Red colors correspond to positive stresses (compression), blue corresponds to negative stresses (tension), and green indicates a zero stress condition. Both plots have horizontal lines a H/10 and H/2 indicating where cell stress states have been extracted for further plotting on the lower two plots. The plot on the lower left shows the stresses along the two measurement lines in principal stress space. Two Hoek-Brown failure envelopes are plotted for Models 587 and 591. The dashed line in this plot represents the volumetric stress axis, where $|\sigma_1| = |\sigma_2|$. The plot on the lower right shows the stresses along the same measurement lines with stress on the y-axis and distance on the x-axis. Note that the scale and position of the x-coordinates on the lower right figure do not line up with the figure(s) above. The x-axis on the bottom plot starts at the slope face near the bottom of the slope.

0.5 Hz Loading

The 0.5 Hz loading (i.e., tuning ratio of 0.17) induces very little dynamic response in the model. The slope behaves roughly as a unit and the maximum velocity at the crest is twice the amplitude of the input velocity – the same as for a flat-ground model and as the free-field response.. The velocity field extrema in the upslope and downslope directions and the velocity time histories for the first 10 cycles of shaking are shown in Figure 5.14. The force-chain and stress field extrema in the upslope and downslope directions (corresponding to the displacement extrema) are shown in Figures 5.15 through 5.17. The compressive force-chain concentration at the toe of the slope is evident Figure 5.15(a). Mild tensile forces are also visible near the toe in 5.15(b). Figure 5.16 (stress downslope extreme) shows that failure is likely at the toe of the slope for Model 587, but that failure is not likely for Model 591.

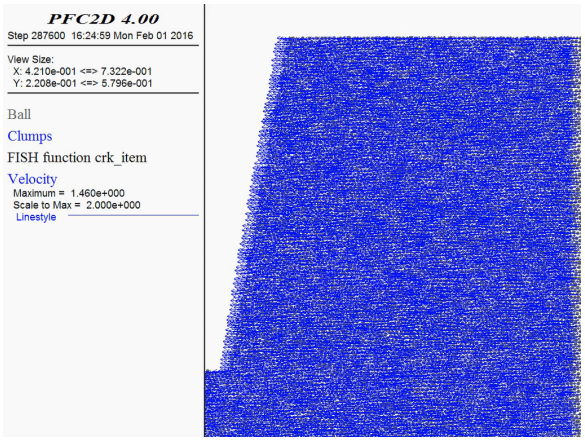

(a) Downslope extreme velocity

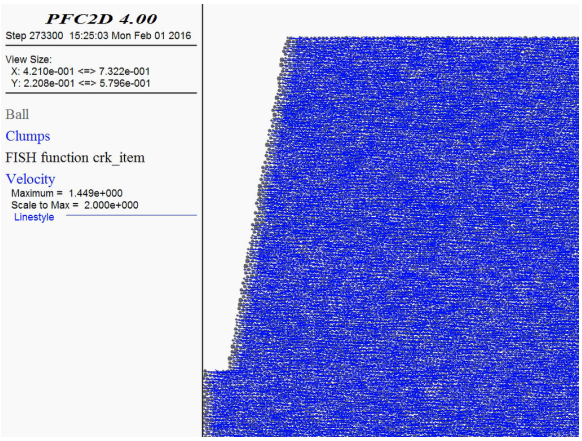

(b) Upslope extreme velocity

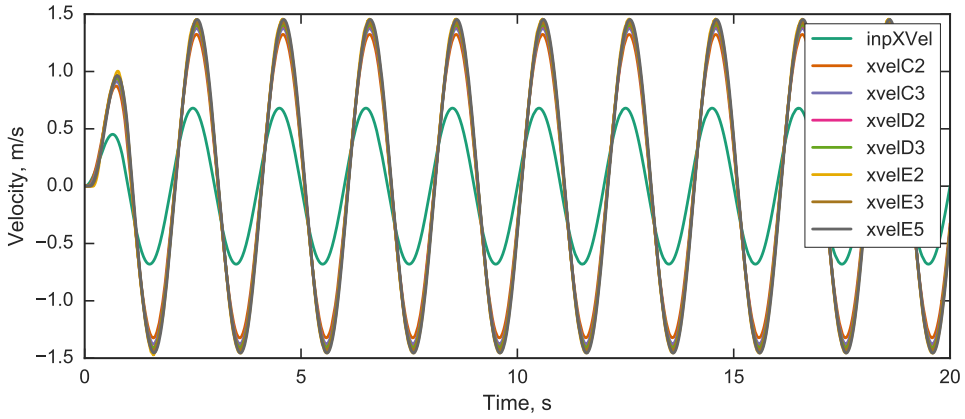

(c) Velocity response of the slope with time. Points with 'E', 'D', and 'C' in the labels correspond to the elevations of the crest, mid-slope, and base, respectively. Points with '2' and '3' in the labels correspond to points at the slope face and set back 65 meters from the slope face, respectively. Point 'E5' corresponds to the furthest monitored point from the crest at the ground surface behind the slope. Refer to Figure 5.12 for the positions of the monitored points within the slope.

Figure 5.14: Velocity response for 0.5 Hz loading on Model 587/591.

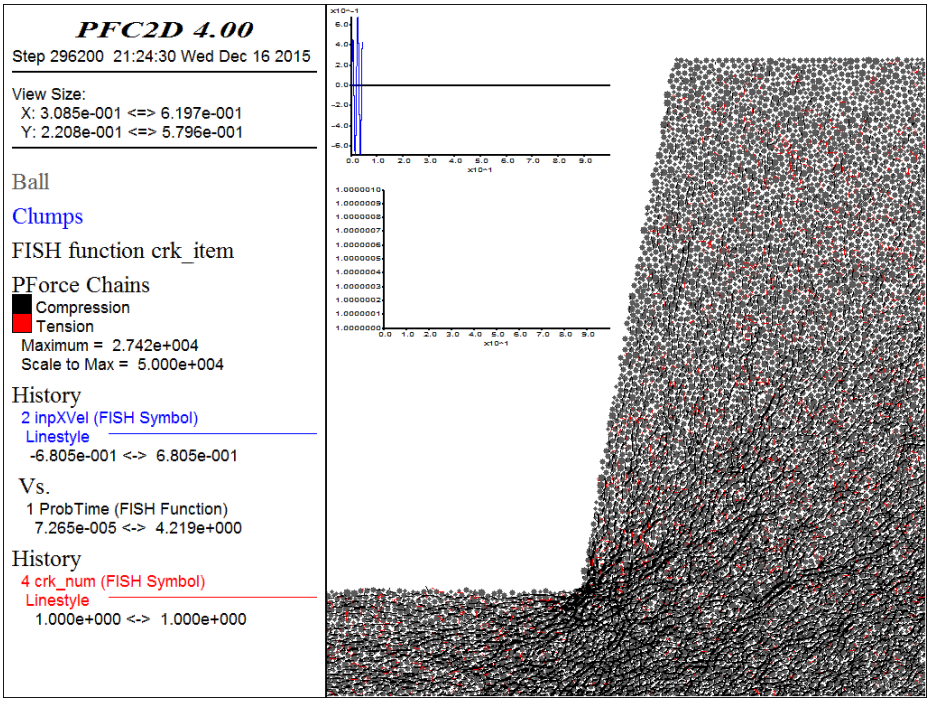

(a) Downslope extreme force

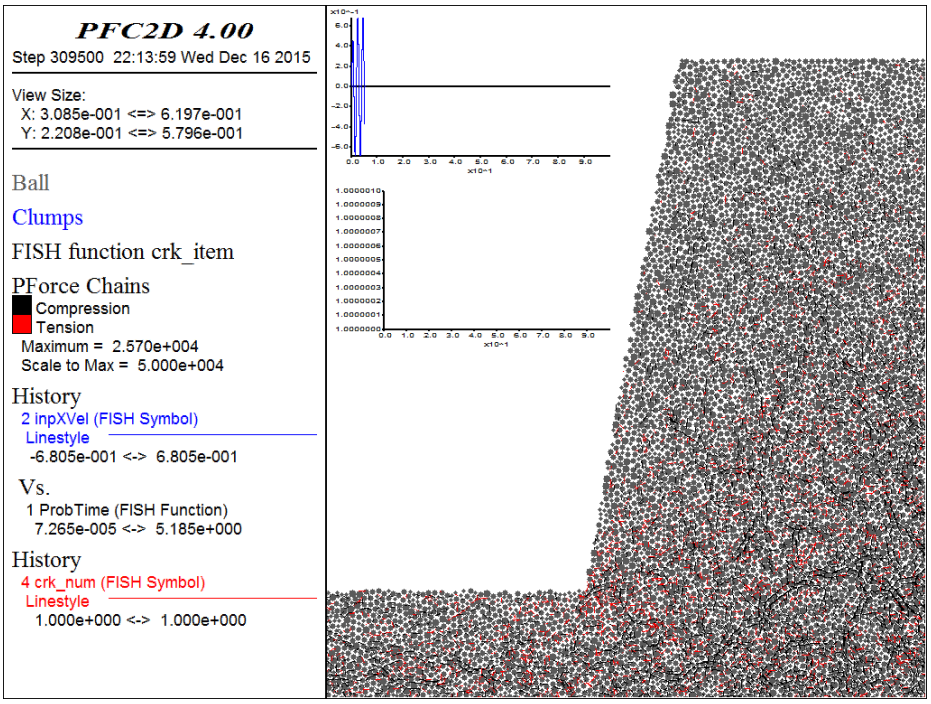

(b) Upslope extreme force

Figure 5.15: Force-chain extrema for 0.5 Hz loading on Model 587/591.

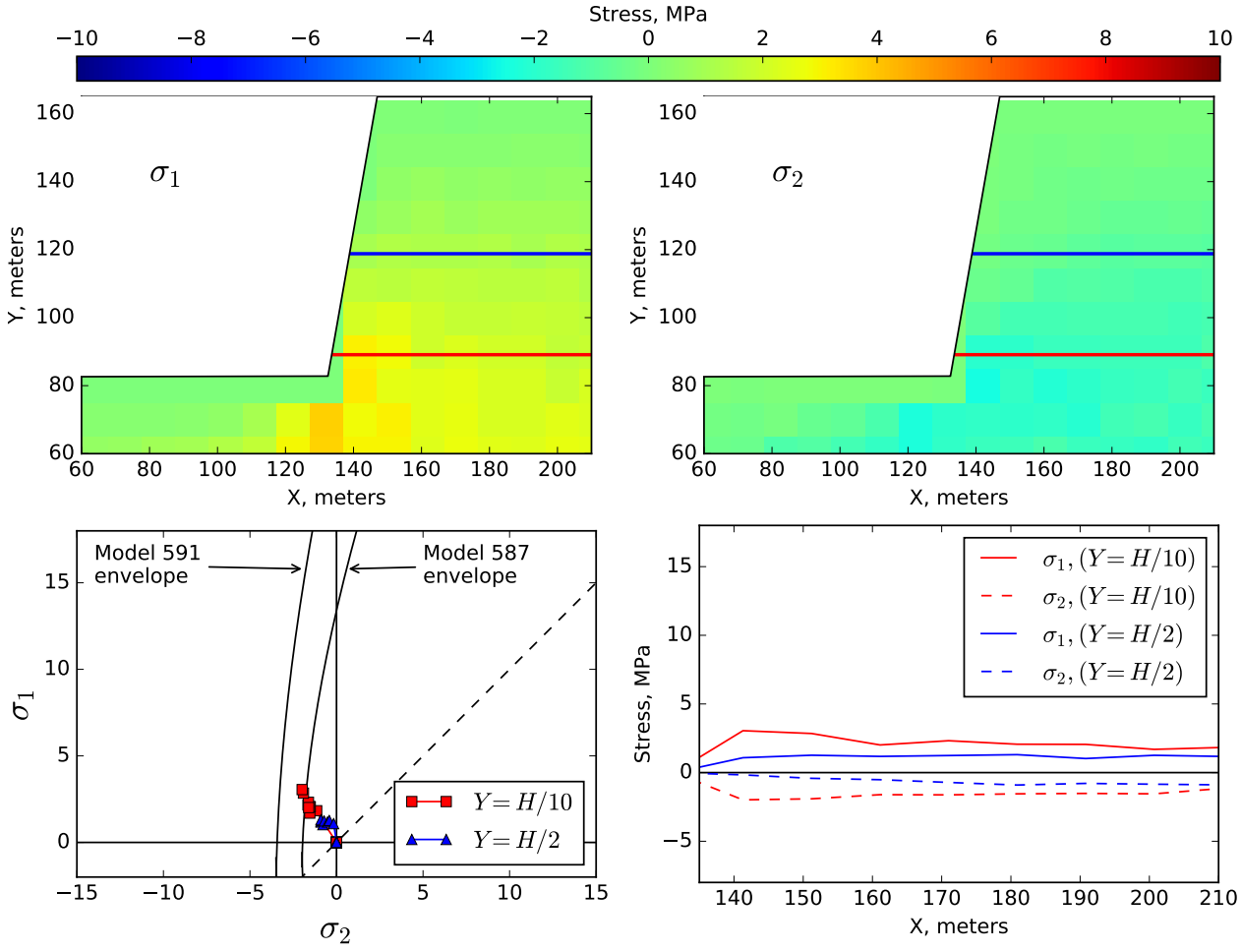

Figure 5.16: Stress state of Model 587/591 at the downslope extreme for 0.5 Hz loading.

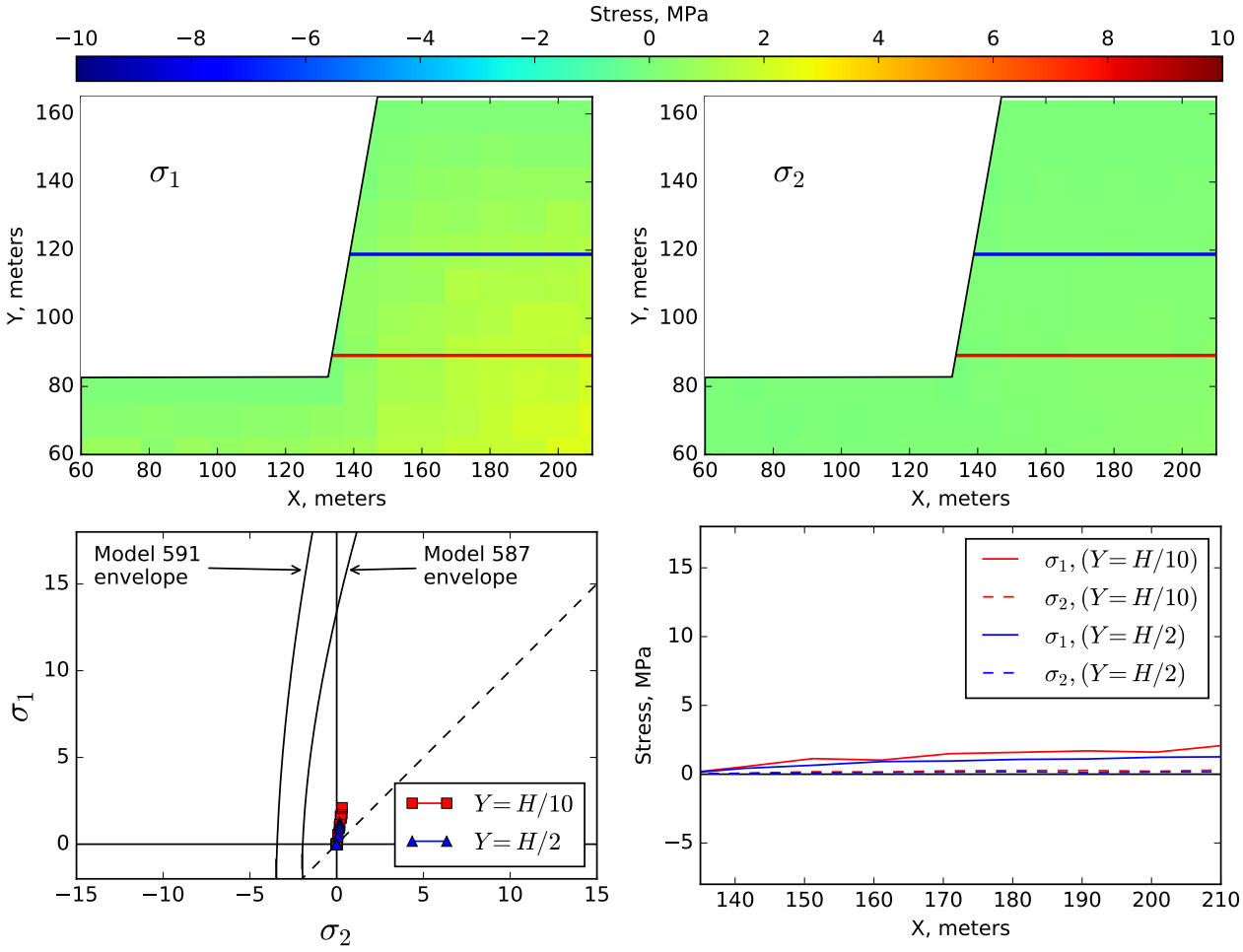

Figure 5.17: Stress state of Model 587/591 at the upslope extreme for 0.5 Hz loading.

1 Hz Loading

The 1 Hz loading (i.e., tuning ratio of 0.34) induces a slight dynamic response. The slope behaves less as a unit as with the 0.5 Hz loading and has a more defined upslope and downslope movement. The velocity extrema shown in Figure 5.18 show relatively more velocity can be observed at the crest than at the toe. The velocity time-history in Figure 5.18(a) shows some slight amplification at the crest relative to the free-field amplification. The force-chain and stress field extrema in the upslope and downslope directions (corresponding to the displacement extrema) are shown in Figure 5.19. Tensile force-chains near the crest, and concentrated compressive force-chains at the toe in the downslope extreme are pronounced. These two sets of force-chains are oriented perpendicular to each other. Tensile forces are also visible at the toe in the upslope extreme. The stress fields in Figures 5.20 and 5.21 indicate that compressive failure at the toe is likely for Model 587 and possible for Model 591, but no tensile failure at the toe is indicated, despite the tensile force concentration. This tensile force concentration may be more critical than the average stresses indicate due to its highly localized nature.

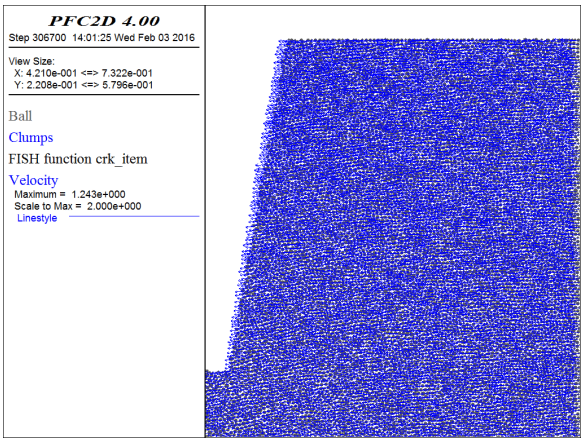

(a) Downslope extreme velocity

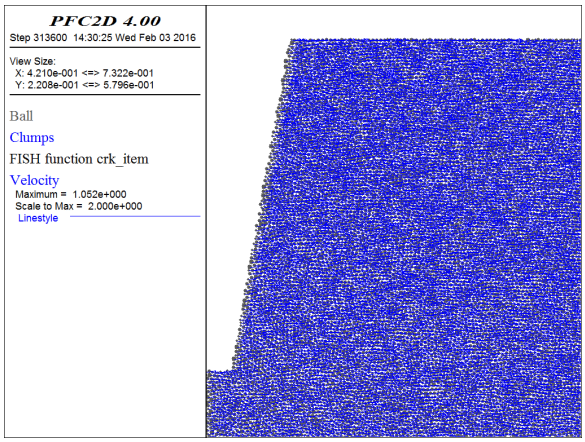

(b) Upslope extreme velocity

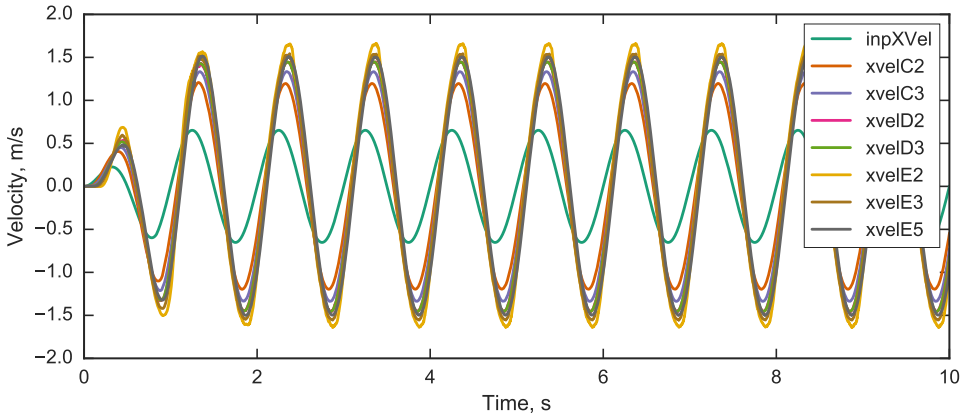

(c) Velocity response of the slope with time. Points with 'E', 'D', and 'C' in the labels correspond to the elevations of the crest, mid-slope, and base, respectively. Points with '2' and '3' in the labels correspond to points at the slope face and set back 65 meters from the slope face, respectively. Point 'E5' corresponds to the furthest monitored point from the crest at the ground surface behind the slope. Refer to Figure 5.12 for the positions of the monitored points within the slope.

Figure 5.18: Velocity response for 1 Hz loading on Model 587/591.

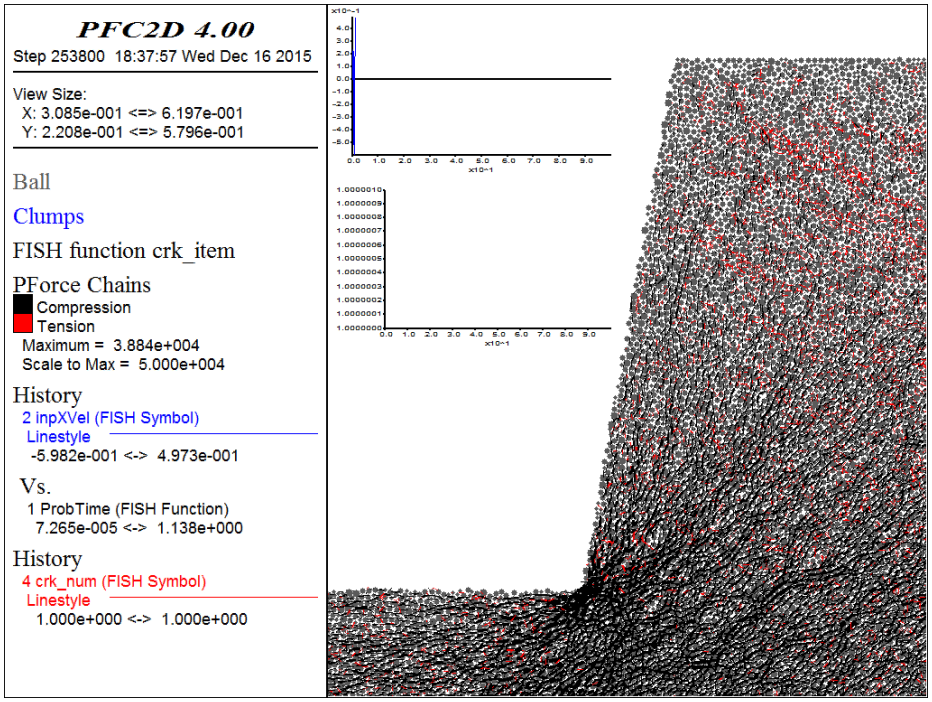

(a) Downslope extreme force

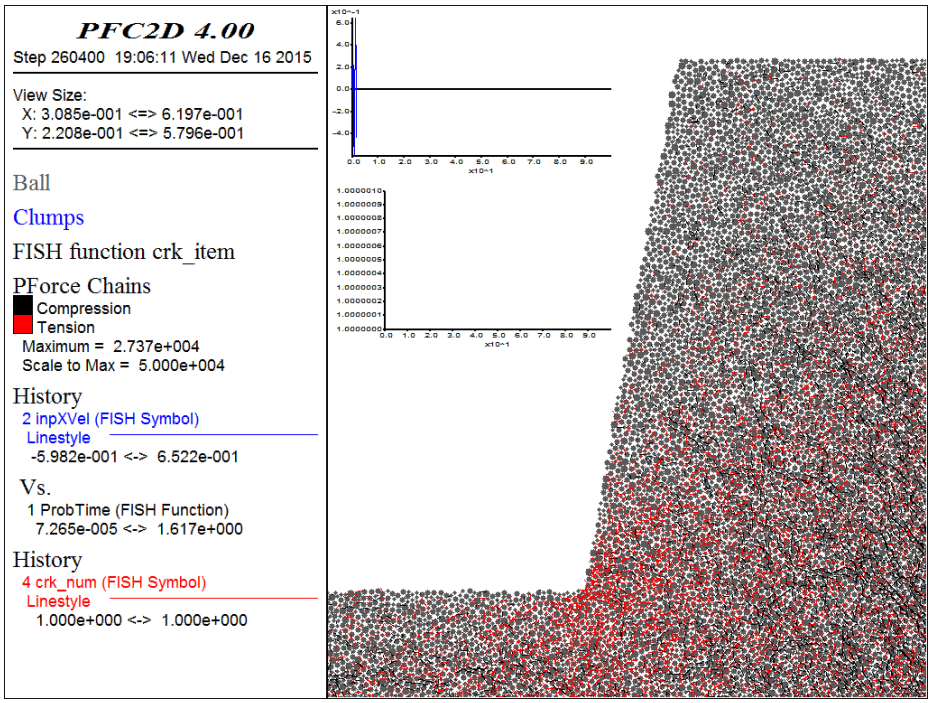

(b) Upslope extreme force

Figure 5.19: Force-chain extrema for 1 Hz loading on Model 587/591.

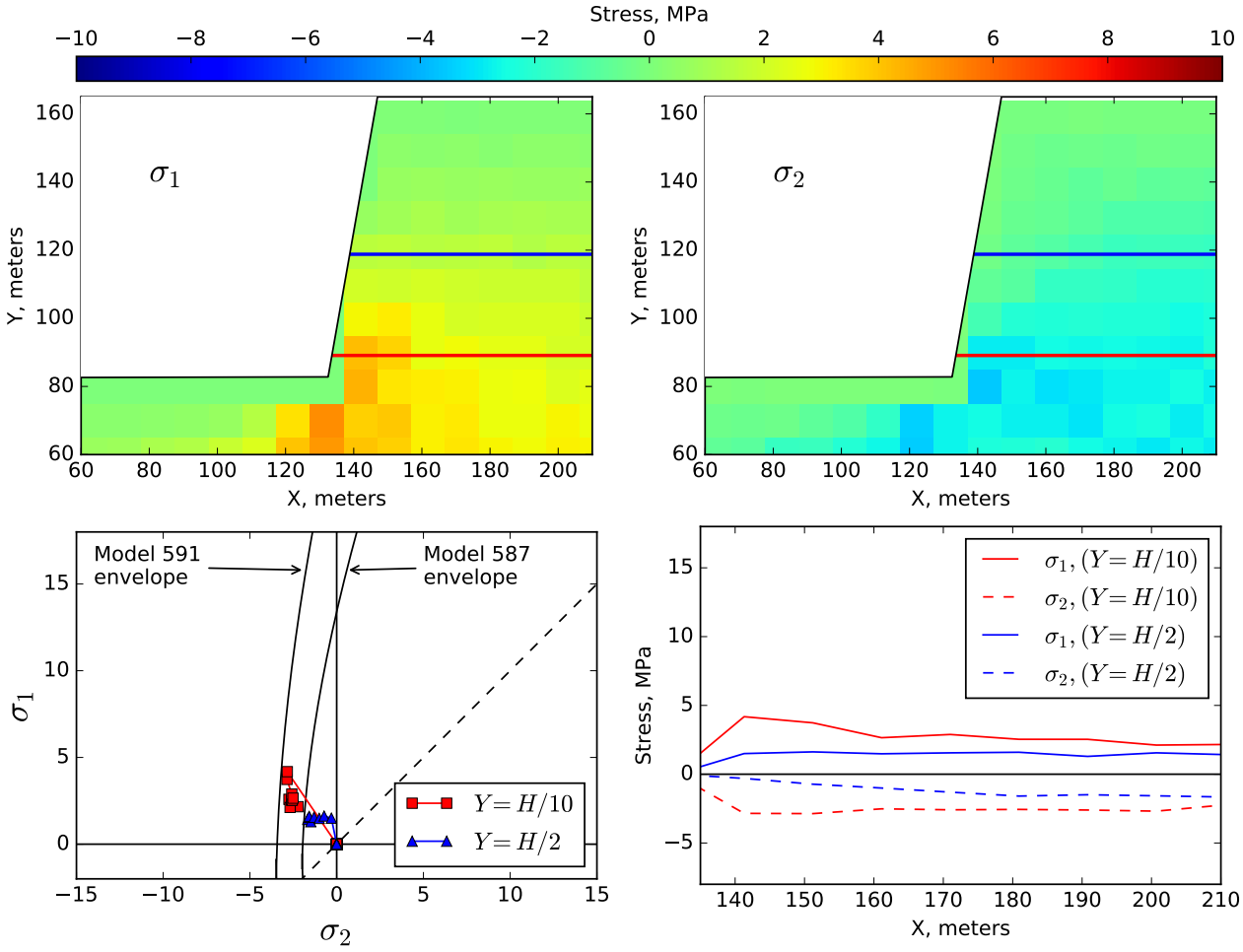

Figure 5.20: Stress state of Model 587/591 at the downslope extreme for 1 Hz loading.

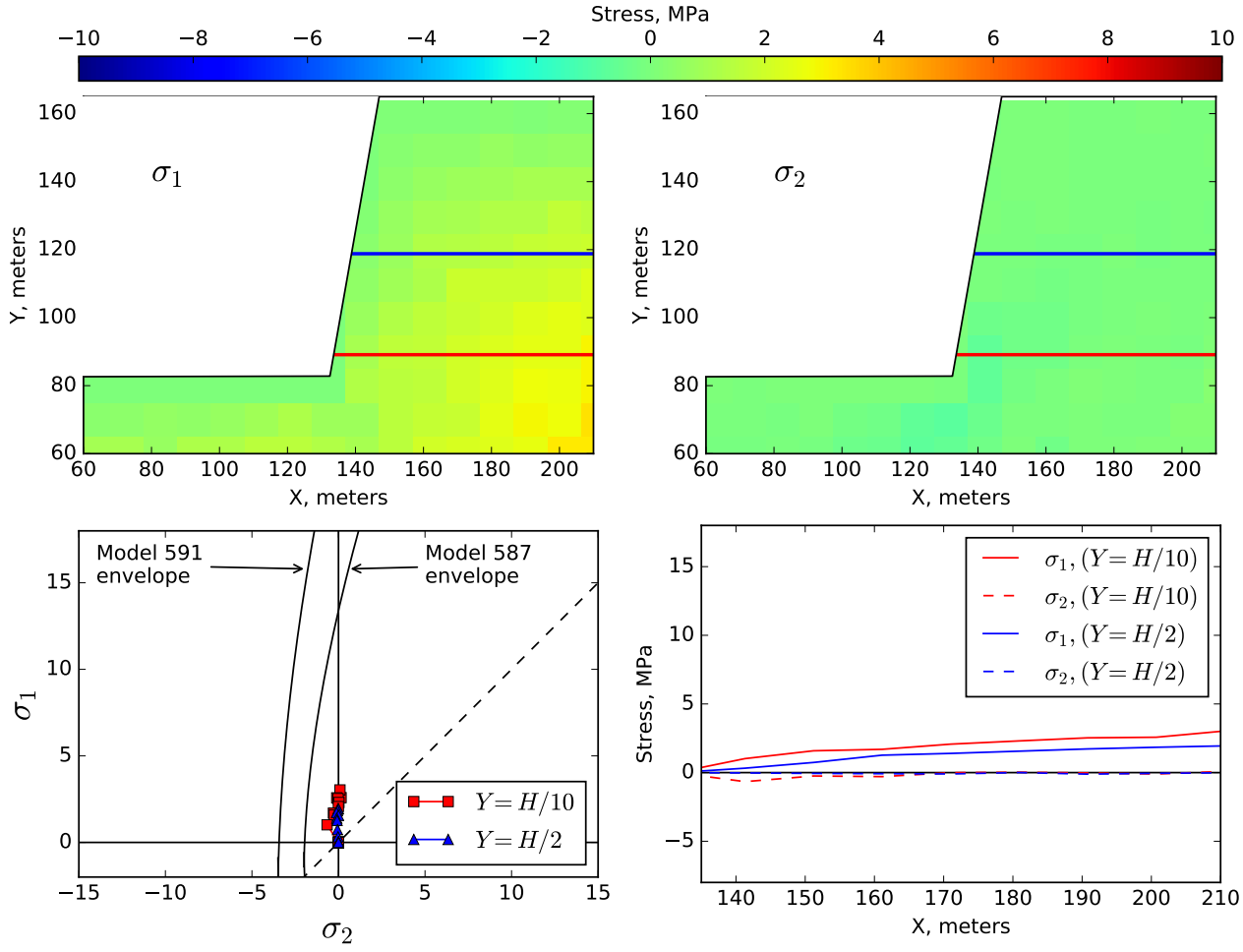

Figure 5.21: Stress state of Model 587/591 at the upslope extreme for 1 Hz loading.

2 Hz Loading

The 2 Hz loading (i.e., tuning ratio of 0.7) induces a strong dynamic response. The slope oscillates with large levels of velocity amplification as shown in Figure 5.22. The force-chain and stress field extrema in the upslope and downslope directions (corresponding to the displacement extrema) are shown in Figures 5.23 through 5.25. The tensile force-chains near the crest of the slope observed in the 1 Hz loading are much more pronounced and have a more clear direction – dipping into the slope at roughly 15 degrees from the horizontal. Compressive force-chains, perpendicular to these tensile force-chains, radiate from the compressive concentration at the toe of the slope. Similar to the force-chain patterns in a Brazilian Tensile (BT) test, the pattern in the downslope extreme force-chain diagram indicates that if tensile failures develop behind the slope crest, the cracks will be likely to propagate down towards the toe. The tensile forces visible at the toe in the upslope extreme are also of greater magnitude than those observed in the 1 Hz loading results. The stress fields in Figures 5.24 and 5.25 indicate that compressive and tensile failures at the toe are both likely for Models 587 and 591. In the downslope extreme, the stresses at H/2 appear to become more critical with distance from the slope face.

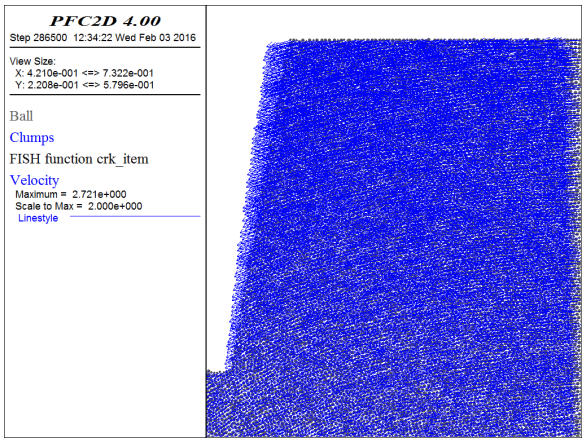

(a) Downslope extreme velocity

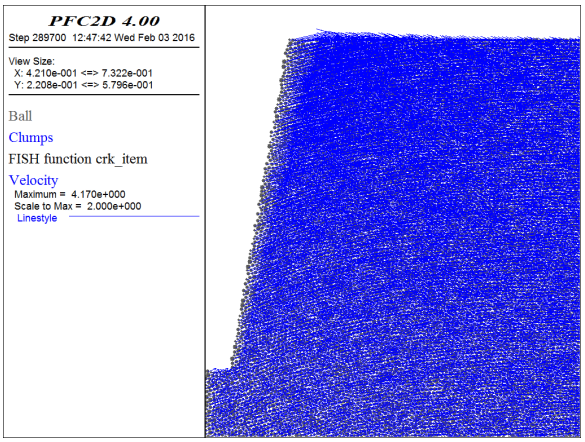

(b) Upslope extreme velocity

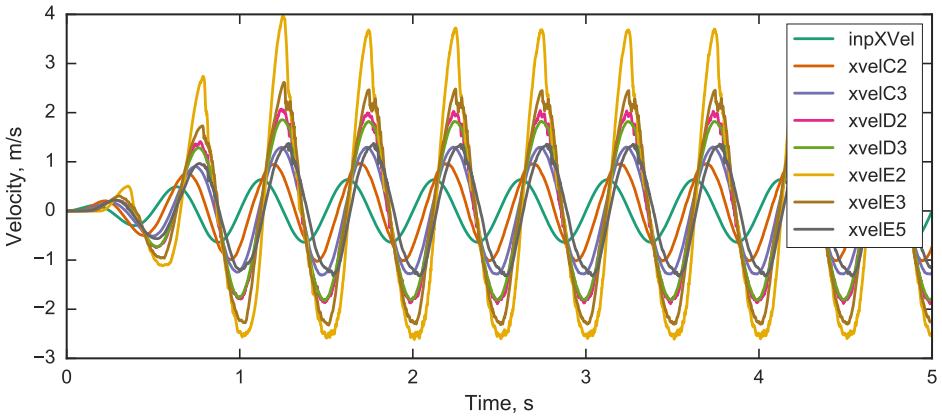

(c) Velocity response of the slope with time.Points with 'E', 'D', and 'C' in the labels correspond to the elevations of the crest, mid-slope, and base, respectively. Points with '2' and '3' in the labels correspond to points at the slope face and set back 65 meters from the slope face, respectively. Point 'E5' corresponds to the furthest monitored point from the crest at the ground surface behind the slope. Refer to Figure 5.12 for the positions of the monitored points within the slope.

Figure 5.22: Velocity response for 2 Hz loading on Model 587/591.

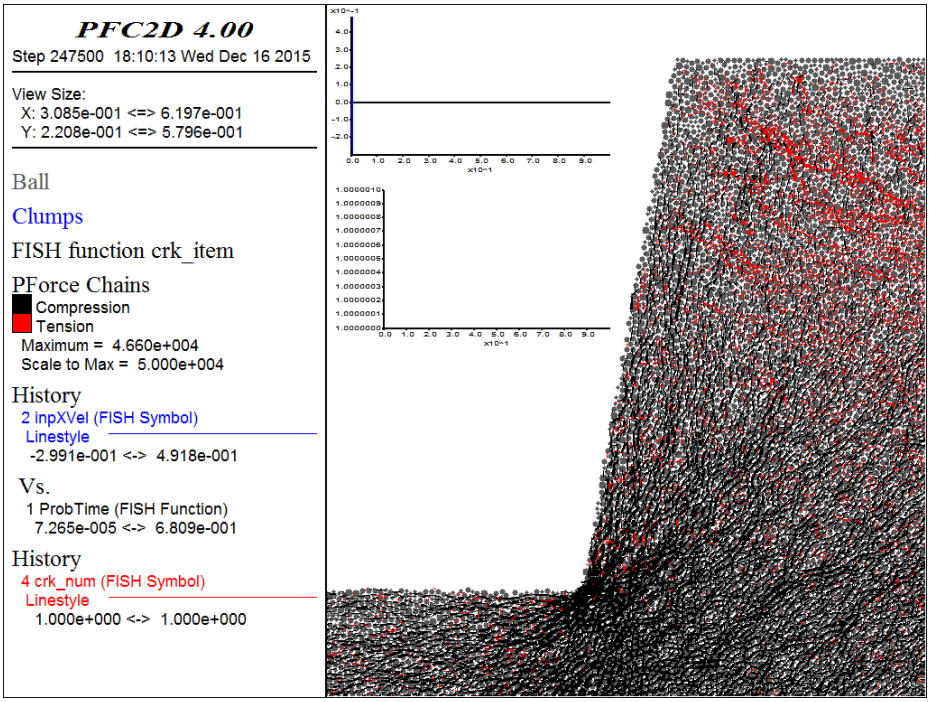

(a) Downslope extreme force

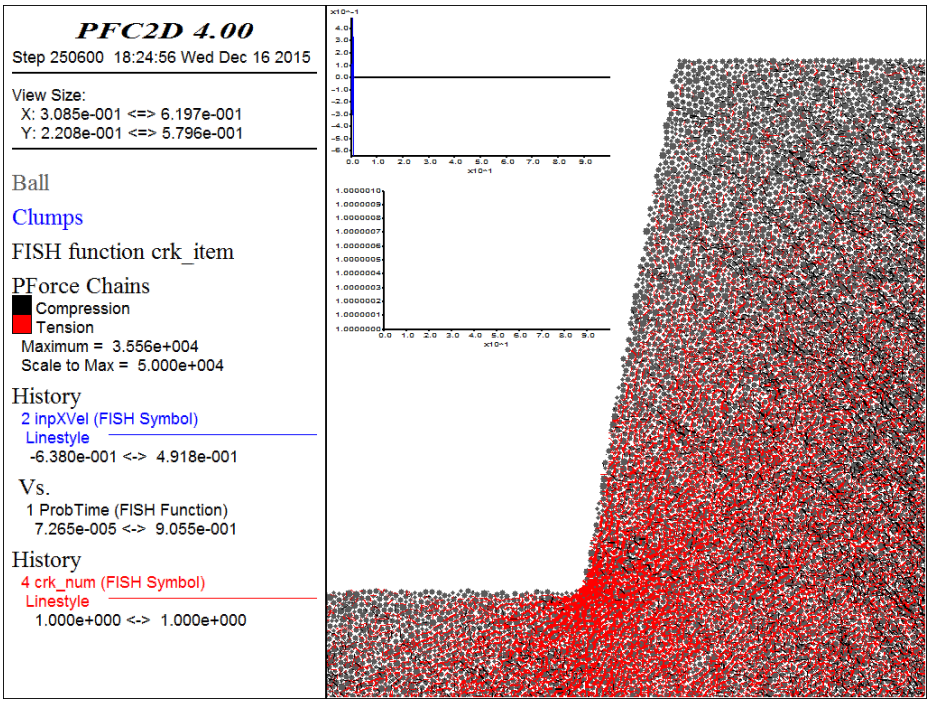

(b) Upslope extreme force

Figure 5.23: Force-chain extrema for 2 Hz loading on Model 587/591.

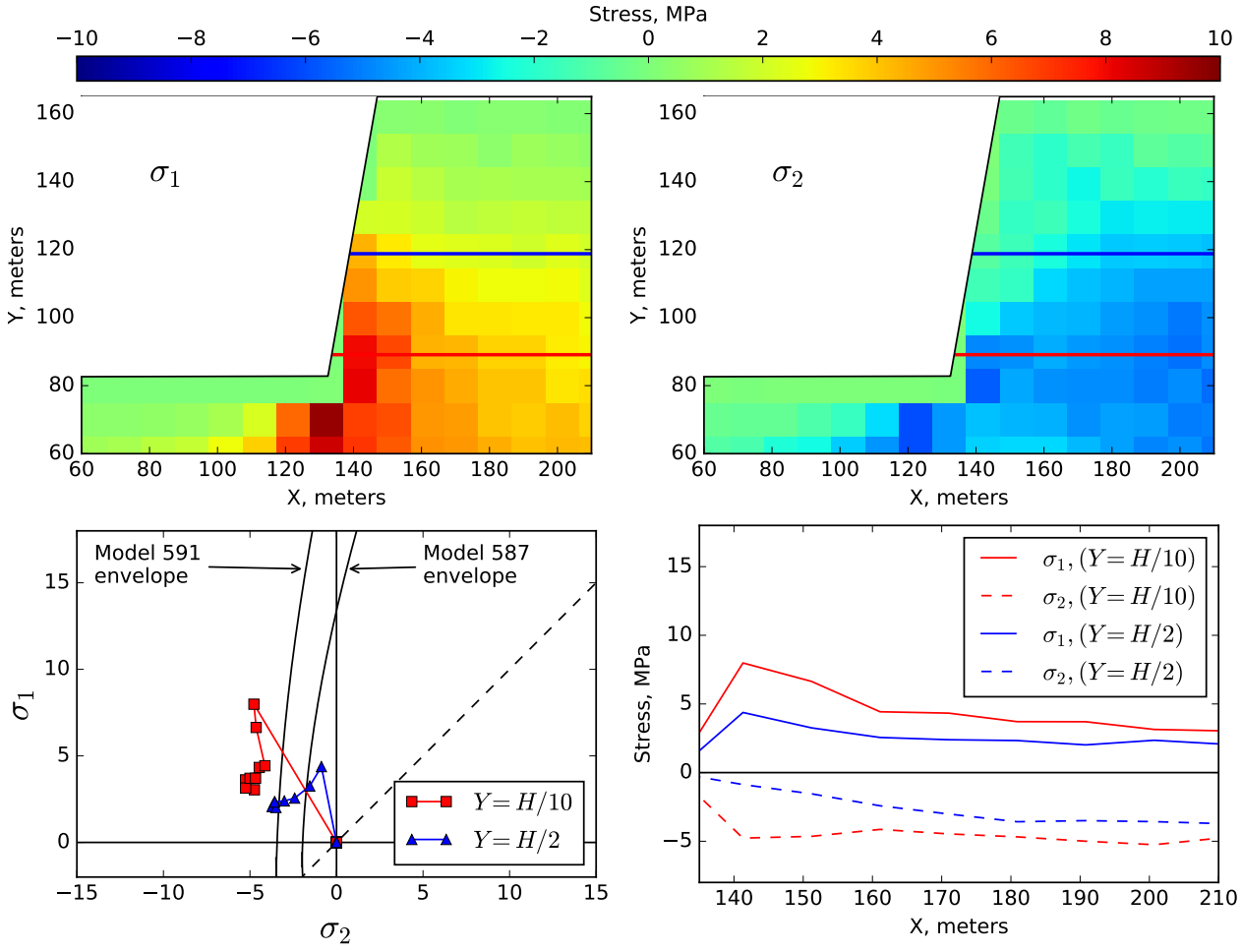

Figure 5.24: Stress state of Model 587/591 at the downslope extreme for 2 Hz loading.

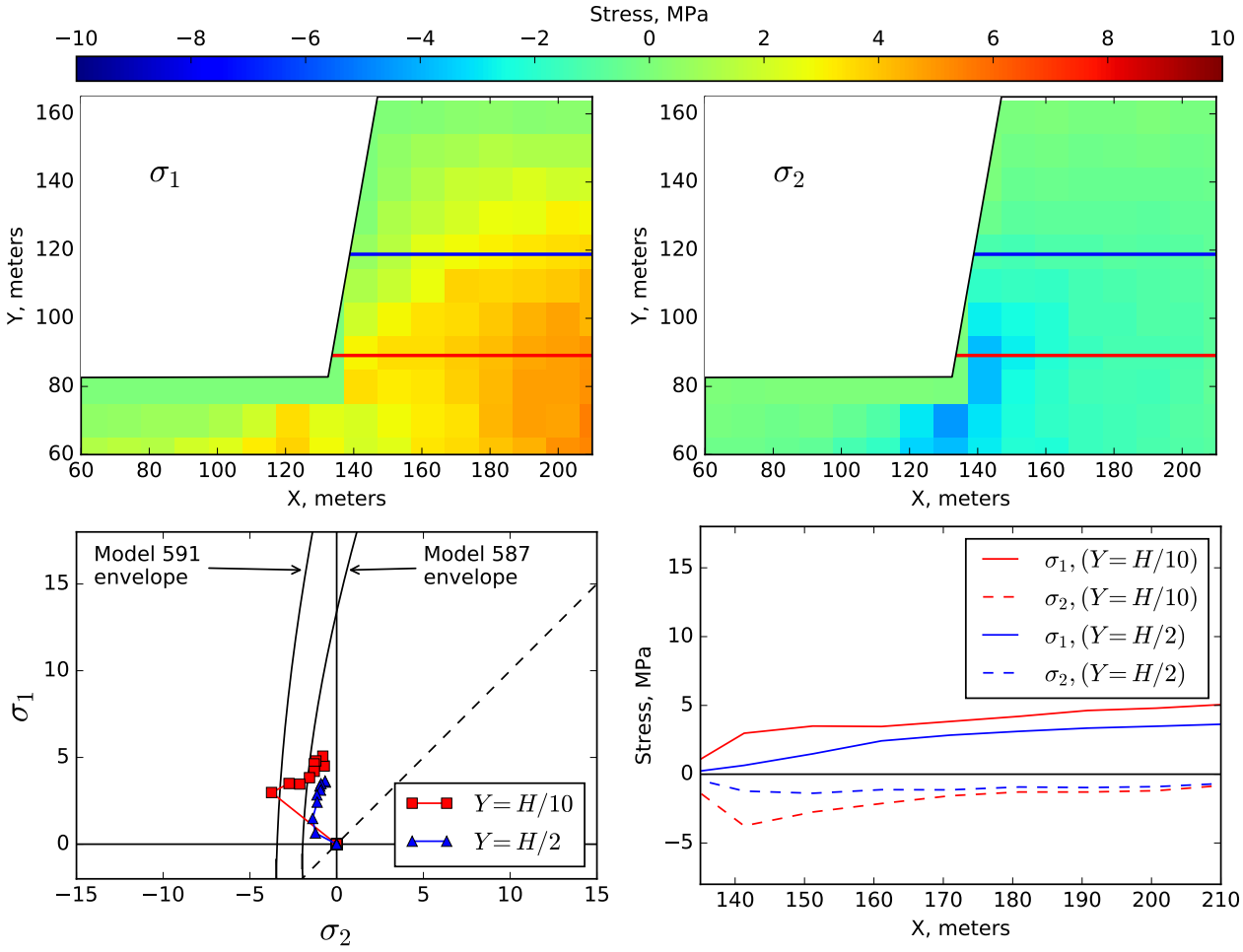

Figure 5.25: Stress state of Model 587/591 at the upslope extreme for 2 Hz loading.

3 Hz Loading

The 3 Hz loading (i.e., tuning ratio of 1.0) induces a very strong dynamic response. The slope oscillates with large levels of velocity amplification as shown in Figure 5.26. The force-chain and stress field extrema in the upslope and downslope directions (corresponding to the displacement extrema) are shown in Figures 5.27 through 5.29. The tensile force-chains near the crest of the slope are much more pronounced than at lower tuning ratios. Compressive force-chains, perpendicular to these tensile force-chains, radiate from the compressive concentration at the toe of the slope. Similar to the force-chain patterns in a Brazilian Tensile (BT) test, the pattern in the downslope extreme force-chain diagram indicates that if tensile failures develop behind the slope crest, the cracks will be likely to propagate down towards the toe. The tensile forces in the slope in the upslope extreme are greatest at the toe, but are also very large throughout nearly the entire slope face. Compressive force-chains in the upslope extreme are perpendicular to the tensile force-chains in an inverse arrangement from the downslope extreme. In this upslope movement case, the force-chains indicate that, if tensile failures develope at the slope face, the cracks will be likely to propagate down and into the slope at about 15 degrees from horizontal. The stress fields in Figures 5.28 and 5.29 indicate that compressive and tensile failures at the toe are both likely for Models 587 and 591. They also indicate that tensile failures much higher up the slope are possible.

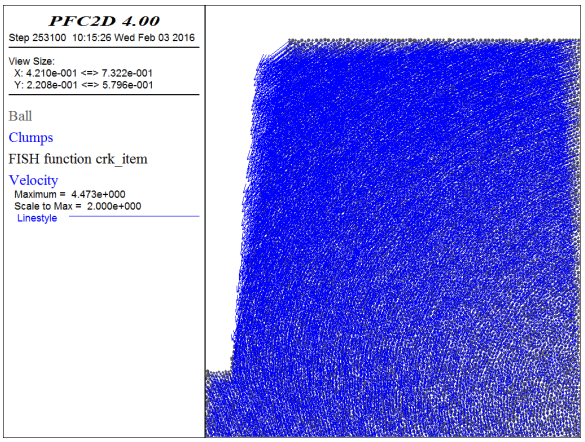

(a) Downslope extreme velocity

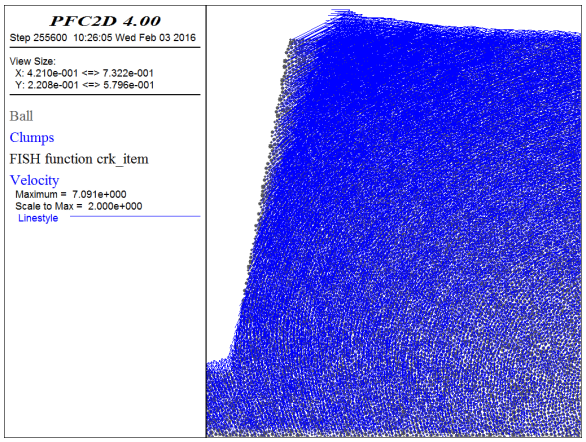

(b) Upslope extreme velocity

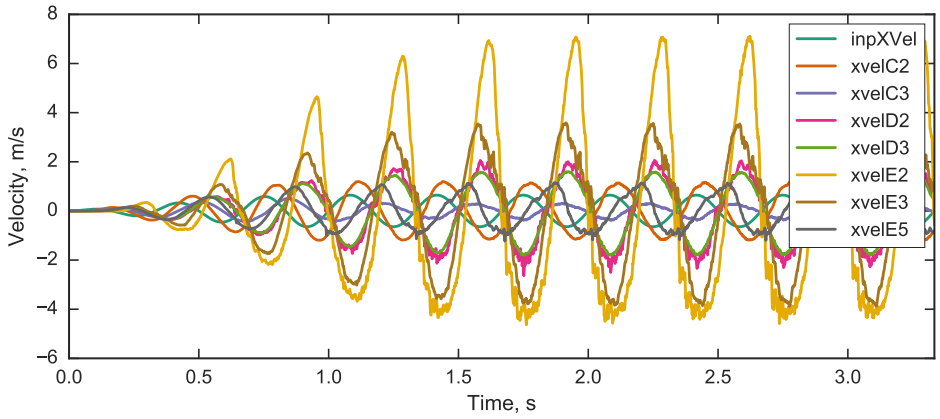

(c) Velocity response of the slope with time.Points with 'E', 'D', and 'C' in the labels correspond to the elevations of the crest, mid-slope, and base, respectively. Points with '2' and '3' in the labels correspond to points at the slope face and set back 65 meters from the slope face, respectively. Point 'E5' corresponds to the furthest monitored point from the crest at the ground surface behind the slope. Refer to Figure 5.12 for the positions of the monitored points within the slope.

Figure 5.26: Velocity response for 3 Hz loading on Model 587/591.

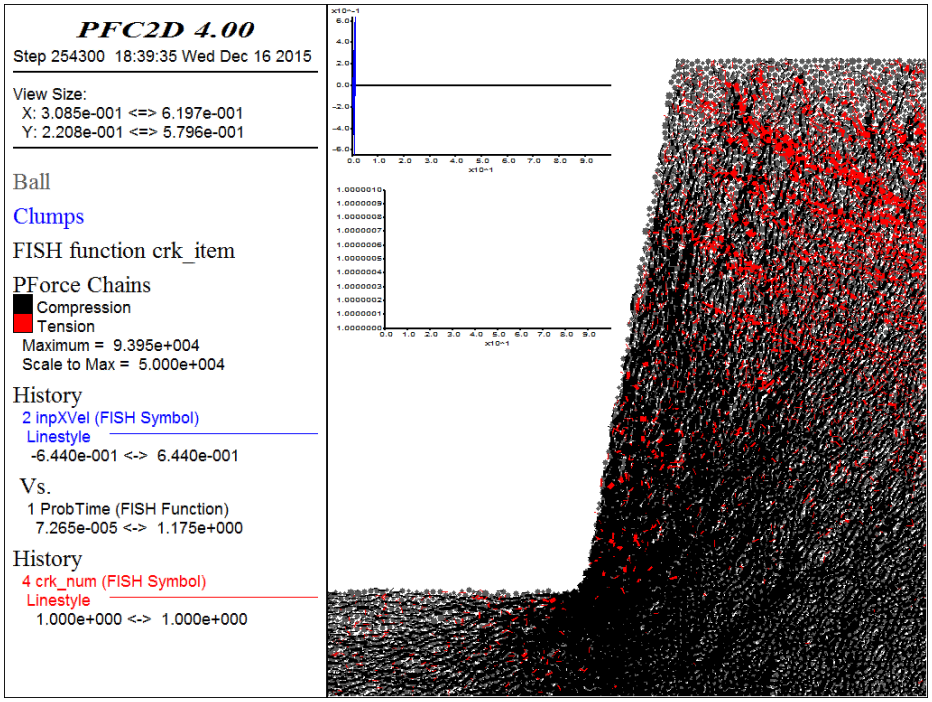

(a) Downslope extreme force

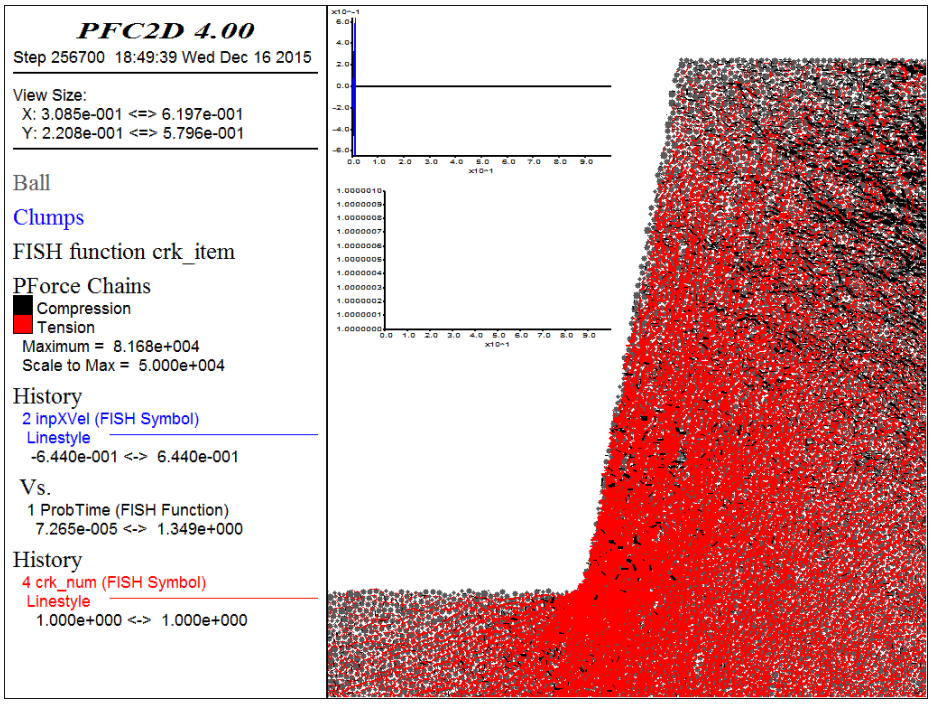

(b) Upslope extreme force

Figure 5.27: Force-chain extrema for 3 Hz loading on Model 587/591.

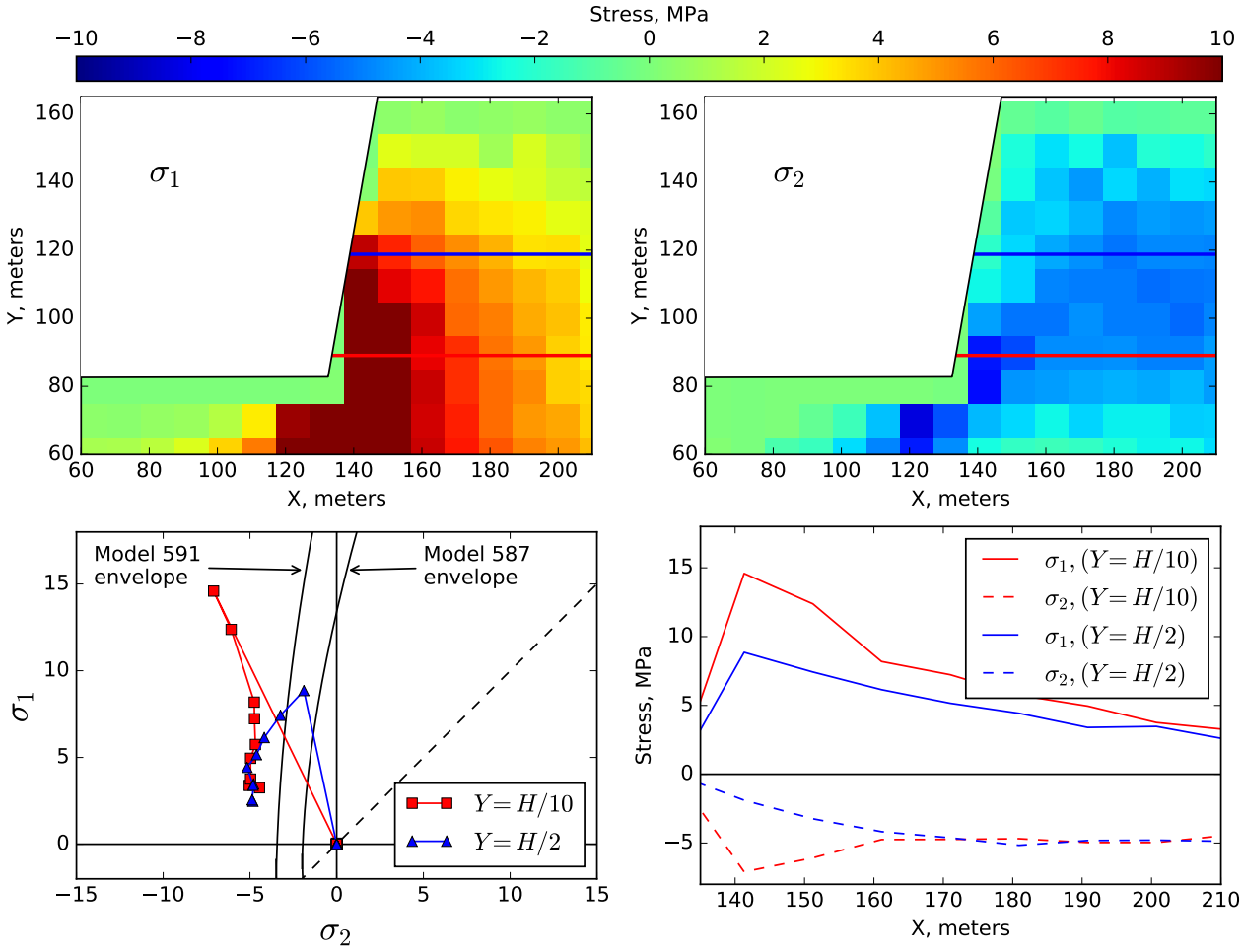

Figure 5.28: Stress state of Model 587/591 at the downslope extreme for 3 Hz loading.

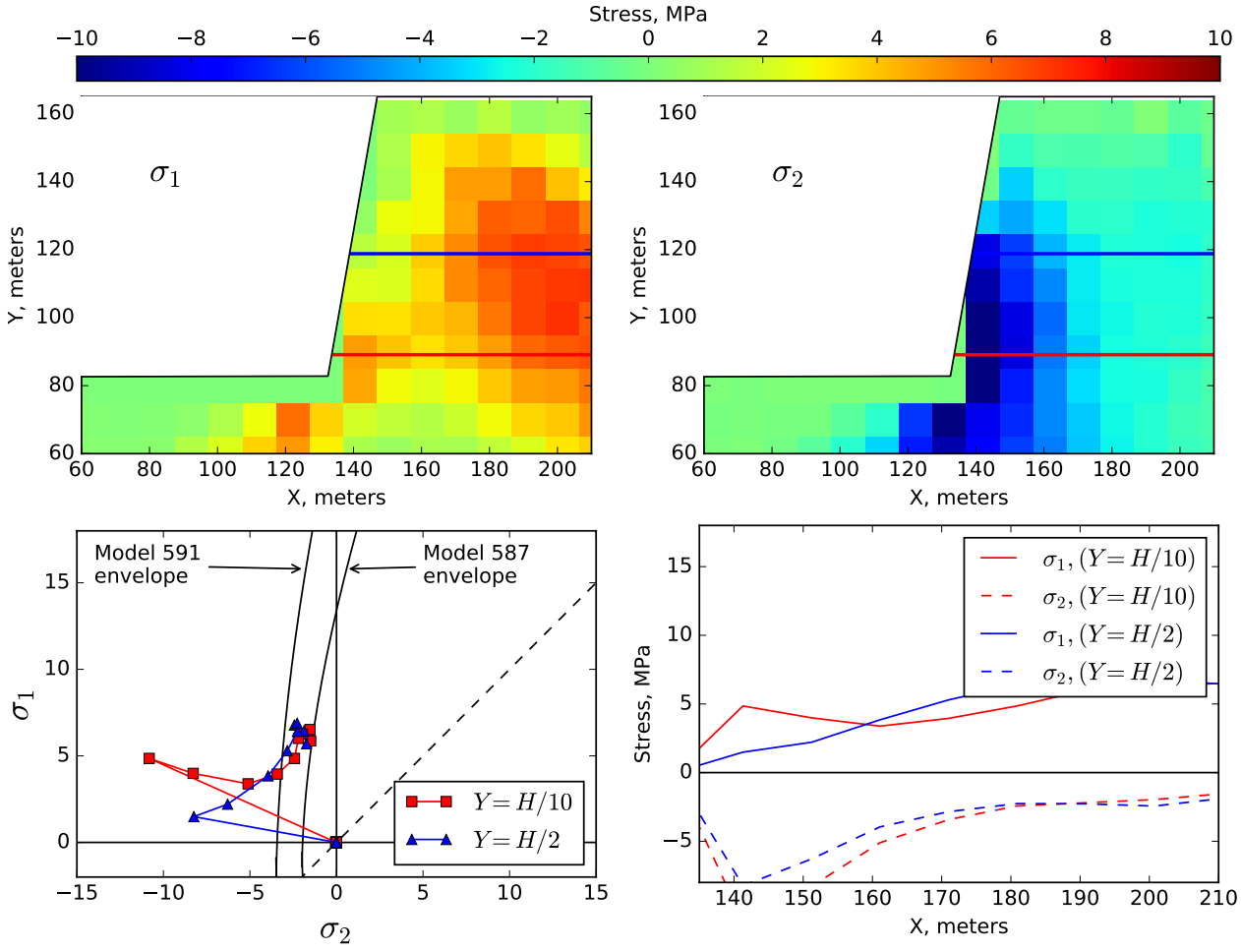

Figure 5.29: Stress state of Model 587/591 at the upslope extreme for 3 Hz loading.

5 Hz Loading

The 5 Hz loading (tuning ratio of 1.7) induces a different dynamic response in the slope than the loadings with tuning ratios at and below 1.0. Because the loading frequency is high compared to the slope frequency, more of the waveform is present within the slope at any given time. For this reason, the figures for the 5 Hz loading show a snapshot of the model state at more than the up and downslope extrema.

Figure 5.30 shows the velocity response of the slope with time.

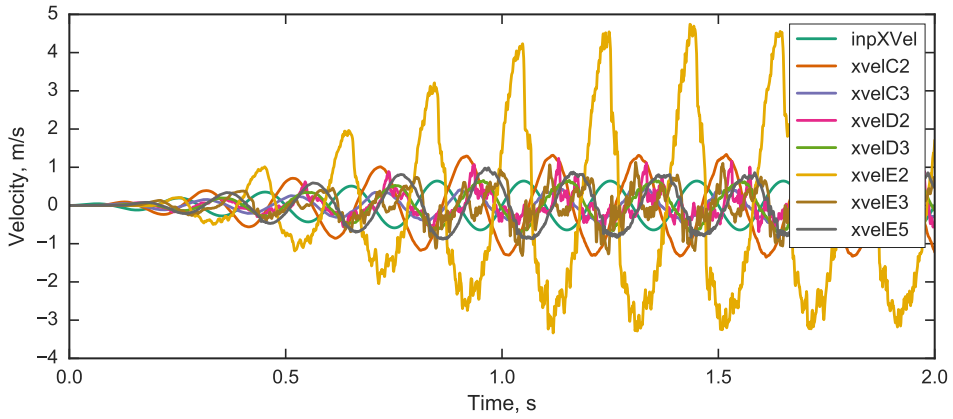

Figure 5.30: Velocity response with time for 5 Hz loading on Model 587/591. Points with 'E', 'D', and 'C' in the labels correspond to the elevations of the crest, mid-slope, and base, respectively. Points with '2' and '3' in the labels correspond to points at the slope face and set back 65 meters from the slope face, respectively. Point 'E5' corresponds to the furthest monitored point from the crest at the ground surface behind the slope. Refer to Figure 5.12 for the positions of the monitored points within the slope.

Eight figures, spaced at $\pi/4$ "steps" over the cycle of input motion are shown in Figures 5.31 through 5.38.

Comments on the states of the models at each of the eight steps shown in Figures 5.31 through 5.38 are presented below:

- **Step 1** (Figure 5.31) – The crest of the slope is experiencing different motion than the

rest of the slope '- the crest is moving out while the toe is moving in. An area of zero apparent velocity is present at the slope face around H/2. A zone of tensile forces can be seen near the slope face. The transverse compressive force-chains indicate cracks initiating in these areas may travel into the slope with a slight upward angle. The stresses in the model indicate that failure due to these tensile forces may occur at the slope face at H/2 or set back from the slope face a bit at H/10. The orientation of tensile and compressive force-chains in this area indicate that cracks initiating here may propagate into the slope at a slightly upward angle and toward the slope face at a slightly downward angle.

- **Step 2** (Figure 5.32) – The particles at the crest begin to move downward as well as outward. The area of zero apparent velocity has moved up and into the slope. The tensile zone seen at the face of the slope in Step 1 has moved deeper into the slope, and strong tensile forces are visible near the crest. There is no distinct pattern of transverse compressive force chains at the crest, which indicates a more erratic force/stress state in this area. This may be the reason that, although there are scattered force-chains of high tension, the cell stresses don't indicate any failure in this area. The stresses at H/10 are critical for Model 587 at the face of the slope, but not for Model 591. The stresses at H/10 increase with distance from the slope face, peaking around 50 meters from the slope face and are critical for Model 591 within 10 meters of the slope face.

- **Step 3** (Figure 5.33) – As the particles at the crest continue to move downward, a zone of compression develops near the slope face. The crest has also moved outward, increasing the tension behind the crest. Compressive force-chains are now visible transverse to these tensile force-chains, and the tensile stresses are visible in the stress plots at this step. The critical stresses in the slope continue to move into the slope, and upward.

- **Step 4** (Figure 5.34) – At this step, the crest is moving downward, but no longer has much outward displacement. The outward displacement of the crest from the velocities observed in preceding steps is approaching a maximum and the resulting

tensile forces behind the crest are pronounced. The compressive forces along the slope face created by the downward movement of the crest, peak around H/2. Note that, although σ_1 is very high at H/2 at the slope face, σ_2 is nearly zero, so compressive failure is not expected due to this condition.

- **Step 5**(Figure 5.35) – Movement at the crest and the toe are out of phase, but in the opposite sign of Step 1. As in Step 1, a point of apparent zero velocity is present near the slope face around H/2. The tensile forces and stresses behind the crest are pronounced, as are the compressive stresses along the slope face from H/2 and below.

- **Step 6** (Figure 5.36) – As the crest continues to move inward, the tensile forces behind the crest are reduced. As in Step 2, he area of zero apparent velocity from the previous step has moved up and into the slope.

- **Step 7** (Figure 5.37) – The area of zero apparent velocity continues to move upward and inward and reaches the top of the slope about H/2 behind the crest. The velocity of the crest, still inward, has a fairly strong upward component.

- **Step 8** (Figure 5.38) – In this step, the tensile forces/stresses develop near the slope face and are strongest at H/2. Step 8 appears to be the precursor to Step 1, which is expected.

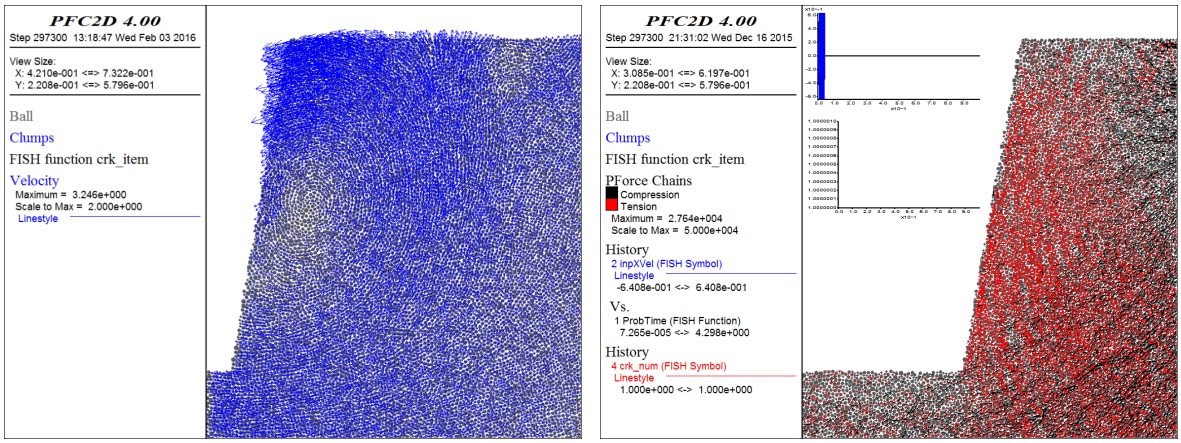

(a) Velocity **(b)** Force-chain

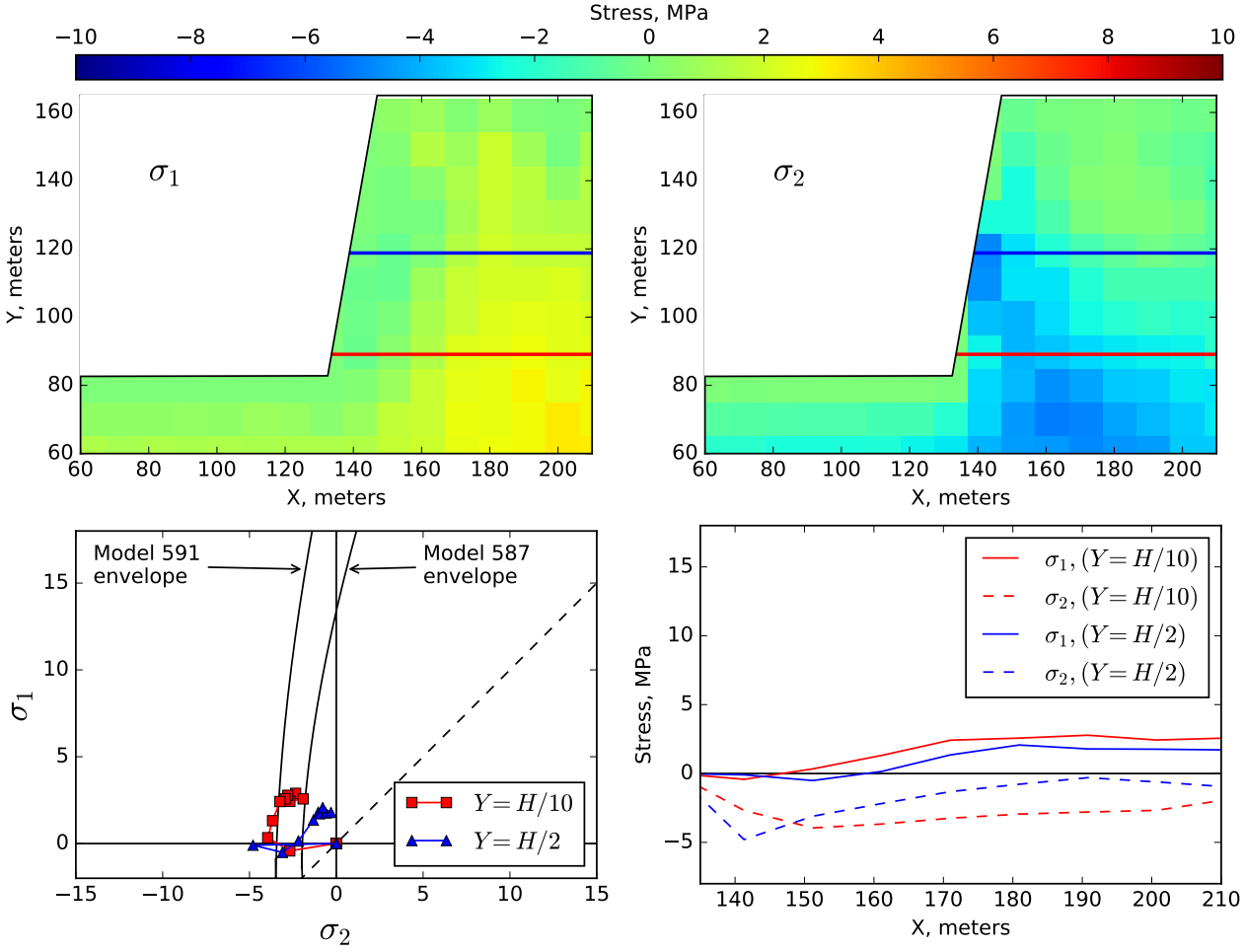

(c) Stress state

Figure 5.31: Velocity, force-chain, and stress states of Model 587/591 at Step 1 for 5 Hz loading.

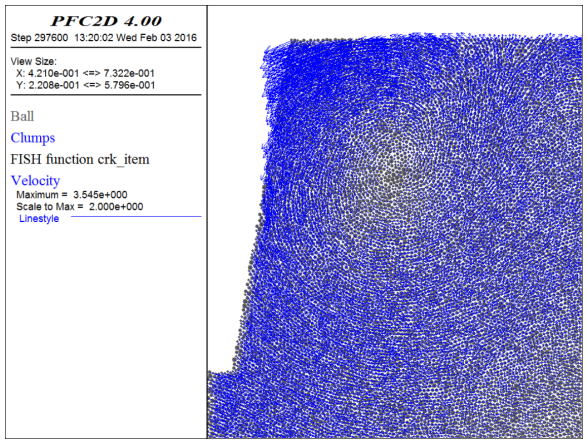

(a) Velocity

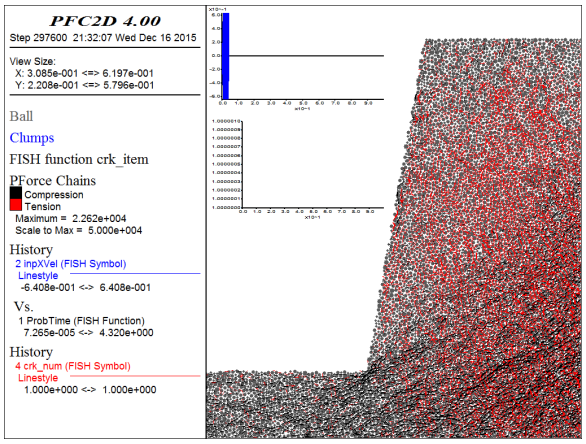

(b) Force-chain

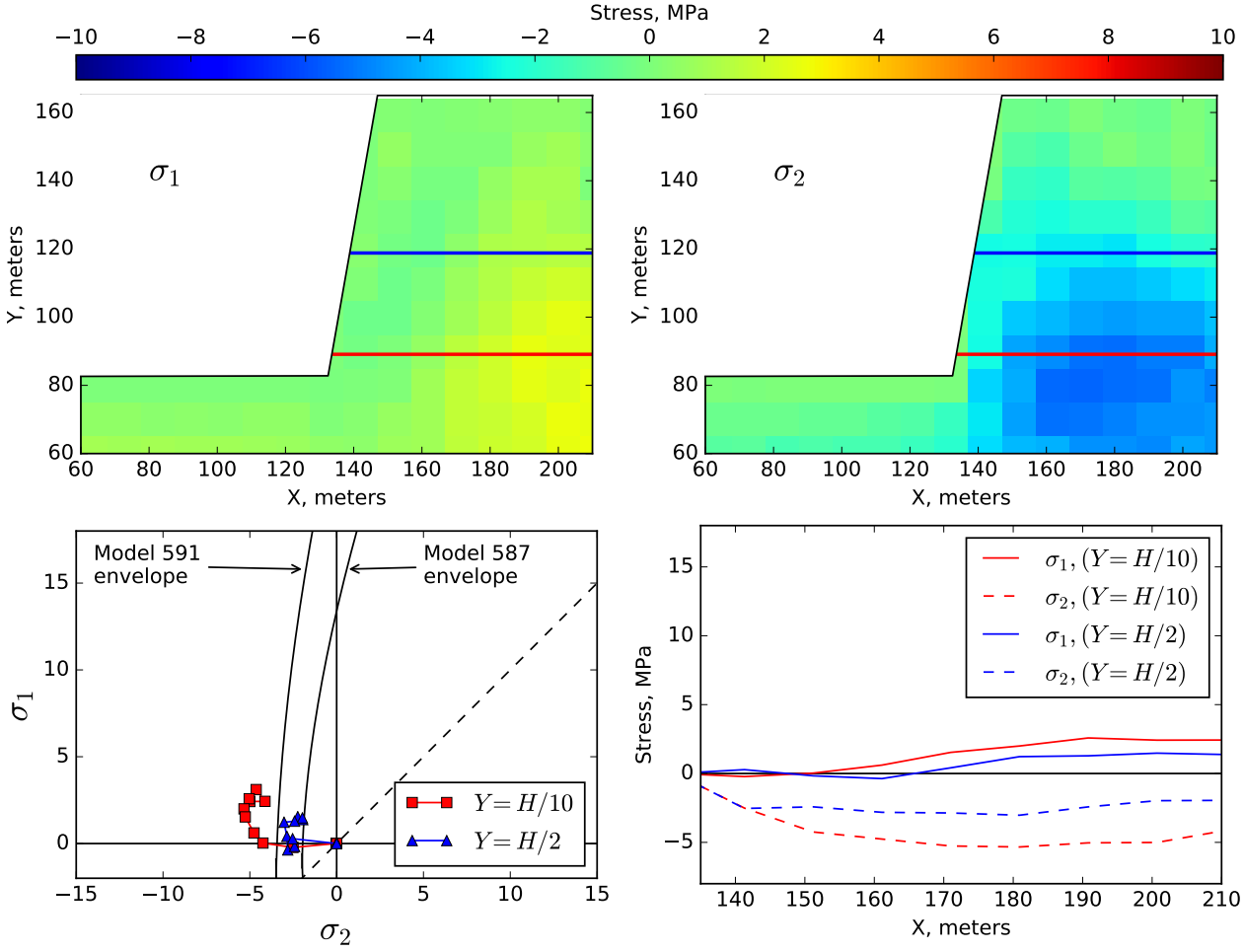

(c) Stress state

Figure 5.32: Velocity, force-chain, and stress states of Model 587/591 at Step 2 for 5 Hz loading.

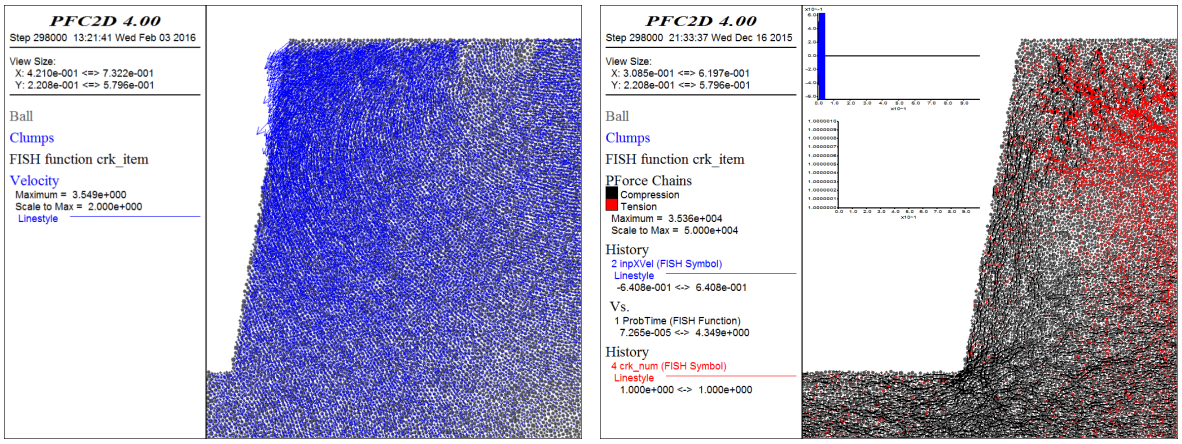

(a) Velocity **(b)** Force-chain

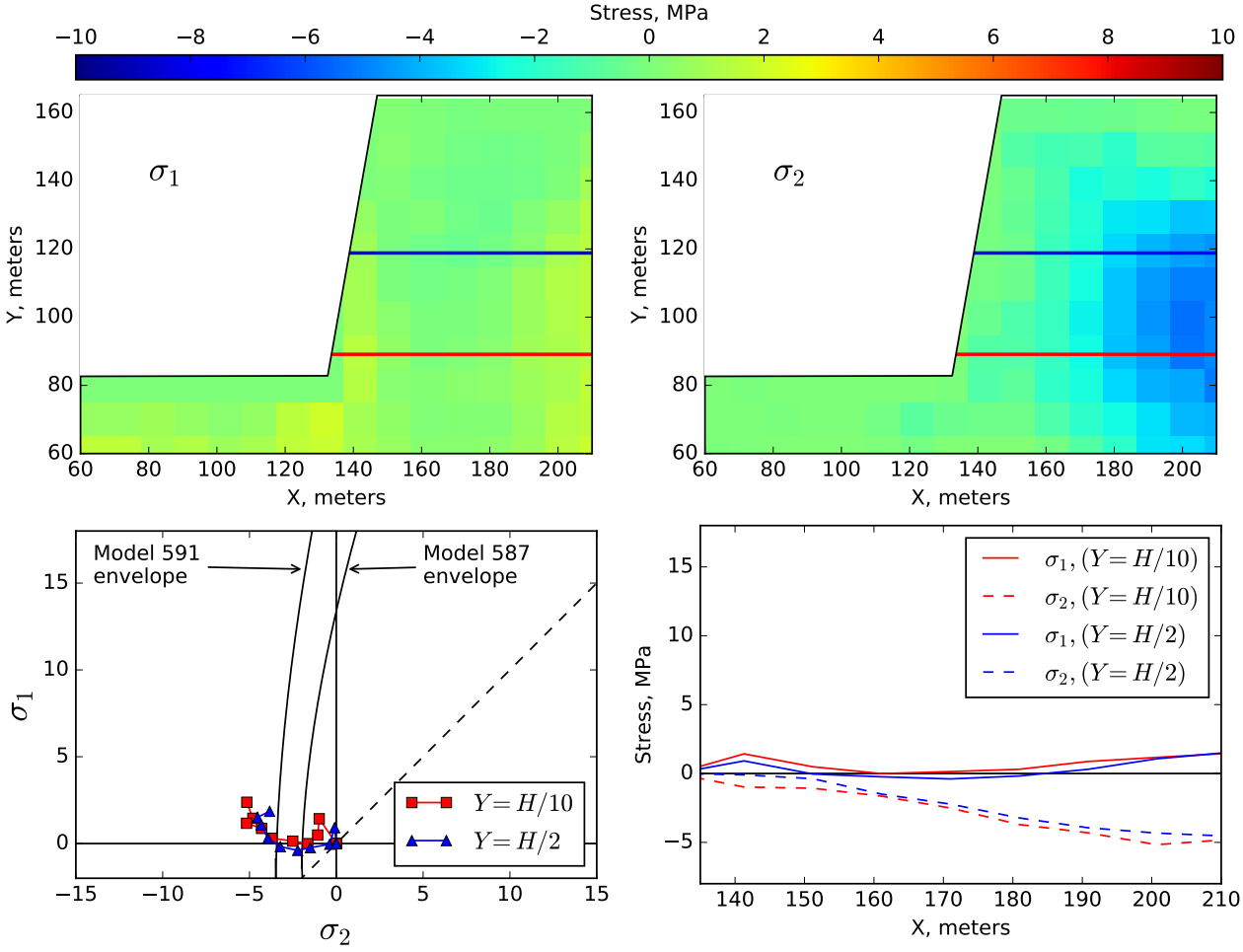

(c) Stress state

Figure 5.33: Velocity, force-chain, and stress states of Model 587/591 at Step 3 for 5 Hz loading.

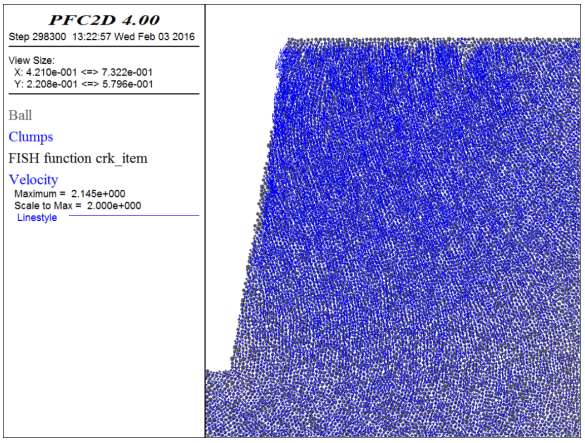

(a) Velocity

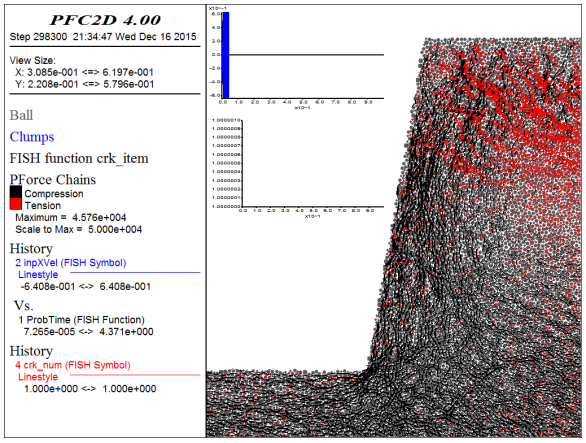

(b) Force-chain

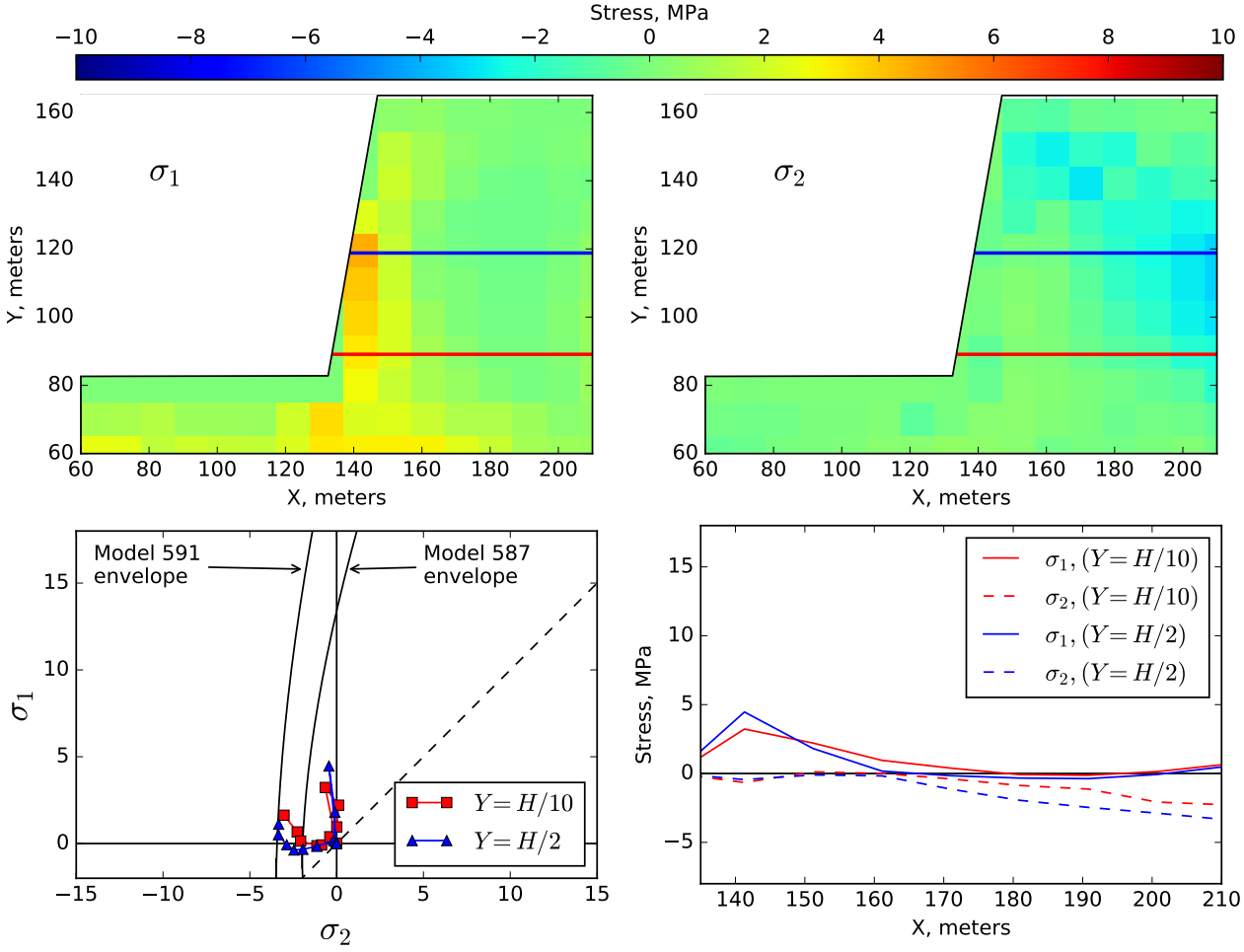

(c) Stress state

Figure 5.34: Velocity, force-chain, and stress states of Model 587/591 at Step 4 for 5 Hz loading.

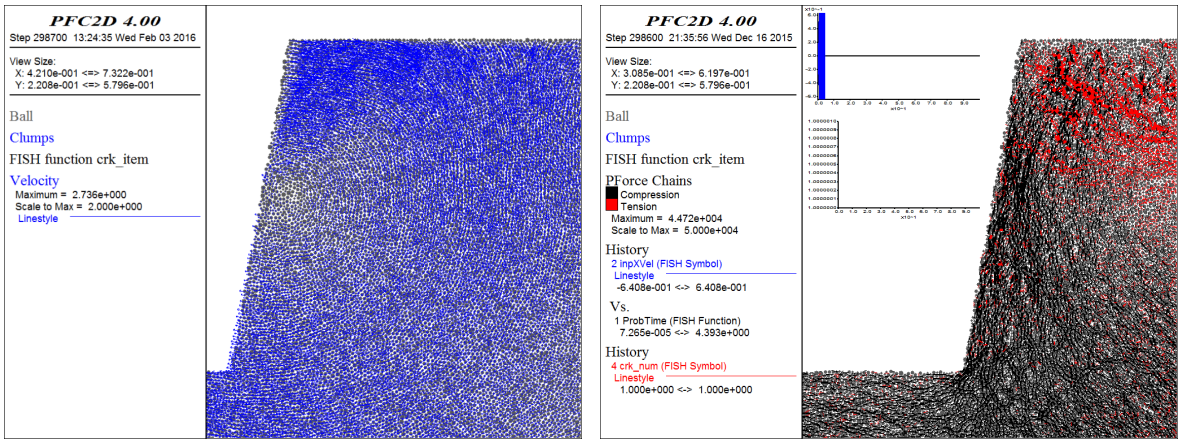

(a) Velocity **(b)** Force-chain

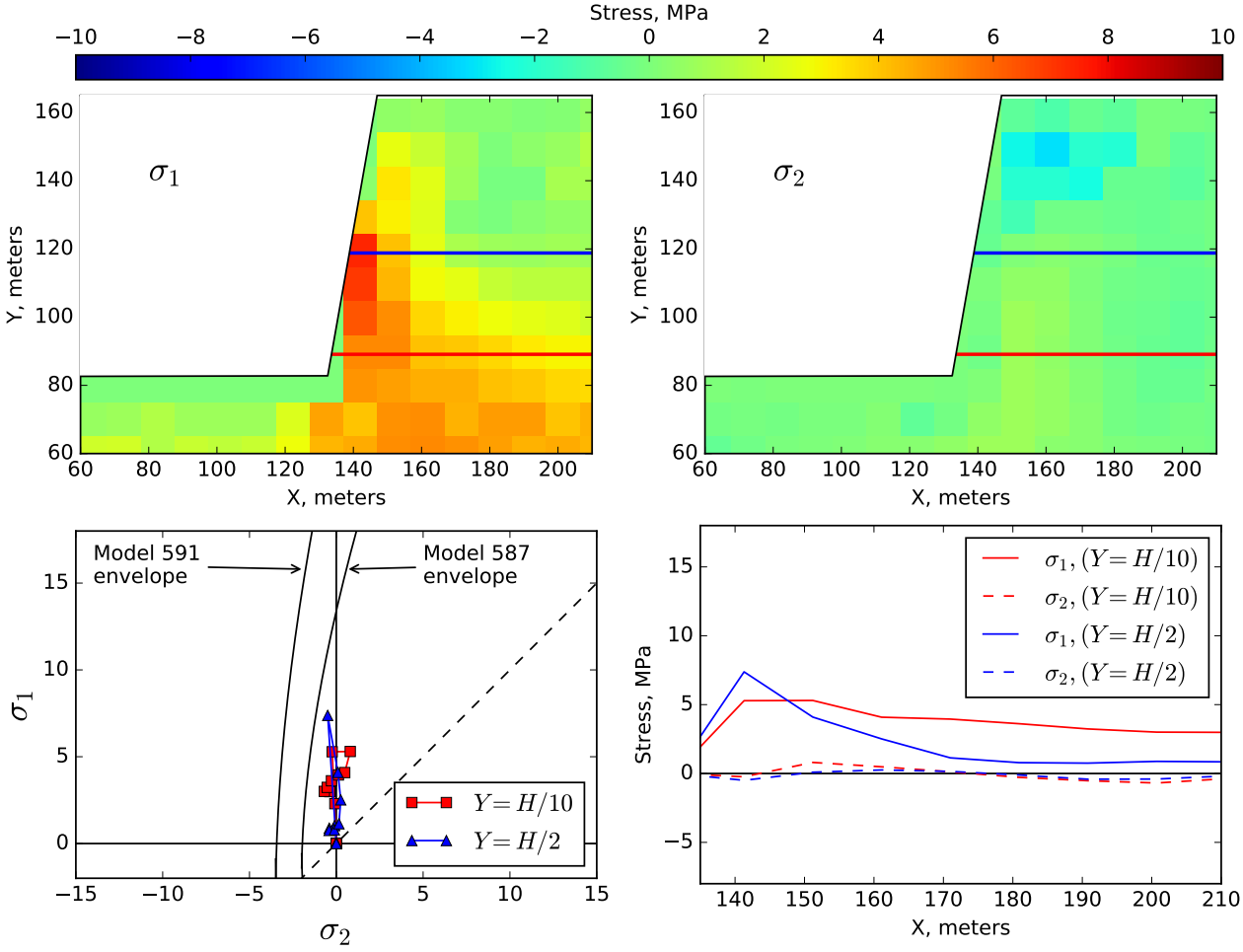

(c) Stress state

Figure 5.35: Velocity, force-chain, and stress states of Model 587/591 at Step 5 for 5 Hz loading.

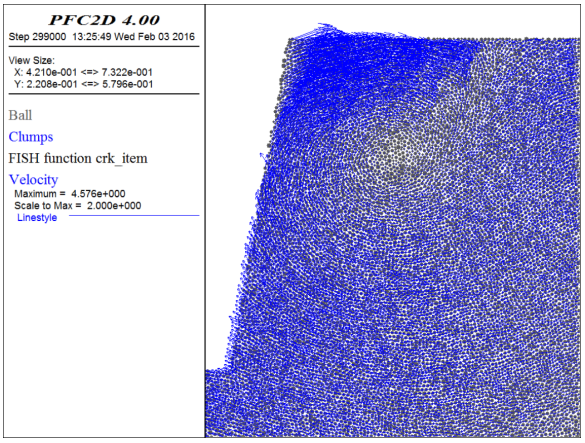

(a) Velocity

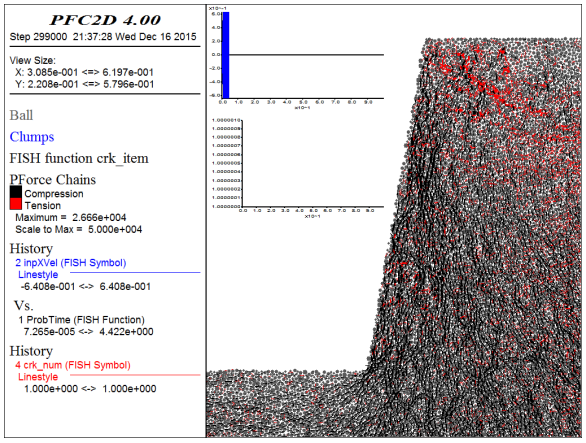

(b) Force-chain

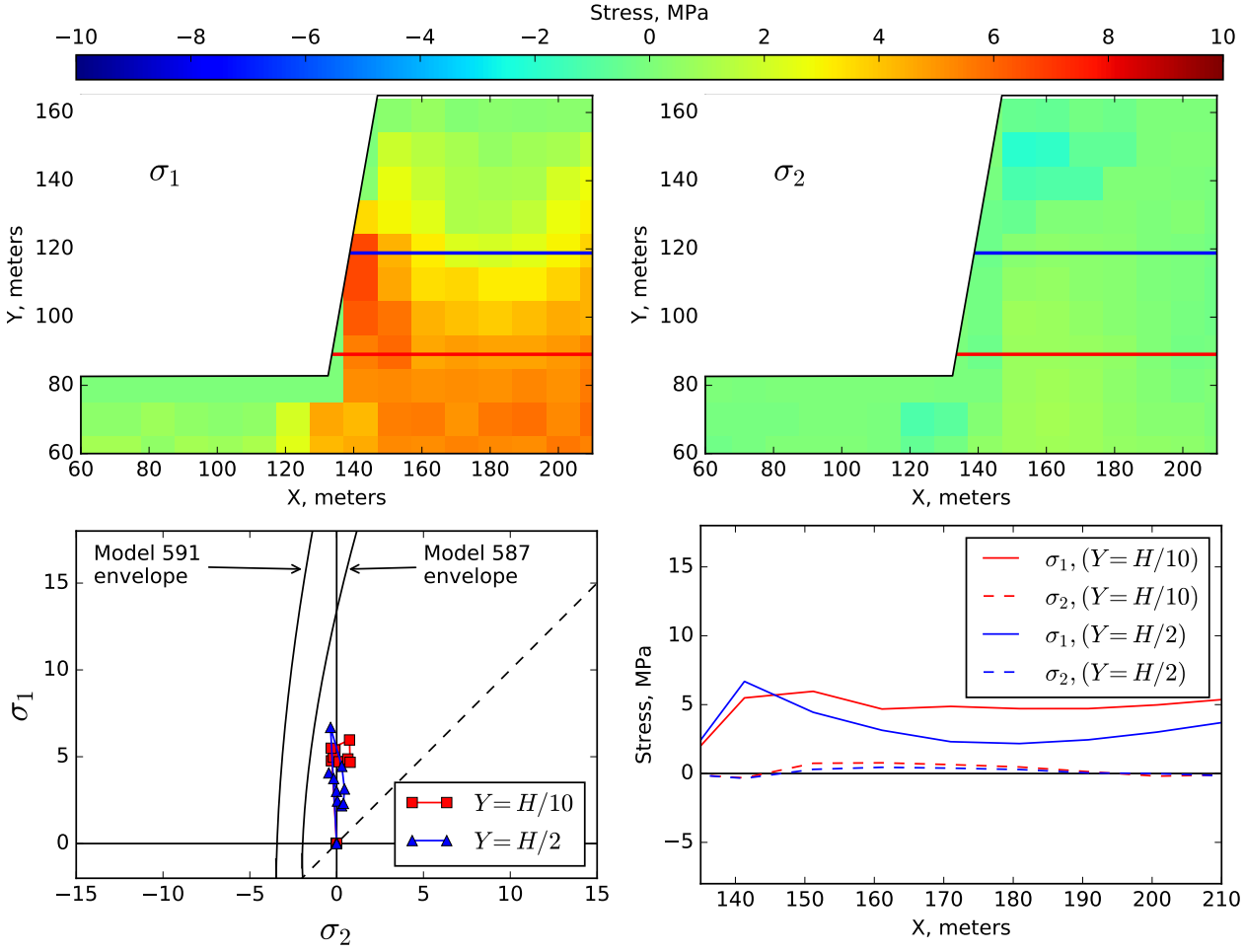

(c) Stress state

Figure 5.36: Velocity, force-chain, and stress states of Model 587/591 at Step 6 for 5 Hz loading.

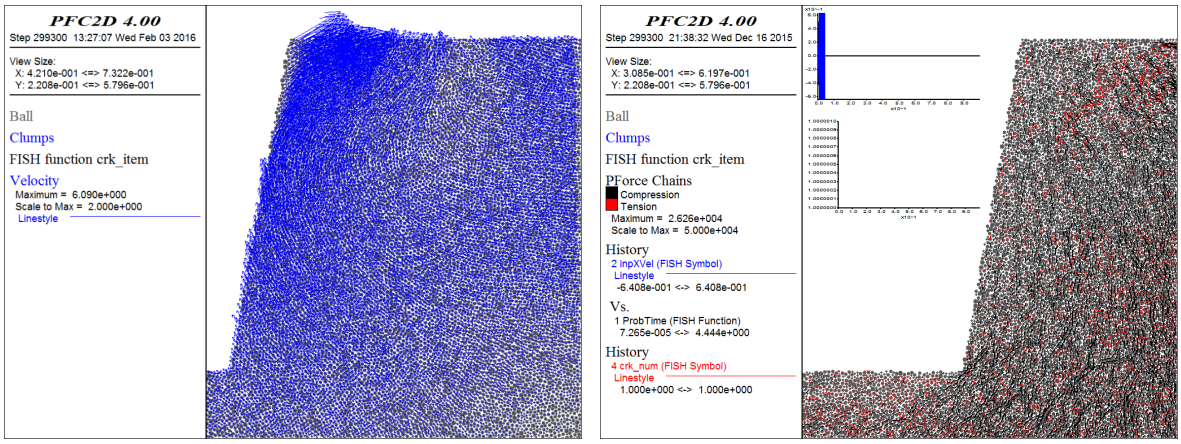

(a) Velocity **(b)** Force-chain

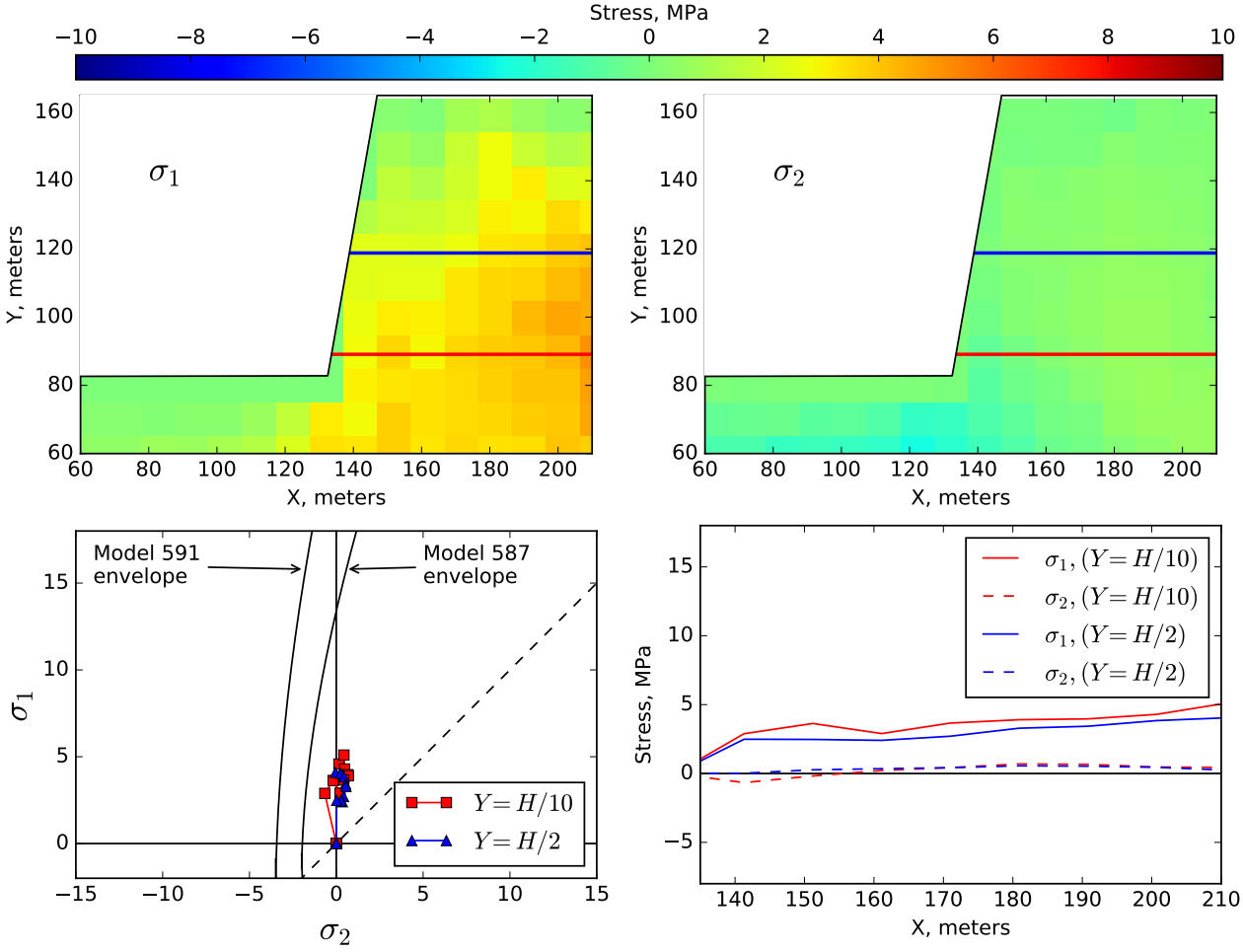

(c) Stress state

Figure 5.37: Velocity, force-chain, and stress states of Model 587/591 at Step 7 for 5 Hz loading.

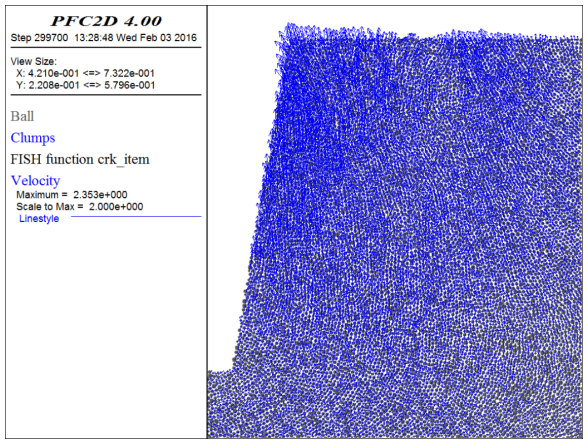

(a) Velocity

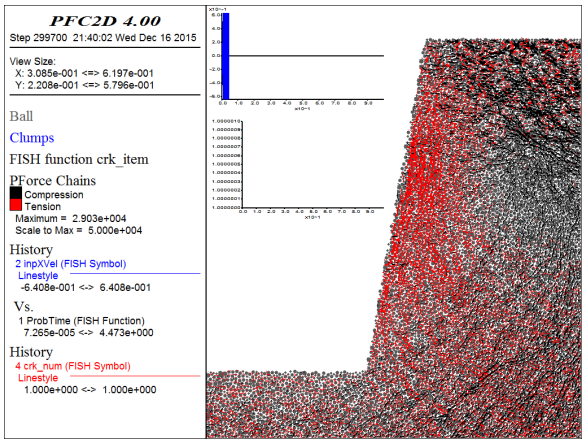

(b) Force-chain

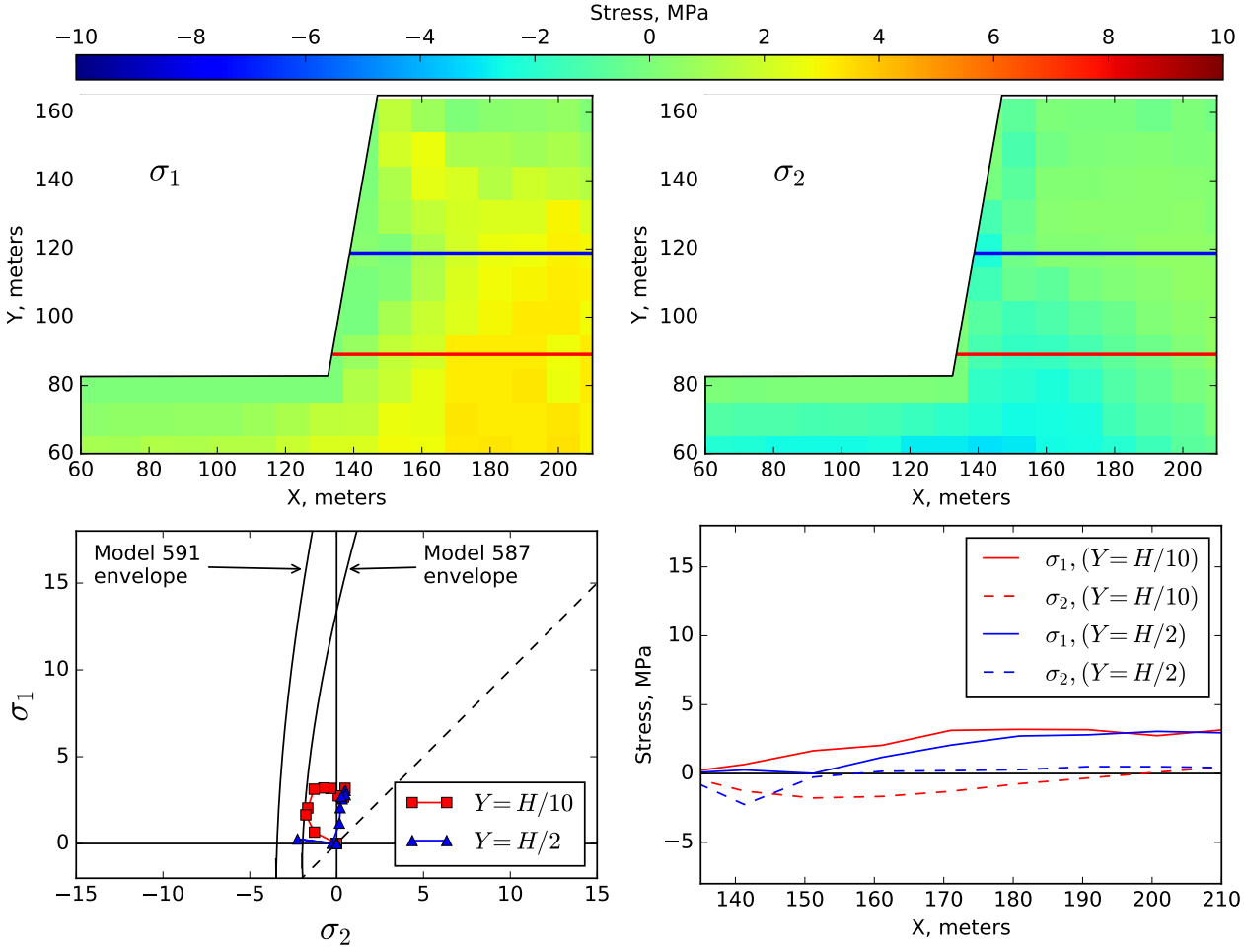

(c) Stress state

Figure 5.38: Velocity, force-chain, and stress states of Model 587/591 at Step 8 for 5 Hz loading.

Velocity Amplification in the Non-Destructive Harmonic Simulations

As shown in the previous sections, the response of the slope to non-destructive harmonic loading varied significantly with loading frequency. The level of amplification due to each loading can be assessed by the velocity apparent amplification factor, AA_V, defined as

$$AA_V = \frac{PV_{cr} - PV_{fff}}{PV_{fff}} \tag{5.4}$$

where PV_{cr} and PV_{fff} are the peak velocities at the crest and free-field in front of the toe, respectively [84]. Figure 5.39 shows the level of velocity amplification for each loading. The figure shows a strong influence of dynamics on the topographic effects.

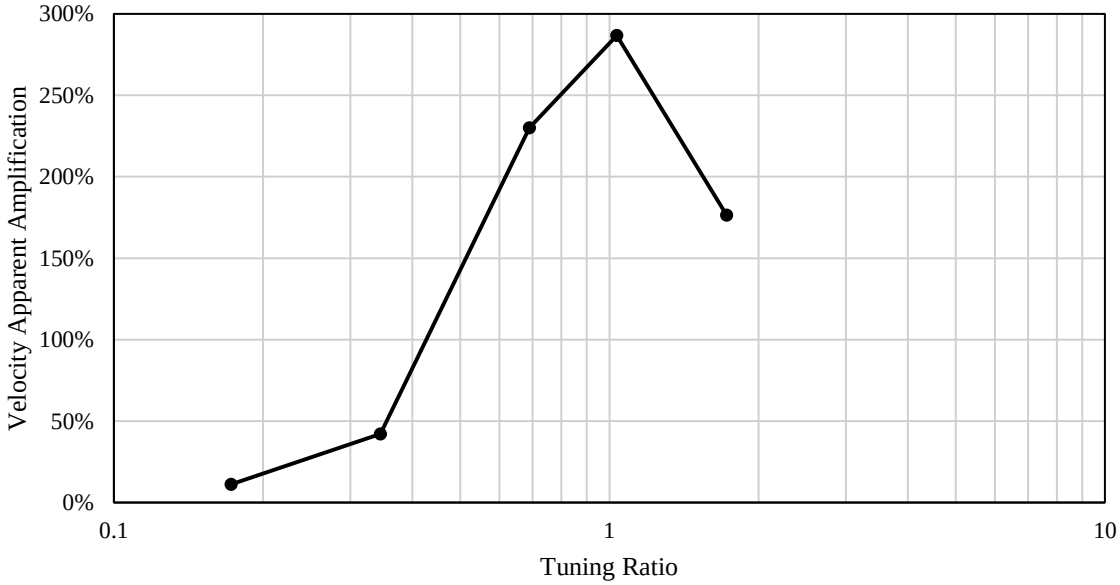

Figure 5.39: Velocity apparent amplification factor AA_V with tuning ratio for Model 587/591 subjected to harmonic loading.

5.4.4 Destructive Harmonic Loading

When subjected to the same harmonic loading suite as in the previous section, Models 587 and 591 experience various levels of damage and failure mechanisms. This section will present the behavior of the two models subjected to strong harmonic ground motion.

Because the loading used in these simulations is very strong and the simulations run for 20 seconds, in some of the simulations, the damage in the model becomes severe and reaches the "no crack boundary". At this point, the simulation's boundary conditions are changed, and the behavior of the slope is more representative of post-shaking run-out than dynamic failure.

Failure Mechanisms and Modes

Multiple failure mechanisms and modes were observed in Models 587 and 591. The terms 'mechanism' and 'mode' have distinct meanings in this document. A failure mechanism is a failure of intact rock mass due to a particular force/stress state at a particular location. A failure mode is a significant movement of rock mass following a failure mechanism.

Some failure mechanisms observed in the models are listed below. The mechanisms are divided by 'primary' and 'secondary'. A 'primary' mechanism is one that can initiate without another failure mechanism preceding it. A 'secondary' mechanism is one that only initiates after another failure mechanism. These labels do not indicate the importance of the failure mechanism to the overall behavior of the slope. And, although they do indicate something about the order of events, a slope may experience multiple primary failure mechanisms. It is worth noting that the definition of the failure modes, and to a lesser extent, the failure mechanisms, are somewhat subjective. The presentation of failure mechanisms and modes provided here may not be exhaustive, and different observers may group the results differently. The mechanisms and modes discussed throughout this chapter are intended to provide a clear, but broad picture of the fundamental behavior of the models being evaluated.

The primary failure mechanisms observed in the slopes were:

- Tensile cracks initiating at the slope face (generally at the toe) and moving into the slope.
- Crushing of the rock mass at the toe.
- Wedge failures created by tensile rupture behind the slope face.

- Scattered tensile and shear failure of material at the crest of the slope.
- Deep tensile cracking at the base of the slope set back from the toe.

Two secondary failure mechanisms were also commonly observed in the simulations:

- Transverse cracking – where sets of cracks initiate and propagate outward from and perpendicular to another crack or set of cracks.
- Deep circular shear failure. This mechanism was often observed after extensive damage due to multiple other mechanisms.

These failure mechanisms are illustrated in Figures 5.40 and 5.41. In the figures, red arrows indicate tensile forces, black arrows indicate compressive forces, yellow dashed arrows indicate tensile cracks and the direction of propagation, and green dashed lines indicate shear cracks.

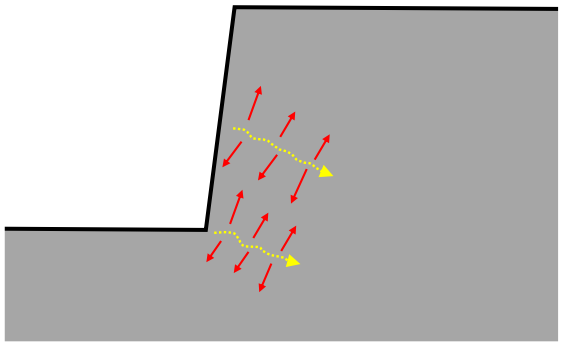

(a) Tensile crack initiating at the slope face

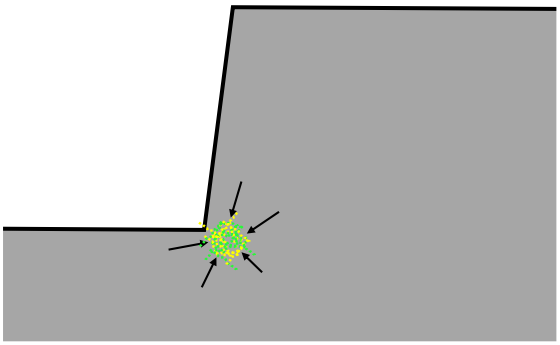

(b) Crushing of the rock mass at the toe

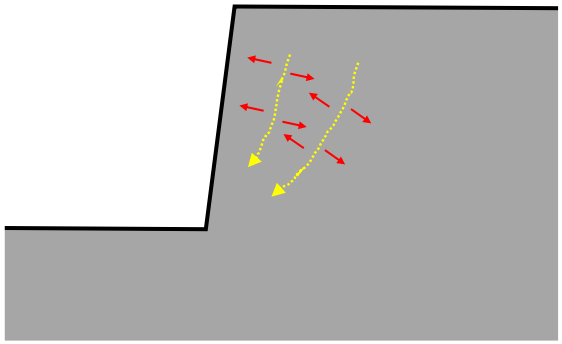

(c) Wedge failure from tensile rupture

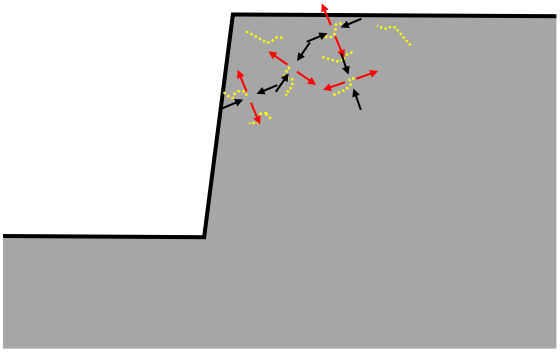

(d) Scattered damage at the crest

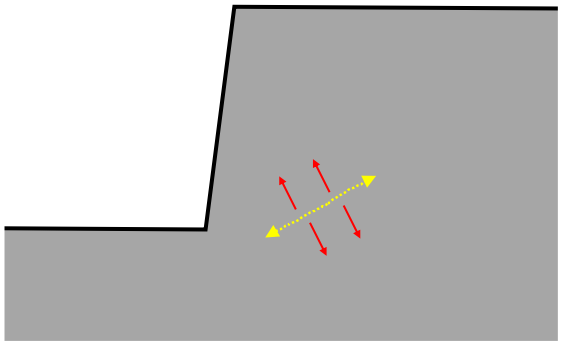

(e) Deep tensile cracking

Figure 5.40: Primary failure mechanisms observed in destructive harmonic loading of Models 587 and 591. Red arrows indicate tensile forces, black arrows indicate compressive forces, yellow dashed arrows indicate tensile cracks and the direction of propagation, and green dashed lines indicate shear cracks.

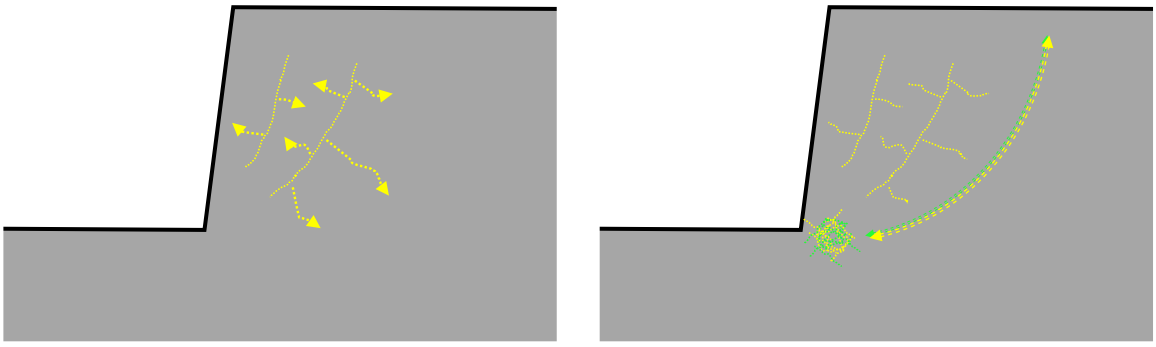

(a) Transverse cracking **(b)** Deep circular shear failure

Figure 5.41: Secondary failure mechanisms observed in the destructive harmonic loading of Models 587 and 591. Yellow dashed arrows indicate tensile cracks and the direction of propagation, and green dashed lines indicate shear cracks. The thinner yellow dashed lines indicate cracks associated with a primary failure mechanism that preceded the secondary mechanism.

Due to these failure mechanisms, the following failure modes were observed in the simulations:

- **Cliff-collapse**: Cliff-collapse involves a relatively shallow failure of intact or partially intact rock along the cliff face, creating a disrupted mass. This falls into the category of a rock fall as presented by Keefer (1984), who describes rock fall as "individual boulders or disrupted masses of rock that descend slopes by bounding, rolling, or free fall" [6]. The term 'disrupted' is used to mean a rock mass that has been broken up into numerous small blocks and rock fragments, after Keefer (2013) [70].

- **Slumping of failure wedges**: Rock slumps involve the movement of large, coherent failure masses along planar to curved sliding surfaces [6].

- **Toppling of discrete blocks near the crest**: Toppling of discrete blocks is preceded by cracking in the model that creates discrete blocks. When these blocks form and topple from the slope, they fall and/or bounce down the slope face. Therefore, toppling can also be categorized as rock fall.

These failure modes are illustrated in Figure 5.42. In these figures, the large, blue arrows indicate the movement of the rock mass.

Keefer (1984), who performed a survey of 40 historical worldwide earthquakes and the resulting landslides, notes that rock falls are the most abundant type of earthquake-induced landslide and require the lowest levels of shaking to initiate. Rock slumps, involving slumping of a coherent rock mass, are a moderately common landslide type in seismic events. Rock slumps are associated with relatively weaker slope materials than rock falls and rock slides and require higher levels of shaking to initiate [6].

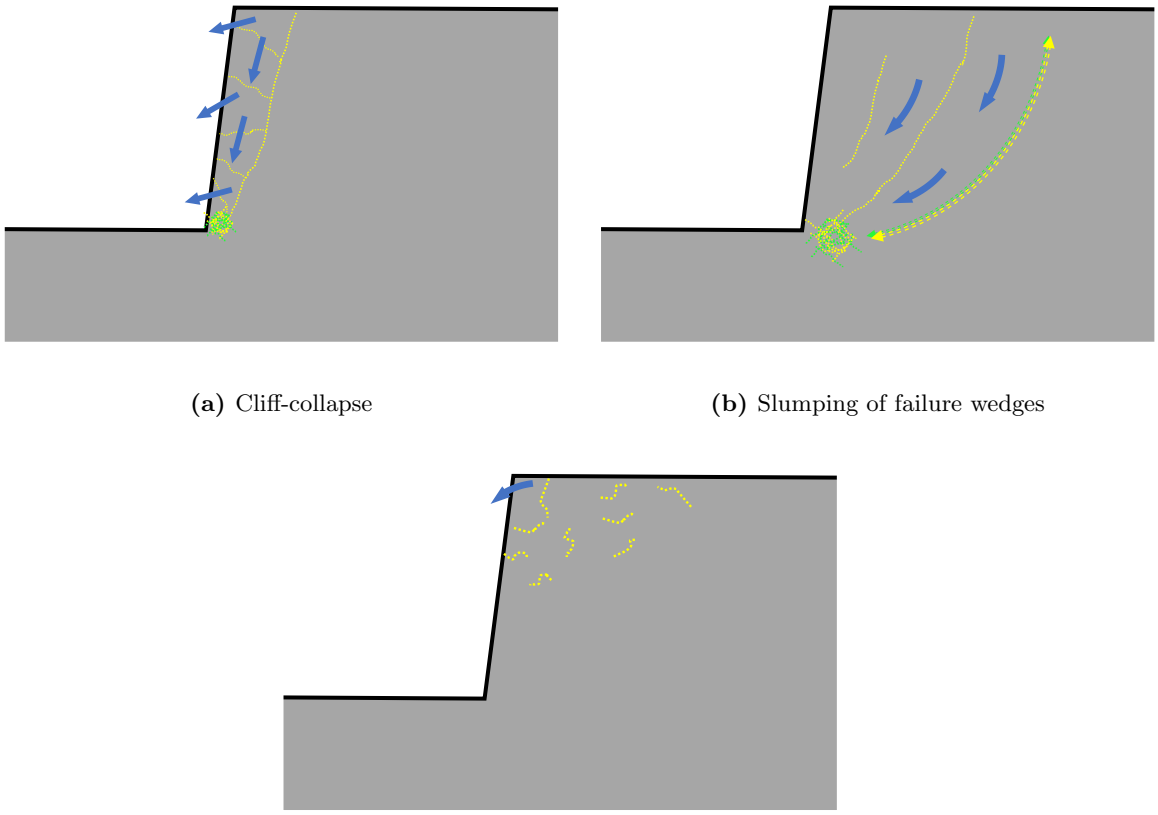

(a) Cliff-collapse

(b) Slumping of failure wedges

(c) Toppling

Figure 5.42: Failure modes observed in destructive harmonic loading of Models 587 and 591. Yellow and green dashed lines indicate tensile and shear damage, respectively. Blue arrows indicate the movement of the rock mass

Model 587 Results

When subjected to the harmonic motion suite, Model 587 experienced a variety of failure mechanisms and modes at different loading frequencies. Table 5.4 summarizes the observed failure mechanisms. Table 5.5 summarizes the observed failure modes.

The numbers in 5.4 and 5.5 indicate the order the events were observed in.

Table 5.4: Failure Mechanisms observed in Model 587 due to harmonic loading.

Loading Frequency, Hz	**Tensile crack into slope**	**Crushing at toe**	**Wedge failure**	**Scattered damage at crest**	**Deep tensile crack**
0.5	–	1	2	–	–
1	1	2	3	–	–
2	1	2	3	–	–
3	1	2	3	–	–
5	–	3	–	1	2

Table 5.5: Failure Modes observed in Model 587 due to harmonic loading.

Loading Frequency, Hz	**Cliff-collapse**	**Slumping**	**Toppling**
0.5	1	–	2
1	1	2	3
2	1	2	3
3	1	–	2
5	1	–	2

The following sections present figures of the failure events from the Model 587 harmonic input simulations.

Model 587 subjected to 0.5 Hz loading

Figure 5.43 shows the sequential failure of Model 587 subjected to a 0.5 Hz loading with a_{max} of 0.25 g and v_{max} of 0.78 m/s.

Failure initiates with a crushing mechanism at the toe at $t = 2.02s$, which is consistent with the approximate stress state plots for the downslope extreme of this loading in Figure 5.16. Following the crushing of material at the toe, a wedge failure from tensile rupture extending from the top of the slope, down to the back of the crushed area, develops at $t = 2.28s$. With continued shaking, this failure wedge begins to collapse and break up. As the slope collapses, damage from impacts between the collapsing slope face and the rest of the slope accumulate. The crest of the portion of the slope behind the failure wedge is particularly damaged, and discrete blocks topple from this area (observed at $t = 7.52s$). After 20 seconds of strong shaking, significant damage has ceased to accumulate, and a large talus pile from the collapsed cliff face buttresses the remaining slope.

The shape of the failure surface for this loading case is very similar to the pseudostatic failure surface for this slope (shown in Figure 5.9). The similarity of these two failures is expected because, as shown by the elastic response of the slope subjected to the 0.5 Hz loading, there is very little topographic amplification for this loading, and the PGA in the model is just below k_y from the pseudostatic simulation.

The velocity time-histories of several monitored points on the slope and the number of cracks that developed in the model over time are shown in Figure 5.44. A clear change in the velocity response of E2 and D2 (corresponding to the crest and a point halfway up the slope face, respectively) can be seen around 2 seconds. The remaining monitored particles, behind the failure surface, continue to respond to the dynamic input relatively undisturbed by the failure event. The number of cracks in the model jumps up very quickly to a few hundred at the initial failure and then gradually increases and the failure mass breaks up and falls from the slope.

An enlarged view of the final slope configuration is shown in Figure 5.45. Particles considered part of the failure volume are identified by their displacements and rotations. Any particle having been displaced more than 0.25 meters or having a rotation greater than 10 degrees is considered 'failed' and colored red in Figure 5.45. The cracks in Figure 5.45 (tensile and shear cracks are shown with yellow and green lines, respectively) show that there is little to no damage to the portion of the slope behind the failure volume.

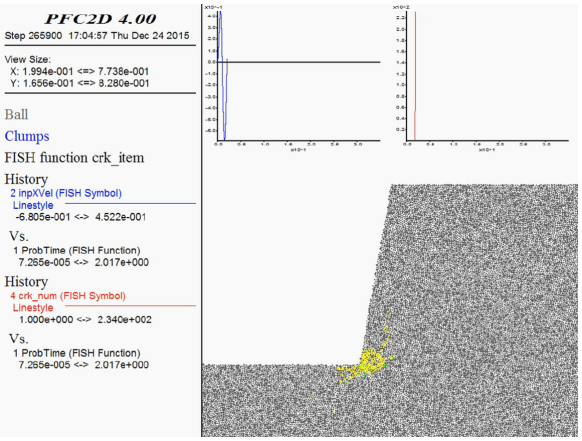

(a) $t = 2.02s$

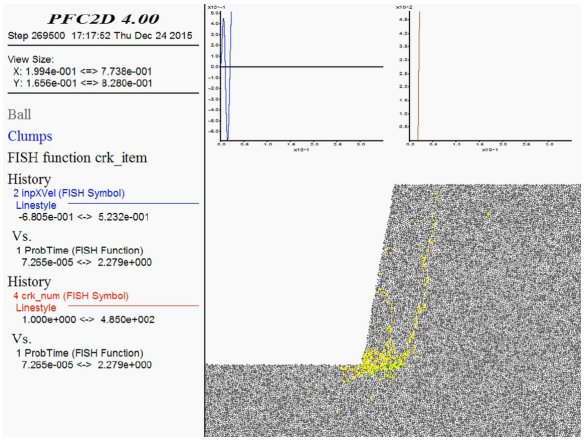

(b) $t = 2.28s$

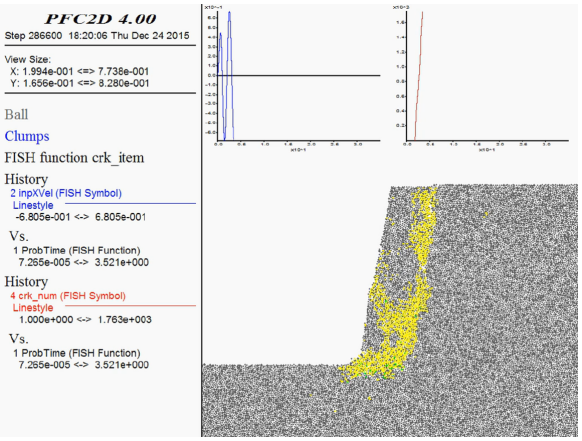

(c) $t = 3.52s$

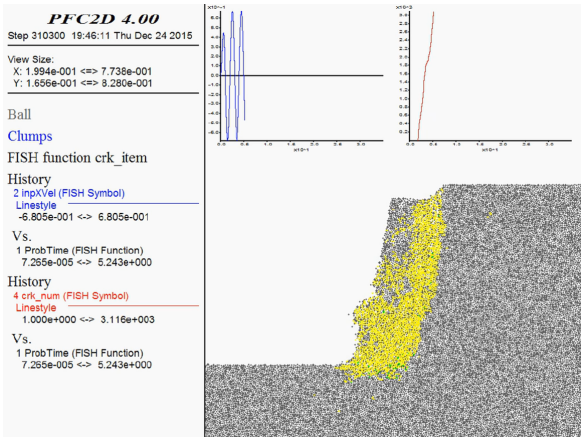

(d) $t = 5.24s$

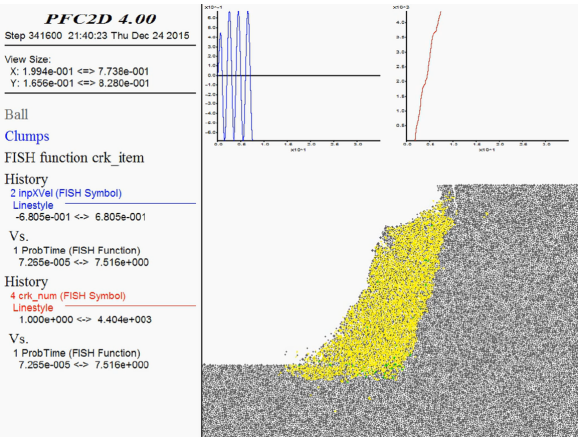

(e) $t = 7.52s$

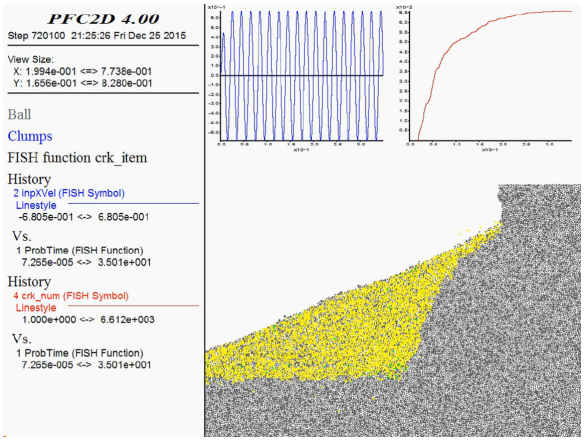

(f) $t = 20.0s$

Figure 5.43: Failure sequence of Model 587 subjected to a 0.5 Hz loading with a_{max} of 0.25 g and v_{max} of 0.78 m/s.

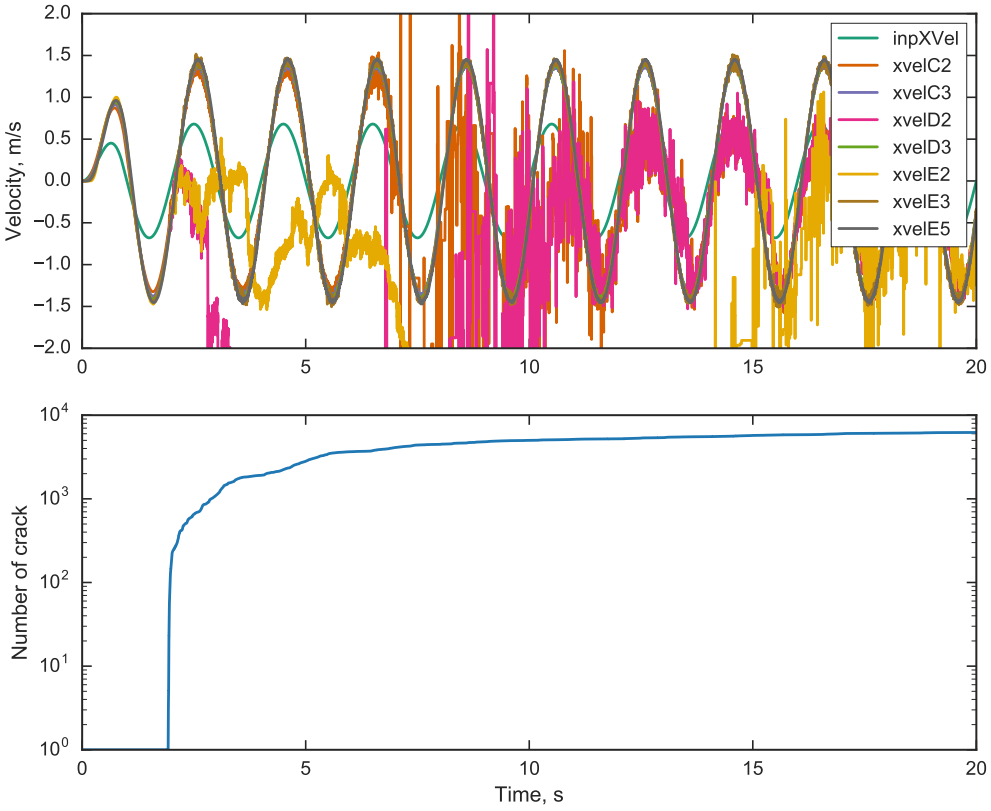

Figure 5.44: Velocity time histories and number of cracks with time for Model 587 subjected to 0.5 Hz destructive harmonic loading. Points with 'E', 'D', and 'C' in the labels correspond to the elevations of the crest, mid-slope, and base, respectively. Points with '2' and '3' in the labels correspond to points at the slope face and set back 65 meters from the slope face, respectively. Point 'E5' corresponds to the furthest monitored point from the crest at the ground surface behind the slope. Refer to Figure 5.12 for the positions of the monitored points within the slope.

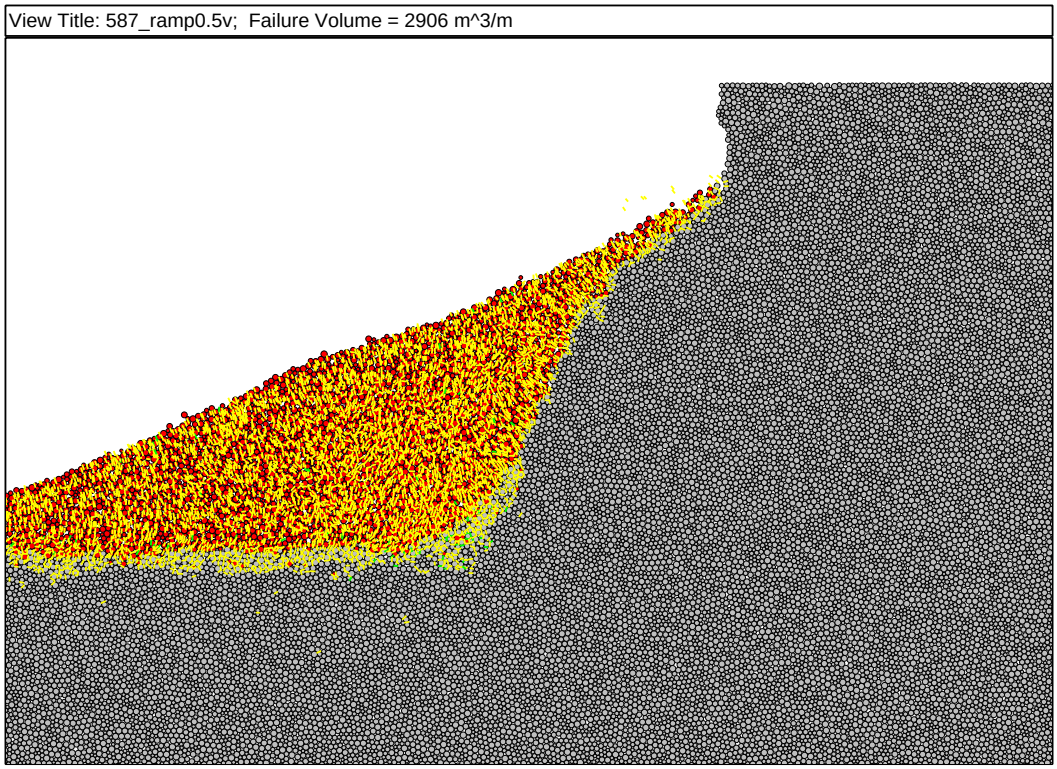

Figure 5.45: Final slope configuration for Model 587 after 20 seconds of a 0.5 Hz loading with a_{max} of 0.25 g and v_{max} of 0.78 m/s. The yellow lines indicate the failure of a parallel bond that has broken in tension. Green lines indicate a shear failure. The failure volume is indicated by red particles. Particles are considered part of the failure volume if their total displacement is greater than 0.25 meters or their rotation is greater than 10 degrees. For reference, the width of the frame in the figure is 185 meters.

Model 587 subjected to 1 Hz loading

Figure 5.46 shows the sequential failure of Model 587 subjected to a 1 Hz loading with a_{max} of 0.5 g and v_{max} of 0.78 m/s.

Failure initiates with a tensile crack at the toe of the slope at t = 0.89s. This failure mechanism was indicated by the force-chains shown in Figure 5.18, but not by the average cell stresses shown in Figure 5.21. As discussed in Section 5.4.3, this is likely due to the highly localized nature of the forces at the toe. Following the tensile crack at the toe, crushing at the toe and wedge failures initiate around t = 1.16s. With continued shaking, transverse cracking occurs and by t = 3.36s, the cliff face is beginning to collapse. By t = 13.3s, a deep-seated circular shear failure has developed, and the failure wedges are beginning to slump and slide along their failure surfaces. During the movement of the failure mass, some toppling of blocks near the crest was also observed.

The velocity time-histories of several monitored points on the slope and the number of cracks that developed in the model over time are shown in Figure 5.47. A clear change in the velocity response of E2 and D2 (corresponding to the crest and a point halfway up the slope face, respectively) can be seen around 1 second. The remaining monitored particles, behind the initial failure surface, continue to respond to the dynamic input until around 3 seconds when E3 and D3 begin to experience a Newmark-like drop off in velocity. The reduced motion of E3 and D3 indicates that the damage beneath these points is creating a base-isolating effect, where a reduced amount of shaking can be applied to the slope due to the compliance of the damaged rock material beneath. The difference in behavior between the points at the slope face (E2 and D2) and points deeper in the slope (E3 and D3) show contrast the signatures of two different failure modes. Points E2 and D2 are part of a cliff-collapse mode and completely lose the signature of the input motion as they experience relative free fall during the collapse. Points E3 and D3 are part of a slumping mode and they follow the input signal fairly well during downslope movement, but slip outward during upslope movement in a traditional Newmark fashion.

The crack time history in Figure 5.47 shows the initial damage due to the tensile crack that initiated at the toe and propagated a few meters into the slope. The crushing of the toe

that followed resulted in a sudden large increase in number of cracks followed by a gradual increase as the slope experienced slumping and breaking up of the failure mass.

An enlarged view of the final slope configuration is shown in Figure 5.48. The failure volume in this figure shows a well-defined circular failure surface that has slumped. The pattern of displacement at the top of the failed portion of the slope steps down showing evidence of the multiple failure wedges that are part of the failure volume. The angle of the surface on these steps show the backward rotation of the failure wedges as they slid along the failure surfaces. The cracks in Figure 5.48 show a moderate amount of damage behind and underneath the failed slope, extending downward into the slope.

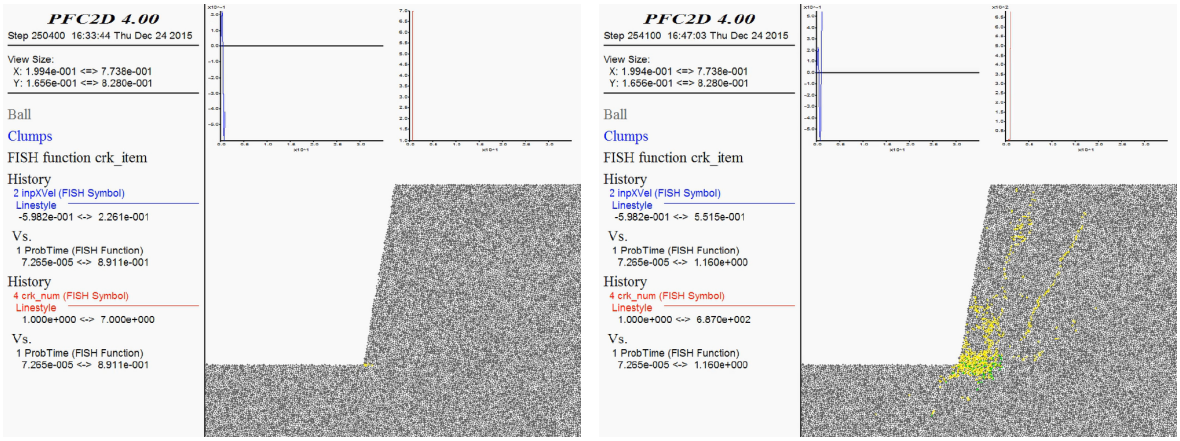

(a) $t = 0.89s$ **(b)** $t = 1.16s$

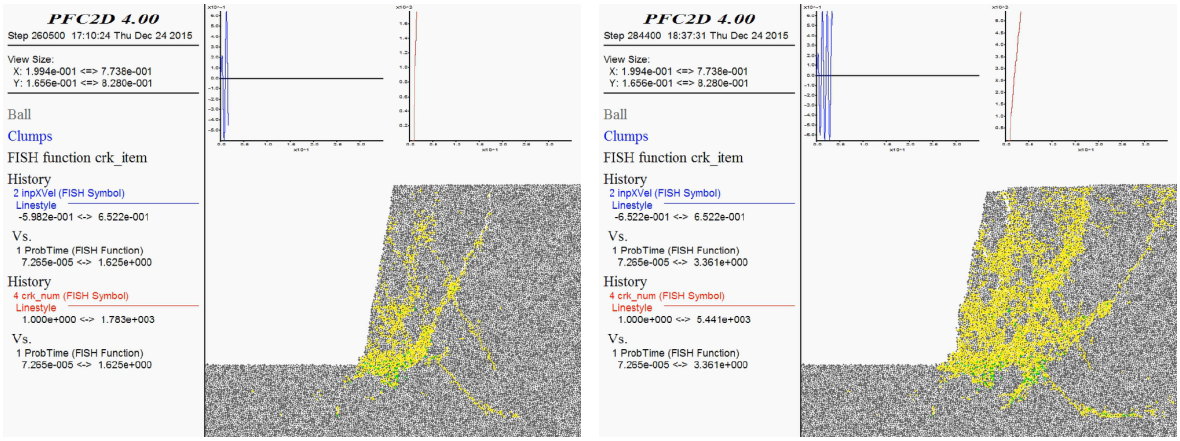

(c) $t = 1.625s$ **(d)** $t = 3.36s$

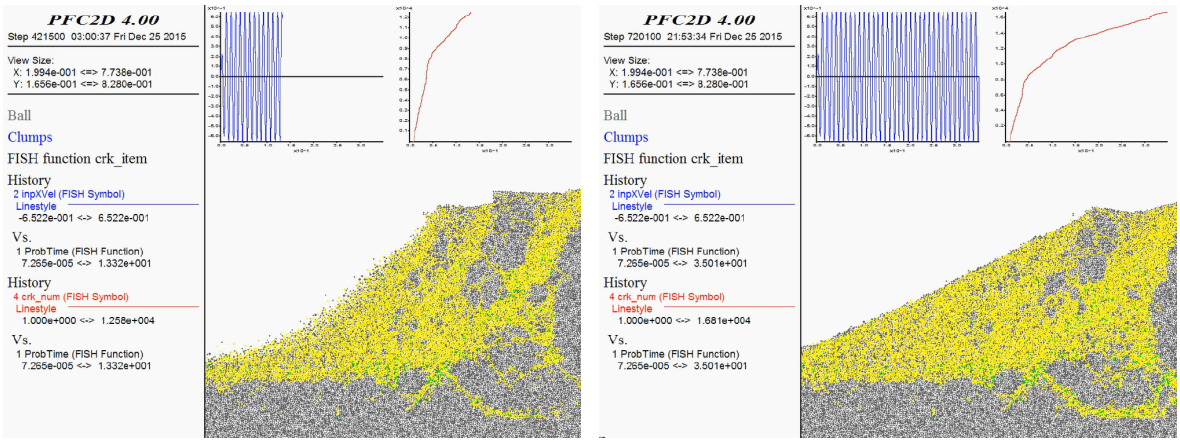

(e) $t = 13.3s$ **(f)** $t = 20.0s$

Figure 5.46: Failure sequence of Model 587 subjected to a 1 Hz loading with a_{max} of 0.5 g and v_{max} of 0.78 m/s.

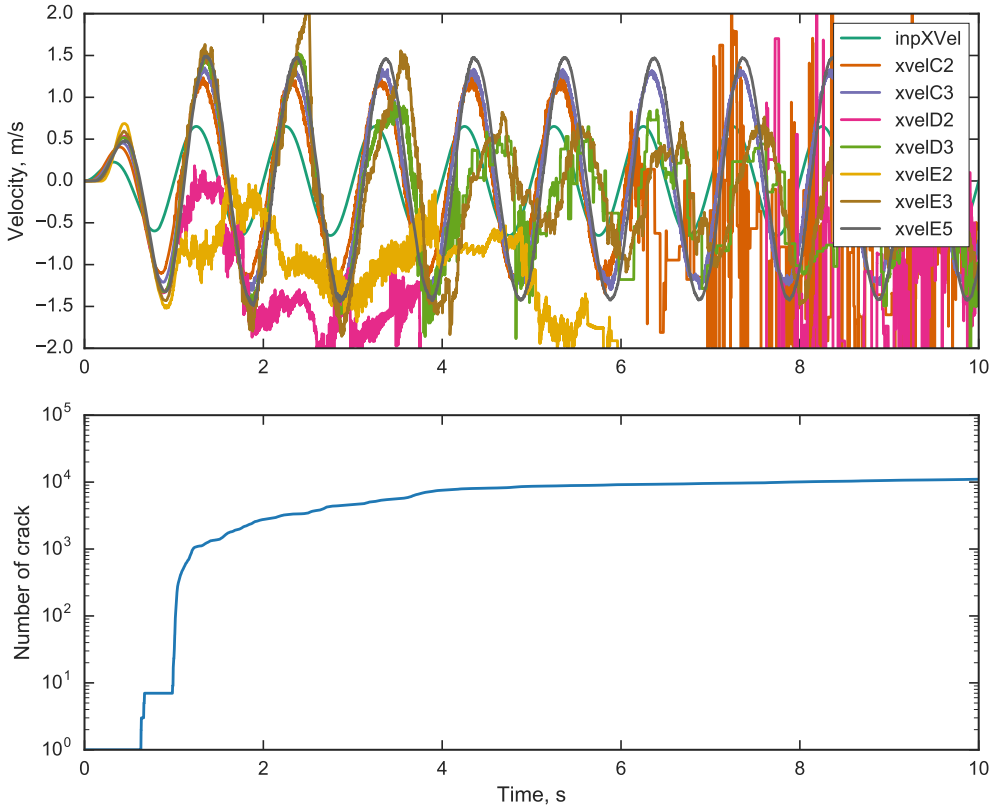

Figure 5.47: Velocity time histories and number of cracks with time for Model 587 subjected to 1 Hz destructive harmonic loading. Points with 'E', 'D', and 'C' in the labels correspond to the elevations of the crest, mid-slope, and base, respectively. Points with '2' and '3' in the labels correspond to points at the slope face and set back 65 meters from the slope face, respectively. Point 'E5' corresponds to the furthest monitored point from the crest at the ground surface behind the slope. Refer to Figure 5.12 for the positions of the monitored points within the slope.

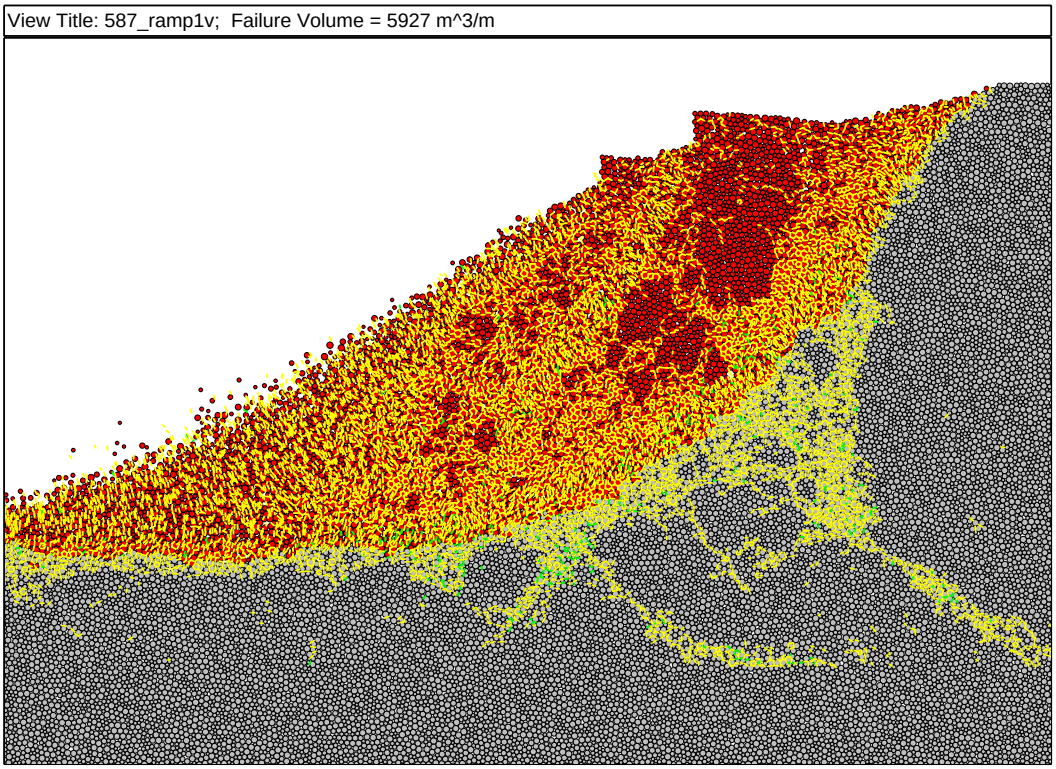

Figure 5.48: Final slope configuration for Model 587 after 20 seconds of a 1 Hz loading with a_{max} of 0.5 g and v_{max} of 0.78 m/s. The yellow lines indicate the failure of a parallel bond that has broken in tension. Green lines indicate a shear failure. The failure volume is indicated by red particles. Particles are considered part of the failure volume if their total displacement is greater than 0.25 meters or their rotation is greater than 10 degrees. For reference, the width of the frame in the figure is 185 meters.

Model 587 subjected to 2 Hz loading

Figure 5.49 shows the sequential failure of Model 587 subjected to a 2 Hz loading with a_{max} of 1.0 g and v_{max} of 0.78 m/s.

Failure initiates with a tensile crack at the toe of the slope at t = 0.56s. This failure mechanism was indicated by the force-chains shown in Figure 5.22, as well as by the average cell stresses shown in Figure 5.25. Following the tensile crack at the toe, crushing at the toe and wedge failures initiate around t = 0.67. With continued shaking, transverse cracking occurs and by t = 2.85s, the cliff face is beginning to collapse, and a deep-seated circular shear failure has developed. At this point in the simulation, the damage to the model is extreme and extends to the bounds of where cracks are allowed to form in the model. Although the base of the model continues to shake, the slope is essentially base-isolated. By t = 11.7s, the failure wedges are beginning to slump and slide along their failure surfaces. During the movement of the failure mass, some toppling of blocks near the crest was also observed. The extensive damage in the model, even behind the deep circular failure surface is sufficient to allow for further mobilization of material.

The velocity time-histories of several monitored points on the slope and the number of cracks that developed in the model over time are shown in Figure 5.50. A clear change in the velocity response of E2 and D2 (corresponding to the crest and a point halfway up the slope face, respectively) can be seen around 0.5 seconds. The remaining monitored particles, behind the initial failure surface, continue to respond to the dynamic input, but the influence of the damage to the model is apparent in the roughness of the signals. The difference in behavior between the points at the slope face (E2 and D2) and points deeper in the slope show that E2 and D2 are unique in being part of a cliff-collapse mode, however, in contrast to the 1 Hz loading, the damage around the model boundaries becomes severe and the dynamic input to the majority of the model is largely lost. Because of the extensive damage, points C2 and C3, which are at the elevation of the toe of the slope, begin to slide and show a Newmark velocity signature, indicating model-wide base-isolation. Only E5, which is at the ground surface near the free-field boundary, where cracking is not allowed in the model, continues to show the signature of the input signal.

The crack time history in Figure 5.50 shows the initial damage due to the tensile crack that initiated at the toe and propagated a few meters into the slope. The crushing of the toe that followed resulted in a sudden large increase in number of cracks followed by a gradual increase as the slope experienced slumping and breaking up of the failure mass.

An enlarged view of the final slope configuration is shown in Figure 5.51. The failure volume in this figure shows a that a significant portion of the slope behind the deep circular failure has moved. The failure wedges nearest the slope face have been completely destroyed. The pattern of displacement at the top of the failed portion of the slope steps down as in the failure due to 1Hz loading. In the case of the 2 Hz loading, the amount of backward rotation of the failure wedges is relatively less. The cracks in Figure 5.51 show an extreme amount of damage behind and underneath the failed slope.

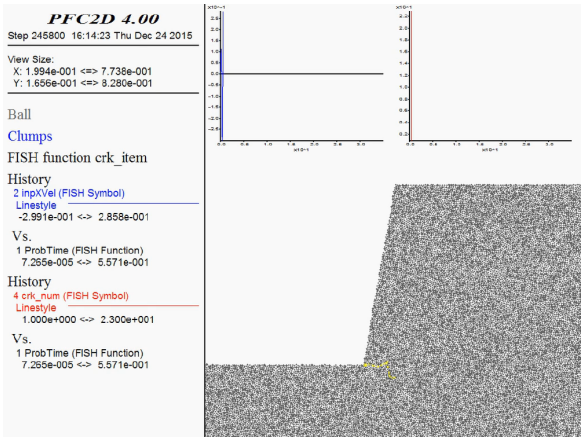

(a) $t = 0.56s$

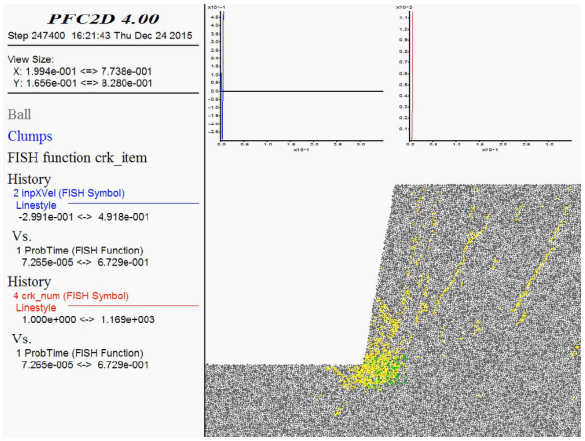

(b) $t = 0.67s$

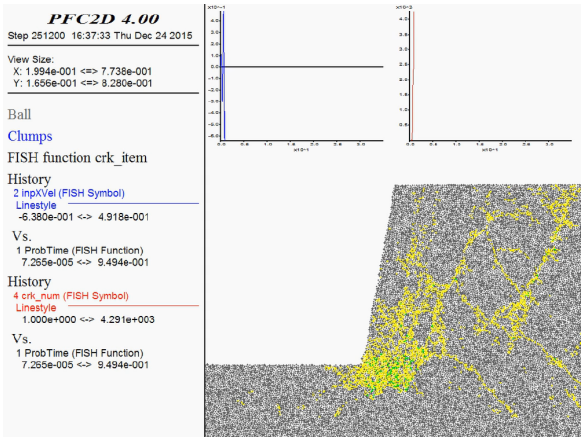

(c) $t = 0.95s$

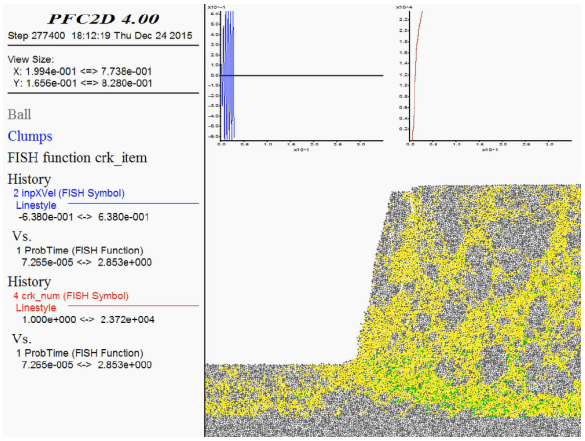

(d) $t = 2.85s$

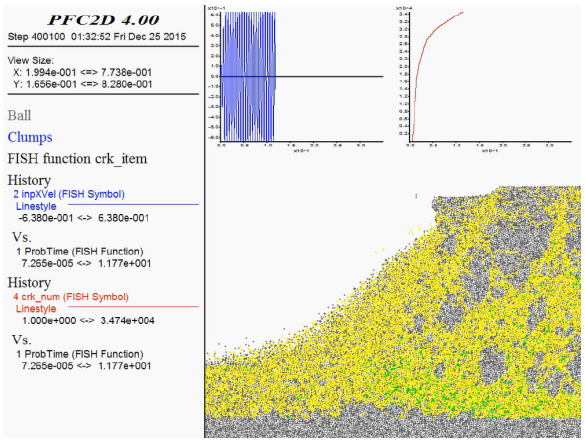

(e) $t = 11.7s$

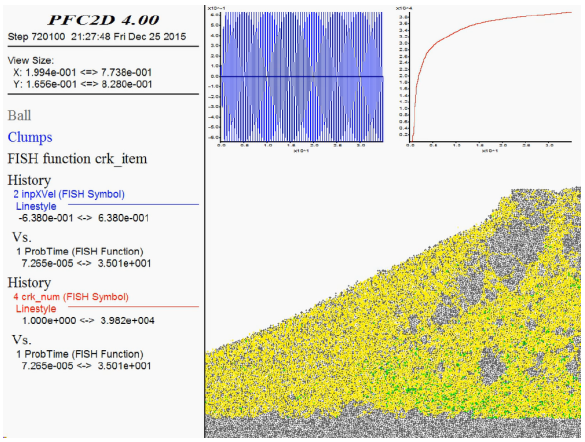

(f) $t = 20.0s$

Figure 5.49: Failure sequence of Model 587 subjected to a 2 Hz loading with a_{max} of 1.0 g and v_{max} of 0.78 m/s.

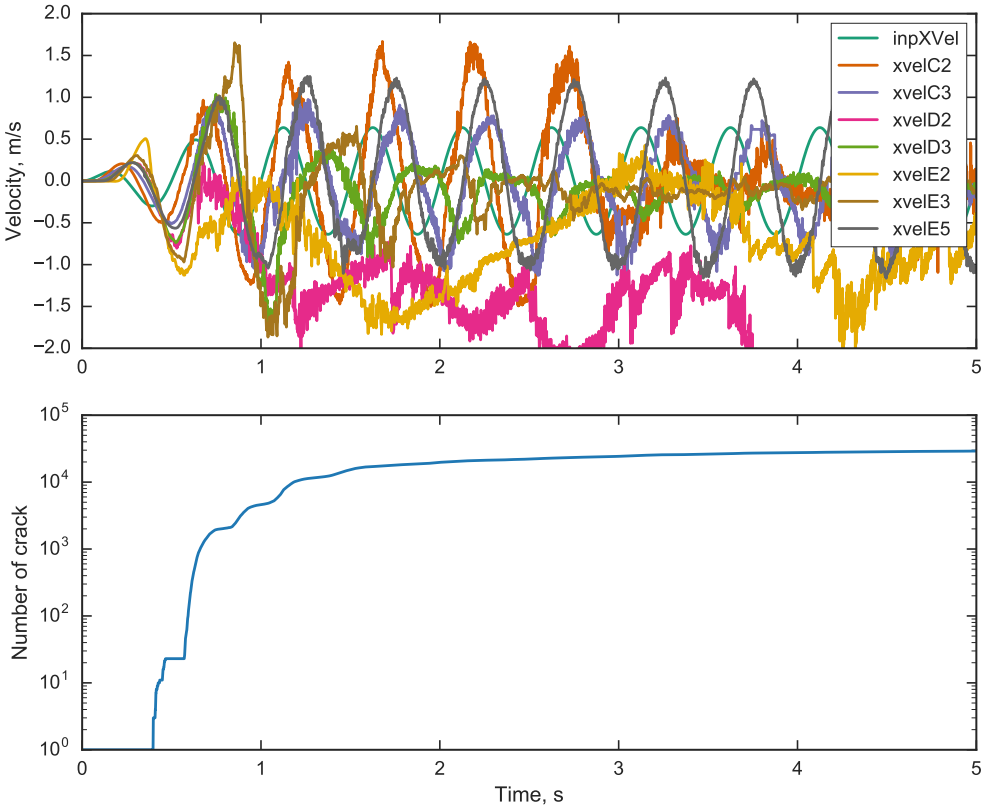

Figure 5.50: Velocity time histories and number of cracks with time for Model 587 subjected to 2 Hz destructive harmonic loading. Points with 'E', 'D', and 'C' in the labels correspond to the elevations of the crest, mid-slope, and base, respectively. Points with '2' and '3' in the labels correspond to points at the slope face and set back 65 meters from the slope face, respectively. Point 'E5' corresponds to the furthest monitored point from the crest at the ground surface behind the slope. Refer to Figure 5.12 for the positions of the monitored points within the slope.

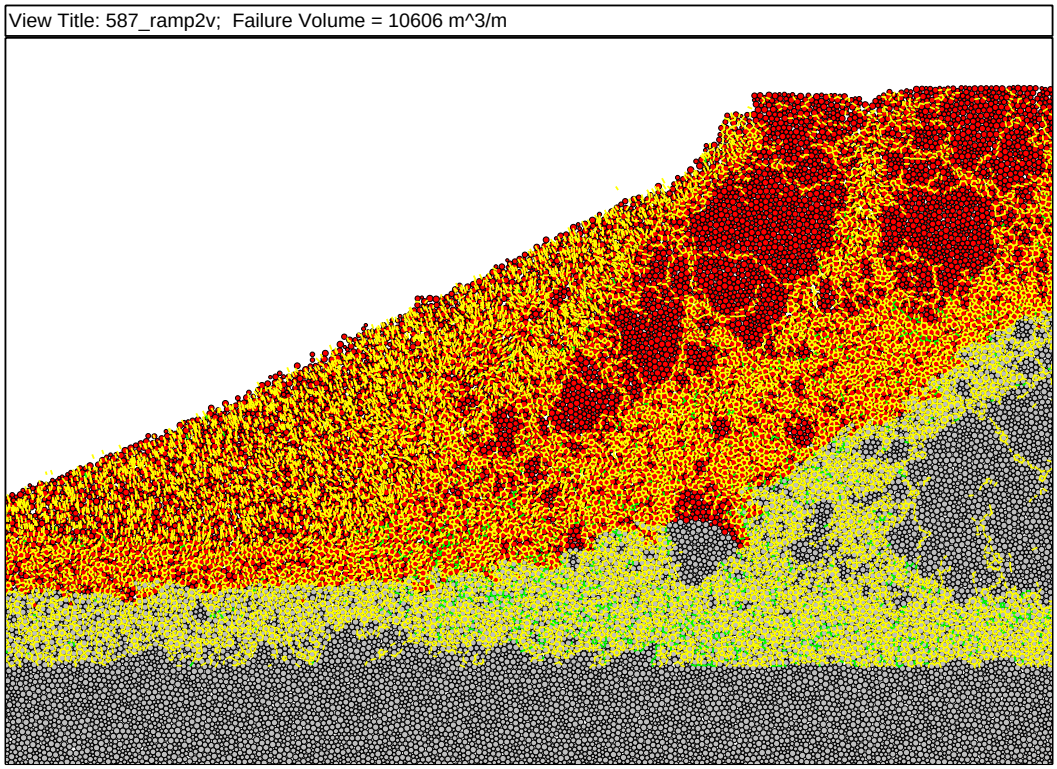

Figure 5.51: Final slope configuration for Model 587 after 20 seconds of a 2 Hz loading with a_{max} of 1.0 g and v_{max} of 0.78 m/s. The yellow lines indicate the failure of a parallel bond that has broken in tension. Green lines indicate a shear failure. The failure volume is indicated by red particles. Particles are considered part of the failure volume if their total displacement is greater than 0.25 meters or their rotation is greater than 10 degrees. For reference, the width of the frame in the figure is 185 meters.

Model 587 subjected to 3 Hz loading

Figure 5.52 shows the sequential failure of Model 587 subjected to a 3 Hz loading with a_{max} of 1.5 g and v_{max} of 0.78 m/s.

Failure initiates with a crushing at the toe of the slope and wedge failures due to tensile rupture at t = 0.54s. Transverse cracks develop by t = 0.71s and at t = 1.05s, a deep circular shear failure has formed, allowing for slumping of the slope mass. Around this time, the damage accumulation has started to reach the extent of where cracks are allowed to form. At t = 3.06s, cliff-collapse and some toppling is evident.

With continued shaking, the damage in the slope continues to accumulate, but there is no significant slumping visible. The material closest to the slope face appears to continue to collapse until nearly the entire slope is buttressed by the talus material.

The velocity time-histories of several monitored points on the slope and the number of cracks that developed in the model over time are shown in Figure 5.53. A clear change in the velocity response at several monitored points shortly after 0.5 seconds is apparent. As with the previous loadings, the cliff-collapse mode is evident in the velocities of E2 and D2. The reduced motion of E3 and D3 indicates that the damage beneath these points is creating a base-isolating effect.

The crack time history in Figure 5.53 shows a sudden large increase in number of cracks followed by a gradual increase as the slope experienced slumping and breaking up of the failure mass.

An enlarged view of the final slope configuration is shown in Figure 5.54. The failure volume in this figure shows that although the displacement is relatively less than for the 1 Hz and 2 Hz loadings, the material bounded by the deep circular failure surface displaced at least 0.5 meters.

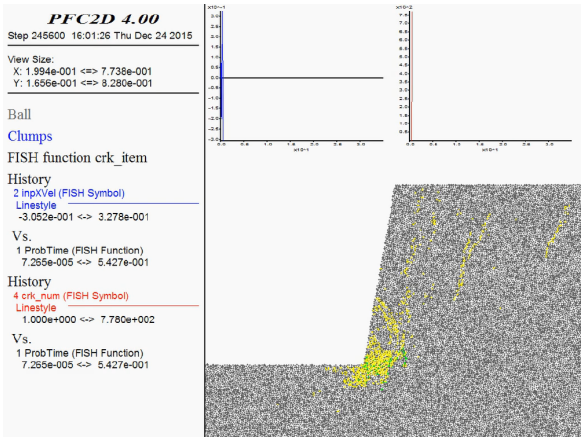

(a) $t = 0.54s$

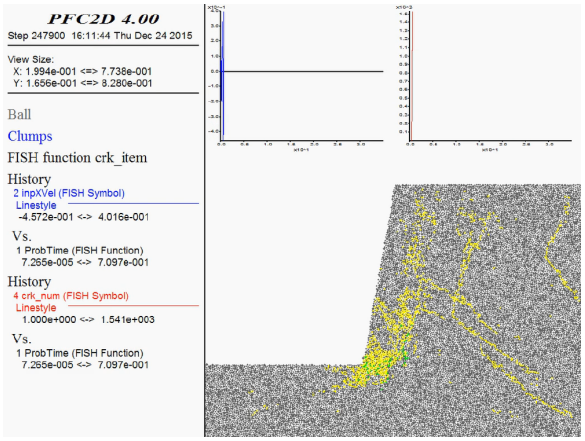

(b) $t = 0.71s$

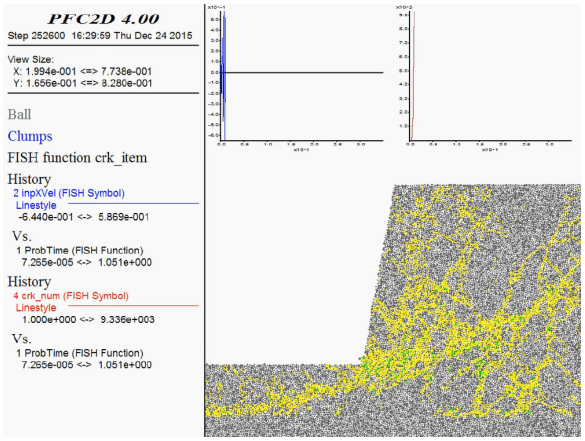

(c) $t = 1.05s$

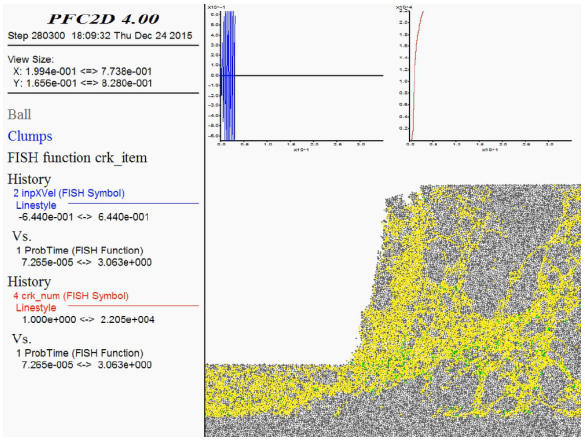

(d) $t = 3.06s$

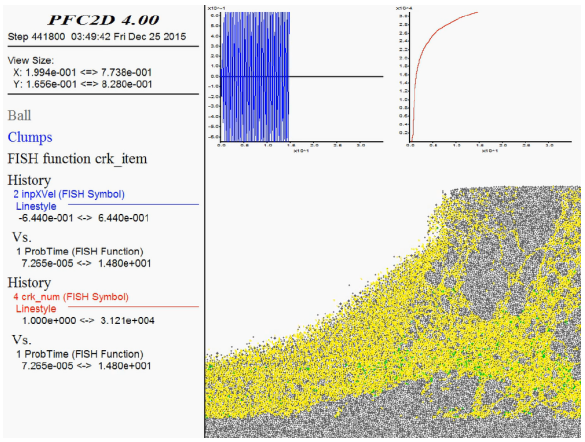

(e) $t = 14.8s$

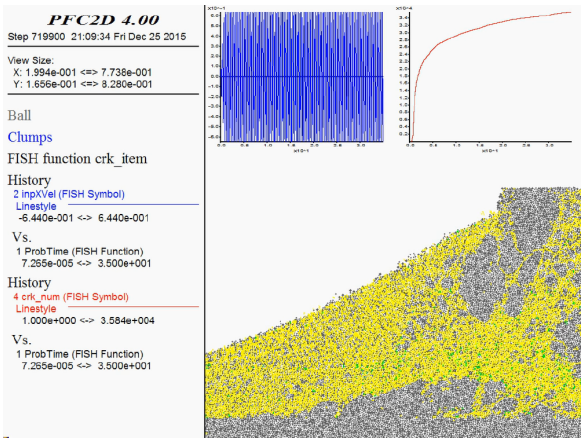

(f) $t = 20.0s$

Figure 5.52: Failure sequence of Model 587 subjected to a 3 Hz loading with a_{max} of 1.5 g and v_{max} of 0.78 m/s.

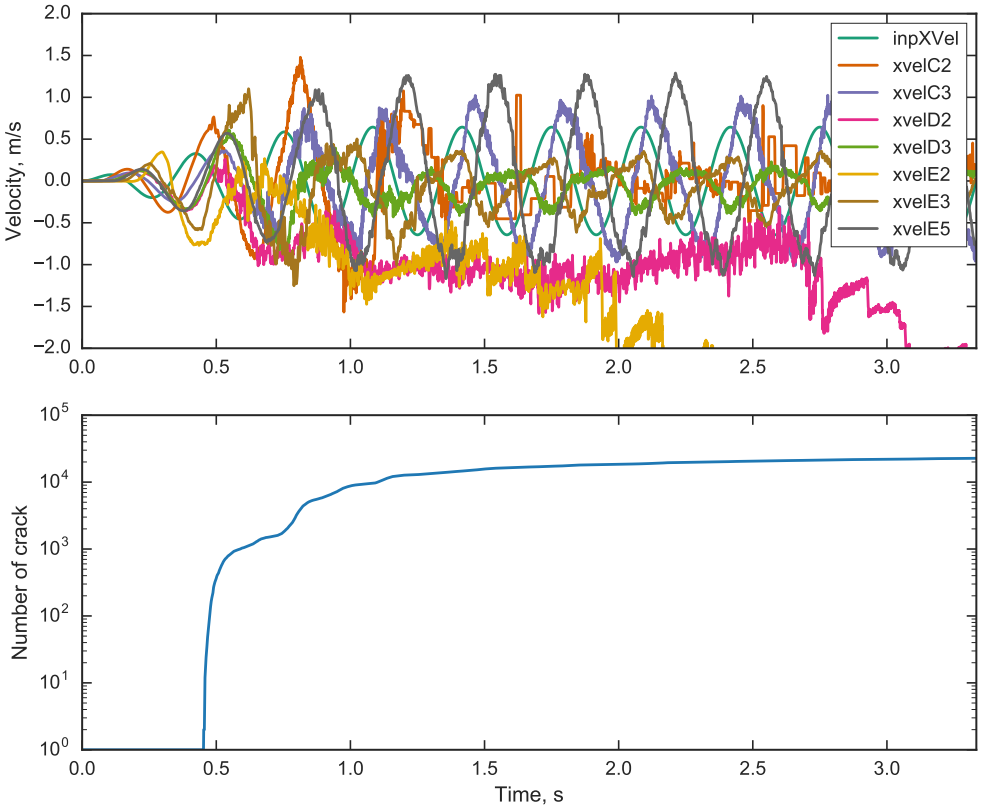

Figure 5.53: Velocity time histories and number of cracks with time for Model 587 subjected to 3 Hz destructive harmonic loading. Points with 'E', 'D', and 'C' in the labels correspond to the elevations of the crest, mid-slope, and base, respectively. Points with '2' and '3' in the labels correspond to points at the slope face and set back 65 meters from the slope face, respectively. Point 'E5' corresponds to the furthest monitored point from the crest at the ground surface behind the slope. Refer to Figure 5.12 for the positions of the monitored points within the slope.

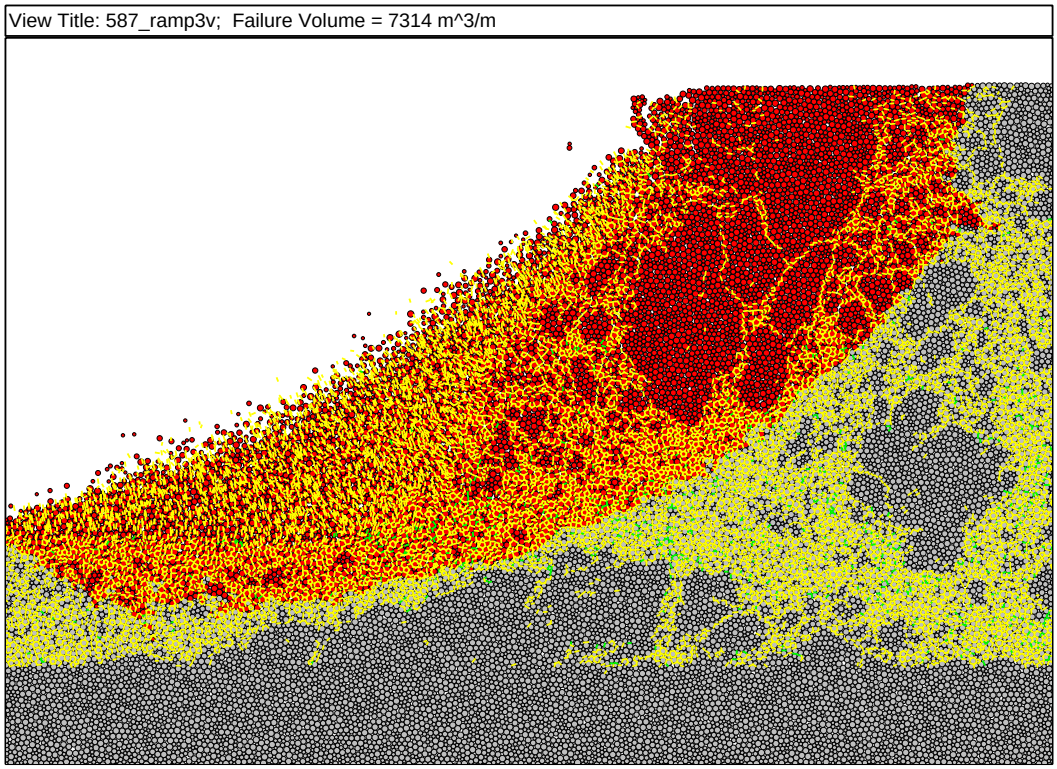

Figure 5.54: Final slope configuration for Model 587 after 20 seconds of a 3.0 Hz loading with a_{max} of 1.5 g and v_{max} of 0.78 m/s. The yellow lines indicate the failure of a parallel bond that has broken in tension. Green lines indicate a shear failure. The failure volume is indicated by red particles. Particles are considered part of the failure volume if their total displacement is greater than 0.25 meters or their rotation is greater than 10 degrees. For reference, the width of the frame in the figure is 185 meters.

Model 587 subjected to 5 Hz loading

Figure 5.55 shows the sequential failure of Model 587 subjected to a 5 Hz loading with a_{max} of 2.5 g and v_{max} of 0.78 m/s.

The failure of the Model 587 slope for the 5 Hz loading is different than the lower frequency loadings. Failure initiates with scattered damage at the crest around t = 0.48s, followed by a deep tensile crack at t = 0.52s. These failure mechanisms are consistent with the observations made for the non-destructive loading of the slope at 5 Hz. The scattered damage at the crest of visible concentrations of stress at the crest of the slope in Steps 4 and 5 (Figures 5.34 and 5.35). Steps 1 and 2 (Figures 5.31 and 5.32) indicated that tensile rupture may occur at H/10, but set back from the face of the slope and that the orientation of a tensile crack forming in this area would be angled slightly upward pointing into the slope. At t = 0.70s, some crushing at the toe occurs, and the material along the cliff face is increasingly damaged. At t = 0.88s, the deep tensile crack has been extended to form a deep circular shear failure and some transverse cracking along the circular failure surface is visible. Around t = 3.84s, cliff-collapse is evident, and some blocks at the crest begin to topple. Also around this time, damage has accumulated along the lower bound of where cracks are allowed in the model. By the end of the simulation, a large talus pile is buttressing the slope, the damaged material at the slope face and crest has run out, and some a block at the crest of the remaining slope is in the process of toppling.

The velocity time-histories of several monitored points on the slope and the number of cracks that developed in the model over time are shown in Figure 5.56. The change in velocity response that signals that failure has occurred and a monitored point is now part of a failure mass occurs first at E2 and D2 between 0.5 and 0.6 seconds. The change in velocity response for E3 and D3 occurs at around 0.8 seconds, corresponding to the development of the deep circular failure surface shown in Figure 5.55(d), which produced a base-isolating effect.

The crack time history in Figure 5.56 shows the initial jump in number of cracks due to the deep tensile crack and scattered damage at the crest followed by a gradual increase in number of cracks with time.

An enlarged view of the final slope configuration is shown in Figure 5.57. As with the 3 Hz simulation on this slope, although significant slumping was not necessarily evident, the material bounded by the deep circular failure surface displaced at least 0.5 meters.

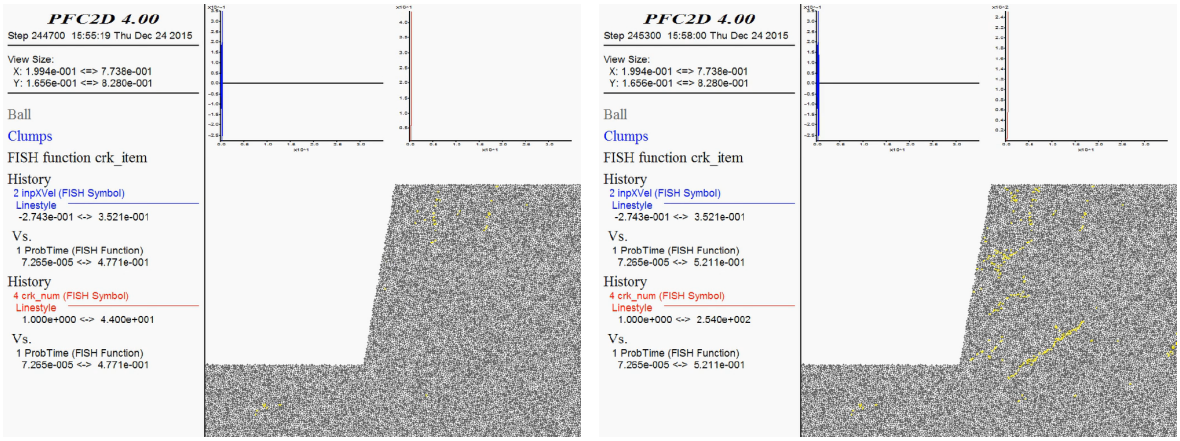

(a) $t = 0.477s$ **(b)** $t = 0.52s$

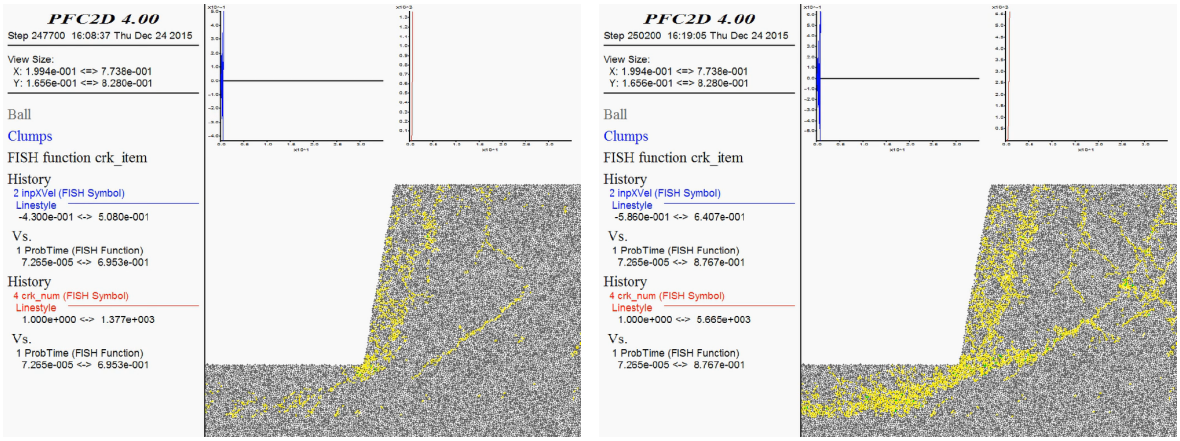

(c) $t = 0.70s$ **(d)** $t = 0.88s$

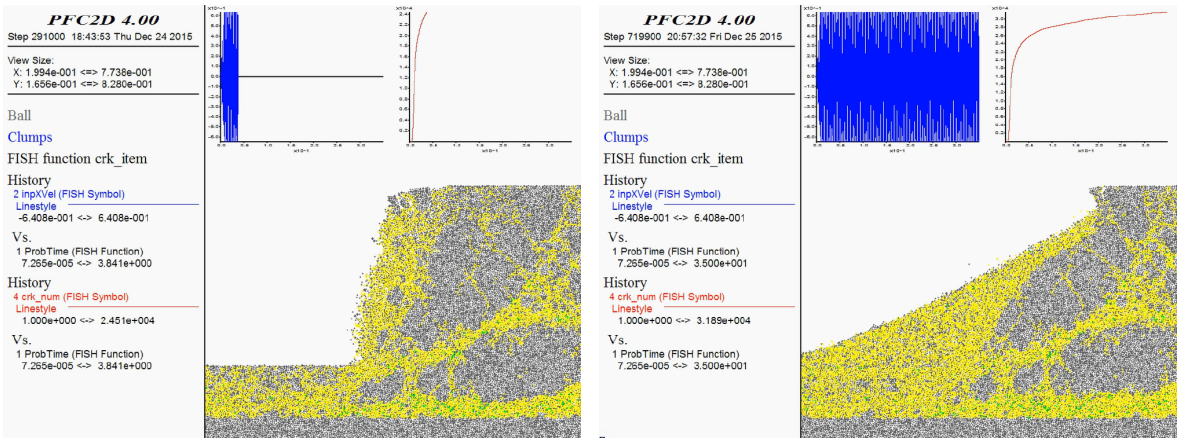

(e) $t = 3.84s$ **(f)** $t = 20.0s$

Figure 5.55: Failure sequence of Model 587 subjected to a 5 Hz loading with a_{max} of 2.5 g and v_{max} of 0.78 m/s.

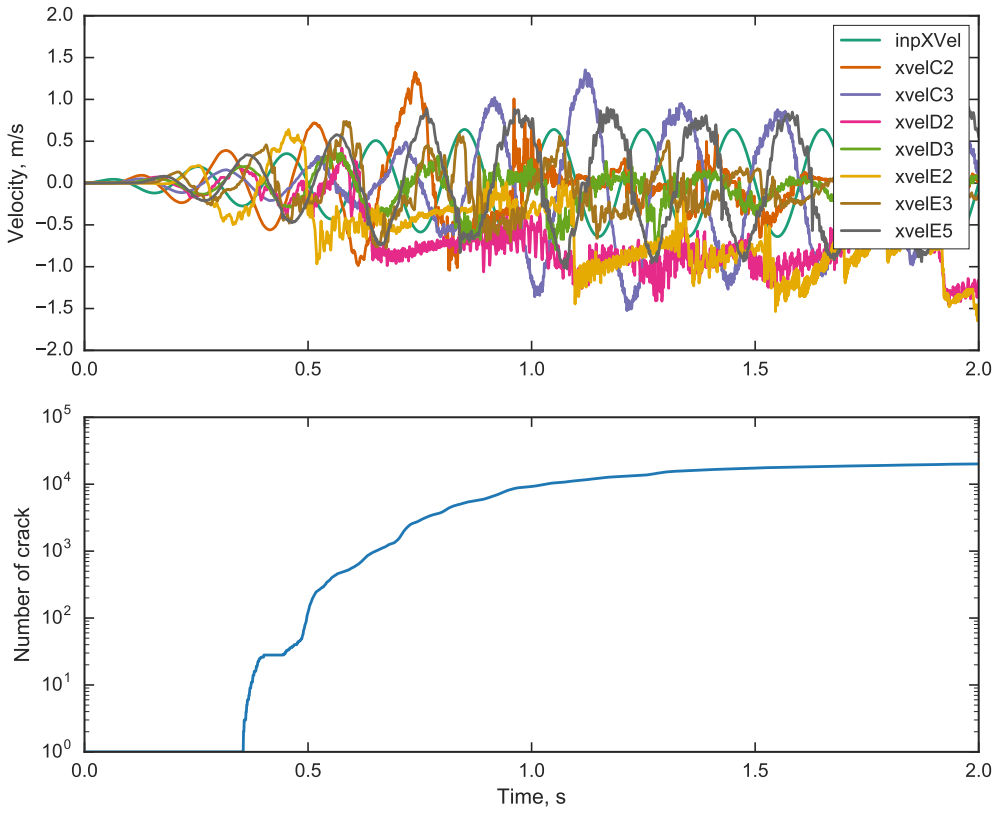

Figure 5.56: Velocity time histories and number of cracks with time for Model 587 subjected to 5 Hz destructive harmonic loading. Ten cycles of input motion are shown. Points with 'E', 'D', and 'C' in the labels correspond to the elevations of the crest, mid-slope, and base, respectively. Points with '2' and '3' in the labels correspond to points at the slope face and set back 65 meters from the slope face, respectively. Point 'E5' corresponds to the furthest monitored point from the crest at the ground surface behind the slope. Refer to Figure 5.12 for the positions of the monitored points within the slope.

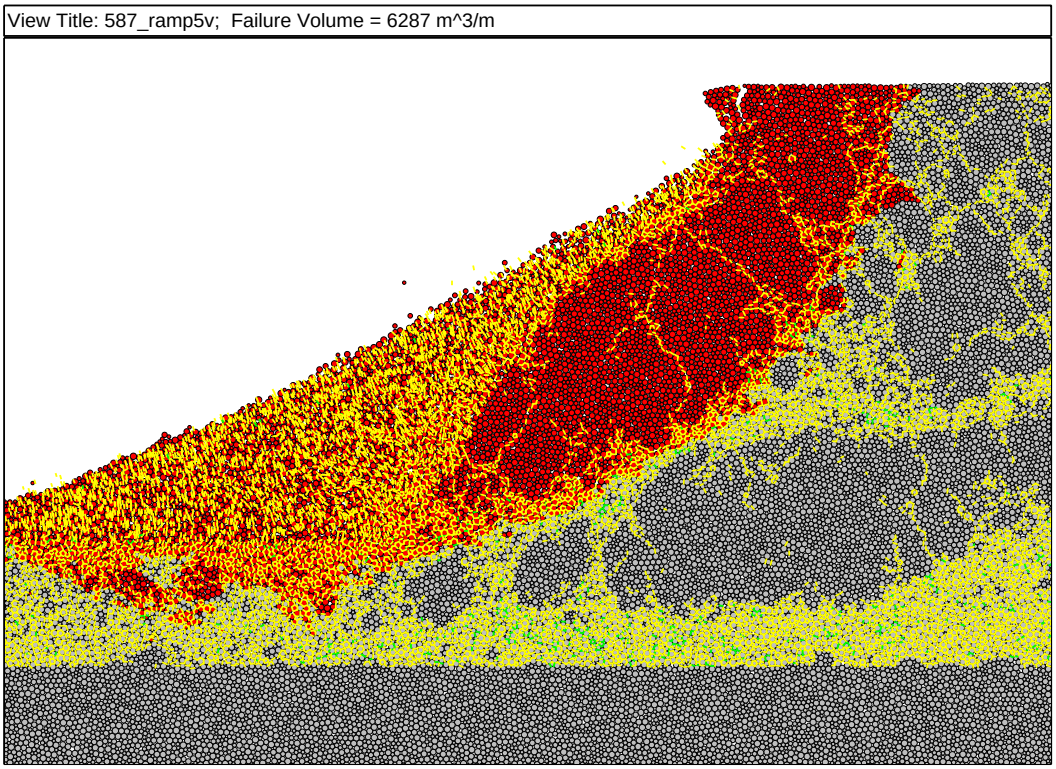

Figure 5.57: Final slope configuration for Model 587 after 20 seconds of a 5 Hz loading with a_{max} of 2.5 g and v_{max} of 0.78 m/s. The yellow lines indicate the failure of a parallel bond that has broken in tension. Green lines indicate a shear failure. The failure volume is indicated by red particles. Particles are considered part of the failure volume if their total displacement is greater than 0.25 meters or their rotation is greater than 10 degrees. For reference, the width of the frame in the figure is 185 meters.

Model 587 Results Summary

Figure 5.58 shows a summary of the simulation results in terms of number of cracks developed in Model 587 with 20 seconds of harmonic loading with tuning ratio. The shape of the curve in Figure 5.58 is very similar to the shape of the velocity apparent amplification curve in Figure 5.39. This indicates that the dynamic amplification is playing an important role in the initiation and accumulation of damage. However, the peak in the number of cracks trend occurs at $TR = 0.7$, rather than $TR = 1.0$, indicating that dynamic amplification alone is not driving the slope's dynamic failure. The decrease in number of cracks above $TR = 0.7$ is particularly striking because the acceleration amplitudes of the motions increase with increased frequency. Lower frequency motions, on the other hand, have higher displacement amplitudes. The trend in Figure 5.58 (particularly the location of the peak) indicates that peak ground displacement (PGD) is also an important factor in the accumulation of damage in rock-slopes).

Figure 5.59 shows a summary of the simulation results regarding failure volume developed in Model 587 with 20 seconds of harmonic loading with tuning ratio. The trend is very similar in shape to the trend in number of cracks with tuning ratio.

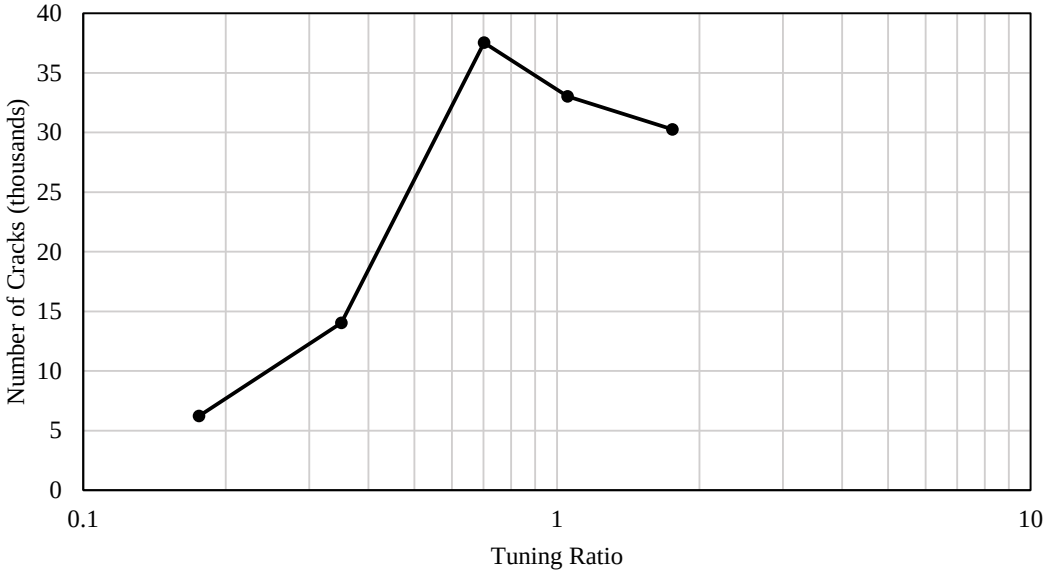

Figure 5.58: Number of cracks developed in Model 587 with 20 seconds of harmonic loading with tuning ratio.

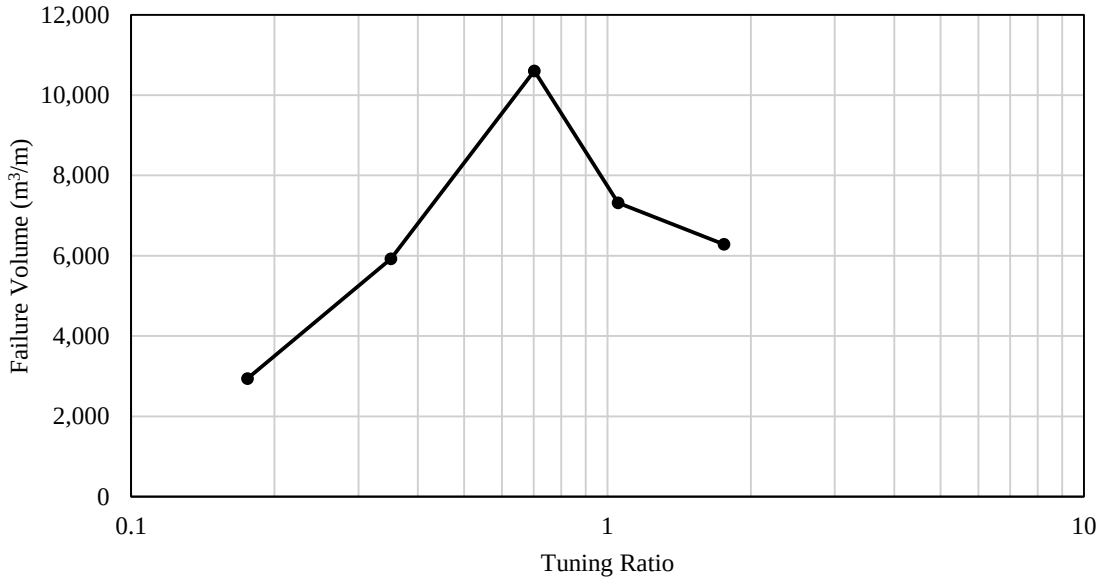

Figure 5.59: Failure volumes developed in Model 587 with 20 seconds of harmonic loading with tuning ratio.

Model 591 Results

When subjected to the harmonic motion suite, Model 591 experienced a variety of failure mechanisms and modes at different loading frequencies. Table 5.6 summarizes the observed failure mechanisms. Table 5.7 summarizes the observed failure modes.

The numbers in Tables 5.6 and 5.7 indicate the order the events were observed in.

Table 5.6: Failure Mechanisms observed in Model 591 due to harmonic loading.

Loading Frequency, Hz	**Tensile crack into slope**	**Crushing at toe**	**Wedge failure**	**Scattered damage at crest**	**Deep tensile crack**
0.5	–	–	–	–	–
1	2	–	1	–	–
2	–	2	1	–	–
3	1	2	–	–	–
5	–	–	–	1	2

Table 5.7: Failure Modes observed in Model 587 due to harmonic loading.

Loading Frequency, Hz	**Cliff-collapse**	**Slumping**	**Toppling**
0.5	–	–	–
1	1	–	2
2	1	3	2
3	1	–	2
5	–	2	1

The following sections present figures of the failure events from the Model 591 harmonic input simulations.

Model 591 subjected to 0.5 Hz loading

As indicated by the stresses during non-destructive loading (Figures 5.16 and 5.17), the 0.5 Hz loading, with a_{max} of 0.25g and v_{max} of 0.78 m/s, did not induce any damage in Model 591.

Model 591 subjected to 1 Hz loading

Figure 5.60 shows the sequential failure of Model 591 subjected to a 1 Hz loading with a_{max} of 0.5 g and v_{max} of 0.78 m/s.

Failure initiates with a failure wedge due to tensile rupture by t = 1.31s. As was observed for the 0.5 Hz loading in model 587, which had a PGA very close to k_y, the shape of the failure surface shown in Figure 5.60(a) is very similar to the pseudostatic failure surface from Model 591 (shown in Figure 5.10). At t = 1.76s, a ensile crack at the toe develops.

With continued shaking, cliff-collapse and toppling are observed by t = 5.88s. By t = 20.0s, the cliff face has collapsed leaving a relatively small talus pile in front of the slope.

The velocity time-histories of several monitored points on the slope and the number of cracks that developed in the model over time are shown in Figure 5.61. A clear change in the velocity response of E2 and D2 (corresponding to the crest and a point halfway up the slope face, respectively) can be seen around 1 second. The remaining monitored particles, behind the initial failure surface, generally continue to respond to the dynamic input. Points E2 and D2 are part of a cliff-collapse mode and completely lose the signature of the input motion as they experience relative free fall during the collapse.

The crack time history in Figure 5.61 shows the initial damage due to the tensile wedge crack just after 1 second. The tensile crack initiating at the toe around 1.7 seconds is also visible as a sharp increase in number of cracks. At around 3.75 seconds another, relatively steep, increase in cracks corresponds to the damage to the failure wedge mass as it breaks up and falls from the cliff face.

An enlarged view of the final slope configuration is shown in Figure 5.62. Other than tensile crack diving down and into the slope from the toe, the portion of the slope left standing is relatively undamaged.

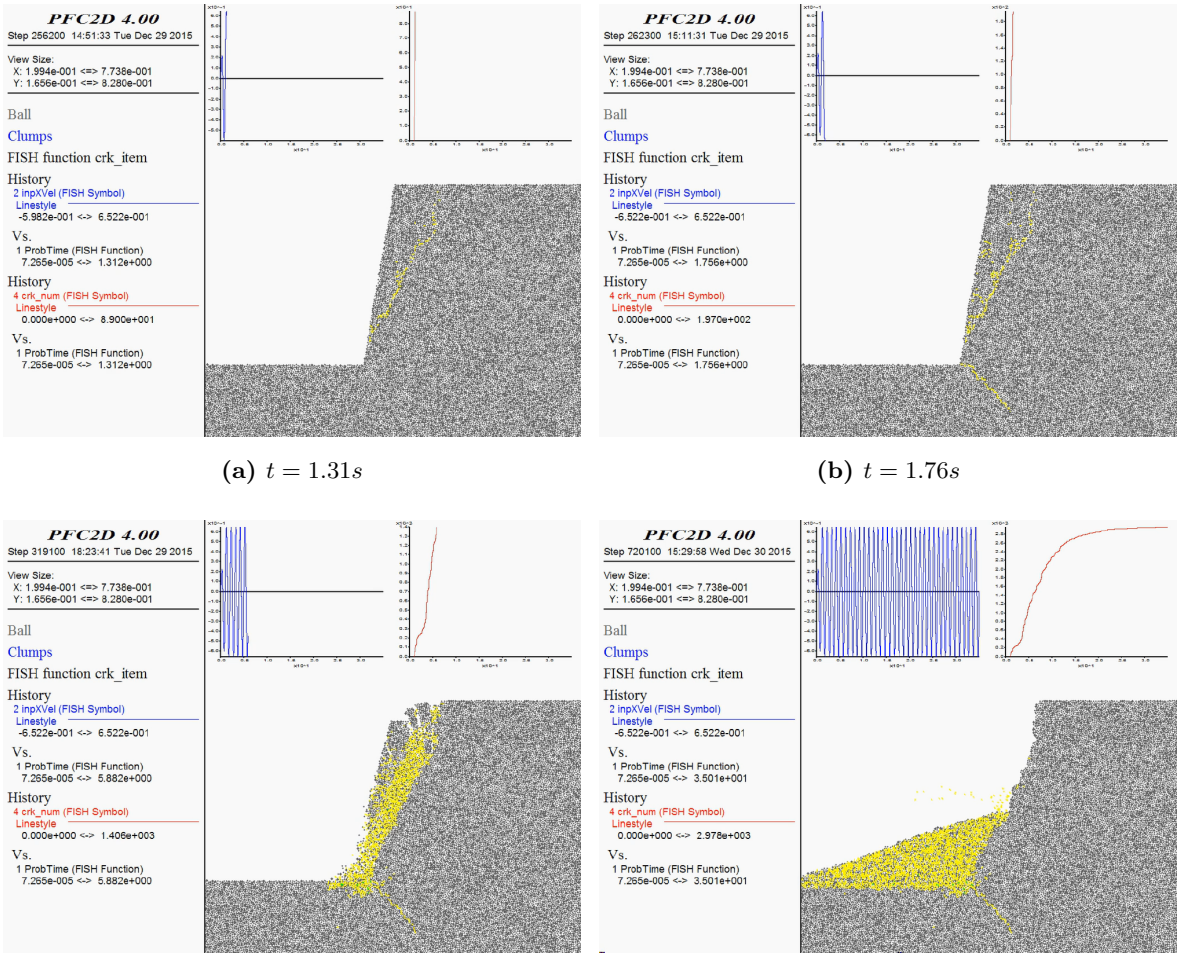

(a) $t = 1.31s$ **(b)** $t = 1.76s$

(c) $t = 5.88s$ **(d)** $t = 20.0s$

Figure 5.60: Failure sequence of Model 591 subjected to a 1 Hz loading with a_{max} of 0.5 g and v_{max} of 0.78 m/s.

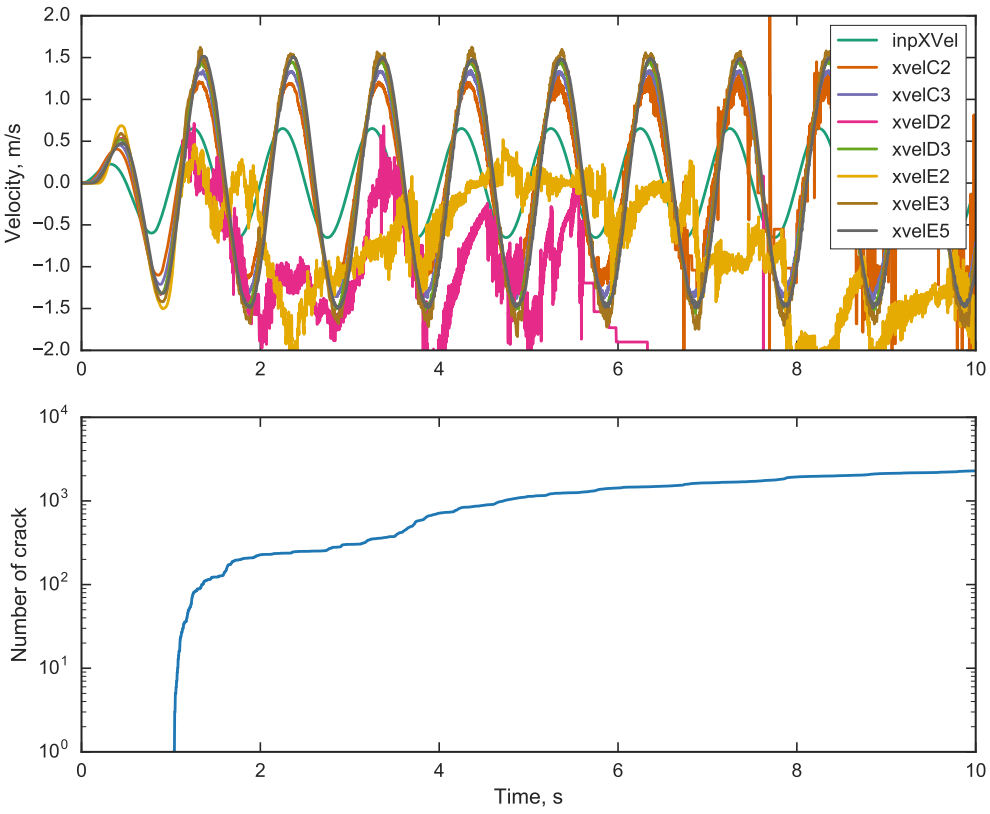

Figure 5.61: Velocity time histories and number of cracks with time for Model 591 subjected to 1 Hz destructive harmonic loading. Ten cycles of input motion are shown. Points with 'E', 'D', and 'C' in the labels correspond to the elevations of the crest, mid-slope, and base, respectively. Points with '2' and '3' in the labels correspond to points at the slope face and set back 65 meters from the slope face, respectively. Point 'E5' corresponds to the furthest monitored point from the crest at the ground surface behind the slope. Refer to Figure 5.12 for the positions of the monitored points within the slope.

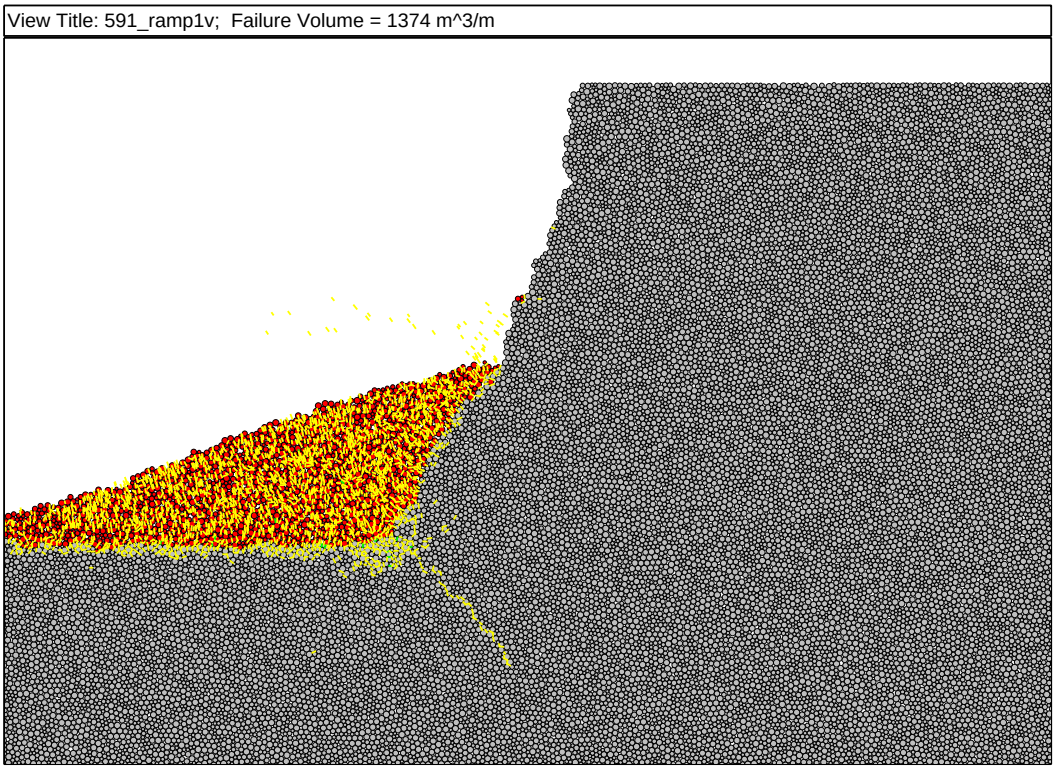

Figure 5.62: Final slope configuration for Model 591 after 20 seconds of a 1 Hz loading with a_{max} of 0.5 g and v_{max} of 0.78 m/s. The yellow lines indicate the failure of a parallel bond that has broken in tension. Green lines indicate a shear failure. The failure volume is indicated by red particles. Particles are considered part of the failure volume if their total displacement is greater than 0.25 meters or their rotation is greater than 10 degrees. For reference, the width of the frame in the figure is 185 meters.

Model 591 subjected to 2 Hz loading

Figure 5.63 shows the sequential failure of Model 591 subjected to a 2 Hz loading with a_{max} of 1.0 g and v_{max} of 0.78 m/s.

Failure initiates with crushing at the toe and failure wedges due to tensile rupture by t = 0.70s. At t - 1.77s, transverse cracking between and behind the failure surfaces defining the wedges has developed.

By t = 5.12s, cliff-collapse and toppling are occurring, and extensive damage has formed throughout the slope mass. As the extensive damage forms, a deep circular shear failure surface begins to develop.

By t = 20.0s, the cliff face has collapsed and the broken up material behind the cliff-collapse is continuing to topple and beginning to slump and slide.

The velocity time-histories of several monitored points on the slope and the number of cracks that developed in the model over time are shown in Figure 5.64. A clear change in the velocity response of E2 and D2 (corresponding to the crest and a point halfway up the slope face, respectively) can be seen around 0.7 seconds. The remaining monitored particles, behind the initial failure surface, continue to respond to the dynamic input, but the influence of the damage to the model is apparent in the roughness of the signals. After about 2 seconds, the monitored particles further back in the slope begin to drop off in velocity amplitude as the slope mass breaks up, and mild base-isolation occurs.

The crack time history in Figure 5.64 shows that the initial crushing of the toe resulted in a sudden large increase in number of cracks followed by a gradual increase as the slope experienced slumping and breaking up of the failure mass.

An enlarged view of the final slope configuration is shown in Figure 5.65. The figure shows that slumping has occurred on the failure surface created by one of the original failure wedges, but that the damage due to the deep circular shear failure was not extensive enough to produce a deep rotational slumping failure mode. Even so, the damage in the slope behind the failure volume is severe.

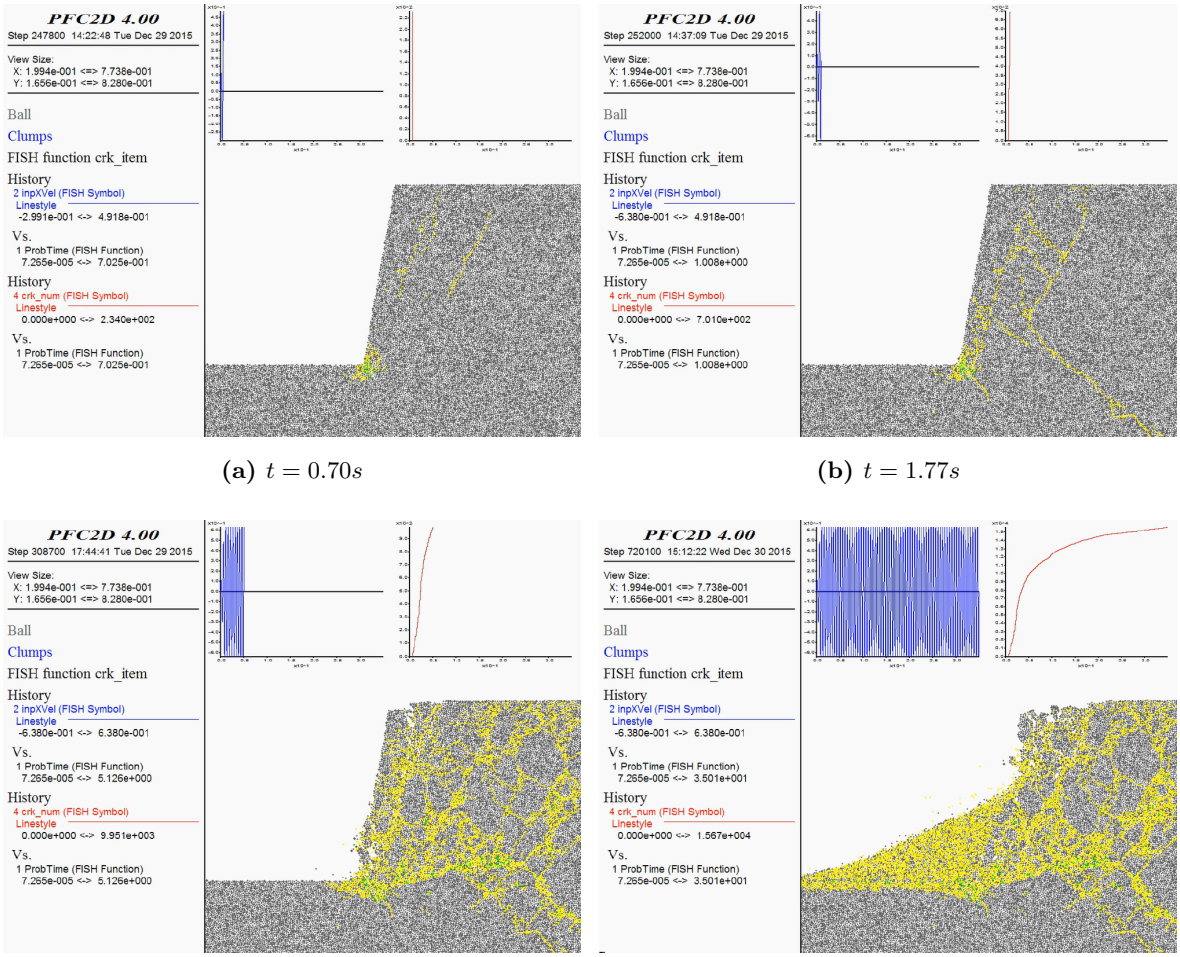

(a) $t = 0.70s$ **(b)** $t = 1.77s$

(c) $t = 5.12s$ **(d)** $t = 20.0s$

Figure 5.63: Failure sequence of Model 591 subjected to a 2 Hz loading with a_{max} of 1.0 g and v_{max} of 0.78 m/s.

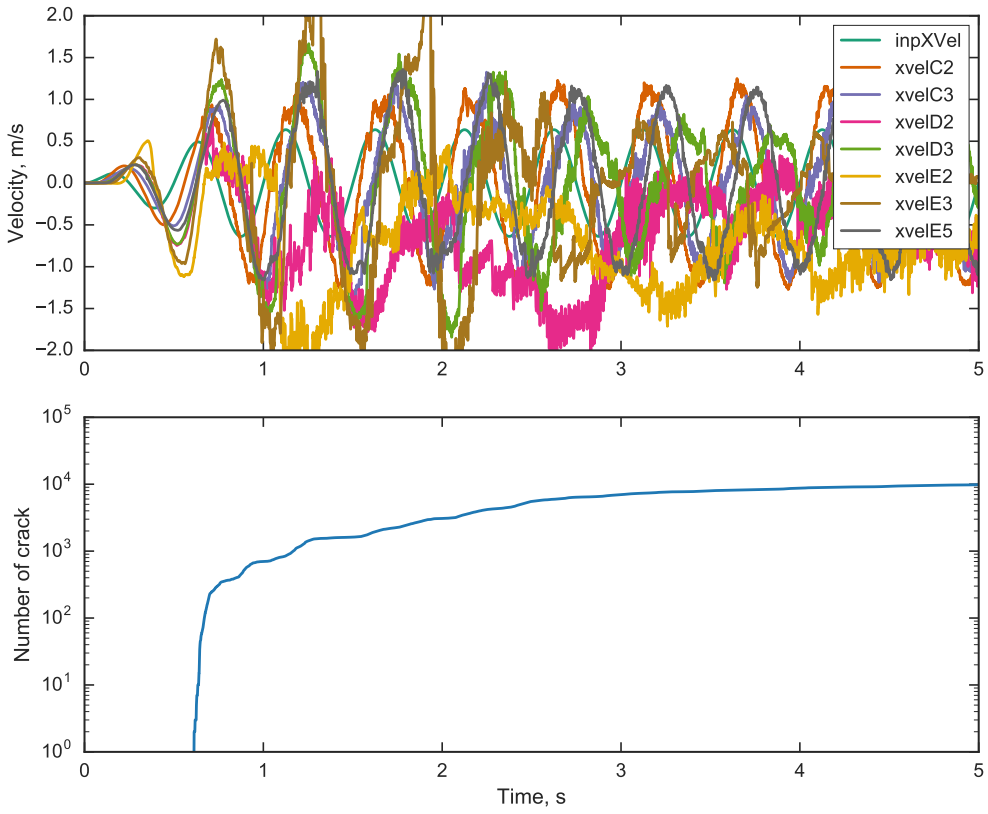

Figure 5.64: Velocity time histories and number of cracks with time for Model 591 subjected to 2 Hz destructive harmonic loading. Ten cycles of input motion are shown. Points with 'E', 'D', and 'C' in the labels correspond to the elevations of the crest, mid-slope, and base, respectively. Points with '2' and '3' in the labels correspond to points at the slope face and set back 65 meters from the slope face, respectively. Point 'E5' corresponds to the furthest monitored point from the crest at the ground surface behind the slope. Refer to Figure 5.12 for the positions of the monitored points within the slope.

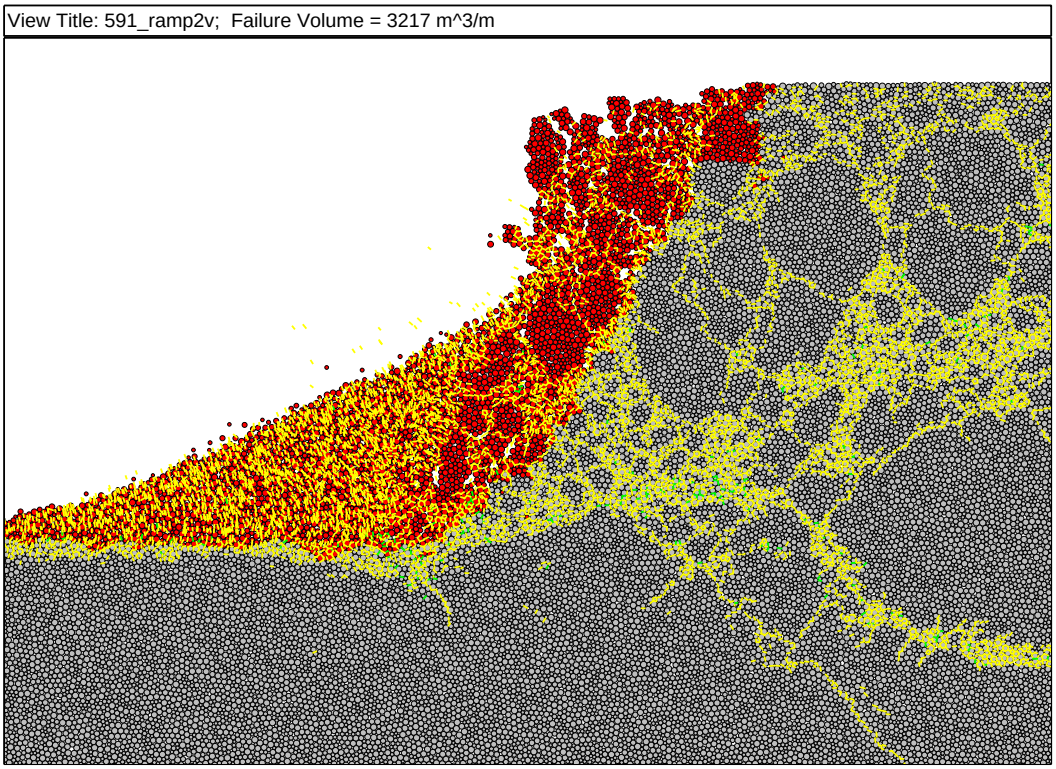

Figure 5.65: Final slope configuration for Model 591 after 20 seconds of a 2 Hz loading with a_{max} of 1.0 g and v_{max} of 0.78 m/s. The yellow lines indicate the failure of a parallel bond that has broken in tension. Green lines indicate a shear failure. The failure volume is indicated by red particles. Particles are considered part of the failure volume if their total displacement is greater than 0.25 meters or their rotation is greater than 10 degrees. For reference, the width of the frame in the figure is 185 meters.

Model 591 subjected to 3 Hz loading

Figure 5.66 shows the sequential failure of Model 591 subjected to a 3 Hz loading with a_{max} of 1.5 g and v_{max} of 0.78 m/s.

Failure initiates with a failure wedge due to tensile rupture by t = 0.64s. At t = 0.7s, tensile cracks at the slope face have initiated and propagated down and into the slope. Two tensile cracks are visible, one at the toe, and the other around H/2. This is the only case of a tensile crack initiating near the face, but not at the toe of the slope. The preceding tensile failure that is beginning to form a wedge appears to be a contributing factor. However, the stresses observed in the non-destructive simulation at this loading are consistent with the initiation of tensile rupture at H/2. The force-chain patterns noted in 5.27 are consistent with the direction of propacation of these tensile cracks.

By t = 20.0s, the cliff face has collapsed and toppling of material from behind the cliff-collapse has ceased.

The velocity time-histories of several monitored points on the slope and the number of cracks that developed in the model over time are shown in Figure 5.67. The velocity response of E2 and D2 (corresponding to the crest and a point halfway up the slope face, respectively) changes, indicating can be seen around 0.75 seconds. The remaining monitored particles, behind the initial failure surface, continue to respond to the dynamic input, but the influence of the damage to the model is apparent in the roughness of the signals.

The crack time history in Figure 5.67 shows that the initial tensile failure wedge resulted in a sudden increase in number of cracks, followed by another increase corresponding to the tensile cracks diving into the slope and the breaking up of the failure mass. The increase in number of cracks during the breaking up of the slope is relatively more gradual than from lower frequency loadings and the weaker Model 587.

An enlarged view of the final slope configuration is shown in Figure 5.68. The figure shows that slumping has occurred on the failure surface created by some of the transverse cracks and failure wedges, but that no deep rotational movement is occurring As with the 2 Hz loading, the damage in the slope behind the failure volume is severe.

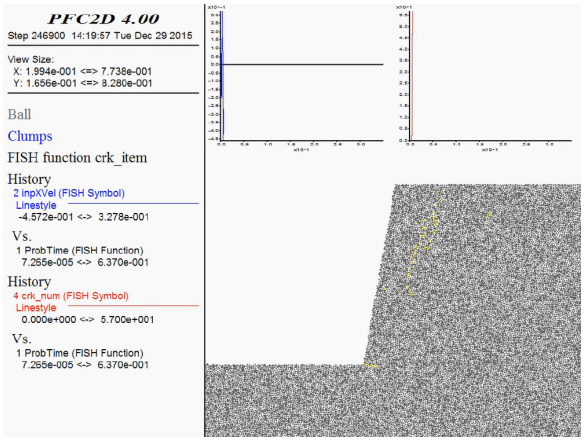

(a) $t = 0.64s$

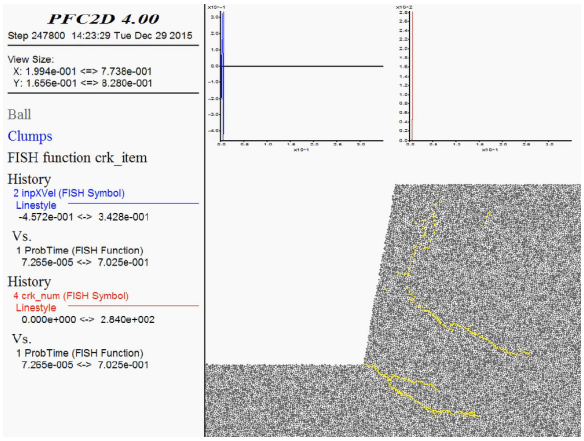

(b) $t = 0.70s$

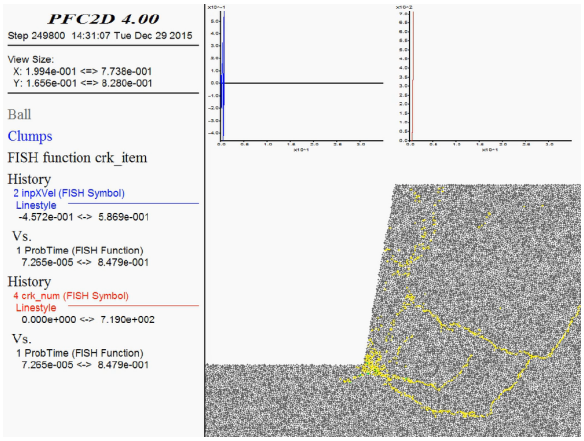

(c) $t = 0.85s$

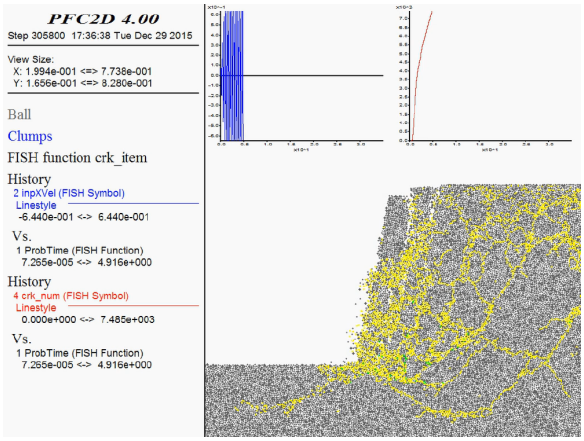

(d) $t = 4.91s$

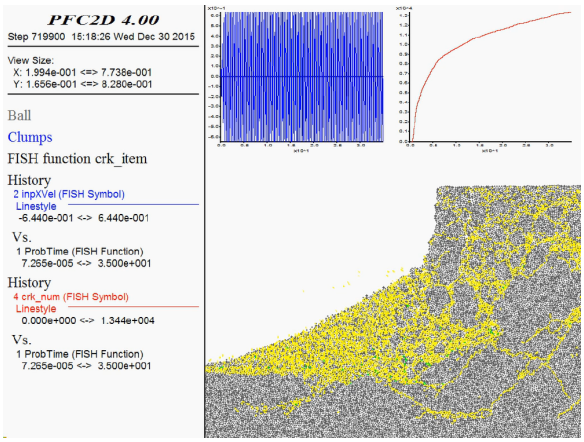

(e) $t = 20.0s$

Figure 5.66: Failure sequence of Model 591 subjected to a 3 Hz loading with a_{max} of 1.5 g and v_{max} of 0.78 m/s.

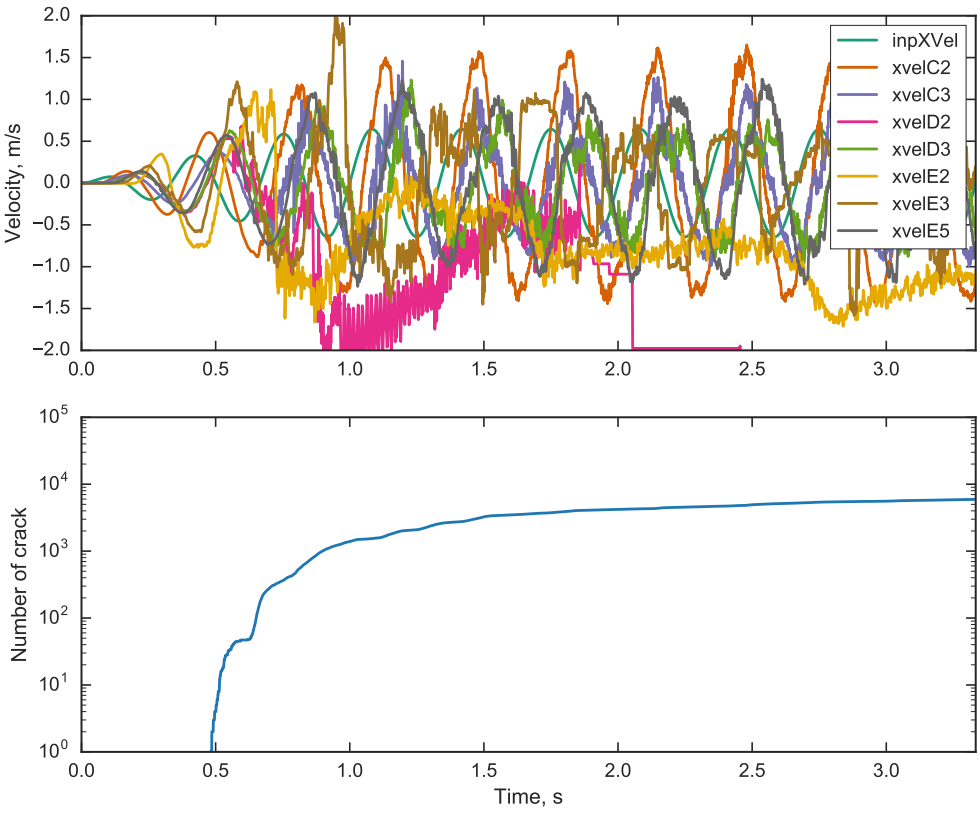

Figure 5.67: Velocity time histories and number of cracks with time for Model 591 subjected to 3 Hz destructive harmonic loading. Ten cycles of input motion are shown. Points with 'E', 'D', and 'C' in the labels correspond to the elevations of the crest, mid-slope, and base, respectively. Points with '2' and '3' in the labels correspond to points at the slope face and set back 65 meters from the slope face, respectively. Point 'E5' corresponds to the furthest monitored point from the crest at the ground surface behind the slope. Refer to Figure 5.12 for the positions of the monitored points within the slope.

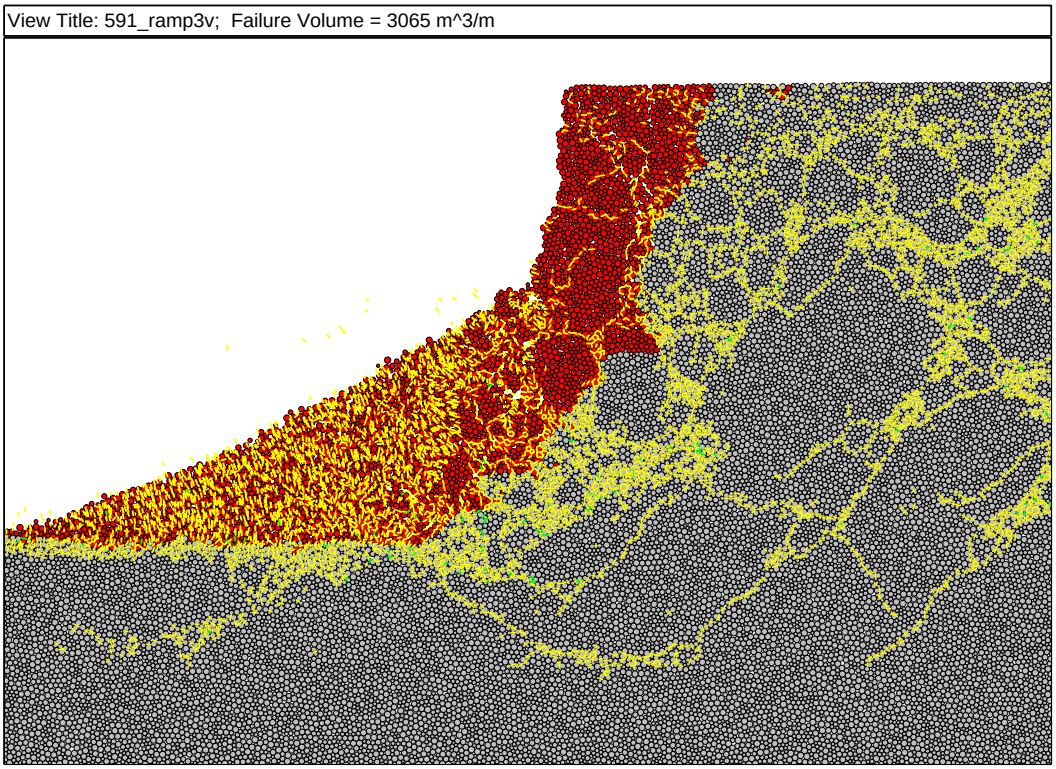

Figure 5.68: Final slope configuration for Model 591 after 20 seconds of a 3 Hz loading with a_{max} of 1.5 g and v_{max} of 0.78 m/s. The yellow lines indicate the failure of a parallel bond that has broken in tension. Green lines indicate a shear failure. The failure volume is indicated by red particles. Particles are considered part of the failure volume if their total displacement is greater than 0.25 meters or their rotation is greater than 10 degrees. For reference, the width of the frame in the figure is 185 meters.

Model 591 subjected to 5 Hz loading

Figure 5.69 shows the sequential failure of Model 591 subjected to a 5 Hz loading with a_{max} of 2.5 g and v_{max} of 0.78 m/s.

Failure initiates with scattered damage at the crest of the slope around t = 0.91s. By t = 1.39s, a deep tensile crack has formed, and the damage at the crest continues to develop. Although the damage a the crest began in a relatively scattered manner, there is an apparent orientation to the cracks at roughly 45 degrees from the horizontal. This pattern corresponds roughly to the path traveled by the apparent zone of zero velocity in Figures 5.31 through 5.38. Relative to the same loading on Model 587, the damage lower in the slope is milder, allowing for more dynamic energy to be transmitted into the slope.

By t = 4.87s, when significant damage near the toe of the slope is occurring, extensive damage starting from the crest and moving downward has occurred, and toppling of blocks off the crest of the slope has begun. At t = 14.0s, one of the cracks oriented at roughly 45 degrees from the horizontal has coalesced with other cracks to form a deep circular shear failure surface that can accommodate a slumping failure mode.

By t = 20.0s, a significant volume of material has toppled off the crest of the slope and the extremely damaged material appears to be continuing to topple.

The velocity time-histories of several monitored points on the slope and the number of cracks that developed in the model over time are shown in Figure 5.70. The velocity responses of the monitored particles change gradually as the damage at the crest of the slope increases and moves deeper into the slope. Monitored particles closer to the slope face and closer to the crest experience changes in velocity signature earlier than those deeper and set back further from the face.

The crack time history in Figure 5.67 shows a relatively gradual increase in number of cracks with time. This crack increase signature is consistent with the different nature of the failure of this slope, which seems to start breaking up higher in the slope with damage gradually occurring deeper and deeper in the slope.

An enlarged view of the final slope configuration is shown in Figure 5.71. The figure shows that slumping has occurred on the deep circular failure surface, and that damage

behind the failure volume is severe.

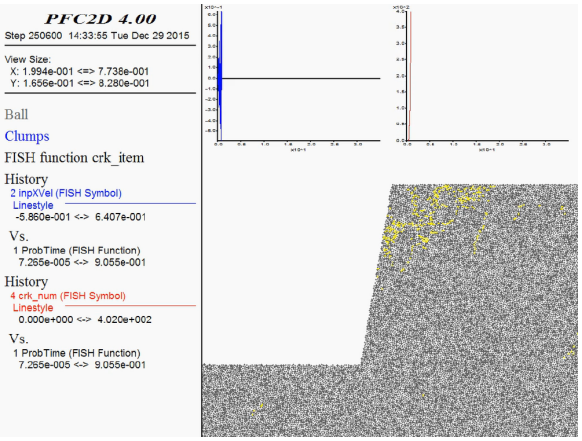

(a) $t = 0.91s$

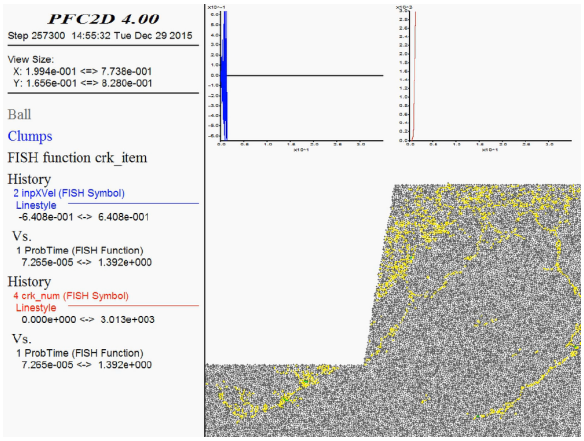

(b) $t = 1.39s$

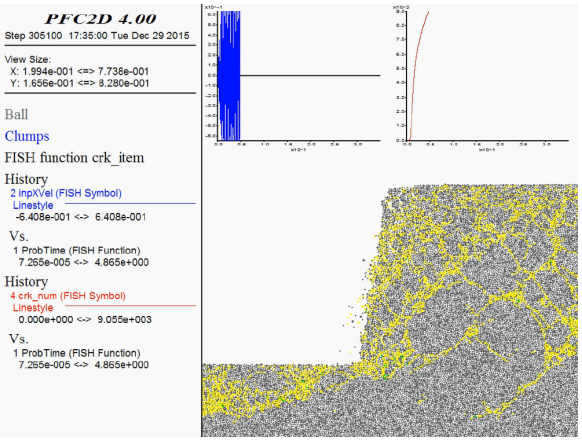

(c) $t = 4.87s$

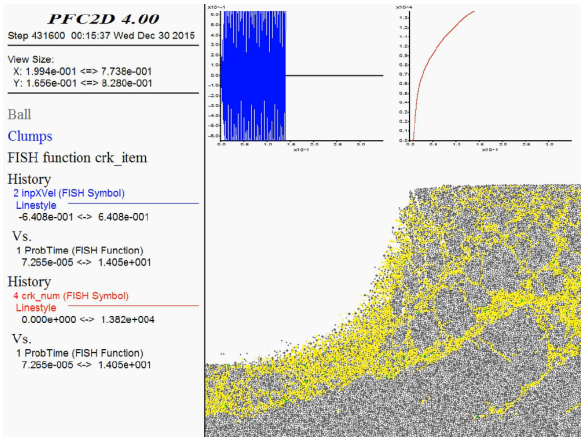

(d) $t = 14.0s$

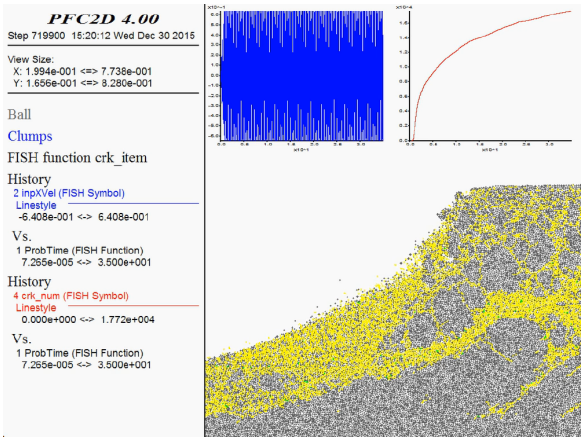

(e) $t = 20.0s$

Figure 5.69: Failure sequence of Model 591 subjected to a 5 Hz loading with a_{max} of 2.5 g and v_{max} of 0.78 m/s.

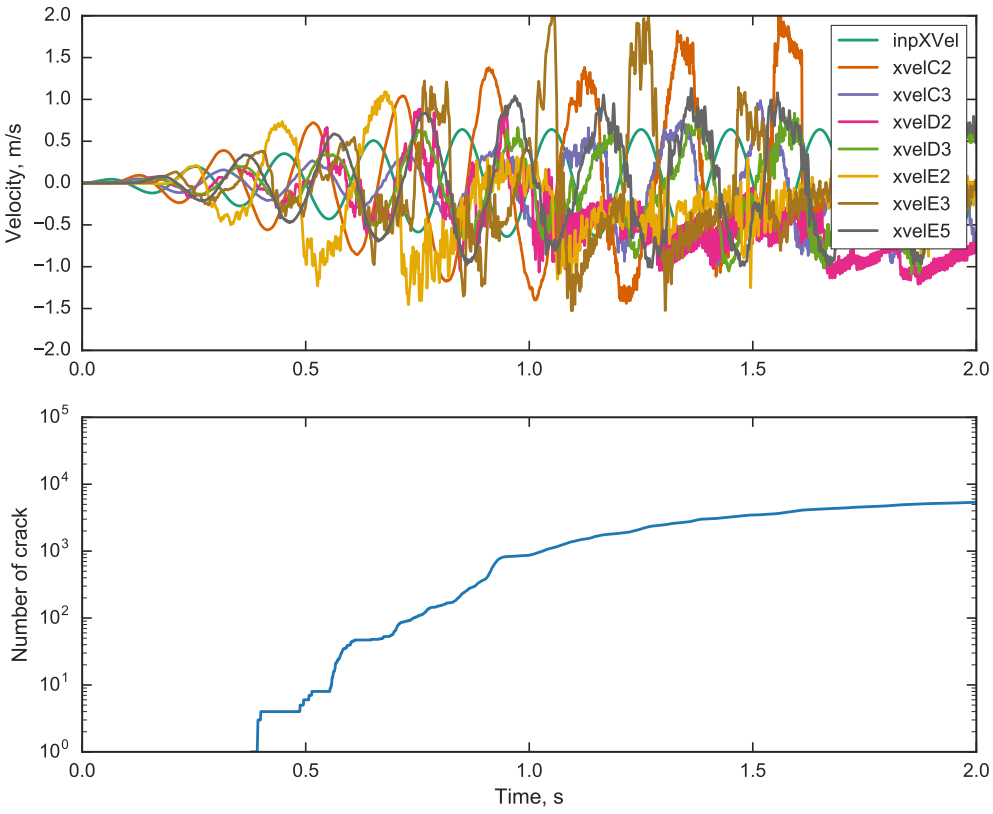

Figure 5.70: Velocity time histories and number of cracks with time for Model 591 subjected to 5 Hz destructive harmonic loading. Ten cycles of input motion are shown. Points with 'E', 'D', and 'C' in the labels correspond to the elevations of the crest, mid-slope, and base, respectively. Points with '2' and '3' in the labels correspond to points at the slope face and set back 65 meters from the slope face, respectively. Point 'E5' corresponds to the furthest monitored point from the crest at the ground surface behind the slope. Refer to Figure 5.12 for the positions of the monitored points within the slope.

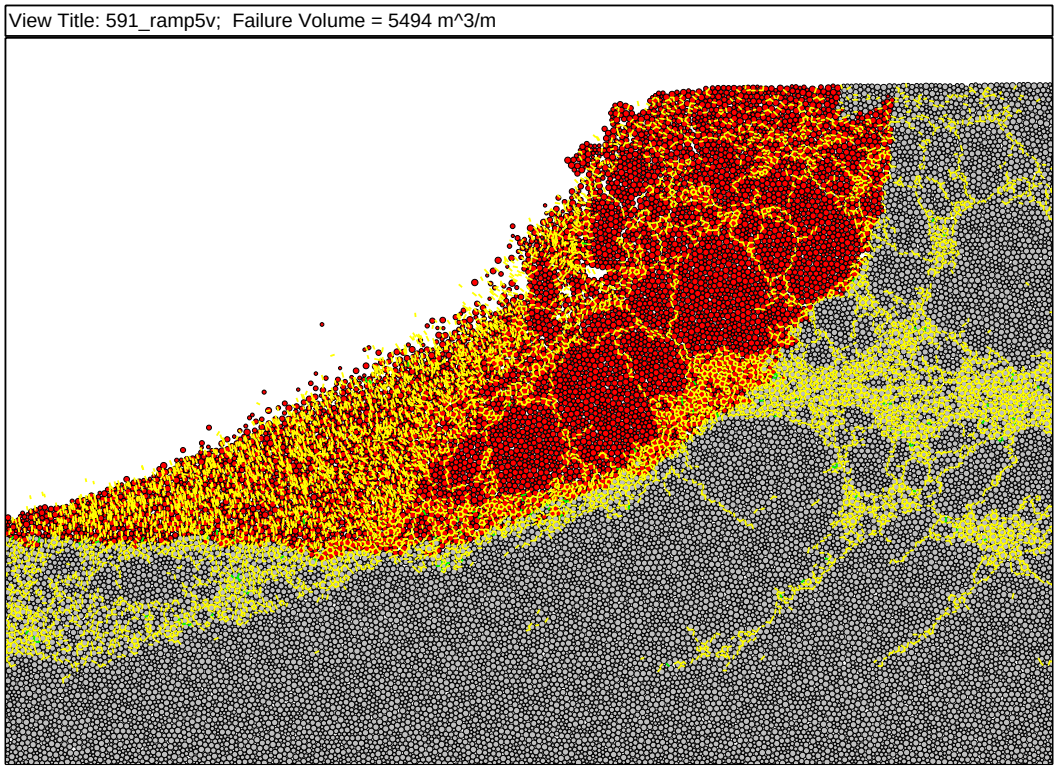

Figure 5.71: Final slope configuration for Model 591 after 20 seconds of a 5 Hz loading with a_{max} of 2.5 g and v_{max} of 0.78 m/s. The yellow lines indicate the failure of a parallel bond that has broken in tension. Green lines indicate a shear failure. The failure volume is indicated by red particles. Particles are considered part of the failure volume if their total displacement is greater than 0.25 meters or their rotation is greater than 10 degrees. For reference, the width of the frame in the figure is 185 meters.

Model 591 Results Summary

Figure 5.72 shows a summary of the simulation results in terms of number of cracks developed in Model 591 with 20 seconds of harmonic loading with tuning ratio. Figure 5.73 shows a summary of the simulation results in terms of failure volume developed in Model 591 with 20 seconds of harmonic loading with tuning ratio. From TR of just above 1.0 and below, the trend in the Model 591 results resembles those from Model 587. In contrast to the results from Model 587, the damage to the Model 591 increases at the highest loading frequency (5 Hz, $TR = 1.7$). The variation of the trend is a result of the differing failure mechanisms and modes observed in the corresponding simulation. Int he 5 Hz loading on Model 591, the damage in the lower portion of the slope, which eventually insulates the slope from dynamic input from the base, occurred later in the simulation than in the Model 587 simulation. As a result, relatively more damage had a chance to accumulate in the upper portion of the slope, which was being severely shaken due to the excitation of the second mode of vibration, which is at the same frequency as the input signal.

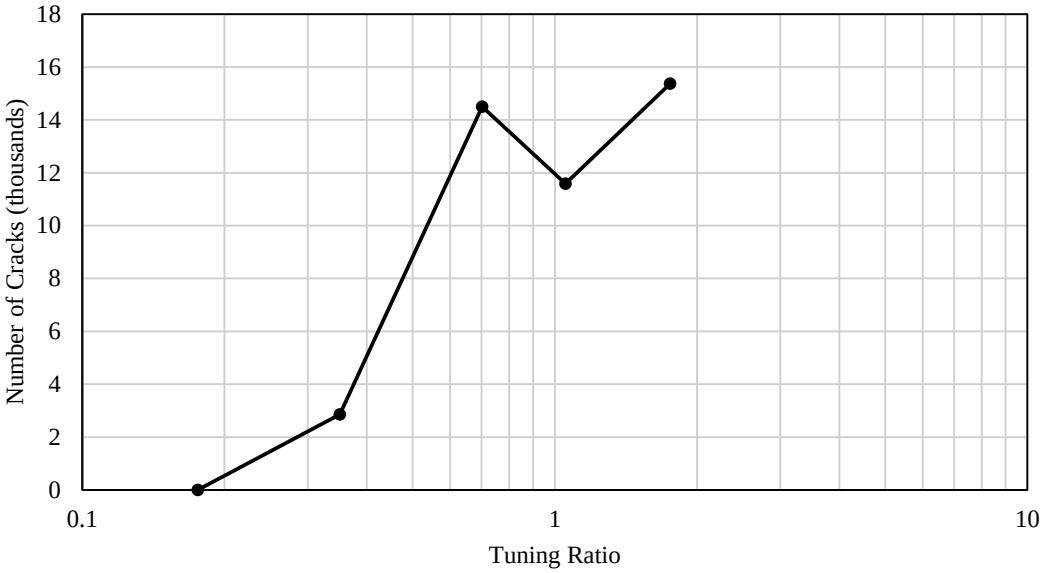

Figure 5.72: Number of cracks developed in Model 591 with 20 seconds of harmonic loading with tuning ratio.

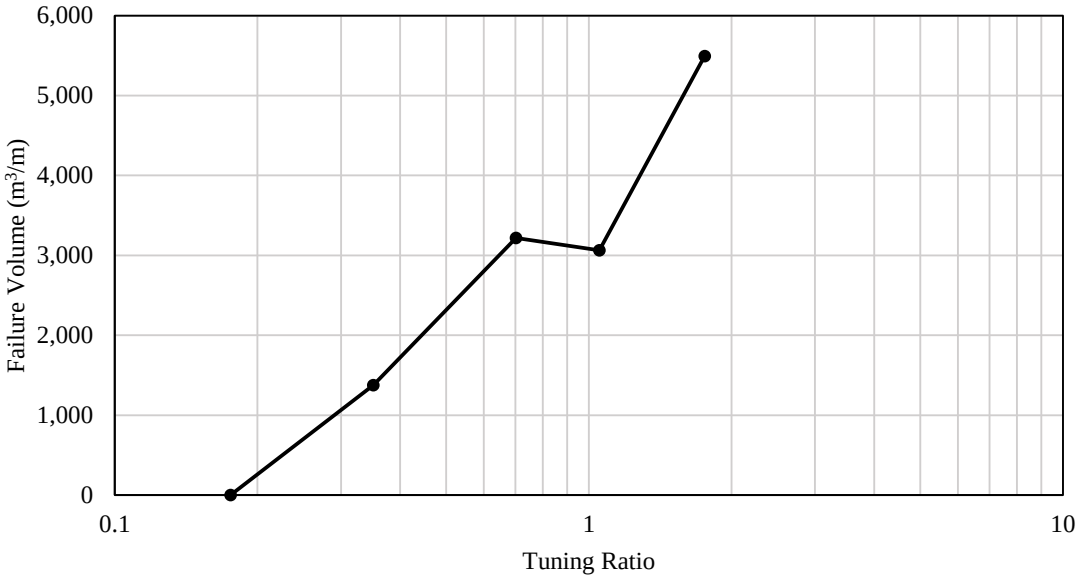

Figure 5.73: Failure volumes developed in Model 591 with 20 seconds of harmonic loading with tuning ratio.

5.5 Results from Recorded Ground Motion Simulations

Model 587 was subjected to the recorded ground motions presented in Table 5.3 in Section 5.3.4. As with the harmonic loading, these simulations were run as both non-destructive and as destructive simulations.

The primary purpose of these simulations is to assess the extent to which the trends observed in the model behavior under harmonic loading are still present when the model is subjected to more realistic motions with more frequency content. The results of the non-destructive simulations are compared with trends of amplification and tuning ratio from the harmonic loading. The results of the destructive simulations are compared with the observed failure mechanisms and modes from the harmonic loading cases, as well as trends in number of cracks and failure volumes.

5.5.1 Non-Destructive Recorded Ground Motion Simulations

The ground motion suite presented in Table 5.3 was first run through the homogeneous slope model without allowing any bonds to break to assess the level of amplification due to the recorded ground motions for comparison with the harmonic motion suite. Figures 5.74 through 5.78 show the velocity time-histories of the recorded ground motions at $v_{max} = 0.78$ m/s.

The apparent amplification of the slope due to the recorded ground motion suite is shown in Figure 5.79. The apparent amplification from the harmonic motion suite is also shown for reference. Relative to the harmonic motions, the amplification from the recorded ground motions is relatively low. The shape of the trend is also somewhat different, with less of a pronounced peak at a tuning ratio of one. The peak velocity apparent amplification from the recorded motions occurs at a tuning ratio of 0.76 (from the Northridge record) and also increases at tuning ratio of 1.55 (from the Richmond Hill ground motion).

Because the recorded ground motions have varying duration and more complex frequency content than the harmonic ground motions, the relative difference in overall amplification levels, and even the offset of the peak amplification appear to be reasonable. The pronounced difference between levels of amplification for the recorded ground motions at tuning ratio of 1.28 and 1.55 (corresponding to the Redcliffs and Richmond Hill motions, respectively) is somewhat surprising since these motions are different horizontal components of the same recorded event. However, the characteristic frequency of the Richmond Hill motion (4.5 Hz) is very close to the frequency of the second mode of vibration of the slope (5 Hz).

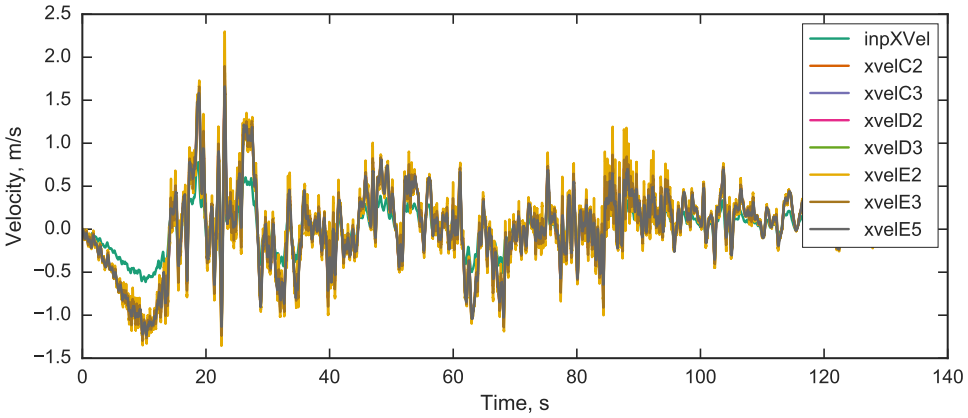

Figure 5.74: Velocity time histories for the homogeneous slope subjected to Michoacan under non-destructive conditions. Refer to Figure 5.12 for the positions of the monitored points within the slope.

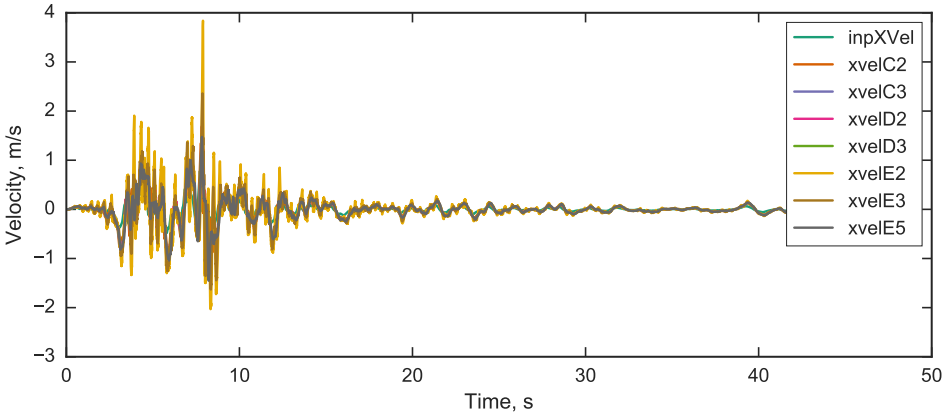

Figure 5.75: Velocity time histories for the homogeneous slope subjected to Northridge under non-destructive conditions. Refer to Figure 5.12 for the positions of the monitored points within the slope.

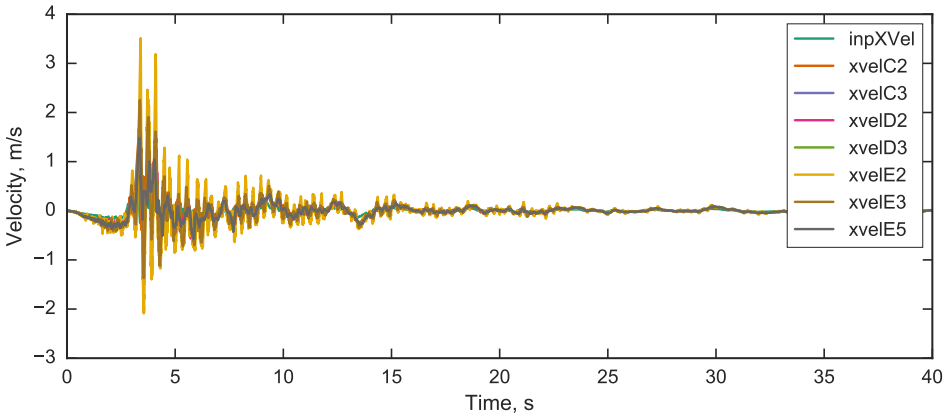

Figure 5.76: Velocity time histories for the homogeneous slope subjected to Loma Prieta under non-destructive conditions. Refer to Figure 5.12 for the positions of the monitored points within the slope.

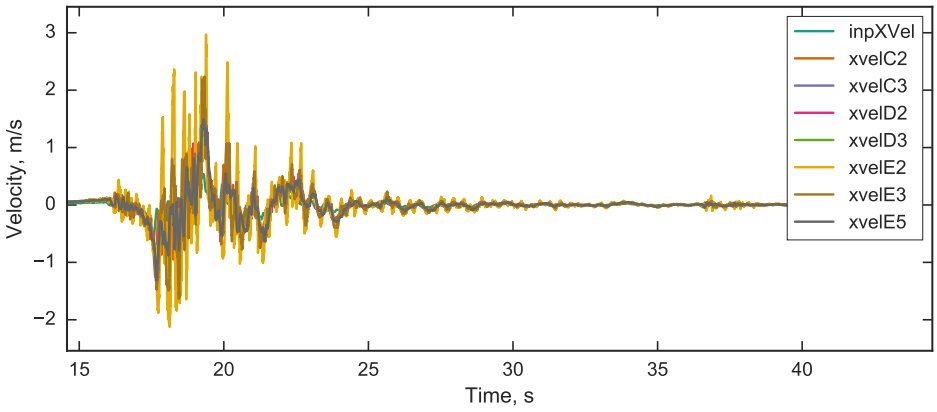

Figure 5.77: Velocity time histories for the homogeneous slope subjected to Redcliffs under non-destructive conditions. Refer to Figure 5.12 for the positions of the monitored points within the slope.

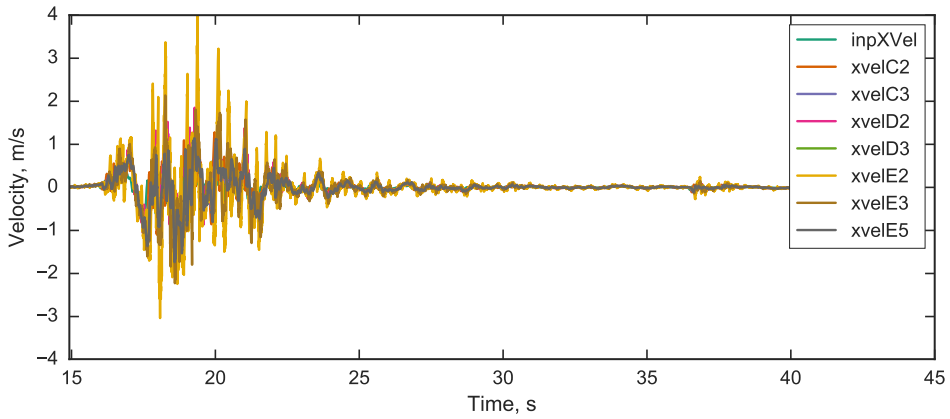

Figure 5.78: Velocity time histories for the homogeneous slope subjected to Richmond Hill under non-destructive conditions. Refer to Figure 5.12 for the positions of the monitored points within the slope.

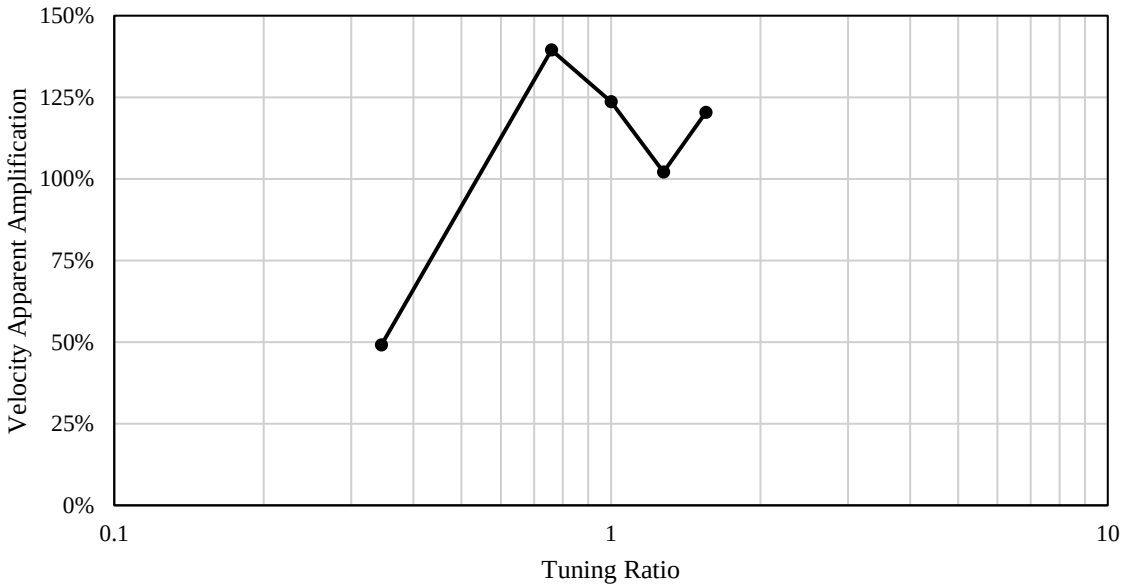

Figure 5.79: Velocity apparent amplification AA_V with tuning ratio for Model 587/591 subjected to recorded ground motion loading.

5.5.2 Destructive Recorded Ground Motion Simulations

Model 587 was subjected to the strong ground motion suite presented in Table 5.3. The observed failure mechanisms and modes, the failure sequence of the individual simulations, and a summary of the results in terms of number of cracks and failure volume are presented in the following sections.

Failure Mechanisms and Modes due to Recorded Ground Motions

When subjected to recorded ground motions, the observed failure mechanisms were fairly uniform, as shown in Table 5.8. In every simulation, the initial failure mechanism was a tensile crack, generally thought to correspond to the development of a wedge failure, initiating near the crest of the slope. After the tensile wedge failure, crushing at the toe occurred. Unlike the harmonic input simulations, no tensile cracks, initiating at the slope face and propagating into the slope were observed. Similarly, no deep tensile cracks, as were observed in the 5 Hz harmonic loadings in Models 587 and 591 were observed. The 'scattered damage at crest' mechanism is less clear because it is difficult to distinguish from a 'tensile wedge failure'. The damage near the crest that is identified as a 'tensile wedge failure' was minor and could be interpreted as 'scattered damage.' As mentioned in the discussion of failure mechanisms and modes for the harmonic simulations, the identification of mechanisms and modes is somewhat subjective. In this case, the broken bonds near the crest of the slope were considered part of a 'tensile wedge failure' mechanism because they became part of a wedge failure over time as the cracks grew and propagated towards the toe of the slope.

The observed failure modes in the recorded ground motion simulations, shown in Table 5.9, are also more uniform than the harmonic ground motion results. In all cases, the first observed failure mode is cliff-collapse. When observed, the second mode is slumping, and toppling of blocks created by the breaking up of the slope mass followed.

The following sections present figures of the failure events from the Model 587 recorded ground motion input simulations.

Table 5.8: Failure Mechanisms observed in Model 587 due to recorded ground motion loading.

Ground Motion	Tensile crack into slope	Crushing at toe	Tensile wedge failure	Scattered damage at crest	Deep tensile crack
Michoacan	–	2	1	–	–
Northridge	–	2	1	–	–
Loma Prieta (G1)	–	2	1	–	–
Redcliffs	–	2	1	–	–
Richmond Hill	–	2	1	–	–

Table 5.9: Failure Modes observed in Model 587 due to harmonic loading.

Loading Frequency, Hz	Cliff-collapse	Slumping	Toppling
Michoacan	1	–	2
Northridge	1	–	2
Loma Prieta (G1)	1	2	3
Redcliffs	1	2	3
Richmond Hill	1	–	2

Model 587 Subjected to Michoacan

Figure 5.80 shows the sequential failure of Model 587 subjected to the Michoacan recorded strong ground motion.

Failure initiates with tensile wedge failure around $t = 14.5s$, however, it is not until around $t = 17.2s$, when crushing at the toe occurs that the initial tensile cracks propagate to form a wedge failure. Once the wedge is formed, the shallow failure mass created by the wedge failures and crushing at the toe breaks up and begins to collapse ($t = 21.6s$). At $t = 23.0s$ a secondary wedge failure develops behind the first failure volume. This secondary wedge begins to break up from the top down, resulting in some toppling of blocks from the top of the slope (seen at $t = 25.6s$). By the end of the simulation, at $t = 128.8s$, the upper third of the secondary wedge has been damaged and run out, and the slope below that is buttressed by the failure volume.

The velocity time histories and number of cracks in the model with time (truncated to show the time period at and surrounding the main failure event) is shown in Figure 5.81. The velocity time-histories show a clear change in response of material near the face of the cliff following the crushing of material at the toe and subsequent cliff-collapse. The number of cracks with time shows that the sudden increase in number of cracks associated with the crushing at the toe and cliff-collapse is preceded by the small number of bonds broken in the initial tensile wedge failure mechanism.

Figure 5.82 shows the final slope configuration. Although there is a wedge of independent material behind the buttressing failure volume, the level of damage to the slope behind the main failure volume is fairly mild.

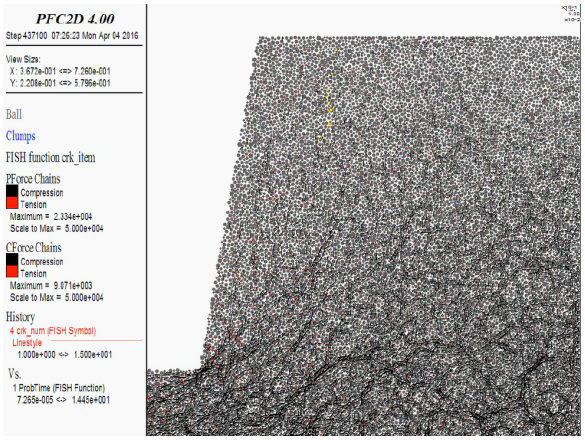

(a) $t = 14.5s$

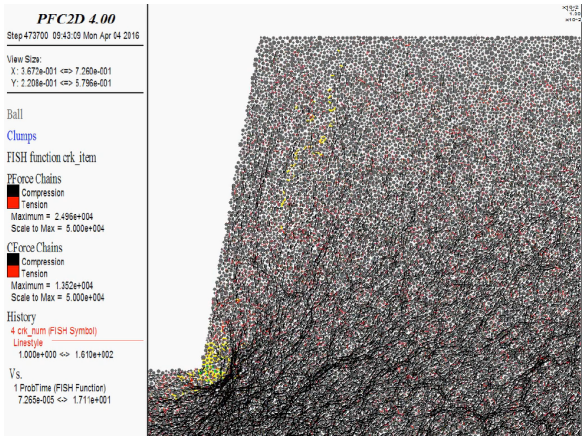

(b) $t = 17.1s$

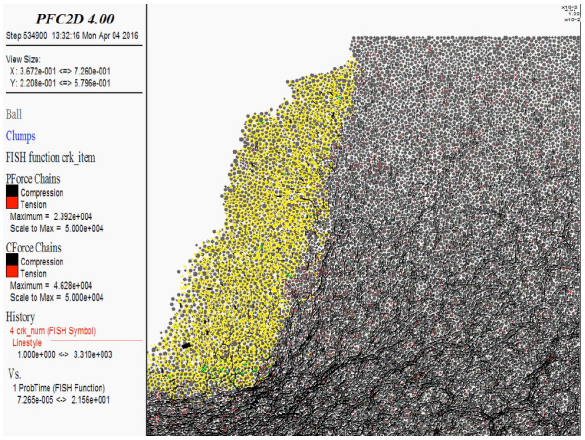

(c) $t = 21.6s$

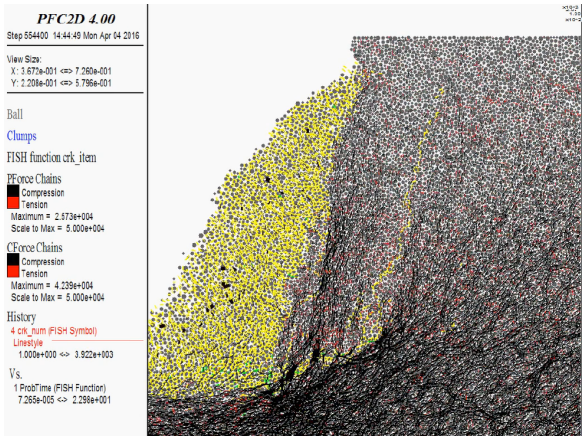

(d) $t = 23.0s$

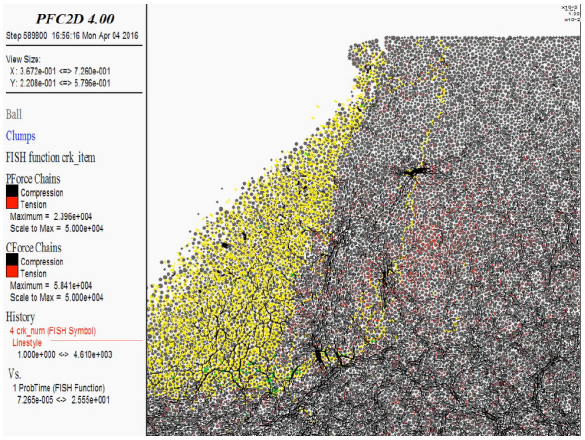

(e) $t = 25.6s$

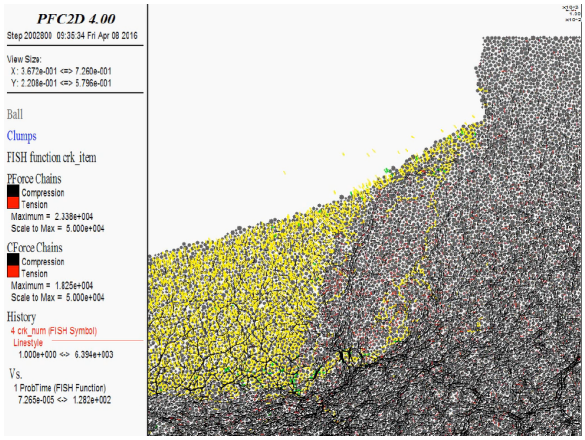

(f) $t = 128.2$

Figure 5.80: Failure sequence of Model 587 subjected to Michoacan.

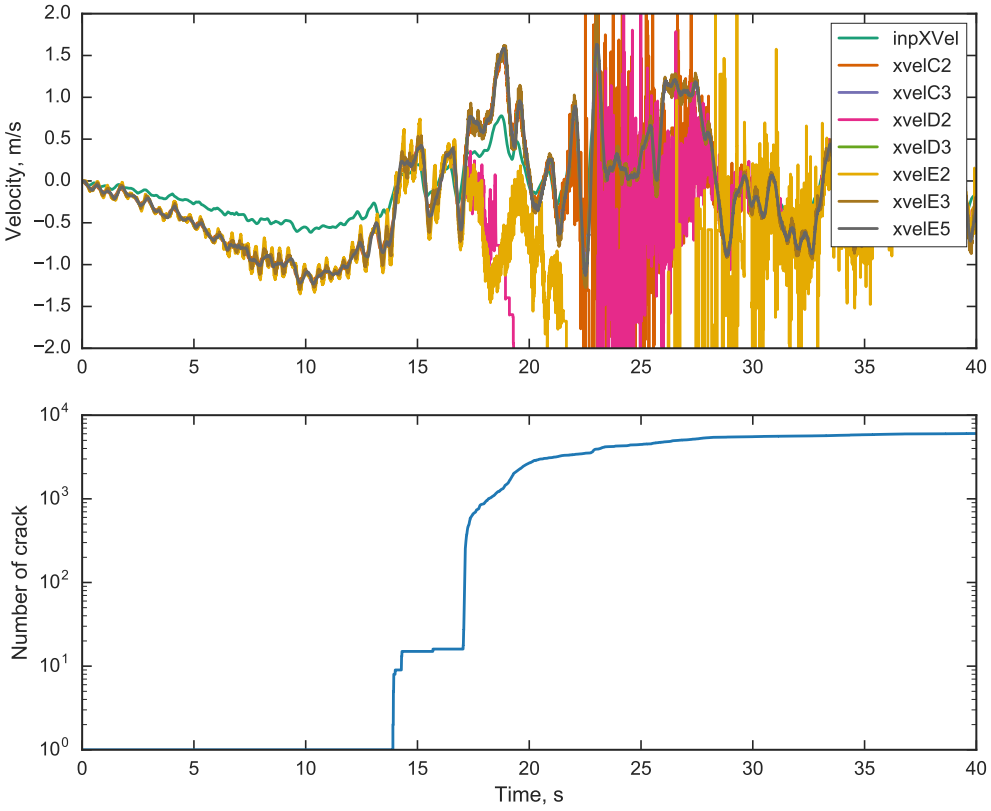

Figure 5.81: Velocity time histories and number of cracks with time for Model 591 subjected to Michoacan destructive harmonic loading. Points with 'E', 'D', and 'C' in the labels correspond to the elevations of the crest, mid-slope, and base, respectively. Points with '2' and '3' in the labels correspond to points at the slope face and set back 65 meters from the slope face, respectively. Point 'E5' corresponds to the furthest monitored point from the crest at the ground surface behind the slope. Refer to Figure 5.12 for the positions of the monitored points within the slope.

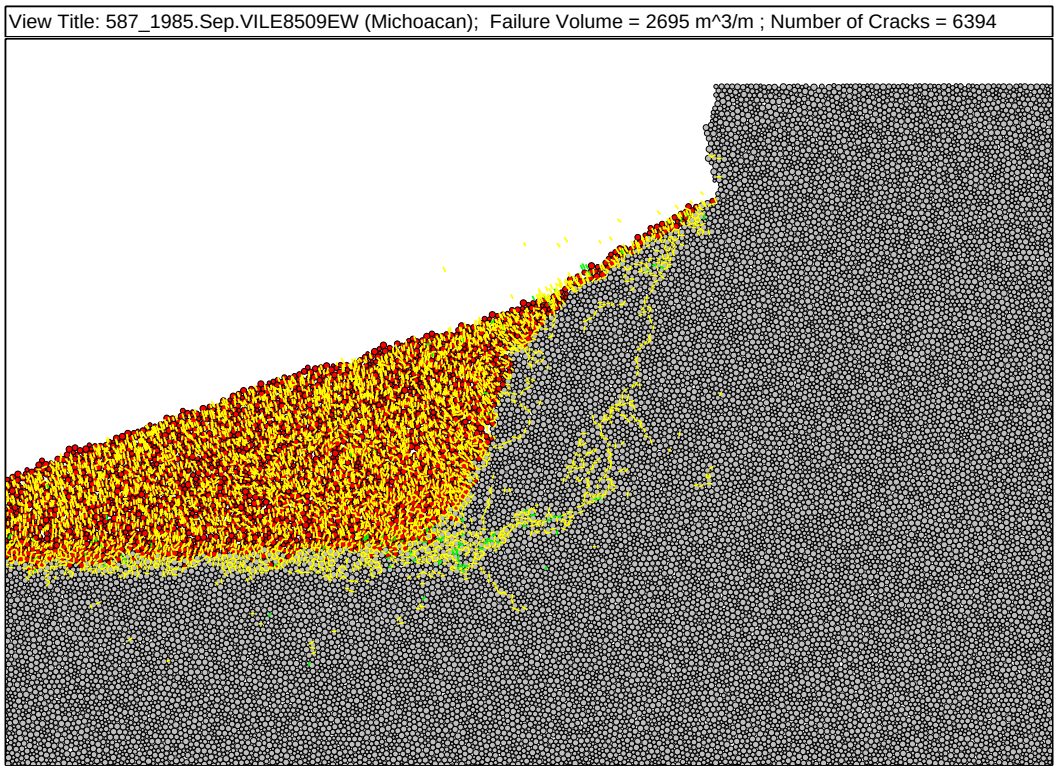

Figure 5.82: Final slope configuration for Model 587 after Michoacan. The yellow lines indicate the failure of a parallel bond that has broken in tension. Green lines indicate a shear failure. The failure volume is indicated by red particles. Particles are considered part of the failure volume if their total displacement is greater than 0.25 meters or their rotation is greater than 10 degrees. For reference, the width of the frame in the figure is 185 meters.

Model 587 Subjected to Northridge

Figure 5.83 shows the sequential failure of Model 587 subjected to the Northridge recorded strong ground motion with a_{max} of 1.0 g and v_{max} of 0.78 m/s. The Northridge motion was run at multiple levels of scaling. The results from the varied scaling levels will be presented in the next section.

Failure initiates with tensile wedge failure around $t = 3.3s$. Shortly after, at $t = 3.4s$, crushing at the toe occurs and by $t = 4.5s$, multiple wedge failures have developed, and the wedge closed to the face of the slope is beginning to break up. By $t = 7.2s$, cliff-collapse is occurring and toppling of blocks from behind the slope is observed. Also at this time, a significant amount of damage begins to develop along the two failure surfaces behind the main cliff-collapse. The damage accumulation along these failure surfaces is significant. By $t = 8.0s$, wide bands of damage define the failure surfaces. By the end of the simulation, at $t = 47.8s$, the upper third of the secondary wedge has been damaged and experienced some slumping but is being buttressed by a large talus pile.

The velocity time histories and number of cracks in the model with time (truncated to show the time period at and surrounding the main failure event) is shown in Figure 5.84. The velocity time-histories show a clear change in response of material near the face of the cliff following the crushing of material at the toe and subsequent cliff-collapse. The number of cracks with time shows a sudden increase in number of cracks associated with the crushing at the toe. Around 7 seconds, a secondary increase in number of cracks is visible, corresponding to the large spike in velocity at this time, and the increased damage along newly generated failure surfaces shown in Figures 5.84(d) and 5.84(e).

Figure 5.85 shows the final slope configuration. The failure volume includes the cliff-collapse material and one of the failure wedges behind the collapsed area. A deep circular failure surface is visible, but the displacement along this failure surface is not significant. Although no significant displacement has accumulated here, clearly the damage pattern indicates a reduction in the overall stability of the slope.

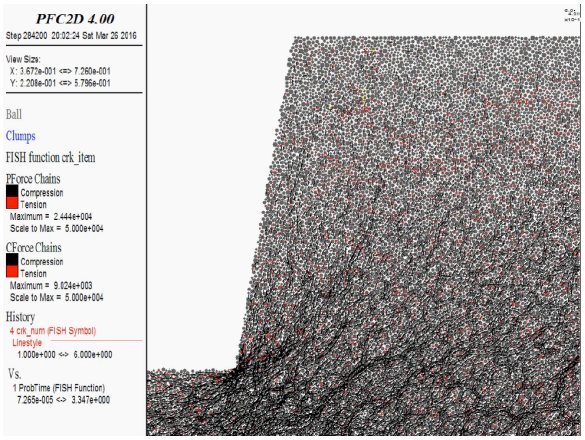

(a) $t = 3.3s$

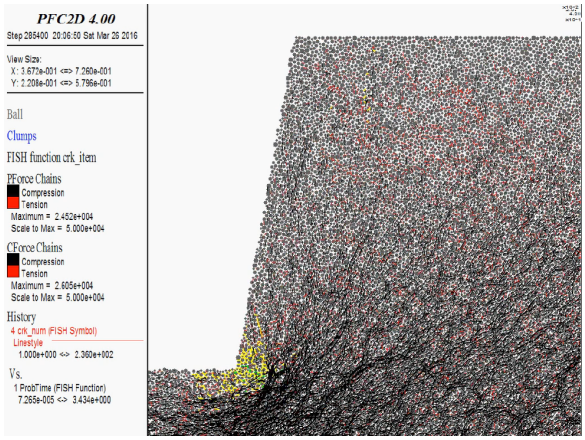

(b) $t = 3.4s$

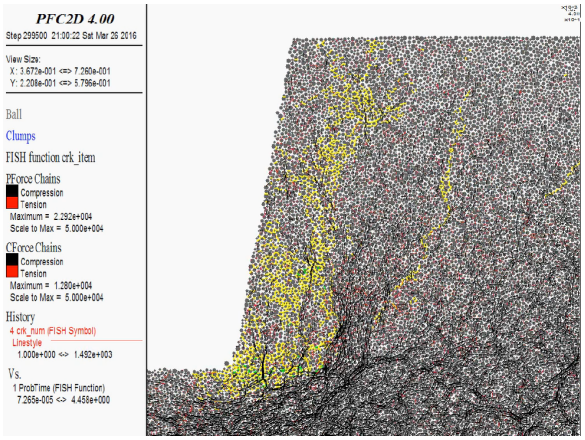

(c) $t = 4.5s$

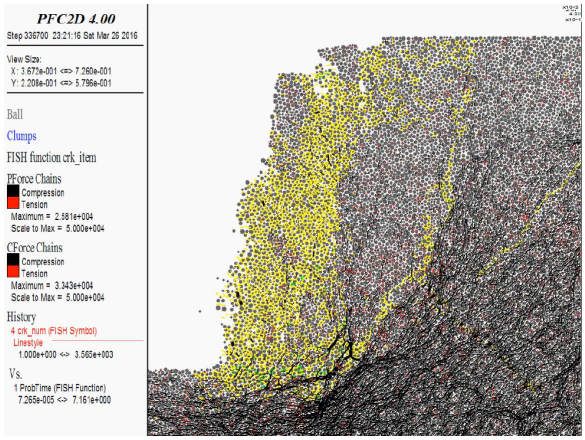

(d) $t = 7.2s$

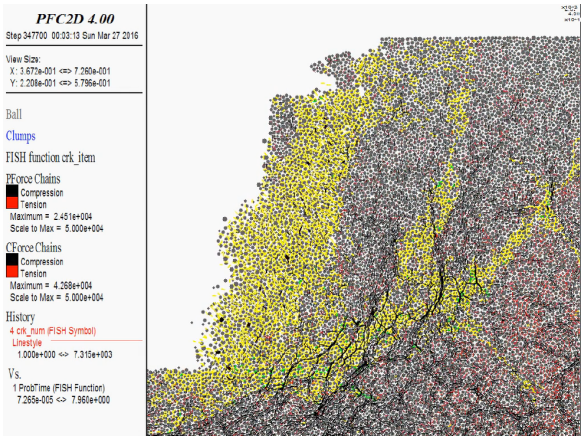

(e) $t = 8.0s$

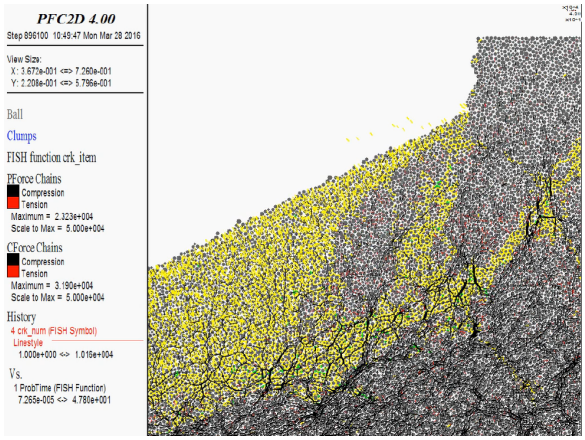

(f) $t = 47.8s$

Figure 5.83: Failure sequence of Model 587 subjected to Northridge.

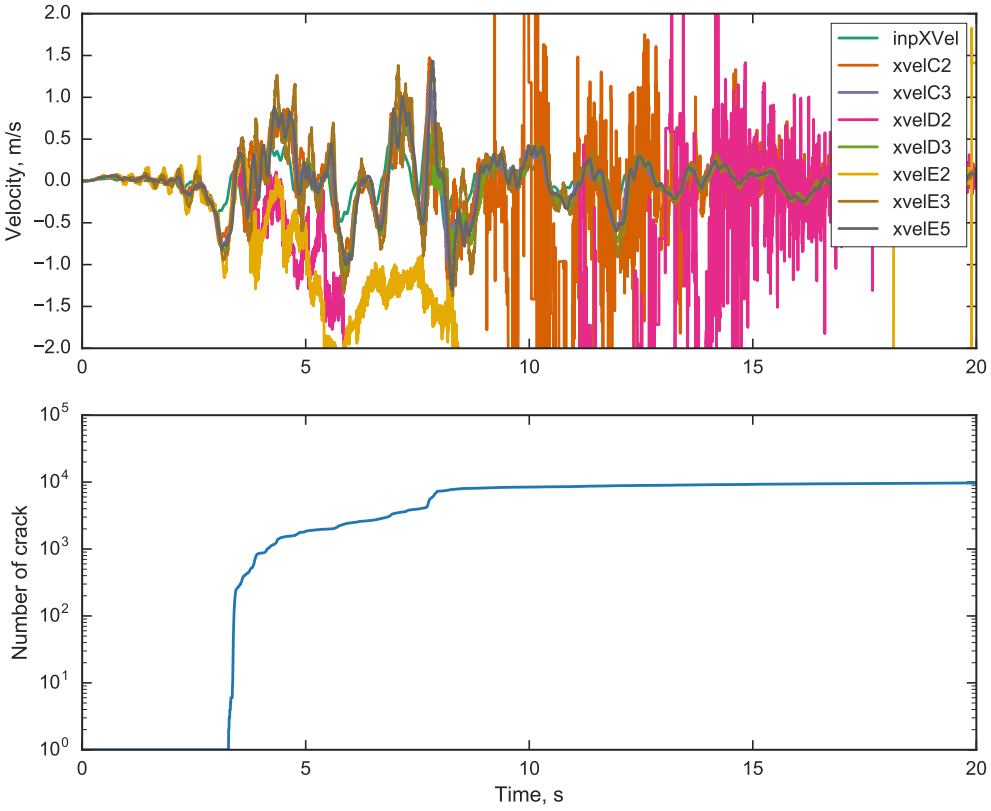

Figure 5.84: Velocity time histories and number of cracks with time for Model 591 subjected to Northridge destructive harmonic loading. Points with 'E', 'D', and 'C' in the labels correspond to the elevations of the crest, mid-slope, and base, respectively. Points with '2' and '3' in the labels correspond to points at the slope face and set back 65 meters from the slope face, respectively. Point 'E5' corresponds to the furthest monitored point from the crest at the ground surface behind the slope. Refer to Figure 5.12 for the positions of the monitored points within the slope.

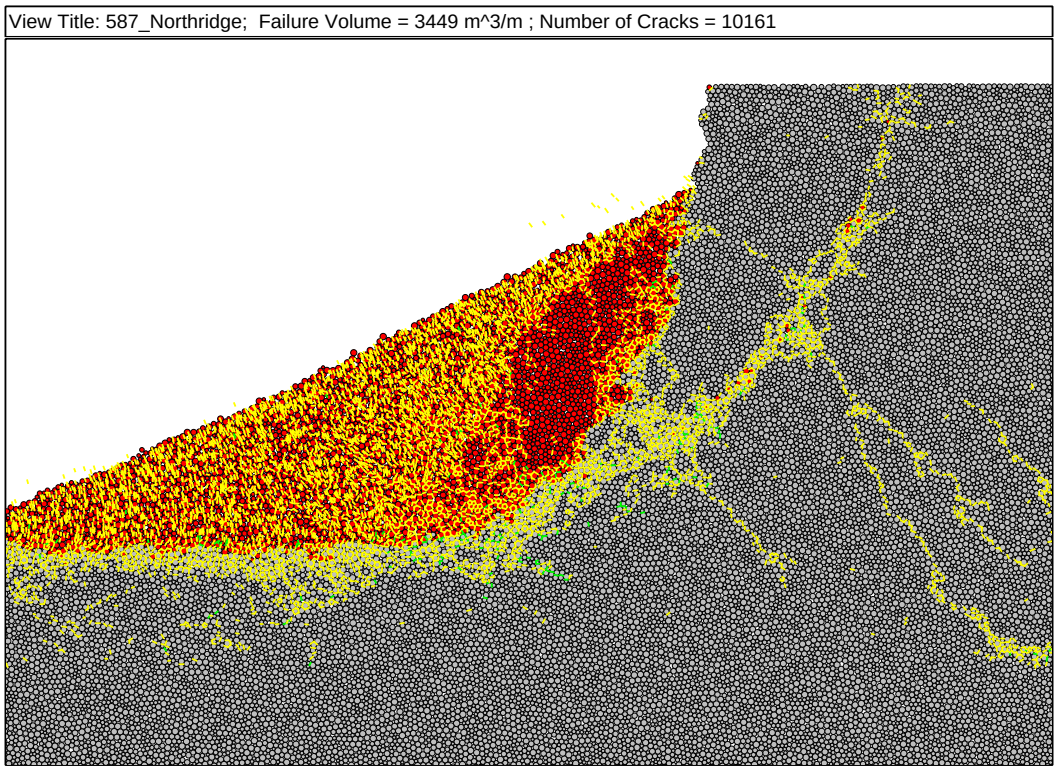

Figure 5.85: Final slope configuration for Model 587 after Northridge. The yellow lines indicate the failure of a parallel bond that has broken in tension. Green lines indicate a shear failure. The failure volume is indicated by red particles. Particles are considered part of the failure volume if their total displacement is greater than 0.25 meters or their rotation is greater than 10 degrees. For reference, the width of the frame in the figure is 185 meters.

Model 587 Subjected to Loma Prieta (G1)

Figure 5.86 shows the sequential failure of Model 587 subjected to recorded the Loma Prieta (G1) strong ground motion with a_{max} of 1.0 g and v_{max} of 0.78 m/s. The Loma Prieta (G1) motion was run at multiple levels of scaling. The results from the varied scaling levels will be presented in the next section.

Failure initiates with tensile wedge failure around $t = 3.1s$. Shortly after, at $t = 3.3s$, rushing at the toe occurs and by $t = 4.2s$, significant damage has developed forming multiple failure surfaces. By $t = 6.4s$, cliff-collapse is occurring and slumping of the wedge behind the slope face is observed. At $t = 11.5s$, toppling of blocks from behind the cliff-collapse zone is observed.

By the end of the simulation, at $t = 40.0s$, the slope is buttressed by a large talus pile and the damage behind the talus pile is severe.

The velocity time histories and number of cracks in the model with time (truncated to show the time period at and surrounding the main failure event) is shown in Figure 5.87. The velocity time-histories show a clear change in response of material near the face of the cliff following the crushing of material at the toe and subsequent cliff-collapse. The small number of cracks from the initial tensile wedge failures is also apparent.

Figure 5.88 shows the final slope configuration. The failure volume includes the cliff-collapse material and one of the failure wedges behind the collapsed area. A deep circular failure surface, as well as extensive damage within and behind this failure surface, is visible, but the displacement along the circular failure surface is not significant. Although no significant displacement has accumulated here, clearly the damage pattern indicates a reduction in the overall stability of the slope.

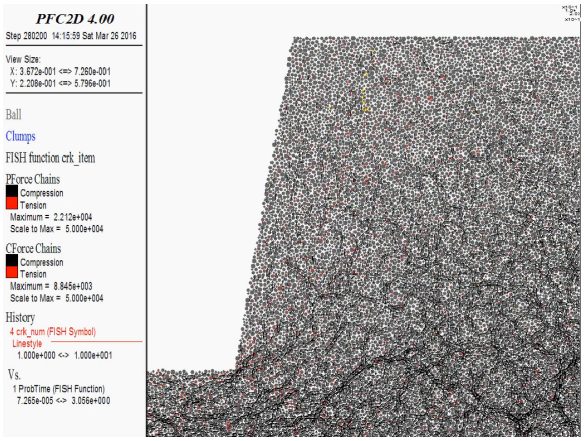

(a) $t = 3.1s$

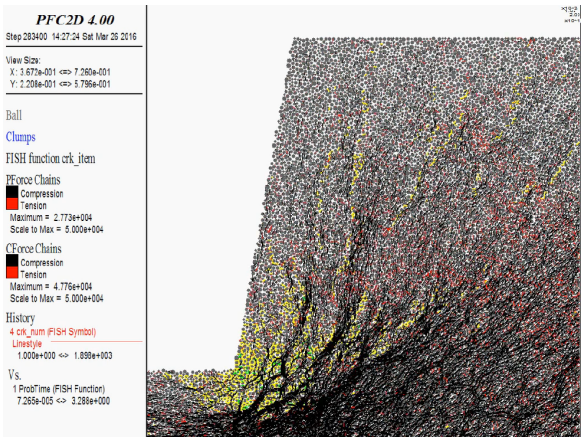

(b) $t = 3.3s$

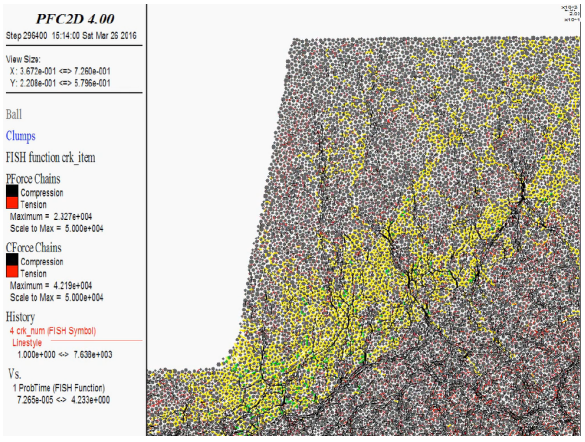

(c) $t = 4.2s$

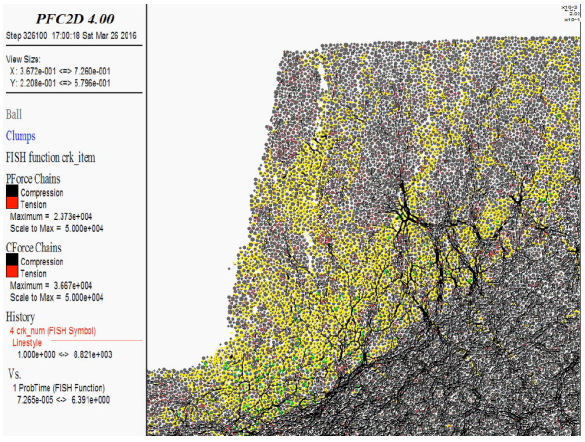

(d) $t = 6.4s$

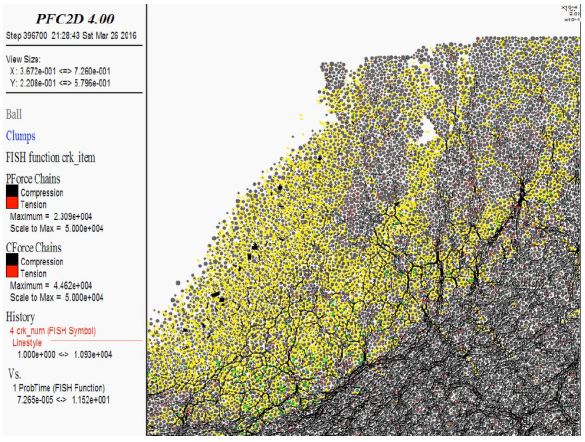

(e) $t = 11.5s$

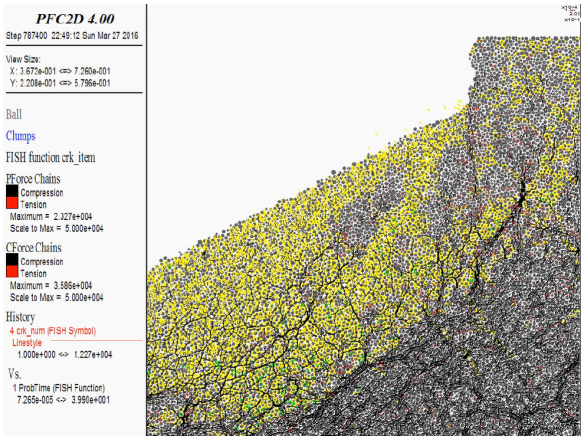

(f) $t = 40.0s$

Figure 5.86: Failure sequence of Model 587 subjected to Loma Prieta (G1).

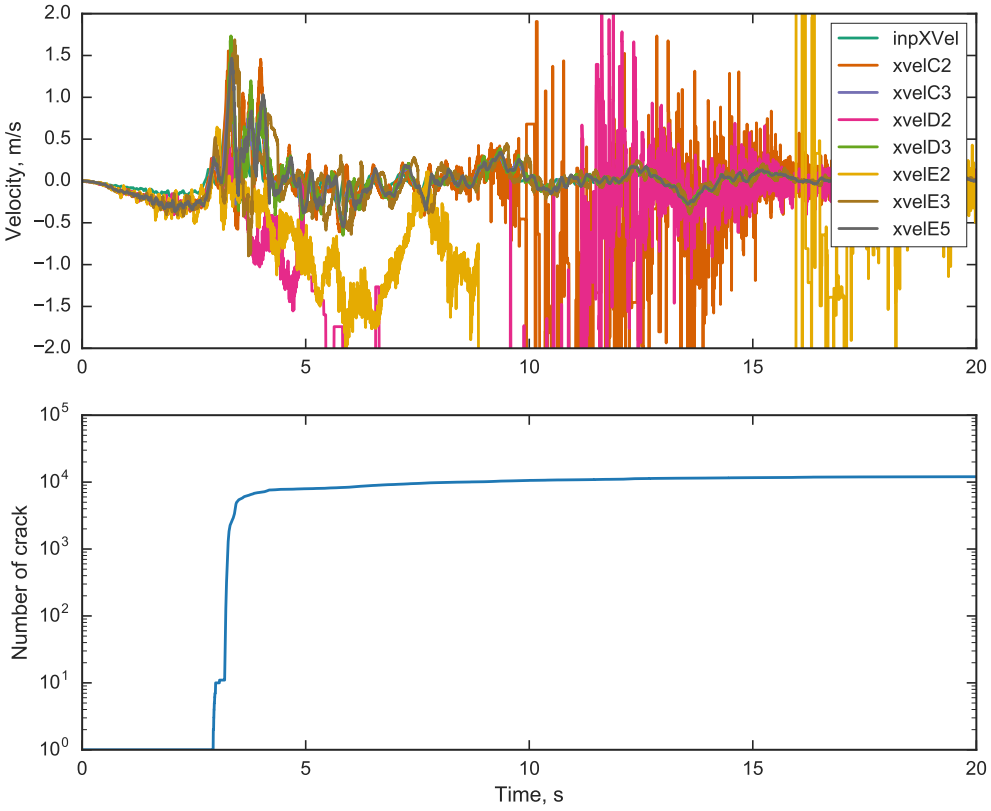

Figure 5.87: Velocity time histories and number of cracks with time for Model 591 subjected to Loma Prieta destructive harmonic loading. Points with 'E', 'D', and 'C' in the labels correspond to the elevations of the crest, mid-slope, and base, respectively. Points with '2' and '3' in the labels correspond to points at the slope face and set back 65 meters from the slope face, respectively. Point 'E5' corresponds to the furthest monitored point from the crest at the ground surface behind the slope. Refer to Figure 5.12 for the positions of the monitored points within the slope.

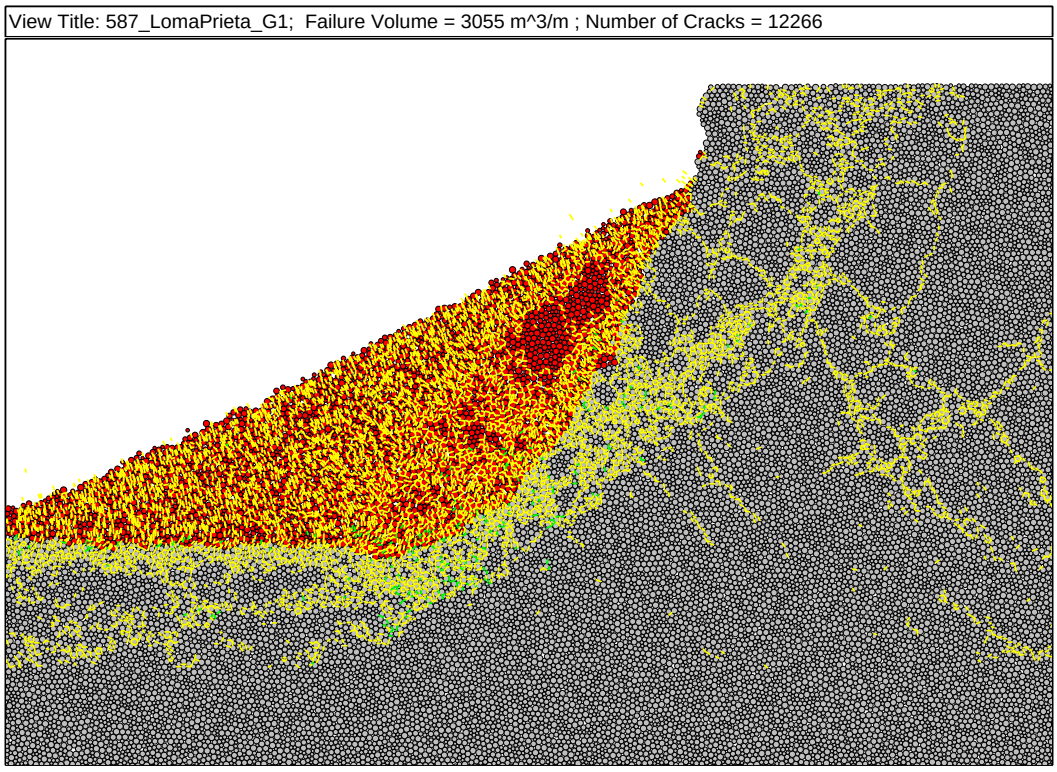

Figure 5.88: Final slope configuration for Model 587 after Loma Prieta (G1). The yellow lines indicate the failure of a parallel bond that has broken in tension. Green lines indicate a shear failure. The failure volume is indicated by red particles. Particles are considered part of the failure volume if their total displacement is greater than 0.25 meters or their rotation is greater than 10 degrees. For reference, the width of the frame in the figure is 185 meters.

Model 587 Subjected to Redcliffs

Figure 5.89 shows the sequential failure of Model 587 subjected to the Redcliffs strong ground motion.

Failure initiates with tensile wedge failure around $t = 17.7s$. Shortly after, at $t = 17.8s$, crushing at the toe occurs. By $t = 20.0s$, cliff-collapse is occurring, and the partial development of a thin, deep failure surface is seen. Slumping of the wedge behind the slope face is observed at $t = 27.2s$.

By the end of the simulation, at $t = 66.2s$, the slope is buttressed by a large talus pile.

The velocity time histories and number of cracks in the model with time (truncated to show the time period at and surrounding the main failure event) is shown in Figure 5.90. The velocity time-histories show a clear change in response of material near the face of the cliff following the crushing of material at the toe and subsequent cliff-collapse.

Figure 5.91 shows the final slope configuration. The failure volume includes the cliff-collapse material and the wedge of material that slid out behind the cliff-collapse. Two deep, partially-developed failure surfaces, with some transverse cracking between them, are also visible.

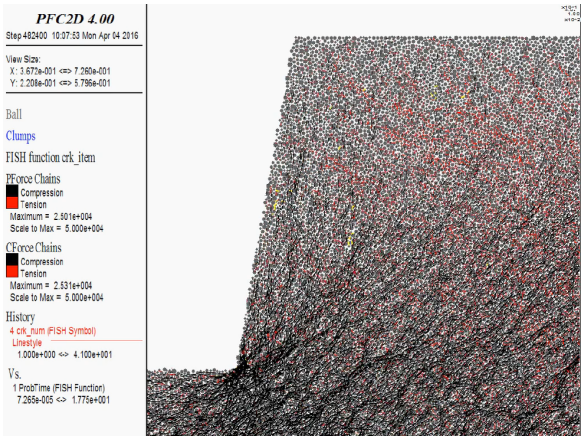

(a) $t = 17.7s$

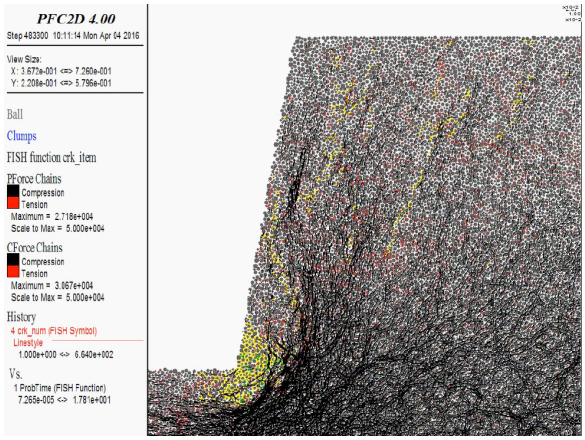

(b) $t = 17.8s$

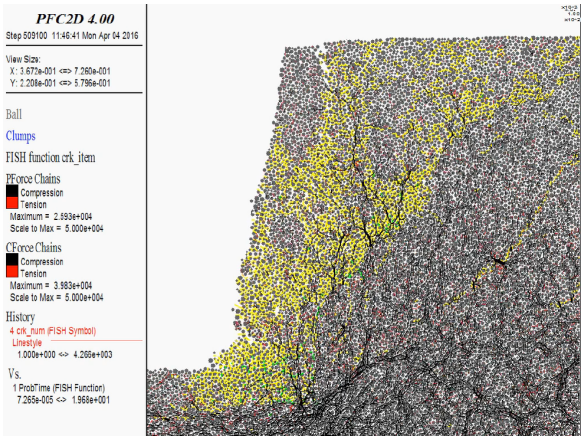

(c) $t = 20.0s$

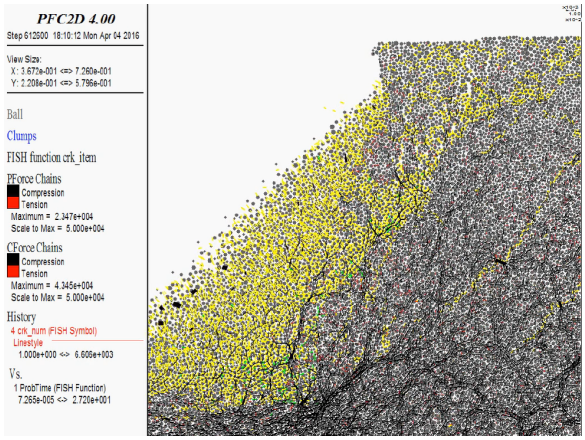

(d) $t = 27.2s$

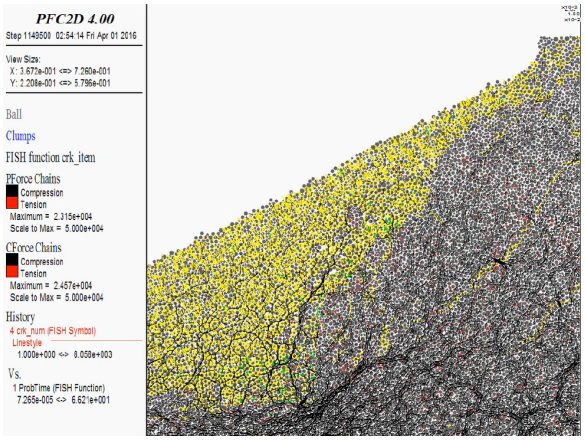

(e) $t = 66.2s$

Figure 5.89: Failure sequence of Model 587 subjected to Redcliffs.

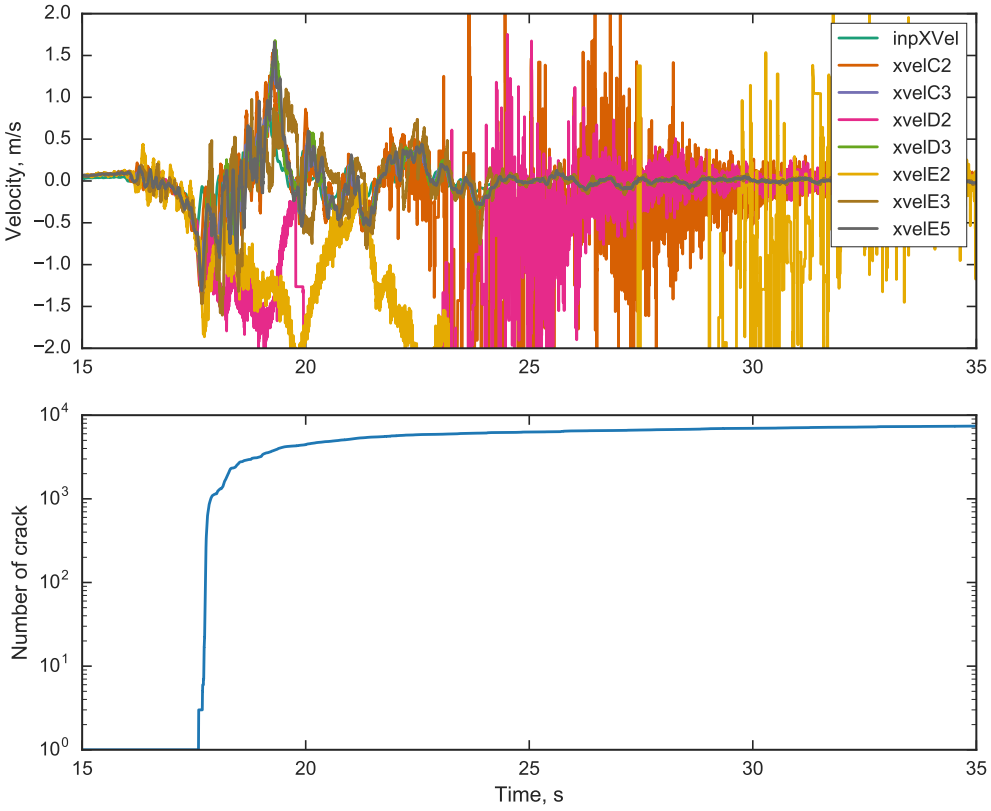

Figure 5.90: Velocity time histories and number of cracks with time for Model 591 subjected to Redcliffs destructive harmonic loading. Points with 'E', 'D', and 'C' in the labels correspond to the elevations of the crest, mid-slope, and base, respectively. Points with '2' and '3' in the labels correspond to points at the slope face and set back 65 meters from the slope face, respectively. Point 'E5' corresponds to the furthest monitored point from the crest at the ground surface behind the slope. Refer to Figure 5.12 for the positions of the monitored points within the slope.

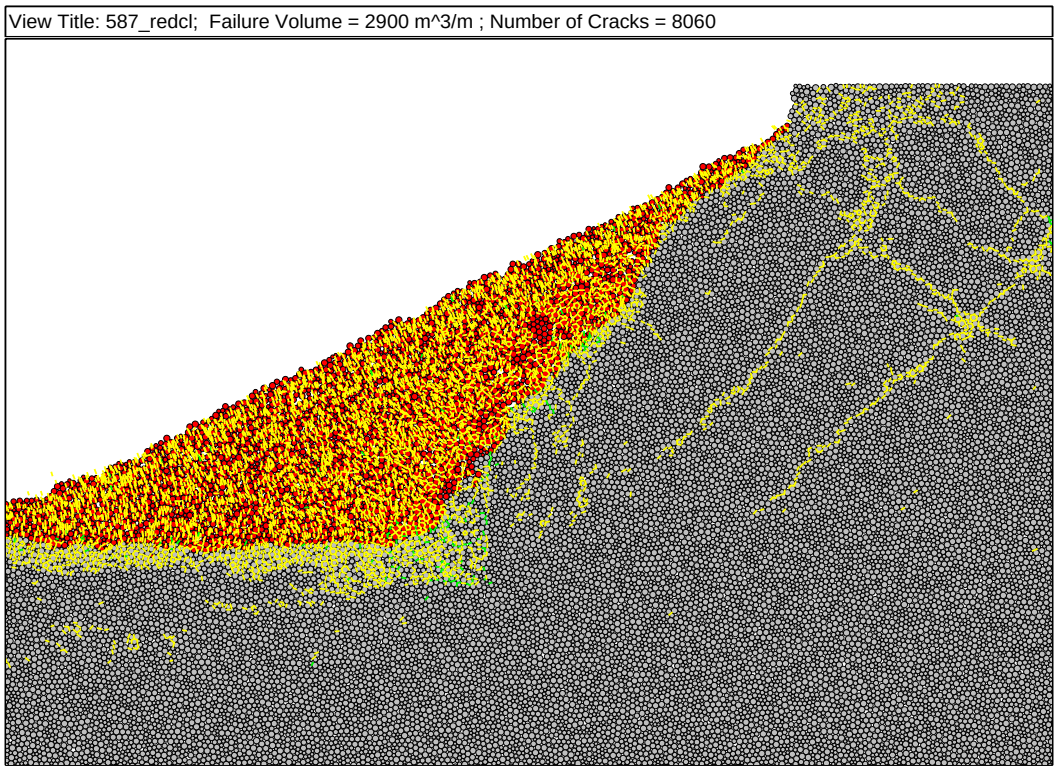

Figure 5.91: Final slope configuration for Model 587 after Redcliffs. The yellow lines indicate the failure of a parallel bond that has broken in tension. Green lines indicate a shear failure. The failure volume is indicated by red particles. Particles are considered part of the failure volume if their total displacement is greater than 0.25 meters or their rotation is greater than 10 degrees. For reference, the width of the frame in the figure is 185 meters.

Model 587 Subjected to Richmond Hill

Figure 5.92 shows the sequential failure of Model 587 subjected to the Richmond Hill strong ground motion with a_{max} of 1.82 g and v_{max} of 0.78 m/s. The Richmond Hill motion was run at multiple levels of scaling. The results from the varied scaling levels will be presented in the next later section.

Failure initiates with ensile wedge failure around $t = 16.4s$. Shortly after, at $t = 16.7s$, crushing at the toe occurs. By $t = 17.6s$, the face of the slope is damaged, and cliff-collapse is imminent. At $t = 17.8s$, a secondary strong pulse creates multiple cracks behind the crushed toe and scattered damage behind the slope. By $t = 19.2$, cliff-collapse is occurring and the damage initially caused by the secondary pulse has become extensive.

By the end of the simulation, at $t = 65.8s$, the slope is nearly completely buttressed by a large talus pile and material at the crest is toppling.

The velocity time histories and number of cracks in the model with time (truncated to show the time period at and surrounding the main failure event) is shown in Figure 5.93. The velocity time-histories show a clear change in response of material near the face of the cliff following the crushing of material at the toe and subsequent cliff-collapse. The initial and secondary onsets of significant damage can be seen in the number of cracks around 16.5 and 18 seconds.

Figure 5.94 shows the final slope configuration. The damage to the slope is extensive compared to the previous recorded strong ground motions.

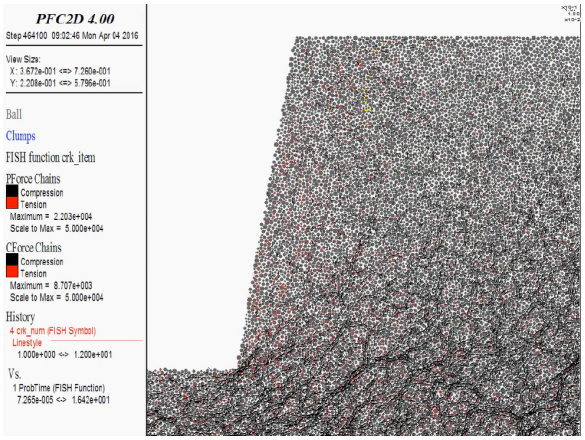

(a) $t = 16.4s$

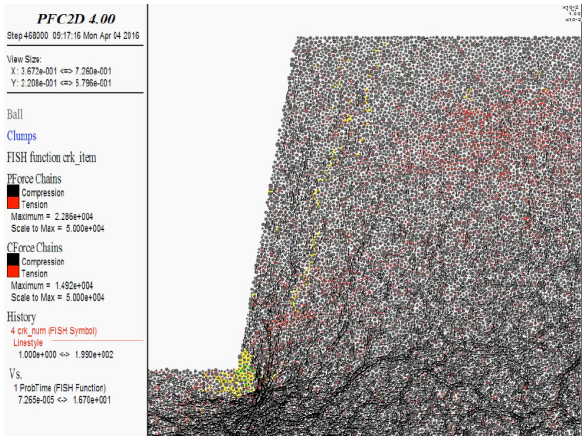

(b) $t = 16.7s$

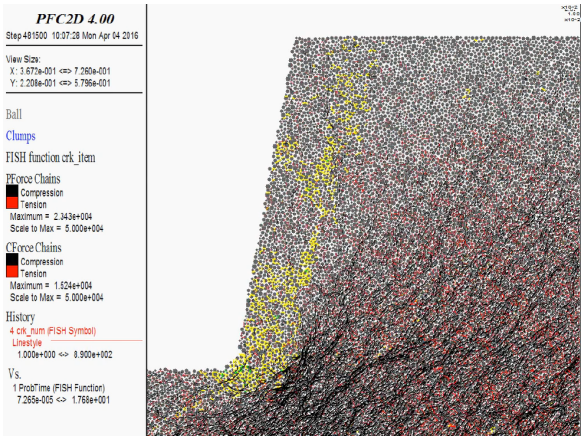

(c) $t = 17.6s$

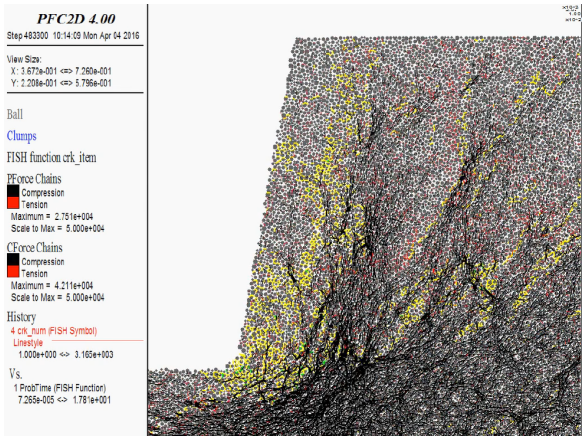

(d) $t = 17.8s$

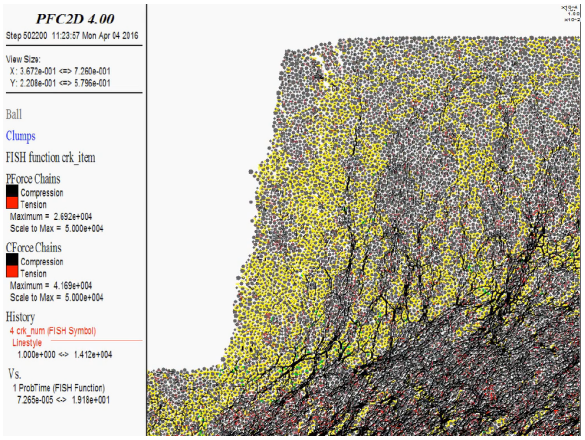

(e) $t = 19.2s$

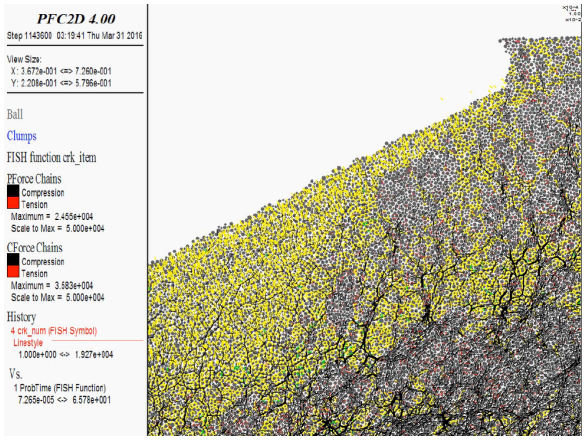

(f) $t = 65.8s$

Figure 5.92: Failure sequence of Model 587 subjected to Richmond Hill.

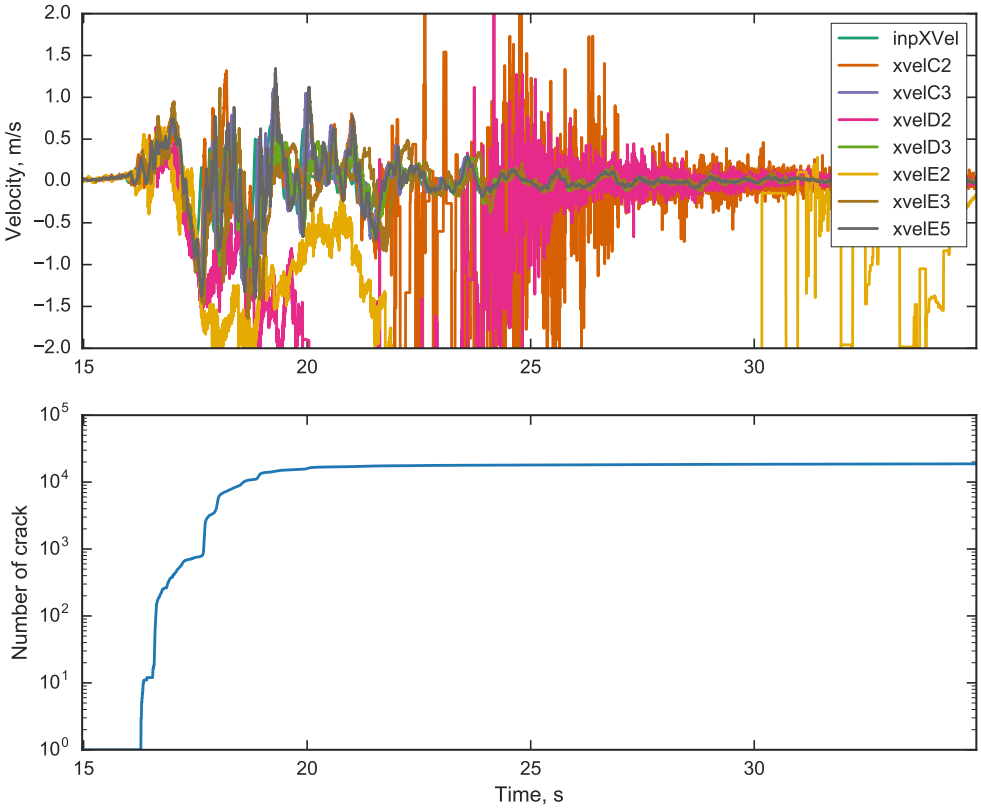

Figure 5.93: Velocity time histories and number of cracks with time for Model 591 subjected to Richmond Hilll destructive harmonic loading. Points with 'E', 'D', and 'C' in the labels correspond to the elevations of the crest, mid-slope, and base, respectively. Points with '2' and '3' in the labels correspond to points at the slope face and set back 65 meters from the slope face, respectively. Point 'E5' corresponds to the furthest monitored point from the crest at the ground surface behind the slope. Refer to Figure 5.12 for the positions of the monitored points within the slope.

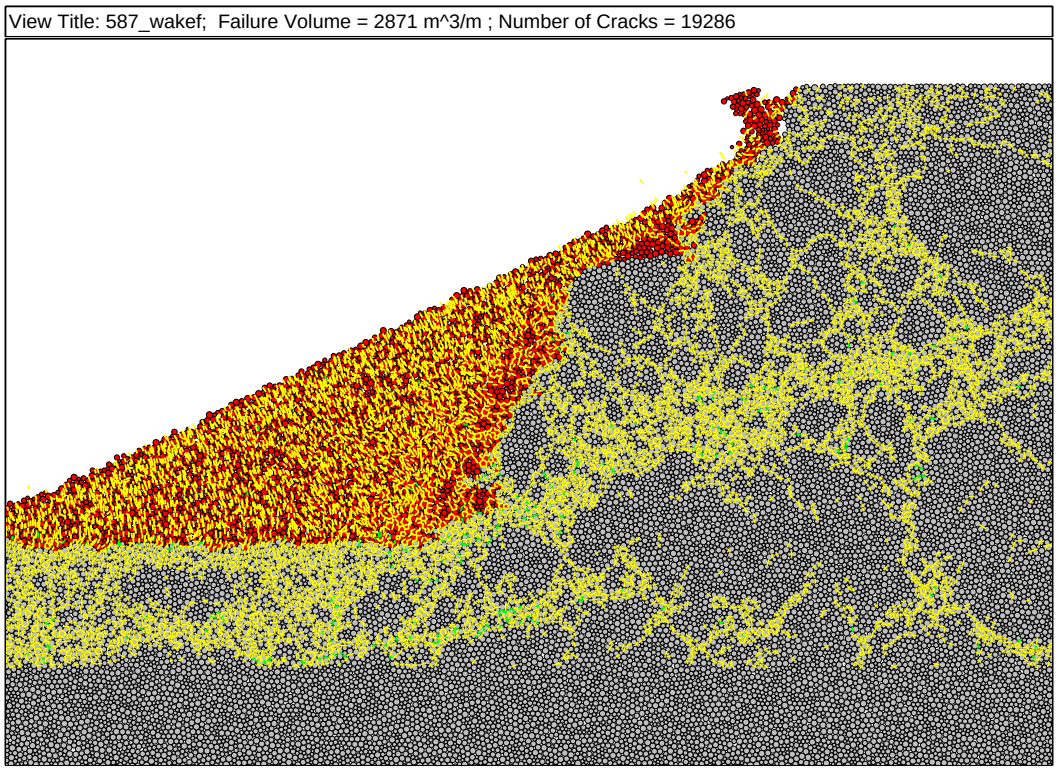

Figure 5.94: Final slope configuration for Model 587 after Richmond Hill. The yellow lines indicate the failure of a parallel bond that has broken in tension. Green lines indicate a shear failure. The failure volume is indicated by red particles. Particles are considered part of the failure volume if their total displacement is greater than 0.25 meters or their rotation is greater than 10 degrees. For reference, the width of the frame in the figure is 185 meters.

Varied Scalings of the Northridge, Loma Prieta (G1), and Richmond Hill Ground Motions

The Northridge, Loma Prieta (G1), and Richmond Hill motions were run at multiple levels of scaling. Table 5.10 presents the levels of varied k_{max} for the motions, where k_{max} is taken as the free-field horizontal acceleration of the motion at the ground surface ($2a_{max}$). The resulting number of cracks in the model and failure volumes and the figures of final slope configurations for Model 587 after the inputs are also presented in the table.

Table 5.10: Variations on the Northridge, Loma Prieta (G1), and Richmond Hill ground motions used on Model 587 and associated number of cracks and failure volumes.

Event	f**[Hz]**	k_{max}**[g]**	**Number of Cracks**	**Failure Volume [m ^{2}/m]**	**Figure Reference**
Northridge	2.2	1.88	10,106	3,449	Figure 5.83
Northridge	2.2	1.24	6,294	2,379	Figure 5.95
Northridge	2.2	0.86	4,133	1,607	Figure 5.96
Northridge	2.2	0.62	973	232	Figure 5.97
Northridge	2.2	0.49	50	0	Figure 5.98
Northridge	2.2	0.36	0	0	–
Loma Prieta (G1)	2.9	1.80	12,266	3,055	Figure 5.88
Loma Prieta (G1)	2.9	1.16	5,942	2,208	Figure 5.99
Loma Prieta (G1)	2.9	0.80	4,585	1,704	Figure 5.100
Loma Prieta (G1)	2.9	0.58	4,486	1,852	Figure 5.101
Loma Prieta (G1)	2.9	0.46	68	0	Figure 5.102
Loma Prieta (G1)	2.9	0.34	20	0	Figure 5.103
Richmond Hill	4.5	3.64	19,286	2,871	Figure 5.94
Richmond Hill	4.5	0.93	4,102	1,614	Figure 5.104
Richmond Hill	4.5	0.70	49	0	Figure 5.105

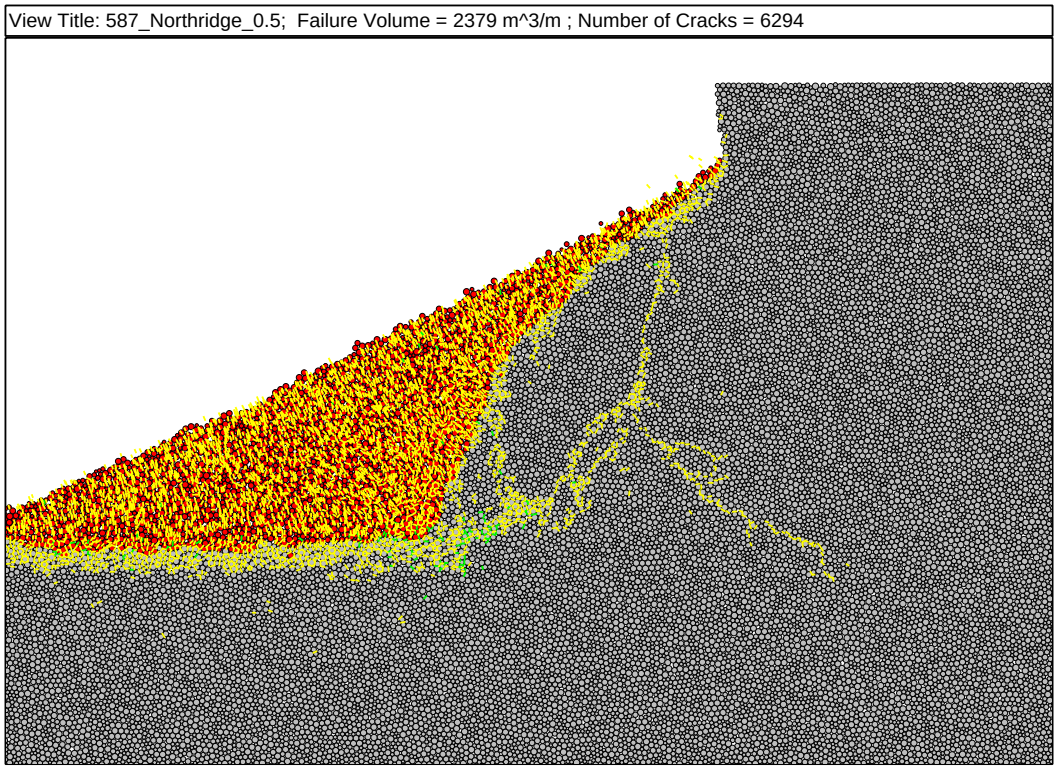

Figure 5.95: Final slope configuration for Model 587 after the Northridge motion scaled to k_{max} of 1.24 g. The yellow lines indicate the failure of a parallel bond that has broken in tension. Green lines indicate a shear failure. Moderate damage was induced behind the failure volume. The failure volume is indicated by red particles. Particles are considered part of the failure volume if their total displacement is greater than 0.25 meters or their rotation is greater than 10 degrees. For reference, the width of the frame in the figure is 185 meters.

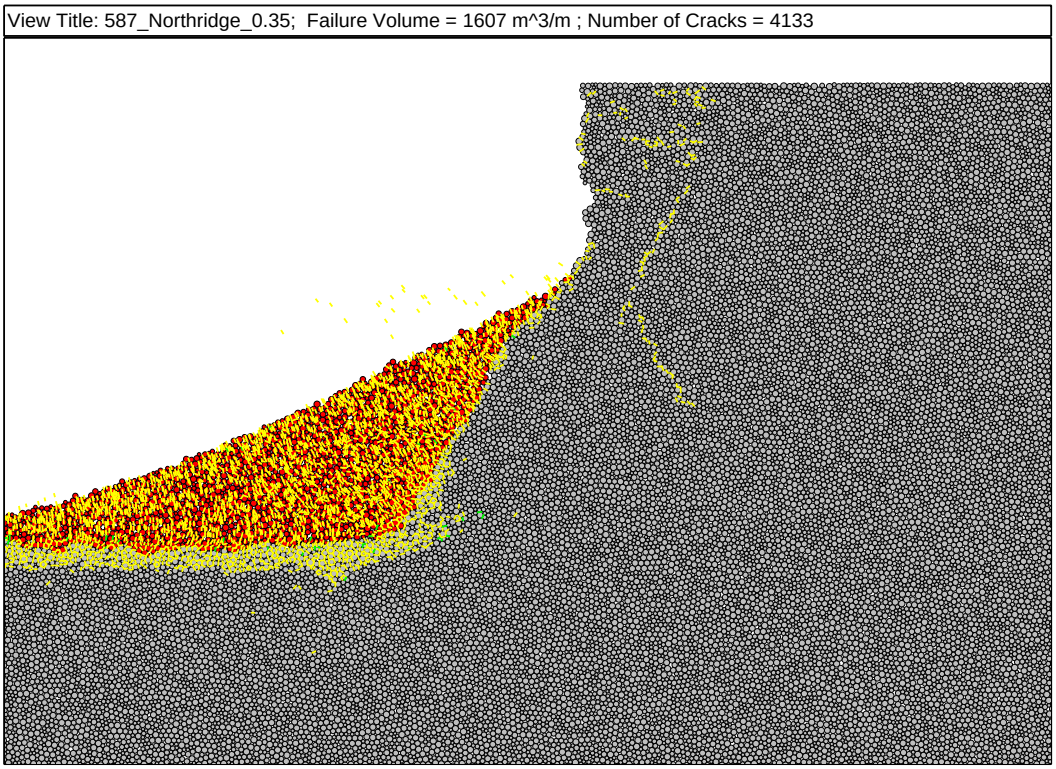

Figure 5.96: Final slope configuration for Model 587 after the Northridge motion scaled to k_{max} of 0.86 g. The yellow lines indicate the failure of a parallel bond that has broken in tension. Green lines indicate a shear failure. Mild damage was induced behind the failure volume. The failure volume is indicated by red particles. Particles are considered part of the failure volume if their total displacement is greater than 0.25 meters or their rotation is greater than 10 degrees. For reference, the width of the frame in the figure is 185 meters.

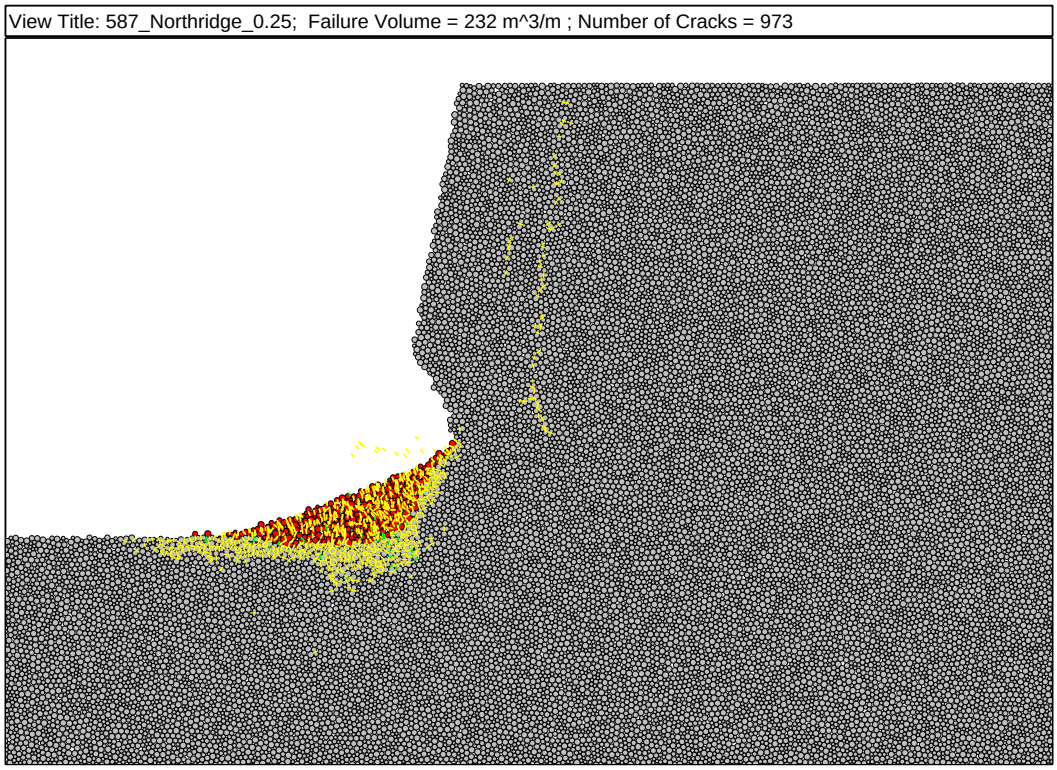

Figure 5.97: Final slope configuration for Model 587 after the Northridge motion scaled to k_{max} of 0.62 g. The yellow lines indicate the failure of a parallel bond that has broken in tension. Green lines indicate a shear failure. The amount of damage behind the failure volume is mild, however, a very precarious geometry has been created. The shape of the failure surface is similar to the static failure of Model 591, but made more critical by the cracking above and behind the overhang. The failure volume is indicated by red particles. Particles are considered part of the failure volume if their total displacement is greater than 0.25 meters or their rotation is greater than 10 degrees. For reference, the width of the frame in the figure is 185 meters.

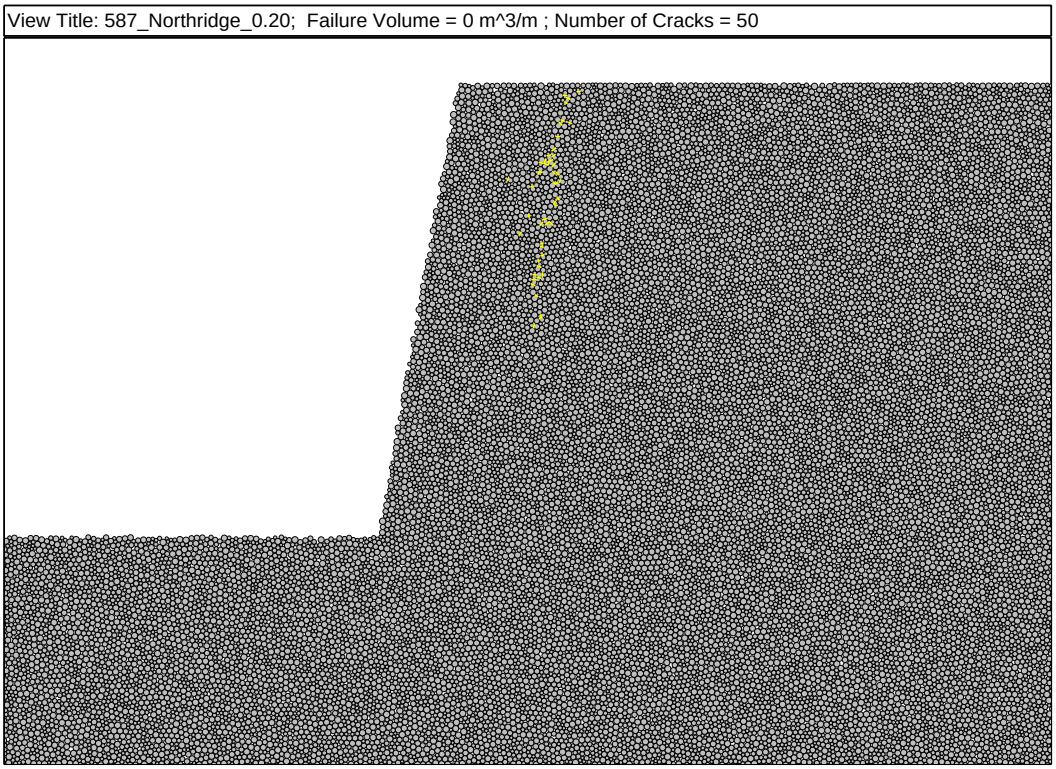

Figure 5.98: Final slope configuration for Model 587 after the Northridge motion scaled to k_{max} of 0.492 g. The yellow lines indicate the failure of a parallel bond that has broken in tension. Green lines indicate a shear failure. No material is lost from the slope, but damage from tensile cracking behind the cliff face can be seen. Particles are considered part of the failure volume if their total displacement is greater than 0.25 meters or their rotation is greater than 10 degrees. For reference, the width of the frame in the figure is 185 meters.

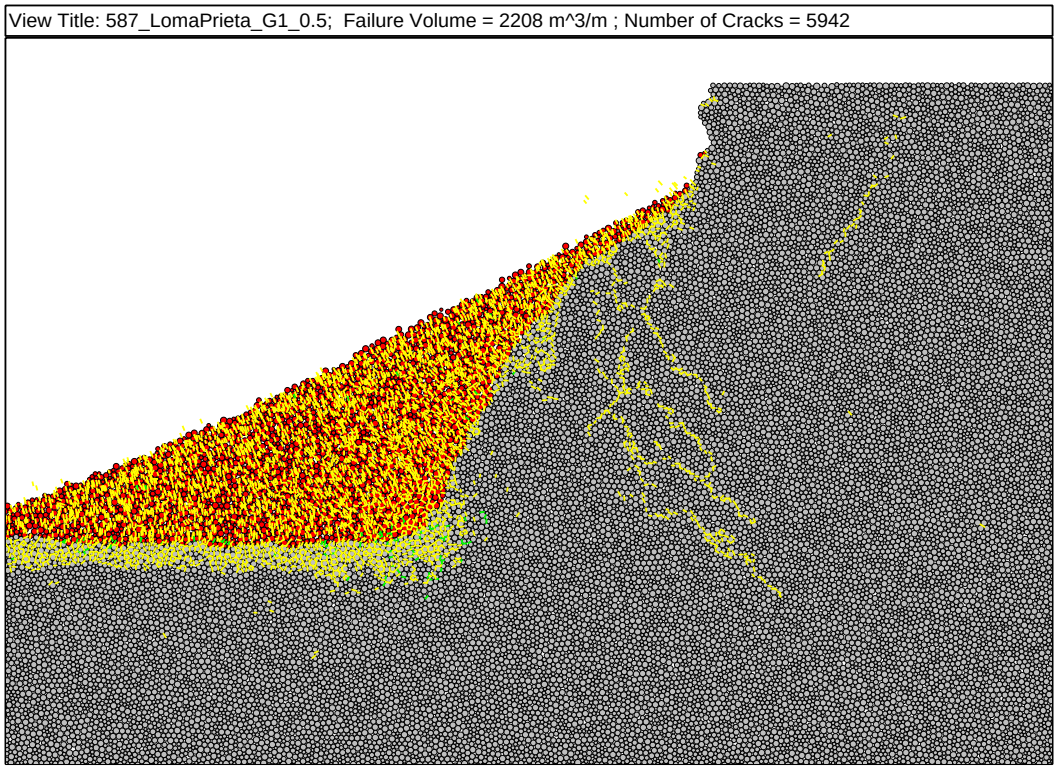

Figure 5.99: Final slope configuration for Model 587 after the Loma Prieta (G1) motion scaled to k_{max} of 1.16 g. The yellow lines indicate the failure of a parallel bond that has broken in tension. Green lines indicate a shear failure. Moderate damage was induced behind the failure volume. The failure volume is indicated by red particles. Particles are considered part of the failure volume if their total displacement is greater than 0.25 meters or their rotation is greater than 10 degrees. For reference, the width of the frame in the figure is 185 meters.

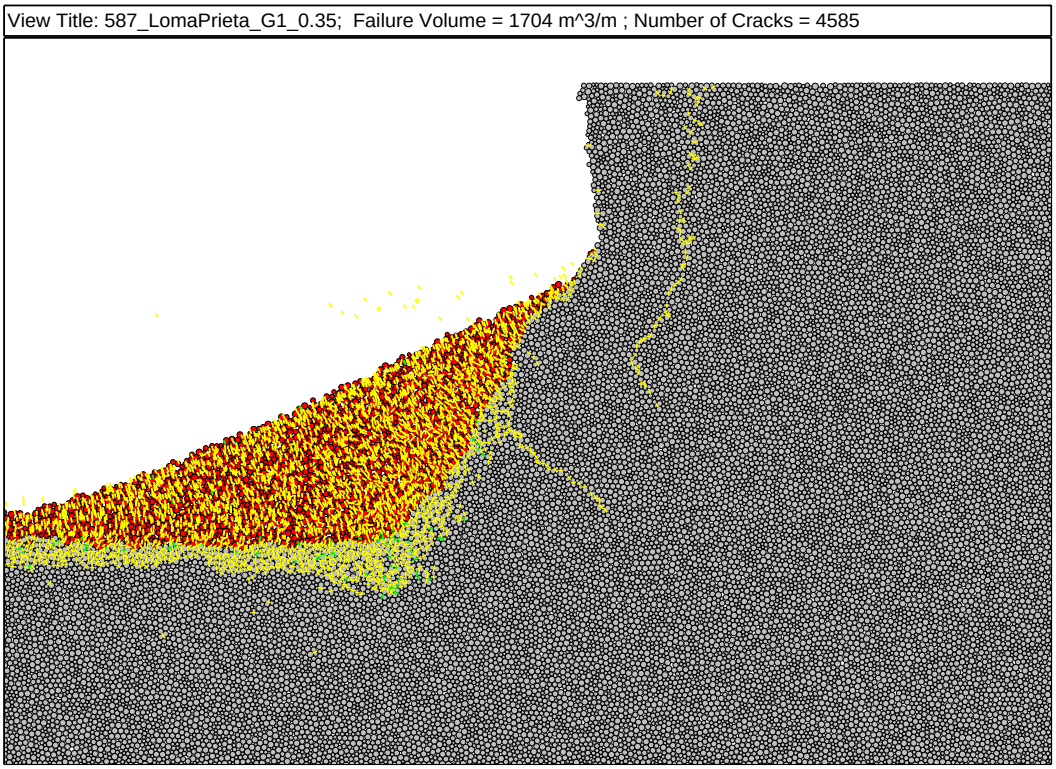

Figure 5.100: Final slope configuration for Model 587 after the Loma Prieta (G1) motion scaled to k_{max} of 0.8 g. The yellow lines indicate the failure of a parallel bond that has broken in tension. Green lines indicate a shear failure. Moderate damage was induced behind the failure volume. The failure volume is indicated by red particles. Particles are considered part of the failure volume if their total displacement is greater than 0.25 meters or their rotation is greater than 10 degrees. For reference, the width of the frame in the figure is 185 meters.

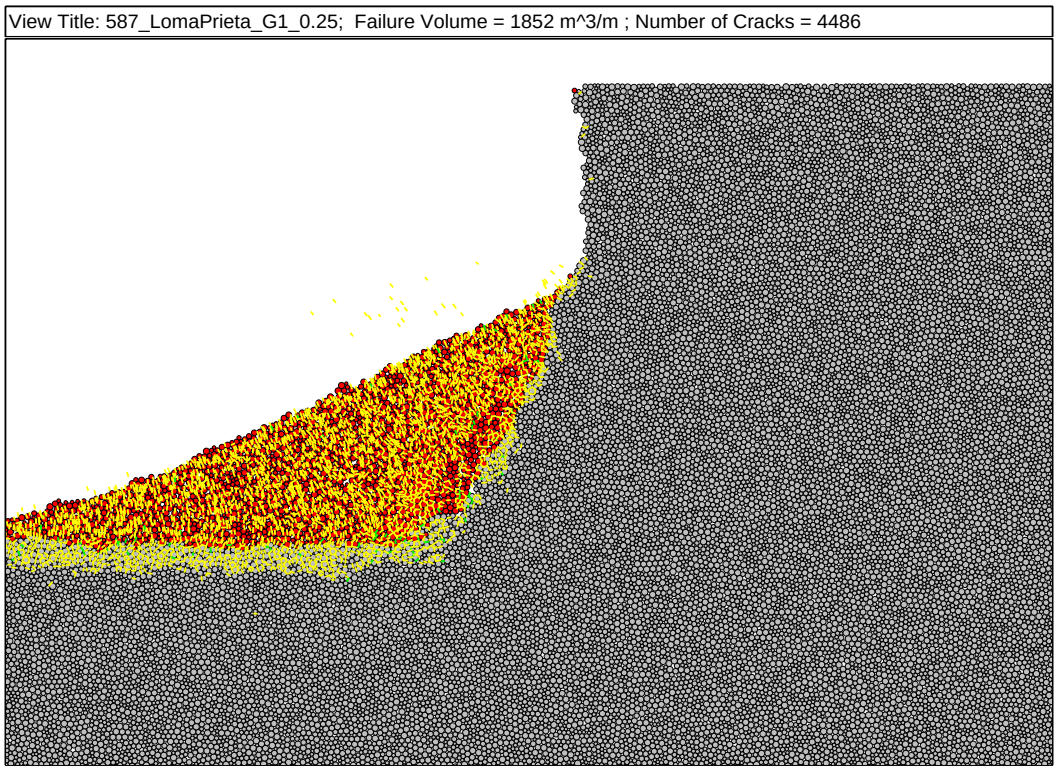

Figure 5.101: Final slope configuration for Model 587 after the Loma Prieta (G1) motion scaled to k_{max} of 0.58 g. The yellow lines indicate the failure of a parallel bond that has broken in tension. Green lines indicate a shear failure. The failure volume is indicated by red particles. Particles are considered part of the failure volume if their total displacement is greater than 0.25 meters or their rotation is greater than 10 degrees. For reference, the width of the frame in the figure is 185 meters.

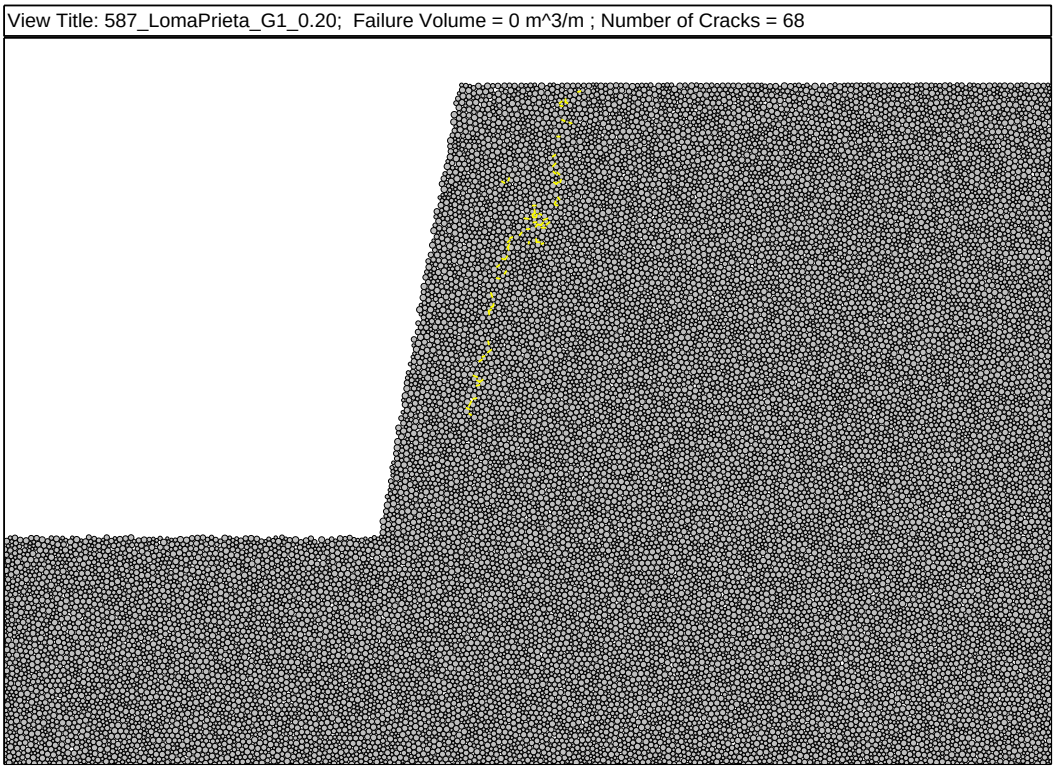

Figure 5.102: Final slope configuration for Model 587 after the Loma Prieta (G1) motion scaled to k_{max} of 0.46 g. The yellow lines indicate the failure of a parallel bond that has broken in tension. Green lines indicate a shear failure. No material is lost from the slope, but damage from tensile cracking behind the cliff face can be seen. Particles are considered part of the failure volume if their total displacement is greater than 0.25 meters or their rotation is greater than 10 degrees. For reference, the width of the frame in the figure is 185 meters.

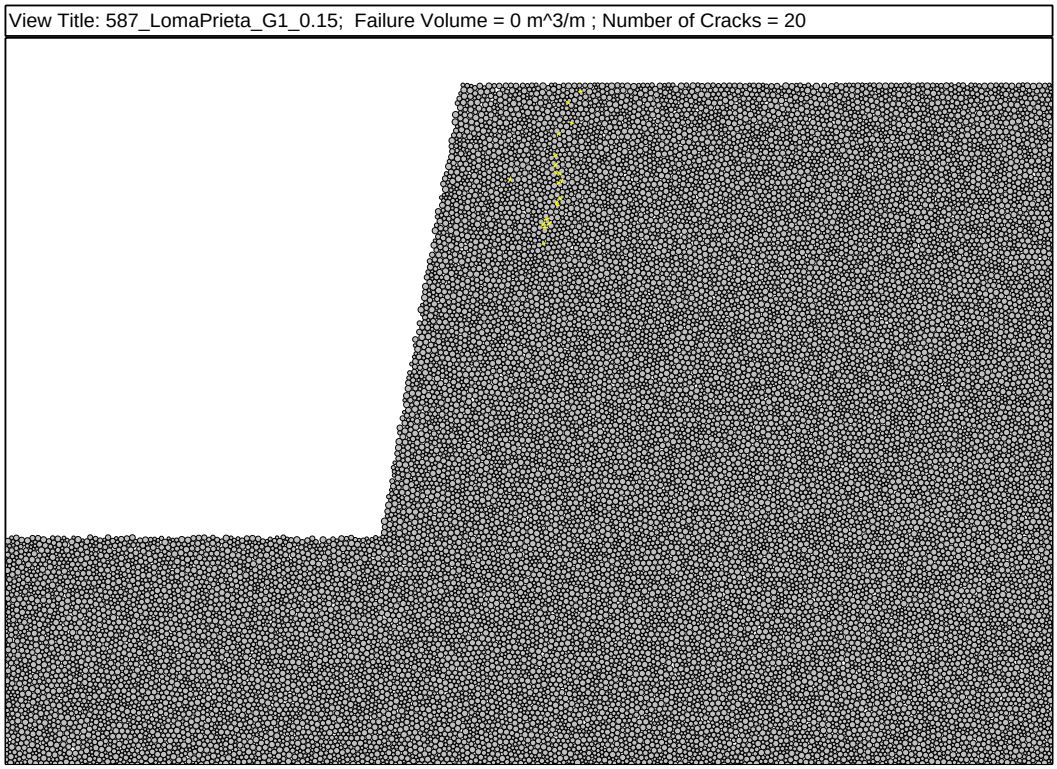

Figure 5.103: Final slope configuration for Model 587 after the Loma Prieta (G1) motion scaled to k_{max} of 0.34 g. The yellow lines indicate the failure of a parallel bond that has broken in tension. Green lines indicate a shear failure. No material is lost from the slope, but damage from tensile cracking behind the cliff face can be seen. Particles are considered part of the failure volume if their total displacement is greater than 0.25 meters or their rotation is greater than 10 degrees. For reference, the width of the frame in the figure is 185 meters.

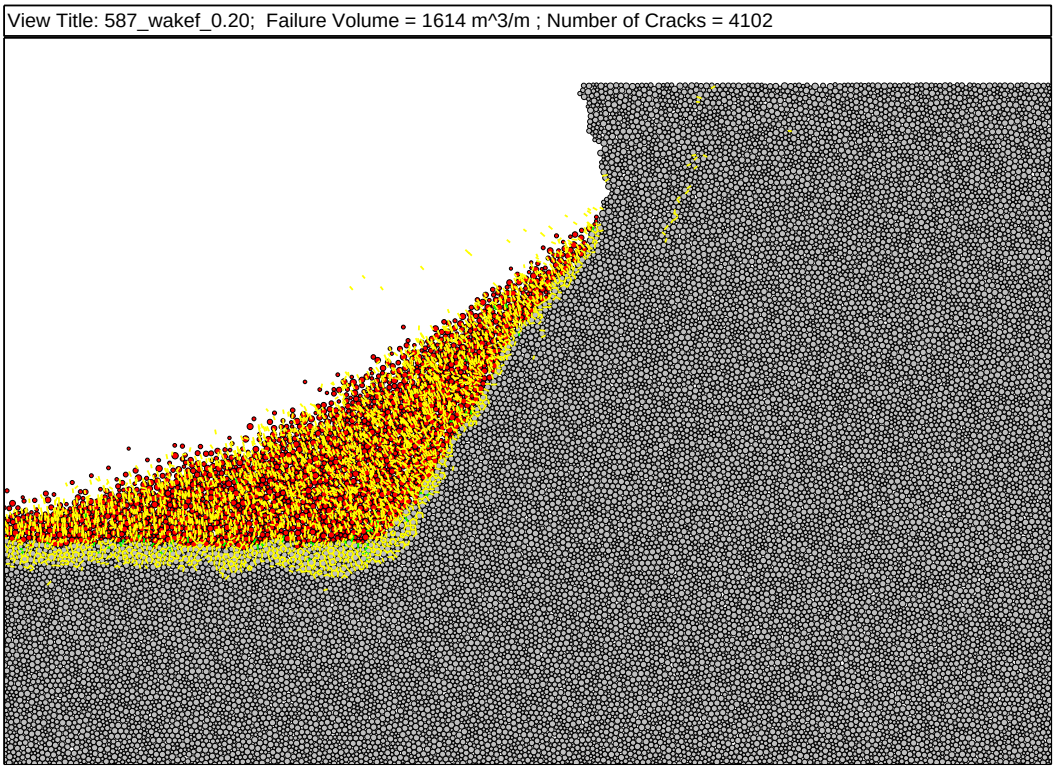

Figure 5.104: Final slope configuration for Model 587 after the Richmond Hill motion scaled to k_{max} of 0.93 g. The yellow lines indicate the failure of a parallel bond that has broken in tension. Green lines indicate a shear failure. Mild damage was induced behind the failure volume. The failure volume is indicated by red particles. Particles are considered part of the failure volume if their total displacement is greater than 0.25 meters or their rotation is greater than 10 degrees. For reference, the width of the frame in the figure is 185 meters.

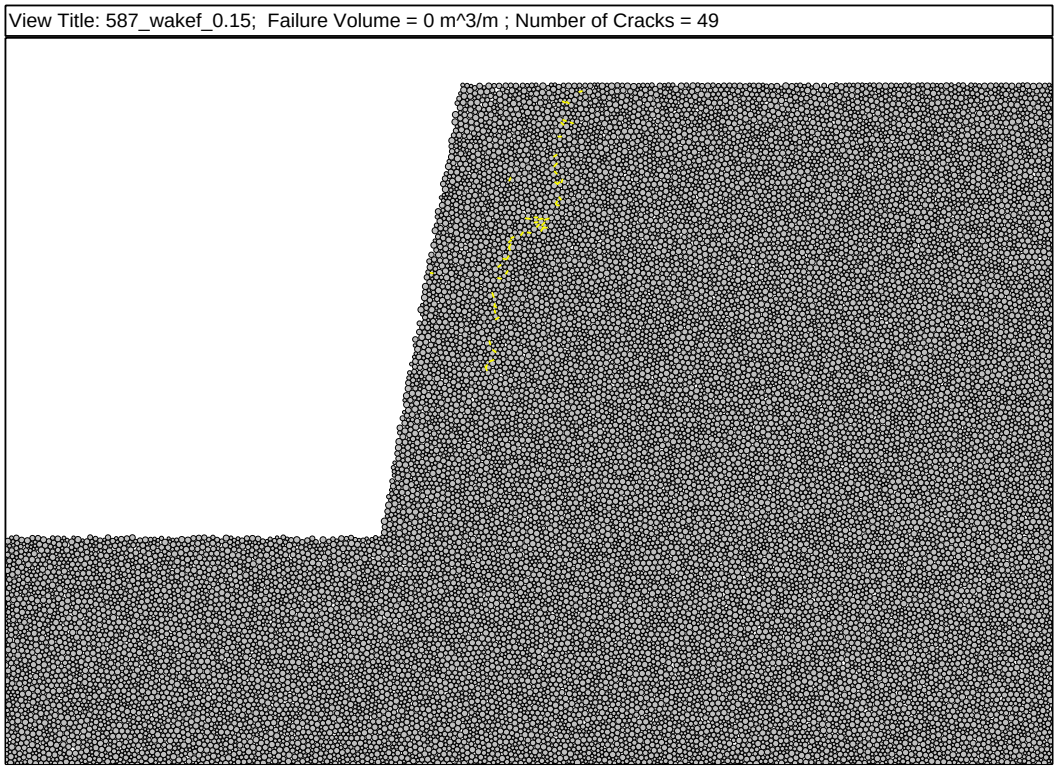

Figure 5.105: Final slope configuration for Model 587 after the Richmond Hill motion scaled to k_{max} of 0.7 g. The yellow lines indicate the failure of a parallel bond that has broken in tension. Green lines indicate a shear failure. No material is lost from the slope, but damage from tensile cracking behind the cliff face can be seen. Particles are considered part of the failure volume if their total displacement is greater than 0.25 meters or their rotation is greater than 10 degrees. For reference, the width of the frame in the figure is 185 meters.

Recorded Ground Motion Results Summary

Figure 5.106 shows a summary of the simulation results in terms of number of cracks developed in Model 587 with recorded ground motion input. Figure 5.107 shows a summary of the simulation results in terms of failure volume developed in Model 587 with recorded ground motion input.

The shape of the two trends is different, unlike the harmonic loading results. The trend in number of cracks with tuning ratio is similar to the Model 591 trend for harmonic loading in that the damage in the model increased for loadings near the second mode frequency. The trend in failure volume with tuning ratio is similar to the Model 587 trend for harmonic loading in that there is a well-defined peak at a tuning ratio in the 0.7 to 0.8 range.

Figure 5.109 shows a summary of the simulation results for different levels of scaling in terms of number of cracks. Figure 5.108 shows a summary of the simulation results for different levels of scaling in terms of failure volume. The decay in number of cracks with k_y/k_{max} is steepest for the Richmond Hill Loading. Very little damage is induced even at $k_y/k_{max} = 0.8$ for the ground motion that caused by far the most damage at the lowest k_y/k_{max} levels. The decay of number of cracks with k_y/k_{max} for the Loma Prieta (G1) and Northridge motions appears to be very reasonable, with both curves having roughly the same shape and the Loma Prieta (G1) curve, which has a tuning ratio of 1.0, plotting slightly above the Northridge curve ($TR = 0.75$). The slight

The change in failure volume with k_y/k_{max} is influenced by the cliff-collapse failure mode. A failure volume of around 1500 to 1700 m^3/m appears to be the approximate threshold for cliff-collapse. The failure volume from the lowest amplitude Northridge motion ($k_y/k_{max} = 0.9$) that produced a non-zero failure volume sits well below this threshold due to the toe collapse with overhanging geometry that was shown in Figure 5.98, however the cracking behind the slope indicates a similar cliff-collapse failure volume can be inferred. Note that for $k_y/k_{max} > 1.0$, no failure volume developed, but rupture of bonds did occur in the slopes. This indicates that k_y/k_{max} may be a good predictor of large runout rock-slope failures, but that strong ground motions below k_y may induce fractures and weaken the slope toward future seismic and static destabilization.

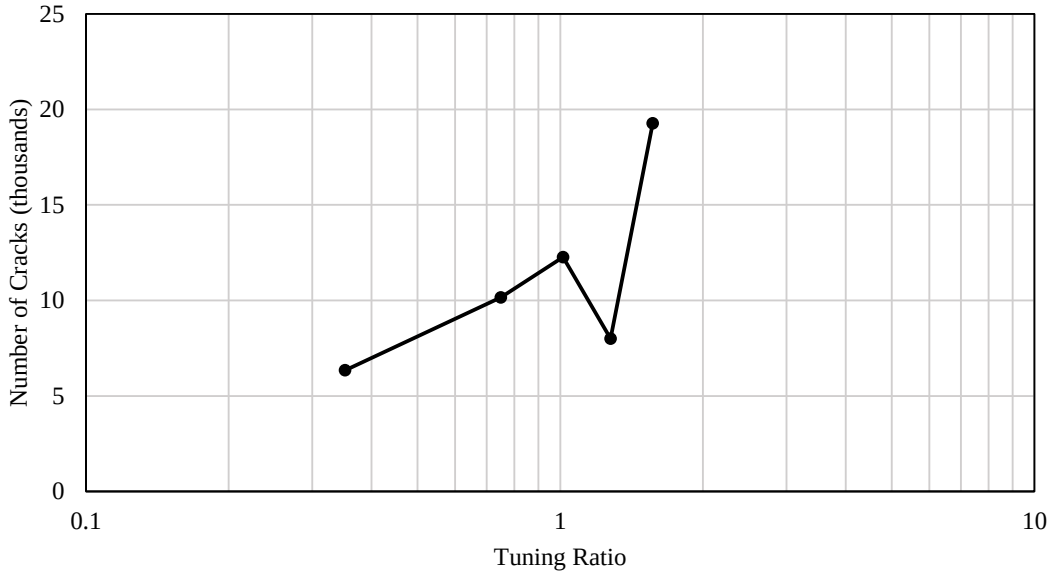

Figure 5.106: Number of cracks developed in Model 587 with recorded ground motion loading with tuning ratio.

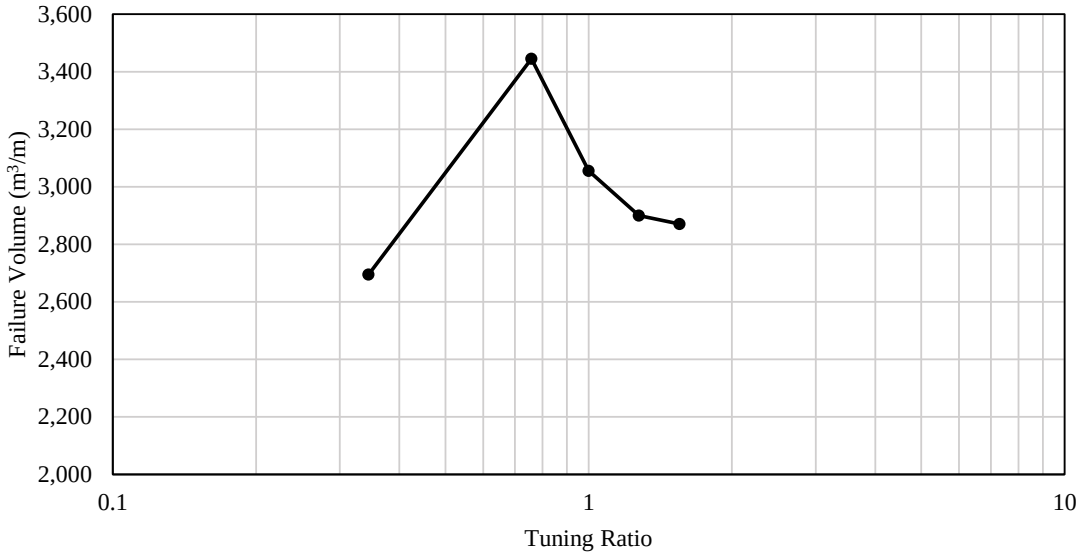

Figure 5.107: Failure volumes developed in Model 587 with recorded ground motion loading with tuning ratio.

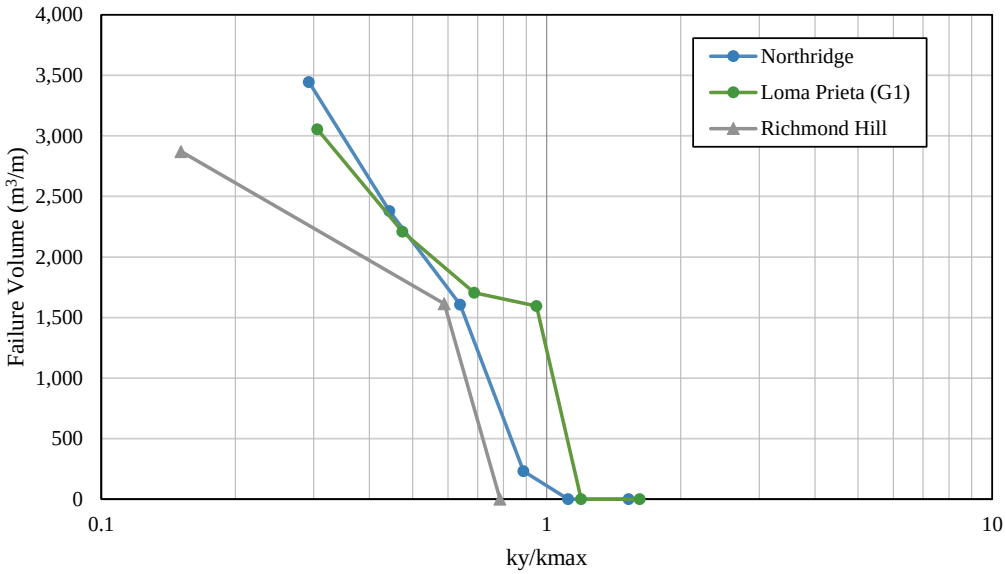

Figure 5.108: Failure volumes developed in Model 587 with different scaled inputs from the Northridge and Loma Prieta (G1) motions.

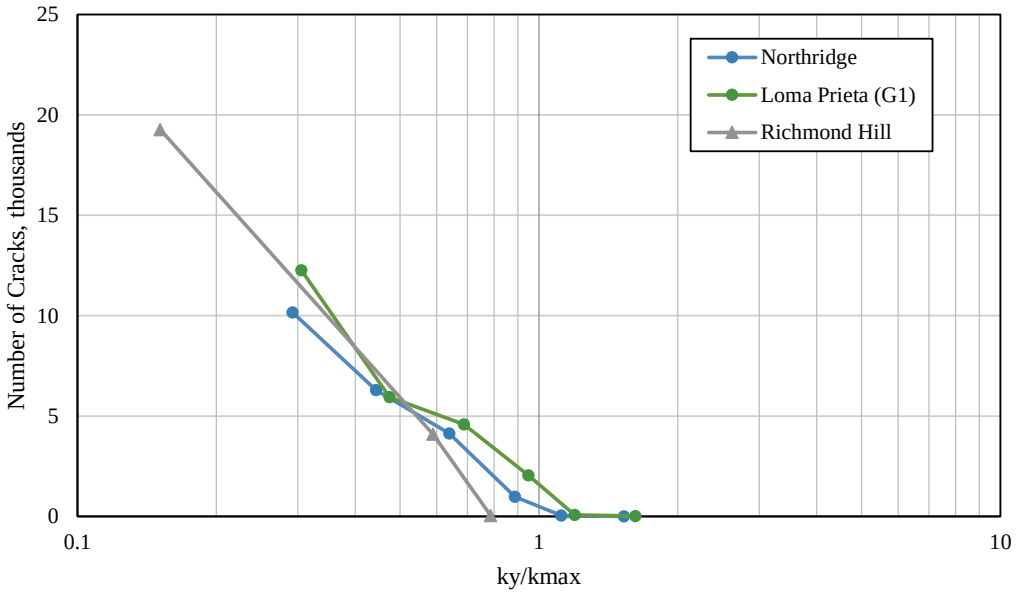

Figure 5.109: Number of cracks developed in Model 587 with different scaled inputs from the Northridge and Loma Prieta (G1) motions.

5.6 Comparison with Newmark Analysis

Newmark (1965) proposed a method for analyzing the behavior of dams and embankments by treating them as rigid masses that slide on inclined planes [23]. Although originally developed for evaluation of dams and embankments, sliding block analysis has become one of the most common methods for assessing the impact of earthquakes on slopes, including rock-slopes [24], [25], [26]. The inputs for a Newmark analysis are the horizontal acceleration yield coefficient, k_y, and an acceleration time history. The method estimates displacements by integrating the parts of the acceleration time history that exceed k_y, then integrating that portion of the signal again to yield the cumulative displacement of the rigid block. A 'coupled' variation of the sliding block analysis considers the dynamic response of the slope. The following explanation of coupled sliding block displacement is taken from the SLAMMER (Seismic LAndslide Movement Modeled using Earthquake Records) user guide [27]:

> Coupled analysis models the interaction of sliding/limited shear stresses on the dynamic response of the sliding mass. In SLAMMER, the dynamic response of the sliding mass is computed using a one-dimensional, modal analysis in the time domain (Rathje and Bray, 1999). The sliding mass is defined by its height, shear-wave velocity, and damping ratio; the shear-wave velocity below the sliding mass is also specified (this can be conservatively taken as rock). The modal analysis has a rigid base, but the effects of a visco-elastic base are modeled through additional damping that is assigned based on the Vs of the base and the Vs of the sliding mass (Lee, 2004). The dynamic response can be modeled as linear elastic or equivalent linear. Coupled analysis is considered the most rigorous and yields the most accurate estimates of displacement for deeper landslides in softer material.

Although sliding block methods yield displacements as output, Bray and Travasarou (2007) suggest that this output is appropriately viewed as an index of seismic performance [28]. A rigid block analysis and coupled analysis were performed on the set of recorded ground

motions (Loma Prieta (G1), Northridge, and Richmond Hill) described in Table 5.10 for BPM simulations. The results of the analysis are summarized in Table 5.11 and shown graphically in Figures 5.110 and 5.113 for rigid and coupled results, respectively. Figures 5.110 and 5.113 show similar trends in behavior of decreasing displacement with increasing k_y/k_{max}, but for values of k_y/k_{max} close to and above 1.0, the rigid block analysis shows no displacement.

Comparison between the BPM results for Model 587 under several strong ground motions and traditional and the sliding block analysis was made to determine whether a simplified analysis had any helpful correlation to the BPM simulations. The BPM simulations with varying k_y/k_{max} ratios for the Loma Prieta, Northridge, and Richmond Hill motions showed good correlations to rigid (Newmark) and coupled sliding block analyses. Plots of the number of cracks in the BPM simulations, and failure volume in the BPM simulations with rigid block displacement are shown in Figures 5.111 and 5.112, respectively. Both comparisons show reasonable trends of increased damage with increasing rigid block displacement, however, the lack of any displacement for relatively low levels of shaking means that no direct comparison can be made for several BPM simulations.

The coupled sliding block analysis provided a better correlation since it accounts for dynamic effects. Figures 5.114 and 5.115 show the number of cracks in the BPM simulations, and failure volume in the BPM simulations with coupled block displacement. As with the rigid block comparison, increased coupled block displacement corresponds to increased BPM damage in terms of both number of cracks and failure volume. In the comparison between sliding block displacements and BPM results, the results of the sliding block analyses are used here as an index value, where increasing magnitudes indicate greater damage to the slope, rather than a literal value of slope displacement. Comparison of the coupled sliding block and BPM results indicate three ranges of coupled displacement with distinct BPM behaviors associated. In the first range, for coupled displacement results from 0.1 to 0.3 inches, cracks developed in the BPM model, but no failure volume developed. This would correspond to a slope that appears to have experienced little to no damage in a seismic event, but has been weakened by damage to the slope internally. One simulation, using the Loma Prieta input motion with $k_y = 0.34$ g, showed no sliding in the coupled displacement

analysis, but did experience some minor cracking, as seen in Figure 5.103. In the second range, for coupled displacements from 0.3 to 2 inches, a fairly constant cliff-collapse failure volume and damage to the slope behind the cliff-collapse was observed in the BPM results. For coupled displacements greater than 2 inches, cliff-collapse with additional failure volumes which increase logarithmically with coupled sliding block displacement is observed.

Note that these threshold values are specific to the Model 587 slope that the displacement results are compared to, but the fundamental behavior described is believed to have applicability for seismic rock-slope stability in general. The influence of slope height, angle, stiffness, and strength on the values of these apparent thresholds is a topic for future research and may provide a path toward a simplified method of analysis of seismically-induced rock-slope failure that accounts for the cliff-collapse phenomenon.

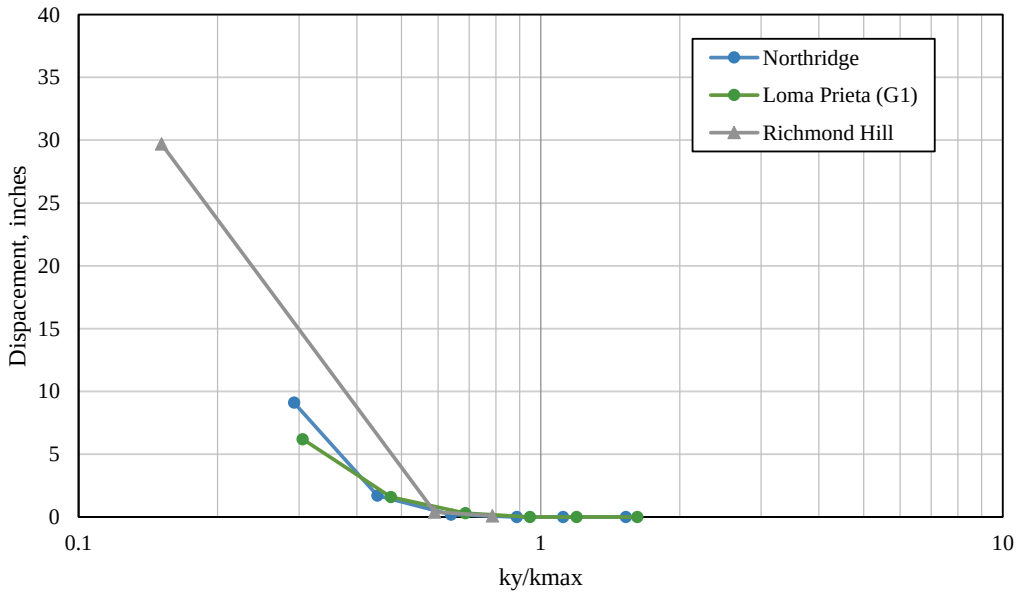

Figure 5.110: Rigid sliding block analysis results with varied k_y/k_{max} for the Northridge, Loma Prieta, and Richmond Hill ground motions.

Table 5.11: Coupled and rigid sliding block analysis results from the on the Northridge, Loma Prieta (G1), and Richmond Hill ground motions.

Event	f**[Hz]**	k_{max}**[g]**	**Rigid Analysis Displacement [in]**	**Coupled Analysis Displacement [in]**
Northridge	2.2	1.88	9.1	19.5
Northridge	2.2	1.24	1.7	5.6
Northridge	2.2	0.86	0.2	1.6
Northridge	2.2	0.62	0	0.3
Northridge	2.2	0.49	0	0.1
Northridge	2.2	0.36	0	0
Loma Prieta (G1)	2.9	1.80	6.2	14.2
Loma Prieta (G1)	2.9	1.16	1.6	5.4
Loma Prieta (G1)	2.9	0.80	0.3	1.8
Loma Prieta (G1)	2.9	0.58	0	0.5
Loma Prieta (G1)	2.9	0.46	0	0.1
Loma Prieta (G1)	2.9	0.34	0	0
Richmond Hill	4.5	3.64	29.7	36
Richmond Hill	4.5	0.93	0.4	0.5
Richmond Hill	4.5	0.70	0.1	0.1

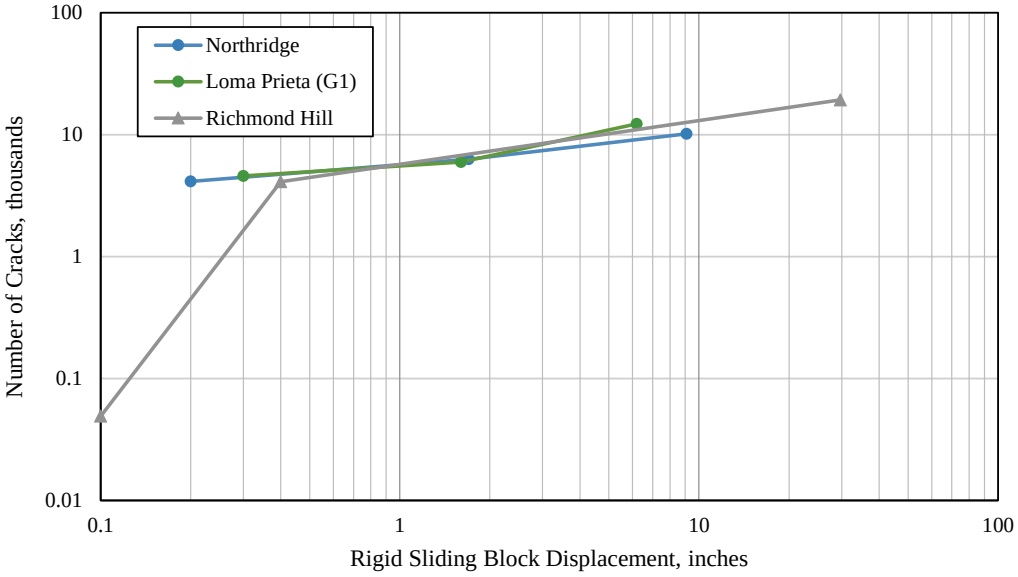

Figure 5.111: Number of cracks in the BPM simulations with rigid sliding block displacement for the Northridge, Loma Prieta, and Richmond Hill ground motions.

Figure 5.112: Failure Volume in the BPM simulations with rigid sliding block displacement for the Northridge, Loma Prieta, and Richmond Hill ground motions.

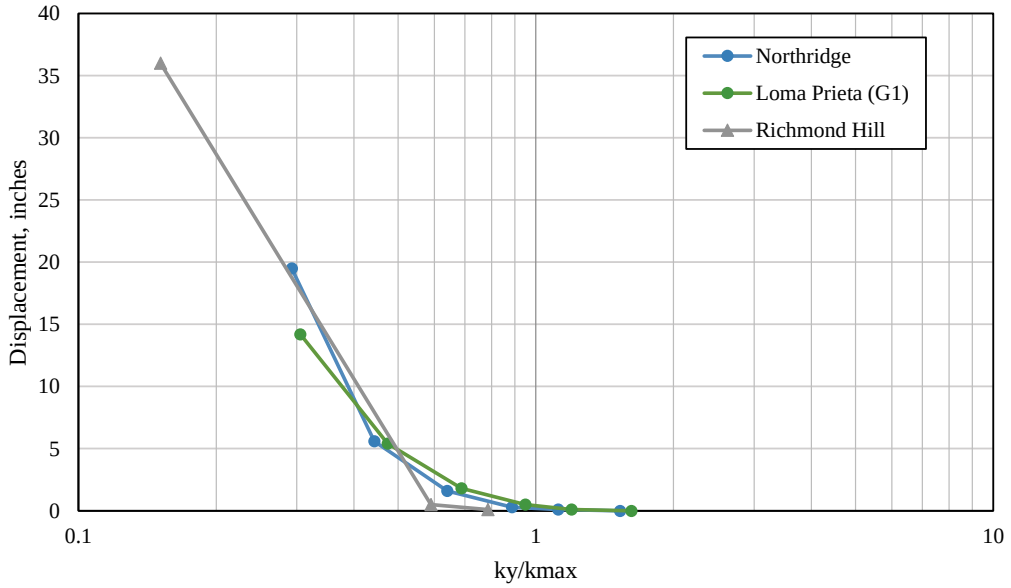

Figure 5.113: Coupled sliding block analysis results with varied k_y/k_{max} for the Northridge, Loma Prieta, and Richmond Hill ground motions.

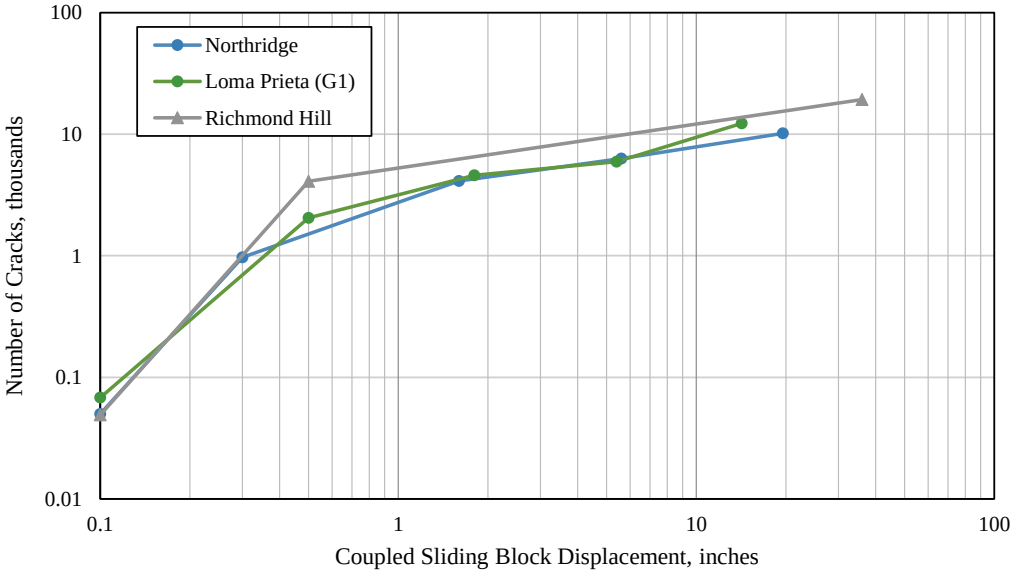

Figure 5.114: Number of cracks in the BPM simulations with coupled sliding block displacement for the Northridge, Loma Prieta, and Richmond Hill ground motions.

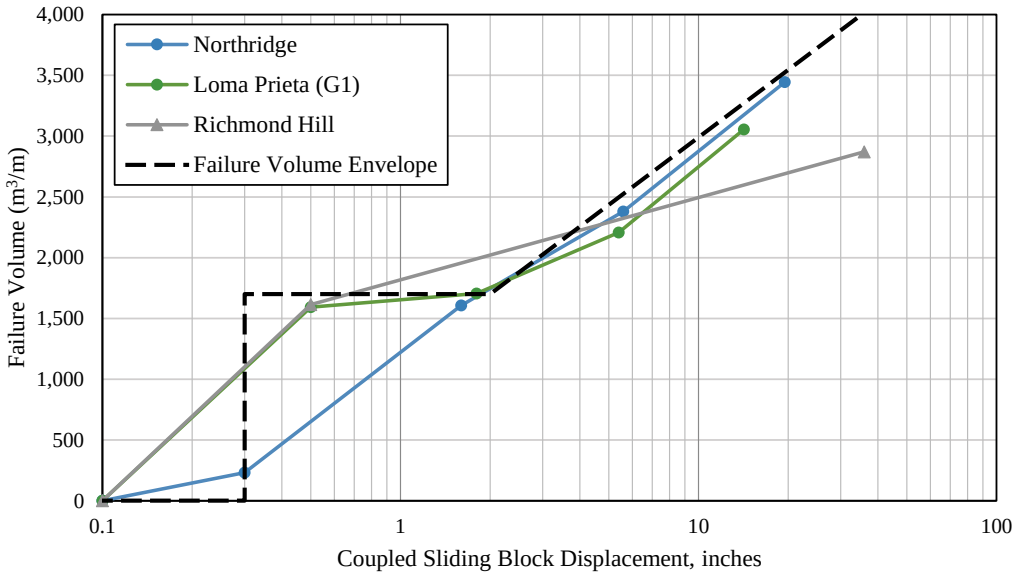

Figure 5.115: Failure Volume in the BPM simulations with coupled sliding block displacement for the Northridge, Loma Prieta, and Richmond Hill ground motions. The dashed line indicates the envelope of BPM failure volume relative the coupled sliding block results. Three distinct ranges of displacement are apparent: 1) 0.3 inches and below, with no failure volume associated, 2) 0.3 to 2 inches, with 1700 m^3/m of failure volume, and 3) 2 inches and greater, were failure volume increases with the log of coupled displacement.

5.7 Summary of Results

The results of the simulations presented above are summarized below:

Static and Pseudostatic Loading Results Summary

Two homogeneous slope models were subjected to static and pseudostatic failure - Model 587 (weaker) and Model 591 (stronger). When subjected to static loading, Models 587 and 591 exhibited shallow cliff-collapse failure and a toe crushing failure with overhanging geometry, respectively. Models 587 and 591 had static factors of safety of 1.9 and 3.5, respectively. Under pseudostatic loading, Models 587 and 591 resulted in shallow cliff-collapse and shallow wedge failure, respectively. Models 587 and 591 had yield accelerations of 0.5 g and 1.15 g, respectively.

Non-damaging Loading Results Summary

Models 587 and 591 have the same stiffness parameters and particle arrangements, so their behavior under non-damaging loading is the same. A series of non-damaging loading cases including a frequency sweep, harmonic motions, and recorded ground motions were applied to the model. The response of the slope to the frequency sweep indicates that the natural frequency of the slope, f_n, (first mode of vibration) is about 2.9 Hz, which is consistent with the empirical formula $f_n = V_s/5H$. The second mode of vibration was observed around 5 Hz.

The response of the model to harmonic inputs of 0.5, 1, 2, 3, and 5 Hz are summarized below:

- The 0.5 Hz motion (tuning ratio of 0.17) induced very little dynamic response in the model and had an apparent amplification factor of 2%. The slope appeared to move as a nearly rigid unit (refer to Figure 5.14). Inspection of the stresses in the model indicated that failure in Model 587, but not in 591 was likely under this loading (Figure 5.16).

- The 1 Hz motion (tuning ratio of 0.34) induced a mild dynamic response in the model

and had an apparent amplification factor of 9%. Some slight relative motion between the crest and toe of the slope was observed (Figure 5.18). Inspection of the stresses and force-chains indicated that Models 587 and 591 are likely to experience crushing failure at the toe of the slope and possibly tensile rupture behind the crest under this loading (Figures 5.19 and 5.20).

- The 2 Hz motion (tuning ratio of 0.7) induced a strong dynamic response in the models and had an apparent amplification factor of 96%. The relative motion between the base and crest of the slope was apparent as the slope oscillated in response to the input motion. The stresses and force-chains indicate that the models are likely to experience crushing failure at the toe of the slope and tensile rupture behind the crest under this loading during downslope movement and that tensile rupture at the toe of the slope is likely during upslope movement (Figures 5.23 and 5.24).

- The 3 Hz motion (tuning ratio of 1.0) induced a very strong dynamic response in the models and had an apparent amplification factor of 224%. The relative motion between the base and crest of the slope was apparent as the slope oscillated in response to the input motion. The stresses and force-chains indicate that the models are likely to experience extensive damage throughout the slope due to both downslope and upslope motion (Figures 5.27 and 5.28).

- The 5 Hz motion (tuning ratio of 1.7) induced a different form of dynamic response in the models than the lower frequency motions. The apparent amplification factor from the 5 Hz loading was 97%. Rather than the rocking motion observed due to 2 and 3 Hz loading, the model's response was dominated by second mode motion where the displacement of the upper half of the slope was out of phase with the lower half of the slope. The resulting stress and force-chain fields indicated that damage was likely to initiate at the crest of the slope, at the midpoint of the slope at the face, and at the base of the slope, but set back about 50 meters from the slope face (Figures 5.31 through 5.38).

The non-damaging simulations of recorded ground motions showed levels of apparent

amplification ranging from 32 to 120%. Figure 5.116 presents a combination of Figures 5.39 and 5.79 to show the amplification relative to the tuning ratio associated with the input motion for harmonic and recorded ground motion loading. The amplification induced by the harmonic and recorded ground motions both show a peak near tuning ratios of one, but the amplification from recorded ground motions is muted compared to the harmonic motions. The amplification from the Richmond Hill motion, associated with a tuning ratio of 1.6, is the maximum for the recorded ground motions, which is a deviation from the trend observed in the harmonic motions. The characteristic frequency of the Richmond Hill motion (4.5 Hz) is near the second mode frequency of the slope (5 Hz) but also has significant frequency content near the first mode of the slope (2.9 Hz) as shown in Figure 5.6. It is suspected that the high level of amplification for this motion is due to combined amplifications associated with the first and second modes of vibration for the slope.

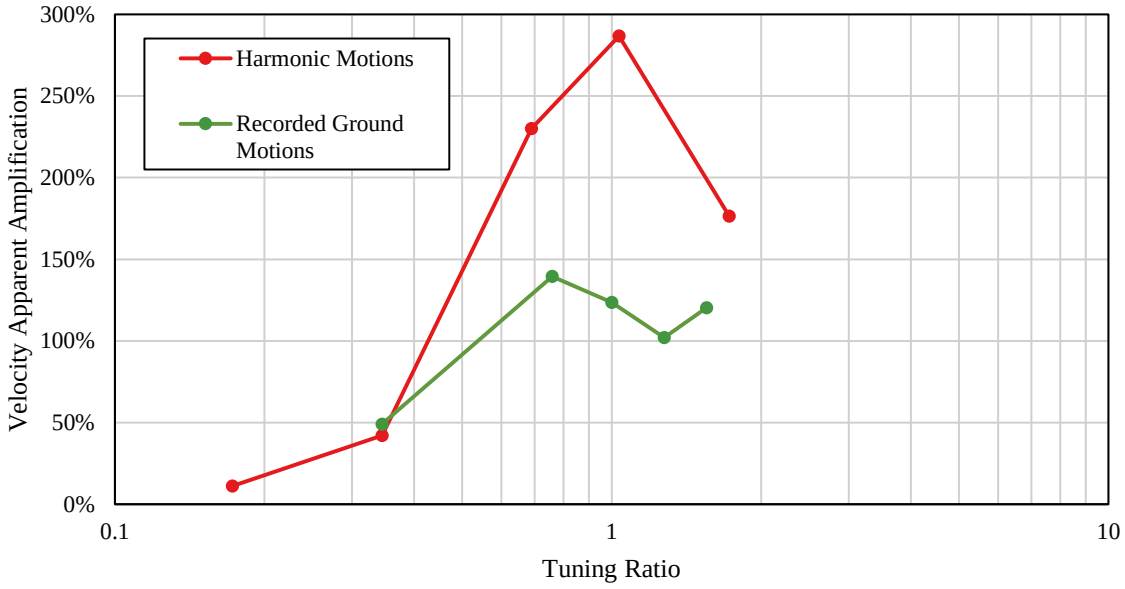

Figure 5.116: Velocity apparent amplification factor AA_v with tuning ratio for Model 587/591 subjected to harmonic and recorded ground motion loading.

Destructive Harmonic Loading Results Summary

Model 587, the weaker of the two homogeneous slopes, experienced a variety of failure mechanisms due to harmonic loading. The observed failure mechanisms included tensile cracking initiating at the face of the slope (usually at the toe) and moving into the slope, crushing at the toe, wedge failures, scattered damage at the crest of the slope, and deep tensile cracking at the base of the slope set back from the toe. At least three failure modes resulted from the mechanisms observed – cliff-collapse, slumping, and toppling. Loading frequencies at and below tuning ratio of 1.0 generally produced the same failure mechanisms and modes in the same order throughout the motion. The most important failure mechanisms associated with these frequencies were crushing at the toe, and tensile rupture leading to wedge failures. Cliff-collapse and toppling were associated with these frequencies, as was slumping, except for in the lowest frequency, lowest acceleration amplitude motion (0.5 Hz). The 5 Hz loading, with a tuning ratio of 1.7, experienced a different set of failure mechanisms – scattered damage at the crest, a deep tensile crack behind the toe of the slope, and crushing at the toe. However, similar failure modes as the rest of the loading cases were observed – cliff-collapse, followed by toppling. Cliff-collapse and toppling were the most commonly observed modes in Model 587, with cliff-collapse being the first mode initiated for all loading cases.

Model 591, the stronger of the two homogeneous slopes, experienced the same failure mechanisms observed in Model 587, but fewer cases of each mechanism were observed due to the increase in strength in the slope. Compared to the Model 587 results, Model 591 had more diverging behavior across loading frequencies in terms of observed failure mechanisms and modes. The most important failure mechanisms associated with the 1, 2, and 3 Hz motions were crushing at the toe, and tensile rupture leading to wedge failures. Cliff-collapse and toppling were associated with these frequencies. Slumping was observed in the 2 Hz loading The 5 Hz loading resulted in a markedly different failure sequence in Model 591. Scattered damage near the slope crest and deep tensile cracking at the base of the slope were the critical failure mechanisms. Failure initiated towards the crest, and progressed deeper into the slope with continued shaking, rather than beginning near the

base and creating a deep failure surface. The 5 Hz loading case on Model 591 was the only dynamic simulation that produced failure, but did not exhibit a cliff-collapse failure mode. Toppling was the most commonly observed failure mode in Model 591, followed by cliff-collapse and slumping. With respect to tuning ratio, both Model 587 and 591 exhibited a peak in level of damage with the 2 Hz motion (tuning ratio of 0.7). In Model 591, the global peak in level of damage was associated with the 5 Hz loading (tuning ratio of 1.7).

In general, for harmonic loading, low-frequency motions, which had lower acceleration amplitudes tended to show less cracking in the model behind the failure surface. The behavior of Model 587 in the 0.5 Hz loading simulation, an of Model 591 in the 1 Hz loading simulation showed little to no damage to the portion of the slope left standing after the dynamic failure event. Both of these simulations involved dynamic loading that was just strong enough to induce failure in the model, according to the non-damaging stress state analysis. In contrast, when subjected to the 1 Hz harmonic motion, the stresses due to dynamic loading were well in excess of the strength of Model 587. The results of the 1 Hz loading on Model 587 showed substantial damage to the portion of the slope left standing after the dynamic failure event, which was observed to be part of an active slump and highly disrupted.

Destructive Recorded Ground Motion Loading Results Summary

Model 587 was subjected to recorded ground motions from Michoacan, Northridge, Loma Prieta, Redcliffs, and Richmond Hill. The observed failure mechanisms due to these loadings scaled to uniform maximum input velocities of 0.78 m/s were relatively uniform compared to the harmonic loading simulations. All recorded ground motions resulted in tensile cracking leading to wedge failure, and crushing at the toe, in that order. The observed failure modes were also more uniform. In all cases, the first observed failure mode is cliff-collapse. Slumping was observed next in the Northridge, Loma Prieta, and Redcliffs simulations. Toppling was the last failure mode observed in all the simulations.

The effects of the tuning ratio of the recorded ground motions on failure volume matched the harmonic loading trend. The effects of tuning ratio of the recorded ground motion on

the number of cracks was more consistent with harmonic results from the simulations of Model 591 because, in addition to a local peak in damage below a tuning ratio of 1.0, the Richmond Hill motion, with a tuning ratio of 1.5 produced the global peak in number of cracks. This global peak for the Richmond Hill motion is also consistent with the trend in apparent amplification in the non-damaging simulations.

Simulations with varying k_y/k_{max} ratios for the Loma Prieta, Northridge, and Richmond Hill motions showed very reasonable trends in damage with levels of shaking. The number of cracks decreased logarithmically with increasing k_y/k_{max}. The failure volume decreased logarithmically with increasing k_y/k_{max} up to k_y/k_{max} ratios between 0.6 and 0.95, where a rapid drop off in failure volume is observed. The drop off in failure volume is associated with the transition in behavior from a simulation with to without an induced cliff-collapse

In general, for recorded ground motions, simulations at all levels of shaking that produced failure resulted in some cracking of the post-shaking slope. For cases with relatively weak loading (k_y/k_{max} close to 1.0) that produced either no failure volumes or very small failure volumes, the initiation of tensile cracking behind the cliff face was observed and appears to create an extremely precarious discontinuity in the slopes (Figure 5.97).

Failure Modes

For the harmonic and recorded ground motion loading cases, cliff-collapse and toppling generally dominated the response of the slopes, with slumping occurring relatively less frequently. The cliff-collapse mode was observed at fairly low levels of shaking (close to k_y/k_max of 1.0) and is preceded by crushing of material at the toe of the slope. Once the material at the toe is compromised, the weight of the slope face looses support, and a cliff-collapse is nearly inevitable, even without continued strong ground motion, indicating that short-duration motions with shaking sufficient to yield material at the toe, are capable of fully developing this failure mode. One simulation of the Northridge earthquake resulted in crushing at the toe and tensile rupture behind the slope face, but did not result in cliff-collapse. It is apparent from the precarious final slope configuration, however, that a cliff-collapse is imminent in this slope's future.

The slumping failure mode, on the other hand, was observed less frequently and was associated with stronger ground shaking. The slumping failure surface also developed more slowly over time with repeated cycles of motion, indicating that relatively longer duration motions may be required to fully develop this mode of failure.

Sliding Block Analysis Results Summary

Both rigid and coupled sliding block analyses provided good correlations with number of cracks and failure volume from the BPM simulations. Coupled analysis, which considers the dynamic response of the slope, generally provided a better correlation involving more points of comparison and clearer trends. The coupled sliding block displacements are used as an index of seismic performance and compared to the behavior of the BPM models. Three distinct behaviors of the BPM models can be associated with three ranges of coupled sliding analysis displacement: (1) cracking, but no failure volume in the BPM models is associated with coupled sliding displacements of up to 0.3 inches, (2) cliff-collapse with no additional failure modes is associated with coupled sliding block displacements between 0.3 and 2 inches, and (3) cliff-collapse with additional failure volumes which increase logarithmically with coupled sliding block displacement is associated with displacements greater than 2 inches.

5.8 Discussion and Implications

The goals of this study were to answer several questions about the role of dynamic response in the development of seismically-induced rock-slope failure for relatively homogeneous, steep rock-slopes:

- From a non-destructive standpoint, how does the level of amplification of the slope change with the frequency content of the input motion?
- What is the nature of the stress field induced in rock-slopes during dynamic loading?
- What failure mechanisms occur in rock-slopes and how are those linked to the dynamic response of the slope?
- Once failure is initiated, how does the failure progress through the slope with continued ground shaking?
- Can simplified methods of analysis, such as sliding block methods, be used to predict the behavior of steep rock-slopes during seismic loading?

The results of this study on homogeneous rock-slopes with the Bonded Particle Model address these questions and provide valuable insight into the fundamental behavior of dynamically loaded steep rock-slopes. This discussion section will describe the applicability and implications of the analyses performed in terms of the overall model behavior, the dynamic response and stresses in the slope, the effects of softening and base-isolation, the importance of failure mechanisms, and the potential for the use of simplified sliding block analyses.

5.8.1 Overall Model Behavior

The overall behavior of the model under dynamic loading appears to be very realistic and replicates several behaviors that are observed in rock-slopes in nature are also observed in the models:

1. Cliff-collapse as a dominant co-seismic failure mode.

2. Rock slumps involving deep-seated, coherent sliding masses.
3. Stepped cliff top profiles from the accumulation of horizontal and vertical displacements toward the slope face.
4. Toppling of discrete blocks from the crest of the slope during strong shaking.
5. The creation of overhanging geometries at the cliff face.
6. Shaking-induced damage to the portion of the rock-slope left standing after seismic loading.

The failure modes observed in the simulations are consistent with observations from Keefer's 1984 survey of landslides caused by earthquakes in several respects. Cliff-collapse and toppling (also called debris avalanche [71], [69] and rock fall [6]) dominate the response of the slopes to dynamic loading. Slumping occurred less frequently and was associated with higher levels of shaking and took more time to fully develop in the model. These results are in agreement with Keefer's conclusions related to the occurrence of similar earthquake-induced landslides. As noted by Keefer (1984) [6]:

> Rock falls... are initiated by the weakest shaking. In particular, these shallow, highly disrupted landslides from steep slopes are probably susceptible to the short-duration, high-frequency shaking characteristic of small earthquakes. Coherent, generally deep-seated landslides are initiated by stronger and probably longer-duration shaking.

The model results are also consistent with some of the observations of rock-slope failures in the Port Hills of New Zealand during the Canterbury Earthquake Sequence (CES), as described in the Chapter 4 and by Massey et al. [17], [16]. Cliff-collapse dominated the response of steep-rock slopes during the CES, and the partial development of deep-seated rock slumps was inferred from the displacement profile at the cliff top. The development of new cracks in the slope, behind the failure surface, as observed in several of the BPM results was also observed and documented in the Port Hills following the CES.

That cliff-collapse dominates the co-seismic response of the model is particularly significant for three reasons: 1) as discussed above, this is the dominant seismically-induced landslide failure mode observed in nature, 2) the consequences of cliff-collapse are severe [6], and 3) the cliff-collapse mode is not well predicted or modeled using traditional techniques for assessing seismically-induced rock-slope failure [16]. The performance of the model demonstrates that BPM is a powerful and important tool for the assessment of the seismic performance of rock-slopes.

5.8.2 Model Response to Non-Damaging Dynamic Loading

The dynamic response of the model is shown to be a strongly influenced by the tuning ratio. Peaks in amplification levels for harmonic and recorded ground motions occur at loading frequencies near the slope natural frequency. Strong amplification was also observed for the Richmond Hill recorded ground motion, which has a characteristic frequency (4.5 Hz) close to the frequency associated with the second mode of the slope (5 Hz). This indicates that the effects of the second mode of vibration may be an important factor in the behavior of rock-slopes in dynamic loading.

The stresses in the model induced by dynamic loading under non-damaging conditions provide a good predictive tool for identifying the nature and location of the initial failure mechanism. Each observed primary failure mechanism (tensile cracking initiating at the slope face, crushing and damage at the toe, wedge failure from tensile rupture, tensile damage at the crest, and deep tensile cracking) was indicated by the force-chains and stress fields evaluated under non-damaging conditions. This has implications for future research and design because a strong difference in the accumulation of damage during shaking was observed for simulations where initial failure mechanisms differed. If an elastic model can be used to predict initial failure mechanisms, and initial failure mechanisms tend to dictate the behavior of the slope, simple elastic simulations using a finite element model may become a valuable tool for assessing the potential for seismically-induced rock-slope failure.

5.8.3 Effects of Dynamics on Rock-Slope Failure Events

Peaks in damage with tuning ratio for Models 587 and 591 occurred with the 2 Hz loading (i.e., tuning ratio of 0.7). This result is striking since the 3 Hz motion has both higher peak acceleration and a tuning ratio of 1.0. The 2 Hz motion, however, has higher peak displacement. This behavior of the slope may be due to either the softening of the slope as damage accrues in the model over time, which shifts its natural frequency closer to 2 Hz, or it may indicate that once failure surfaces form, displacements have a greater impact on the slope than accelerations. Provided that the acceleration of a motion is sufficient to induce sliding on the newly formed failure surfaces, lower frequency motions may induce more displacements in the slope mass, which becomes disrupted with accumulated displacement. This is attributed to both softening of the slope and the influence of peak ground displacement producing the effect that the maximum damage occurs at tuning ratios of about 0.7.

The induced failure in the models resulted in a marked change in dynamic response. Figure 5.117 shows the dynamic response of Model 587 to the 1 Hz loading under non-damaging and damaging loading. The sharp drop off in dynamic response around 1 second for monitored points at the slope face corresponds a cliff-collapse failure. A softening of the slope, as well as base-isolation, is apparent in the gradual change in dynamic response for particles monitored deeper into the slope (about H/1.2 from the slope face). These points have reduced velocity amplitudes and become out of phase with the rest of the slope. The change in dynamic response for these points corresponds to the development of a slumping failure.

One of the effects of base-isolation in the slopes was the reduction in damage accumulation after the development of a deep-seated failure surface. The rate of damage accumulation slows down substantially after an initial period of rapid increase in number of cracks for models were base isolation occurred. In contrast, when Model 591 was subjected to the 5 Hz loading and failure initiated towards the crest and progressed deeper into the slope with continued shaking, the rate of damage accumulation was more gradual to begin with and begins to slow down only after a significant number of cracks have developed. Figure 5.118

illustrates these two distinct damage accumulation patterns by comparing the number of cracks with time in Model 591 subjected to a 2 Hz loading and a 5 Hz loading. The initial failure mechanisms in Model 591 due to the 2 Hz and 5 Hz motions are observed to be different and are the reason behind the base-isolation observed in the 2 Hz simulation and not observed in the 5 Hz simulation. Since the initial failure mechanism can dictate the evolution of damage due to seismic loading, the identification of the possible initial failure mechanisms is a critical step in predicting seismic rock-slope performance.

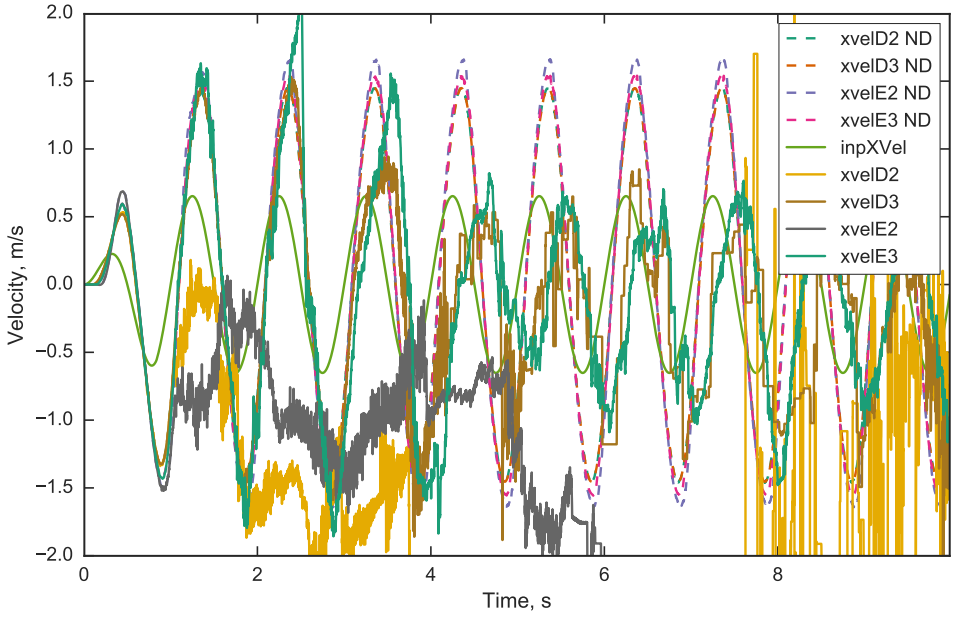

Figure 5.117: Dynamic response of Model 587 to the 1 Hz loading under non-damaging and damaging loading. The non-damaging results are shown in dashed lines and have the identifier 'ND' in the legend. Points with 'E', and 'D'in the labels correspond to the elevations of the crest and mid-slope, respectively. Points with '2' and '3' in the labels correspond to points at the slope face and set back 65 meters from the slope face, respectively. Refer to Figure 5.12 for the legend relating the identifiers to the position within the model.

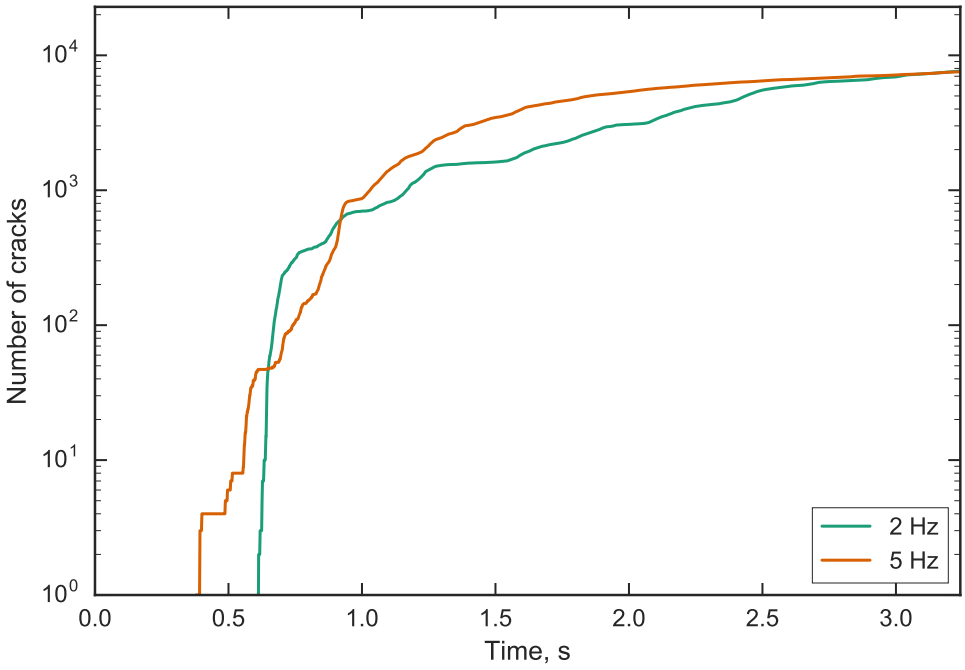

Figure 5.118: Number of cracks with time for the 2 Hz and 5 Hz loading of Model 591. In the 2 Hz loading, the rate of damage accumulation drops off after an initial rapid increase in number of cracks. In the 5 Hz loading, the rate of damage accumulation is more gradual to begin with and begins to slow down only after a significant number of cracks have developed.

5.8.4 Stability of Rock-Slopes After Seismic Loading

The damage in the portion of the slope left standing after the dynamic failure event provides an indication of the weakening of the slope due to dynamic loading and whether it may be predisposed to future failure under seismic or static conditions. In this area, the results from the harmonic and recorded ground motion simulations deviate. Harmonic motions with low acceleration amplitudes, but were strong enough to induce cliff-collapse, produced little to no damage to the portion of the slope left standing after the dynamic failure event. This would indicate a post-shaking stability equal to or greater than the pre-shaking stability. The results from the recorded ground motion simulations are considered to be more reliable than the harmonic ground motion simulations, however, because they contain more realistic broadband frequency content. Results from the recorded ground motion simulations, however, indicate that the post-shaking stability of rock-slopes subjected to strong shaking may be significantly lower than their pre-shaking condition. This result is supported by field observations and is considered to represent a more realistic and more conservative understanding of the stability of rock-slopes after seismic loading.

5.8.5 Applicability of Sliding Block Methods

Coupled sliding block analysis shows promise as a potential tool for evaluating the seismic performance of rock-slopes if the co-seismic displacement index is calibrated to identify more complex dynamic rock-slope behaviors. Rigid sliding block analysis does not appear to be appropriate for this use since it does not incorporate dynamic effects and did not provide enough points of comparison for the BPM simulations.

Three distinct behaviors in the BPM models (1 –cracking, but no cliff-collapse, 2 – cliff-collapse, and 3 –cliff-collapse plus additional failures) were found to correlate well with coupled sliding block displacements for three recorded ground motions. The associated range of coupled sliding block displacements (1 –up to 0.3 inches, 2 –0.3 to 2 inches, and 3 –2 inches and greater, respectively) are specific to the Model 587 BPM results, but the fundamental behavior described is believed to have applicability for seismic rock-slope stability in general. The influence of slope height, angle, stiffness, and strength on the values of these apparent

sliding block displacement correlations is a topic for future research. This may provide a path toward a simplified method of analysis of seismically-induced rock-slope failure that accounts for the cliff-collapse phenomenon.

5.9 Conclusions

The Bonded Particle Model is a powerful tool for assessing the seismic behavior and performance of rock slopes. The behavior of the developed model shows strong agreement with numerous case-studies presented in the literature. Cliff-collapse, rock toppling, and rock slumping modes are all captured in the simulations, with cliff-collapse being the most prevalent and requiring the lowest levels of shaking to initiate. This study of steep, homogeneous rock-slopes provides several insights into the fundamental mechanics of rock-slopes under seismic loading.

The dynamic response of the slope dictates the development of stresses that result in the initiation of fracturing and eventual global slope failure. Where fracturing initiates in the slope can dictate the evolution of failure throughout a strong shaking event –in some cases providing base-isolation through the development of a deep-seated failure surface, which insulates the slope from dynamic input, and in other cases allowing significant dynamic loading to continue to impact the slope and produce continually increasing damage with time.

The tuning ratio is an important factor in the magnitude of the impact of seismically-induced rock-slope failure. Due to the softening effects of damage accumulation, and higher peak displacements and velocities associated with lower frequency motions, loading frequencies slightly below the natural frequency have the potential to induce the greatest failure volumes. The fracturing induced by dynamic loading not only impacts the mass associated with the failure volume but also affects the remaining portion of the slope left standing after a seismic event. Fracturing in the post-shaking slope, particularly when associated with the partial development of failure mode, can produce extremely precarious slope configurations that may not have any external manifestations.

Several of the key behaviors observed in the model can be associated with coupled sliding block displacements. Because sliding block analysis is much simpler than a fully

dynamic BPM analysis, a link between these two methods would be a valuable tool for the future of seismic rock-slope stability analysis. Good correlation between these methods has been demonstrated here, however, continued research is needed to account for numerous additional variables that are known to impact slope stability and dynamics and must be incorporated into any reliable link between the two methods.

Chapter 6

THE EFFECTS OF DISCONTINUITIES ON DYNAMIC ROCK-SLOPE STABILITY

6.1 Introduction

This chapter presents a parametric study of the effects of discontinuities on the dynamic behavior and performance of rock-slopes. Discontinuities in rock come from a variety of sources, including bedding planes, foliations, fractures, joints, and faults [85], [86]. The effect of discontinuities on rock-slope stability varies with the nature and extent of discontinuities, overall slope geometry, and intact rock mass engineering properties [11], [12]. Stead and Wolter (2015) provide a summary of the importance of structural geology on rock-slope stability. They present several case-studies providing examples of how discontinuities often control rock-slope stability, failure mechanisms, and failure modes [10]. These effects have been well-studied under static conditions, and, to a lesser extent, pseudostatic conditions [10, 12, 87, 88].

In Chapter 4, discontinuities were shown to play an important role in the nature of dynamic rock-slope failure in the Port Hills case-studies in terms of the extent of failure, the sensitivity of the slope to tuning ratio, and the levels of damage within the portion of the rock-slope left standing after a seismic event. However, the discontinuities used in those models were mostly random, not systematically varied, and their influence was somewhat obscured by additional structural features including geologic layers and weathering. In Chapter 5, the effects of dynamic response on a homogeneous rock-slope with no discontinuities was assessed. In this chapter, the dynamic failure of Bonded Particle Model (BPM) rock-slope models with discontinuities of varying inclination, spacing, and persistence will be presented.

The aim of the parametric study is to provide insight in how discontinuities influence the dynamic response and dynamic stability of rock-slopes. Specific questions that will be

addressed include:

- How does discontinuity persistence, spacing, and orientation affect the natural frequency of rock-slopes?
- What effect, if any, do discontinuities play in the frequency-dependency of the initiation of failure in rock-slopes? Are the frequency-related effects on homogeneous rock-slopes observed in rock-slopes with pre-existing discontinuities?
- Do fracturing rock-slopes experience failure by initiation of new fractures, or by coalescence of existing joints?
- Do the observed fracturing patterns due to dynamic loading match the patterns expected from previous research on static rock-slope fracture or do new fracture patterns develop due to dynamic stresses?

The following sections will present the rock-slope models developed for the parametric study, the loading conditions the slopes were subjected to, the behavior of the slopes under loading, and provide a discussion of the results and their implications.

6.2 Rock-Slope Models

The rock-slope models developed for the parametric study fall into three main categories: 1) without discontinuities (one slope), 2) with persistent discontinuities (23 slopes), and 3) with non-persistent discontinuities (18 slopes). Slopes with persistent discontinuities are those whose discontinuities terminate either at the surface, or within the model, but beyond the "no crack boundary". The "no crack boundary" is a portion of the model offset 10 meters from the lateral boundaries and 12 meters from the base where the BPM bonds are not allowed to break. Illustrations of the "no crack boundary" are provided in Sections 6.2.2 through 6.2.4. All slopes have a face angle of 80 degrees, and a height of 20 meters.

Table 6.1 shows the microproperties of the parametric study models.. The average particle radius is 0.15 meters and is uniformly distributed over plus and minus 50 percent of the average. A local damping ratio of 2 percent was used in the simulations.

The resulting macroproperties of the models are shown in Table 6.2

Table 6.1: BPM microproperties for parametric study BPM models. Property symbols: $k_{n(bond)}$ is the normal stiffness of the bond, N_{bond} is the normal (tensile) strength of the bond, $\rho_{particle}$ is the particle density, and ϕ is the interparticle and smooth joint friction angle.

$k_{n(bond)}$ [N/m^2]	N_{bond} [N/m^2]	$\rho_{particle}$ [kg/m^3]	ϕ [degrees]
1.9E+10	5.0E+04	2800	30

Table 6.2: Rock mass engineering properties for parametric study BPM models. Rock property symbols: σ_c is unconfined compressive strength, σ_t is tensite strength, E is the elastic modulus, V_s is the shear wave velocity, ρ is the density, and ϕ is the internal friction angle and the joint friction angle.

σ_c[MPa]	σ_t[MPa]	E [GPa]	Vs [m/s]	ρ [kg/m^3]	ϕ [degrees]
50.0	5.0	6.5	1500	2200	30

The next sections will present the specific geometries of rock-slope models. Note that a very wide range of geometric conditions is considered, but that intact rock mass properties remain the same across all models. The purpose of using a single rock mass across all slopes is to limit the number of variables and focus the study exclusively on the role of discontinuity geometry. A side-effect of this approach is that the strength and stiffness of models in the study varies dramatically. The relatively high strength of some of the models is not unrealistic, as high-strength, intact rock masses do exist in nature. However, the dynamic inputs required to initiate failure in these models be unreasonable. Similarly, to bound the natural frequencies of the models in this study, the frequencies of input motions (at least at the levels of shaking used) can exceed reasonable values. These aspects of the parametric study, which stem from the breadth of parameters evaluated, are acknowledged. And because the goal of the parametric study is to provide comparisons between different rock-slopes under different conditions, these extreme values are still considered acceptable and will provide valuable and meaningful results.

6.2.1 Discontinuities in the Models

The models presented in this chapter contain a variety of discontinuity configurations. As mentioned above, discontinuities in rock can come from a variety of sources. Authors frequently use the terms discontinuity, joint, flaw, and fracture interchangeably to describe any discontinuity in a rock mass [89], [90], [91], [29]. In this chapter, the terms discontinuity and joint will be used interchangeably to mean any pre-existing discontinuity in the slope models. New discontinuities in the model that develop during loading will be called cracks.

Multiple terms can also be used to describe the geometry of a joint set. These terms usually include descriptions of joint orientation, spacing, length, rock bridge length, and joint step angles [89], [92], [90]. Figure 6.1 from [89] shows the a set of discontinuity parameters that were adopted for the models in this study They include orientation (β), spacing (d), joint length (L_j), rock bridge length (L_r), and joint step angle (γ). All of these parameters, except β, are used to describe the joint sets presented in the following sections. Instead of orientation relative to a principal stress direction, the dip of the joint – the angle of the joint inclination measured clockwise from horizontal – is used to describe orientation.

The joint parameters above describe the amount of jointing in the rock mass using spacing, joint length, and rock bridge length. It is useful to combine these terms to describe the amount of jointing using a single parameter. Dershowitz and Herda [91] and Mauldon and Dershowitz [93] present several several possible terms to use the amount of jointing in a rock mass (they use the term fracture to describe discontinuities of all kinds): fracture spacing, fracture intensity, fracture porosity, fracture frequency, fracture persistence, dimensionless fracture density, and degree of development. Dershowitz and Mauldon proposed using the term abundance as an umbrella term for the amount of fracturing in a rock mass and the terms density, intensity, and porosity to describe the fracture abundance in 1, 2, and 3 dimensions, respectively. The 'PXY' system follows this proposed terminology [94]. In the PXY system, the 'X' term denotes the dimension of the sampling space, and the 'Y' term denotes the dimension of the sample measurement. The sampling space can have either one dimension (a line), two dimensions (an area), or three dimensions (a volume). The sample measurement can have the same dimensions and also includes a zero dimension option for

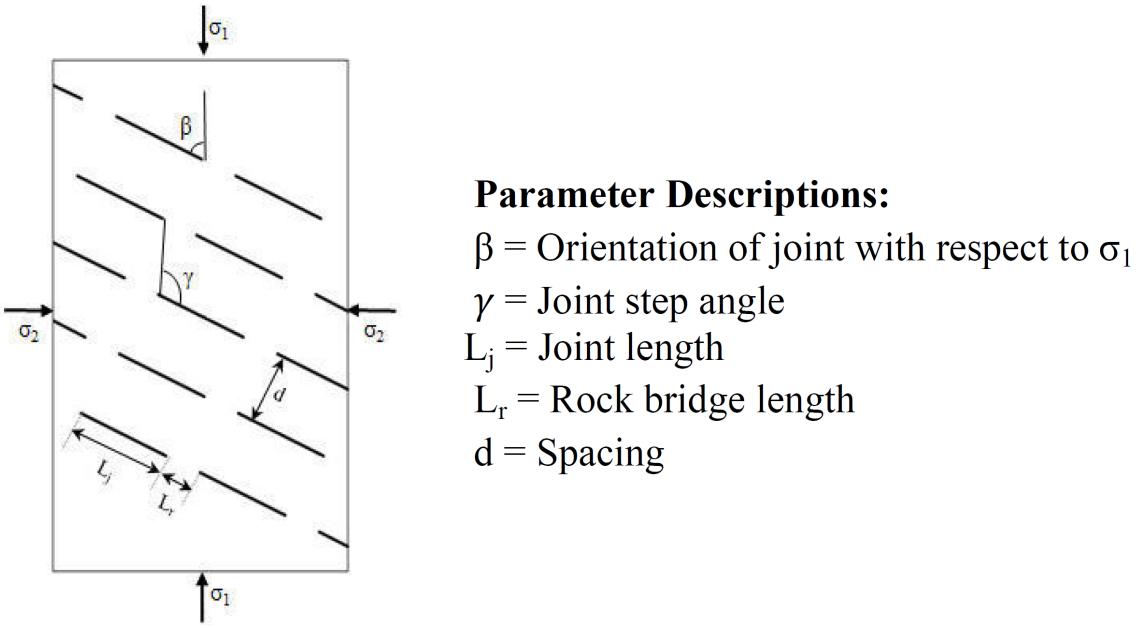

Figure 6.1: Joint geometry parameters from [89].

a count of fractures. For example, P01 would describe the number of fractures encountered along a line. P21, which is the intensity measure used in this study, described the length of fractures present in a given area. Figure 6.2 from [94] presents the PXY scheme for description of fracture abundance.

Using the joint set parameters shown in Figure 6.1, the P21 intensity can be described by:

$$P21 = \frac{L_j}{L_j + L_{rb}} * \frac{1}{d} \tag{6.1}$$

		Dimension of Measurement				
		0	1	2	3	
Dimension of Sample	1	P10 *No of fractures per unit length of borehole*	P11 *Length of fractures per unit length*			*Linear Measures*
	2	P20 *No of fractures per unit area*	P21 *Length of fractures per unit area*	*P22 Area of fractures per area*		*Areal Measures*
	3	P30 *No of fractures per unit volume*		P32 *Area of fractures per unit volume*	P33 *Volume of fractures per unit volume*	*Volumetric Measures*
		Density		*Intensity*	*Porosity*	

Figure 6.2: Fracture abundance measures from [94].

6.2.2 Homogeneous Slope

The homogeneous (without discontinuities) slope as described above is shown in Figure 6.3. The model identification designation for the homogeneous slope is '600'. Slope names correspond to the sequential steps of model development and are essentially arbitrary. This homogeneous slope is very strong and stiff relative to the jointed models, and, as mentioned above, the levels of loading required to initiate failure in the slope may not be realistic. It provides a useful point of reference, however, for change in natural frequency and yield acceleration due to the joints introduced in the rest of the parametric models.

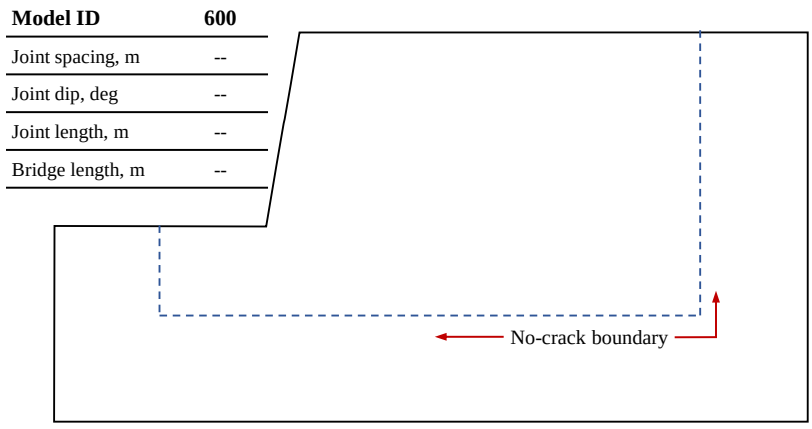

Figure 6.3: Slope geometry for the Model 600 slope. The slope has no pre-existing discontinuities. For reference, the slope height is 20 meters, and the slope face angle is 80 degrees.

6.2.3 Slopes with Persistent Discontinuities

The slopes with persistent discontinuities have the ID numbers 601 – 611, and 613 – 624. Within this set of slopes, discontinuity dips were varied from 20 degrees from horizontal to 110 degrees from horizontal for slopes with discontinuity spacing of 3 meters. For slopes with discontinuity dips of 60 and 70 degrees from horizontal, three additional joint spacings, 1, 4, and 6 meters, were developed. For slopes with discontinuity dips of 80 degrees from horizontal, seven additional joint spacings, 1, 3, 4, 5, 6, 7, and 8 meters, were developed. Table 6.3 summarizes the geometries of slopes with persistent discontinuities used in this study.

The primary failure mechanisms associated with rock-slopes with persistent discontinuities that dip into the slope are flexural toppling and shearing across the joints (cross-joint shear) [9]. Slopes with non-persistent joints that dip out of the slope at a steeper angle than the slope face can fail in sliding, without any fracture of intact rock material, and are outside of the scope of this study. Slopes with joints between vertical inclinations and inclinations can fail in buckling. These mechanisms are illustrated in Figure 6.4.

The susceptibility of rock-slopes to flexural toppling under static conditions has been well-studied and the influence of joint dip and spacing has been demonstrated by several researchers [95], [96], [97], [50] , [98], [99], [100]. Joint dip has multiple levels of influence on flexural toppling.

One of the conditions for flexural toppling is slip between rock columns [50]. Goodman and Bray (1976) proposed the following equation to expain the kinematic conditions necessary for the initiation of slip between rock columns on joints:

$$\alpha \geq 90^o + \phi_j - \beta \tag{6.2}$$

where α is the angle of the slope face, ϕ_j is the joint interface friction angle, and β is the dip [95]. Given that the slopes in this parametric study have a constant α of 80 degrees and ϕ_j of 30 degrees, Equation 6.2 can be used to determine the minimum dip needed for susceptibility to flexural toppling ($\beta_{min,k}$) based purely on kinematics and friction:

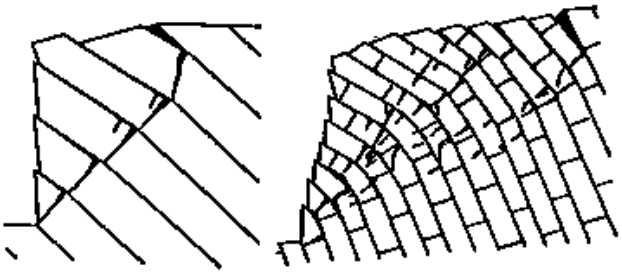

(a) flexural toppling

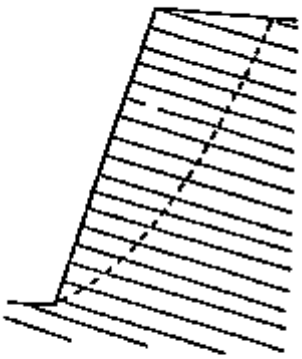

(b) Cross-joint shear

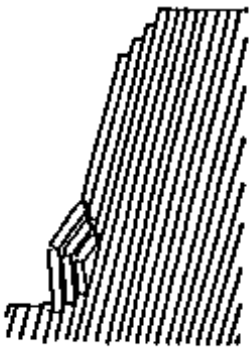

(c) Buckling

Figure 6.4: Common rock-slope failure mechanisms for slopes with persistent discontinuities (after [9]).

$$\beta_{min,k} = 90^o + 30^o - 80^o = 40^o \tag{6.3}$$

Where flexural toppling is kinematically possible, the slopes susceptibility to this failure mechanism is influenced by the joint friction, dip, face angle, slope height, and rock tensile strength. It is worth noting that the kinematic condition in Equation 6.2 is based on static conditions, where the weight of each column points directly down. Under pseudostatic conditions, where weight vectors have horizontal components, the criterion would require an adjustment for this change. Relative to static conditions, the weight vector would have higher magnitude and be rotated clockwise. Some corresponding clockwise rotation in the minimum dip for flexural slip can be expected. However, under dynamic conditions, which is the focus of this study, the flexural slip limitation is not necessarily applicable, because joints have the ability to open and close during cyclic loading.

Adhikari et al. proposed design charts for evaluating the susceptibility of rock-slopes to flexural toppling. Figure 6.5 shows an example of a design chart for slopes with joint friction angles of 30 degrees. In the figure, H_{cr} is a dimensionless parameter that describes the slope's susceptibility to flexural toppling failure:

$$H_{cr} = \frac{\gamma H^2}{(\sigma_t / F.S.)d} \tag{6.4}$$

where γ is the unit weight, H is the slope height, σ_t is the tensile strength of the rock, $F.S.$ is the factor of safety, and d is the joint spacing [50]. Lower values of H_{cr} are more critical than higher values. It is apparent from the chart that joint dips of 70 to 80 degrees are most critical for slopes with face angles of 80 degrees and joint friction angles of 30 degrees under static conditions. Under static conditions, slopes with joint dips of 90 degrees or greater are considered infinitely stable (against flexural toppling) because there is no component of the column weight normal to the joints to induce flexure. Under pseudostatic and dynamic loading, this is not the case, so a shift of the susceptibility for relative joint dips is anticipated.

Outside of the ranges of susceptibility for flexural toppling, persistently-jointed rock-slopes can fail in other mechanisms, like cross-joint shearing. Adhikary et al. acknowledge

this and recommend that other slope failure mechanisms be considered when the resistance of a slope to flexural toppling is high.

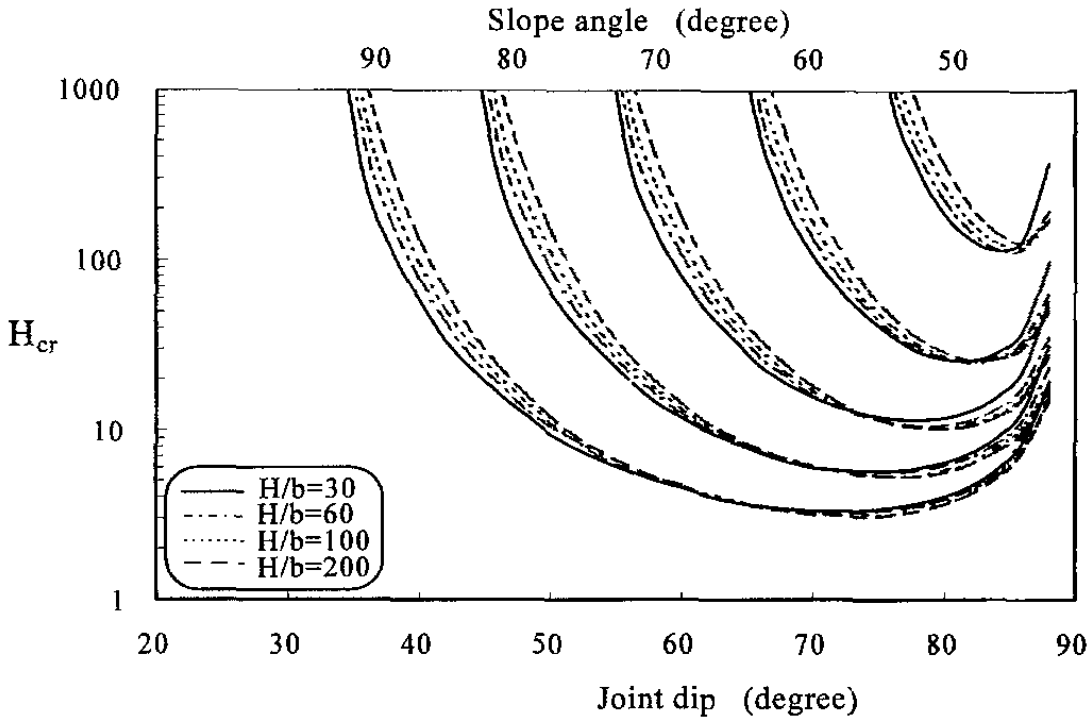

Figure 6.5: Design chart for evaluating the dimensionless parameter H_{cr} for assessing the flexural toppling stability of rock-slopes with joint friction angles of 30 degrees from Adhikary et al. [50].

Figures 6.6 through 6.13 present the discontinuity geometries applied to the BPM models. Figures 6.14 and 6.15 show examples of a closely spaced joint geometry (Model 606) and a widely spaced joint geometry (Model 621), respectively, applied to the BPM model.

Table 6.3: Discontinuity geometries for rock-slope models with persistent discontinuities.

Model	Discontinuity Spacing, m	Discontinuity Dip, degrees
601	2	20
602	2	30
603	2	40
604	2	45
605	2	50
606	2	60
607	2	70
608	2	80
609	2	90
610	2	100
611	1	80
613	3	80
614	4	80
615	5	80
616	6	80
617	7	80
618	8	80
619	1	70
620	4	70
621	6	70
622	1	60
623	4	60
624	6	60

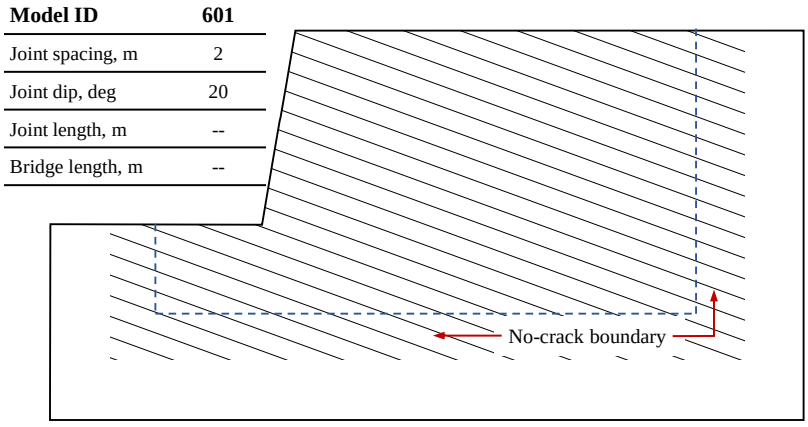

(a) Model 601

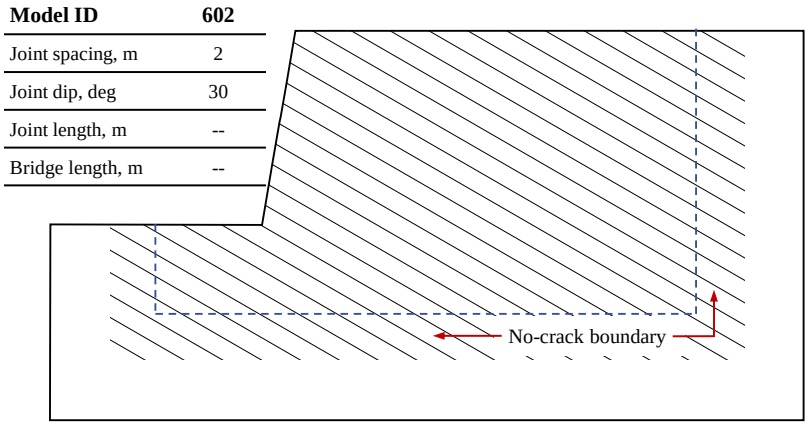

(b) Model 602

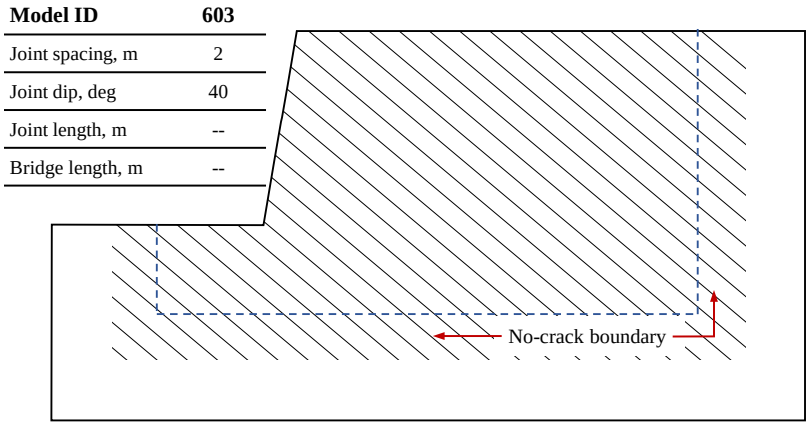

(c) Model 603

Figure 6.6: Discontinuity geometries for slopes with persistent discontinuities. Models of 601, 602, and 603 are shown. For reference, the slope height is 20 meters, and the slope face angle is 80 degrees.

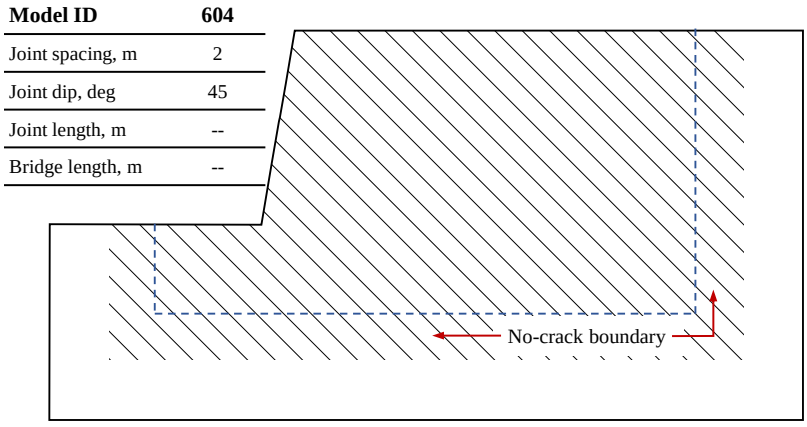

(a) Model 604

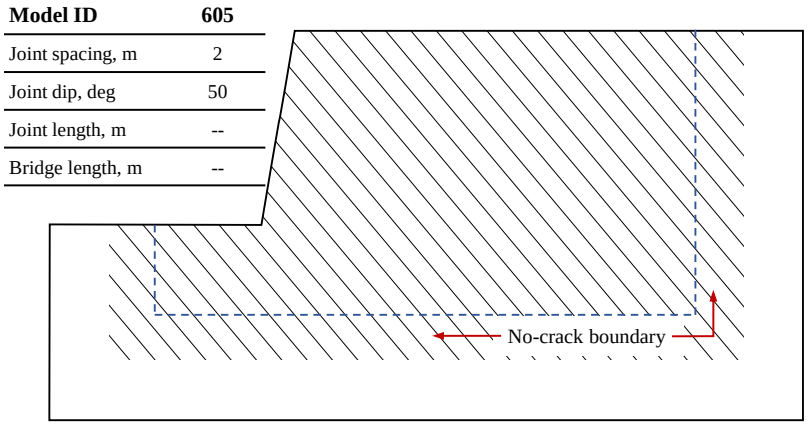

(b) Model 605

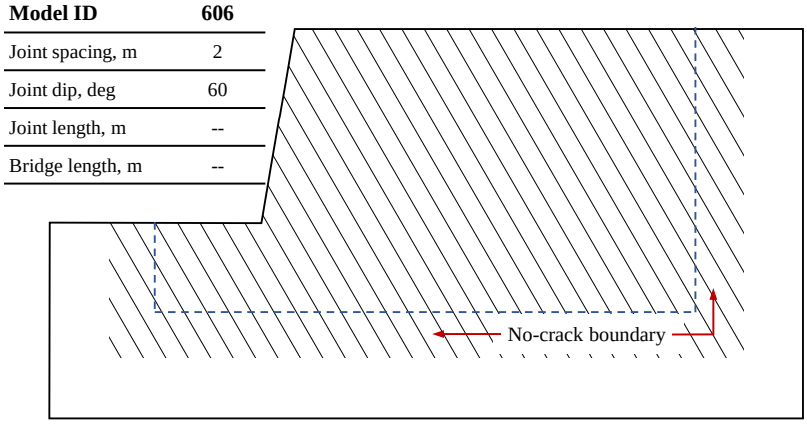

(c) Model 606

Figure 6.7: Discontinuity geometries for slopes with persistent discontinuities. Models of 604, 605, and 606 are shown. For reference, the slope height is 20 meters, and the slope face angle is 80 degrees.

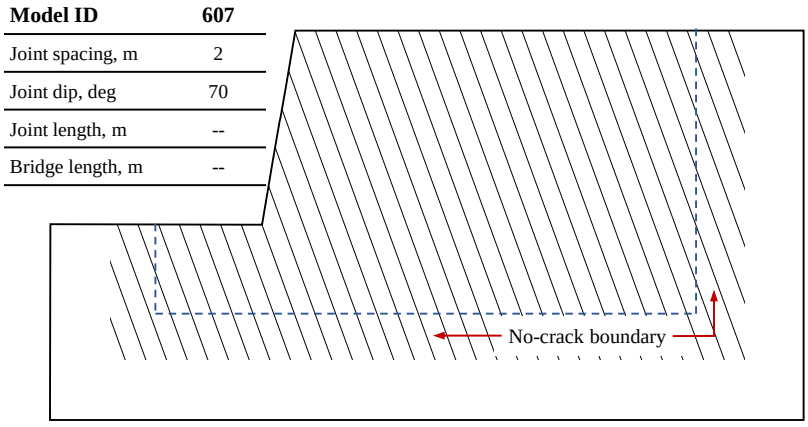

(a) Model 607

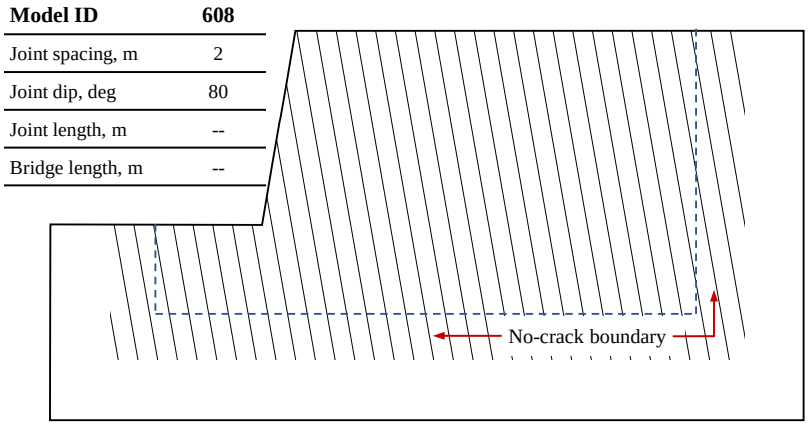

(b) Model 608

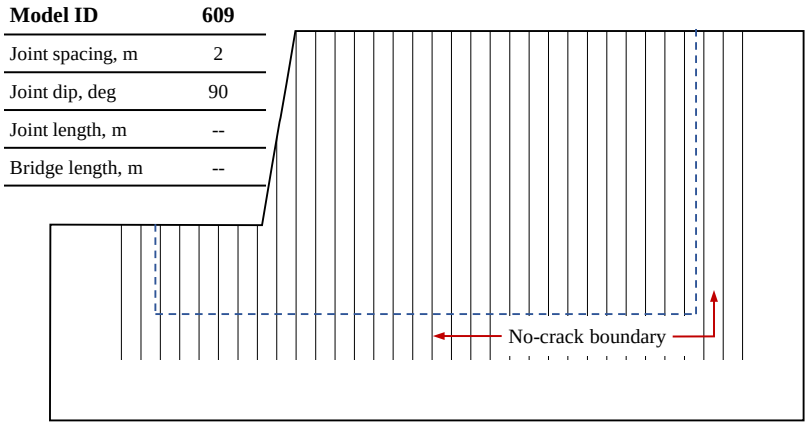

(c) Model 609

Figure 6.8: Discontinuity geometries for slopes with persistent discontinuities. Models of 607, 608, and 609 are shown. For reference, the slope height is 20 meters, and the slope face angle is 80 degrees.

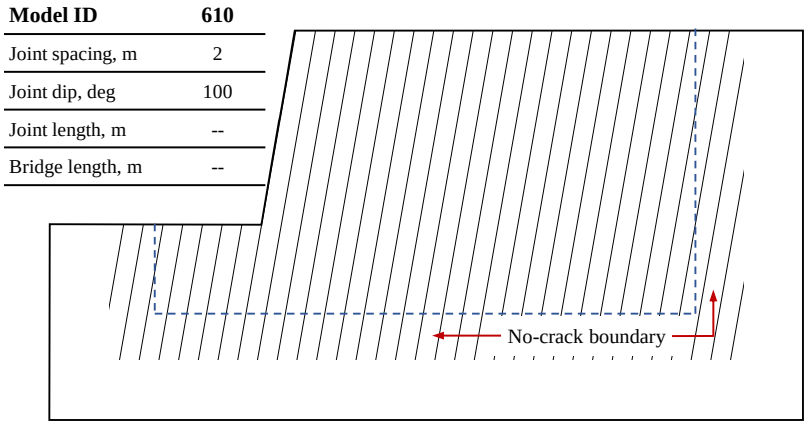

(a) Model 610

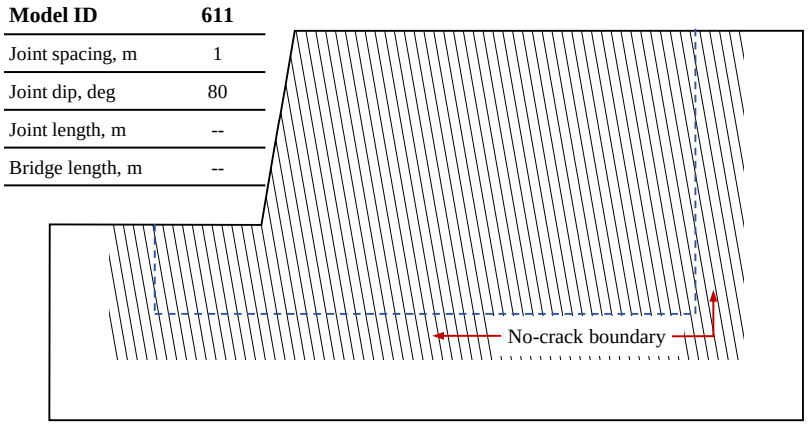

(b) Model 611

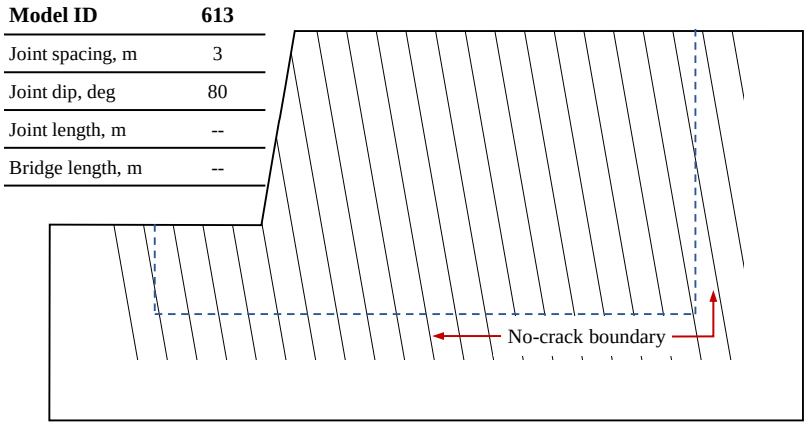

(c) Model 613

Figure 6.9: Discontinuity geometries for slopes with persistent discontinuities. Models of 610, 611, and 613 are shown. For reference, the slope height is 20 meters, and the slope face angle is 80 degrees.

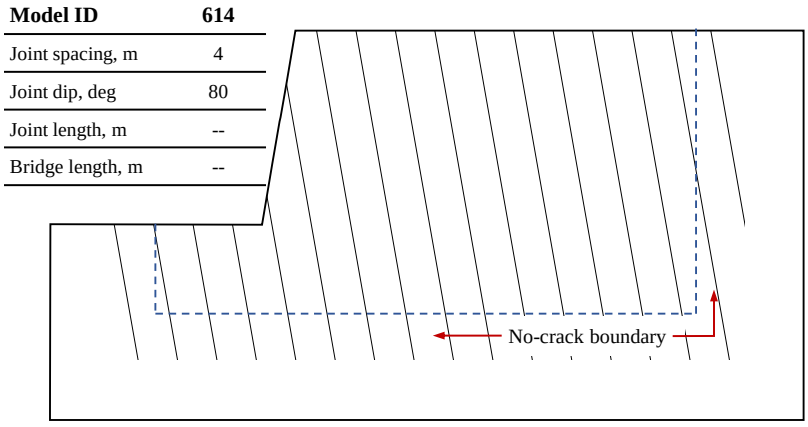

(a) Model 614

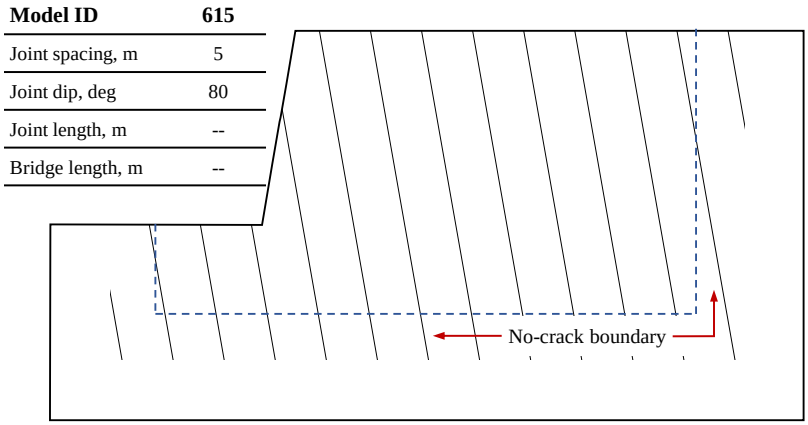

(b) Model 615

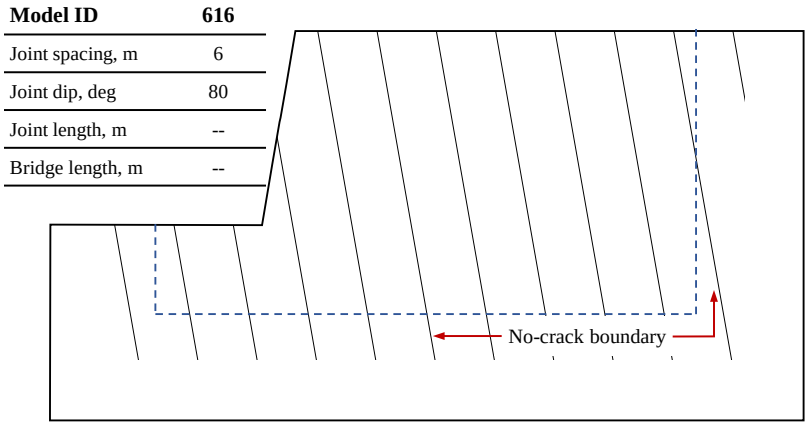

(c) Model 616

Figure 6.10: Discontinuity geometries for slopes with persistent discontinuities. Models of 614, 615, and 616 are shown. For reference, the slope height is 20 meters, and the slope face angle is 80 degrees.

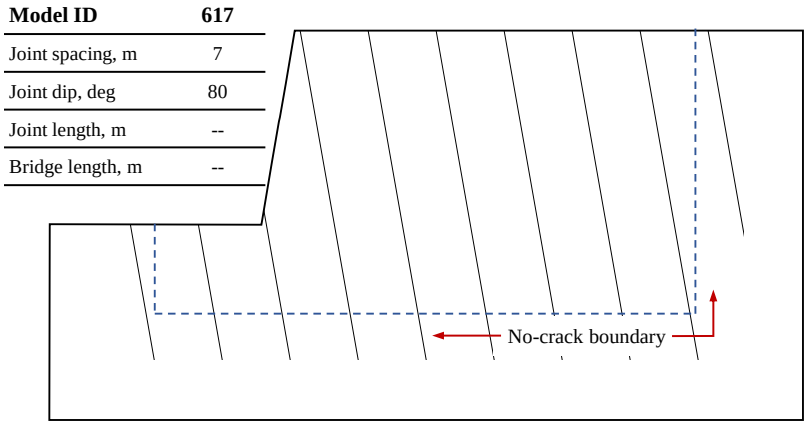

(a) Model 617

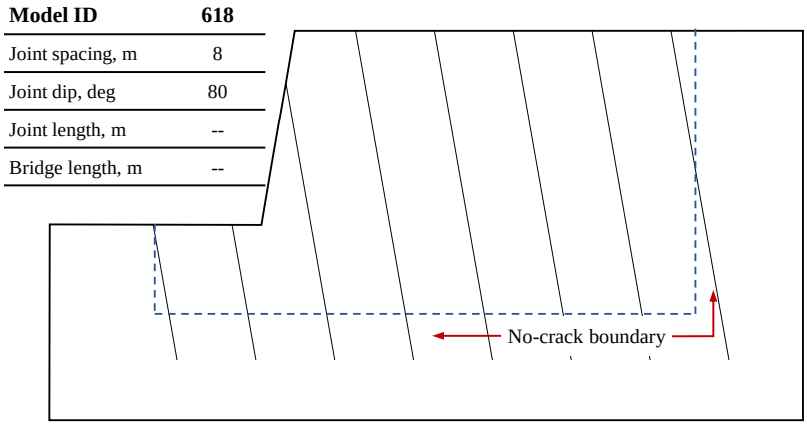

(b) Model 618

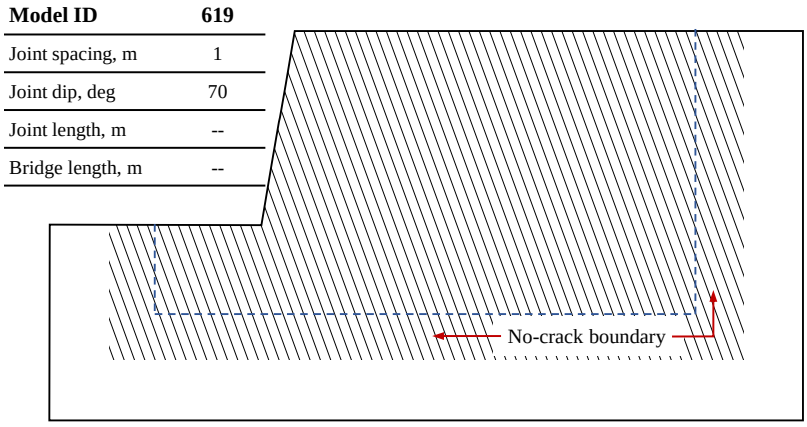

(c) Model 619

Figure 6.11: Discontinuity geometries for slopes with persistent discontinuities. Models of 617, 618, and 619 are shown. For reference, the slope height is 20 meters, and the slope face angle is 80 degrees.

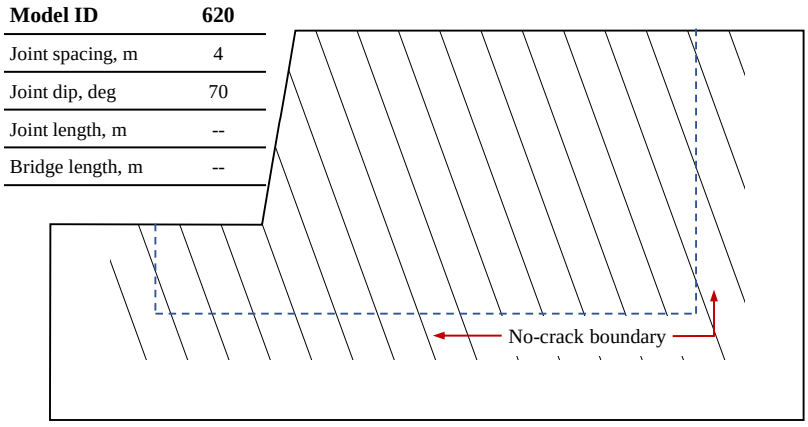

(a) Model 620

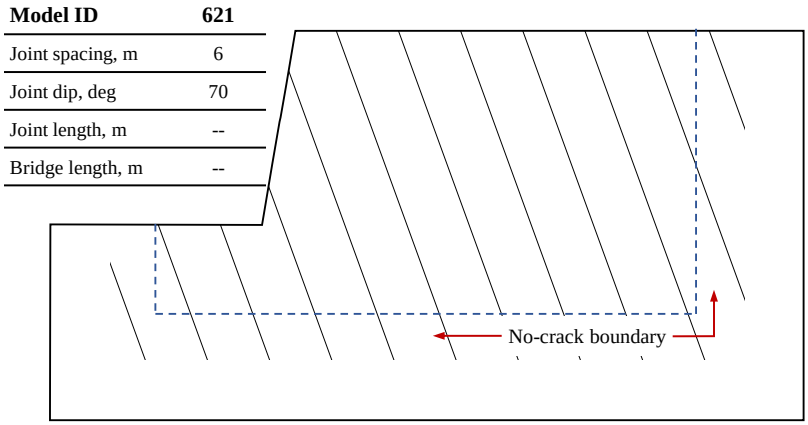

(b) Model 621

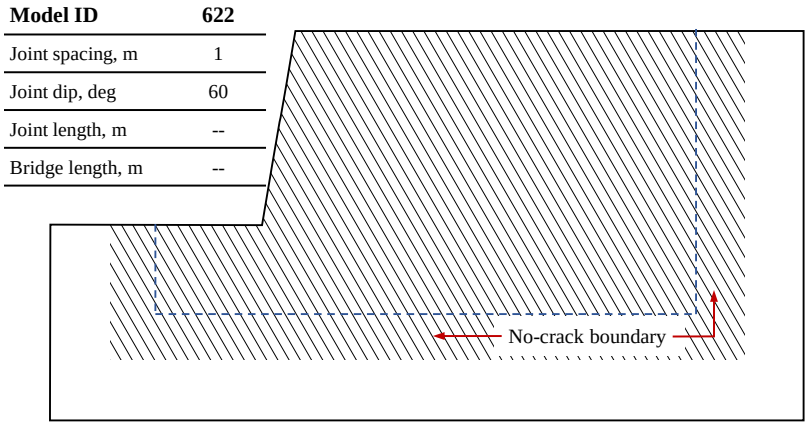

(c) Model 622

Figure 6.12: Discontinuity geometries for slopes with persistent discontinuities. Models of 620, 621, and 622 are shown. For reference, the slope height is 20 meters, and the slope face angle is 80 degrees.

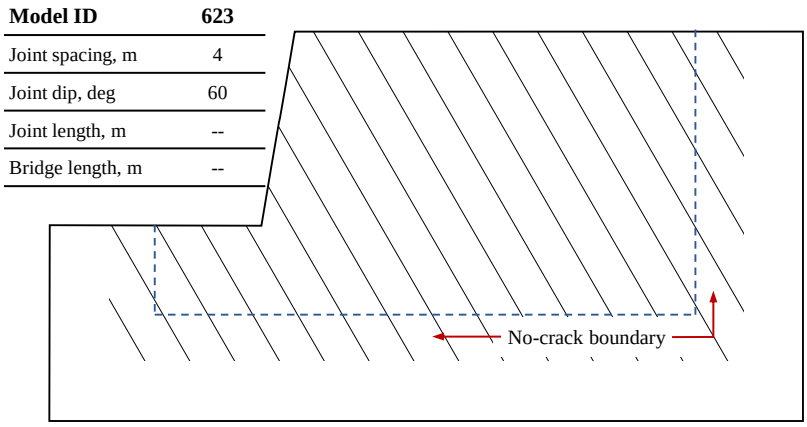

(a) Model 623

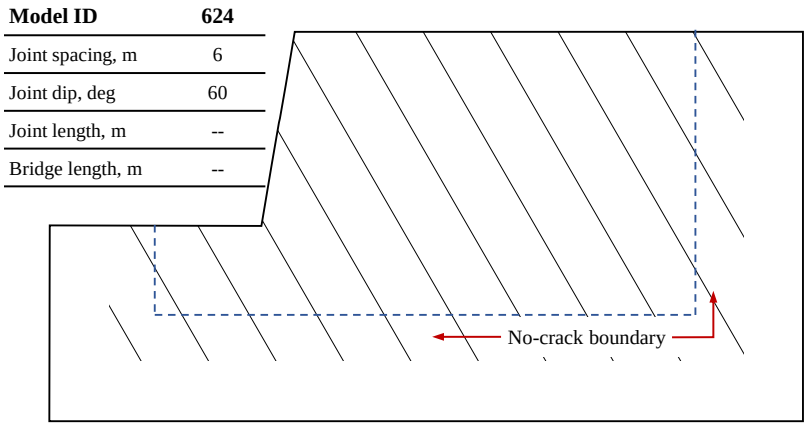

(b) Model 624

Figure 6.13: Discontinuity geometries for slopes with persistent discontinuities. Models of 623 and 624 are shown. For reference, the slope height is 20 meters, and the slope face angle is 80 degrees.

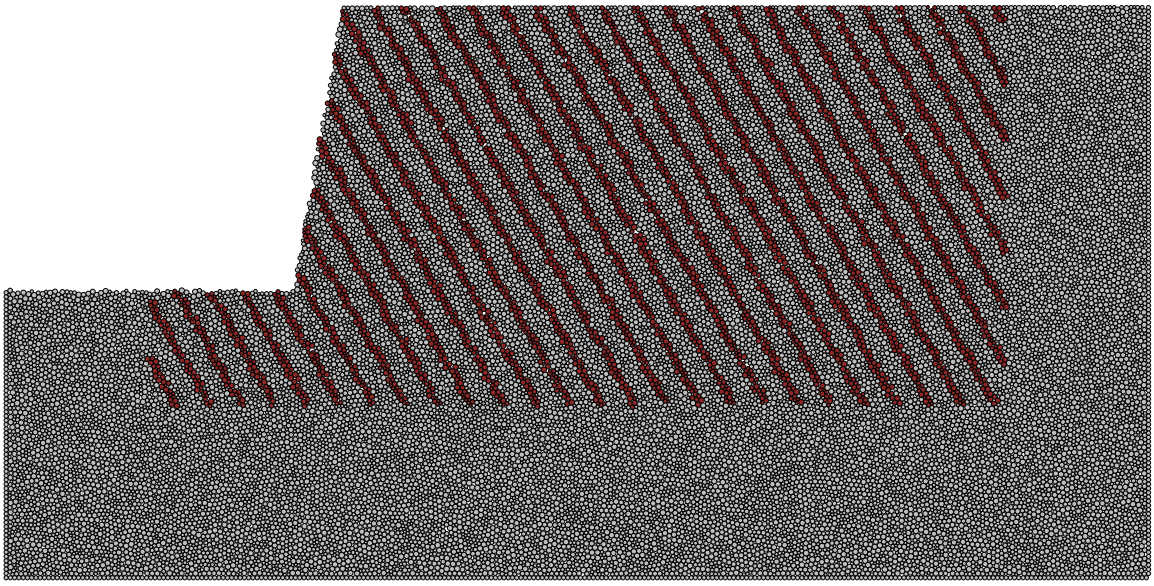

Figure 6.14: Example of the discontinuity geometry applied to the BPM model. Model 606 – having discontinuity spacing and dip of 2 meters and 60 degrees, respectively – is shown.

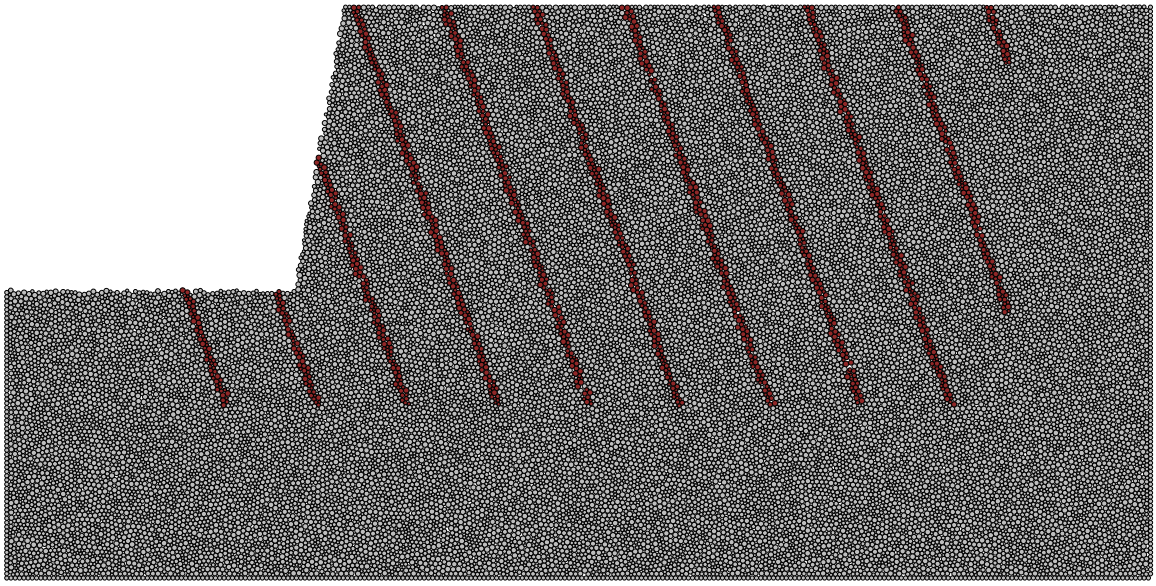

Figure 6.15: Example of the discontinuity geometry applied to the BPM model. Model 621 – having discontinuity spacing and dip of 6 meters and 60 degrees, respectively – is shown.

6.2.4 Slopes with Non-persistent Discontinuities

The slopes with non-persistent discontinuities have Model numbers 643 through 660. Within this set of slopes, discontinuity spacing was held constant at 2 meters, and rock bridge length was kept constant at 3 meters. Joint dip was varied from 0 to 150 degrees in increments of 30 degrees. For each joint orientation, three rock bridge lengths, 3, 6, and 9 meters, were used. The corresponding P21 joint intensity values for these rock bridge lengths are 0.25, 0.333, and 0.375 m/m^2. The joint step angle was varied such that the location of a rock bridge was at the center of the adjacent joint. Table 6.4 summarizes the geometries of slopes with non-persistent discontinuities used in this study.

The influence of non-persistent joints of rock-slope stability under static conditions has been well-studied [10, 11, 101, 102]. In general terms, increasing joint intensity by increased persistence, decreased spacing, or introduction of multiple joint sets decreases the stability of a rock-slope [10]. The influence of joints is also known to be more pronounced in dip slopes than in anti-dip slopes. In dip slopes, fracture coalescence creates critical sliding planes. In anti-dip slopes, fractures generally cross joints to create a failure surface [9, 101].

Coalescence –the connection of pre-existing joints through propagation– is known to occur most commonly through wing cracks extending from the tips of existing joints. This behavior has been demonstrated experimentally by Park and Bobet (2009) [90] and numerically using BPM as shown in Figure 6.16 by Camones et al. (2013).

Figure 6.17 shows examples of dip slope failure mechanisms. Sketches of coalescence of co-planar joints (Figure 6.17a) and coalescence due to en-echelon tensile failures between joints, forming a stepped-path failure (Figure 6.17b) are shown. The stepped-path failure mechanism is common in rock-slope failures, and leads to stepped block sliding, as shown in Figure 6.17c.

In anti-dip slopes, the coalescence of pre-existing joints does not form a sliding surface. Anti-dip slopes can fail due to the development of a cross-joint shear surface, or by block toppling, if independent blocks are created. Figure 6.18 shows examples of cross-joint shear and block toppling in anti-dip slopes.

Figures 6.19 through 6.24 present the discontinuity geometries applied to the BPM

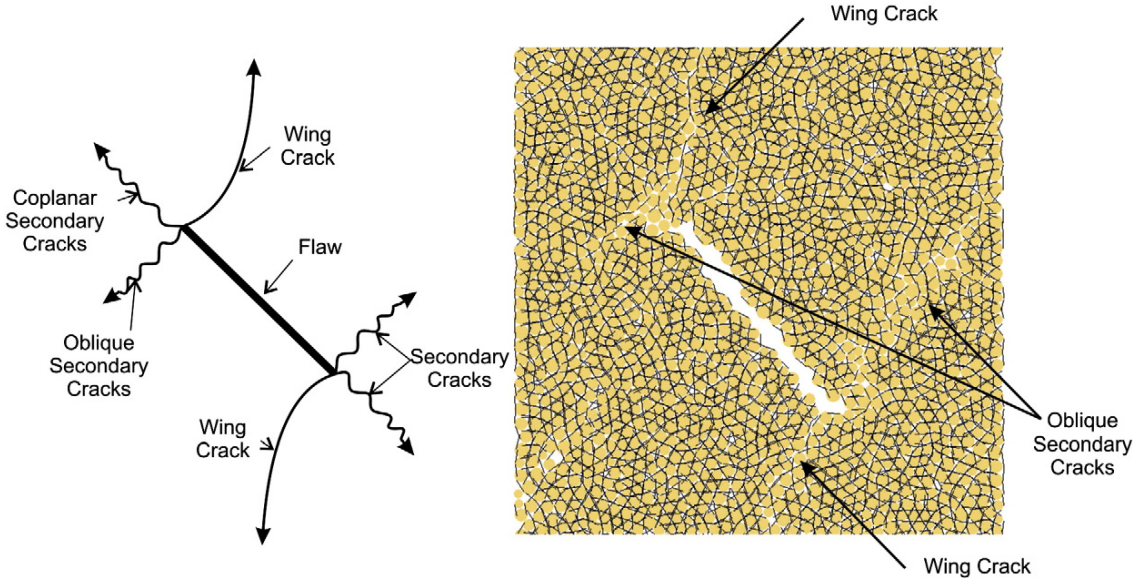

Figure 6.16: Camones et al. [103].

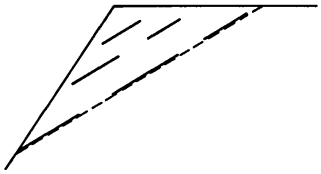

(a) Co-planar fracture coalescence (from [101])

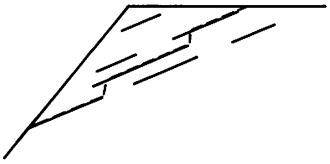

(b) En-echelon fracture coalescence (from [101])

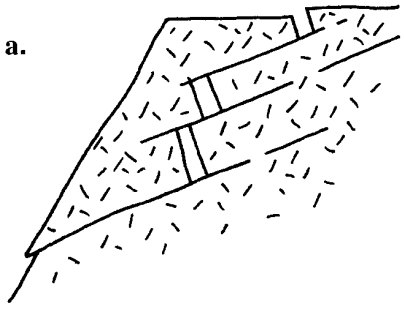

(c) Stepped block sliding (from [8])

Figure 6.17: Failure mechanisms for dip slopes with non-persistent discontinuities.

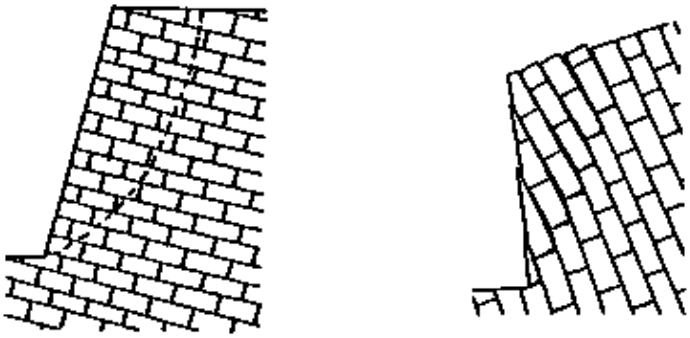

(a) Cross-joint shear failure in a blocky, anti-dip slope

(b) Toppling geometry in a blocky, anti-dip slope.

Figure 6.18: Failure mechanisms for anti-dip slopes (from [9]).

models. Figures 6.25, 6.26 and 6.27 show a examples of horizontally jointed (Model 644), dip slope (Model 650), and anti-dip slope (Model 559) discontinuity geometry, respectively, applied to the BPM model.

Table 6.4: Discontinuity geometries for rock-slope models with non-persistent discontinuities.

Model	Discontinuity Spacing, m	Discontinuity Dip, degrees	Discontinuity Length, m	Rock Bridge Length, m	Joint Intensity, m/m^2
643	2	0	3	3	0.25
644	2	0	6	3	0.333
645	2	0	9	3	0.375
646	2	30	3	3	0.25
647	2	30	6	3	0.333
648	2	30	9	3	0.375
649	2	60	3	3	0.25
650	2	60	6	3	0.333
651	2	60	9	3	0.375
652	2	90	3	3	0.25
653	2	90	6	3	0.333
654	2	90	9	3	0.375
655	2	120	3	3	0.25
656	2	120	6	3	0.333
657	2	120	9	3	0.375
658	2	150	3	3	0.25
659	2	150	6	3	0.333
660	2	150	9	3	0.375

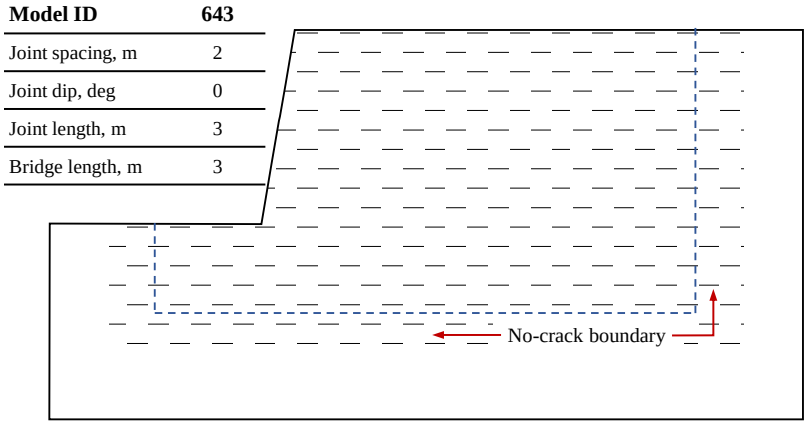

(a) Model 643

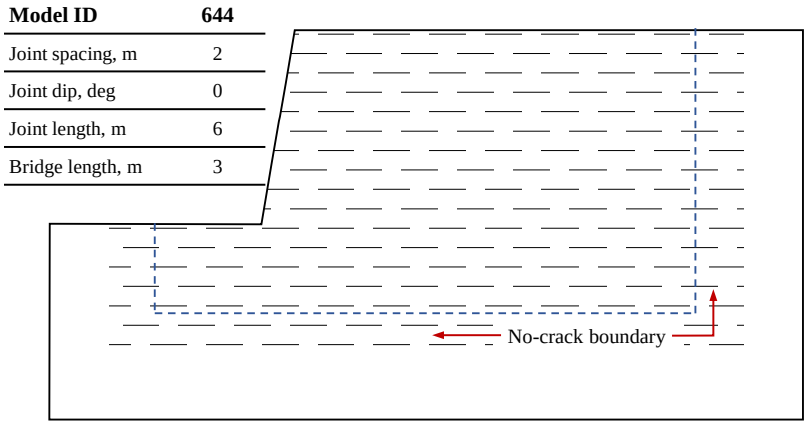

(b) Model 644

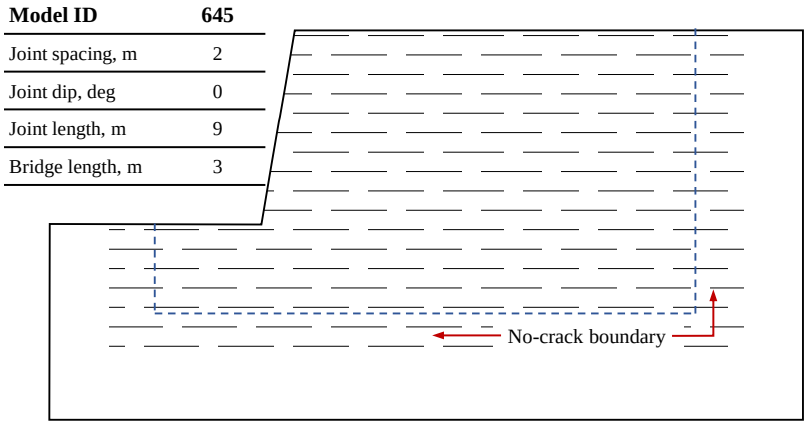

(c) Model 645

Figure 6.19: Discontinuity geometries for Models 643, 644, and 645, which have discontinuity dips of 0 degrees. For reference, the slope height is 20 meters, and the slope face angle is 80 degrees.

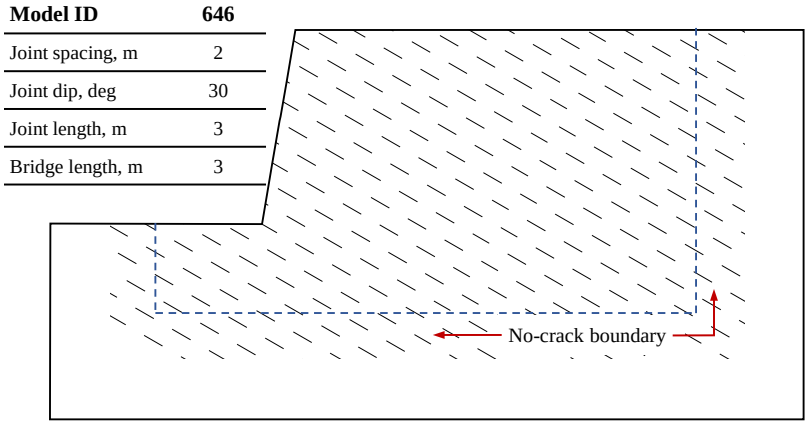

(a) Model 646

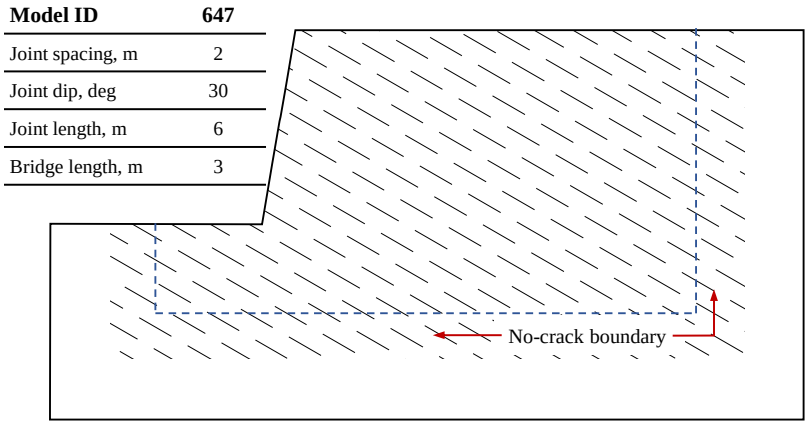

(b) Model 647

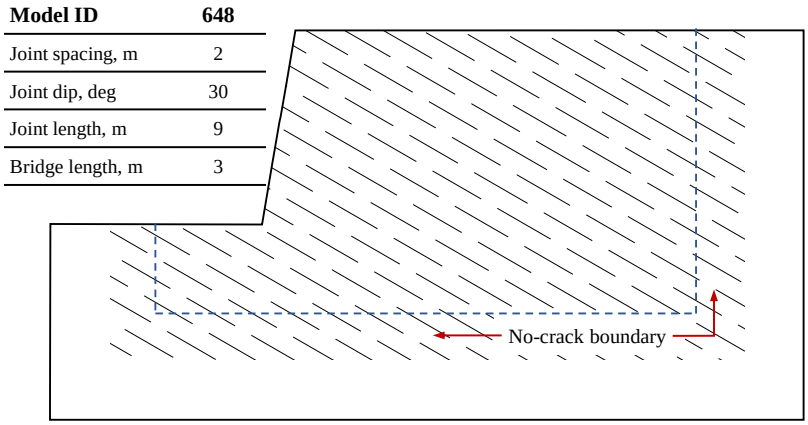

(c) Model 648

Figure 6.20: Discontinuity geometries for Models 646, 647, and 648, which have discontinuity dips of 30 degrees. For reference, the slope height is 20 meters, and the slope face angle is 80 degrees.

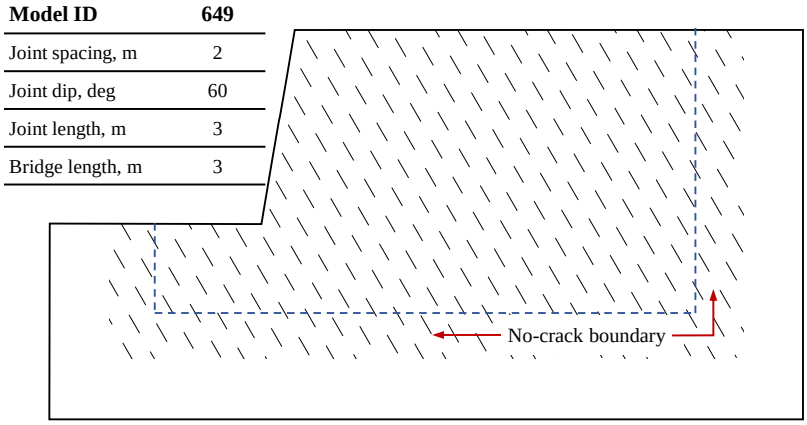

(a) Model 649

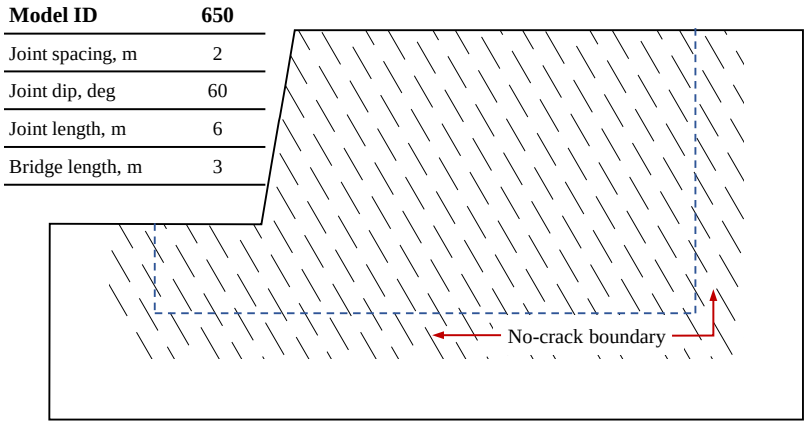

(b) Model 650

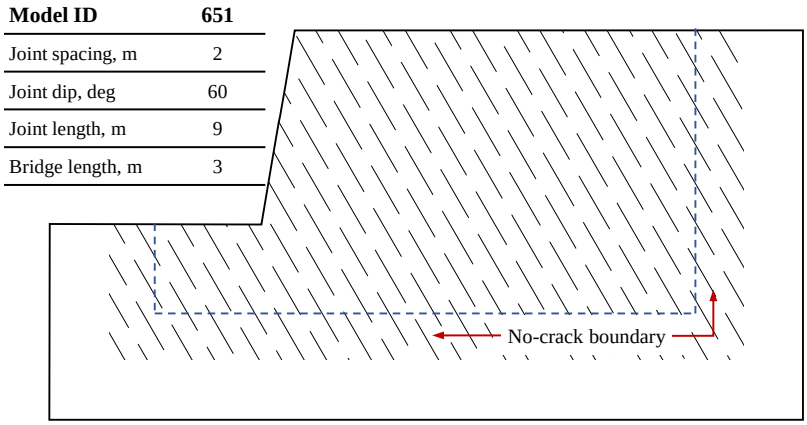

(c) Model 651

Figure 6.21: Discontinuity geometries for Models 649, 650, and 651, which have discontinuity dips of 60 degrees. For reference, the slope height is 20 meters, and the slope face angle is 80 degrees.

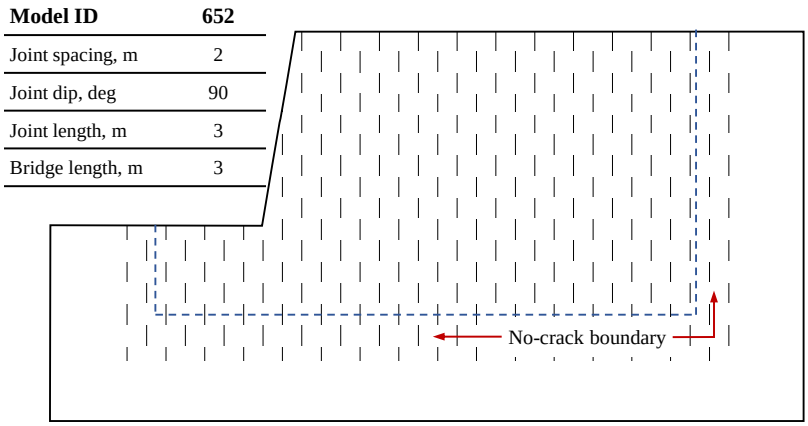

(a) Model 652

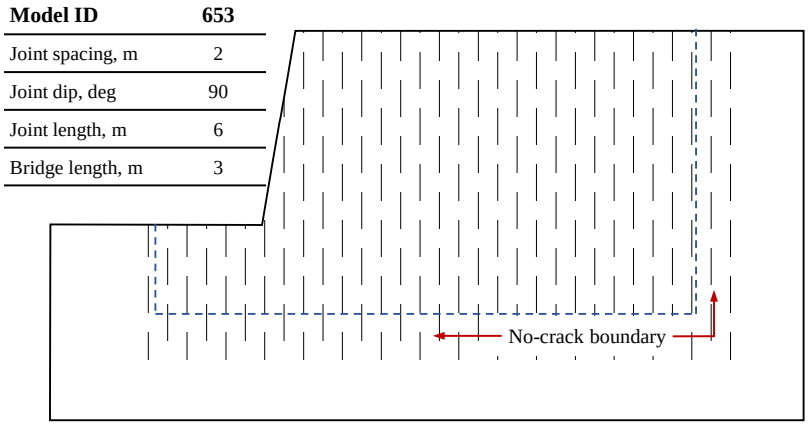

(b) Model 653

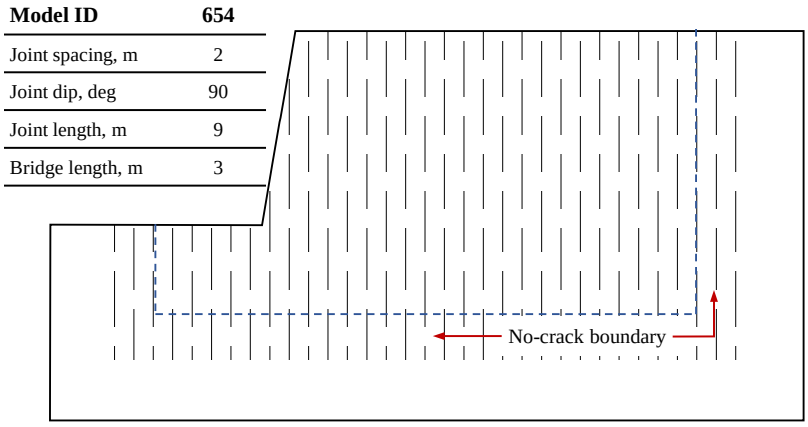

(c) Model 654

Figure 6.22: Discontinuity geometries for Models 652, 653, and 654, which have discontinuity dips of 90 degrees. For reference, the slope height is 20 meters, and the slope face angle is 80 degrees.

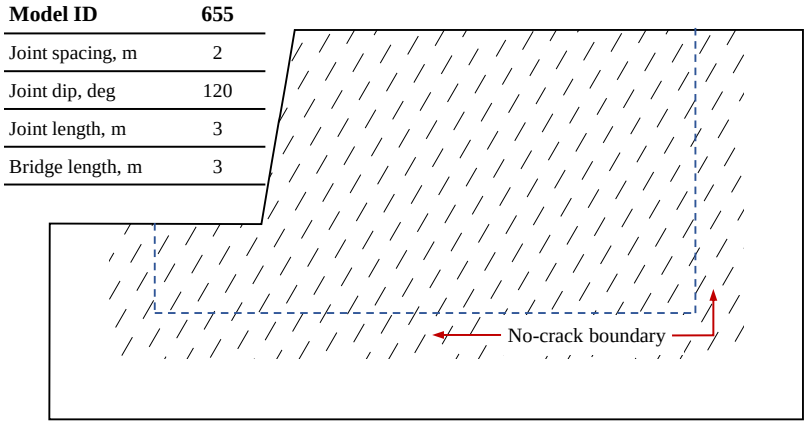

(a) Model 655

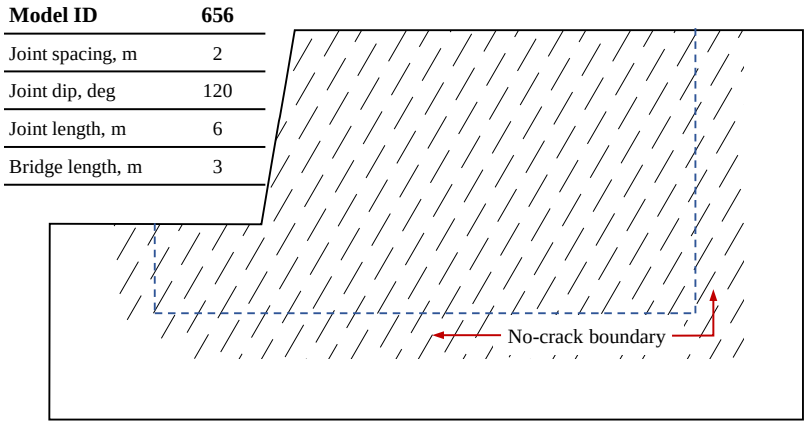

(b) Model 656

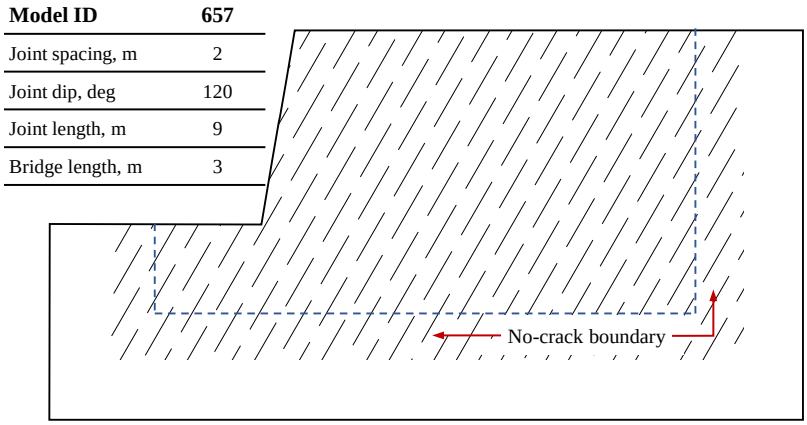

(c) Model 657

Figure 6.23: Discontinuity geometries for Models 655, 656, and 657, which have discontinuity dips of 120 degrees. For reference, the slope height is 20 meters, and the slope face angle is 80 degrees.

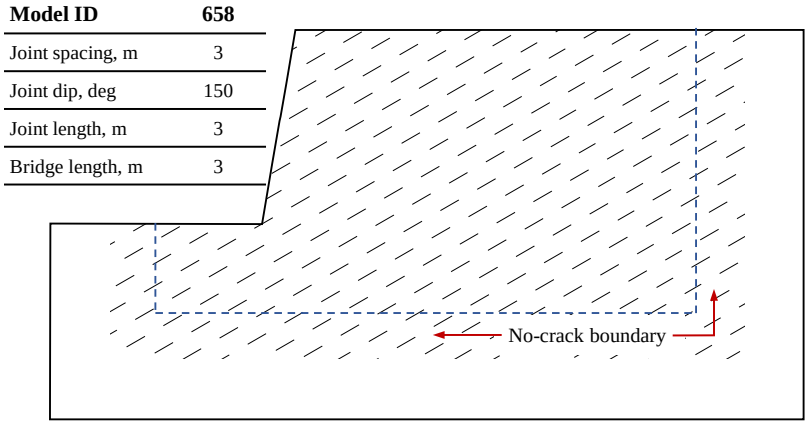

(a) Model 658

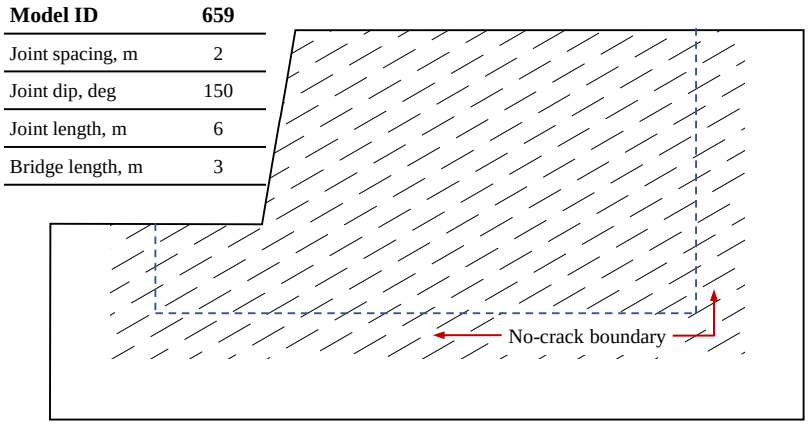

(b) Model 659

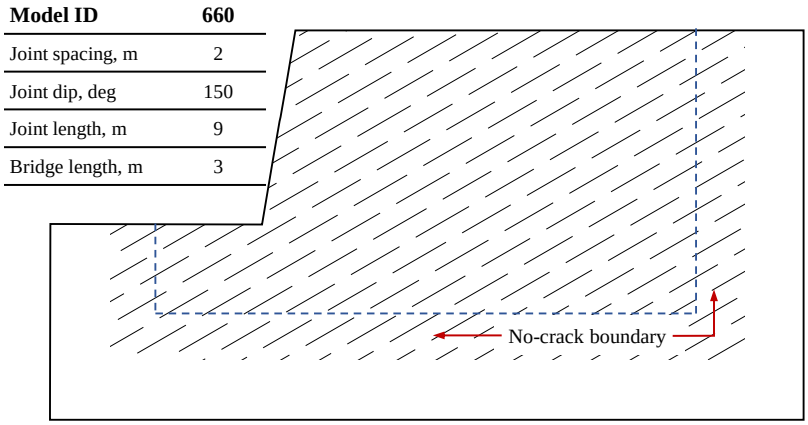

(c) Model 660

Figure 6.24: Discontinuity geometries for Models 658, 659, and 660, which have discontinuity dips of 120 degrees. For reference, the slope height is 20 meters, and the slope face angle is 80 degrees.

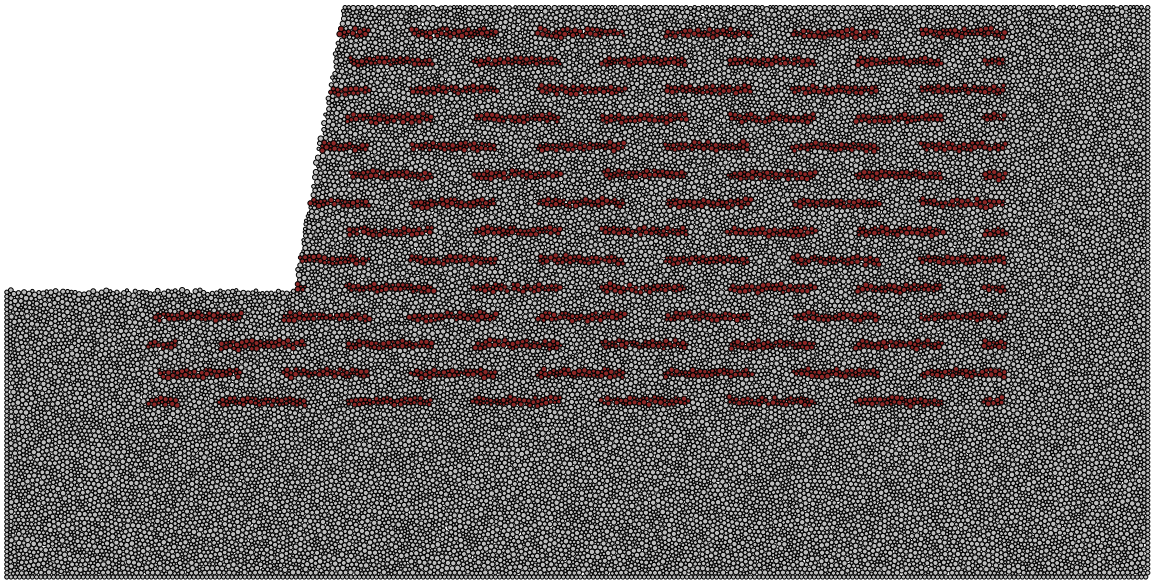

Figure 6.25: Example of the discontinuity geometry applied to the BPM model. Model 644 – having discontinuity spacing, dip, and length of 3 meters, 0 degrees, and 6 meters, respectively, and rock bridge length of 3 meters – is shown.

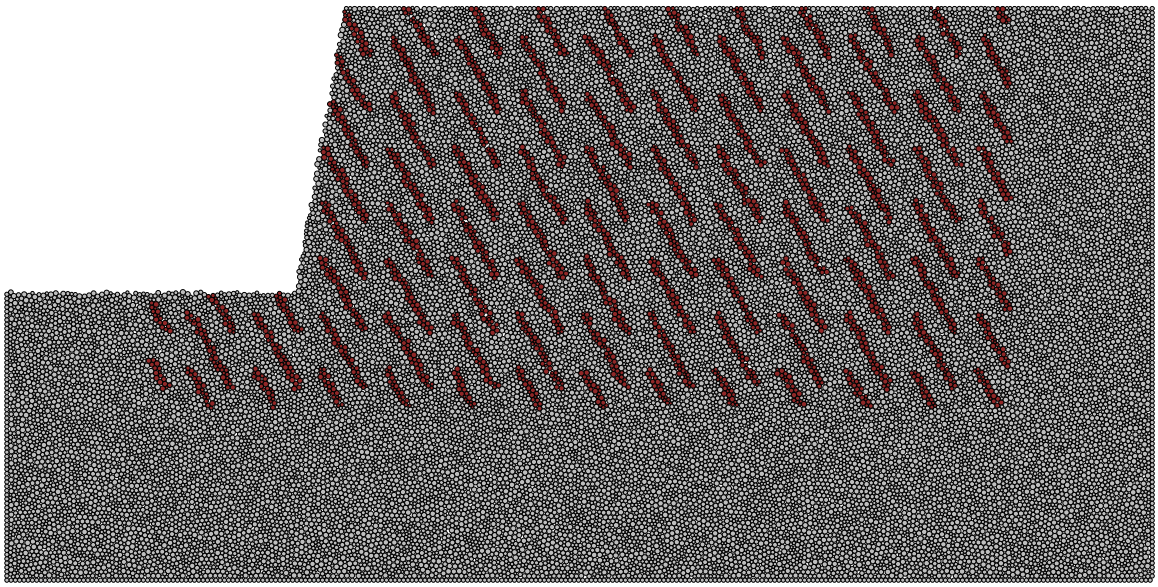

Figure 6.26: Example of the discontinuity geometry applied to the BPM model. Model 650 – having discontinuity spacing, dip, and length of 3 meters, 60 degrees, and 6 meters, respectively, and rock bridge length of 3 meters – is shown.

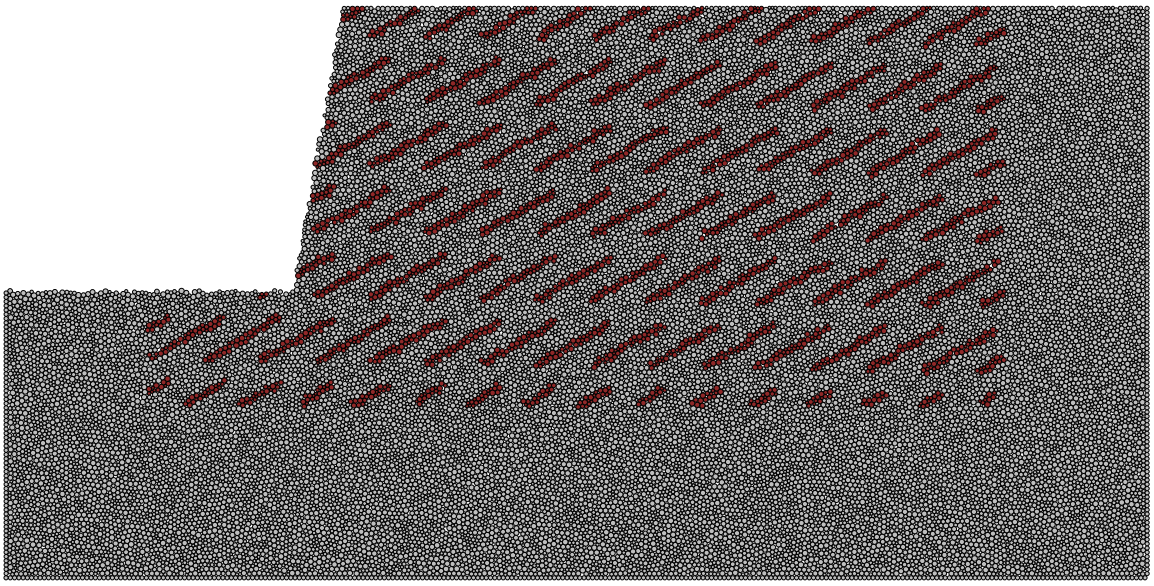

Figure 6.27: Example of the discontinuity geometry applied to the BPM model. Model 659 – having discontinuity spacing, dip, and length of 3 meters, 120 degrees, and 6 meters, respectively, and rock bridge length of 3 meters – is shown.

6.3 Loading Cases

The loading the the models were subjected to include:

- Pseudostatic loading,
- A non-destructive frequency sweep,
- A destructive, ramping amplitude harmonic motion suite

The following sections describe the loading conditions.

6.3.1 Pseudostatic Loading

The slopes were evaluated under pseudostatic loading to determine the pseudostatic yield acceleration, k_y. The pseudostatic yield acceleration is determined by increasing the horizontal acceleration coefficient, k, on the slope model in increments of 0.25 g. In cases where k_y was 0.25 g or less, the pseudostatic loading was reapplied in increments of 0.1 g. Between incremental applications of k, the model is allowed to come to rest. During the time where the model comes to equilibrium, a high level of damping is used to prevent damage in the model due to the shock of instantaneous horizontal acceleration. The yield acceleration, k_y is taken as the horizontal acceleration applied to the model at the initiation of failure.

6.3.2 Frequency Sweep

A frequency sweep with loading frequencies of 1 to 30 Hz and a constant input acceleration of 0.01 g (after an initial ramping period at 1 Hz) was applied to the models. The purpose of the frequency sweep is to evaluate the natural frequency/frequencies of the slope model.

6.3.3 Ramping Amplitude Harmonic Motions

A series of harmonic motions with ramping amplitude were run through the models. The input acceleration amplitude, a, of the harmonic motions was varied linearly with time from 0 to 3.5 g in 20 seconds. Frequencies of 1 Hz, 3 Hz, 5 Hz, 7 Hz, 9 Hz, and 11 Hz were used.

The frequencies of loading applied to the models were determined by the natural frequency of the slopes, which are presented in Section 6.4.2.

With input motions of the same input acceleration with time, but different frequencies, the velocity and displacement amplitudes vary significantly. Velocity and displacement amplitudes for harmonic loading are related to acceleration amplitude by:

$$|v| = \frac{|a|g}{2\pi f} \tag{6.5}$$

and

$$|d| = \frac{|a|g}{(2\pi f)^2} \tag{6.6}$$

where $|a|$, $|v|$, and $|d|$, are the acceleration, velocity, and displacement amplitudes, respectively of a harmonic signal with frequency, f, and g is gravitational acceleration.

The maximum input accelerations amplitudes, a_{max} (which are the same for all motions), and associated maximum input velocities and displacements, v_{max} and d_{max}, respectively, are shown for reference in Table 6.5.

Table 6.5: Maximum input acceleration, velocity, and displacements for the ramping amplitude harmonic input suite.

Loading Frequency, Hz	$\boldsymbol{a_{max}}$, **g**	$\boldsymbol{v_{max}}$, **m/s**	$\boldsymbol{d_{max}}$, **m**
1	3.5	5.5	0.870
3	3.5	1.8	0.097
5	3.5	1.1	0.035
7	3.5	0.8	0.018
9	3.5	0.6	0.011
11	3.5	0.5	0.007

6.4 Results

6.4.1 Pseudostatic Analysis

The results of the pseudostatic analysis of the three slope categories (without discontinuities, with persistent discontinuities, and with non-persistent discontinuities) are presented in the following sections. Not all of the pseudostatic simulations produced meaningful results. In some cases, unbonded particles at the cliff face or crest were dislodged by the pseudostatic loading and the damage caused by the impact of the particle on the ground in front of the slope triggered an end of simulation with a result that was not meaningful. The majority of the pseudostatic simulations successfully captured a global slope stability, and their results provide sufficient information to draw conclusions on the influence of joint structure on yield acceleration.

Pseudostatic Analysis of the Homogeneous Slope

When subjected to pseudostatic loading, Model 600 yielded at a horizontal seismic coefficient of 5.5 g. This k_y is outside the range of values typically of interest for evaluating the co-seismic stability of rock-slopes because it is outside of observed seismic loading. As mentioned in Section 6.2, Model 600 is much stronger than most of the other slopes in this study because it has no pre-existing discontinuities. Even with such a high value of k_y, Model 600 provides a point of reference for the level of influence of the joints present in other models. The yield acceleration of Model 600, which other models will be compared to is denoted as $k_{y,600}$ in the following sections.

Pseudostatic Analysis of Slopes with Persistent Discontinuities

When subjected to pseudostatic loading, the slopes with persistent discontinuities showed values of k_y ranging from 0.2 to 3.5 g. Table 6.6 shows the yield accelerations for all the models where the simulations produced meaningful results. Where the simulations did not produce meaningful results, a dash is placed in the k_y column.

Figure 6.28 shows a plot of k_y for different joint dips for slopes with 2-meter joint spacing. The k_y figures are normalized as a percentage of the yield acceleration of Model

600, $k_{y,600}$. As discussed in Section 6.2.3, the restriction of flexural toppling slopes to have dips less than 90 degrees under static conditions does not apply to pseudostatic loading cases. The anticipated shift to the right in dip associated with minimum stability relative to the Adhikari design chart in Figure 6.5 is confirmed by Figure 6.28. A vertical dashed line on the figure shows the kinematic limit on flexural toppling after Goodman and Bray (1976). A rapid drop in k_y is visible to the right of the line. The result on the line at a dip of 40 degrees is an example of a slope that experienced failure that falls outside of the Goodman and Bray slip criterion. The relatively large k_y for this dip is consistent with a scenario where flexural toppling is not permitted but a cross-joint shear failure can develop. The kinematic condition for flexural slip is simply used here to provide a useful point of reference for a marked change in k_y for the results presented in Figure 6.28.

Joint spacing also has an influence on flexural toppling failure, with wider joint spacing allowing for more resistance to tensile failure in flexure, and therefore, greater stability. Figure 6.29 shows the relationship between k_y and joint spacing for joints with dips of 60, 70, and 80 degrees. The increase in k_y with joint spacing is linear in the range of dips where spacing was altered. The slope of the linear trend for slopes with dips in this range is roughly the same.

The results of the pseudostatic analysis verify that the BPM models behave in a reasonable manner.

Table 6.6: Pseudostatic yeild acceleration, k_y, for BPM slope models with persistent discontinuities.

Model	Discontinuity Spacing, m	Discontinuity Dip, degrees	Pseudostatic Yield (k_y), g
601	2	20	–
602	2	30	–
603	2	40	3.5
604	2	45	–
605	2	50	–
606	2	60	1.0
607	2	70	0.75
608	2	80	0.5
609	2	90	0.2
610	2	100	0.75
611	1	80	–
613	3	80	1.0
614	4	80	1.25
615	5	80	1.5
616	6	80	1.5
617	7	80	2.0
618	8	80	2.5
619	1	70	–
620	4	70	1.25
621	6	70	1.75
622	1	60	–
623	4	60	1.5
624	6	60	2.0

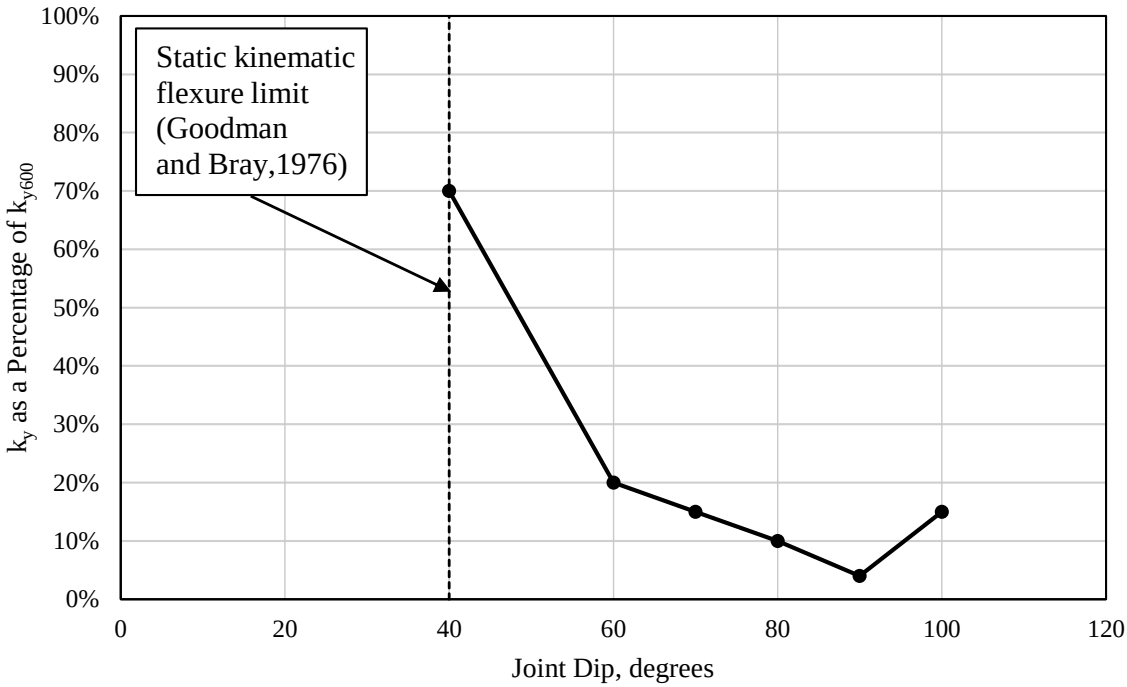

Figure 6.28: Pseudostatic yield accelerations k_y for slopes with persistent discontinuities, normalized to the yield acceleration of the homogeneous slope $k_{y,600}$, with variation in joint dip with constant joint spacing of 2 meters. The vertical dashed line at dip = 40 degrees marks the limit of static flexural toppling according to equation 6.2 from Goodman and Bray [95]. The rapid drop in k_y across the static flexural toppling susceptibility line indicates a change in failure mechanism in the pseudostatic simulation from cross-joint shearing to flexural toppling.

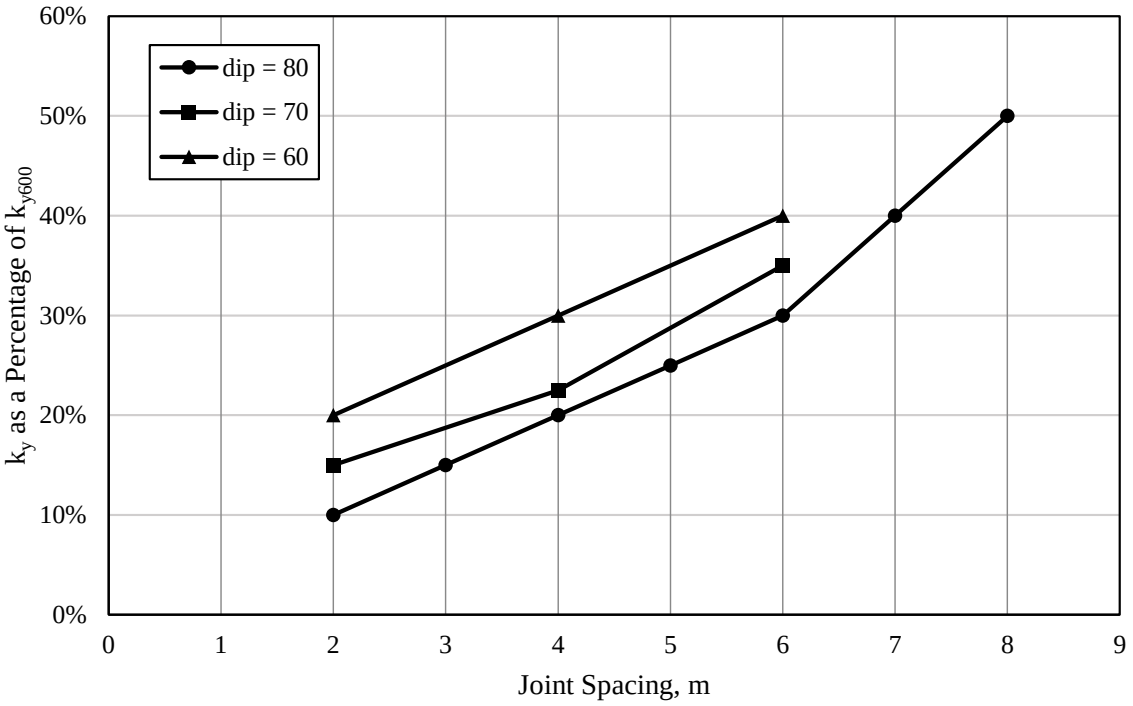

Figure 6.29: Pseudostatic yield accelerations k_y for slopes with persistent discontinuities, normalized to the yield acceleration of the homogeneous slope $k_{y,600}$, with variation in joint spacing with joint dips of 60, 70, and 80 degrees. The variation in k_y with joint spacing is generally consistent in the 2-meter to 6-meter spacing range. At spacings greater that 6-meters, the trend of increasing k_y with spacing steepens, possibly indicating a change in failure mechanism from flexural toppling to shearing failure as the columns get less slender.

Pseudostatic Analysis of Slopes with Non-persistent Discontinuities

When subjected to pseudostatic loading, the slopes with non-persistent discontinuities showed values of k_y ranging from 0.5 to 4.5 g. Table 6.7 shows the yield accelerations for all the models where the simulations produced meaningful results. Where simulations did not produce meaningful results, a dash is shown in the k_y column.

Figure 6.30 shows the influence of joint dip for multiple joint intensities on k_y. The influence of the joint intensity varies with dip, and the critical dips appear to be different at different intensity levels. Figures 6.31, 6.32, and 6.33 show the influence of joint intensity on k_y for horizontally and vertically dipped, anti-dip, and dip slopes, respectively. Horizontally and vertically dipped slopes have similar changes in k_y due to change in joint intensity, with vertically jointed slopes being uniformly more resistant to pseudostatic failure than horizontally jointed slopes. Figure 6.32 shows that the pseudostatic stability of anti-dip slopes is relatively insensitive to changes in joint intensity. Figure 6.33 shows that the pseudostatic stability of dip slopes is more sensitive to changes in joint intensity than anti-dip, horizontally, or vertically dipped slops.

These results are consistent with expectations based on findings on the influence of joint intensity on the static stability of rock-slopes.

Table 6.7: Pseudostatic yeild acceleration, k_y, for BPM slope models with non-persistent discontinuities.

Model	Joint Dip, degrees	Joint Intensity, m/m^2	Pseudostatic Yield (k_y), g
643	0	0.25	3.0
644	0	0.333	2.0
645	0	0.375	1.0
646	30	0.25	3.5
647	30	0.333	2.5
648	30	0.375	2.5
649	60	0.25	4.0
650	60	0.333	–
651	60	0.375	3.5
652	90	0.25	4.5
653	90	0.333	3.5
654	90	0.375	2.0
655	120	0.25	4.5
656	120	0.333	1.5
657	120	0.375	1.0
658	150	0.25	3.5
659	150	0.333	2.5
660	150	0.375	0.5

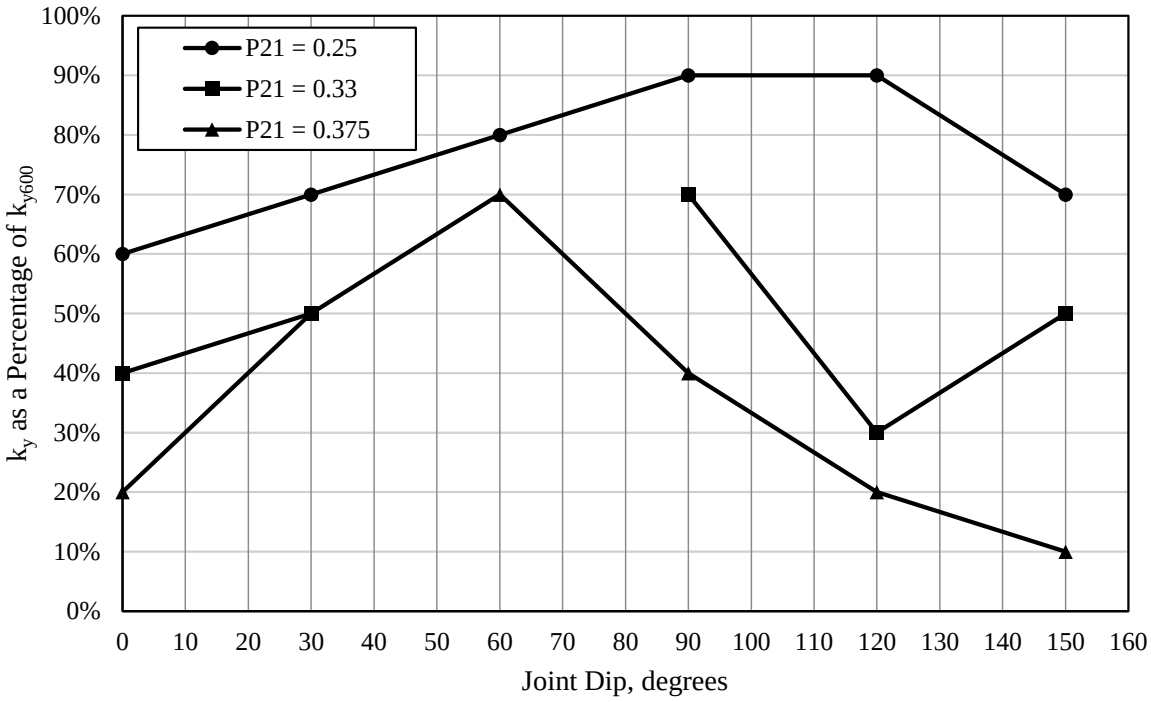

Figure 6.30: Pseudostatic yield accelerations k_y for slopes with non-persistent discontinuities, normalized to the yield acceleration of the homogeneous slope $k_{y,600}$, with variation in joint dip with constant joint spacing of 3 meters and P21 values of 0.25, 0.333, and 0.375.

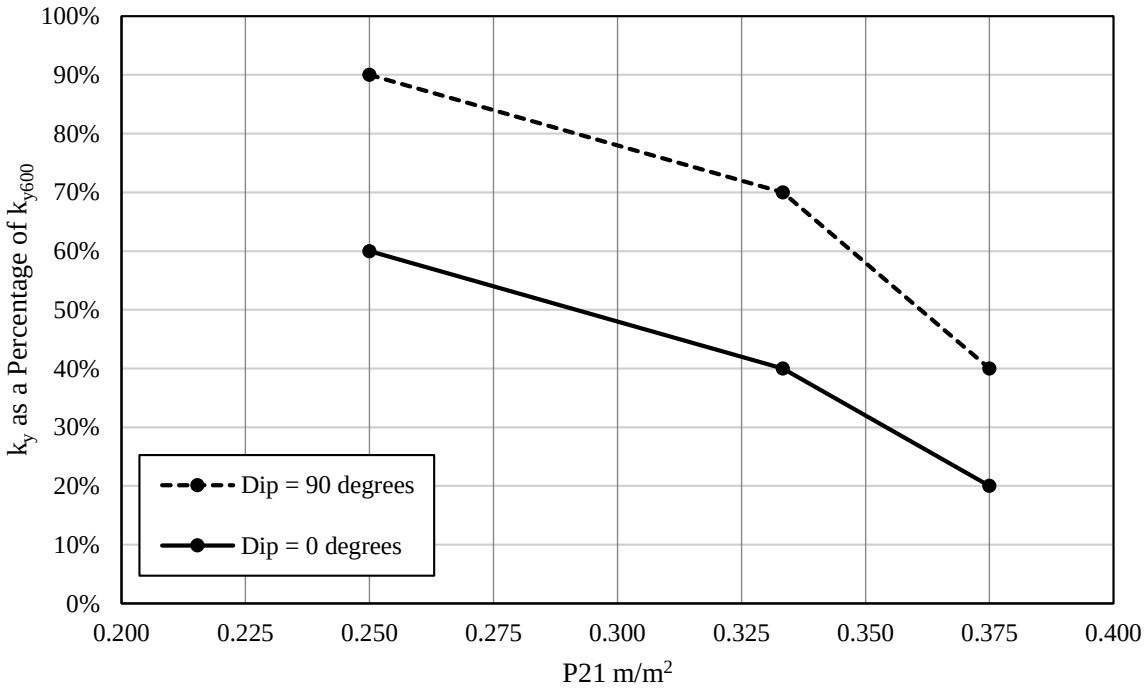

Figure 6.31: Pseudostatic yield accelerations k_y for slopes with non-persistent discontinuities, normalized to the yield acceleration of the homogeneous slope $k_{y,600}$, for horizontally and vertically jointed slopes with variation in P21 with constant joint spacing of 3 meters.

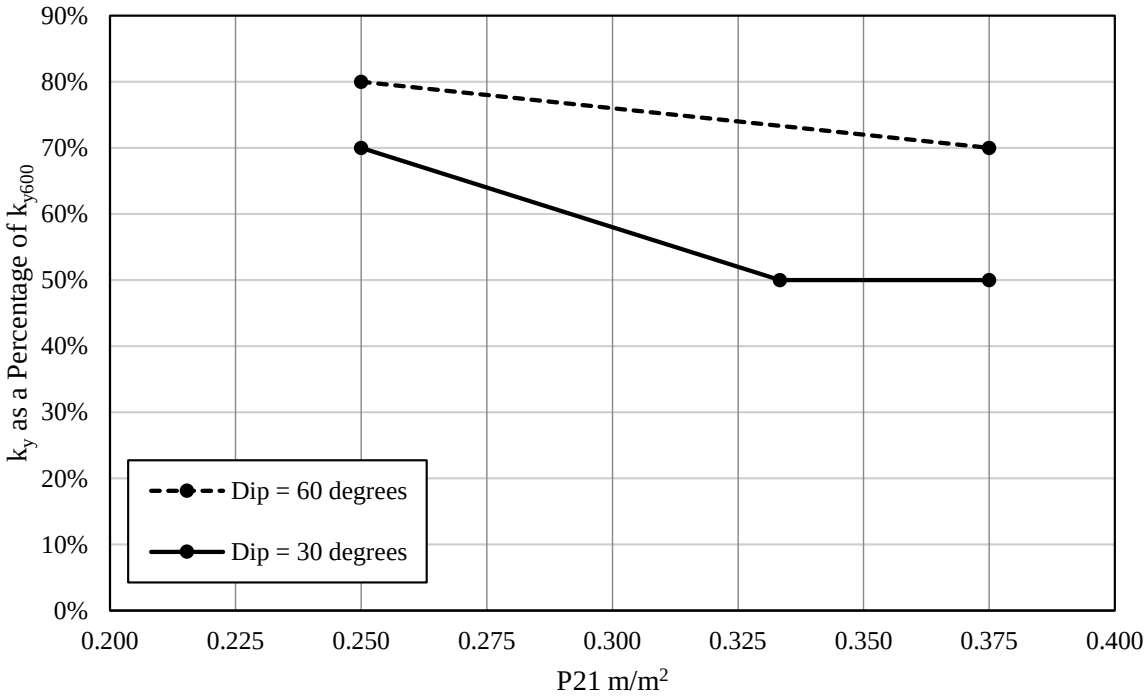

Figure 6.32: Pseudostatic yield accelerations k_y for slopes with non-persistent discontinuities, normalized to the yield acceleration of the homogeneous slope $k_{y,600}$, for anti-dip slopes with variation in P21 with constant joint spacing of 3 meters.

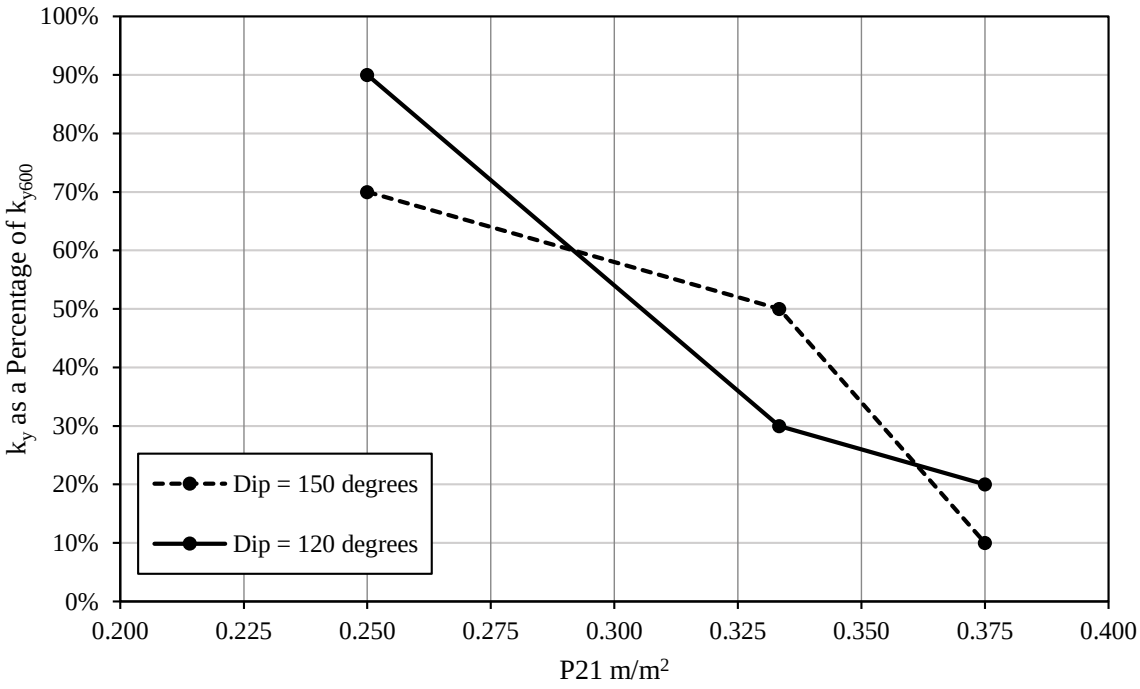

Figure 6.33: Pseudostatic yield accelerations k_y for slopes with non-persistent discontinuities, normalized to the yield acceleration of the homogeneous slope $k_{y,600}$, for dip slopes with variation in P21 with constant joint spacing of 3 meters.

6.4.2 Frequency Sweep Analysis

The results of the frequency sweep analysis on the homogeneous slope, slopes with persistent discontinuities, and slopes with non-persistent discontinuities are presented in the following sections.

Frequency Sweep Analysis of the Homogeneous Slope

A plot of the frequency response of Model 600, the homogeneous slope, is shown in Figure 6.34. The natural frequency is taken as the lowest frequency where the amplification peaks and the whole of the slope appears to experience some amplification – 14.2 Hz for this slope. Similar to the response of the 80-meter tall homogeneous slope from Chapter 5, the second mode of vibration, where only the crest is being amplified is visible at a frequency of approximately 1.7 times the natural frequency.

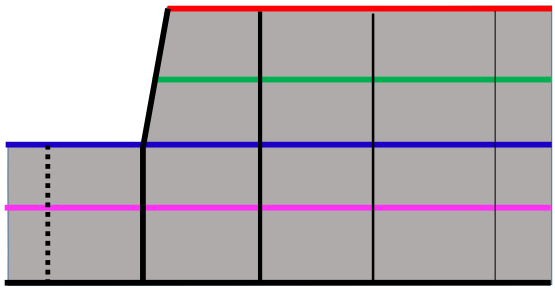

Graphical legend for monitored particles in BPM slopes. Line colors correspond to elevations and line widths and types correspond to position from the slope face.

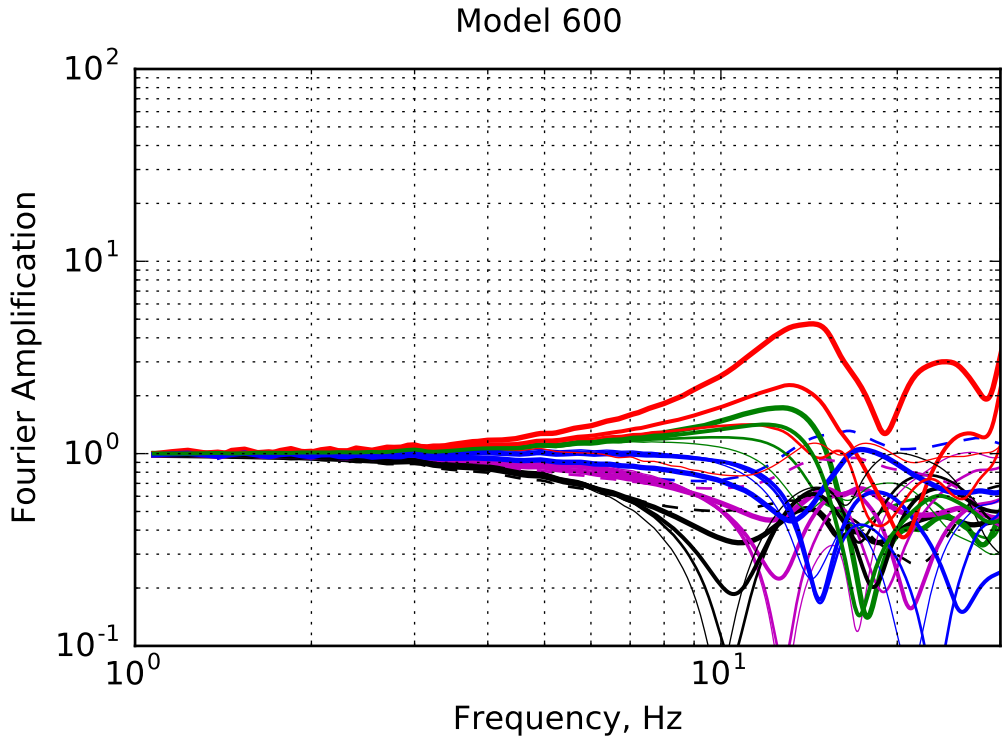

Figure 6.34: Frequency domain Fourier amplitude amplification of acceleration in Model 600 relative to base input from a 1 to 30 Hz frequency sweep. The first mode of the slope is at about 14 Hz with a second mode at around 24 Hz.

Frequency Sweep Analysis of Slopes with Persistent Discontinuities

An example of the frequency response of a slope (Slope 606) with persistent discontinuities is shown in Figure 6.35. Figures of the frequency response of the entire set of slopes with persistent discontinuities are provided in Appendix F. The results of the frequency sweep analysis on slopes with persistent discontinuities are presented in Table 6.8.

The natural frequency of the slopes is affected by the joint dip and the joint spacing. Joint spacing has a much more pronounced effect on the natural frequency than joint dip in the range of dips and spacing evaluated in this study. Figure 6.36 shows the variation in slope natural frequency with joint spacing for slopes with 60, 70, and 80 degree dips. Natural frequency varies from 0.5 Hz to 4.5 Hz roughly linearly with joint spacing increasing from 1 to 8 meters for the 80-degree dip slopes. Fewer slopes with dips of 60 and 70 degrees were generated for the parametric study, however, the trend in natural frequency with spacing for slopes with those dips for the range tested are consistent with the trend in slopes with 80-degree dips.

Figure 6.37 shows the variation in slope natural frequency with joint dip for slopes with 2-, 4-, and 6-meter joint spacing. The trend for slopes with 2-meter spacing shows a clear minimum at a dip of 80 degrees with a gentle increase in frequency for lower dips and a slightly steeper increase in frequency for dips higher than 80 degrees. Compared to the effect of joint spacing on natural frequency, the influence of dip is modest, varying only from 2 to 3 Hz for the 2-meter spacing slopes with dips from 20 to 110 degrees. The slopes of the 4- and 6-meter spacing slopes suggest that the influence of dip may increase with increasing spacing.

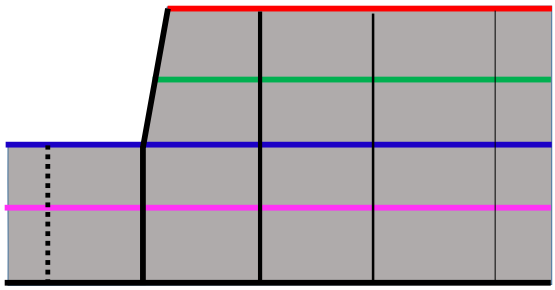

Graphical legend for monitored particles in BPM slopes. Line colors correspond to elevations and line widths and types correspond to position from the slope face.

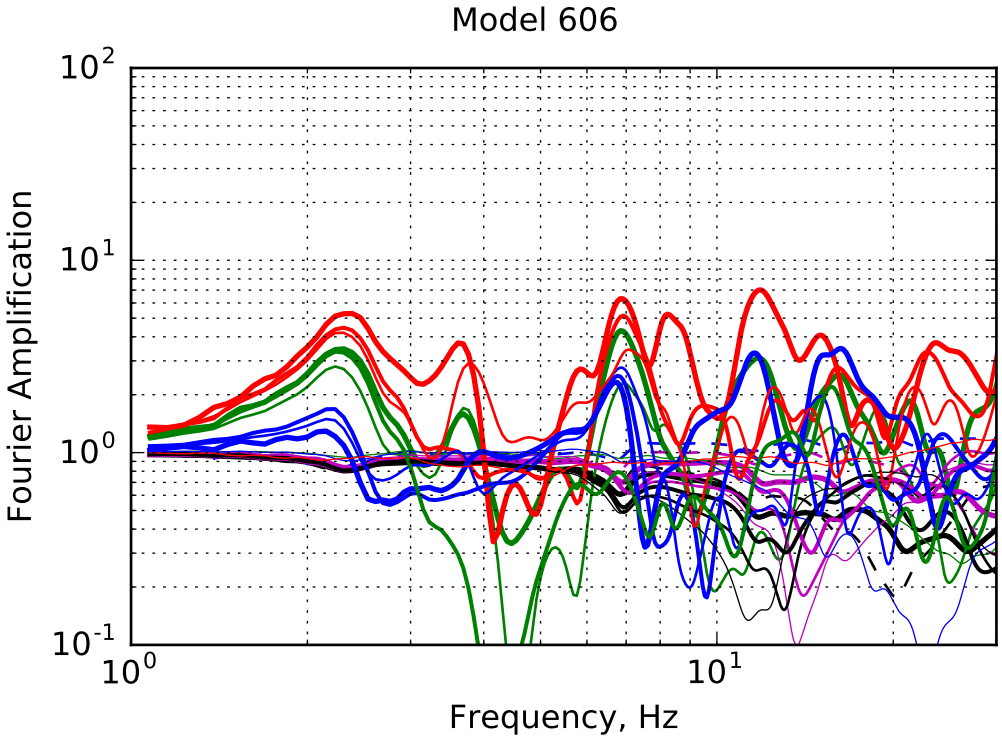

Figure 6.35: Frequency domain Fourier amplitude amplification of acceleration in Model 606 (joint spacing = 2 meters, dip = 60 degrees) relative to base input from a 1 to 30 Hz frequency sweep. The first mode of the slope is at about 2.3 Hz.

Table 6.8: Natural frequency for BPM slope models with persistent discontinuities.

Model	Discontinuity Spacing, m	Discontinuity Dip, degrees	Natural Frequency, Hz
601	2	20	2.9
602	2	30	2.85
603	2	40	2.7
604	2	45	2.6
605	2	50	2.5
606	2	60	2.3
607	2	70	2.1
608	2	80	2.0
609	2	90	2.1
610	2	100	2.6
611	1	80	0.5
613	3	80	2.7
614	4	80	2.8
615	5	80	3.0
616	6	80	3.4
617	7	80	4.0
618	8	80	4.4
619	1	70	1.7
620	4	70	3.2
621	6	70	3.9
622	1	60	1.7
623	4	60	3.4
624	6	60	4.4

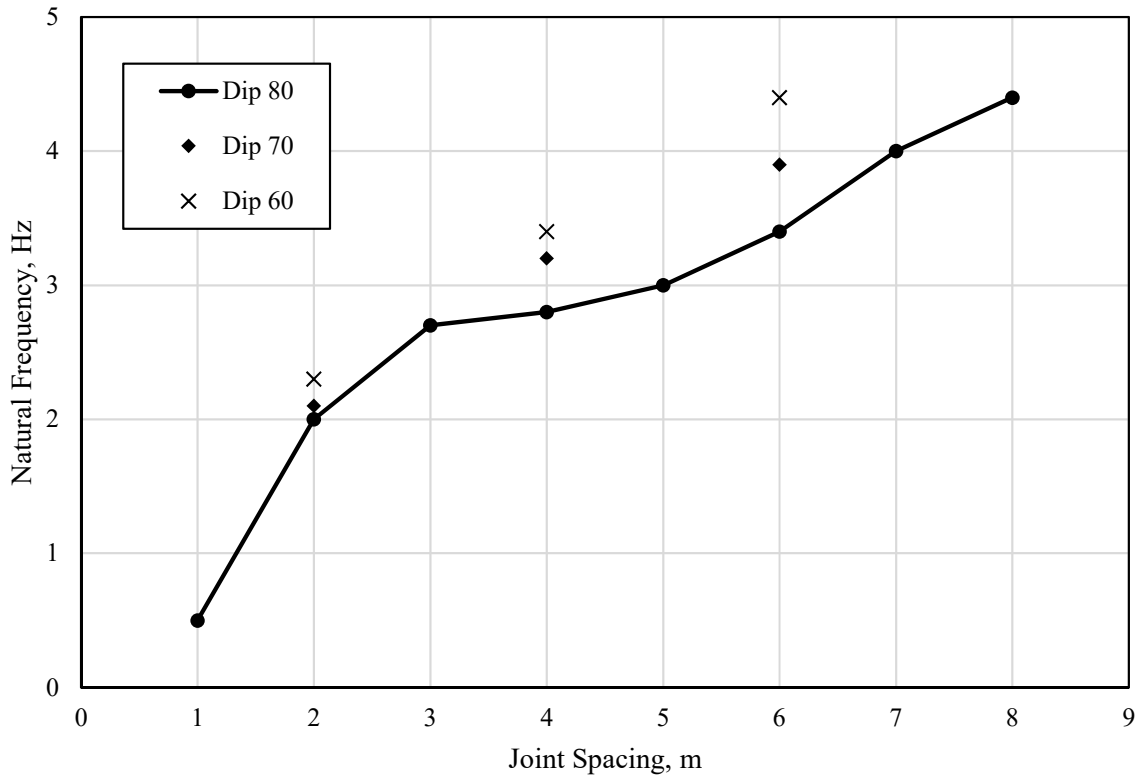

Figure 6.36: Variation in natural frequency with joint spacing for slopes with persistent joints and dips of 60, 70, and 80 degrees. The variation in natural frequency is roughly linearly with joint spacing increasing from 1 to 8 meters for the 80-degree dip slopes. The variation in natural frequency for joint spacing ranging from 2 to 6 meters for 60- and 70-degree dip slopes follows a similar trend.

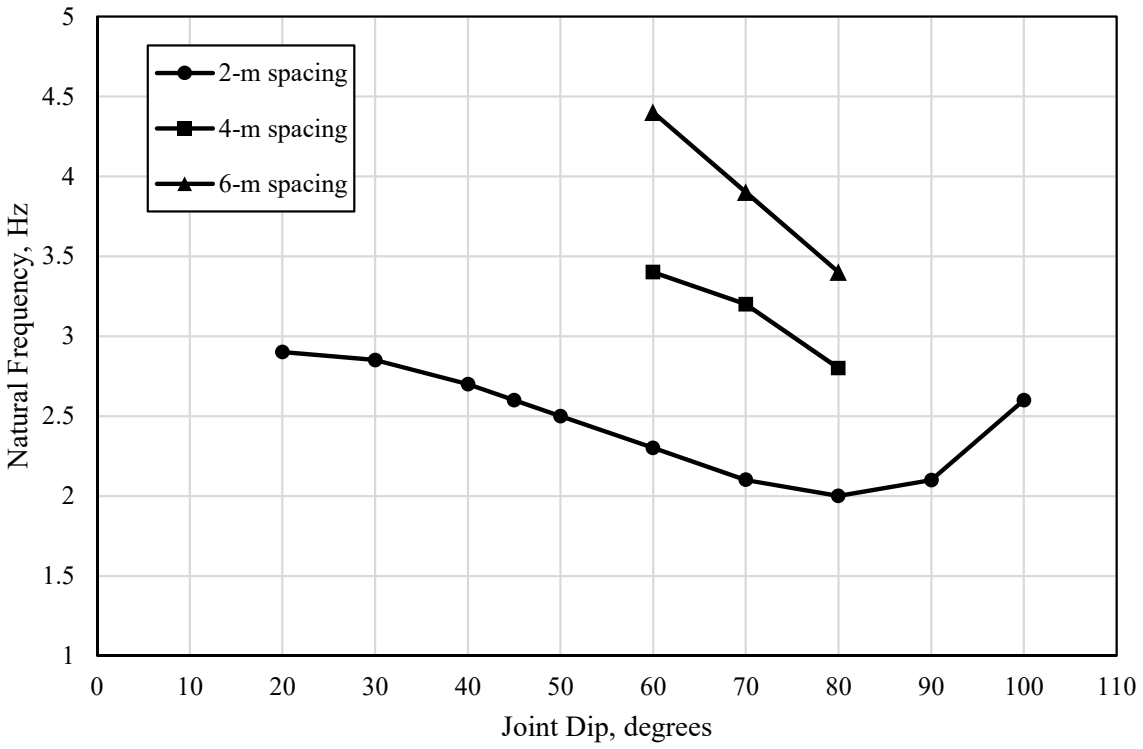

Figure 6.37: Variation in natural frequency with joint dip for slopes with persistent joints and joint spacing of 2, 4, and 6 meters. The minimum slope natural frequency occurs at dips of 80 degrees for slopes with 2-meter spacing and for slopes with 4- and 6-meter spacing in the range of dips tested.

Frequency Sweep Analysis of Slopes with Non-persistent Discontinuities

An example of the frequency response of a slope (Slope 650) with persistent non-discontinuities is shown in Figure 6.38. Figures of the frequency response of the entire set of slopes with non-persistent discontinuities are provided in Appendix XX. The results of the frequency sweep analysis on slopes with persistent discontinuities are presented in Table 6.9.

Table 6.9: Natural frequency for BPM slope models with non-persistent discontinuities.

Model	Joint Dip, degrees	Joint Intensity, m/m^2	Natural Frequency, Hz
643	0	0.25	9.8
644	0	0.333	7.5
645	0	0.375	6.7
646	30	0.25	9.1
647	30	0.333	6.2
648	30	0.375	5.1
649	60	0.25	10.5
650	60	0.333	7.2
651	60	0.375	5.9
652	90	0.25	9.9
653	90	0.333	7.4
654	90	0.375	6.2
655	120	0.25	9.7
656	120	0.333	6.4
657	120	0.375	5.5
658	150	0.25	9.4
659	150	0.333	6.3
660	150	0.375	5.1

The natural frequency of the slopes is affected by the joint dip and the joint intensity. Joint intensity has a much more pronounced effect on the natural frequency than joint dip

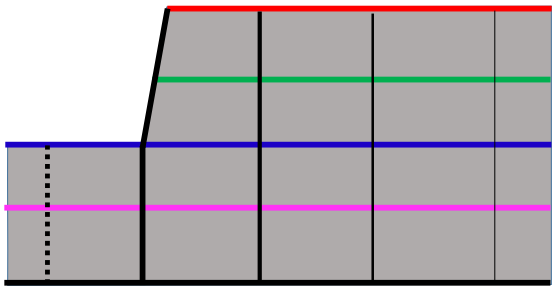

Graphical legend for monitored particles in BPM slopes. Line colors correspond to elevations and line widths and types correspond to position from the slope face.

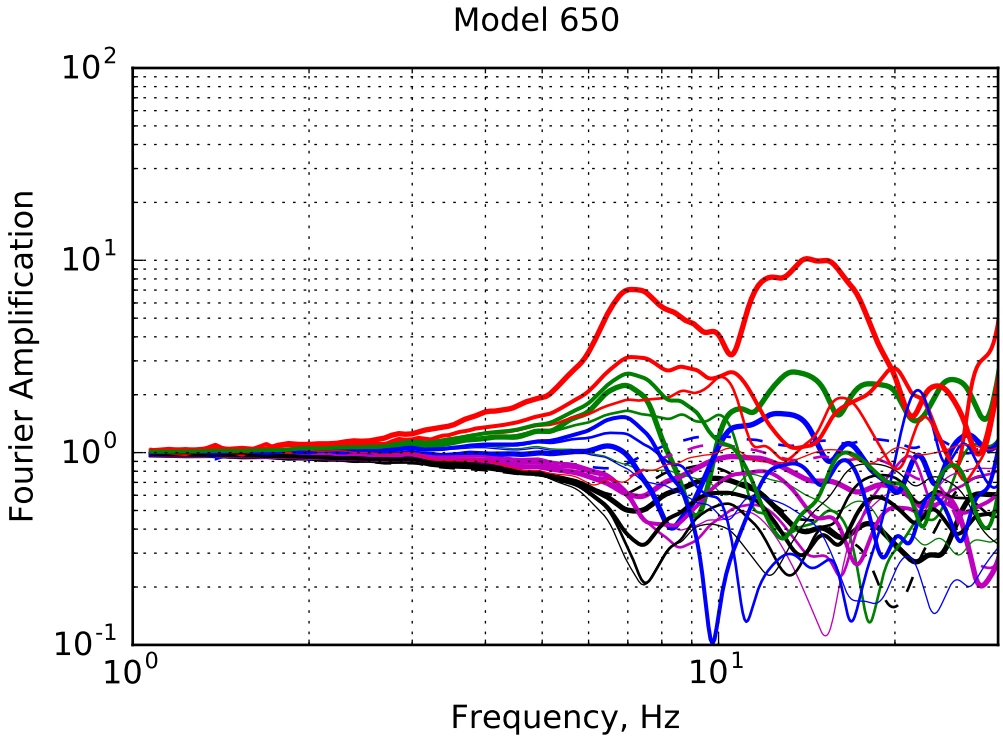

Figure 6.38: Frequency domain Fourier amplitude amplification of acceleration in Model 650 (dip = 60 degrees, P21 = 0.333) relative to base input from a 1 to 30 Hz frequency sweep. The first mode of the slope is at about 7.2 Hz.

in the range of dips and intensity evaluated in this study. Figure 6.39 shows the variation in slope natural frequency with joint intensity for multiple sets of slopes, including the homogeneous slope and some slopes with persistent joints as presented in the previous section. A second order polynomial fit to the slopes with non-persistent joints, slopes with persistent joints and the same joint spacing as the non-persistent joint set (2 meters), and the homogeneous slope is also shown. The polynomial fit shows a clear relationship between natural frequency and P21 for constant joint spacing, regardless of whether joints are persistent or non-persistent.

Figure 6.40 shows the variation in slope natural frequency with joint dip for slopes with P21 of 0.25, 0.333, and 0.375. Note that the data points at dip = 180 degrees are repetitions of the dip = 0 data points. The variation in natural frequency with joint dip is cyclic, with a slight asymmetry between dip and anti-dip slopes. The shape of the trend for P21 = 0.333 and 0.375 are nearly identical, while the trend for P21 = 0.25 is similar in shape, but the amplitude of the variation in natural frequency with dip is less. Compared to the effect of joint intensity on natural frequency, the influence of dip is modest, varying only about 1 Hz for a given joint intensity.

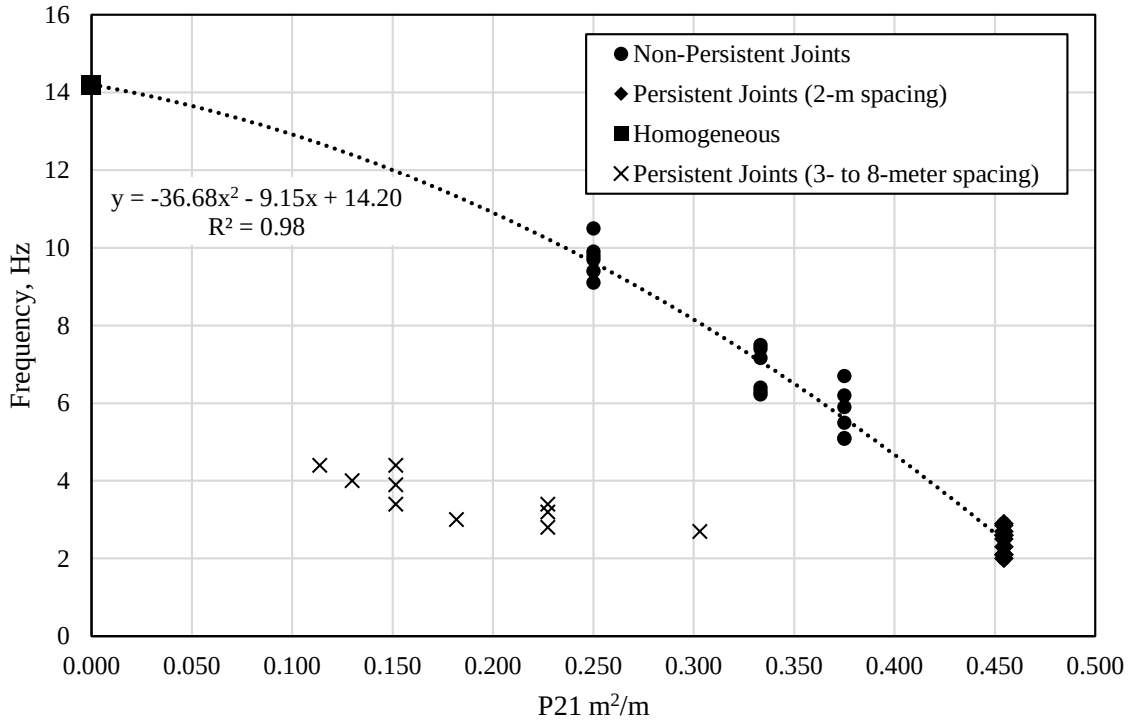

Figure 6.39: Variation in natural frequency with joint intensity. Slopes with non-persistent joints, as well as the homogeneous slope and slopes with persistent joints are shown. The polynomial fit to the homogeneous slope and slopes with 2-meter joint spacing shows a clear relationship between intensity and natural frequency for a given joint spacing, regardless of whether joints are persistent or non-persistent.

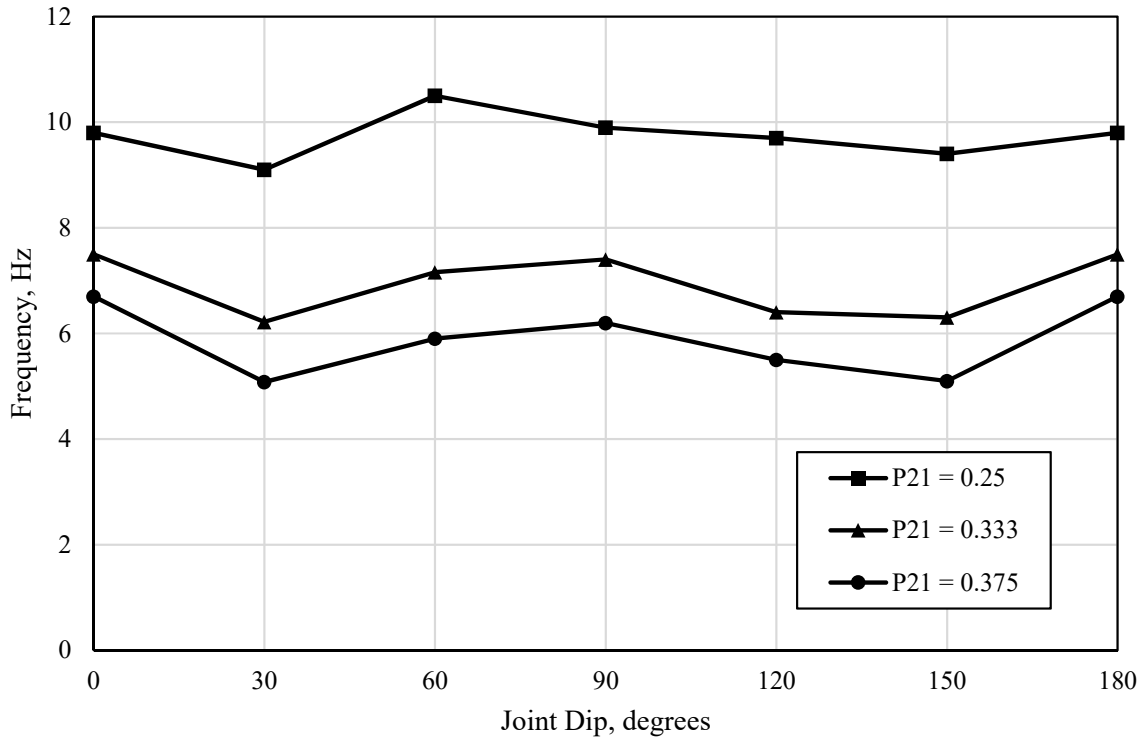

Figure 6.40: Variation in natural frequency with joint dip for slopes with non-persistent joints. The variation in natural frequency with joint dip is cyclic, with a slight asymmetry between dip and anti-dip slopes.

6.4.3 Dynamic Failure Analysis

The results of the dynamic failure simulations on the parametric slopes are presented in the following sections. For slopes with persistent and non-persistent discontinuities, a selection of model simulation images during different timesteps are presented to illustrate the observed failure mechanisms. For all slopes in the parametric study, plots of the number of cracks generated in the models relative to the peak input acceleration throughout the loading are presented.

Dynamic Failure Analysis of the Homogeneous Slope

When subjected to ramping amplitude harmonic loading of 5, 7, 9, and 11 Hz, Model 600 experienced varying levels of damage and showed varying levels of input acceleration required to initiate failure. Figure 6.41 shows the number of cracks generated in Model 600 with input acceleration for the loading frequencies applied. At any input acceleration on the x-axis, the curve with the highest number of cracks indicates which loading resulted in the most damage at the given level of input acceleration. Similarly, for any given number of cracks on the y-axis, the curve with the lowest input acceleration indicates which loading required the lowest level of shaking to induce the at level of damage. In other words, any given curve that plots above and/or to the left of another curve is a more critical loading case than the curves below and/or to the right. Figure 6.41 shows that loading frequencies closest to the natural frequency of the slope induced damage first. With continued increase in input acceleration, the lower frequency loadings of 5 and 7 Hz appear to become more critical. Recall, however, that the purpose of the parametric study is to evaluate the initiation of failure, rather than it's progression, and that by the end of the simulations, the input accelerations are extremely high. Although some inferences related to the model results at these high input accelerations will be made, the levels of damage by the end of the simulations can be severe, and their response may not be realistic.

When compared to the yield acceleration from the pseudostatic simulation (k_y = 5 g for Model 600), the PGA required to initiate failure, PGA_f, appears to be significantly lower than k_y for all frequencies. However, the initiation of dynamic failure is by a tensile

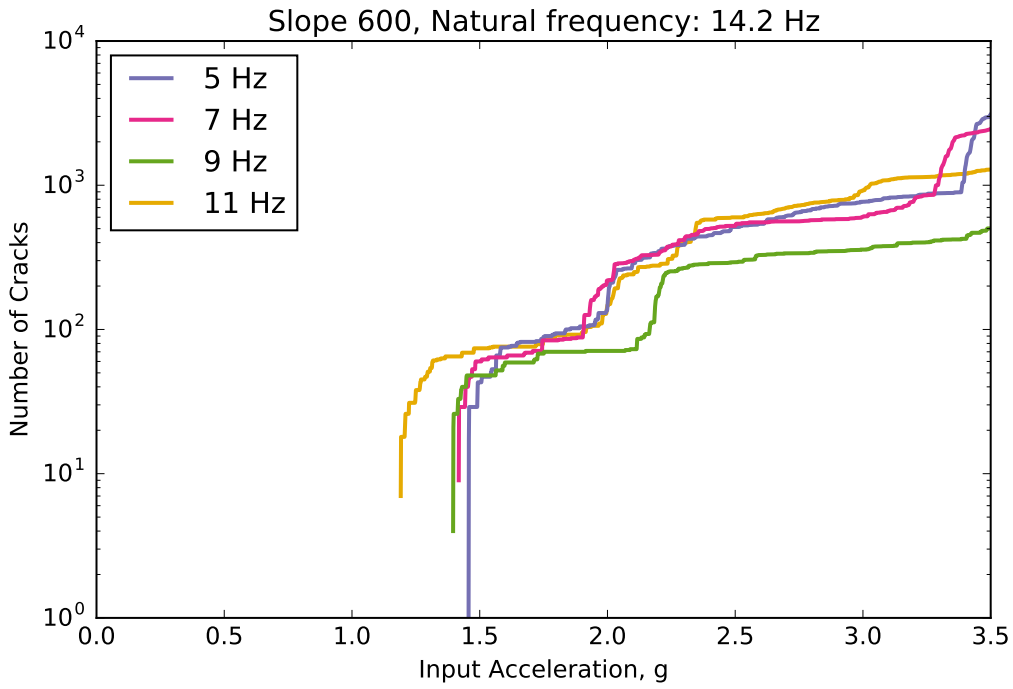

Figure 6.41: Number of cracks generated in Model 600 with input acceleration for multiple harmonic loading frequencies. Loading frequencies closest to the natural frequency initiate failure at the lowest levels of input acceleration.

crack initiating at the toe and diving into the model as shown in Figure 6.42. This failure mechanism was observed in some simulations in the previous Chapter 5 but to a lesser extent. The tensile crack that develops is deep and influences the behavior of the simulation in terms of wave propagation in ways that are not well-quantified. It appears that Model 600, which is at the extremes of strength, natural frequency, and levels of shaking at failure initiation, may be outside a reasonable range for evaluation as discussed in Section 6.2.

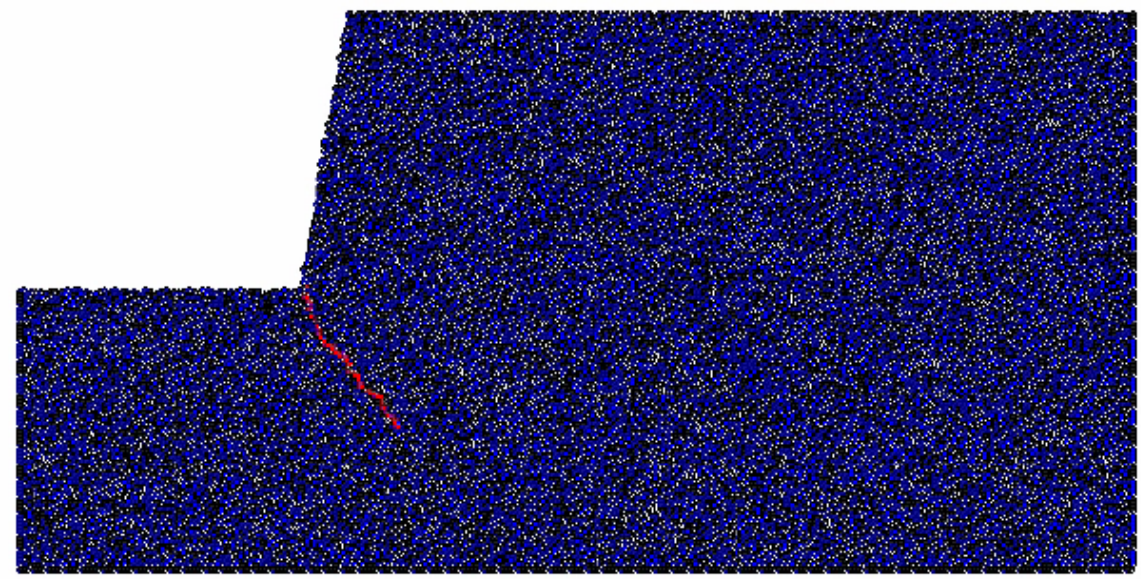

Figure 6.42: Image of the initiation of failure in Model 600 due to 5 Hz loading. The initial failure mechanism is a tensile crack that starts at the toe and dives deep into the model.

This section presents the results of the dynamic failure analysis from harmonic ground motions of various frequencies on rock-slopes with persistent discontinuities. Examples of two simulations involving Model 606 and 621 subjected to a 5 Hz harmonic input are presented to illustrate some of the behaviors observed in this set of simulations. The accumulation of damage in terms of the of cracks with input acceleration is shown for all models for all tested loading frequencies. Loading frequencies of 1, 3, 5, and 7 Hz were used in the dynamic analysis of models with persistent discontinuities because the natural frequencies for these slopes generally fall within that range.

Figure 6.43 shows the sequential failure of Model 606 subjected to a 5 Hz ramping amplitude harmonic input. The at-rest model in shown in Figure 6.43a. In Figure 6.43b, the influence of the dynamic loading can be seen in the force-chains in each column. Tensile forces on the upslope side of the columns and compressive forces on the downslope side of the columns indicate flexure. These flexural forces are concentrated near the lower portion of the slope near the face at this point in time. Some scattered damage near the crest of the slope is visible in this frame. As the input wave propagates upward, the flexure in the columns moves up and to the right, as shown in Figure 6.43c, where flexure is observed deeper and higher in the slope, and another wave is arriving at the toe. Some cracking at the top of the slope and the toe is also visible in Figure 6.43c. In Figure 6.43d, flexural failure has occurred from the toe of the slope, as observed in the previous frame, all the way to the top of the slope creating structurally-independent columnar blocks. The contrast in dynamics created by the newly formed flexural cracks across the pre-existing joints is evident in Figure 6.43e where the flexural forces are visible beneath the failure zone, but not above. The columnar blocks are beginning to topple over here and continue to topple in Figure 6.43f. Figure 6.43f also shows that a secondary flexural toppling failure has occurred beneath the original flexural toppling failure surface.

Figure 6.44 shows the sequential failure of Model 621 subjected to a 5 Hz ramping amplitude harmonic input. In Figure 6.44a, the flexure in the columns is evident by the tensile and compressive force-chain patterns. Failure initiates in a column due to tensile

failure in Figure 6.44b. In Figure 6.44c, another column, not adjacent to the first failed column fails. And in Figure 6.44d, the column between these two has failed in a location offset from the plane created by the cracks on the adjacent columns. Scattered damage at the top and crest of the slope is also visible. Figure 6.44f shows that a cross-joint shearing failure has also occurred, and the material experiencing the most displacement appears to be due to this cross-joint shearing, rather than the deeper cracks. This final slope frame shows a failure mode less like the flexural toppling observed in Model 606 and more like a wedge failure were a relatively shallow wedge of rock material may slide from the slope face.

Figures 6.45 through 6.67 show the accumulation of damage in terms of number of cracks with input acceleration is shown for all models for all tested loading frequencies. At any input acceleration on the x-axis, the curve with the highest number of cracks indicates which loading resulted in the most damage at the given level of input acceleration. Similarly, for any given number of cracks on the y-axis, the curve with the lowest input acceleration indicates which loading required the lowest level of shaking to induce the given level of damage. In other words, any given curve that plots above and/or to the left of another curve is a more critical loading case than the curves below and/or to the right. The relative positions of the lines, particularly at the initiation of damage in the models, indicates the manner, if any, that frequency content is affecting the dynamic stability of the model. Wider spacing between the curves indicates a greater effect of frequency content.

The figures show two characteristic frequency-related behaviors for slopes with persistent discontinuities: either 1) the slope is more susceptible to damage due to lower frequency inputs, or 2) the slope is more susceptible to damage due to inputs whose frequency is closest to the slope natural frequency. Slopes that were more susceptible to lower frequency inputs, regardless of their natural frequencies are slopes that failed in flexural toppling like the Model 606 failure illustrated in Figure 6.43. Slopes that were sensitive to tuning ratio were either slopes with shallow dips that stable against flexural toppling according to the Goodman and Bray kinematic restriction, or slopes with very wide joint spacing. As with structural columns, the wide rock columns associated with wide joint spacing experience shear failure, rather than flexural failure. Whether because of the width of columns or the shallow dip of the joints, models with persistent discontinuities that failed in shear showed

some sensitivity to tuning ratio. Slopes that failed in a flexural toppling manner showed sensitivity to low frequencies. This result is consistent with the analysis of single toppling blocks under dynamic loading by Gibson (2015) [104]. Gibson showed that as the length of time that a block is subjected to dynamic loading increases, the more likely it is to topple.

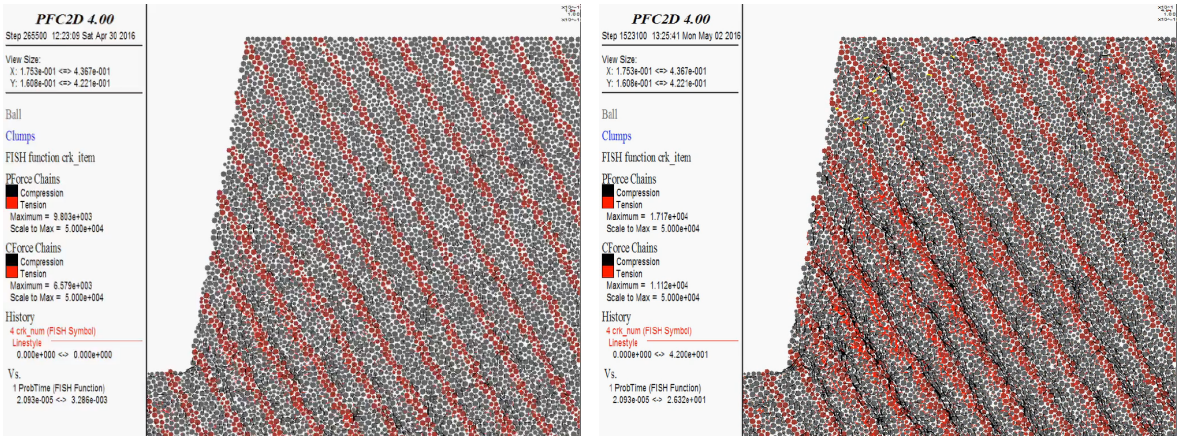

(a) **(b)**

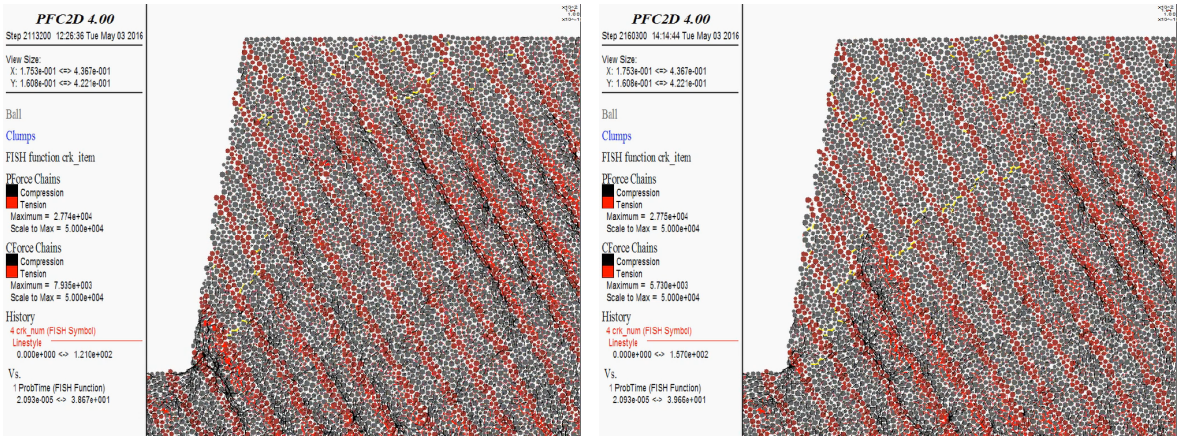

(c) **(d)**

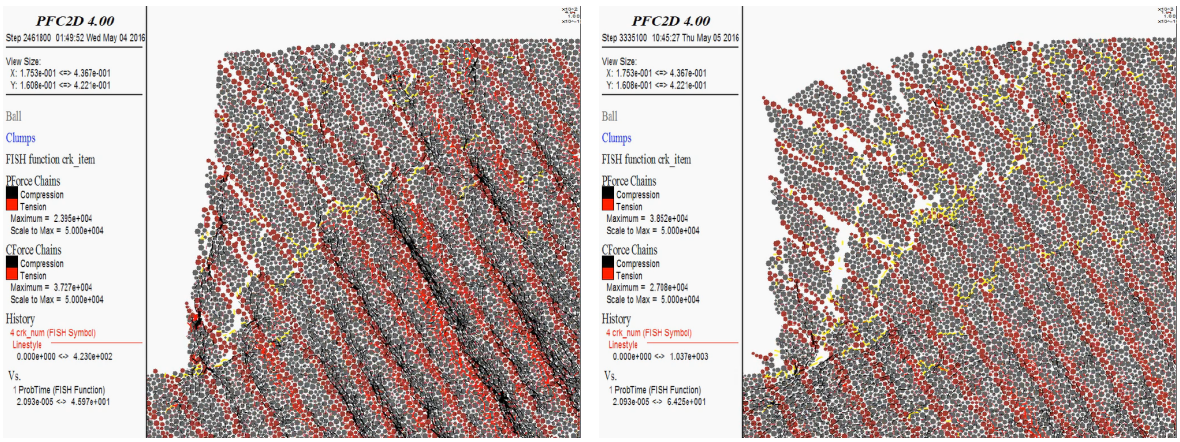

(e) **(f)**

Figure 6.43: Failure sequence of Model 606 subjected to a 5 Hz loading.

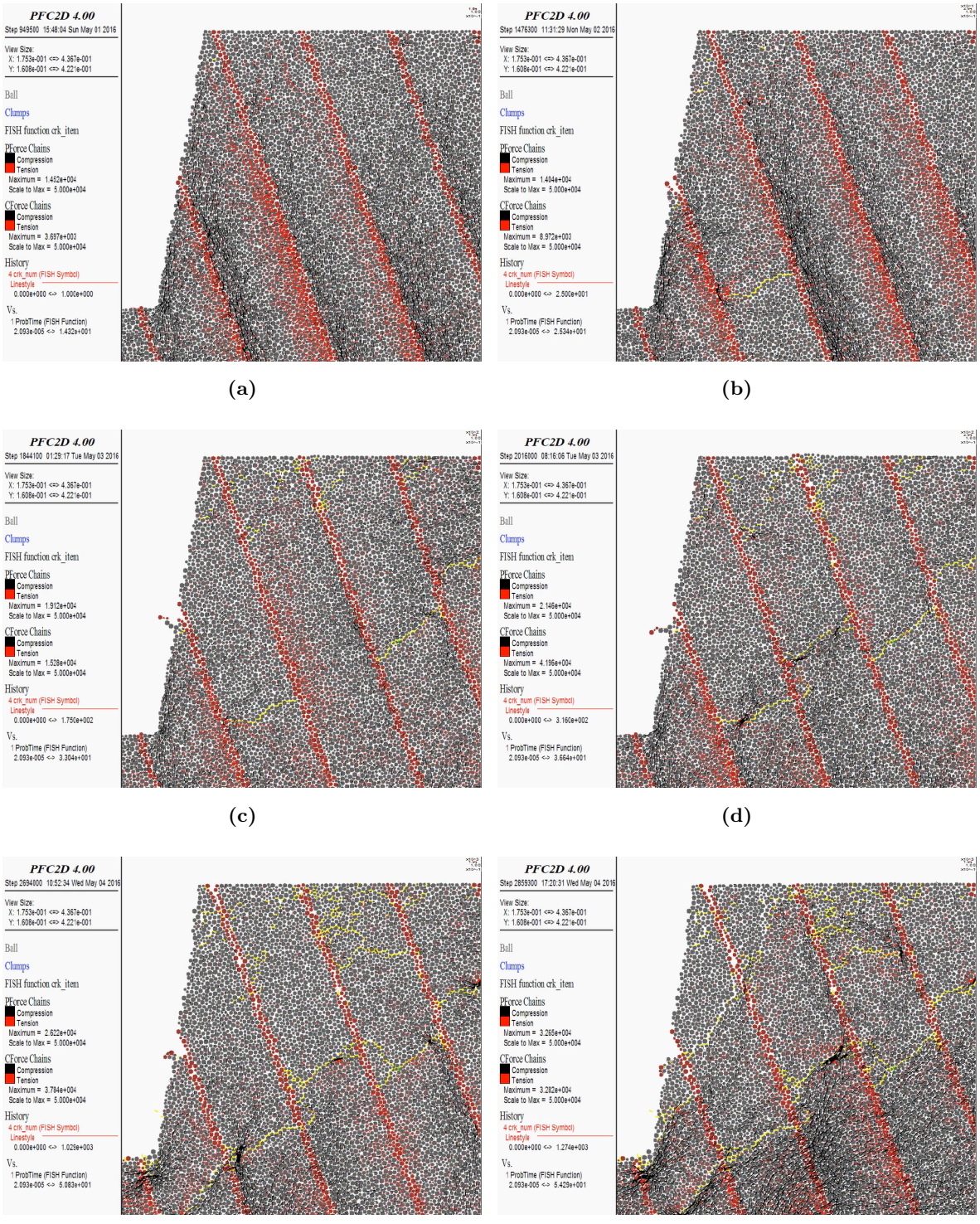

Figure 6.44: Failure sequence of Model 621 subjected to a 5 Hz loading.

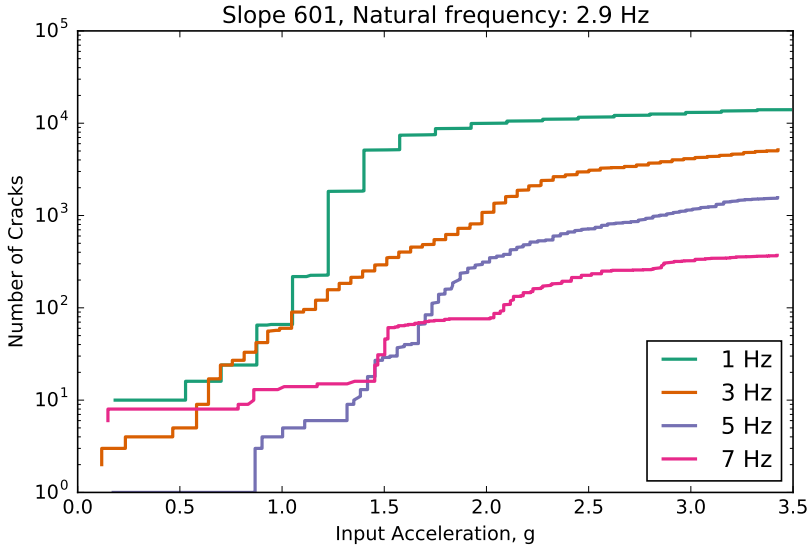

Figure 6.45: Number of cracks generated in Model 601 with input acceleration for multiple harmonic loading frequencies. The slightly more critical signature of the 3 Hz curve at failure initiation indicates a mild tuning ratio effect on dynamic stability.

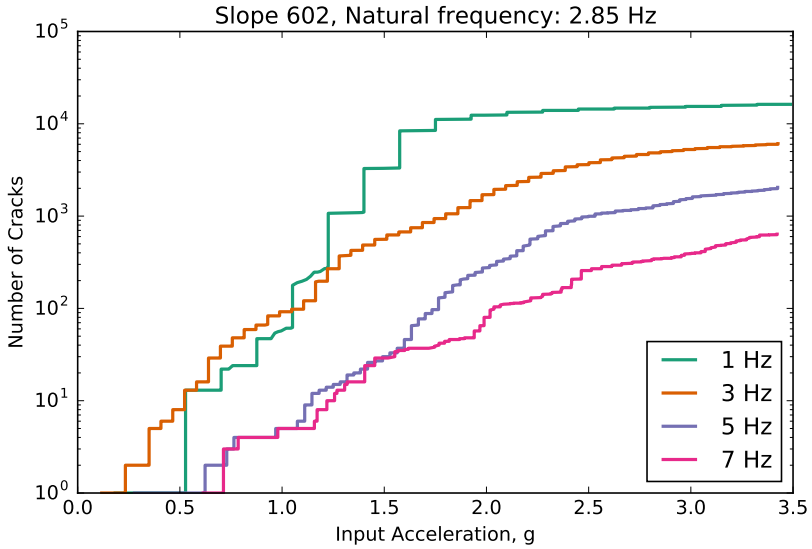

Figure 6.46: Number of cracks generated in Model 602 with input acceleration for multiple harmonic loading frequencies. The position of the 3 Hz curve as most critical up to input acceleration of about 1.0 g indicates a tuning ratio effect on dynamic stability.

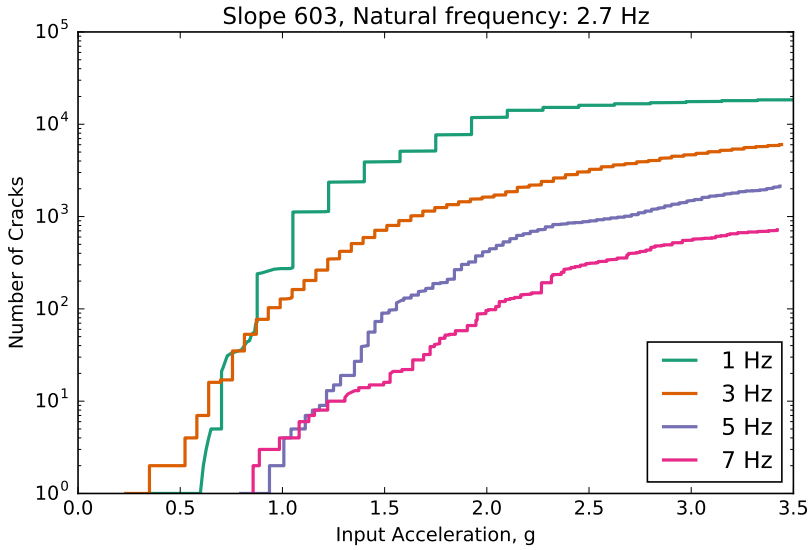

Figure 6.47: Number of cracks generated in Model 603 with input acceleration for multiple harmonic loading frequencies. The position of the 3 Hz curve as most critical up to input acceleration of about 0.7 g indicates a tuning ratio effect on dynamic stability.

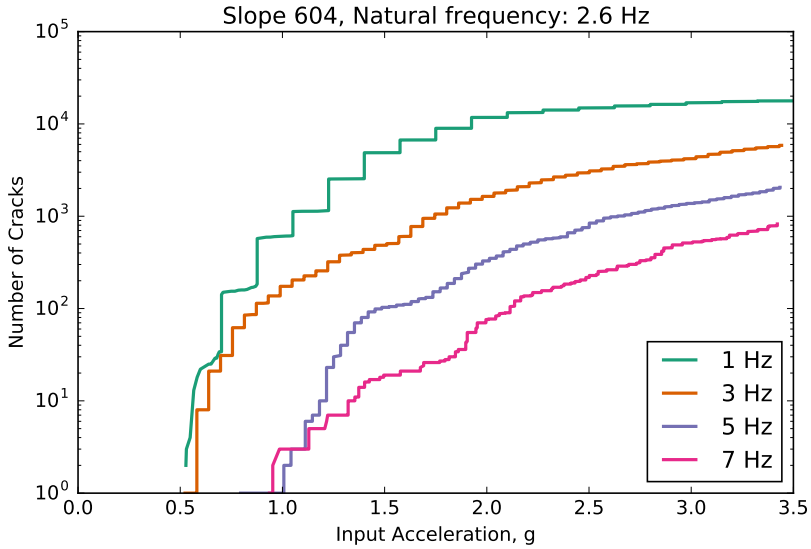

Figure 6.48: Number of cracks generated in Model 604 with input acceleration for multiple harmonic loading frequencies. The position of the 1 Hz curve as most critical over the entire simulation indicates no tuning ratio effect on dynamic stability. The order of the curves indicates that lower loading frequencies are uniformly more critical than higher loading frequencies.

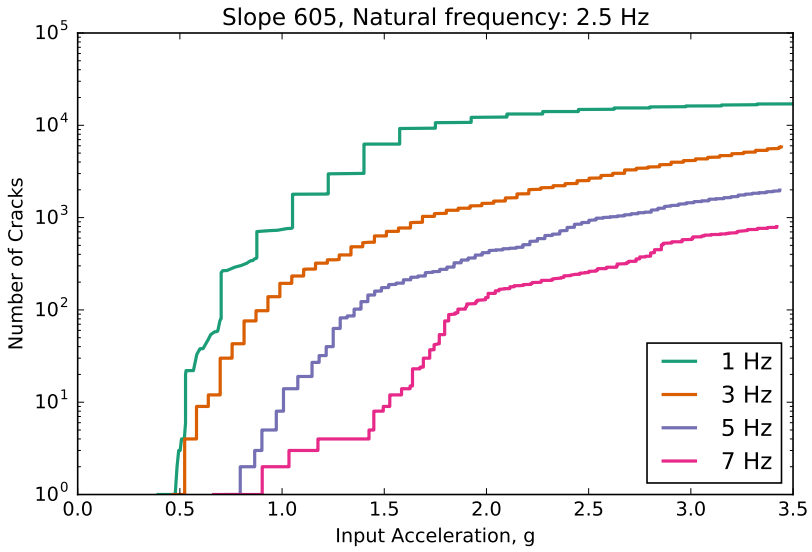

Figure 6.49: Number of cracks generated in Model 605 with input acceleration for multiple harmonic loading frequencies. The position of the 1 Hz curve as most critical over the entire simulation indicates no tuning ratio effect on dynamic stability. The order of the curves indicates that lower loading frequencies are uniformly more critical than higher loading frequencies.

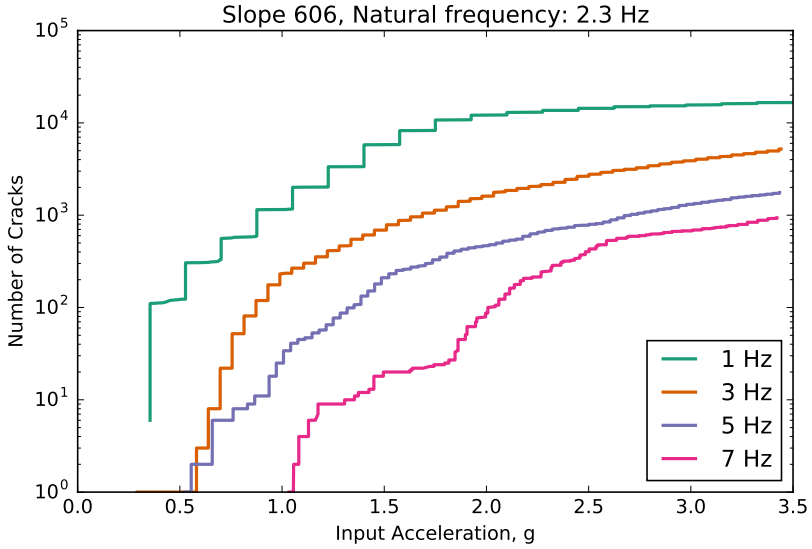

Figure 6.50: Number of cracks generated in Model 606 with input acceleration for multiple harmonic loading frequencies. The position of the 1 Hz curve as most critical over the entire simulation indicates no tuning ratio effect on dynamic stability. The order of the curves indicates that lower loading frequencies are uniformly more critical than higher loading frequencies.

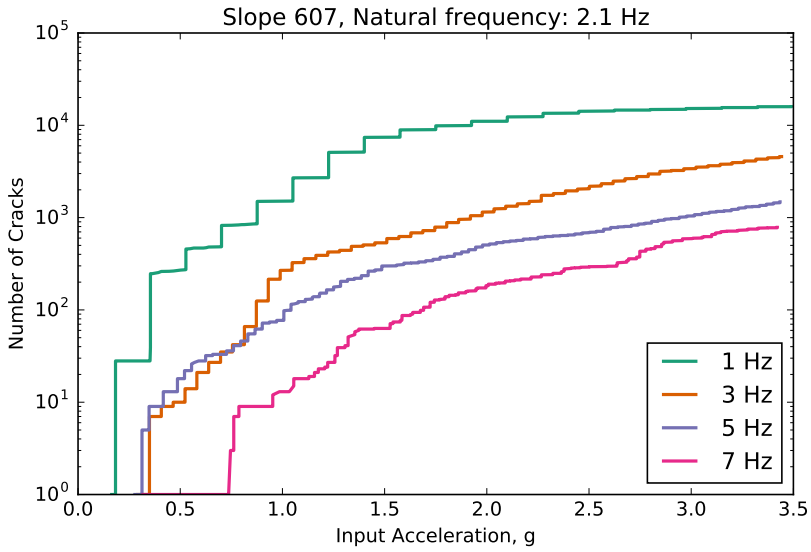

Figure 6.51: Number of cracks generated in Model 607 with input acceleration for multiple harmonic loading frequencies. The position of the 1 Hz curve as most critical over the entire simulation indicates no tuning ratio effect on dynamic stability. The order of the curves indicates that lower loading frequencies are nearly uniformly more critical than higher loading frequencies.

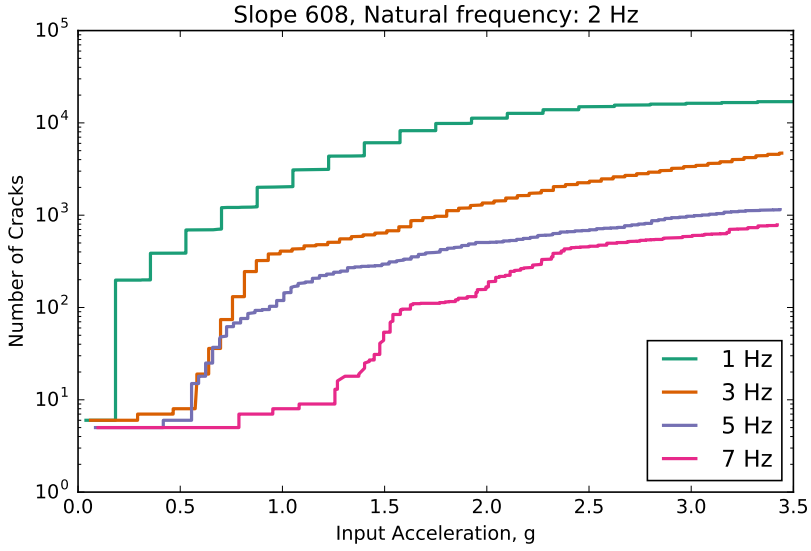

Figure 6.52: Number of cracks generated in Model 608 with input acceleration for multiple harmonic loading frequencies.The position of the 1 Hz curve as most critical over the entire simulation indicates no tuning ratio effect on dynamic stability. The order of the curves indicates that lower loading frequencies are nearly uniformly more critical than higher loading frequencies.

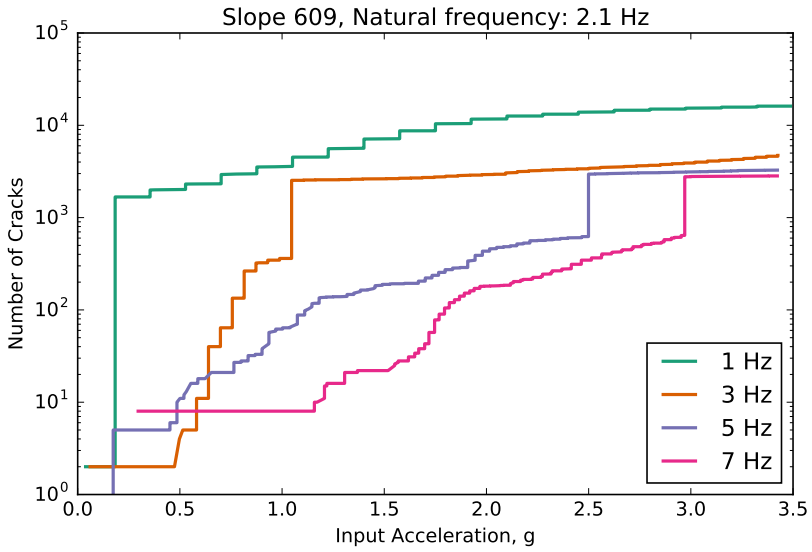

Figure 6.53: Number of cracks generated in Model 609 with input acceleration for multiple harmonic loading frequencies.The position of the 1 Hz curve as most critical over the entire simulation indicates no tuning ratio effect on dynamic stability. The order of the curves indicates that lower loading frequencies are nearly uniformly more critical than higher loading frequencies.

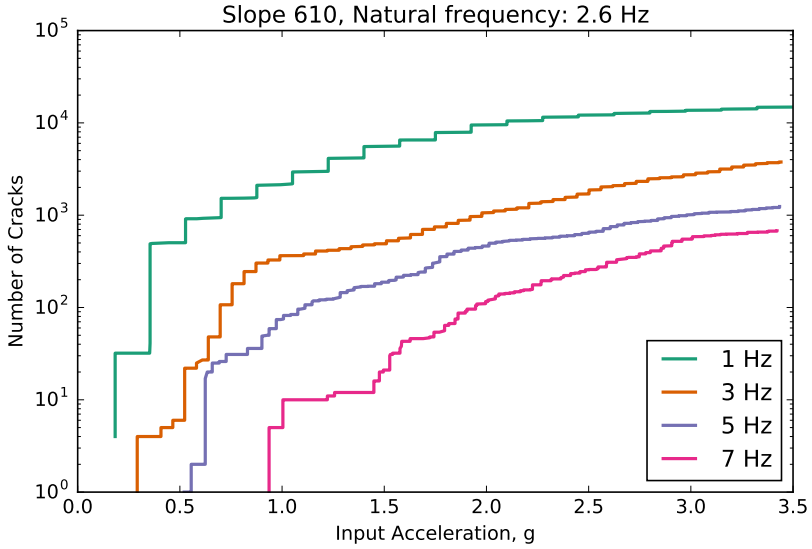

Figure 6.54: Number of cracks generated in Model 610 with input acceleration for multiple harmonic loading frequencies. The position of the 1 Hz curve as most critical over the entire simulation indicates no tuning ratio effect on dynamic stability. The order of the curves indicates that lower loading frequencies are uniformly more critical than higher loading frequencies.

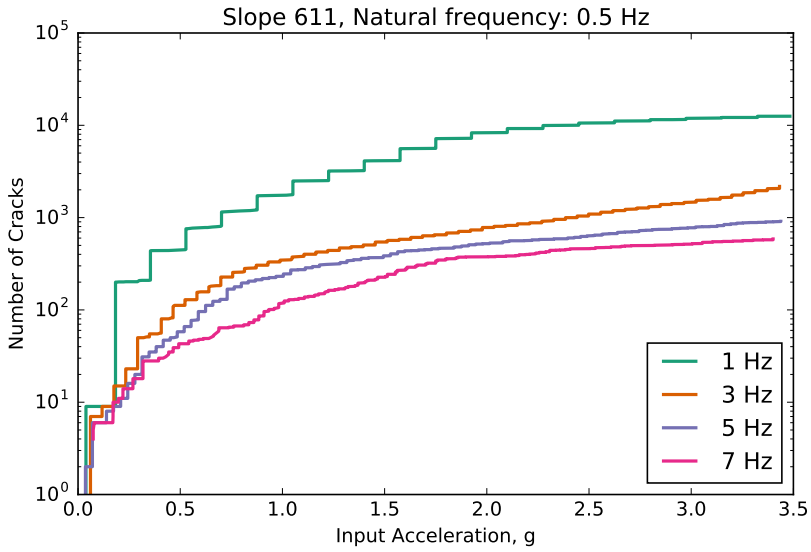

Figure 6.55: Number of cracks generated in Model 611 with input acceleration for multiple harmonic loading frequencies. The position of the 1 Hz curve as most critical over the entire simulation indicates no tuning ratio effect on dynamic stability. The order of the curves indicates that lower loading frequencies are nearly uniformly more critical than higher loading frequencies.

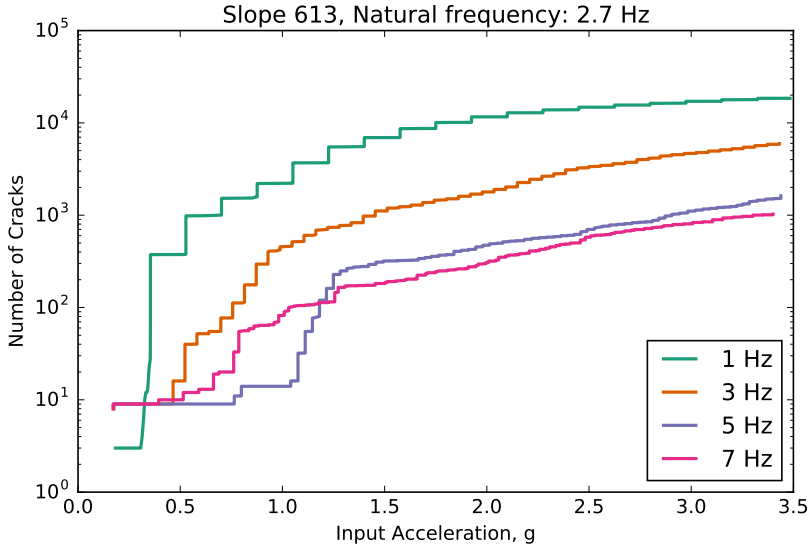

Figure 6.56: Number of cracks generated in Model 613 with input acceleration for multiple harmonic loading frequencies. The position of the 1 Hz curve as most critical over the entire simulation indicates no tuning ratio effect on dynamic stability. The order of the curves indicates that lower loading frequencies are nearly uniformly more critical than higher loading frequencies.

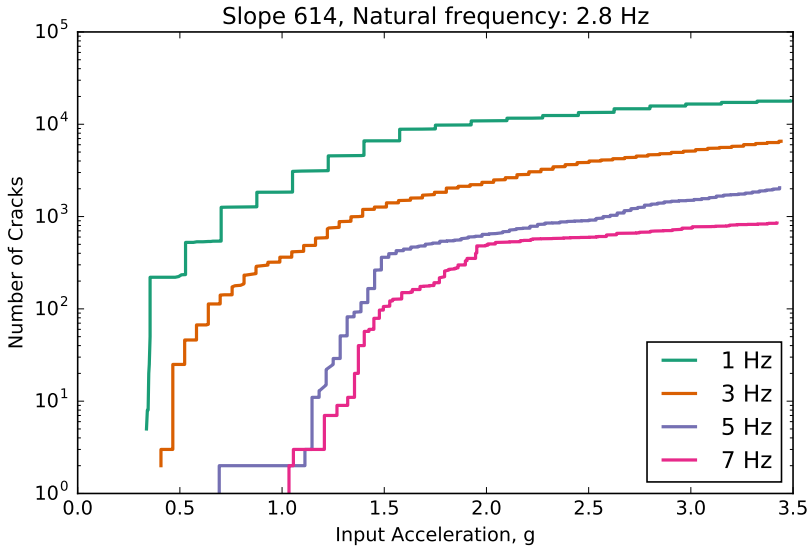

Figure 6.57: Number of cracks generated in Model 614 with input acceleration for multiple harmonic loading frequencies.The position of the 1 Hz curve as most critical over the entire simulation indicates no tuning ratio effect on dynamic stability. The order of the curves indicates that lower loading frequencies are nearly uniformly more critical than higher loading frequencies.

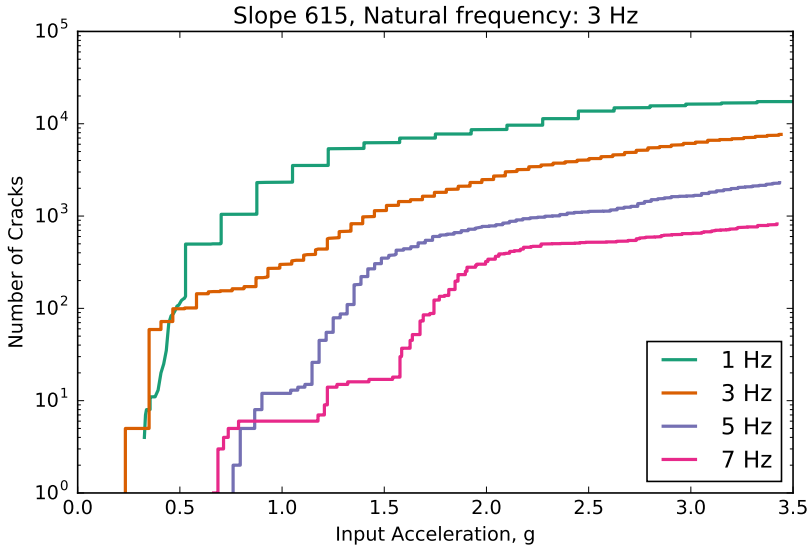

Figure 6.58: Number of cracks generated in Model 615 with input acceleration for multiple harmonic loading frequencies. The slightly more critical signature of the 3 Hz curve at failure initiation indicates a mild tuning ratio effect on dynamic stability.

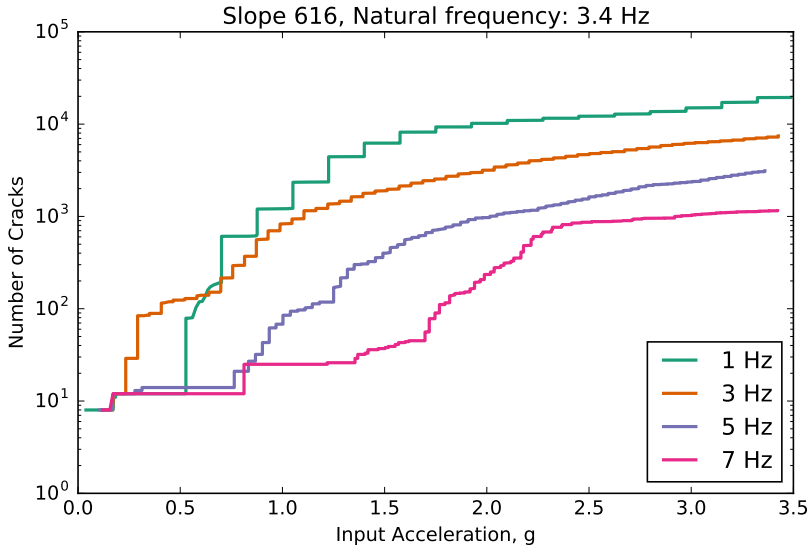

Figure 6.59: Number of cracks generated in Model 616 with input acceleration for multiple harmonic loading frequencies.

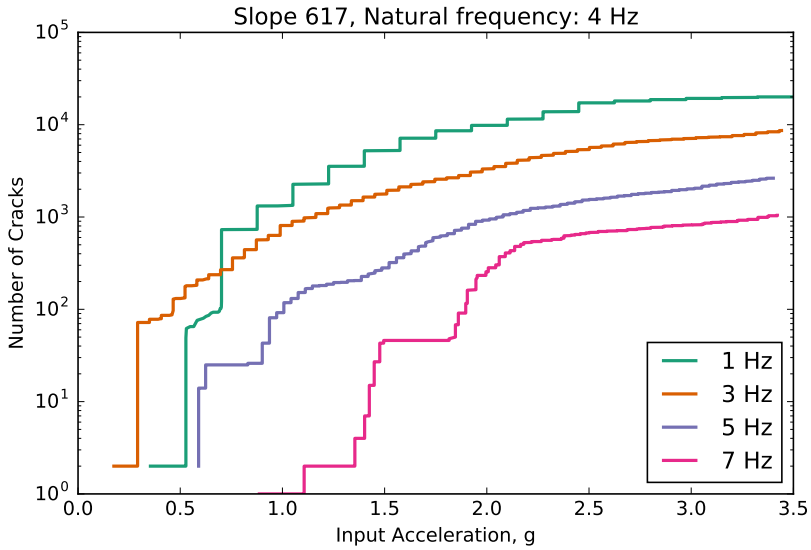

Figure 6.60: Number of cracks generated in Model 617 with input acceleration for multiple harmonic loading frequencies.

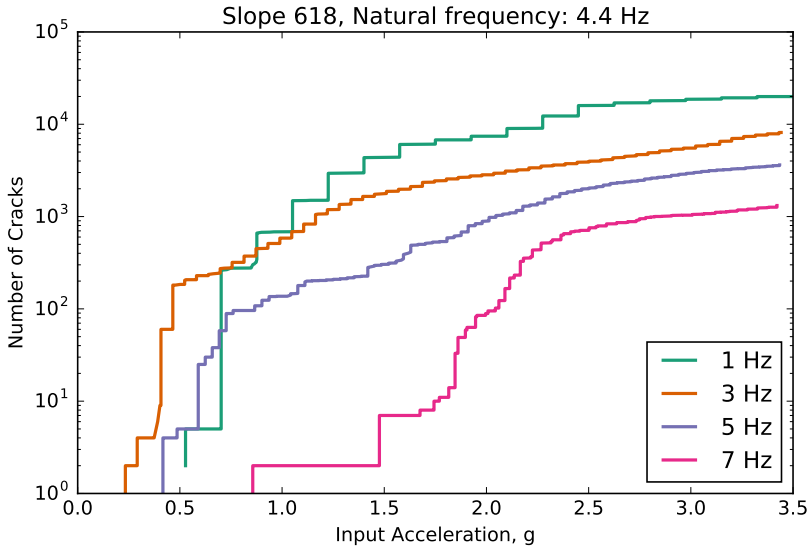

Figure 6.61: Number of cracks generated in Model 618 with input acceleration for multiple harmonic loading frequencies. The position of the 3 Hz curve as most critical up to input acceleration of about 0.8 g indicates a tuning ratio effect on dynamic stability.

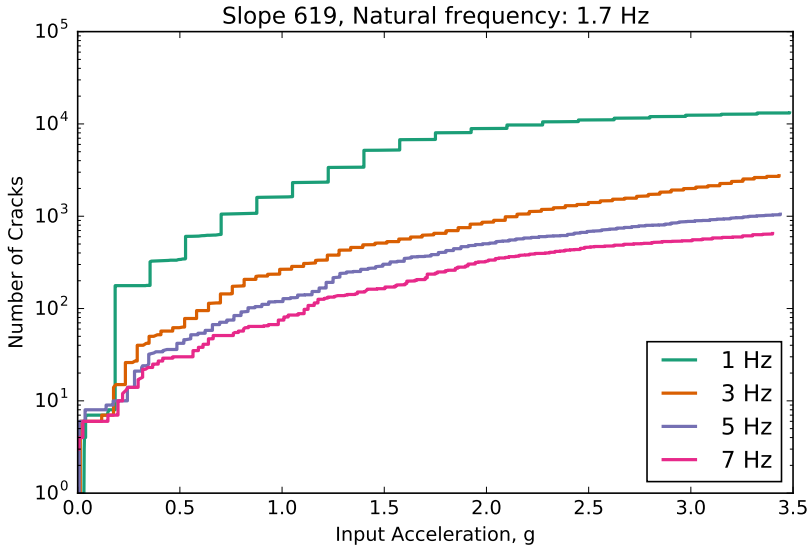

Figure 6.62: Number of cracks generated in Model 619 with input acceleration for multiple harmonic loading frequencies. The position of the 1 Hz curve as most critical over the entire simulation indicates no tuning ratio effect on dynamic stability. The order of the curves indicates that lower loading frequencies are nearly uniformly more critical than higher loading frequencies.

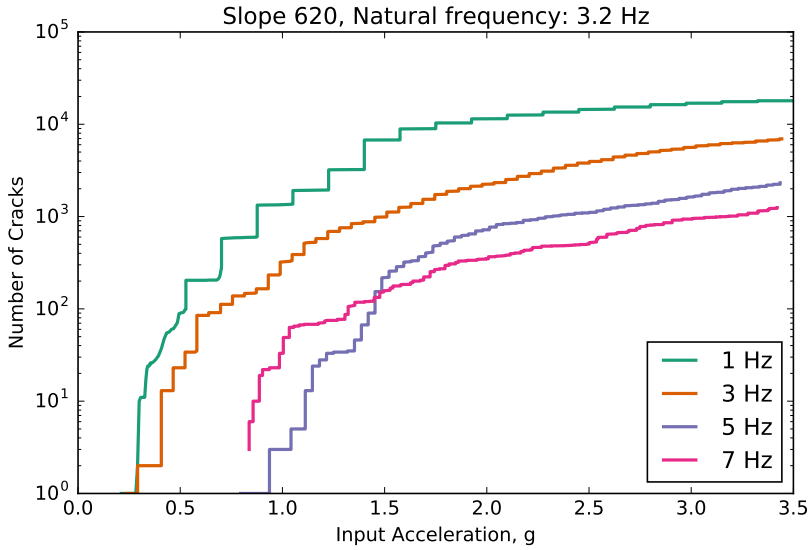

Figure 6.63: Number of cracks generated in Model 620 with input acceleration for multiple harmonic loading frequencies. The position of the 1 Hz curve as most critical over the entire simulation indicates no tuning ratio effect on dynamic stability. The order of the curves indicates that lower loading frequencies are nearly uniformly more critical than higher loading frequencies.

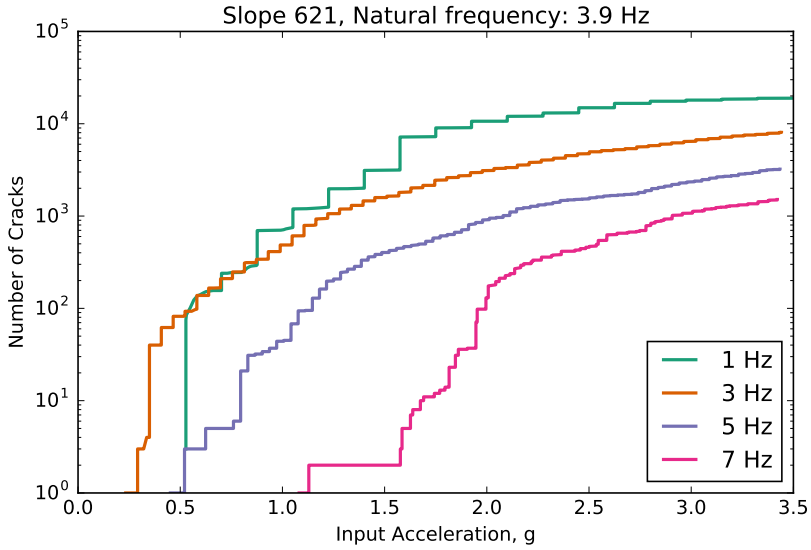

Figure 6.64: Number of cracks generated in Model 621 with input acceleration for multiple harmonic loading frequencies. The position of the 3 Hz curve as most critical up to input acceleration of about 0.5 g indicates a tuning ratio effect on dynamic stability.

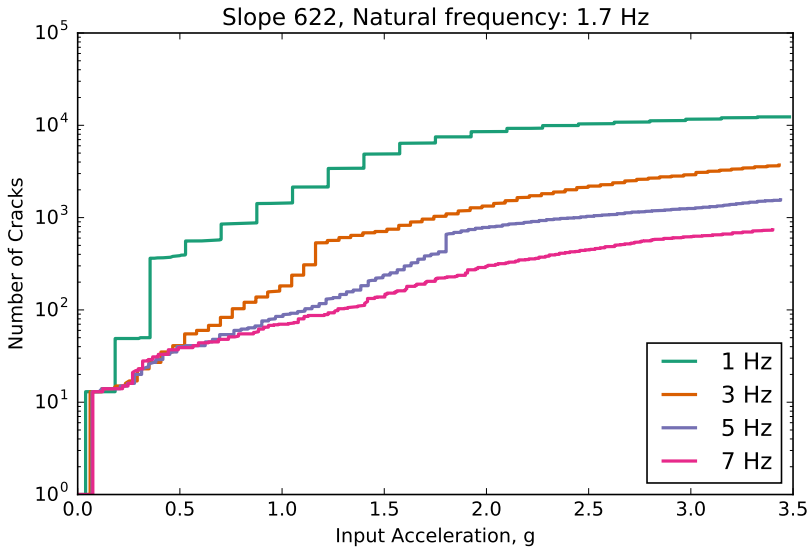

Figure 6.65: Number of cracks generated in Model 622 with input acceleration for multiple harmonic loading frequencies. The position of the 1 Hz curve as most critical over the entire simulation indicates no tuning ratio effect on dynamic stability. The order of the curves indicates that lower loading frequencies are nearly uniformly more critical than higher loading frequencies.

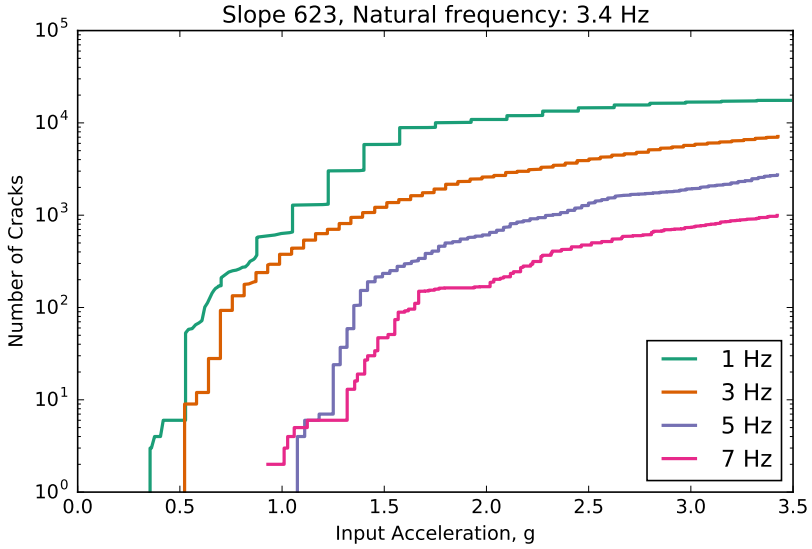

Figure 6.66: Number of cracks generated in Model 623 with input acceleration for multiple harmonic loading frequencies. The position of the 1 Hz curve as most critical over the entire simulation indicates no tuning ratio effect on dynamic stability. The order of the curves indicates that lower loading frequencies are nearly uniformly more critical than higher loading frequencies.

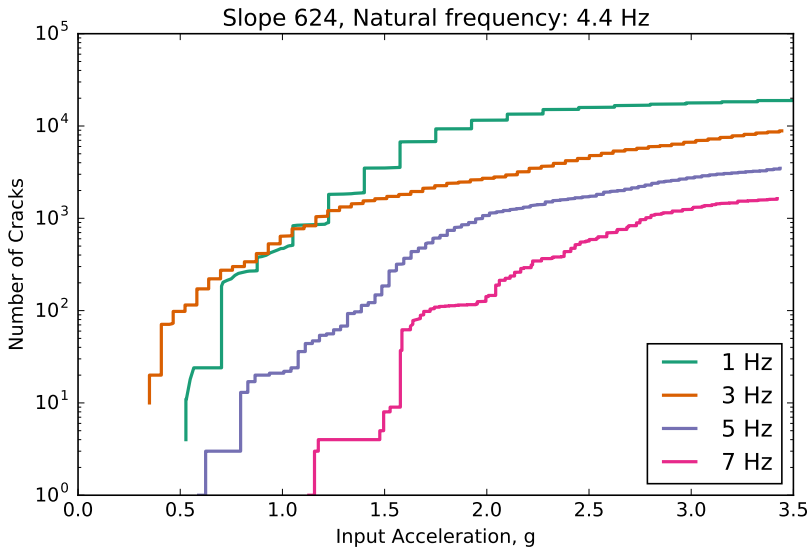

Figure 6.67: Number of cracks generated in Model 624 with input acceleration for multiple harmonic loading frequencies. The position of the 3 Hz curve as most critical up to input acceleration of about 1.2 g indicates a tuning ratio effect on dynamic stability.

Summary of the Dynamic Failure Analysis of Slopes with Persistent Discontinuities

The preceding results, particularly the sensitivity of the slopes with persistent joints to frequency content can be summarized as follows: Slopes that had dips between 45 and 110 degrees and joint spacing of up to 4 meters exhibited no sensitivity to tuning ratio and were nearly uniformly more sensitive to lower frequency input than higher frequency input. Slopes that were kinematically restricted from flexural toppling or had joint spacing greater than 4 meters exhibit sensitivity to tuning ratio. The type of frequency effect (either low frequency or tuning ratio) and the qualitative level of sensitivity to frequency are presented in Table 6.10. The qualitative assessment of sensitivity to frequency content is based on visual inspection of Figures 6.45 through 6.67. The relative spacing between the curves of number of cracks with input acceleration for different frequencies provides an indication of the sensitivity to frequency content. The curves are assessed at the initiation of fracturing in the slope. Sensitivity levels are given the following levels: slight, mild, moderate, and strong.

The minimum PGA to initiate failure, PGA_f, and the ratio of PGA_f to the pseudostatic yield for the slope, k_y, are also presented in Table 6.10. Multiple definitions of 'initiation of failure', from the breaking of the first bond, to the development of complete failure surface, are possible. Based on observations of the failure sequences (as shown in Figures 6.43 and 6.44), a threshold of 10 cracks (i.e., 10 broken bonds) was selected as the initiation of failure. At ten broken bonds, the slopes typically were observed to have a sufficient level of damage in the models to either form discrete blocks or indicate the beginning of a failure surface.

PGA_f for a range of joint spacings for slopes, with dips of 60, 70, and 80 degrees, are shown in Figure 6.68. No clear trend of increased PGA_f with increased joint spacing is observed. The relative difference between this behavior and the pseudostatic behavior of these slopes as shown in Figure 6.29, where the increase in resistance to failure with increasing spacing was very clear, is a subject for future research. It is suspected that the impacts associated with opening and closing of joints during cyclic loading are playing a role in this change in behavior.

The effect of joint dip on PGA_f is shown in Figure 6.69. The pseudostatic k_y is also

shown on the figure for comparison. Both pseudostatic and dynamic analyses have clear minima at steep dip angles – 90 degrees in the pseudostatic case and 80 degrees in the dynamic case. At the static kinematic flexure limit from Goodman and Bray, both trends show a maximum, but the dynamic maximum is significantly lower than the pseudostatic maximum. The relative shape of the pseudostatic and dynamic failure trends indicate that a pseudostatic analysis can provide a good approximation of dynamic behavior under conditions where slopes are prone to flexural toppling failure, but will be unconservative where other failure mechanisms (e.g., cross-joint shearing) are critical.

The transition from a flexural toppling mechanism to a cross-joint shearing mechanism and the factors that influence those behaviors will be an interesting topic for future research. Results from this parametric study suggest that two fundamental constraints control the behavior of persistently jointed rock-slopes under dynamic loading – the Goodman and Bray kinematic restriction and the width of rock columns. As addressed by Adhikari et al. [50], when resistance to flexural toppling is high, slopes may fail under other mechanisms. Slopes with shallow dips, which are insusceptible to failure due to joint friction, or slopes with wide joint spacing, which are capable of resisting large flexural loads, may fail in shear. Figure 6.70 shows the tuning ratio sensitivity types for slopes of varying joint dip and spacing evaluated in this study. For dips less than the limiting dip from Goodman and Bray, slopes are sensitive to tuning ratio under dynamic loading. For joint spacing greater than 4 meters, slopes are also sensitive to tuning ratio. Slopes in the lower right quadrant of Figure 6.70 are sensitive to low frequency content. Slopes with low-frequency sensitivity are associated with flexural toppling failure.

Table 6.10: Summary of dynamic analysis results for slopes with persistent discontinuities.

Model	Spacing, m	Dip, degrees	Type of Frequency Sensitivity*	Level of Frequency Sensitivity	PGA_f , g	$\frac{PGA_f}{k_y}$
601	2	20	TR	mild	0.405	–
602	2	30	TR	moderate	1.089	–
603	2	40	TR	moderate	1.310	0.37
604	2	45	LF	mild	1.313	–
605	2	50	LF	mild	1.315	
606	2	60	LF	strong	0.722	0.72
607	2	70	LF	moderate	0.407	0.54
608	2	80	LF	strong	0.397	0.80
609	2	90	LF	strong	0.402	2.01
610	2	100	LF	moderate	0.579	0.77
611	1	80	LF	mild	0.180	0.72
613	3	80	LF	moderate	0.394	0.53
614	4	80	LF	moderate	0.697	0.70
615	5	80	TR	slight	0.735	0.59
616	6	80	TR	moderate	0.252	0.17
617	7	80	TR	moderate	0.604	0.30
618	8	80	TR	moderate	0.818	0.33
619	1	70	–	–	0.385	1.54
620	4	70	LF	mild	0.679	0.60
621	6	70	TR	moderate	0.727	0.42
622	1	60	LF	slight	0.169	0.68
623	4	60	LF	mild	1.092	0.73
624	6	60	TR	moderate	0.721	0.36

* LF = sensitivity to low frequencies, TR = sensitivity to tuning ratio

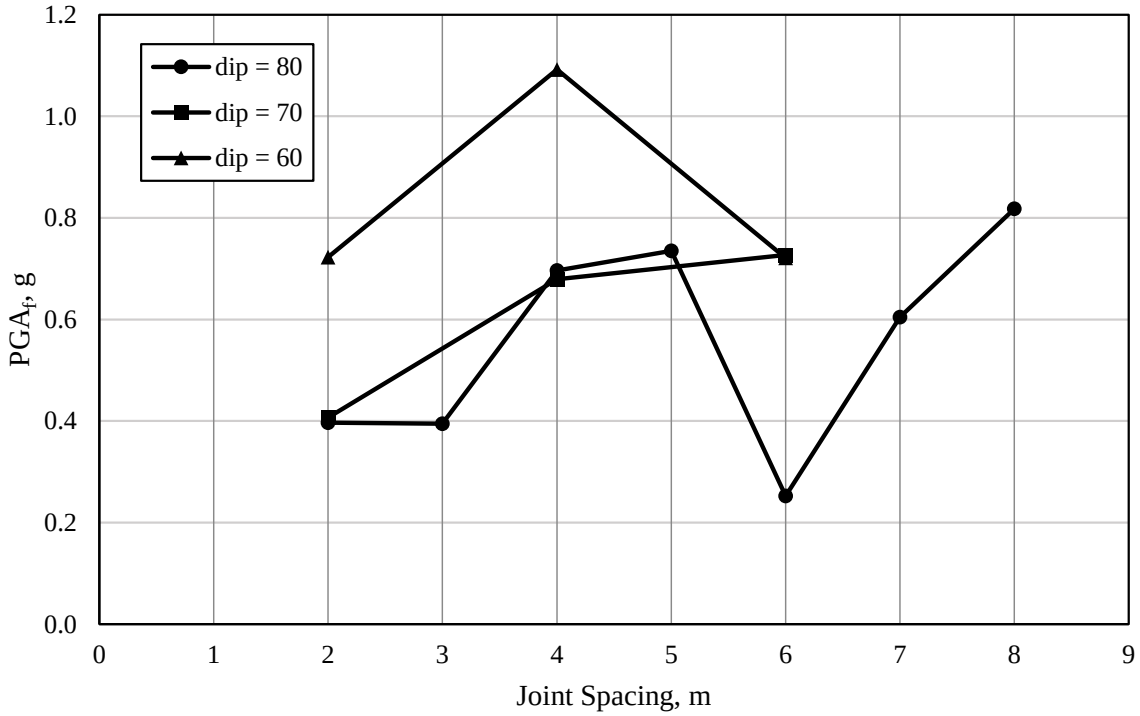

Figure 6.68: Minimum PGA_f from dynamic loading for slopes with persistent discontinuities with joint spacing.

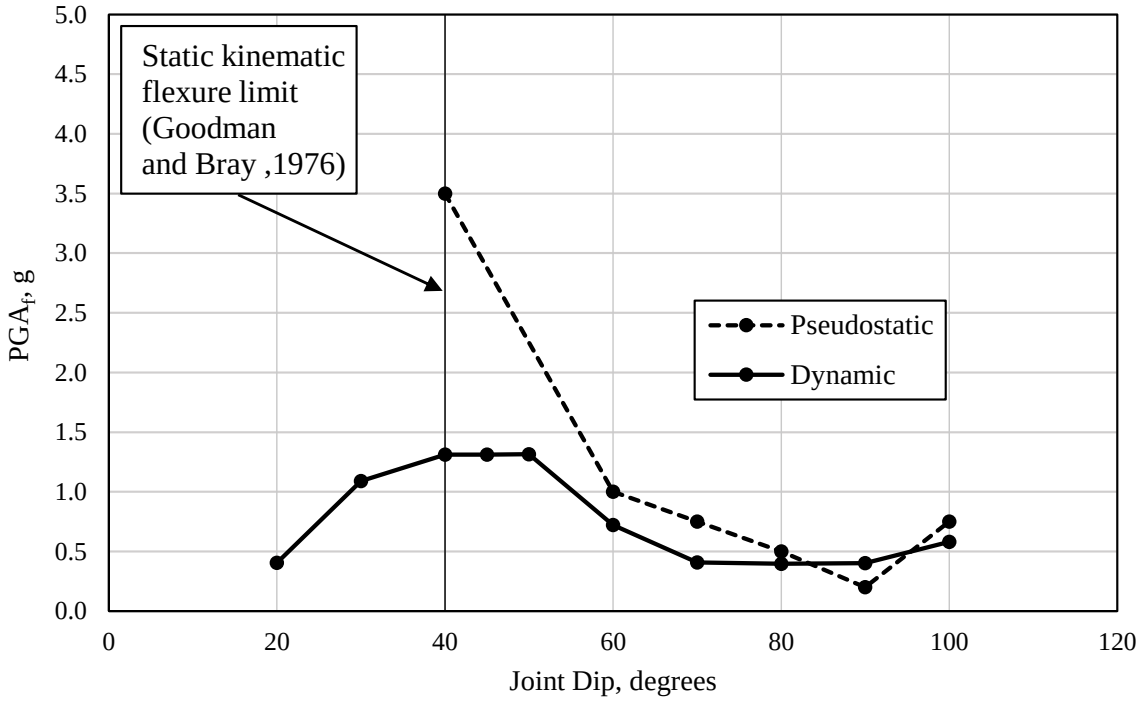

Figure 6.69: Minimum PGA_f from dynamic loading with joint dip. The pseudostatic k_y is also shown for comparison. The minima in the curves, at 80 degrees for dynamic loading, and 90 degrees for pseudostatic loading, are apparent. The curves are similar in shape for dips of 60 and greater. The vertical line at dip = 40 degrees marks the limit of static flexural toppling according to equation 6.2 from Goodman and Bray [95]. The pseudostatic stability increases sharply here, and the dynamic stability has a maximum between 40 and 50 degrees, but at significantly lower levels of acceleration than the pseudostatic case.

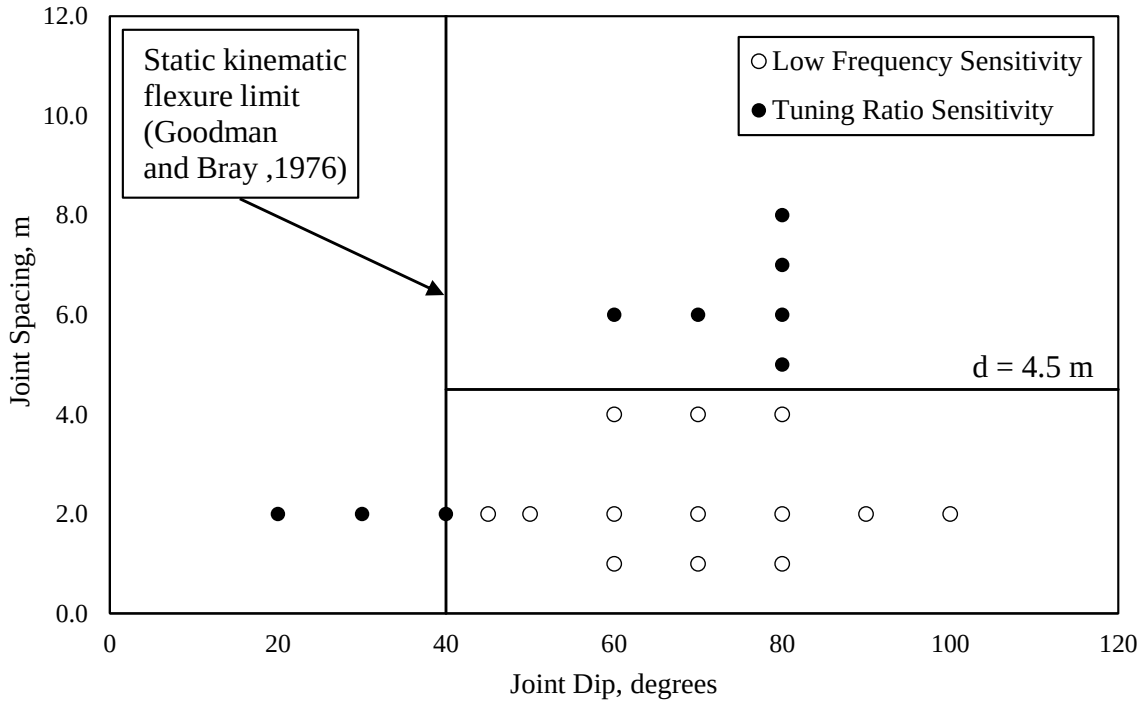

Figure 6.70: Type of frequency sensitivity for slopes with persistent joints over a range of joint spacing and dip. A dip boundary in sensitivity type is apparent at the limit of static flexural toppling according to equation 6.2 from Goodman and Bray [95]. For dips on and less than the static kinematic flexure limit, slopes are sensitive to tuning ratio under dynamic loading. A spacing boundary between 4 and 5 meters is also apparent. Slopes with spacing plotting above the horizontal line at d = 4.5 are sensitive to tuning ratio under dynamic loading. Slopes that fall in the lower right quadrant of the plot are sensitive to low-frequency content and are associated with flexural toppling failure.

Dynamic Failure Analysis of Slopes with Non-persistent Discontinuities

This section presents the results of the dynamic failure analysis from harmonic ground motions of various frequencies on rock-slopes with non-persistent discontinuities. Examples of three simulations involving Model 644, 650, and 659 subjected to a 5 Hz harmonic input are presented to illustrate some of the behaviors observed in this set of simulations. The accumulation of damage in terms of number of cracks with input acceleration is shown for all models for all tested loading frequencies. Loading frequencies of 5, 7, 9, and 11 Hz were used in the dynamic analysis of models with non-persistent discontinuities because the natural frequencies for these slopes generally fall within that range.

Figure 6.71 shows the sequential failure of Model 644 (horizontally dipped) subjected to a 5 Hz ramping amplitude harmonic input. Figure 6.71a shows the patterns of compressive and tensile force-chains in Model 644 during downslope displacement. Compressive force-chains travel around and between the horizontal joints, and have maximum magnitudes near the toe of the slope. Tensile force-chains are visible near the top and crest of the slope in relatively lower magnitudes. In Figure 6.71b, tensile cracking has developed at the crest of the slope and an independent block has been created. In Figure 6.71c, continued damage near the crest, but moving deeper into the slope can be seen. The cracks in the model are generally vertical wing cracks extending from the tips of the pre-existing horizontal joints. As the damage moves deeper into the slope, as shown in Figure 6.71d, the base-isolating effect of the coalesced fractures is visible in the sharp difference in force-chain magnitude above and below the coalesced fractures. Following the creation of a large, structurally-independent block with a base of stepped, horizontal fractures, Figures 6.71e and 6.71f show the breaking up of the slope mass. Rather than sliding as a single, blocky mass, displacements accumulate first at the slope face and progress backward into the slope as the block breaks up.

Figure 6.72 shows the sequential failure of Model 650 subjected to a 5 Hz ramping amplitude harmonic input. The pattern of compressive and tensile force-chains during downslope displacement is shown in Figure 6.72a. As with Model 644, the compressive force-chains travel around and between the joints, but in a different pattern due to the

different orientation of the joints. The upslope displacement extreme is shown in Figure 6.72b. During this point in the slope's motion, tensile force-chains dominate the slope and also travel around the pre-existing joints, with concentrations at the joint tips. Some cracking at the crest of the slope is visible in this frame. Figure 6.72c shows the cracks that developed as a result of the tensile force concentrations shown in the previous frame. In Figure 6.72d, the cracks have continued to accumulate in the slope near the base and slope face. In Figure 6.72e, cracks linking the pre-existing joints essentially cover the entire slope, and the slope is mostly made up of small independent blocks. Although the blocks are independent (meaning that no bonds exist between them), they are kinematically-restricted from moving by the surrounding blocks and orientation of the joints. Blocks closest to the slope face are the least restricted, and Figure 6.72f shows these blocks beginning to rotate outward from the slope face in a toppling failure mode as illustrated in 6.18b from [9].

Figure 6.73 shows the sequential failure of Model 559 subjected to a 5 Hz ramping amplitude harmonic input. At the downslope extreme displacement, shown in Figure 6.73a, the compressive forces near the toe travel around and between the joints, but in a relatively less obstructed manner than in Models 644 and 650 because the dip of the joints is oriented towards the toe. A point of high tensile force concentration at the tip of a crack can be observed about two-thirds of the way up the slope. In the next frame (Figure 6.73b) a wing crack that initiated due to the tensile force concentration can be seen, and another tensile force concentration has developed at the tip of the next joint down. Another wing crack develops at the tip of this joint (seen in Figure 6.73c). This pattern of sequential coalescence of joints progressing down the slope in a stepped manner continues, as shown in Figure 6.73d. By the time shown in Figure 6.73e, an independent sliding mass has been created by the coalesced joints. Again, the base-isolating effect of the joints is clearly visible by the sharp difference in force-chain magnitude above and below the coalesced fractures. The entire block above the coalesced fractures appears to be moving downslope and a block at the toe has become independent and is toppling out from the toe. In Figure 6.73f, extensive damage in the slope beneath the sliding mass can be seen, and another set of coalesced joints within the sliding mass has created a smaller sliding mass near the slope face.

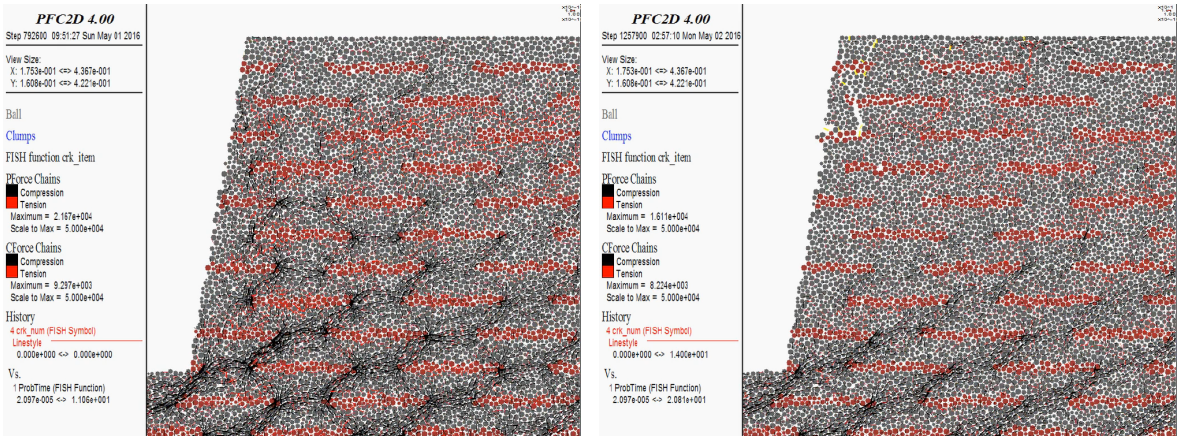

(a) **(b)**

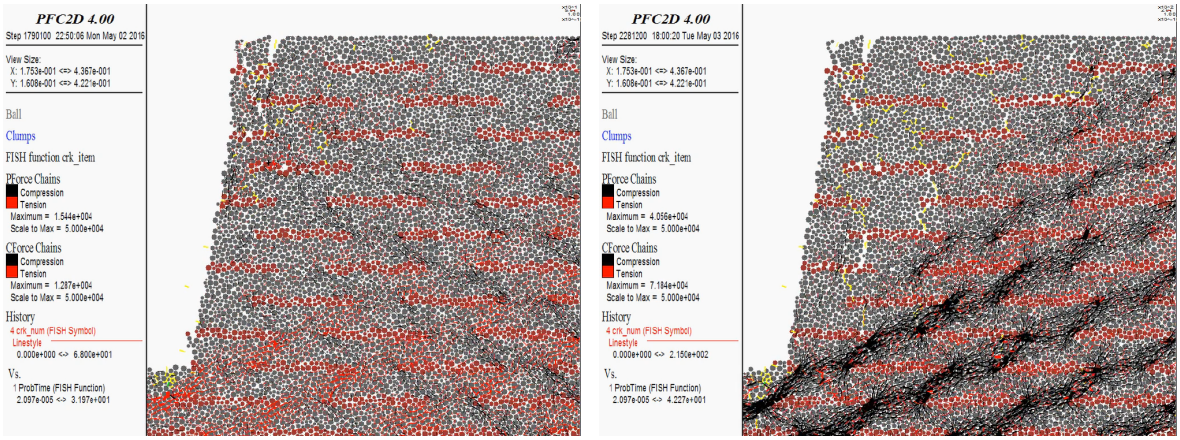

(c) **(d)**

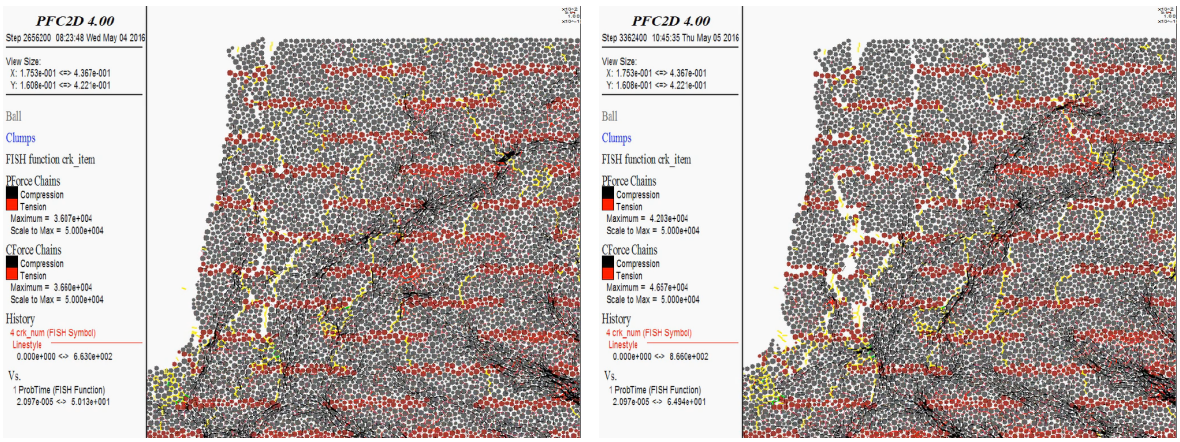

(e) **(f)**

Figure 6.71: Failure sequence of Model 644 subjected to a 5 Hz loading.

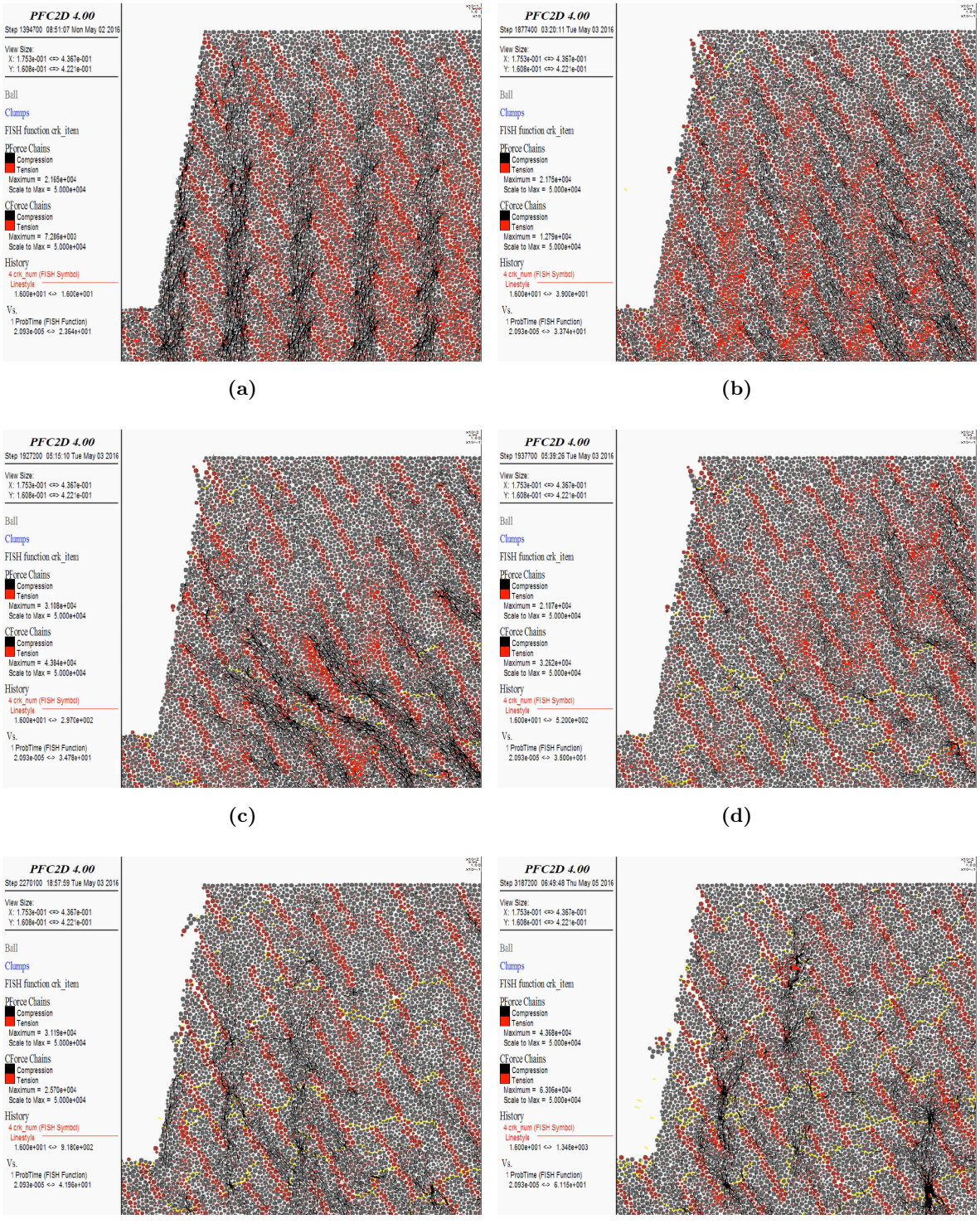

Figure 6.72: Failure sequence of Model 650 subjected to a 5 Hz loading.

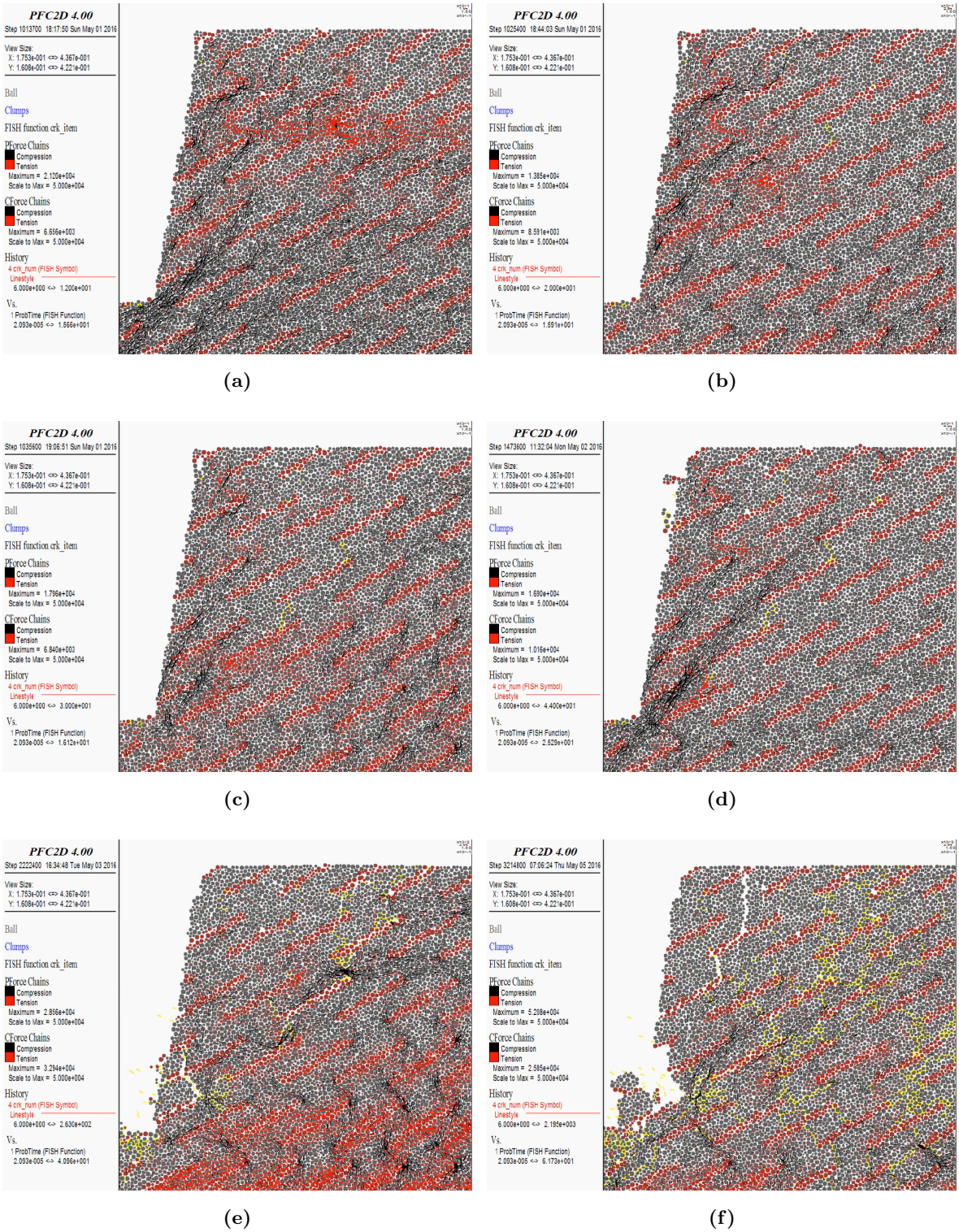

(a) **(b)**

(c) **(d)**

(e) **(f)**

Figure 6.73: Failure sequence of Model 659 subjected to a 5 Hz loading.

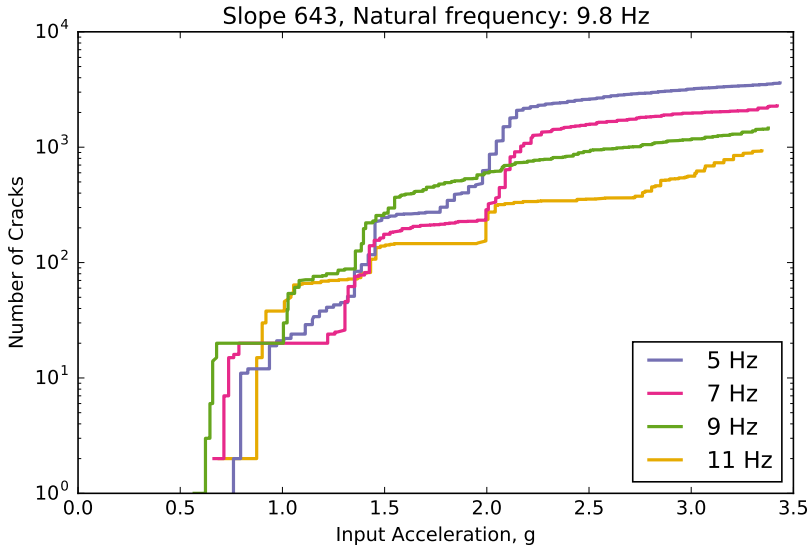

Figure 6.74: Number of cracks generated in Model 643 with input acceleration for multiple harmonic loading frequencies.

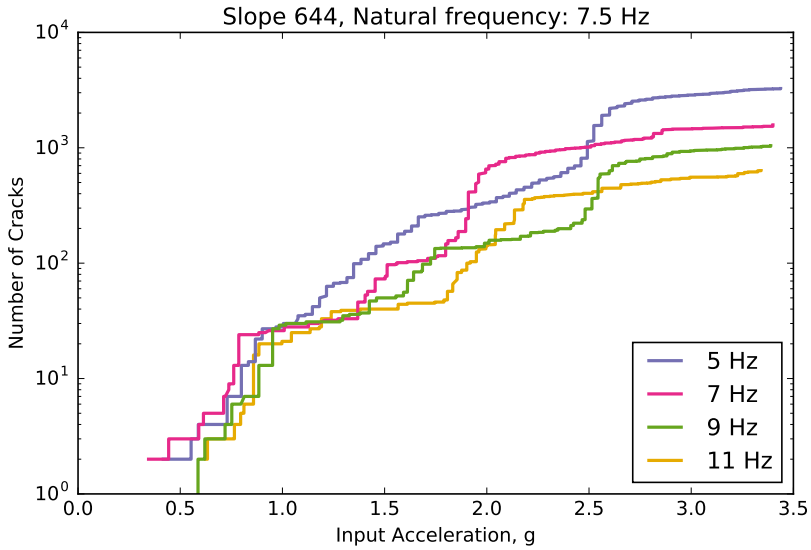

Figure 6.75: Number of cracks generated in Model 644 with input acceleration for multiple harmonic loading frequencies.

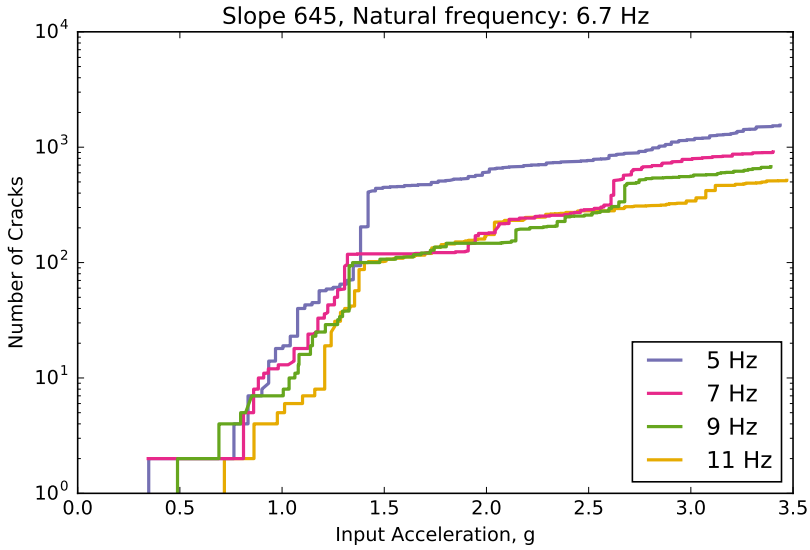

Figure 6.76: Number of cracks generated in Model 645 with input acceleration for multiple harmonic loading frequencies.

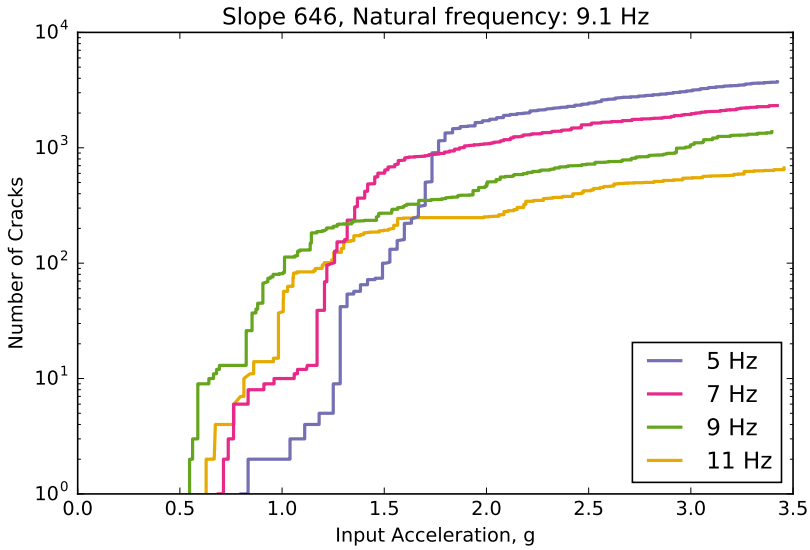

Figure 6.77: Number of cracks generated in Model 646 with input acceleration for multiple harmonic loading frequencies.

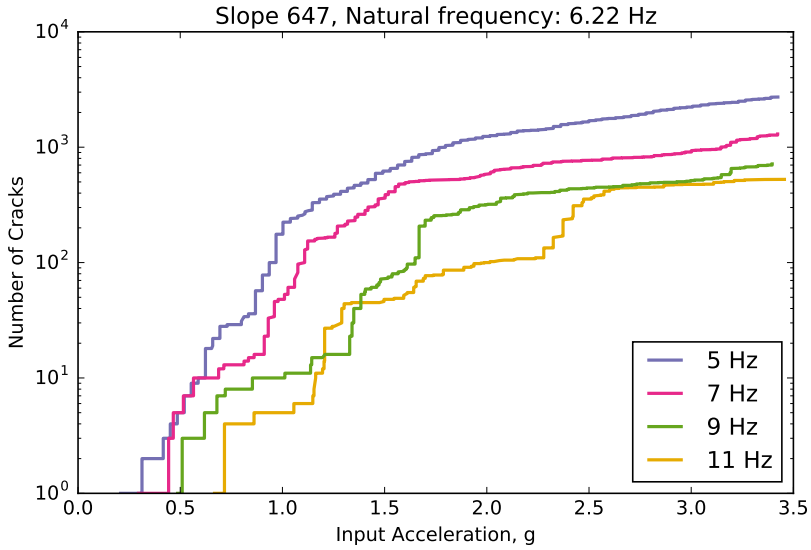

Figure 6.78: Number of cracks generated in Model 647 with input acceleration for multiple harmonic loading frequencies.

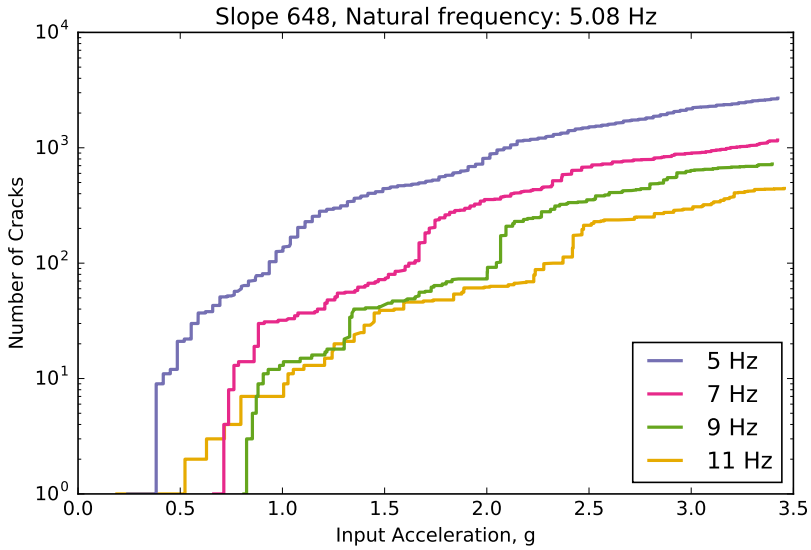

Figure 6.79: Number of cracks generated in Model 648 with input acceleration for multiple harmonic loading frequencies.

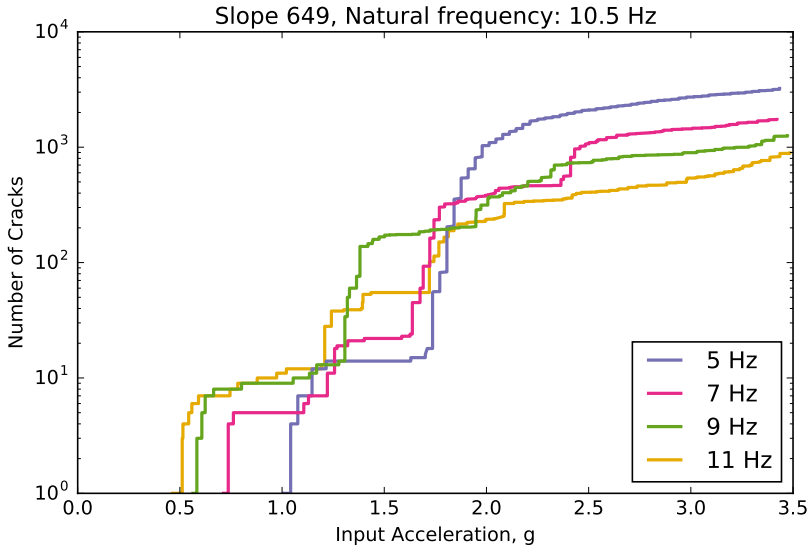

Figure 6.80: Number of cracks generated in Model 649 with input acceleration for multiple harmonic loading frequencies.

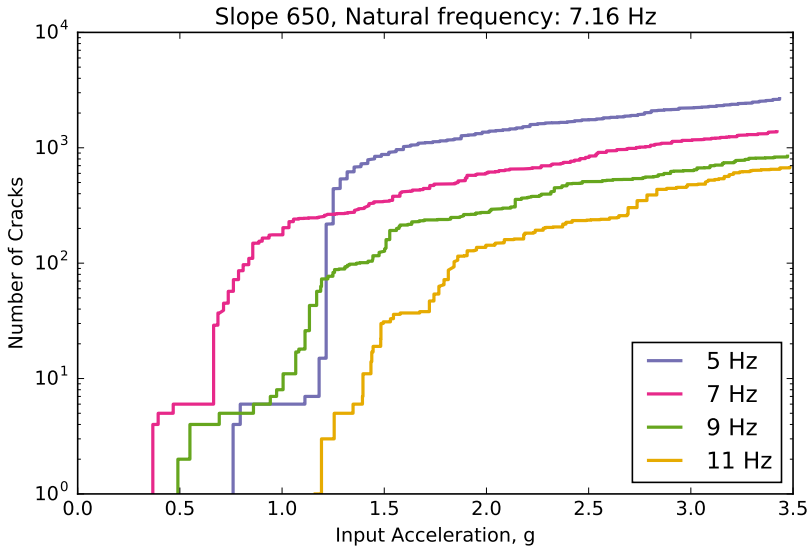

Figure 6.81: Number of cracks generated in Model 650 with input acceleration for multiple harmonic loading frequencies.

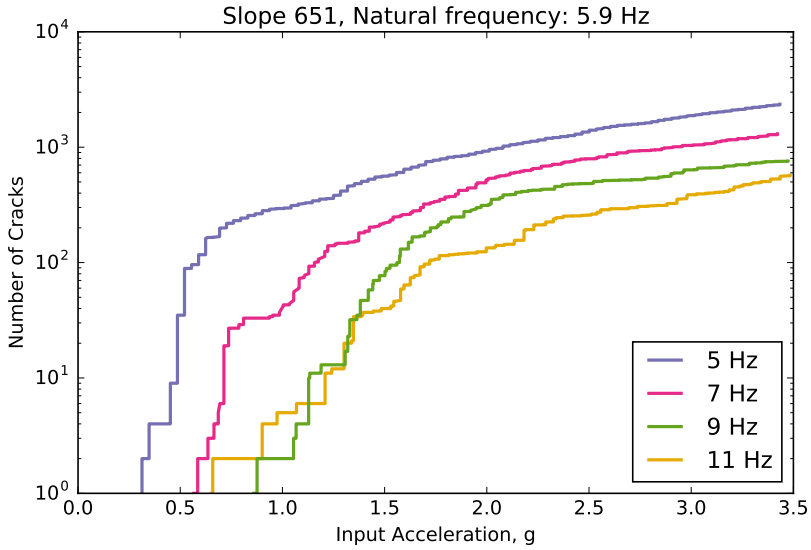

Figure 6.82: Number of cracks generated in Model 651 with input acceleration for multiple harmonic loading frequencies.

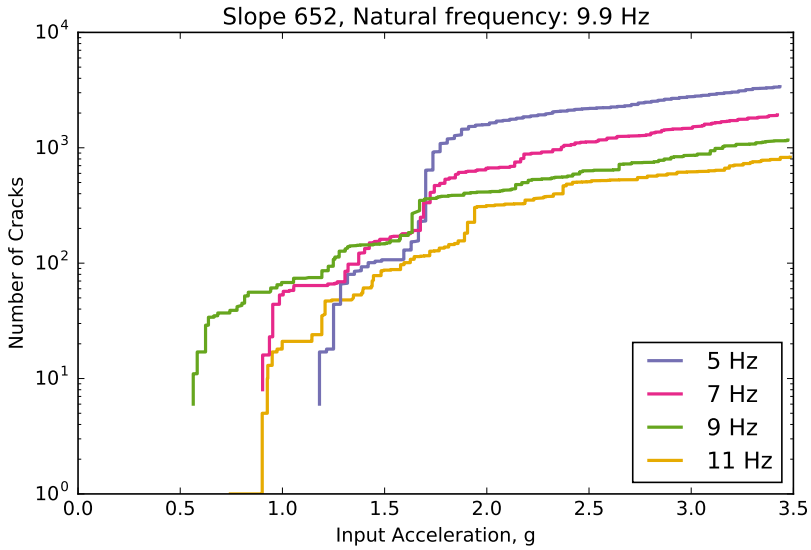

Figure 6.83: Number of cracks generated in Model 652 with input acceleration for multiple harmonic loading frequencies.

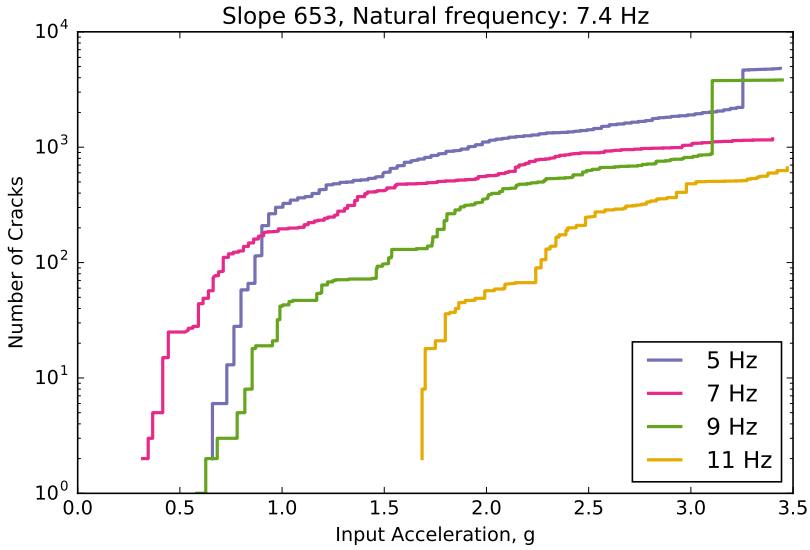

Figure 6.84: Number of cracks generated in Model 653 with input acceleration for multiple harmonic loading frequencies.

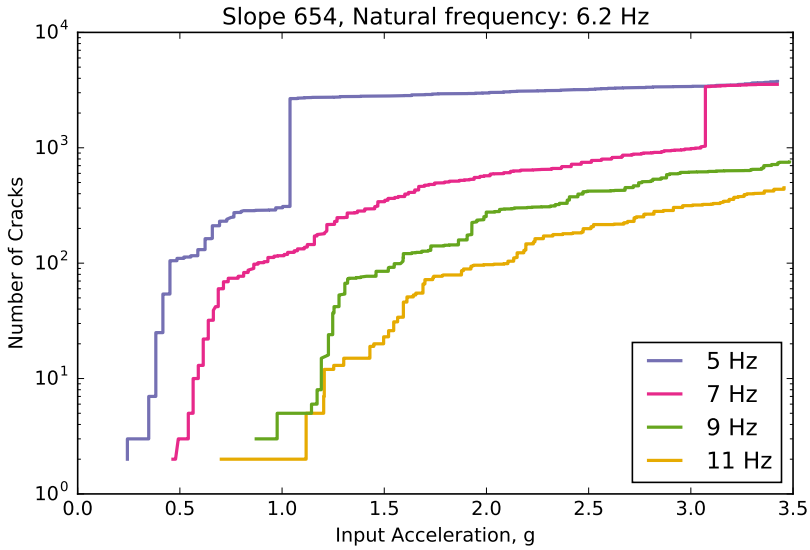

Figure 6.85: Number of cracks generated in Model 654 with input acceleration for multiple harmonic loading frequencies.

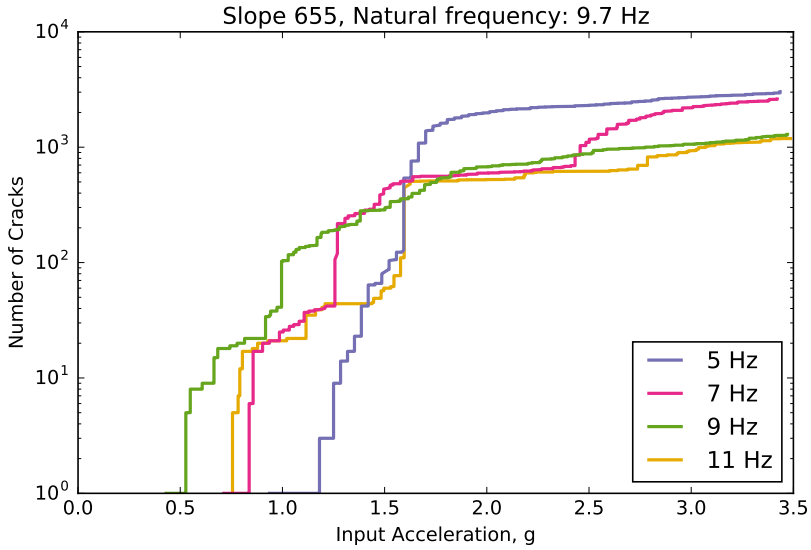

Figure 6.86: Number of cracks generated in Model 655 with input acceleration for multiple harmonic loading frequencies.

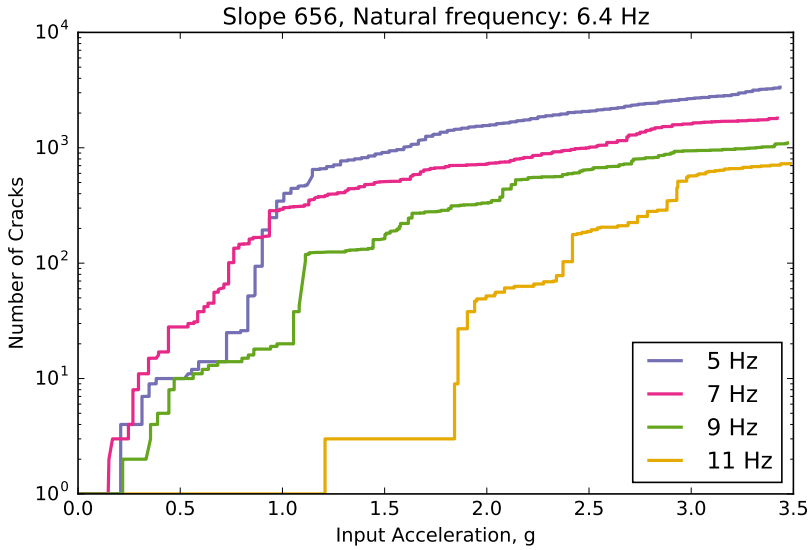

Figure 6.87: Number of cracks generated in Model 656 with input acceleration for multiple harmonic loading frequencies.

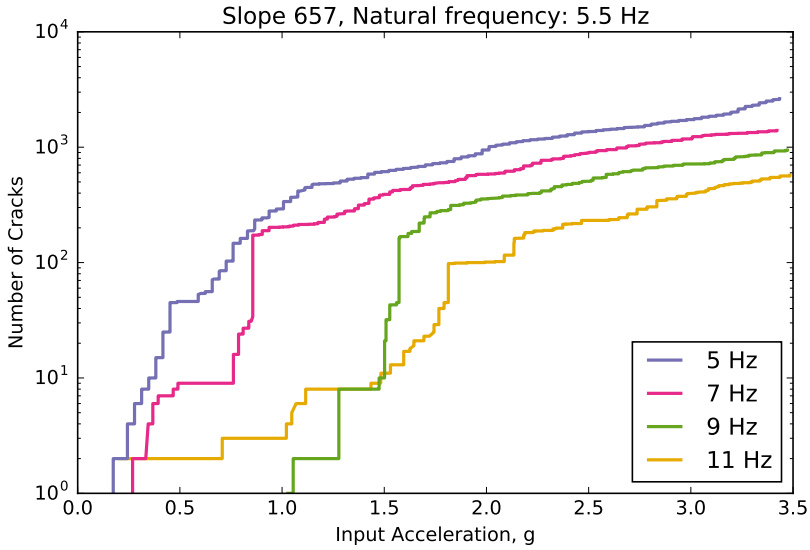

Figure 6.88: Number of cracks generated in Model 657 with input acceleration for multiple harmonic loading frequencies.

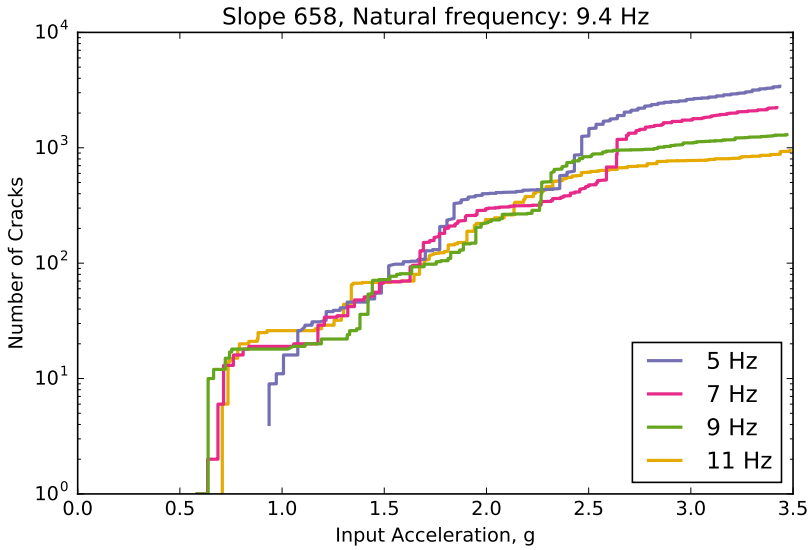

Figure 6.89: Number of cracks generated in Model 658 with input acceleration for multiple harmonic loading frequencies.

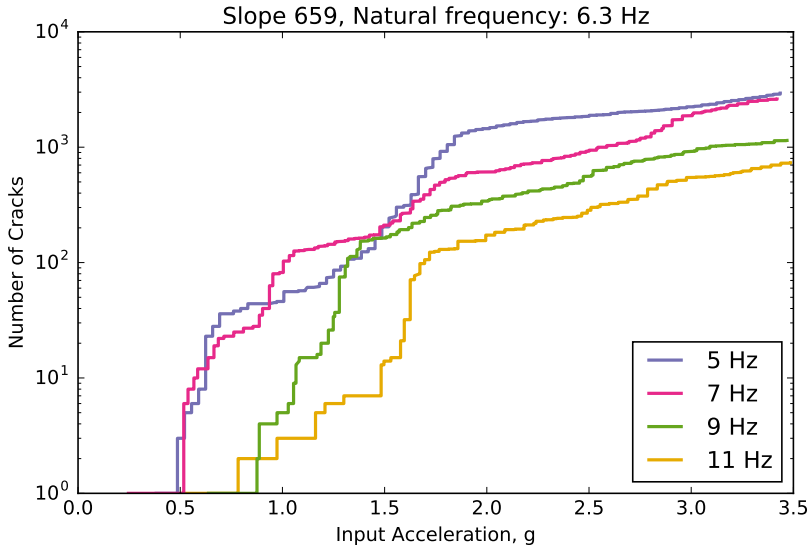

Figure 6.90: Number of cracks generated in Model 659 with input acceleration for multiple harmonic loading frequencies.

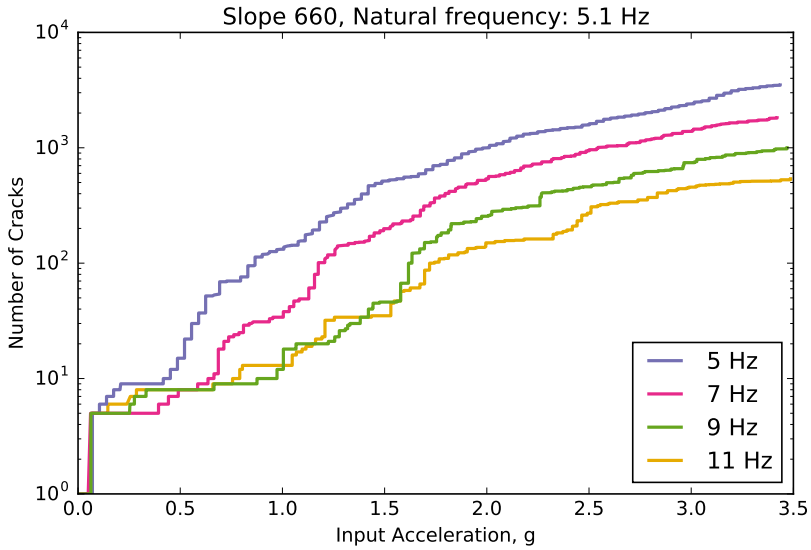

Figure 6.91: Number of cracks generated in Model 660 with input acceleration for multiple harmonic loading frequencies.

Summary of the Dynamic Failure Analysis of Slopes with Non-persistent Discontinuities

The results above, particularly the sensitivity of the slopes with non-persistent joints to frequency content can be summarized as follows: For all dips and joint intensities tested, some influence of tuning ratio, ranging from slight to strong, was observed. The qualitative level of sensitivity to frequency are presented in Table 6.11.

The qualitative assessment of sensitivity to frequency content is based on visual inspection of Figures 6.74 through 6.91. The relative spacing between the curves of number of cracks with input acceleration for different frequencies provides an indication of the sensitivity to frequency content. The curves are assessed at the initiation of fracturing in the slope. Sensitivity levels are given the following levels: slight, mild, moderate, and strong.

The minimum PGA to initiate failure, PGA_f, and the ratio of PGA_f to the pseudostatic yield for the slope, k_y, are also presented in Table 6.11. Multiple definitions of 'initiation of failure', from the breaking of the first bond, to the development of complete failure surface, are possible. Based on observations of the failure sequences (as shown in Figures 6.25, 6.26 and 6.27), a threshold of 10 cracks (i.e., 10 broken bonds) was selected as the initiation of failure. At ten broken bonds, the slopes typically were observed to have a sufficient level of damage in the models to either form discrete blocks or indicate the beginning of a failure surface.

The PGA_f for slopes with non-persistent discontinuities of varying dip with three levels of joint intensity are shown in Figure 6.92. PGA_f generally increases with decreasing joint intensity with some exceptions. Slopes with dips of 0 degrees showed the opposite trend – PGA_f increased with increasing joint intensity. The slopes with dips of 120 degrees had a minimum PGA_f associated with the mid-range intensity. Figure 6.93 shows the PGA_f for these slopes as a percentage of the pseudostatic yield, k_y. For slopes with P21 of 0.25 and 0.33 m/m^2, PGA_f/k_y ranges from 25 to 80 % with the lowest ratios occurring for slopes with dips of 90 degrees. For slopes with P21 of 0.375 m/m^2, PGA_f/k_y ranges from about 30 to 180 %. with the minimum PGA_f/k_y occurring at a dip of 60 degrees and the maximum values occurring at dips of 0 and 150 degrees.

Figures 6.94, 6.95, and 6.96 show the influence of joint intensity on PGA_f for horizontally

and vertically dipped, anti-dip, and dip slopes, respectively. These figures complement Figure 6.92 by showing the same results in a different space. They show that vertically-dipped, anti-dip, and dip slopes have relatively linear PGA_f to P21 relationships with PGA_f decreasing with increasing P21, as discussed above. Horizontally-dipped slopes also have a relatively linear PGA_f to P21 relationship, but with PGA_f increasing with increasing P21.

Because the initiation of failure in these slopes is occurring due to the extension of pre-existing joints, the resistance of the BPM to fracture is a key parameter driving the behavior. The random arrangement of particles at the tips of pre-existing joints has a significant influence on the resistance to fracture, so a fair amount of variability in the results is to be expected. Further study of the interaction of dynamic stresses and pre-existing joint sets with the bonded particle model should include multiple versions of slopes with the same joint set properties that vary the random particle arrangement to capture the distribution of possible model behaviors.

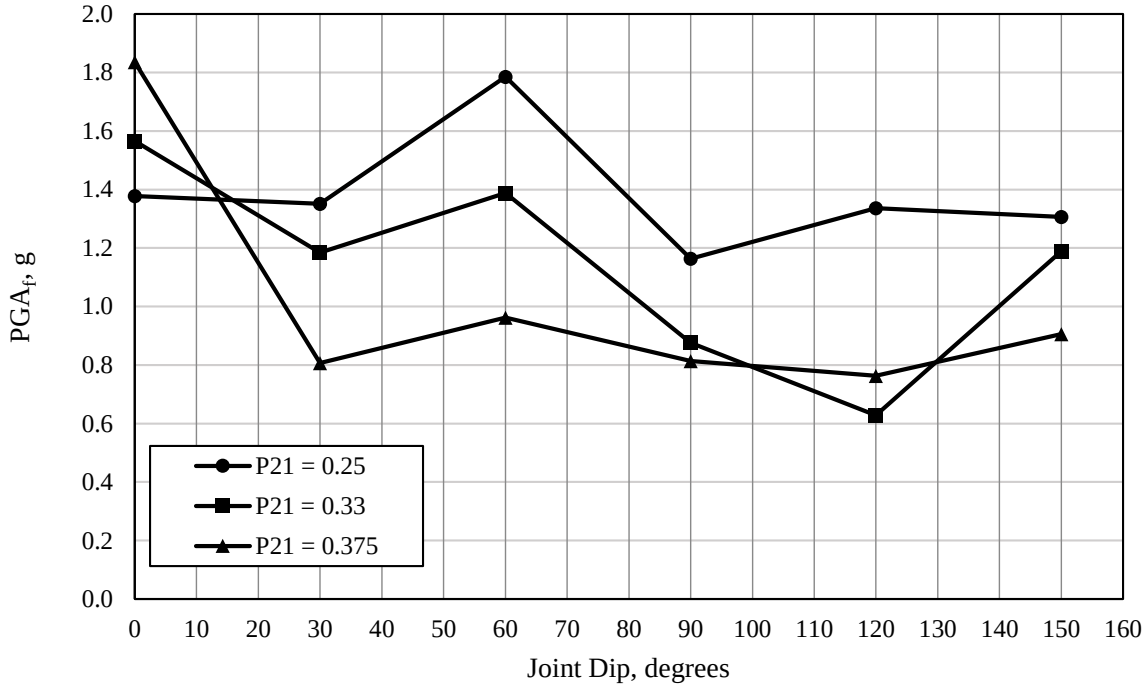

Figure 6.92: Minimum PGA_f from dynamic loading with joint dip for slopes with non-persistent discontinuities.

Table 6.11: Summary of dynamic analysis results for slopes with non-persistent discontinuities.

Model	Joint Dip, degrees	Joint Intensity, m/m^2	Level of Sensitivity	PGA_f , g	$\frac{PGA_f}{k_y}$
643	0	0.25	mild	1.377	0.45
644	0	0.333	slight	1.566	0.78
645	0	0.375	mild	1.836	1.84
646	30	0.25	mild	1.352	0.39
647	30	0.333	mild	1.184	0.48
648	30	0.375	mild	0.806	0.32
649	60	0.25	mild	1.785	0.45
650	60	0.333	moderate	1.388	–
651	60	0.375	moderate	0.962	0.28
652	90	0.25	moderate	1.163	0.26
653	90	0.333	strong	0.875	0.25
654	90	0.375	strong	0.813	0.41
655	120	0.25	moderate	1.336	0.30
656	120	0.333	mild	0.628	0.42
657	120	0.375	mild	0.763	0.76
658	150	0.25	slight	1.306	0.37
659	150	0.333	moderate	1.189	0.48
660	150	0.375	slight	0.905	1.81

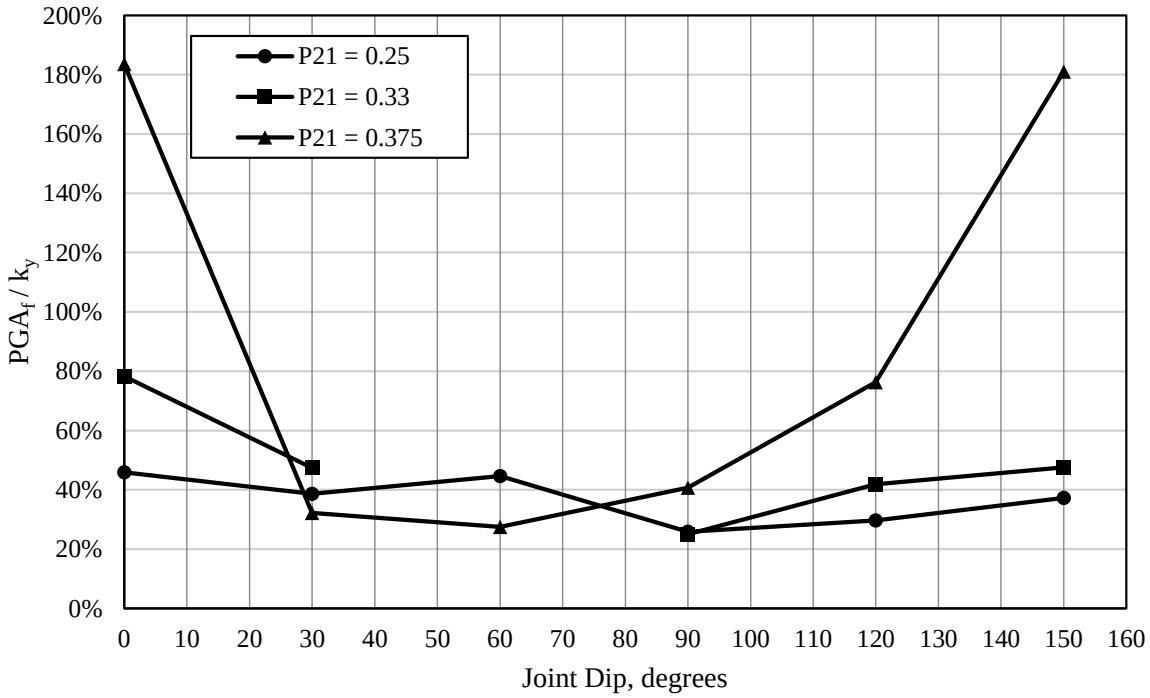

Figure 6.93: Minimum PGA_f from dynamic loading as a percentage of pseudostatic yield acceleration, k_y, with joint dip for slopes with non-persistent discontinuities.

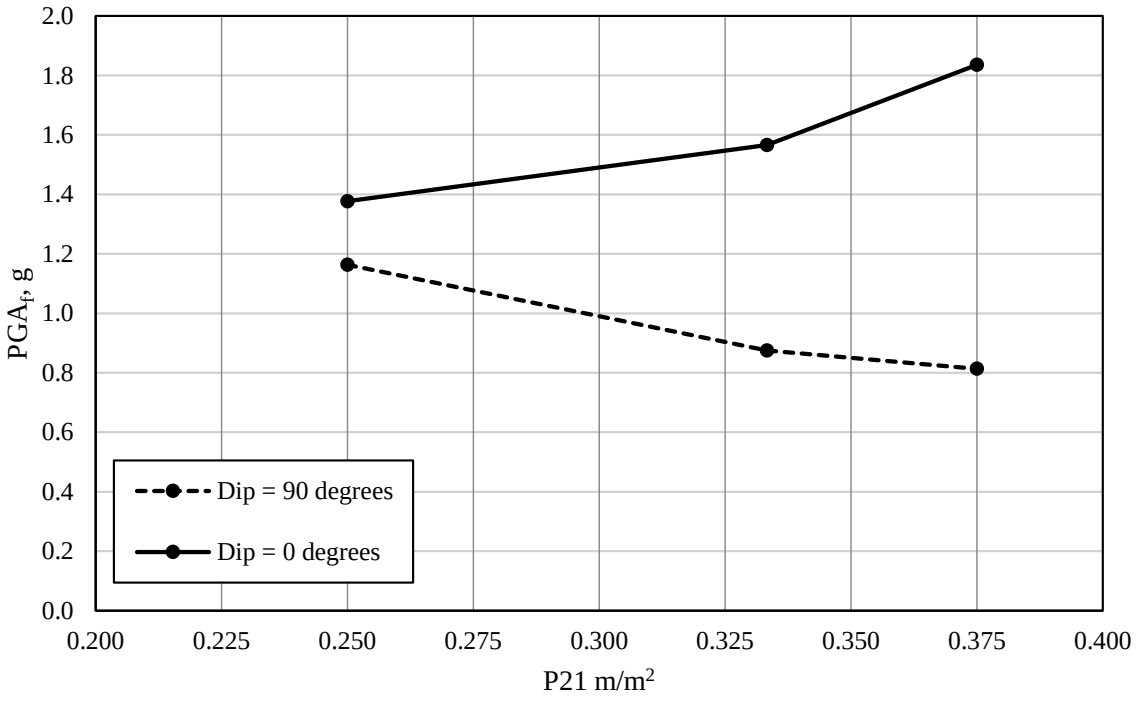

Figure 6.94: Minimum PGA_f from dynamic loading with P21 for horizontally and vertically dipped slopes.

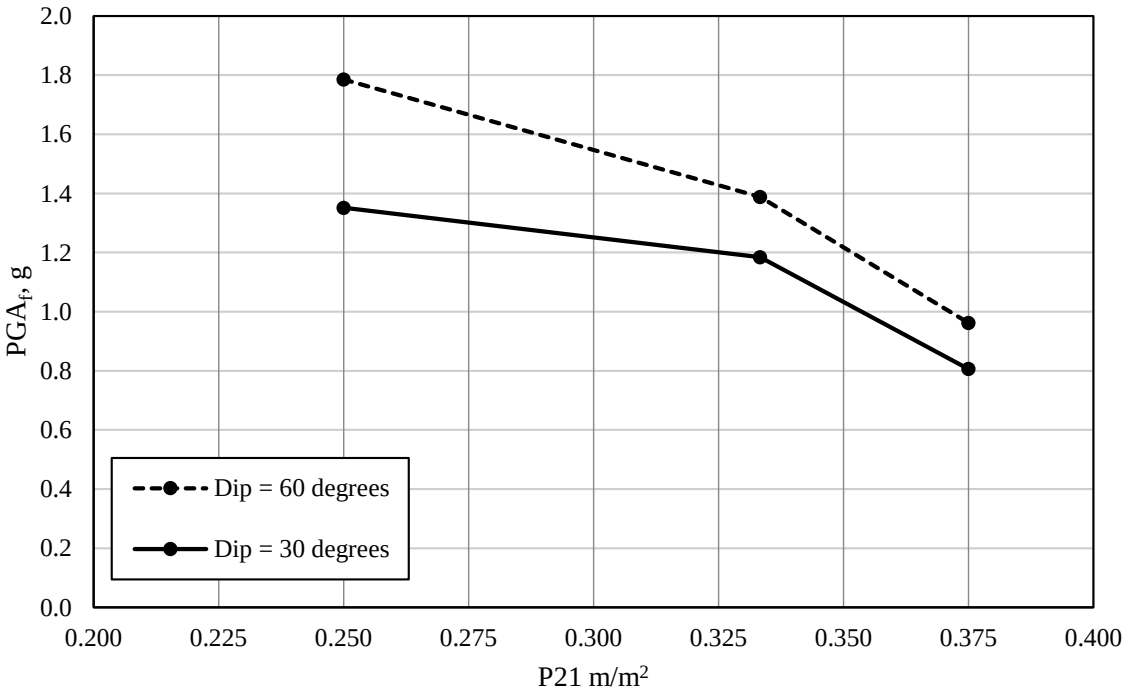

Figure 6.95: Minimum PGA_f from dynamic loading with P21 for anti-dip slopes.

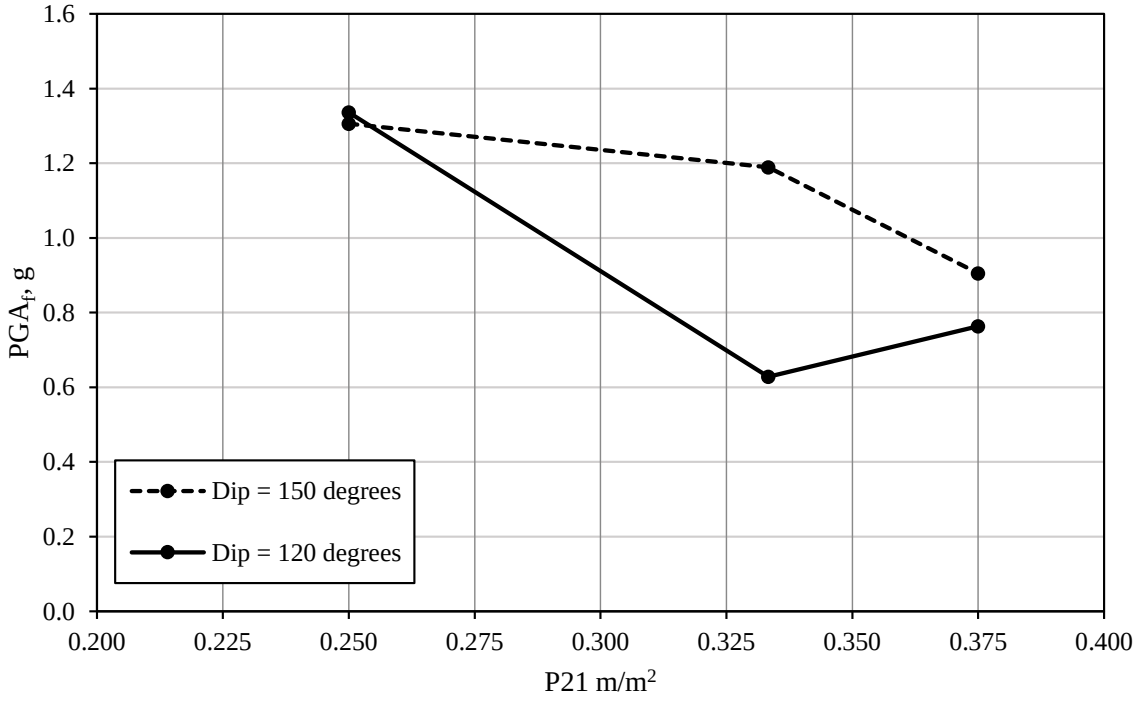

Figure 6.96: Minimum PGA_f from dynamic loading with P21 for dip slopes.

6.5 Parametric Study Discussion

The goals of this portion of the research were to answer several questions about the role of discontinuities on the fundamental behavior and performance of rock-slopes. Specifically, questions posed were:

- How does discontinuity persistence, spacing, and orientation affect the natural frequency of rock-slopes?
- What effect, if any, do discontinuities play in the frequency-dependency of the initiation of failure in rock-slopes? Are the frequency-related effects on homogeneous rock-slopes observed in rock-slopes with pre-existing discontinuities?
- How do discontinuities affect the behavior of rock-slopes in dynamic loading relative to their behavior under a simple pseudostatic loading?
- Do fracturing rock-slopes experience failure by initiation of new fractures, or by coalescence of existing joints?
- Do the observed fracturing patterns due to dynamic loading match the patterns expected from previous research on static rock-slope fracture or do new fracture patterns develop due to dynamic stresses?

Models of rock-slopes with persistent and non-persistent discontinuities were tested under multiple loading conditions to assess the dynamic characteristics of the slopes and their response to strong ground motion. By comparing the behaviors of the models of varying joint geometric properties, the role of the joint set in the behavior and performance can be addressed.

The following sections discuss the results of this parametric study regarding the research question posed.

6.5.1 The Effect of Joint Set Parameters on the Pseudostatic Stability of Rock-slopes

Pseudostatic Stability of Rock-Slopes with Persistent Joints

The pseudostatic stability of slopes with persistent joints is highly dependent on the dip of the joints. Whether or not the slope is susceptible to the flexural toppling failure mode is the driver of the dip-dependent stability. A marked change in behavior occurs at shallow joint dips where the friction of the joints does not allow for slip, which is a prerequisite for flexural toppling failure (see Figure 6.28). Where slopes with persistent joints do not fail in flexural toppling, other failure modes, such as cross-joint shear have to develop for failure to occur. Joint spacing also has an effect on the pseudostatic stability. The pseudostatic stability of slopes increases roughly linearly with increased joint spacing (see Figure 6.29).

Pseudostatic Stability of Rock-Slopes with Non-Persistent Joints

The pseudostatic stability of slopes with non-persistent joints is affected by joint intensity, but the effect is dependent on the dip of the joint set. Slopes with horizontal and vertical joint sets have a moderate drop in pseudostatic stability with increasing joint dip (see Figure 6.31). Dip slopes have a strong drop in pseudostatic stability with increasing joint intensity (see Figure 6.33). Anti-dip slopes have a slight drop in pseudostatic stability with increasing joint intensity (see Figure 6.32). The relative difference in the effect of joint intensity between dip and anti-dip slopes in the models is consistent with the literature. Because dip slopes generally fail through the extension and coalescence of existing joints, and anti-dip slopes require rupture of intact rock material across joints to form a failure surface, the model results are to be expected and help to verify that the model is behaving realistically.

6.5.2 The Effect of Joint Set Parameters on the Natural Frequency of Rock-Slopes

Natural Frequency of Rock-Slopes with Persistent Discontinuities

The natural frequency of rock-slopes is affected by the orientation and spacing of persistent joints. Joint spacing has a much more pronounced effect on the natural frequency than

joint dip. The increase in slope natural frequency with increased joint spacing (i.e., wider rock columns) is roughly linear (see Figure 6.36). The effect of joint dip on slope natural frequency is non-linear, with the minimum natural frequencies (i.e., the softest slopes) associated with very steep dip angles and maximum slope natural frequencies for very shallow dip angles (see Figure 6.37).

Natural Frequency of Rock-Slopes with Non-Persistent Discontinuities

The natural frequency of rock-slopes with non-persistent discontinuities is affected by the orientation and intensity of joints. Similar to the behavior of slopes with persistent discontinuities, the intensity of the joints has a much more pronounced effect on the natural frequency that the dip of the joints. As shown in Figure 6.39, for a given joint spacing, the change in natural frequency appears to be a quadratic function of joint intensity for both persistent and non-persistent joints. The effect of joint direction –either dip or anti-dip– for slopes with dips of equal, but opposite angles from the ground surface, is even less pronounced than the dip angle itself (see Figure 6.40). It appears that when it comes to the variation in natural frequency of rock-slopes due to non-persistent joints, intensity is the key parameter.

6.5.3 The Effect of Joint Set Parameters on the Initiation of Failure Due to Dynamic Loading

Initiation of Dynamic Failure of Rock-Slopes with Persistent Discontinuities

The effect of joint spacing on the initiation of dynamic failure of rock-slopes with persistent discontinuities is not clear (see Figure 6.68). This is in contrast to the pseudostatic stability of the same models, where stability increased linearly with increased joint spacing. It is suspected that the impacts associated with opening and closing of joints during cyclic loading are playing a role in this change in behavior.

The effects of joint dip on the initiation of dynamic failure are dependent on whether failure is associated with a flexural toppling or a cross-joint shear mechanism. In the flexural toppling mode, models are insensitive to tuning ratio, but sensitive to low-frequency content

(see Figure 6.70). The minimum levels of shaking required to initiate failure under these conditions are roughly consistent with the pseudostatic k_y, indicating that for the flexural toppling mode, a pseudostatic analysis may provide a reasonable approximation of stability under seismic loading. In the cross-joint shear mode, models are sensitive to tuning ratio and the levels of shaking required to initiate failure are in the range of 15 to 40% of the pseudostatic k_y, indicating that pseudostatic analysis is unconservative in this case (see Figure 6.69).

Initiation of Dynamic Failure of Rock-Slopes with Non-Persistent Discontinuities

Relative to the simulations on homogeneous slopes presented in Chapter 5, and simulations on slopes with persistent discontinuities, the simulation results for slopes with non-persistent discontinuities contain a fair amount of scatter (see Figure 6.92). This is to be expected because of the increased uncertainty related to the interaction between the pre-existing joint tips and the random particle arrangement of the BPM matrix. Even so, the behavior of the models, particularly related to the initiation of fractures, provides significant insight into the role of non-persistent discontinuities in dynamic rock-slope behavior. The extension and coalescence of pre-existing discontinuities in the models follows well-established patterns from physical and experimental fracture mechanics models of rock. Fractures tend to initiate from the tips of pre-existing joints as wing cracks, and the level of shaking required to produce these crack extensions is roughly the same for joint sets of all orientations. This is significant because it indicates similar levels of damage to dip and anti-dip slopes for similar levels of shaking. While the levels of damage are similar, however, the effect of the damage for dip slopes may be to create sliding blocks, whereas interlocked toppling blocks would be generated in anti-dip slopes, so the behavior of the slopes following damage will be different.

The levels of shaking required to initiate failure generally range from 30 to 80% of the yield acceleration, indicating that pseudostatic analysis is an unconservative approach to dynamic rock-slope stability for slopes with non-persistent joints. However, in some cases, for joint sets with high intensity and horizontal or shallow anti-dip orientations, the levels of shaking required to initiate failure were higher than k_y. Vertically-dipped, anti-dip, and dip

slopes have relatively linear decreases in the level of input to initiate failure with increased joint intensity (see Figures 6.94, 6.95, 6.96). Horizontally dipped slopes appear to be less sensitive to joint intensity.

6.6 Conclusions

The Bonded Particle Model is a powerful tool for assessing the seismic behavior and performance of rock slopes with pre-existing discontinuities. Some important features of the initiation of failure, including the impacts associated with the opening and closing of joints and the uncertainties related to crack tip geometries, will require further research to address. However, significant understanding of dynamic rock-slope behavior has been gained through this parametric study. The behavior of the developed model shows strong agreement with patterns of crack propagation, extension, and coalescence in rock as presented in the literature and expands the understanding of how those phenomena develop under dynamic loading.

This study shows that the dynamic interaction of seismic waves on with pre-existing discontinuities cannot be conservatively simplified by the use of pseudostatic analysis in most cases. Slopes where flexural toppling failure is expected to dominate the behavior are an exception. For this category of slope, a pseudostatic analysis may be appropriate. Slopes with non-persistent pre-existing joints experience failure through the coalescence of existing joints forming structurally-independent blocks. Slopes with persistent pre-existing joints experience failure through the fracture of intact rock material between existing joints.

Chapter 7
CONCLUSIONS

This chapter will present the conclusions of the research presented in this dissertation including the simulation of case-studies from the Port Hills region of New Zealand, the evaluation of the influence of ground motion characteristics on homogeneous rock-slopes, and the influence of discontinuities of the dynamic behavior and performance of rock-slopes. The work addresses several questions raised by the NEESROCK project including:

1. What is the role of input ground motion characteristics, particularly frequency content and amplitude, on the initiation of fracture in rock-slopes during seismic events?
2. What is the role of joint structure (orientation, spacing, and persistence) on rock-slope dynamics?
3. What is the role of joint structure on dynamic rock-slope stability?
4. Which slope and input motion parameters influence the consequences of seismically-induced rock-slope failure events (e.g., the displaced volume of the failure event)?
5. To what extent, if any, does earthquake shaking fracture and thus condition slopes for subsequent failure under non-seismic conditions?
6. For a range of common geologic conditions, how do dynamic rock-slope failures initiate and progress? Do failures occur as a single event or in a staged, episodic manner?

7.1 Conclusions

7.1.1 Model Development

A rational approach to the selection of micro stiffness parameters based on the inherent double elasticity of a parallel-bonded BPM assembly has been described and verified. The ability of the BPM model to accurately capture the dynamic flexural behavior of a cantilever

beam and wave transmission, reflection, and absorption was verified with analytical solutions and experimental data. A pseudo-periodic boundary using clump logic was developed and implemented to create free-field response columns for boundary control. The advantage of the pseudo-periodic boundary is that it allows the use of one-dimensional free-field response columns to provide control of lateral model boundaries. Its implementation is entirely within the PFC2D program, making it more efficient than other other methods involving coupling with an external code. These boundary conditions provide the ability to model dynamic input in simple rock-slope configurations in a well-established 2-D dynamic analysis framework.

7.1.2 Simulations of Seismic Rock-Slope Failures in New Zealand

The seismically-induced cliff collapse observed throughout the Port Hills area during the Canterbury Earthquake Sequence (CES) were not captured with traditional rock-slope analysis methods. Using a fully dynamic bonded particle model, the cliff-collapse at two Port Hills sites was successfully modeled. Several features of the rock-slope failures induced during the CES were captured by the model including, different levels of material loss from different geologic units leading to the development of overhanging and benched geometry, and newly formed and/or dilated cracks near the post-failure cliff face. The model results indicate that these collapses were due to a combination of weathering, fractures, and dynamic stresses near the slope face.The PFC model was unable to capture the cliff top displacement at the level of resolution used. This indicates that although BPM is a powerful tool, it may only be appropriate for use as a supplement to, rather than a replacement for, traditional methods. The fact that the results from tradition methods employed by GNS were fairly successful where the BPM models were not, and vice versa, provides a strong argument for using multiple methods of evaluation

By observing the failure mechanisms that lead to the cliff-collapse in the models, we have an indication of the mechanisms that likely contributed to the field behavior. Based on the tensile stresses observed near the cliff face in the weathered zone, and the increases in damage due to extension of pre-existing fractures, it appears that a combination of

dynamic stresses at the cliff face, weathering, and pre-existing fractures all contributed to the observed cliff-collapse in the Port Hills during the Canterbury Earthquake Sequence.

Based on the results of the long-duration loading simulations, the following conclusions are made:

- It appears that cliff-collapse is not a strictly short-duration feature. While other failure modes may (or may not) develop with continued strong ground motion, cliff-collapse appears to continue to occur in repeated cycles of strong ground motion.

- In several cases, the depth of cliff-collapse exceed the depth of weathering in the slopes. This indicates that slopes are still susceptible to cliff-collapse after the weathered material has been "shed" from the slope face.

- The seismic performance of rock-slopes appears to be frequency-dependent, but not uniformly so. The nature of the frequency-dependence is strongly influenced by the particular failure mechanisms induced by the ground motion. When evaluating rock-slopes for potential seismic performance, then, the identification of potential failure mechanisms will be an important step.

- Although the similarity in behavior of four models with random joint sets indicates that the random joint pattern is not dictating the behavior of the slope, the dissimilarity in behavior when the random joints are removed, and the weathered properties are applied throughout the slope, suggests that the presence of the joints, regardless of their orientation, may dictate the behavior of the slope.

The simulations of the dynamic behavior of rock-slopes in the Port Hills highlights the importance of the initial failure mechanisms and the force and stress states that cause them.

7.1.3 Evaluation of Ground Motion Characteristics on Homogeneous Rock-Slopes

The homogeneous rock-slope provided the opportunity to approximate and evaluate the stress tests in steep rock slopes before the initiation of dynamic failure. This analysis, combined with the destructive simulations provides further (and more quantitative) insight into

the mechanisms of dynamic rock-slope behavior. The behavior of the modeled slopes shows strong agreement with numerous case-studies presented in the literature. Cliff-collapse, rock toppling, and rock slumping modes are all captured in the simulations, with cliff-collapse being the most prevalent and requiring the lowest levels of shaking to initiate. This study provides several insights into the fundamental mechanics of rock-slopes under seismic loading.

The dynamic response of the slope dictates the development of stresses that result in the initiation of fracturing and eventual global slope failure. Where fracturing initiates in the slope can dictate the evolution of failure throughout a strong shaking event. In some cases fractures initiate near the base of the slope, providing base-isolation through the development of a deep-seated failure surface, which insulates the slope from dynamic input. In other cases, fractures initiate near the crest, allowing significant dynamic loading to continue to impact the slope and produce continually increasing damage with time.

The tuning ratio is a major factor in the magnitude of the impact of seismically-induced rock-slope failure. Due to the softening effects of damage accumulation, and higher peak displacements and velocities associated with lower frequency motions, loading frequencies slightly below the natural frequency have the potential to induce the greatest failure volumes. The fracturing caused by dynamic loading not only impacts the mass associated with the failure volume but also affects the remaining portion of the slope left standing after a seismic event. Fracturing in the post-shaking slope, particularly when associated with the partial development of failure mode, can produce extremely precarious slope configurations that may not have any external manifestations.

Several of the key behaviors observed in the model can be associated with coupled sliding block displacements. Because sliding block analysis is much simpler than a fully dynamic BPM analysis, a link between these two methods would be a valuable tool for the future of seismic rock-slope stability analysis. Good correlation between these methods has been demonstrated here, however, continued research is needed to account for numerous additional variables that are known to impact slope stability and dynamics and must be incorporated into any reliable link between the two methods.

7.1.4 Parametric Study

The Bonded Particle Model is a powerful tool for assessing the seismic behavior and performance of rock slopes with pre-existing discontinuities. Some important features of the initiation of failure, including the impacts associated with the opening and closing of joints and the uncertainties related to crack tip geometries, will require further research to address. However, significant understanding of dynamic rock-slope behavior has been gained through this parametric study. The behavior of the developed model shows strong agreement with patterns of crack propagation, extension, and coalescence in rock as presented in the literature and expands the understanding of how those phenomena develop under dynamic loading.

This study shows that the dynamic interaction of seismic waves on with pre-existing discontinuities cannot be conservatively simplified by the use of pseudostatic analysis in most cases. Slopes where flexural toppling failure is expected to dominate the behavior are an exception. For this category of slope, a pseudostatic analysis may be appropriate. Slopes with non-persistent pre-existing joints experience failure through the coalescence of existing joints forming structurally-independent blocks. This coalescence appears to occur in a staged, episodic manner. Slopes with persistent pre-existing joints experience failure through the fracture of intact rock material between existing joints.

7.2 Recommendations for Future Research

The research presented in this dissertation answers many questions about the behavior and performance of rock-slopes during earthquakes. However, it has raised several questions, as well. Questions posed by the results of the research are much more specific and targeted than the NEESROCK project questions that were addressed. The increasing specificity in posed questions stems from the increased fundamental understanding of the topic gained through this research. A short list of proposed topics for future research is presented below:

- **Linking elastic, pre-failure stresses to dynamic failure behavior:** The stresses associated with wave interaction with steep slopes was shown to have a strong influence on the failure mechanisms and modes experienced by the slopes. The evaluation of

stresses was made with the bonded particle model, which is not the most efficient tool for elastic simulations. Future research that involves a link between elastic stresses and full dynamic failure may enable prediction of dynamic rock-slope failures, including failure modes and volumes, with a more efficient continuum tool. This could involve BPM simulations of dynamic failure events for a wide range of slope height, angle, stiffness, and strength. A characterization of the range of failure behaviors under these conditions and an analysis of the stress-states of the model just before the initiation of failure could then be made.

- **Linking general dynamic failure modes to sliding block methods:** The failure events of a homogeneous rock-slope subjected to a range of recorded ground motions were shown to correspond to distinct levels of coupled sliding block analysis, however, continued research is needed to account for numerous additional variables that are known to impact slope stability and dynamics. A wide range of slope variables must be incorporated into any reliable link between the two methods.

- **Impacts of opening and closing joints:** Rock-slopes with persistent joints were shown to have dramatically reduced stability under dynamic loading than under pseudostatic loading when the slopes failed in shear across the joints. This has been attributed to the impacts associated with the opening and closing of joints. The nature of these impacts was not studied but appears to have a significant influence on the initiation of damage under certain conditions. A study of these impacts should include the use of additional numerical tools where joint roughness can be more explicitly defined than with BPM.

- **Interaction between stress waves and discontinuities:**The nature and extent of fractures in rock are known to have significant impacts on rock mass strength and rock-slope stability. This research indicates that these features and their effects on dynamic rock mass strength and rock-slope stability are also affected by the interactions between fractures and stress waves. Future research should explore the nature of this interaction with a particular focus on how the physical size of waveforms and fractures dictate their interaction.

BIBLIOGRAPHY

[1] D. K. Keefer and M. C. Larsen, "Assessing Landslide Hazards," *Science*, no. May, pp. 1136–1138, 2007.

[2] G. Plafker and G. E. Ericksen, "Nevados Huascaran Avalanches, Peru," in *Rockslides and Avalanches, 1 Natural Phenomena* (B. Voight, ed.), pp. 277–314, 1978.

[3] P. Sun, Y.-p. Yin, S.-r. Wu, and L.-w. Chen, "Does vertical seismic force play an important role for the failure mechanism of rock avalanches? A case study of rock avalanches triggered by the Wenchuan earthquake of May 12, 2008, Sichuan, China," *Environmental Earth Sciences*, vol. 66, pp. 1285–1293, sep 2011.

[4] Q. Xu, X.-M. Fan, R.-Q. Huang, and C. V. Westen, "Landslide dams triggered by the Wenchuan Earthquake, Sichuan Province, south west China," *Bulletin of Engineering Geology and the Environment*, vol. 68, pp. 373–386, jun 2009.

[5] USGS, "Worldwide OVerview of Large Lansdlides of the 20th and 21st Centuries," 2010.

[6] D. K. Keefer, "Landslides caused by earthquakes," *Geological Society of America Bulletin*, no. 4, 1984.

[7] G. Hancox, N. Perrin, and R. V. Dissen, "GNS SCIENCE IMMEDIATE REPORT: Landslide Reconnaissance Flight February 24 2011," Tech. Rep. February, GNS Science, 2011.

[8] R. E. Goodman and D. S. Keiffer, "Behavior of Rock in Slopes," *Journal of Geotechnical and Geoenvironmental Engineering*, no. August, pp. 675–684, 2000.

[9] Ö. Aydan, "The effects of earthquakes on rock slopes," in *American Rock Mechanics Association*, 2013.

[10] D. Stead and A. Wolter, "A critical review of rock slope failure mechanisms: The importance of structural geology," *Journal of Structural Geology*, vol. 74, pp. 1–23, 2015.

[11] K. Terzaghi, "Stability of Steep Slopes on Hard Unweathered Rock," *Geotechnique*, vol. 12, no. 4, pp. 251–270, 1962.

[12] E. Eberhardt, "Rock Slope Stability Analysis - Utilization of Advanced Numerical Techniques," 2003.

[13] S. A. Sepúlveda, W. Murphy, R. W. Jibson, and D. N. Petley, "Seismically induced rock slope failures resulting from topographic amplification of strong ground motions: The case of Pacoima Canyon, California," *Engineering Geology*, vol. 80, no. 3-4, pp. 336–348, 2005.

[14] T. Topal, M. K. Akin, and M. Akin, "Rockfall hazard analysis for an historical Castle in Kastamonu (Turkey)," *Natural Hazards*, vol. 62, pp. 255–274, oct 2011.

[15] R. Huang, J. Zhao, N. Ju, G. Li, M. L. Lee, and Y. Li, "Analysis of an anti-dip landslide triggered by the 2008 Wenchuan earthquake in China," *Natural Hazards*, vol. 68, pp. 1021–1039, apr 2013.

[16] C. Massey, F. Della Pasqua, C. Holden, A. Kaiser, L. Richards, J. Wartman, M. J. McSaveney, G. Archibald, M. Yetton, and L. Janku, "Rock slope response to strong earthquake shaking," *Landslides*, no. February, 2016.

[17] C. I. Massey, M. J. McSaveney, T. Taig, L. Richards, N. J. Litchfield, D. A. Rhoades, G. H. McVerry, B. Lukovic, D. W. Heron, W. Ries, and R. J. Van Dissen, "Determining Rockfall Risk in Christchurch Using Rockfalls Triggered by the 2010-2011 Canterbury Earthquake Sequence," *EARTHQUAKE SPECTRA*, vol. 30, pp. 155–181, feb 2014.

[18] D. K. Keefer, "The importance of earthquake-induced landslides to long-term slope erosion and slope-failure hazards in seismically active regions," *Geomorphology*, vol. 10, pp. 265–284, aug 1994.

[19] E. L. Harp and M. A. Noble, "An Engineering Rock Classification to Evaluate Seismic Rock-Fall Susceptibility and its Application to the Wasatch Front," *Association of Engineering Geologists Bulletin*, vol. 30, no. 3, pp. 293–319, 1993.

[20] E. Hoek and M. Diederichs, "Empirical estimation of rock mass modulus," *International Journal of Rock Mechanics and Mining Sciences*, vol. 43, pp. 203–215, feb 2006.

[21] S. B. Miles and D. K. Keefer, "Toward a Comprehensive Areal Model of Earthquake-Induced Landslides," no. February, pp. 19–28, 2009.

[22] S. L. Kramer, *Geotechnical Earthquake Engineering*. Prentice Hall, 1996.

[23] N. M. Newmark, "Effects of Earthquakes on Dams and Embankments," *Géotechnique*, vol. 15, no. 2, pp. 139–160, 1965.

[24] R. W. Jibson, "Predicting Earthquake-Induced Landslide Dispacements Using Newmark's Sliding Block Analysis," tech. rep., Transportation Research Record, 1993.

[25] K. Allstadt, J. E. Vidale, and a. D. Frankel, "A Scenario Study of Seismically Induced Landsliding in Seattle Using Broadband Synthetic Seismograms," *Bulletin of the Seismological Society of America*, vol. 103, pp. 2971–2992, oct 2013.

[26] V. Kveldsvik, A. M. Kaynia, F. Nadim, R. Bhasin, B. Nilsen, and H. H. Einstein, "Dynamic distinct-element analysis of the 800m high Åknes rock slope," *International Journal of Rock Mechanics and Mining Sciences*, vol. 46, pp. 686–698, jun 2009.

[27] R. Jibson, E. Rathje, M. Jibson, and Y. Lee, "SLAMMER - Seismic LAndslide Movement Modeled using Earthquake Records," 2013.

[28] J. D. Bray and T. Travasarou, "Simplified Procedure for Estimating Earthquake-Induced Deviatoric Slope Displacements," *Journal of Geotechnical and Geoenvironmental Engineering*, vol. 133, no. 4, pp. 381–392, 2007.

[29] D. Stead, E. Eberhardt, and J. Coggan, "Developments in the characterization of complex rock slope deformation and failure using numerical modelling techniques," *Engineering Geology*, vol. 83, pp. 217–235, feb 2006.

[30] A. Fakhimi and T. Villegas, "Application of Dimensional Analysis in Calibration of a Discrete Element Model for Rock Deformation and Fracture," *Rock Mechanics and Rock Engineering*, vol. 40, pp. 193–211, jun 2006.

[31] R. Peerlings, R. de Borst, W. Brekelmans, and M. Geers, "Localisation issues in local and nonlocal continuum approaches to fracture," *European Journal of Mechanics - A/Solids*, vol. 21, pp. 175–189, jan 2002.

[32] L. Jing, "A review of techniques, advances and outstanding issues in numerical modelling for rock mechanics and rock engineering," *International Journal of Rock Mechanics and Mining Sciences*, vol. 40, pp. 283–353, apr 2003.

[33] A. Bobet, A. Fakhimi, S. Johnson, J. Morris, F. Tonon, and M. R. Yeung, "Numerical Models in Discontinuous Media : Review of Advances for Rock Mechanics Applications," no. November, pp. 1547–1561, 2009.

[34] P. A. Cundall and R. D. Hart, "Numerical Modelling of Discontinua," *Engineering Computations*, vol. 9, no. 2, pp. 101–113, 1992.

[35] D. Potyondy and P. Cundall, "A bonded-particle model for rock," *International Journal of Rock Mechanics and Mining Sciences*, vol. 41, pp. 1329–1364, dec 2004.

[36] N. Cho, C. Martin, and D. Sego, "A clumped particle model for rock," *International Journal of Rock Mechanics and Mining Sciences*, vol. 44, pp. 997–1010, oct 2007.

[37] D. Mas Ivars, "Bonded Particle Model for Jointed Rock Mass," 2010.

[38] D. Mas Ivars, M. E. Pierce, C. Darcel, J. Reyes-Montes, D. O. Potyondy, R. Paul Young, and P. a. Cundall, "The synthetic rock mass approach for jointed rock mass modelling," *International Journal of Rock Mechanics and Mining Sciences*, vol. 48, pp. 219–244, feb 2011.

[39] Y. Wang and F. Tonon, "Dynamic validation of a discrete element code in modeling rock fragmentation," *International Journal of Rock Mechanics and Mining Sciences*, vol. 48, pp. 535–545, jun 2011.

[40] K. J. L. Stone and V. Merrien-Soukatchoff, "Physical and numerical modeling of chalk slopes.pdf," in *Landslides and Climate Change* (McInnes, Jakeways, Fairbank, and Maithie, eds.), Taylor & Francis, 2007.

[41] L. Y. G. Cheung, *Micromechanics of Sand Production in Oil Wells*. Phd, University of London, 2010.

[42] G. Marketos and C. O'Sullivan, "A micromechanics-based analytical method for wave propagation through a granular material," *Soil Dynamics and Earthquake Engineering*, vol. 45, pp. 25–34, feb 2013.

[43] J. Olson, R. Narayanasamy, J. Holder, A. Rauch, and B. Comacho, "DEM Study of Wave Propagation in Weak Sandstone," pp. 335–339, 1999.

[44] R. Resende, L. N. Lamas, J. V. Lemos, and R. Calçada, "Micromechanical Modelling of Stress Waves in Rock and Rock Fractures," *Rock Mechanics and Rock Engineering*, vol. 43, pp. 741–761, may 2010.

[45] J. F. Hazzard, "Numerical investigation of induced cracking and seismic velocity changes in brittle rock," *Geophysical Research Letters*, vol. 31, no. 1, pp. 31–34, 2004.

[46] ICG, "Particle Flow Code 2D," 2012.

[47] I. Itasca Consulting Group, "PFC2D FISH in PFC2D - 01 FISH Beginner's Guide," 2008.

[48] J. Yoon, "Application of experimental design and optimization to PFC model calibration in uniaxial compression simulation," *International Journal of Rock Mechanics and Mining Sciences*, vol. 44, pp. 871–889, sep 2007.

[49] Y. Wang and F. Tonon, "Calibration of a discrete element model for intact rock up to its peak strength," no. July 2009, pp. 447–469, 2010.

[50] D. P. Adhikary, a. V. Dyskin, R. J. Jewell, and D. P. Stewart, "A study of the mechanism of flexural toppling failure of rock slopes," *Rock Mechanics and Rock Engineering*, vol. 30, no. 2, pp. 75–93, 1997.

[51] I. Itasca Consulting Group, "PFC2D Theory and Background - 04 Clump Logic," 2008.

[52] I. Itasca Consulting Group, "PFC2D Theory and Background - 01 General Formulation," 2008.

[53] I. Hawkes, M. Mellor, and S. Gariepy, "Deformation of rocks under uniaxial tension," *International Journal of Rock Mechanics and Mining Sciences & Geomechanics Abstracts*, vol. 10, pp. 493–507, nov 1973.

[54] I. Itasca Consulting Group, "PFC2D Theory and Background - 02 Contact Models," 2008.

[55] B. Engquist and A. Majdat, "Absorbing boundary conditions for numerical simulation of waves," in *Proceedings of the National Academy of Sciences of the United States of America*, vol. 74, pp. 1765–1766, 1977.

[56] P. A. Cundall, R. R. Kunar, P. C. Carpenter, and J. Marti, "Solution of Infinite Dynamic Problems by Finite Modelling in the Time Domain," in *International Conference on Applied Mathematique Modeling*, 1978.

[57] C. Peng and M. N. Toksz, "An optimal absorbing boundary condition for finite difference modeling of acoustic and elastic wave propagation," *Journal of the Acoustical Society of America*, vol. 95, no. 2, pp. 733–745, 1993.

[58] J.-P. Berenger, "A Perfectly Matched Layer for the Absorption of Electromagnetic Waves," *Journal of Computational Physics*, vol. 114, pp. 185–200, oct 1994.

[59] C. K. Tam, L. Auriault, and F. Cambuli, "Perfectly Matched Layer as an Absorbing Boundary Condition for the Linearized Euler Equations in Open and Ducted Domains," *Journal of Computational Physics*, vol. 144, pp. 213–234, jul 1998.

[60] J. Lysmer and R. L. Kuhlemeyer, "Finite Dynamic Model for Infinite Media," *Journal of the Engineering Mechanics Division*, pp. 859–877, 1969.

[61] I. Itasca Consulting Group, "FLAC Manual - Dynamic Analysis," 2011.

[62] L. Arnold, J. Wartman, M. Maclaughlin, and D. Keefer, "Wave dynamics and boundary condition verifications in PFC2D," in *4th Itasca Symposium on Applied Numerical Modeling*, (Lima, Peru), 2016.

[63] I. Itasca Consulting Group, "PFC2D User's Guide - 03 Problem Solving with PFC2D," 2008.

[64] D. M. Boore, S. C. Harmsen, and S. T. Harding, "Wave scattering from a step change in surface topography," *Bulletin of the Seismological Society of America*, vol. 71, no. 1, pp. 117–125, 1981.

[65] S. H. Potter, J. S. Becker, D. M. Johnston, and K. P. Rossiter, "An overview of the impacts of the 2010-2011 Canterbury earthquakes," *International Journal of Disaster Risk Reduction*, vol. 14, pp. 6–14, 2015.

[66] B. a. Bradley, M. C. Quigley, R. J. Van Dissen, and N. J. Litchfield, "Ground motion and seismic source aspects of the canterbury earthquake sequence," *Earthquake Spectra*, vol. 30, no. 1, pp. 1–15, 2014.

[67] W. S. A. Saunders and J. S. Becker, "A discussion of resilience and sustainability: Land use planning recovery from the Canterbury earthquake sequence, New Zealand," *International Journal of Disaster Risk Reduction*, vol. 14, pp. 73–81, 2015.

[68] G. Dellow, M. Yetton, C. Massey, G. Archibald, D. J. A. Barrell, D. Bell, Z. Bruce, A. Campbell, T. Davies, G. D. Pascale, M. Easton, P. J. Forsyth, C. Gibbons, P. Glassey, H. Grant, R. Green, G. Hancox, R. Jongens, P. Kingsbury, J. Kupec, D. Macfarlane, B. Mcdowell, B. Mckelvey, I. Mccahon, I. Mcpherson, J. Molloy, J. Muirson, M. O. Halloran, N. Perrin, C. Price, S. Read, N. Traylen, R. V. Dissen, M. Villeneuve, and I. Walsh, "LANDSLIDES CAUSED BY THE 22 FEBRUARY 2011 CHRISTCHURCH EARTHQUAKE AND MANAGEMENT OF LANDSLIDE RISK IN THE IMMEDIATE AFTERMATH," *Bulletin of the New Zealand Society for Earthquake Engineering*, vol. 44, no. 4, pp. 227–238, 2011.

[69] C. I. Massey, T. Taig, B. Lukovic, W. Ries, F. D. Pasqua, G. Archibald, and D. Heron, "Canterbury Earthquakes 2010 / 11 Port Hills Slope Stability : Risk assessment for Redcliffs," Tech. Rep. 78, GNS Science Consultancy Report, 2014.

[70] D. K. Keefer, "Landslides generated by earthquakes: Immediate and long-term effects," in *Treatise on Geomophology* (J. F. Shroder, ed.), ch. 5.11, pp. 250–266, Elsevier Inc., 2013.

[71] C. I. Massey, T. Taig, B. Lukovic, W. Ries, F. D. Pasqua, and G. Archibald, "Canterbury Earthquakes 2010 / 11 Port Hills Slope Stability : Debris avalanche risk assessment for Richmond Hill," Tech. Rep. August, GNS Science Consultancy Report, 2014.

[72] L. Arnold, J. Wartman, C. Massey, M. Maclaughlin, and D. Keefer, "Insights into the Seismically-Induced Rock-slope Failures in the Canterbury Region Using the Discrete Element Method," no. November, 2015.

[73] E. Hoek, "Putting numbers to geology an engineer ' s viewpoint," *Quarterly Journal of Engineering Geology*, vol. 32, no. 1, pp. 1 – 19, 1999.

[74] F. I. Makdisi and H. B. Seed, "A Simplified Procedure for Estimating Earthquake-Induced Deformations in Dams and Embankments," tech. rep., Earthquake Engineering Research Center, 1977.

[75] X.-p. Z. Louis and N. Yuen, "Displacement field analysis for cracking processes in bonded-particle model," pp. 13–21, 2014.

[76] B. A. Bradley and M. Cubrinovski, "Near-source strong ground motions observed in the 22 February 2011 Christchurch earthquake," *Bulletin of the New Zealand Society for Earthquake Engineering*, vol. 44, no. 4, pp. 181–194, 2011.

[77] C. V. Houtte, O. J. Ktenidou, T. Larkin, and A. Kaiser, "Reference stations for christchurch," *Bulletin of the New Zealand Society for Earthquake Engineering*, vol. 45, no. 4, pp. 184–195, 2012.

[78] C. M. Wood, B. R. Cox, L. M. Wotherspoon, and R. A. Green, "Dynamic site characterization of Christchurch strong motion stations," *Bulletin of the New Zealand Society for Earthquake Engineering*, vol. 44, no. 4, pp. 195–204, 2011.

[79] A. Fakhimi and E. Alavi Gharahbagh, "Discrete element analysis of the effect of pore size and pore distribution on the mechanical behavior of rock," *International Journal of Rock Mechanics and Mining Sciences*, vol. 48, pp. 77–85, jan 2011.

[80] S. Song and T. H. Heaton, "Prediction of Collapse from PGV and PGD," in *15th World Conference on Earthquake Engineering*, 2012.

[81] C. Wang, D. Tannant, and P. Lilly, "Numerical analysis of the stability of heavily jointed rock slopes using PFC2D," *International Journal of Rock Mechanics and Mining Sciences*, vol. 40, pp. 415–424, apr 2003.

[82] E. M. Rathje, F. Faraj, S. Russell, and J. D. Bray, "Empirical Relationships for Frequency Content Parameters of Earthquake Ground Motions," *Earthquake Spectra*, vol. 20, no. 1, pp. 119–144, 2004.

[83] S. A. Ashford and N. Sitar, "Seismic Response of Steep Natural Slopes," tech. rep., EERC, 1994.

[84] S. A. Ashford, N. Sitar, and M. Asce, "Simplified Method for Evaluating Seismic Stability of Steep Slopes," no. February, pp. 119–128, 2002.

[85] L. A. Pierson and R. Van Vickle, "Rockfall Hazard Rating System," tech. rep., FHWA-SA-93-057, 1993.

[86] M. Tsesarsky, "Deformation mechanisms and stability analysis of undermined sedimentary rocks in the shallow subsurface," *Engineering Geology*, vol. 133-134, pp. 16–29, apr 2012.

[87] Ö. Aydan and H. Kumsar, "An Experimental and Theoretical Approach on the Modeling of Sliding Response of Rock Wedges under Dynamic Loading," *Rock Mechanics and Rock Engineering*, vol. 43, pp. 821–830, mar 2009.

[88] N. Sitar, M. M. Maclaughlin, and D. M. Doolin, "Influence of Kinematics on Landslide Mobility and Failure Mode," *Journal of Geotechnical and Geoenvironmental Engineering*, no. June, pp. 716–728, 2005.

[89] M. Bahaaddini, G. Sharrock, and B. K. Hebblewhite, "A comparison of physical and numerical experiments on artificial jointed rock masses using PFC 3D," in *Continuum and Distinct Element Numerical Modeling in Geomechanics*, 2011.

[90] C. H. Park and A. Bobet, "Crack coalescence in specimens with open and closed flaws: A comparison," *International Journal of Rock Mechanics and Mining Sciences*, vol. 46, no. 5, pp. 819–829, 2009.

[91] W. S. Dershowitz and H. H. Herda, "Interpretation of fracture spacing and intensity," in *Rock Mechanics*, pp. 757–766, 1992.

[92] M. Bahaaddini, G. Sharrock, B. K. Hebblewhite, and R. Mitra, "Statistical analysis of the effect of joint geometrical parameters on the mechanical properties of non-persistent jointed rock masses," in *American Rock Mechanics Association*, 2012.

[93] M. Mauldon and W. Dershowitz, "A Multi-Dimensional System of Fracture Abundance Measures," 2000.

[94] W. Dershowitz, "Derivation of Basic Fracture Properties," 2008.

[95] R. E. Goodman and J. W. Bray, "Toppling of Rock Slopes," 1976.

[96] O. Aydan and T. Kawamoto, "The Stability of Slopes and Underground Openings Against Flexural Toppling and Their Stabilisation," *Rock Mechanics and Rock Engineering*, vol. 25, no. 3, pp. 143–165, 1992.

[97] D. P. Adhikary, A. V. Dyskin, and R. J. Jewell, "Numerical modelling of the flexural deformation of foliated rock slopes," *Continuum*, vol. 33, no. 6, pp. 595–606, 1996.

[98] M. Amini, A. Majdi, and Ö. Aydan, "Stability Analysis and the Stabilisation of Flexural Toppling Failure," *Rock Mechanics and Rock Engineering*, vol. 42, pp. 751–782, dec 2008.

[99] A. Majdi and M. Amini, "Analysis of geo-structural defects in flexural toppling failure," *International Journal of Rock Mechanics and Mining Sciences*, vol. 48, pp. 175–186, feb 2011.

[100] Z. Zhang, T. Wang, S. Wu, and H. Tang, "Rock toppling failure mode influenced by local response to earthquakes," *Bulletin of Engineering Geology and the Environment*, 2015.

[101] H. Einstein, D. Veneziano, G. Baecher, and K. O'Reilly, "The effect of discontinuity persistence on rock slope stability," *International Journal of Rock Mechanics and Mining Sciences & Geomechanics Abstracts*, vol. 20, pp. 227–236, oct 1983.

[102] L. Scholtès and F.-V. Donzé, "Modelling progressive failure in fractured rock masses using a 3D discrete element method," *International Journal of Rock Mechanics and Mining Sciences*, vol. 52, pp. 18–30, jun 2012.

[103] L. A. M. Camones, E. D. A. Vargas, R. P. de Figueiredo, and R. Q. Velloso, "Application of the discrete element method for modeling of rock crack propagation and coalescence in the step-path failure mechanism," *Engineering Geology*, vol. 153, pp. 80–94, feb 2013.

[104] M. D. Gibson, *Prediction of Seismic Rock Slope Failure Modes and Displacements Using Simplified Single Block Methods*. Doctor of philosophy, University of Washington, 2013.

[105] C. Fairhurst, "Fundamental Considerations Relating To The Strength Of Rock," *Report on the Workshop on Extreme Ground Motions at Yucca Mountain*, 2004.

[106] T. L. Anderson, *Fracture Mechanics Fundamentals and Applications*. Taylor & Francis, 2005.

[107] D. Roylance, "Introduction to Fracture Mechanics," 2001.

[108] A. A. Griffith, "The Phenomena of Rupture and Flow in Solids," *Philisophical Transactions of the Royal Society of London*, vol. 221, no. Series A, Containing Pepers of a Methematical or Physical Character, pp. 163–198, 1921.

[109] A. K. Chopra, *Dynamics of Structures*. Prentice Hall, 2007.

[110] B. Indraratna, "Development and applications of a synthetic material to simulate soft sedimentary rocks," *Geotechnique*, vol. 40, no. 2, pp. 189–200, 1990.

[111] L. Dobereiner and M. H. Freitas, "Geotechnical properties of weak sandstone," *Geotechnique*, vol. 36, no. 1, pp. 79–94, 1986.

[112] P. Joseph and H. Einstien, "Rock Modeling Using the Centrifuge," tech. rep., Air Force Engineering and Services Center, 1988.

[113] I. Itasca Consulting Group, *PFC2D FISH in PFC2D - 02 FISH Refence*. 2008.

Appendix A

FRACTURE MECHANICS

A.1 Rupture at the Atomic Level

The fundamentals of fracture mechanics begin at the atomic level. Two atoms, bonded as a solid, have an equilibrium distance, x_o, where the interatomic force is zero and the attractive energy is at a maximum [105]. Figure A.1 shows the changes in force and energy with distance. There are two requirements for a bond to be ruptured:

1. The bond strength, t_{max}, must be exceeded.

2. The atoms must separate to a distance where there is no longer attractive energy between them. If this separation distance is not achieved, the atoms will return to their equilibrium spacing, even if the bond strength has been exceeded.

The implication of this on fracture mechanics is that there is both a stress and an energy requirement to create a fracture (a rupture of atomic bonds) in a material.

A.2 Stress Intensity

The separation of atoms can be the result of either tensile or shear loading. There are three fundamental modes of fracture - one in tension and two in shear [106]. Figure A.2 shows the three modes. For this summary, only tensile (Mode I) fractures will be discussed.

Each mode has its own stress itensity function. Stress intensity is a measure of the stress concentration at the tip of the crack caused by the discontinuity in the material. For Mode I, the stress intensity, K_I is:

$$K_I = \lim_{r \to 0} \sqrt{2\pi r}\sigma \tag{A.1}$$

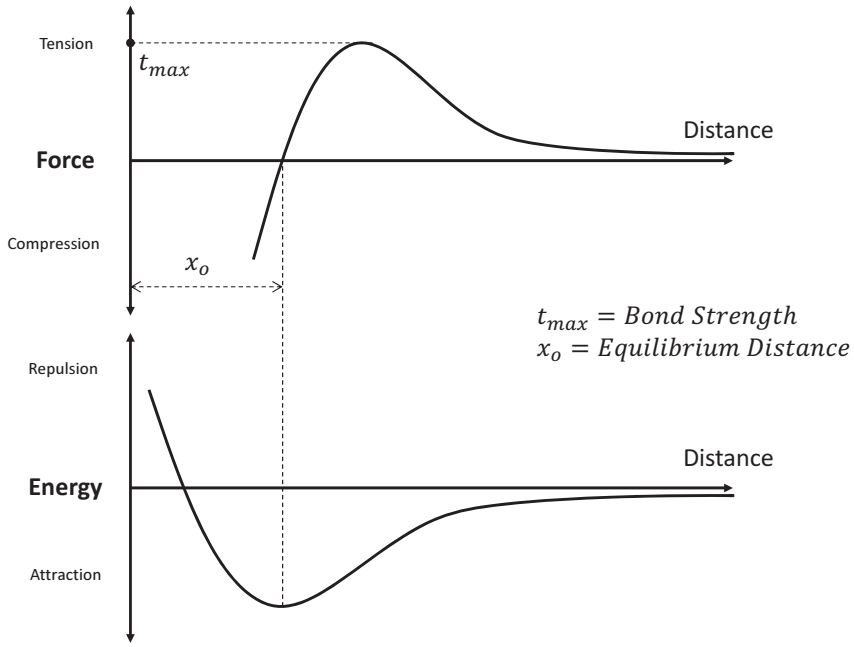

Figure A.1: Atomic Force and Energy with Distance

where r is the distance from the crack tip and σ is stress normal to the direction of the crack [107].

Equation A.1 is dependent on geometry and often not simple to evaluate. Most fracture mechanics references provide tables for solutions for K_I for common specimen geometries. For the case of a single crack in an infinite plate (Figure A.3), K_I is shown in Equation A.2. Solutions for stress intensity for any geometry are all of units $Stress\sqrt{Length}$.

$$K_I = \sigma\sqrt{\pi a} \tag{A.2}$$

where a is one half of the crack length [106]. The half crack length is used because an

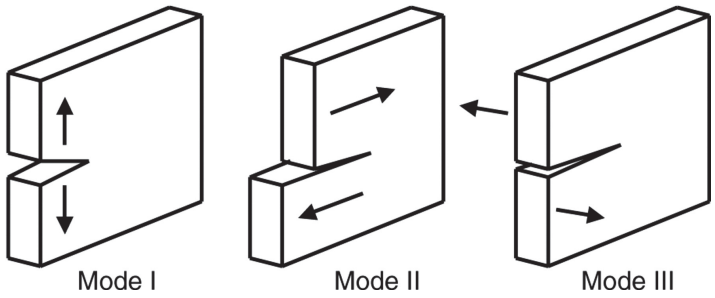

Figure A.2: Modes of Fracture

elliptical crack in an infinite plate is symmetric about the minor axis of the ellipse and only one half of the infinite plate needs to be considered.

A.3 Fracture in an Idealized Material

A. A. Griffith used the concept of energy required for atomic separation to establish a criterion for fracture of brittle materials in 1921 [108]. An infinite plate with an elliptical crack can be used as an illustration for Griffith's fracture criterion. A depiction of such a plate is shown in Figure A.3. The plate is loaded in tension perpendicular to the long axis of the ellipse. Since tension cannot be transmitted across the crack, the stress 'flows' around the crack resulting in a stress concentration at the crack tip (Figures A.4 and A.5).

In a perfectly rigid material, as a becomes very large compared to b, the radius at the crack tip approaches zero and the stress concentration factor approaches ∞. Far from the crack tip, the stress approaches the far-field stress, σ_o [107]. See Figure A.6.

The stress singularity at the crack tip makes it desireable to have a criteron for fracture

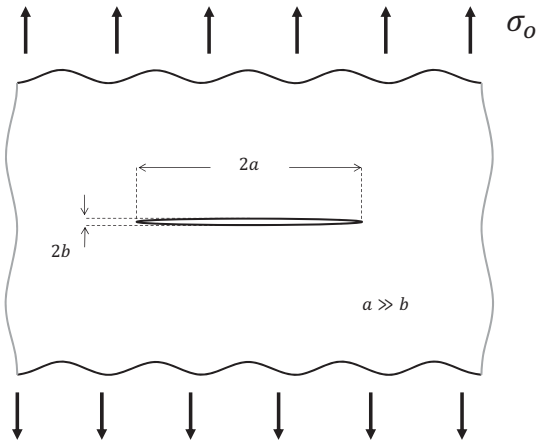

Figure A.3: An Elliptical Crack in a Loaded Infinite Plate

based on energy requirements rather than stress requirements [107]. Griffith developed *A Theoretical Criterion of Rupture* based on the theorem of minimum energy which states that

> *[T]he equilibrium state of an elastic solid body, deformed by specified surface forces, is such that the potential energy of the whole system is a minimum.*

Griffith's new criterion for rupture added that

> *[T]he equilibrium position, if equilibrium is possible, must be one in which rupture of the solid has occurred, if the system can pass from the unbroken to the broken condition by a process involving a continuous decrease in potential energy.* [108]

There are three sources of change in energy related to the extension of a crack:

1. Potential energy of the applied forces, W.

   The energy contribution of the applied forces is the work ($force * distance$) done on the system. Equation A.3 shows the relationship between work and strain energy.

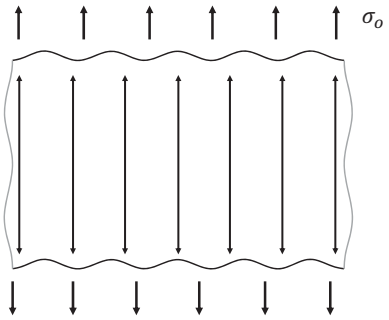

Figure A.4: Infinite Plate with No Crack

2. Strain energy of the loaded plate, U.

   The strain energy is the energy stored in the plate due to the deformation caused by loading.

3. Surface energy of the crack surfaces, S.

   Surface energy is the energy associated with the intermolecular forces on the surface of a solid or liquid. The surface energy per unit area, or specific surface energy (γ), is the same as 'surface tension'.

The relationships between these energies and the system and material properties (E, γ, a, and σ) have been established by Griffith, Love, and others [105] and are shown in equations A.3 through A.5. These three sources of change in energy can be summed to obtain the change in potential energy, ΔP, for the system (Equation A.6).

$$\Delta W = -2\Delta U \tag{A.3}$$

$$\Delta U = \frac{\pi a^2 \sigma^2}{E} \tag{A.4}$$

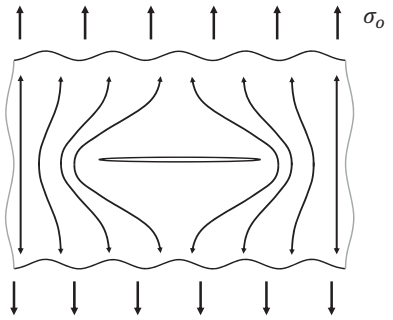

Figure A.5: Stress Flow Around a Crack

$$\Delta S = 4a\gamma \tag{A.5}$$

where γ is the specific surface energy.

$$\Delta P = \Delta W + \Delta U + \Delta S \tag{A.6}$$

Equations A.3 through A.6 are combined in Equation A.7 to give the change in potential energy for the system in terms of the system and material properties.

$$\Delta P = 4a\gamma - \frac{\pi a^2 \sigma^2}{E} \tag{A.7}$$

According to Griffith's failure criterion, fracture will occur when conditions are such that crack extension will result in a continuous decrease in ΔP. A plot of ΔP v. crack length, a, is shown in Figure A.7. Looking at the graphical representation of Equation A.7, it is easy to see that beyond a critical crack length, a_{crit}, for a given stress state, the system potential energy will continually decrease and, therefore, fracture will occur. The partial derivative of ΔP with respect to a is zero at the critical crack length.

$$\frac{\partial(\Delta P)}{\partial c} = 0 = 4\gamma - \frac{2\pi a \sigma^2}{E} \tag{A.8}$$

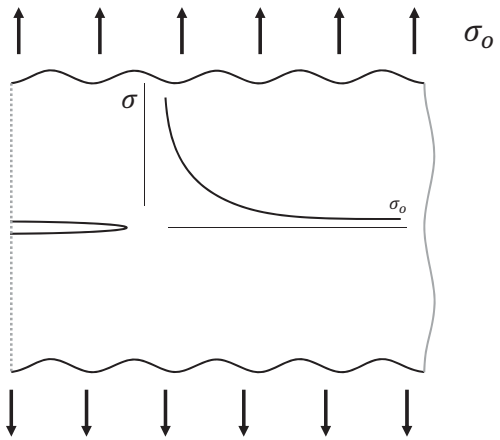

Figure A.6: Stress at a Crack Tip in a Loaded Infinite Plate

Of course, for a stable crack with a constant stress state, there is no reason for the crack to extend, so the concept of a critical crack length is a bit abstract. Perhaps a more intuitive way to look at the change in system potential energy is to look at several ΔP curves for different stress states as is shown in Figure A.8. This figure shows how an increasing stress state produces a decreasing critical crack length, which will lead to fracture when $a_{crit} = a$. The dependency of the global strength of the infinite plate on the length of the crack indicates a fundamental relationship between internal structure and resistance to rupture. Even in cases where a material is seemingly intact, micro-cracks and micro-crack size, have a strong influence on the material's ultimate strength. In other words, the macro-strength of a material is always dependent on the size of discontinuities in the material.

Equation A.8 can also be written as:

$$\sigma_{crit} = \sqrt{\frac{2E\gamma}{\pi a}} \tag{A.9}$$

The applied stress that causes fracture to initiate in this system, σ_{crit}, is a function of

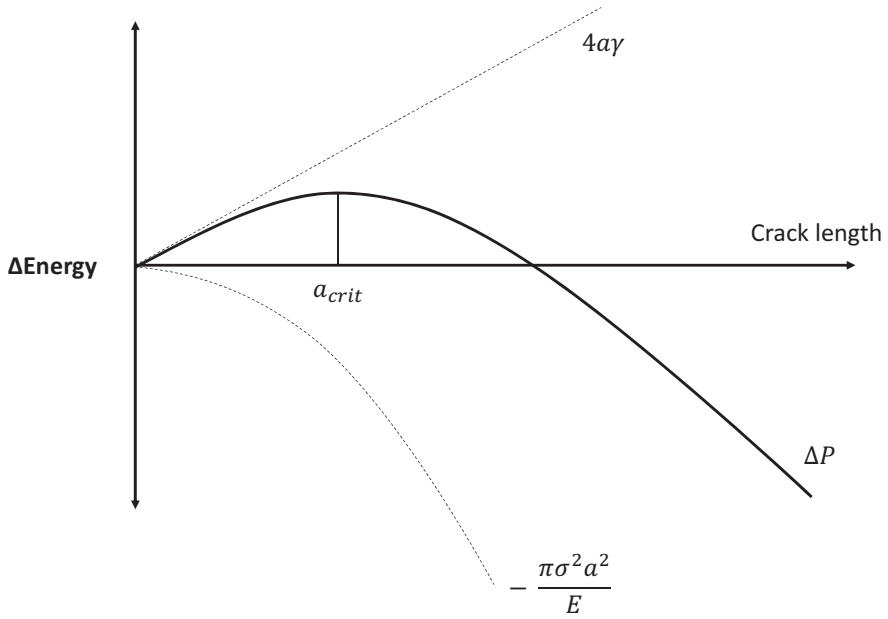

Figure A.7: Change in Potential Energy with Crack Length

crack length, so it is not a material property. E and γ, however, are materal properties. A rearrangement of Equation A.9 shows that $\sigma_{crit}^2 a$ is equal to material constants and must be constant itself.

$$\sigma_{crit}^2 = 2E\gamma = \textbf{const} \tag{A.10}$$

Recalling Equation A.2 for stress intensity in an infinite plate, we see that $\sigma_{crit}^2 \pi a$ is the square of the Mode I stress intensity at the initiation of fracture. The stress intensity at the initiation of fracture (or the critical stress intensity) is called the 'fracture toughness', K_{IC}.

$$K_{IC} = \sigma_{crit}\sqrt{\pi a} \tag{A.11}$$

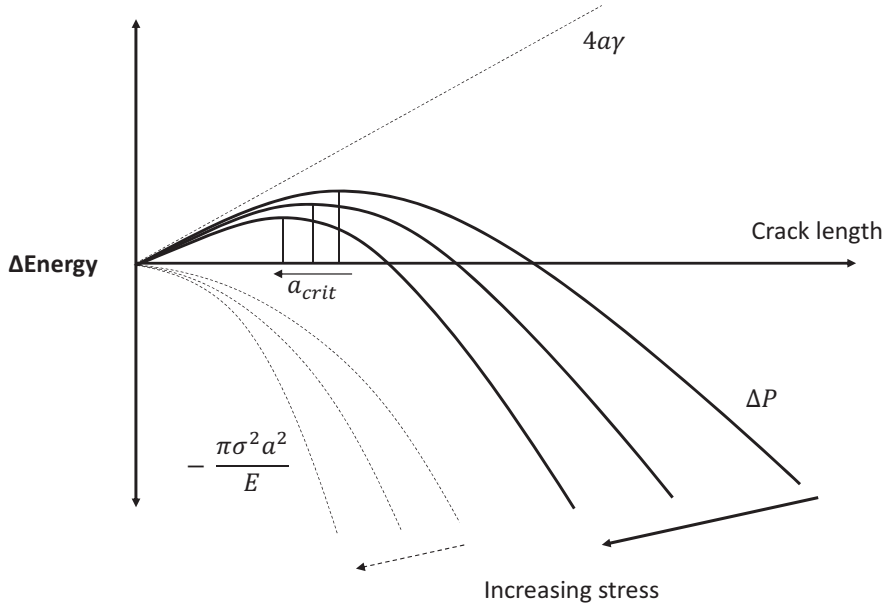

Figure A.8: Change in Potential Energy with Crack Length with Increasing Applied Stress

Fracture toughness is a material property that describes a material's resistance to fracture. According to Griffith's theory, a material's fracture toughness considers the fundamental energy requirement for rupture at the atomic level. The units of fracture toughness ($Stress\sqrt{Length}$) demonstrate the dependence of a material's macro-strength on the size of 'flaws' or cracks.

Appendix B

ANALYTICAL SOLUTION FOR A DYNAMIC CANTILEVER BEAM

The primary purpose of this centrifuge experiment was to provide data for the calibration of a bonded-particle model (BPM). A BPM simulates the ARM with an assembly of rigid particles and elastic springs. One important question to answer when calibrating a model against an experiment is how well the experiment behaved. An analytical model for the experiment performed in the centrifuge would give an indication of how closely the experiment matched idealized conditions.

B.1 Formulation of the analytical model

The theory needed for the formulation of the analytical model for the natural frequencies and mode shapes of an elastic cantilever beam can be found in Chopra's *Dynamics of Structures* Chapter 16 [109].

B.1.1 Symbols used in this section

E	Young's modulus
G_s	Specific gravity
ξ	Damping ratio
w	Beam width
t	Beam thickness
L	Beam length
ω	Natural frequency
$\overline{\omega}$	Loading frequency
Φ	Mode shape
u	Beam displacement
R_d	Dynamic response factor
$T(f)$	Transfer function

A cantilever with a distributed mass is an infinite degree of freedom system. Only the first four modes were considered initially, however, because they account most of the system's response. The timestep of the input motions limits the range of frequencies that can be excited such that only two of the modes are truly considered.

The natural frequencies can be described by:

$$\omega_n = \frac{\alpha_n}{L^2}\sqrt{\frac{EI}{m}} \tag{B.1}$$

No simple solution for α_n exists, so Chopra provides them from a numerical solution: $\alpha_1 = 3.516$, $\alpha_2 = 22.03$, $\alpha_3 = 6.70$, $\alpha_4 = 120.9$. The mode shape corresponding to each natural vibration mode is:

$$\Phi_n(x) = \cosh\beta_n x - \cos\beta_n x - \frac{\cosh\beta_n L - \cos\beta_n L}{\sinh\beta_n L - \sin\beta_n L}(\sinh\beta_n x - \sin\beta_n x) \tag{B.2}$$

Figure B.1 shows the first 4 mode shapes. Once the mode shapes and natural frequencies are determined, modal analysis can be performed on the system. For each considered mode,

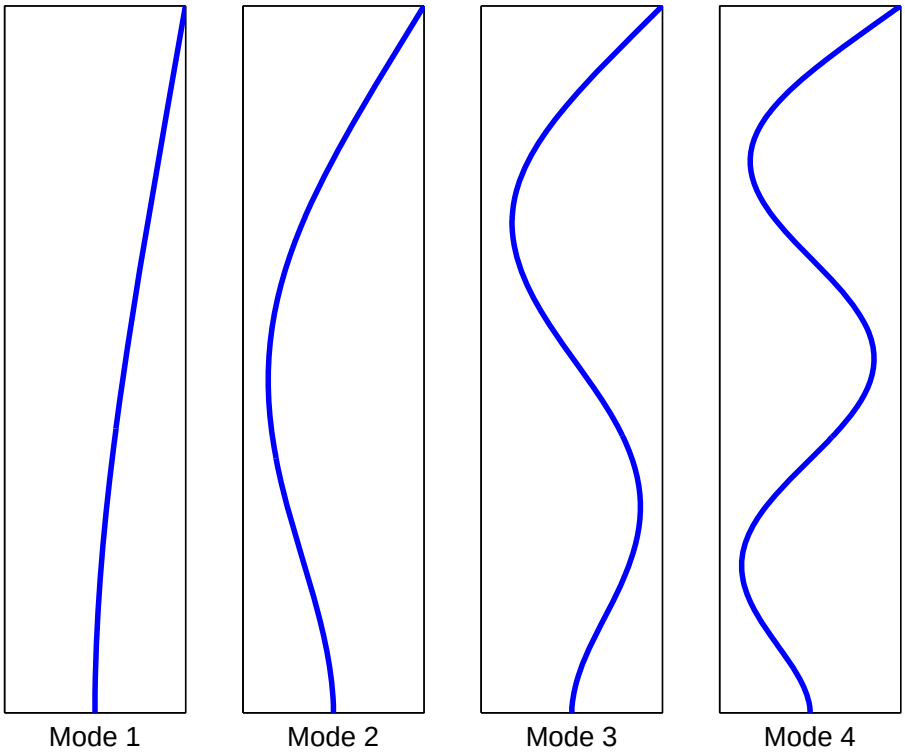

Figure B.1: Mode Shapes

the modal dynamic parameters are found:

$$M_n = \int_0^L \Phi_n^2(x) m(x) dx \tag{B.3}$$

$$P_n = -\int_0^L \Phi_n(x) |\ddot{u}(x)| m(x) dx \tag{B.4}$$

$$K_n = \frac{M_n}{\omega_n^2} \tag{B.5}$$

$$\Xi_n = \xi_n n^2 \tag{B.6}$$

where M_n, P_m, K_n, Ξ_n are the modal mass, load, stiffness and damping, respectively. Note that the modal damping equation is arbitrary and simply provides higher levels of damping at higher modes.

Once these modal parameters are determined, each mode can be analyzed as a single degree of freedom (SDOF) system and the responses summed. The steady state response to harmonic loading for a SDOF system is given by:

$$u(t) = C \sin \overline{\omega} t + D \cos \overline{\omega} t \tag{B.7}$$

where

$$C = \frac{P}{K} \frac{1 - (\frac{\overline{\omega}}{\omega_n})^2}{[1 - (\frac{\overline{\omega}}{\omega_n})^2]^2 + [2\xi(\frac{\overline{\omega}}{\omega_n})]^2} \tag{B.8}$$

and

$$D = \frac{P}{K} \frac{-2\xi(\frac{\overline{\omega}}{\omega_n})}{[1 - (\frac{\overline{\omega}}{\omega_n})^2]^2 + [2\xi(\frac{\overline{\omega}}{\omega_n})]^2} \tag{B.9}$$

The amplification, or the modal dynamic response factor (R_{nd}) is the ratio between the amplitude of this dynamic response and the static input displacement amplitude:

$$R_{nd} = \frac{1}{\sqrt{C^2 + D^2}} \tag{B.10}$$

R_{nd},evaluated over a range of frequencies produces a modal transfer function, $T_n(f)$, which can be applied to a general input motion in the frequency domain to determine the modal response. These modal transfer functions can be combined to create a global transfer function, $T(f)$, that includes the effects of all considered modes. The modal transfer functions are combined in this way:

$$T(f) = T_1(f) + T_2(f) + \cdots + T_n(f) - (n - 1) \tag{B.11}$$

$T(f)$ is shown in Figure 2.

B.2 Comparison with experimental results

All inputs for the analytical model (except for damping) were taken from measurements taken in the lab. The Youngs modulus and damping were adjusted to get the best fit of natural frequency and amplification. The inputs to the analytical model are: E, G_s, ξ, w, t, L.

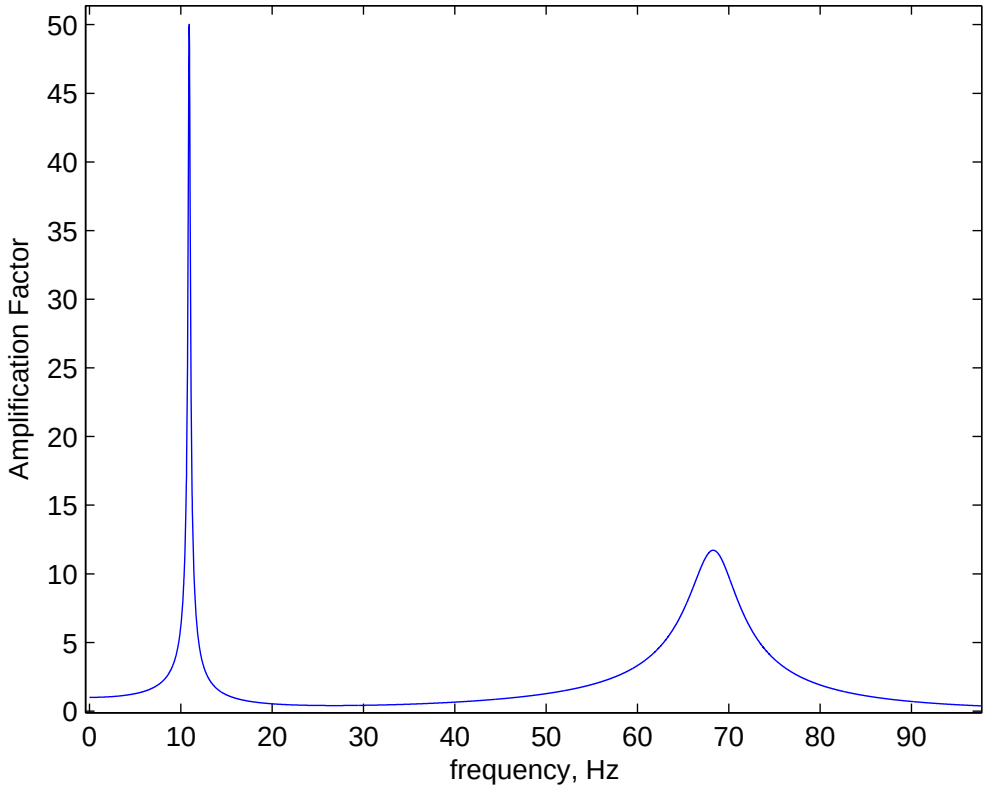

Figure B.2: Transfer Function for a Cantilever Beam with Distributed Mass

The analytical solution shows good agreement with the experimental results in most respects. Figures 3, 4, 5 and 6, 7, 8 show the analytical and experimental results in the time and frequency domains.

B.2.1 Time Domain Observations

At low frequencies, the analytical model under-predicts the response and at the natural frequency, the analytical model over-predicts the response. These trends are seen more clearly in the frequency domain.

B.2.2 Frequency Domain Observations

Consistent with the time domain observations, the amplification at low frequencies is lower in the analytical solution. At the natural frequency, the amplification is greater, but in a much more narrow band than the experimental results. The experimental results show a less clear natural frequency and a broadband amplification about that frequency.

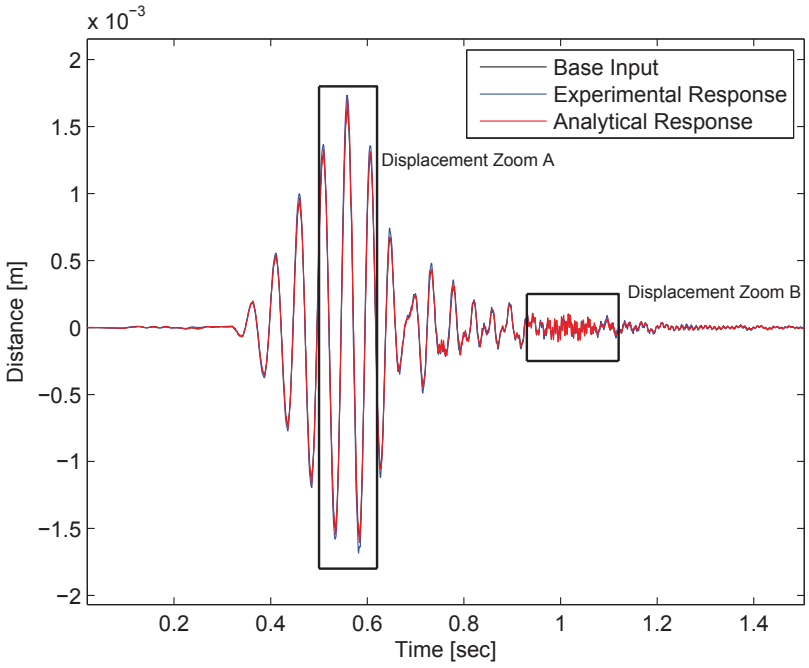

Figure B.3: Displacement Response

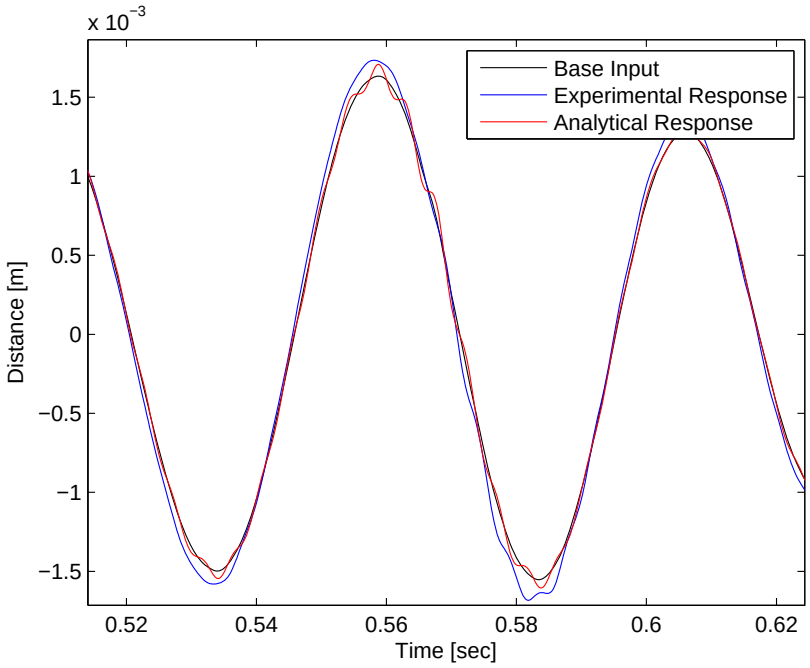

Figure B.4: Displacement Zoom A

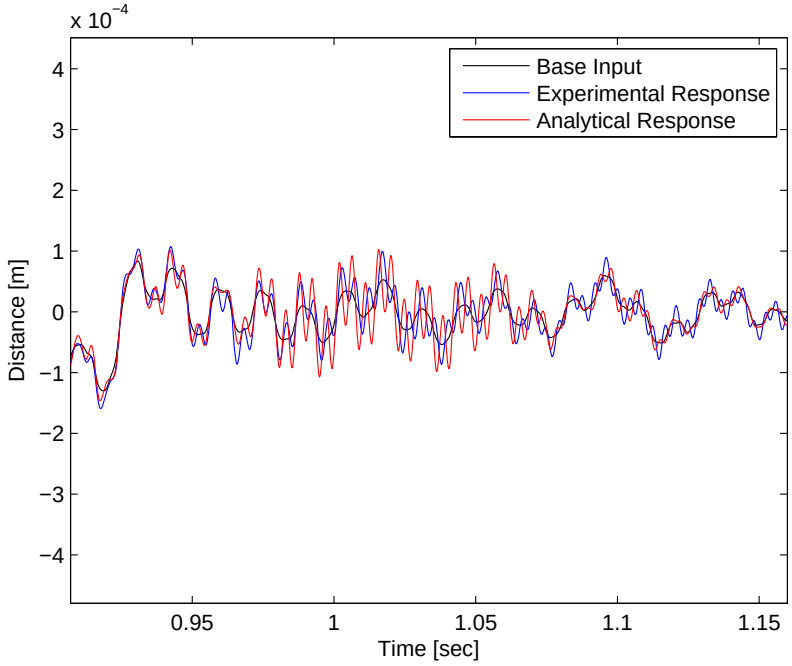

Figure B.5: Displacement Zoom B

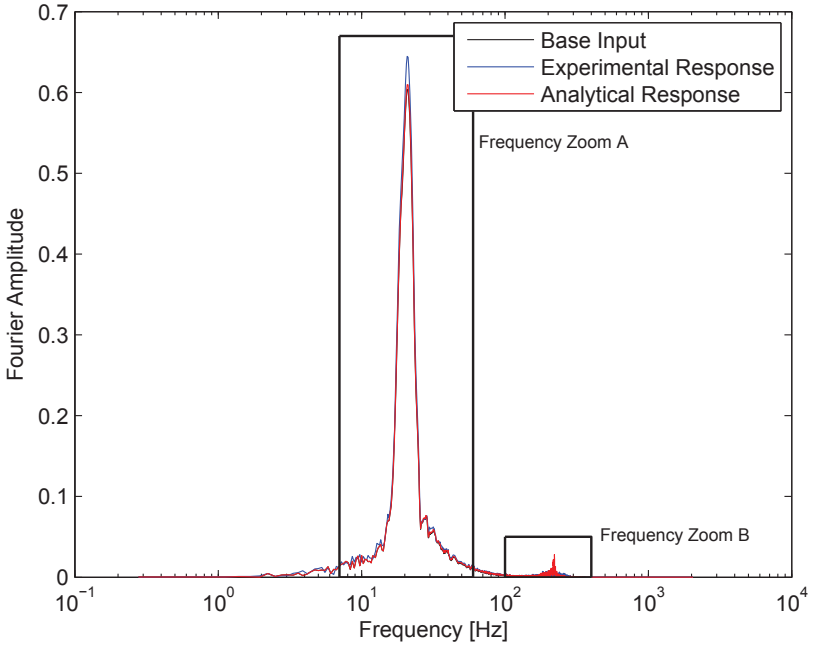

Figure B.6: Frequency Response

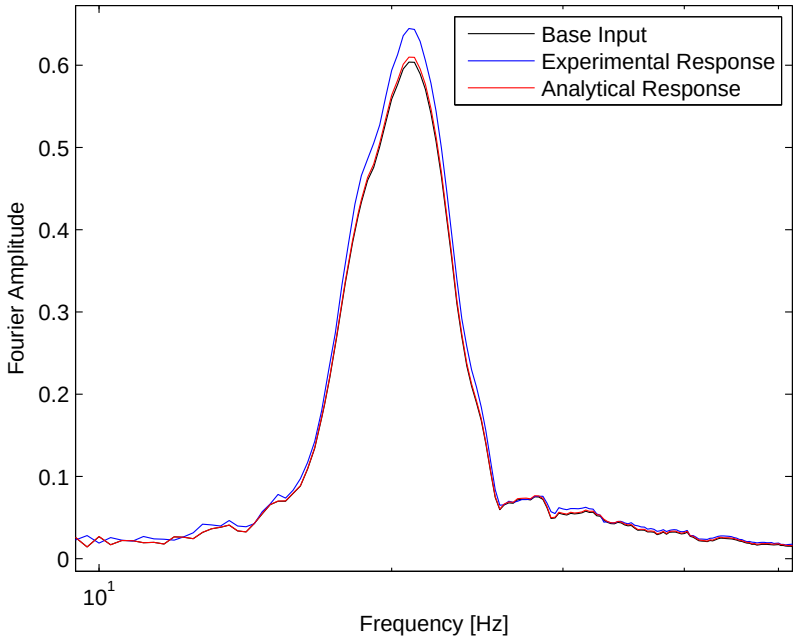

Figure B.7: Frequency Zoom A

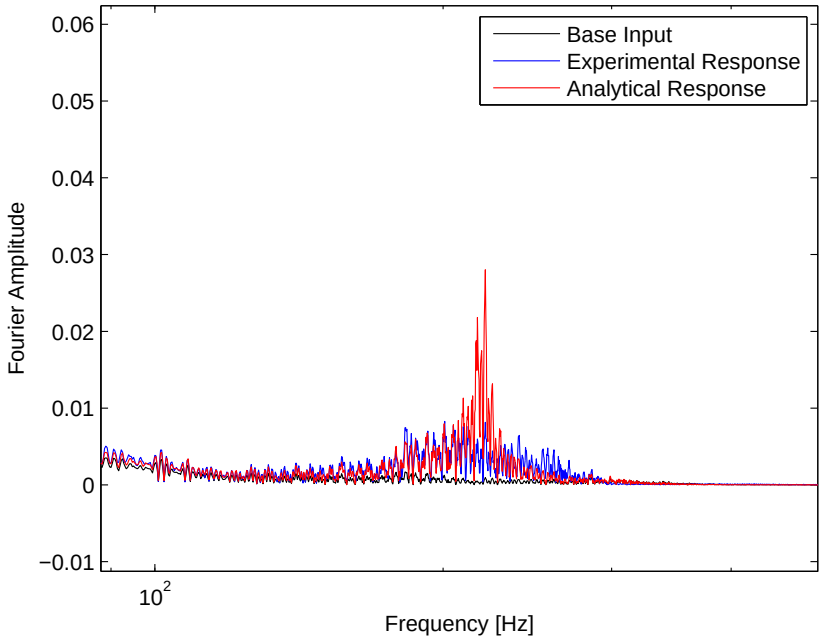

Figure B.8: Frequency Zoom B

B.2.3 Conclusions

The inability of the analytical solution to perfectly match the experimental results is no surprise, but the results show good agreement overall. There are several possible contributing factors to the discrepancies: the material itself may not be perfectly elastic and the glue connection had some compliance. Other contributing factors could include the placement of the sensors and the output signal filtering process.

The analytical solution provides a guide for how far from the ideal the experiment performed and how well any other idealized model could be expected to match the experiment. Really, it gives us a benchmark to quantify the acceptability of level of agreement between the PFC results and the experiment.

Appendix C

PHYSICAL TESTING

C.1 Development of an Analogue Rock Material

An artificial material is desirable for physical investigations because, unlike most natural materials, an artificial material can be made fairly homogeneous so that the influence of different variables on behavior can be looked at independently. The analogue rock material (ARM) developed for this study had two purposes: 1) to serve as a rock-like material for physical modeling and 2) to provide a target for the calibration of the PFC model. Indraratna (1990) provides several considerations for the development of such a material as well as several potential ingredients [110]. Based on these recommendations, a gypsum, sand, and water mix was selected and several recipes were tested. The material was subjected to three common laboratory tests: 1) unconfined compressive strength (UCS), 2) Brazilian tensile strength (BT), and 3) a three point bending test on a single edge notched beam (SENB), which can provide the material's fracture toughness (K_{IC}). Figure C.1 shows the initial testing conditions as well as the approximate scale of the samples. The final selected recipe was 59% sand, 24% gypsum, and 17% water by weight. A summary of its engineering properties can be found in Table C.1. It is similar to a weak sandstone [111].

Table C.1: ARM engineering properties

Compressive modulus (E_c)	4 GPa
Flexural modulus (E_{flex})	3 GPa
Unconfined compressive strenth (σ_c)	15 MPa
Tensile strength (σ_t)	3 Mpa
Fracture toughness (K_{IC})	0.95 MPa$\sqrt{m}$

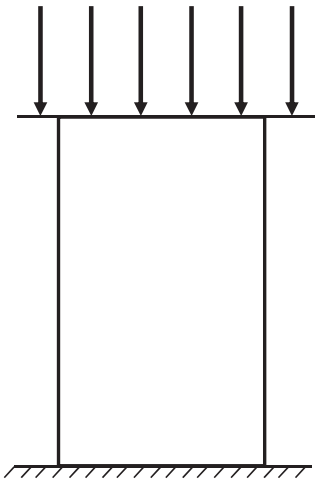

(a) UCS test sample illustration

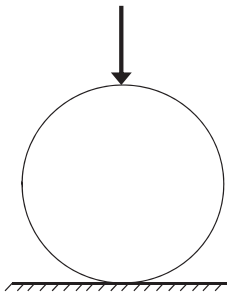

(b) BT test sample illustration

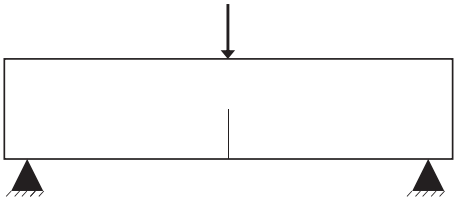

(c) SENB test sample illustration

Figure C.1: Laboratory test setups

C.2 UC Davis Centrifuge Test

In September 2012, a small centrifuge test was performed on the Schaevitz centrifuge at the NEES Center for Geotechnical Modeling at the University of California, Davis.

C.2.1 Purpose

The purpose of the test was to provide high g-level and dynamic calibration data for the numerical model and also to investigate the viability of the model material for rock fracture and rock-slope experiments for future centrifuge tests.

Two types of samples were tested: beams and slopes. The beam were made in a variety of configurations with internal cracks of different orientations and lengths. A completely intact beam was also tested as a baseline. The cracks in the beams were formed during the casting process by inserting thin plastic sheets (about 0.5-mm thick) into the mold before pouring the gypsum mix. The mold was designed to allow the plastic sheets to be removed during the curing process. By a process of trial and error, it wad determined hat the sheets could be removed between 5 and 7 minutes of pouring without damaging the specimen or allowing the discontinuity to close and seal itself. When the fully cured samples were broken for investigation of the cracks, the surfaces were observed to be clean (i.e., no sealing) and had a distinct boundary formed by the edge of the sheet. The cracks formed in the beams, therefore, where thin discontinuities whose respective sides were not in contact and which terminated in intact material. These discontinuities are different for natural fractures rock in that there is no direct contact between the faces and that a crack tip radius of 0.25-mm is fairly dull.

Figure C.2 shows the full set of beams that were tested. Beams were created with cracks of varying length and orientation. A completely intact beam was also tested as a baseline. The cracks in the beams were formed during the casting process by inserting thin plastic sheets (approximately 0.5-mm thick) into the mold before pouring the mix. The mold was designed to allow the plastic sheets to be removed during the curing process. By a process of trial and error, it was determined that the sheets could be removed between 5 and 7 minutes of pouring without damaging the specimen or allowing the discontinuity to close and seal

itself. When the fully cured samples were broken, and the surfaces of the discontinuities exposed, they were observed to be clean (i.e. no sealing) and had a distict boundary formed by the edge of the plastic sheet. The cracks formed in the beams, therefore, were thin discontinuities whose respective sides were not in contact and terminated in intact material.

Figure C.3 shows the slope configurations tested.

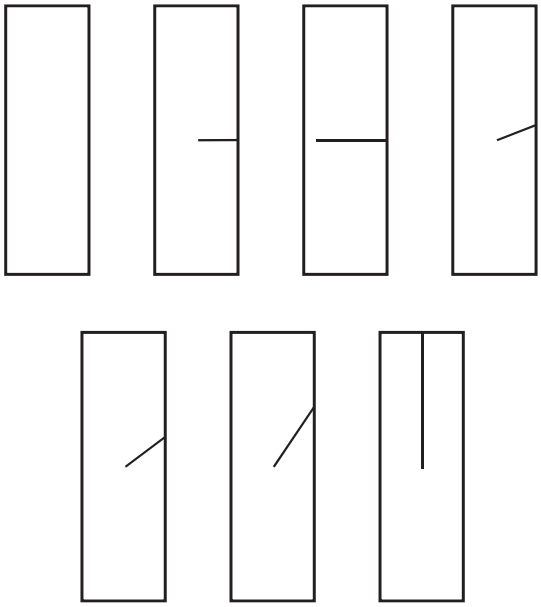

Figure C.2: Centrifuge beam models with pre-existing cracks of varying length and orientation.

C.2.2 Beam Tests

The ARM was formed into beams and glued to a stiff platform forming a cantilever for dynamic testing. As shown in Figure C.5, accelerometers were attached to the platform, the base and the top of the model to record the input and capture the beam's response. The glue used to attach the model to the platform was very stiff, and no significant difference between the recorded acceleration of the centrifuge platform and the base of the beam was observed. The material was tested in a centrifuge at 20g. The increase in g-level allows the beam to be interpreted as a larger prototype-scale model according to centrifuge scaling

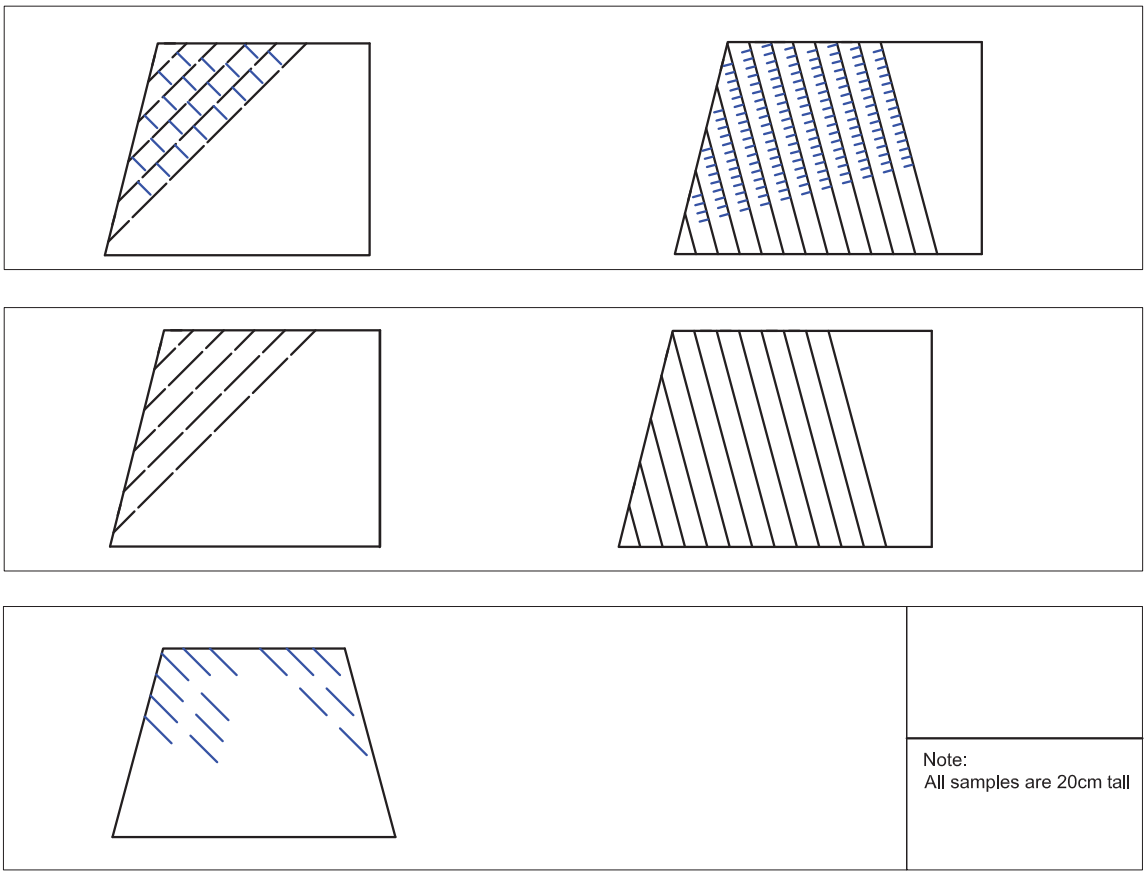

Figure C.3: Centrifuge slope models. Top row left: a sliding slope with two joint sets. Top row right: a toppling slope with two joint sets. Middle row left: a sliding slope with one joint set. Middle row left: a toppling slope with one joint set. Bottom row: a double-sided slope with an anti-dip joint set on the left and a dip joint set on the right.

laws [112]. At 20g, the prototype dimensions of the cantilever beam are 4-m by 1-m by 0.4-m. For the sake of consistency, all experimental and numerical results will be presented in prototype dimensions.

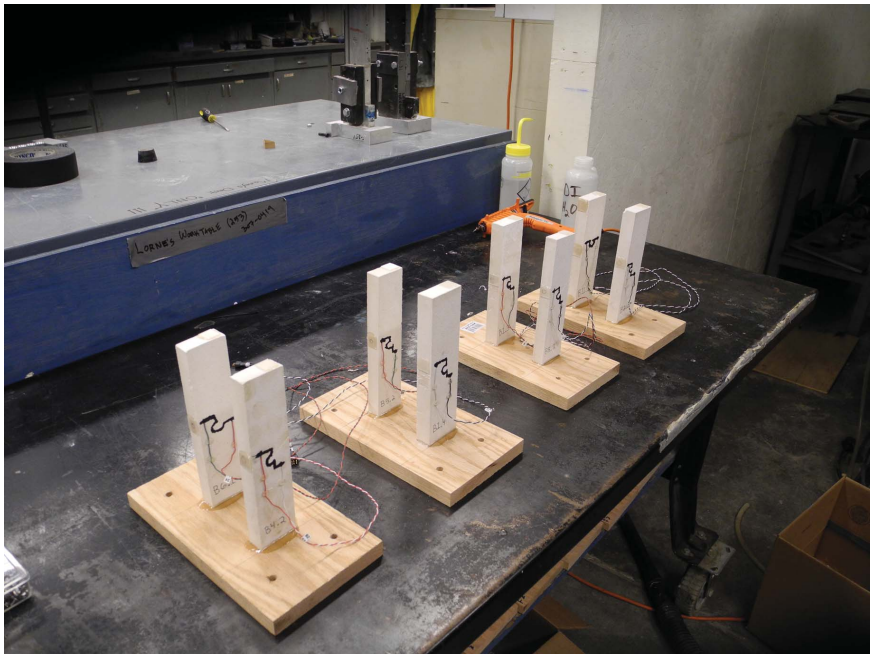

Figure C.4: Centrifuge test samples

The beams were subjected to loading in the range of 1 to 30 Hz with a frequency sweep motion with a maximum amplitude of about 0.3 g. Figure C.6 shows the input motion as recorded by the accelerometer on the shaking base.

C.2.3 Slope Tests

The slopes tested at UC Davis were designed in conjunction with Xianglong Li, a visiting researcher from China University of Geosciences. The primary purpose of this centrifuge campaign was to evaluate the viability of the ARM for use in future centrifuge experiments. All the slope specimens were designed to test different failure mechanisms of interest. Of the five slopes tested, four failed under dynamic loading, and of these four, two provided insight into failure modes of simple rock-slopes.

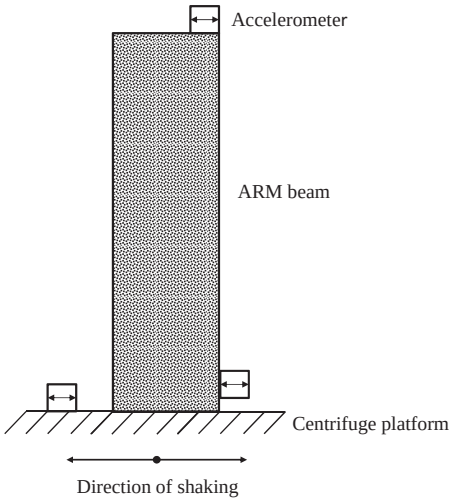

Figure C.5: Centrifuge test setup

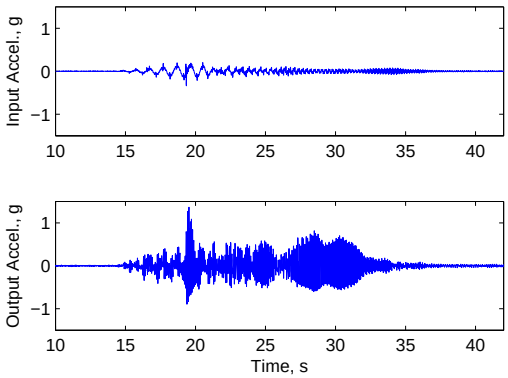

Figure C.6: Centrifuge motion - input and output

The behavior of the two flexual toppling slopes are of particular interest because they most closely resemble the slope geometries that will be tested in the model verification stage. Both of these slopes failed under dynamic loading as intended, indicating that the ARM is a viable material for this kind of simulation - strong enough to spin up to high g-levels and weak enough to break by shaking. The two tests also gave some insights into the role of secondary cracks in the nature of the slope failure. Between the two tests, some differences worth mentioning are: (i) the depth of the failure surface, (ii) the displacement of the failure mass, (iii) the extent of damage above the failure surface, and (iv) the extent of damage below the failure surface. The relative behaviors of the slopes are shown in Table C.2 in very general terms. The physical models on which these observations are based are shown in Figures C.7 and C.8.

Table C.2: UC Davis Slope Test Observations

Feature	**Intact column slope**	**Pre-cracked column slope**
Depth of failure surface	deep	less deep
Displacement of failure mass	less	more
Damage above failure surface	less	more
Damage below failure surface	less	more

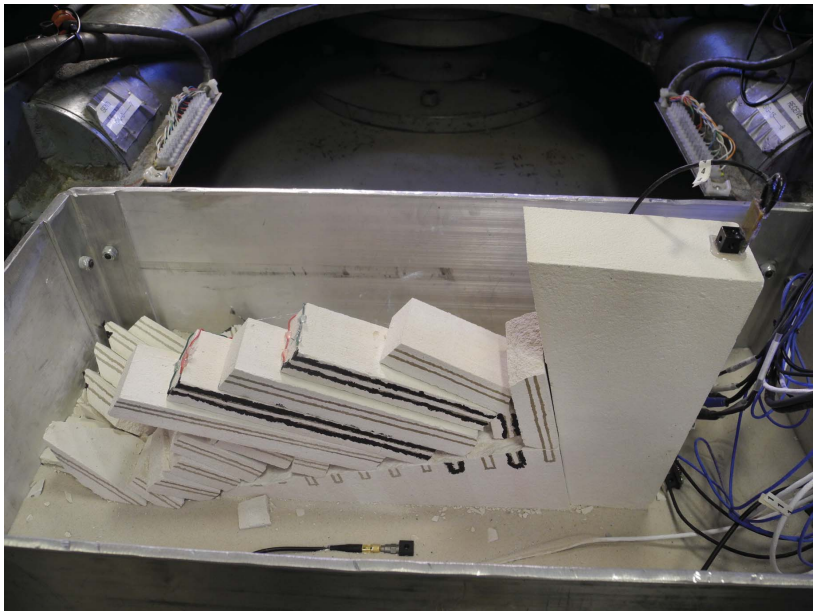

Figure C.7: Post failure photo of a flexural toppling slope with intact columns

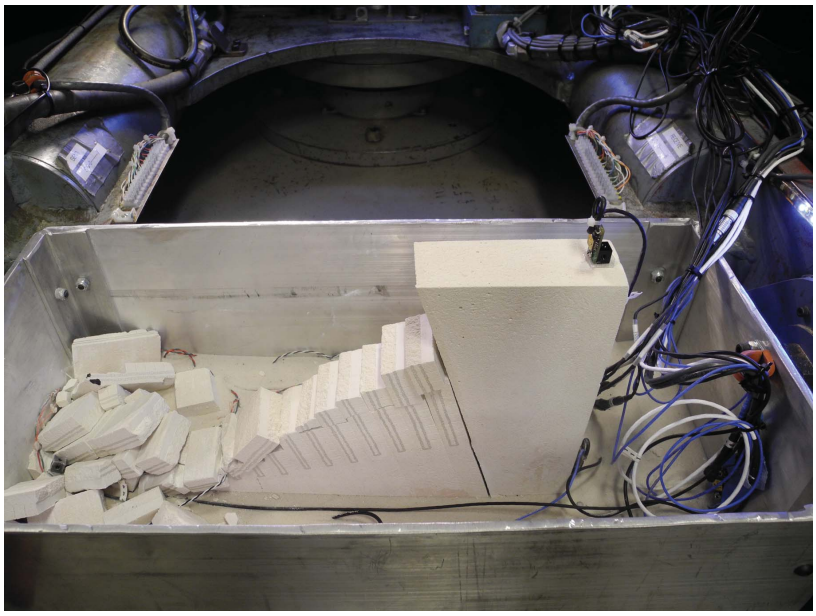

Figure C.8: Post failure photo of a flexural toppling slope with pre-cracked columns

Appendix D

PARTICLE RESOLUTION OPTIMIZATION

Like the calculation timestep, the particle resolution is an important model parameter that affects the quality of the simulations and the time it takes to run them. Particle resolution (the number of particles across a given model dimension) is directly changed via the particle radius. A higher particle resolution will result in higher precision in the results and a better approximation of the mechanical behavior of a granular material whose physical grains are smaller than the model particle radius. The cost of this improved model performance is runtime.

At a minimum, the particle resolution must be sufficiently high that the target mechanical behavior can be captured. Different model behaviors (wave transmission, fracture, shear and compression failure, e.g.) are all affected by the resolution. Each behavior of interest needs to be considered and several researchers have provided guidelines for appropriate particle resolutions for different simulations. The UDEC manual provides the minumum resolution for wave transmission in discrete elements. Wanne 2008 address the relationship between particle resolution, fracture mechanics and thermal expansion. Potyondy and Cundall 2004 address different strength mechanisms (fracture in particular). These guidelines provide a lower bound for the particle resolution to be used in DEM simulations. The lower bound is controlled by the DEM model's ability to approximate continuous mechanical behavior with a discontinuum.

Above the lower bound, the particle resolution affects the consistency of the numerical results. For any given particle resolution, a variation in the random packing of particles can have an influence on the model's behavior. A change in random seed is analagous to casting a new sample of the same concrete mix or testing a diferent core of the same intact rock. Therefore, simulations of models with different random seeds will be unique and tend to be normally distributed about some mean. Given the variation in results for a given

particle resolution, the munber of tests required to achieve a specified confidence level in the measured mean response can be found using:

$$N = \lfloor \left(\frac{Z_\alpha \sigma}{\beta} \right)^2 \rfloor \tag{D.1}$$

where N is the number of samples required, Z_α is the standard normal variable for a target confidence level, and β is the error. N, with the runtime associated with a simulation at a given particle resolution gives the total computer runtime required to achieve the specified confidence level.

This method was used to find an optimal particle radius for the dynamic beam simulations used in the dynamic calibration process. Five particle resolution levels were compared with mean particle radius ranging from 3.75×10^{-4} meters to 2.25×10^{-3} meters. These radii are presented as fractions of the radius that was eventually selected for the work (1.5×10^{-4} meters).

The models were subjected to a frequency sweep motion and their natural frequencies, f_n, maximum Fourier amplitudes, $c_{n,max}$, and peak acceleration response, PAR, were measured. The highest resolution model's runtime was over 150 hours, making it impractical to include that model in the study. For the remaining four resolution levels, 50 unique simulations were run and the mean and standard deviations of the three dynamic response measurements were compared. Runtime decreased exponentially with increase in mean particle radius as shown by Figure D.4. Figures D.1 through D.3 show the levels of variability in the different parameters for different mean particle radii. Natural frequency shows a steady decrease in C_v with decrease in r_{mean} while $C_{n,max}$ and PAR show no discernible trend. Assuming an allowed error of 5% from the mean, the number of simulations required to achieve 90%, 95%, and 99% confidence levels was calculated for each response measurement. The runtimes required to achieve those levels are shown in Figures D.5 through D.7.

Figure D.5 shows that f_n has a clear minimum runtime at $r_{mean} = 0.75$, while $C_{n,max}$ and PAR have continually decreasing runtime with increasing r_{mean}. To balance these trends, an average radius of $r_{mean} = 1$ was selected for continued simulations.

Although not the focus of this project, this simple example indicates that it may be

possible to quantify the ideal particle resolution for any given particulate DEM simulation. Additionally, since the variation is due only to the randomized placement of the particles, it may be possible to quantify the expected variation in response using only the resolution and particle size distribution without building models or running simulations. Selection of particle resolution is currently treated as more of an art than a science. This topic warrants further investigation for future research.

Figure 3.15b is an example of the BPM for the beam at the original particle resolution from all my previous models.

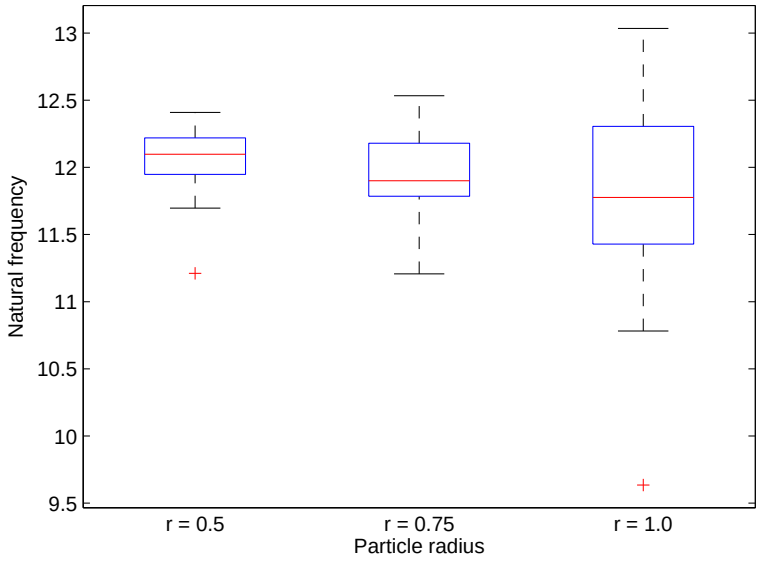

Figure D.1: Boxplots for beam natural frequency with particle radius

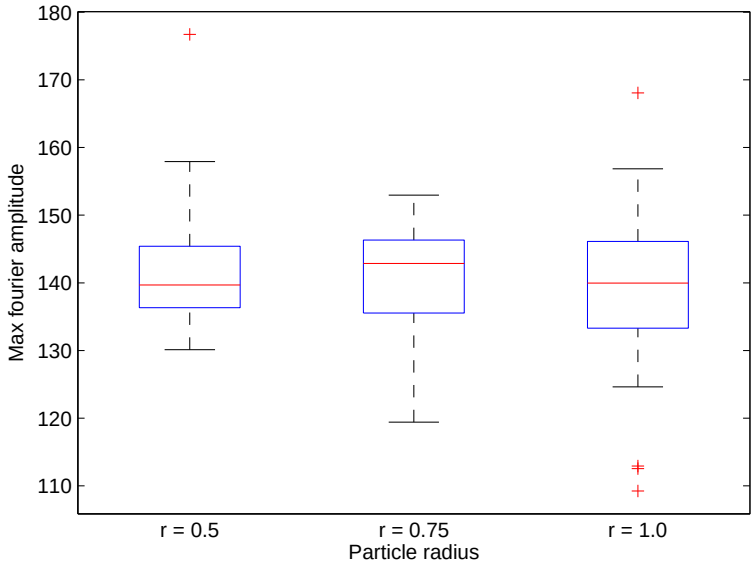

Figure D.2: Boxplots for beam max Fourier amplitude with particle radius

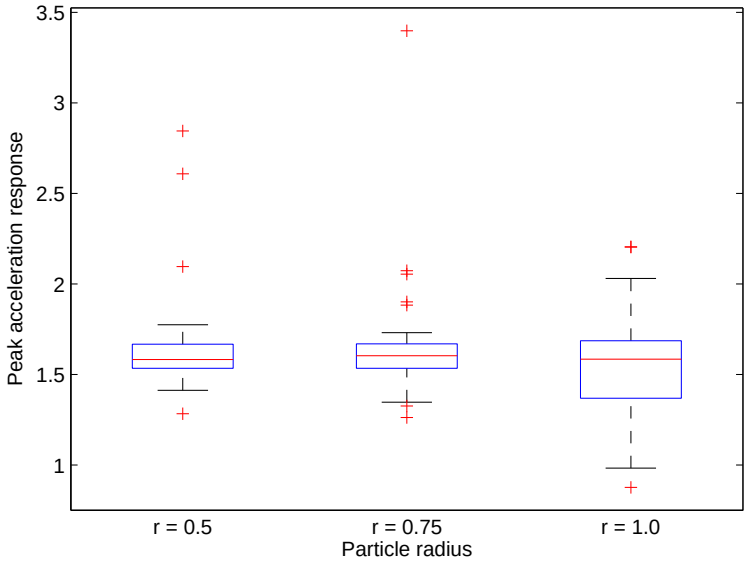

Figure D.3: Boxplots for beam peak acceleration response with particle radius

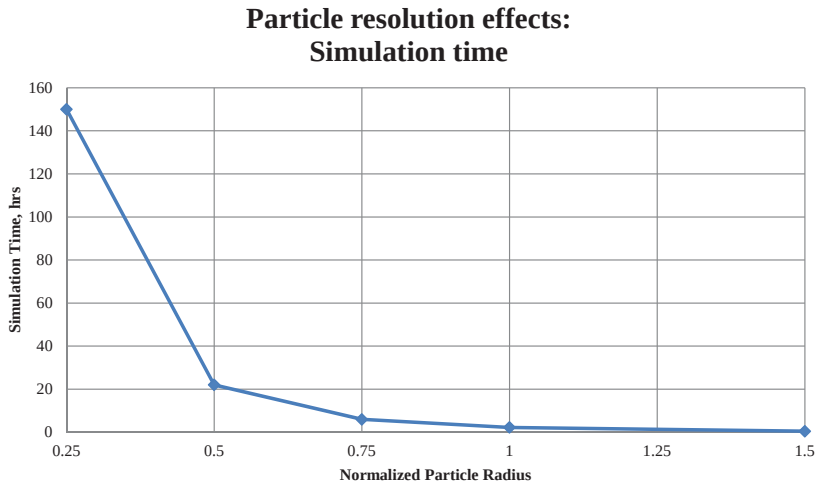

Figure D.4: Runtime for the dynamic simulations v. particle radius

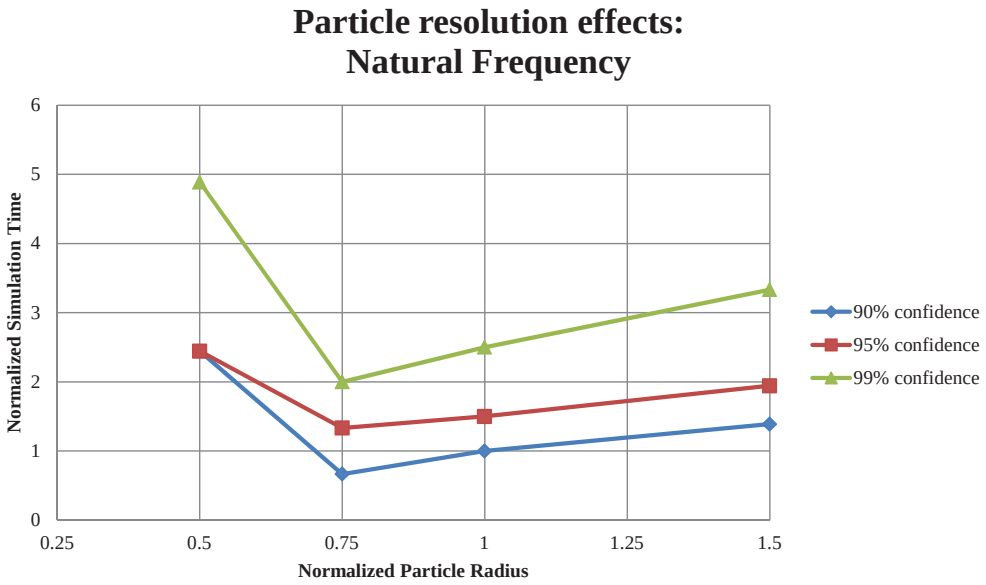

Figure D.5: Natural frequency runtime optimization

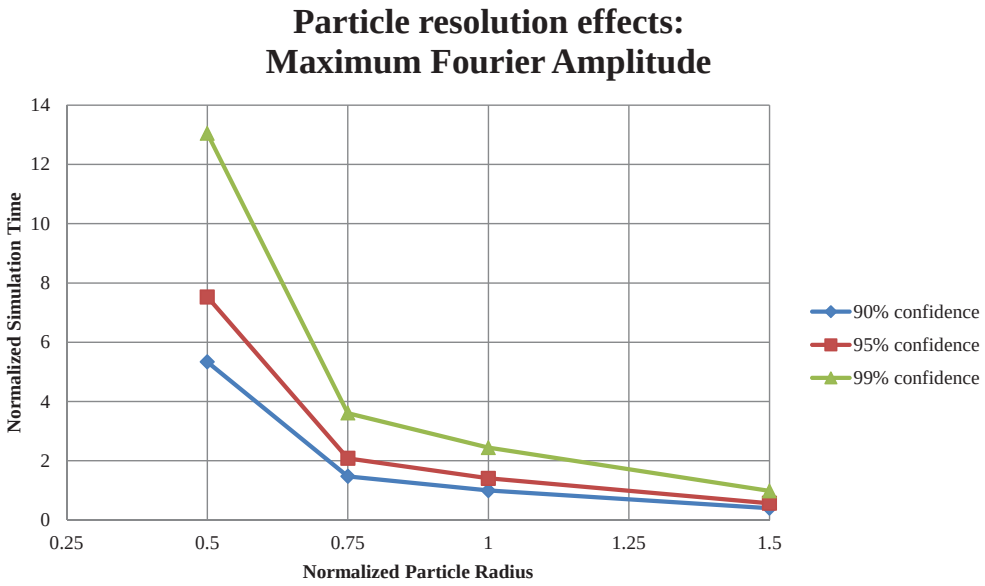

Figure D.6: Maximum Fourier amplitude runtime optimization

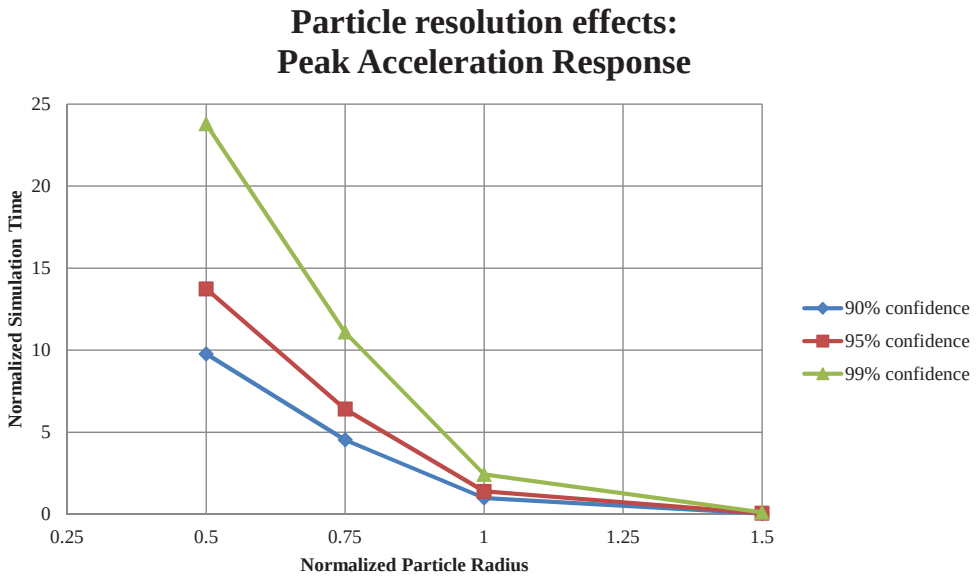

Figure D.7: Peak response acceleration runtime optimization

Appendix E

FISH FOR PFC2D SIMULATIONS

E.1 Introduction

This appendix contains FISH code used to build and control the PFC models presented in this dissertation. The reader is referred to the PFC *FISH Reference Guide* [113] for more details on the FISH language and it's interaction with the PFC program. In short, FISH is a programming language that can be used to define new commands and routines within PFC. FISH is a compiler, rather than an interpreter and FISH functions are compiled at their time of definition. Variables in FISH are global, so functions take no arguments and return no variables, because variable become part of the global namespace upon being mentioned in a FISH function. FISH functions may be called through the PFC command line, or by other FISH functions. It is also possible to insert PFC commands within FISH functions.

The code examples provided below have the following syntax highlighting scheme: PFC commands are highlighted in blue, intrinsic PFC code-supported FISH functions (i.e., not user-defined) are highlighted in green, strings are highlighted in orange, and comments are *highlighted in gray italics*. User-defined variables and functions are not highlighted.

E.2 Building the Model

The following outlines the sets of functions and commands used to build the PFC slope model domain.

```
1  ; fname SLP_build.pfc
2
3  call dirs.fis
4  dirs
5  set cwdir fis_dir
6  call b_sigma.fis
7  call BoundaryFunctions.fis
8  call BuildModel.fis
9  call cell_adjust.fis
10 call cleanup_BPM.fis
11 call count_contacts.fis
12 call count_particles.fis
13 call CrackArray.fis
14 call crack_wall_SLP.fis
```

```
call extra_ball_mem.fis
call fill_SLP.fis
call FixitySwitches.fis
call fnames_BPM.fis
call get_ss_SLP.fis
call grav_DBM.fis
call history_from_python.fis
call install_bonds_BPM.fis
call ListPreservation.fis
call m_cells_slope.fis
call make_vessel_SLP.fis
call plotColors.fis
call PropertyCalculator.fis
call seat_SLP.fis
call SlopeCut.fis
call snapshot.fis
call SmoothJointAdd.fis
call SmoothJointFlagDelete.fis
call SmoothJointInstall.fis
call timestep_BPM.fis
call video_BPM.fis
call wall_addr_BPM.fis

; the following are required here because arrays are used in LayerBuilder.fis
set stype 'SLP'
name_set
fnames
call matfile
mat_prop
call jntfile
call LayerBuilder.fis
call weathering.fis
call JointArray.fis

; building the model
set cwdir bat_dir
set log off
set logfile lgfile
set log on overwrite
make_vessel
fill
domainWall
FreeFieldYFixOff
ClumpYFixOff
set glev glevel_
grv
cycle 10000
property friction 1000
delete wall 1
set fishcall FC_BALL_DEL ListPreservation
fix spin
make_cut
set fishcall FC_BALL_DEL remove ListPreservation
cycle 10000
install_bonds
buildFractureDomain
free spin
property friction p_friction
buildLayers
cycle 5000
resetdisp
;weatherSlope
jointsByLayer
pause
cycle 1
crk_init
set fishcall FC_PB_DEL updateContactStiff
cycle 10000
tinit
set fishcall FC_CYC_MOT timestep
```

```
set fishcall FC_CYC_MOT FreeFieldVelocity
LateralBoundaryLinks
CreateDashpots
cycle 1000
set fishcall FC_CYC_MOT remove timestep
set fishcall FC_CYC_MOT BoundControl
ClumpXFixOff
FreeFieldXFixOff
InputXFixOff
SideStaticXForce
xBalance
instrument
set time 0
start_history
cycle 120000
layerDamping
cycle 70000
write_history
ResetDisp
save inifile
```

```
; example build batch file
new
;-------------------------------------------------------------------------------
define name_set
  pset = 585
  seed = '_1'
  jntset = 500
  tfac = 0.5
end
set random 1
call SLP_build.pfc
new
;-------------------------------------------------------------------------------
```

```
; BPM_prop_600prp ;
;-------------------------------------------------------------------------------
define mat_prop
glevel_ = 100
geologicLayers
;Particle properties
th         = 1.00     ; m - Thickness of the speciment in the z-direction
kn_ks      = 1.75     ; --
nb_sb      = 1.0    ; --
Sb         = Nb/nb_sb   ; N/m
r_avg      = 0.0015   ; m
p_friction     = 0.6    ; --
p_density    = 2800     ; kg/m^3
porosity     = 0.14     ; --

r_dev      = 1/3
rlo        = r_avg - r_avg/3
rhi        = r_avg + r_avg/3
; Ratio of bond material stiffness to particle stiffness
r_k        = 0.1
c_mult       = r_k/(1 + r_k)
pb_mult      = 1/(1 + r_k)
r_mult_pb    = 1.0

stiffnessCalculator
strengthCalculator

;Vessel properties
w_stiff      = n_k1     ; N/m
;Confining pressure
sxxreq       = -1.01e5 ; Pa
syyreq       = -1.01e5 ; Pa
sig_tol      = 0.01     ; percent
```

```
34
35  ;Damping
36  vnorm = 0.5
37  vr = 1
38  vshear = vnorm/vr
39  end
40  ;-------------------------------------------------------------------------------
41  define numberOfLayers
42    numberOfLayers = 2
43  end
44  numberOfLayers
45  ;-------------------------------------------------------------------------------
46  define geologicLayers
47    array ucsLayers(numberOfLayers,3);1)Best estimate UCS, 2)Lower estimate percent of
          UCS, 3) Depth of weathering zone
48    array  vsLayers(numberOfLayers)
49    array   hLayers(numberOfLayers)
50    array   mLayers(numberOfLayers)
51    array rhoLayers(numberOfLayers)
52    array  xiLayers(numberOfLayers)
53    array jntLayers(numberOfLayers)
54
55    ucsLayers(1,1) = 5.0e6
56    ucsLayers(2,1) = 5.0e9
57
58    ucsLayers(1,2) = 1.0
59    ucsLayers(2,2) = 1.0
60
61    ucsLayers(1,3) = 1
62    ucsLayers(2,3) = 1
63
64    vsLayers(1) = 1500.0
65    vsLayers(2) = 1500.0
66
67    hLayers(1) = 0.3
68    hLayers(2) = 0.0
69
70    mLayers(1) = tan(0*degrad)
71    mLayers(2) = tan(0*degrad)
72
73    rhoLayers(1) = 2200
74    rhoLayers(2) = 2200
75
76    xiLayers(1) = 0.02
77    xiLayers(2) = 0.02
78
79    jntLayers(1) = '500'
80    jntLayers(2) = '500'
81
82    loop n (1,numberOfLayers)
83      vsBase = vsLayers(n)
84      if vsBase > vsMax
85        vsMaxIndex = n
86        vsMax = vsBase
87      end_if
88
89      UCSBase = UCSLayers(n,1)
90      if UCSBase > UCSMax
91        UCSMaxIndex = n
92        UCSMax = UCSBase
93      end_if
94    end_loop
95
96    VsToKn = vsMax
97    UCSToNb = UCSMax
98    KnFromWaveSpeeds
99    BondStrengthFromUCS
100 end
101 ;-------------------------------------------------------------------------------
```

```
; SLP_jnt_set_500.jnt
;-------------------------------------------------------------------------------
define jointset_geom
   JointInstallFlag = 0
   SpacingOfJoints = 2.00/glevel_
   JointStepAngle = 1.0
   DipOfJoints = 1.0
   subJointLength = 1.0/glevel_
   rockBridgeLength =1.0/glevel_
   VariationInJointLength = 0.0/glevel_
   VariationInJointSpacing = 0.0/glevel_
   VariationInSubJointDip = 0.0
   VariationInJointDip = 0.0
end
jointset_geom
;-------------------------------------------------------------------------------
```

The following functions are used to build the slope model.

```
; fname BPM_fnames.fis
;-------------------------------------------------------------------------------
define fnames
  if stype = 'SLP'
    scode = '_j' + string(jntset)
  end_if
  if stype = 'UCS'
    scode = ''
  end_if
  motionType = type(motion)
  if motionType = 1
    motionC = ''
  else
    if motion = '_pseudo'
      motionC = motion + string(kh)
    else
      if motion = '_sine'
        motionC = motion + string(freqency)
      else
        motionC = motion
      end_if
    end_if
  end_if

  finfile = sav_dir + stype + scode + motionC + '_fin_' + string(pset) + seed + '.sav
      '
  histfile = his_dir + stype + scode + motionC +'_'+ string(pset) + seed + '.his'
  inifile = sav_dir + stype + scode + '_ini_' + string(pset) + seed + '.sav'
  jntfile = jnt_dir + 'SLP_jnt_set_' + string(jntset) + '.jnt'
  lgfile = log_dir + stype + scode + motionC +'_'+ string(pset) + seed + '.log'
  loadfile = fis_dir + 'load_' + stype + '.fis'
  matfile = prp_dir + 'BPM_prop_' + string(pset) + '.prp'
  statefile = state_dir + stype + scode + motionC +'_'+ string(pset) + seed
  vidfile_1 = vid_dir + stype + scode + motionC +  '_vid_' + string(pset) + seed + '
      _vv' + '.avi'
  vidfile_2 = vid_dir + stype + scode + motionC +  '_vid_' + string(pset) + seed + '
      _pf' + '.avi'

end
;-------------------------------------------------------------------------------
```

```
;-------------------------------------------------------------------------------
define ClumpSides
  xBoundLeft = xLeft - r_avg
  xBoundRight = xRight + r_avg
  yBoundBottom = yBottom + r_avg
  yBoundTop = yTop; - r_avg

```

```
  yBall = yBoundBottom

  loop while yBall <= yBoundTop
    command
      ball radius = r_avg x = xBoundLeft y = yBall
      ball radius = r_avg x = xBoundRight y = yBall
    end_command
    b1 = ball_near2(xBoundLeft,yBall)
    b2 = ball_near2(xBoundRight,yBall)

    clp = cl_add(null,b1)
    clp = cl_add(clp,b2)

    cl_color(clp) = 2

    yBall = yBall + 2*r_avg

  end_loop
  ClumpXFixOn
  ClumpYFixOn
  ClumpRFixOn
  command
    property density = p_density  ks = s_k1  kn = n_k1
  end_command
end
;-------------------------------------------------------------------------------
define ParticleSides
  xBoundLeft = xLeft - r_avg
  xBoundRight = xRight + r_avg
  yBoundBottom = yBottom + r_avg
  yBoundTop = yTop; - r_avg

  yBall = yBoundBottom
  loop while yBall <= yBoundTop
    command
      ball radius = r_avg x = xBoundLeft y = yBall
      ball radius = r_avg x = xBoundRight y = yBall
    end_command
    b1 = ball_near2(xLeft,yBall)
    b2 = ball_near2(xRight,yBall)

    bp = b1
    b_mem_slot = b_bound_next_mem
    cell_bph = bound_bph
    link_particle
    bound_bph = cell_bph

    b_mem_slot = b_ff_next_mem
    cell_bph = ff_bph
    link_particle
    ff_bph = cell_bph

    bp = b2
    b_mem_slot = b_bound_next_mem
    cell_bph = bound_bph
    link_particle
    bound_bph = cell_bph

    b_mem_slot = b_ff_next_mem
    cell_bph = ff_bph
    link_particle
    ff_bph = cell_bph

    b_extra(b1,b_side_flag_mem) = 0
    b_extra(b2,b_side_flag_mem) = 1

    yBall = yBall + 2*r_avg
  end_loop
  FreeFieldXFixOn
  FreeFieldYFixOn
```

```
78    FreeFieldRFixOn
79  end
80  ;-------------------------------------------------------------------------------
81  define ParticleBase
82    xBoundLeft = xLeft - r_avg
83    xBoundRight = xRight + 2*r_avg
84    yBoundBottom = yBottom - r_avg
85    yBoundTop = yTop + r_avg
86
87    xBall = xBoundLeft
88    loop while xBall <= xBoundRight
89      command
90        ball radius = r_avg x = xBall y = yBoundBottom
91      end_command
92      b1 = ball_near2(xBall,yBottom)
93      b2 = ball_near2(xBall,yBoundTop)
94
95      bp = b1
96      b_mem_slot = b_input_next_mem
97      cell_bph = input_bph
98      link_particle
99      input_bph = cell_bph
100
101     bp = b1
102     b_mem_slot = b_bound_next_mem
103     cell_bph = bound_bph
104     link_particle
105     bound_bph = cell_bph
106
107     xBall = xBall + 2*r_avg
108   end_loop
109   InputXFixOn
110   InputYFixOn
111   InputRFixOn
112 end
113 ;-------------------------------------------------------------------------------
114 define InitiateLinkedLists
115   bound_bph = null
116   input_bph = null
117   ff_bph = null
118   main_bph = null
119 end
120 ;-------------------------------------------------------------------------------
121 define FillZone
122   nBalls = nBalls + 1000
123   tot_vol = (xRight - xLeft)*(yTop - yBottom)
124   newNumBalls = nBalls + int((1.0 - porosity)*tot_vol/(pi*r_avg^2))
125   mult  = 1.6
126   rlo_0   = rlo/mult
127   rhi_0 = rhi/mult
128   command
129     generate tries 1000000 id = nBalls,newNumBalls radius = rlo_0,rhi_0  x = xLeft,
          xRight  y = yBottom,yTop
130     property density = p_density  ks = s_k1  kn = n_k1
131     wall kn = w_stiff  nodes = (xLeft,yTop) (xLeft,yBottom) (xRight,yBottom) (xRight,
          yTop)
132   end_command
133   nBalls = newNumBalls + 3
134 end
135 ;-------------------------------------------------------------------------------
136 define FreeFieldPlacement
137   ffWidth = r_avg*20
138   gap = 3*ffWidth
139
140   num = ffWidth/r_avg
141   remainder = num - int(num)
142   plus = r_avg + (1-remainder)*r_avg
143   ffWidth = ffWidth + plus
144
145   xffLeft = 0 - gap - ffWidth
```

```
  yffLeft = 0
  xffRight = width + gap
  yffRight = 0

  xMinBound = xffLeft
  xMaxBound = xffRight + gap
  yMinBound = 0
  yMaxBound = height

  layerLeftLim = 0 + gap
  layerRightLim = width - gap
end
;-------------------------------------------------------------------------------
define BuildModels
  command
    set disk th
    damp viscous normal vnorm
    damp viscous shear vshear
  end_command

  xLeft = xffLeft
  xRight = xLeft + ffWidth
  yBottom = 0
  yTop = height

  ClumpSides
  ParticleBase
  FillZone

  xLeft = 0
  xRight = width

  ParticleSides
  ParticleBase
  FillZone

  xLeft = xffRight
  xRight = xffRight + ffWidth

  ClumpSides
  ParticleBase
  FillZone

end
;-------------------------------------------------------------------------------
define AdjustDims
  num = height/r_avg
  remainder = num - int(num)
  plus = r_avg + (1-remainder)*r_avg
  height = height + plus

  num = width/r_avg
  remainder = num - int(num)
  plus = r_avg + (1-remainder)*r_avg
  width = width + plus
end
;-------------------------------------------------------------------------------
define ColorBound
  bp = bound_bph
  loop while bp # null
    if b_color(bp) = DefaultBallColor
      b_color(bp) = BoundaryBallColor
    else
      b_color(bp) = DefaultBallColor
    end_if
    bp = b_extra(bp,b_bound_next_mem)
  end_loop
end
;-------------------------------------------------------------------------------
define ColorFF
```

```
  bp = ff_bph
  loop while bp # null
    if b_color(bp) = DefaultBallColor
      b_color(bp) = BoundaryBallColor
    else
      b_color(bp) = DefaultBallColor
    end_if
    bp = b_extra(bp,b_ff_next_mem)
  end_loop
end
;------------------------------------------------------------------------------
define ColorInput
  bp = input_bph
  loop while bp # null
    if b_color(bp) = DefaultBallColor
      b_color(bp) = BoundaryBallColor
    else
      b_color(bp) = DefaultBallColor
    end_if
    bp = b_extra(bp,b_input_next_mem)
  end_loop
end
;------------------------------------------------------------------------------
define RadiusMult
  bp = ball_head
  loop while bp # null
    memType = type(b_extra(bp,b_bound_next_mem))
    if memType = 1
      if b_clump(bp) = null
        b_rad(bp) = b_rad(bp)*mult
      end_if
    end_if
    bp = b_next(bp)
  end_loop
end
;------------------------------------------------------------------------------
define fill
  extra_ball_mem
  InitiateLinkedLists

  FreeFieldPlacement

  wxr = xMaxBound + gap + ffWidth
  wxl = xMinBound - gap - ffWidth
  command
    wall id = 1  kn = w_stiff  nodes = (wxr,yMaxBound) (wxl,yMaxBound)
  end_command

  BuildModels
  RadiusMult

  command
    solve
    delete wall 2 3 4
    solve
  end_command
  SetSize
end
;------------------------------------------------------------------------------
define LateralBoundaryLinks
  bp = ff_bph
  loop while bp # null
    if b_extra(bp,b_side_flag_mem) = 0
      clp = clump_near2(b_x(bp) - gap - ffWidth/2,b_y(bp))
    else
      clp = clump_near2(b_x(bp) + gap + ffWidth/2,b_y(bp))
    end_if
    b_extra(bp,b_ref_clump_mem) = clp
    bp = b_extra(bp,b_ff_next_mem)
  end_loop
```

```
end
;-------------------------------------------------------------------------------
define ResetDisp
  bp = ball_head
  loop while bp # null
    b_xdisp(bp) = 0
    b_ydisp(bp) = 0
    bp = b_next(bp)
  end_loop
end
;-------------------------------------------------------------------------------
define xBalance
  bp = ff_bph
  leftForce = 0
  rightForce = 0
  loop while bp # null
    sideFlag = b_extra(bp,b_side_flag_mem)
    if sideFlag = 0
      leftForce = leftForce + b_extra(bp,b_xfst_mem)
    else
      rightForce = rightForce + b_extra(bp,b_xfst_mem)
    end_if
    bp = b_extra(bp,b_ff_next_mem)
  end_loop

  leftForce = abs(leftForce)
  rightForce = abs(rightForce)

  ForceDiff = leftForce - rightForce
  DiffMag = ForceDiff/(leftForce+rightForce)/2

  CorrectDiff
end
;-------------------------------------------------------------------------------
define CorrectDiff
  CountMainBase

  bp = input_bph

  loop while bp # null
    mainFlag = b_extra(bp,b_main_flag_mem)
    if mainFlag = 1
      CorrectingForce = -ForceDiff/BaseNum
      b_xfap(bp) = CorrectingForce
      b_extra(bp,b_xfst_mem) = CorrectingForce
    end_if
    bp = b_extra(bp,b_input_next_mem)
  end_loop

end
;-------------------------------------------------------------------------------
define CountMainBase
  bp = input_bph
  loop while bp # null
    if b_x(bp) > 0
      if b_x(bp) < width
        BaseNum = BaseNum + 1
        b_extra(bp,b_main_flag_mem) = 1
      end_if
    end_if
    bp = b_extra(bp,b_input_next_mem)
  end_loop
end
;-------------------------------------------------------------------------------
define domainWall
  dwXLeft = 0 - gap/2
  dwXRight = width + gap/2
  dwYBottom = 0 - ffWidth/2
  dwYTop = height + ffWidth/2

```

```
  command
    wall kn = w_stiff  nodes = (dwXLeft,dwYTop) (dwXLeft,dwYBottom) (dwXRight,
        dwYBottom) (dwXRight,dwYTop) close
  end_command
end
;-------------------------------------------------------------------------------
define zapDomainWall
  ; fishcall 8 (FC_CONT_CREATE)
  cpz = fc_arg(0)
  wpz = c_ball2(cpz)
  if pointer_type(wpz) = 101
    bpz = c_ball1(cpz)
    ii = b_delete(bpz)
  end_if
end
;-------------------------------------------------------------------------------
define fractureDomain
  ; xObject
  ; yObject
  ; crackBuffer


  ;this does not need to be inside this function
  fractureBuffer = 4*ffWidth
  fracture_xMin = 0 + fractureBuffer
  fracture_xMax = width - fractureBuffer
  fracture_yMin = 0 + 1.5*fractureBuffer
  ;fracture_yMin = 0 + height/2 + r_avg*6

  fractureDomain = 0
  section
    if xObject < fracture_xMin
      fractureDomain = 1
      StrengthFactor = 1000
      exit section
    end_if
    if xObject > fracture_xMax
      fractureDomain = 1
      StrengthFactor = 1000
      exit section
    end_if
    if yObject < fracture_yMin
      fractureDomain = 1
      StrengthFactor = 1 + 999*(fracture_yMin - yObject)^3
      ;StrengthFactor = 1000
    end_if
  end_section

;   if motion = '_pseudo'
;     fractureDomain = 0
;     pseudostaticFractureDomain
;   end_if

end
;-------------------------------------------------------------------------------
define pseudostaticFractureDomain
  ; xObject
  ; yObject

  fractureRadius = height/2 + ffWidth
  xFZ = dx_a
  yFZ = height

  distFZ = sqrt((xFZ-xObject)^2 + (yFZ-yObject)^2)

  if distFZ >= fractureRadius
    fractureDomain = 1
    StrengthFactor = 1 + 9999(distFZ-fractureRadius)^3
  end_if
end
```

```
;-------------------------------------------------------------------------------
define buildFractureDomain
  UCSToNb = 5e6
  BondStrengthFromUCS
  StrengthCalculator
  oldStrength_s = pbs_strength
  oldStrength_n = pbn_strength
  cp = contact_head
  loop while cp # null
    xObject = c_x(cp)
    yObject = c_y(cp)
    if fractureDomain = 1
      pbp = c_pb(cp)
      if pbp # null
        pb_nstrength(pbp) = oldStrength_n*StrengthFactor
        pb_sstrength(pbp) = oldStrength_s*StrengthFactor
      end_if
    end_if
    cp = c_next(cp)
  end_loop
end
;-------------------------------------------------------------------------------
define colorFractureDomain
  bp = ball_head
  loop while bp # null
    xObject = b_x(bp)
    yObject = b_y(bp)
    if fractureDomain = 1
      b_color(bp) = 1
    end_if
    bp = b_next(bp)
  end_loop
end
;-------------------------------------------------------------------------------
```

```
; cell_adjust.fis

define get_cell_sigma
  ; calculates the components of the stress tensor for a single cell based on
  ; the average stresses of the particles within the cell
  cell_stress_xx = 0
  cell_stress_yy = 0
  cell_stress_xy = 0
  cell_stress_yx = 0
  pnum = mem(cell_p + _cell_pnum)
  bp = mem(cell_p + _cell_bph)

  loop while bp # null
    get_sigma
    cell_stress_xx = cell_stress_xx + sigma_xx
    cell_stress_yy = cell_stress_yy + sigma_yy
    cell_stress_xy = cell_stress_xy + sigma_xy
    cell_stress_yx = cell_stress_yx + sigma_yx
    bp = b_extra(bp,b_cell_bnext_mem)
  end_loop

  mem(cell_p + _cell_sxx) = cell_stress_xx/pnum
  mem(cell_p + _cell_syy) = cell_stress_yy/pnum
  mem(cell_p + _cell_sxy) = cell_stress_xy/pnum
  mem(cell_p + _cell_syx) = cell_stress_yx/pnum

  avg_sig = (mem(cell_p + _cell_sxx) + mem(cell_p + _cell_syy))/2
  cell_sdiff = abs((avg_sig - abs(sxxreq))/sxxreq)
  mem(cell_p + _cell_sdiff) = cell_sdiff
;   ii = out('cell_stress = ' + string(avg_sig))
end
;-------------------------------------------------------------------------------

define cell_rad_mult
```

```
  ; multiplies the radius of every particle in a cell by a pre-defined radius
  ; multiplier, r_mult
  bp = mem(cell_p + _cell_bph)
  loop while bp # null
    section
    ; count number of contacts
    ; if the number of contacts is less than 3, don't apply the radius reduction
    ; this will help prevent floaters
    cc = 0
    cp = b_clist(bp)
    loop while cp # null
      if c_nforce(cp) > 0
        cc = cc + 1
      end_if
      if c_ball1(cp) = bp
        cp = c_b1clist(cp)
      else
        cp = c_b2clist(cp)
      end_if
    end_loop
    if cc < 3
      old_radius = b_rad(bp)
      new_radius = old_radius/r_mult
      b_rad(bp) = new_radius
    else
      old_radius = b_rad(bp)
      new_radius = old_radius*r_mult
      b_rad(bp) = new_radius
    end_if
    end_section
    bp = b_extra(bp,b_cell_bnext_mem)
  end_loop
end
;-------------------------------------------------------------------------------
define count_floaters
  bp = ball_head
  fcount = 0
  loop while bp # null
    cc = 0
    cp = b_clist(bp)
    loop while cp # null
      if c_ball1(cp) = bp
        cp = c_b1clist(cp)
      else
        cp = c_b2clist(cp)
      end_if
      cc = cc + 1
    end_loop
    if cc < 4
      fcount = fcount + 1
      b_color(bp) = FloatBallColor
    end_if
    bp = b_next(bp)
  end_loop
  ii = out('Number of floaters: ' + string(fcount))
end
```

```
; timestep_BPM
; takes the average PFC-computed timestep from a set of cycles and sets the
; timestep for the rest of the simulation
;-------------------------------------------------------------------------------
define tinit
  tsp_0 = tdel
  nn = 0
end
;-------------------------------------------------------------------------------
define timestep
    t_count = t_count + 1
    if t_count > 500
```

```
      if tsp_0 # 0
        tsp = tdel
        tsp_0 = (tsp_0*nn + tsp)/(nn+1)
        nn = nn + 1
        t_count = 0
      end_if
    end_if
end
;------------------------------------------------------------------------------
define timestep_2
tsp_0 = tsp_0*tfac ; tfac = 0.5 was found to be most appropriate
end
```

```
; fname install_bonds_BPM.fis

define install_bonds
  command
    property pb_kn = pbn_stiff pb_ks = pbs_stiff pb_radius = r_mult_pb
    property pb_nstrength = pbn_strength pb_sstrength = pbs_strength
  end_command

  cp = contact_head
  loop while cp # null
    initialForce = c_nforce(cp)
    pbp = c_pb(cp)
    if pbp # null
      pb_nforce(pbp) = initialForce
    end_if
    c_kn(cp) = n_k2
    c_ks(cp) = s_k2
    cp = c_next(cp)
  end_loop
end
```

```
; JointArray.fis
;------------------------------------------------------------------------------
define lineDef
  array v1(dim)
  array v2(dim)
end
;------------------------------------------------------------------------------
define jointsByLayer
  loop currentLayer (1,numberOfLayers)
    section
      jntfile = jnt_dir + 'SLP_jnt_set_' + jntLayers(currentLayer) + '.jnt'
      command
        call jntfile
      end_command
      if JointInstallFlag = 0
        exit section
      end_if
      minSpacingCheck
      jointArray
      drawJoints
      buildJoints
    end_section
  end_loop
end
;------------------------------------------------------------------------------
define jointArray
  joint_head = null
  joint_mem
  DipOfJointsRadians = DipOfJoints*degrad
  JointStepAngleRadians = JointStepAngle*degrad
  LengthOfJoints = 2*sqrt(height^2 + width^2)
  NumberOfJoints = int(LengthOfJoints/SpacingOfJoints)
  jointSubverticalFlag

```

```
  loop n (1,NumberOfJoints)
    jointLength = LengthOfJoints
    jointDipRadians = DipOfJointsRadians
    if modelIntersection = 1
      link_joint
    end_if
    xJoint = xJoint + dxJoint
    yJoint = yJoint + dyJoint
  end_loop
end
;-------------------------------------------------------------------------------
define minSpacingCheck
  minJointSpacing = r_avg*4
  if SpacingOfJoints < minJointSpacing
    oo = out('Joint spacing too small. SpacingOfJoints adjusted from ' +string(
        SpacingOfJoints) + ' to ' + string(minJointSpacing))
    SpacingOfJoint = minJointSpacing
  end_if
end
;-------------------------------------------------------------------------------
define modelIntersection
  modelIntersection = 0
  cp = contact_head
  section
    loop while cp # null
      if c_ondisk(cp,xJoint,yJoint,DipOfJointsRadians,jointLength/2) = 1
        modelIntersection = 1
        exit section
      else
      cp = c_next(cp)
      end_if
    end_loop
  end_section
end
;-------------------------------------------------------------------------------
define jointSubverticalFlag
  jointSubverticalFlag = 0
  jsvf = 0
  if DipOfJoints >= 45
    if DipOfJoints <= 135
      jointSubverticalFlag = 1
      jsvf = 1
    end_if
  end_if
  if jsvf = 1
    xJoint = -LengthOfJoints/2
    yJoint = height/2
    dxJoint = SpacingOfJoints/cos(DipOfJointsRadians-pi/2)*(1+VariationInJointSpacing
        *grand)
    dyJoint = tan(JointStepAngleRadians)*SpacingOfJoints
    dxJoint = abs(dxJoint)
  else
    xJoint = width/2
    yJoint = -LengthOfJoints/2
    dxJoint = tan(JointStepAngleRadians)*SpacingOfJoints
    dyJoint = SpacingOfJoints/sin(pi/2-DipOfJointsRadians)*(1+VariationInJointSpacing
        *grand)
    dyJoint = abs(dyJoint)
  end_if
end
;-------------------------------------------------------------------------------
define link_joint
  joint_ad = joint_head
  joint_head = get_mem(5)
  mem(joint_head + _joint_next) = joint_ad
  mem(joint_head + _joint_x) = xJoint
  mem(joint_head + _joint_y) = yJoint
  mem(joint_head + _joint_dip_rad) = jointDipRadians
  mem(joint_head + _joint_length) = jointLength
end
```

```
;-------------------------------------------------------------------------------
define joint_mem
  _joint_next   = 0
  _joint_x    = 1
  _joint_y    = 2
  _joint_dip_rad  = 3
  _joint_length = 4
end
;-------------------------------------------------------------------------------
define jointVerticies
  v1(1) = xJoint - jointLength/2*cos(jointDipRadians)
  v2(1) = xJoint + jointLength/2*cos(jointDipRadians)
  v1(2) = yJoint + jointLength/2*sin(jointDipRadians)
  v2(2) = yJoint - jointLength/2*sin(jointDipRadians)
end
;-------------------------------------------------------------------------------
define subJointVerticies
  v1(1) = xSubJoint - subJointLength_n/2*cos(subJointDipRadians)
  v2(1) = xSubJoint + subJointLength_n/2*cos(subJointDipRadians)
  v1(2) = ySubJoint + subJointLength_n/2*sin(subJointDipRadians)
  v2(2) = ySubJoint - subJointLength_n/2*sin(subJointDipRadians)
end
;-------------------------------------------------------------------------------
define buildJoints
  joint_p = joint_head
  even = 0
  loop while joint_p # null
    even = even + 1
    xJointOffset = 0
    yJointOffset = 0
    xJoint = mem(joint_p + _joint_x)
    yJoint = mem(joint_p + _joint_y)
    jointDipRadians = mem(joint_p + _joint_dip_rad)
    jointLength = mem(joint_p + _joint_length)
    jointVerticies

    if even = 2
      xJointOffset = (subJointLength + rockBridgeLength)/2*cos(jointDipRadians)
      yJointOffset = -(subJointLength + rockBridgeLength)/2*sin(jointDipRadians)
      even = 0
    end_if

    NumberOfSubJoints = int(jointLength/(subJointLength + rockBridgeLength))
    dxSubJoint = (subJointLength + rockBridgeLength)*cos(jointDipRadians)
    dySubJoint = -(subJointLength + rockBridgeLength)*sin(jointDipRadians)
    xSubJoint = v1(1) + xJointOffset
    ySubJoint = v1(2) + yJointOffset
    loop n (1,NumberOfSubJoints)
      subJointLength_n = subJointLength*(1+VariationInJointLength*grand)
      subJointDipRadians = jointDipRadians + VariationInSubJointDip*grand*degrad
      buildSubJoint
      subJointVerticies
      xSubJoint = xSubJoint + dxSubJoint
      ySubJoint = ySubJoint + dySubJoint
    end_loop
    joint_p = mem(joint_p + _joint_next)
  end_loop
end
;-------------------------------------------------------------------------------
define buildSubJoint
  VsToKn = vsLayers(currentLayer)
  KnFromWaveSpeeds
  stiffnessCalculator

  sjDip = subJointDipRadians/degrad
  sjKn = n_k1*0.5
  sjKs = s_k1*0.5
  sjRmult = 1.0
  sjFric = p_friction
  sjDa = 0
```

```
  sjBondMode = 0
  sjBondN = 0
  sjBondCoh = 0
  sjBondFric = 0
  sjStrainMode = 1
  sjGap = 0

  cp = contact_head
  loop while cp # null
    if subJointInstallFlag = 1
      sjInitialForce
      sjFn = sjNForce
      sjFs = sjSForce
      installSmoothJoint
      oo = out('Smooth-Joint installed at contact ' + string(cp))
      sjCount = sjCount + 1
    end_if
    cp = c_next(cp)
  end_loop
end
;-------------------------------------------------------------------------------
define sjInitialForce
  ; contact normal and shear forces
  cNForce = c_nforce(cp)
  cSForce = c_sforce(cp)
  ; bond normal and shear forces
  pbp = c_pb(cp)
  if pbp # null
    pbNForce = pb_nforce(pbp)
    pbSForce = pb_nforce(pbp)
  else
    pbNForce = 0.0
    pbSForce = 0.0
  end_if

  sumNForce = cNForce + pbNForce
  sumSForce = cSForce + pbSForce

  ; directions
  xNormal = c_xun(cp)
  yNormal = c_yun(cp)

  if xNormal = 0.0
    cNormalDegrees = 90
  else
    cNormalDegrees = atan(yNormal/xNormal)/degrad
  end_if

  sjNormalDegrees = 90.0 - sjDipDegrees
  relativeDegrees = sjNormalDegrees - cNormalDegrees
  relativeRadians = degrad*relativeDegrees

  ; smooth-joint forces
  sjNForce = sumNForce*cos(relativeRadians) - sumSForce*sin(relativeRadians)
  sjSForce = sumNForce*sin(relativeRadians) + sumSForce*cos(relativeRadians)

  if sjNForce < 0
    sjNForce = -sjNForce
    sjSForce = -sjSForce
  end_if
end
;-------------------------------------------------------------------------------
define subJointInstallFlag
  subJointInstallFlag = 0
  if c_ondisk(cp,xSubJoint,ySubJoint,subJointDipRadians,subJointLength_n/2)=1
    xObject = c_x(cp)
    yObject = c_y(cp)
    ObjectLayerNumber
    if LayerID = currentLayer
      if crackDomain = 1
```

```
242         subJointInstallFlag = 1
243       end_if
244     end_if
245   end_if
246
247 end
248 ;------------------------------------------------------------------------------
249 define crackDomain
250   ; xObject
251   ; yObject
252   ; crackBuffer
253
254   crackBuffer = 3*ffWidth
255   crack_xMin = 0 + crackBuffer
256   crack_xMax = width - crackBuffer
257   crack_yMin = 0 + crackBuffer
258   crack_yMax = height
259
260   crackDomain = 0
261   section
262     if xObject < crack_xMin
263       exit section
264     end_if
265     if xObject > crack_xMax
266       exit section
267     end_if
268     if yObject < crack_yMin
269       exit section
270     end_if
271     if yObject > crack_yMax
272       exit section
273     end_if
274     crackDomain = 1
275   end_section
276 end
277 ;------------------------------------------------------------------------------
278 define printJoints
279   joint_p = joint_head
280   loop while joint_p # null
281     xJoint = mem(joint_p + _joint_x)
282     yJoint = mem(joint_p + _joint_y)
283     jointDipRadians = mem(joint_p + _joint_dip_rad)
284     jointLength = mem(joint_p + _joint_length)
285     oo = out(string(joint_p)+','+string(xJoint)+','+string(yJoint)+','+string(
          jointDipRadians)+','+string(jointLength))
286     joint_p = mem(joint_p +_joint_next)
287   end_loop
288 end
289 ;------------------------------------------------------------------------------
290 define drawJoints
291   plot_item
292   joint_p = joint_head
293   loop while joint_p # null
294     xJoint = mem(joint_p + _joint_x)
295     yJoint = mem(joint_p + _joint_y)
296     jointDipRadians = mem(joint_p + _joint_dip_rad)
297     jointLength = mem(joint_p + _joint_length)
298     jointVerticies
299     ii = set_color(0)
300     oo = draw_line(v1,v2)
301     joint_p = mem(joint_p +_joint_next)
302   end_loop
303 end
304 ;------------------------------------------------------------------------------
305 define drawSubJoints
306   plot_item
307   ii = set_color(1)
308   oo = draw_line(v1,v2)
309 end
310 ;------------------------------------------------------------------------------
```

```
define colorJoints
  bp = ball_head
  loop while bp # null
    if b_extra(bp,b_sj_mem) = 1
      b_color(bp) = 13
    end_if
    bp = b_next(bp)
  end_loop
end
;-------------------------------------------------------------------------------
```

```
define SmoothJointAdd
  newContact = fc_arg(0)
  cp = newContact
  if SmoothJointCheck = 1
    section
    newGap = 0
    newDip = 0
    sjCount = 0
    bp = b1
    SmoothJointPropSum
    bp = b2
    SmoothJointPropSum
    if sjCount = 0
      ii = out('Error: No smooth joint contact information found to be copied')
      exit section
    end_if
    j_gap = newGap/sjCount
    j_dip = newDip/sjCount
    cp = newContact
    install_sj
    newSJCount = newSJCount + 1
    end_section
  end_if
end
;-------------------------------------------------------------------------------
define SmoothJointCheck
  SmoothJointCheck = 0
  b1 = c_ball1(cp)
  b2 = c_ball2(cp)
  section
    if b_extra(b1,b_sj_mem) = 1
      SmoothJointCheck = 1
      bcheck = 1
      bxcheck = b_x(b1)
      bycheck = b_y(b1)
      b_color(b1) = 1
      exit section
    end_if
    if b_extra(b2,b_sj_mem) = 1
      SmoothJointCheck = 1
      bcheck = 2
      bxcheck = b_x(b2)
      bycheck = b_y(b2)
      b_color(b2) = 1
      exit section
    end_if
  end_section
end
;-------------------------------------------------------------------------------
define SmoothJointPropSum
  cp = b_clist(bp)
  loop while cp # null
    if c_type(cp) = 5
      read_joints
      if sj_active = 1
        calcDip = atan2(sj_yun,sj_xun) - 90*degrad
        newDip = newDip + calcDip
        newGap = newGap + sj_gap
```

```
        sjCount = sjCount + 1
      end_if
    end_if
    if c_ball1(cp) = bp
      cp = c_b1clist(cp)
    else
      cp = c_b2clist(cp)
    end_if
  end_loop
end
;-------------------------------------------------------------------------------
```

```
; SmoothJointInstall.fis
;-------------------------------------------------------------------------------
define installSmoothJoint
  c_model(cp) = 'udm_SmoothJoint'

  ; Smooth-joint model properties
  c_prop(cp,'sj_dip')   = sjDip        ; joint dip
  c_prop(cp,'sj_kn')    = sjKn       ; normal stiffness
  c_prop(cp,'sj_ks')    = sjKs       ; shear stiffness
  c_prop(cp,'sj_rmul')  = sjRmult    ; radius multiplier
  c_prop(cp,'sj_fric')  = sjFric     ; friction coefficient
  c_prop(cp,'sj_da')    = sjDa       ; dilation angle
  c_prop(cp,'sj_bmode')   = sjBondMode  ; bond mode (See Theory and Background
      section 2.2.2)
  c_prop(cp,'sj_bns')   = sjBondN    ; bond normal strength (tension)
  c_prop(cp,'sj_bcoh')  = sjBondCoh    ; bonded system cohesion
  c_prop(cp,'sj_bfa')   = sjBondFric  ; bonded system friction angle
  c_prop(cp,'sj_large')   = sjStrainMode  ; large-strain mode flag
  c_prop(cp,'sj_Fn')    = sjFn       ; joint normal force
  c_prop(cp,'sj_xFs')     = sjFs       ; joint shear force

  ; Smooth-joint model internal state variables
  ; read-write
  c_prop(cp,'sj_gap')   = sjGap    ; gap (gap > 0 is open)


  ; set b_sj_mem to 1 for each particle
  b_extra(c_ball1(cp),b_sj_mem) = 1
  b_extra(c_ball2(cp),b_sj_mem) = 1

end
;-------------------------------------------------------------------------------
define read_joints
  ; Smooth-joint model internal state variables
  sj_active   = c_prop(cp,'sj_active')
  sj_xun    = c_prop(cp,'sj_xun')
  sj_yun    = c_prop(cp,'sj_yun')
  sj_area   = c_prop(cp,'sj_A')
  sj_rad    = c_prop(cp,'sj_rad')
  sj_bss    = c_prop(cp,'sj_bss')
  sj_gap    = c_prop(cp,'sj_gap')
  sj_un   = c_prop(cp,'sj_Un')
  sj_us   = c_prop(cp,'sj_xUs')
  sj_fn   = c_prop(cp,'sj_Fn')
  sj_fs   = c_prop(cp,'sj_xFs')
end
;-------------------------------------------------------------------------------
```

```
; LayerBuilder.fis
;-------------------------------------------------------------------------------
define buildLayers
  bp = ball_head
  loop while bp # null
    yObject = b_y(bp)
    xObject = b_x(bp)
    objectLayerNumber
```

```
    b_dens(bp) = rhoLayers(layerID)*(1+porosity)
    bp = b_next(bp)
  end_loop

  cp = contact_head
  loop while cp # null
    yObject = c_y(cp)
    xObject = c_x(cp)
    objectLayerNumber
    contactLayerProperties
    cp = c_next(cp)
  end_loop
end
;------------------------------------------------------------------------------
define layerDamping
  bp = ball_head
  loop while bp # null
    yObject = b_y(bp)
    xObject = b_x(bp)
    objectLayerNumber
    b_damp(bp) = xiLayers(layerID)*pi
    bp = b_next(bp)
  end_loop

  clp = clump_head
  loop while clp # null
    yObject = cl_y(clp)
    xObject = cl_x(clp)
    objectLayerNumber
    cl_damp(clp) = xiLayers(layerID)*pi
    clp = cl_next(clp)
  end_loop
end
;------------------------------------------------------------------------------
define objectLayerNumber
  layerID = 0
  useX = xObject
  section
  loop k (1,numberOfLayers)
    if useX < layerLeftLim
      useX = layerLeftLim
    end_if
    if useX > layerRightLim
      useX = layerRightLim
    end_if
    yLayer = mLayers(k)*useX + hLayers(k)*height
    if yObject > yLayer
      layerID = k
      exit section
    end_if
    layerID = k
  end_loop
  end_section
end
;------------------------------------------------------------------------------
define contactLayerProperties
  VsToKn = vsLayers(layerID)
  UCSToNb = ucsLayers(layerID,1)
  KnFromWaveSpeeds
  BondStrengthFromUCS
  stiffnessCalculator
  strengthCalculator
  c_kn(cp) = n_k2
  c_ks(cp) = s_k2
  pbp = c_pb(cp)
  if pbp # null
    pb_kn(pbp) = pbn_stiff
    pb_ks(pbp) = pbs_stiff
    pb_nstrength(pbp) = pbn_strength
    pb_sstrength(pbp) = pbs_strength
```

```
  end_if
end
;-------------------------------------------------------------------------------
define colorByLayer
  bp = ball_head
  loop while bp # null
    yObject = b_y(bp)
    xObject = b_x(bp)
    objectLayerNumber
    b_color(bp) = LayerBallColor + layerID -1
    bp = b_next(bp)
  end_loop
end
;-------------------------------------------------------------------------------
define layerCounter
  bp = ball_head
  loop while bp # null
    yObject = b_y(bp)
    xObject = b_x(bp)
    objectLayerNumber
    if layerID = 1
      layerOneCount = layerOneCount + 1
    end_if
    if layerID = 2
      layerTwoCount = layerTwoCount + 1
    end_if
    if layerID = 3
      layerThreeCount = layerThreeCount + 1
    end_if
    bp = b_next(bp)
  end_loop

  oo = out('There are ' + string(layerOneCount) + ' particles in layer one.')
  oo = out('There are ' + string(layerTwoCount) + ' particles in layer two.')
  oo = out('There are ' + string(layerThreeCount) + ' particles in layer three.')
end
;-------------------------------------------------------------------------------
```

```
; weathering.fis
;-------------------------------------------------------------------------------
define weatherSlope
  countSlopeCorners
  cp = contact_head
  loop while cp # null
    xObject = c_x(cp)
    yObject = c_y(cp)
    pbp = c_pb(cp)
    if pbp # null
      weatheringFactor
      pb_nstrength(pbp) = pb_nstrength(pbp)*wFactor
      pb_sstrength(pbp) = pb_sstrength(pbp)*wFactor
    end_if
    cp = c_next(cp)
  end_loop
end
;-------------------------------------------------------------------------------
define countSlopeCorners
  cornerCount = 0
  loop n (1,10)
    corner = xSlopeFace(n)
    if type(corner) = 2
      cornerCount = cornerCount + 1
    end_if
  end_loop
end
;-------------------------------------------------------------------------------
define weatheringFactor
  ; Reduction in strength by 1) dfsf(distance from slope face) and 2) layerID
  ObjectLayerNumber
```

```
  minW = ucsLayers(LayerID,2)
  weatheringLimit = float(ucsLayers(LayerID,3))/glevel_
  if yObject > ySlopeFace(1)
    distFromSlopeFace
    wd = dfsf/weatheringLimit
    if wd > 1
      wFactor = 1
    else
      wFactor = (1-minW)*sqrt(wd) + minW
    end_if
  else
    wFactor = 1
  end_if
end
;-------------------------------------------------------------------------------
define distFromSlopeFace

  dfsf = width

  loop n (1,cornerCount)
    xLine1 = xSlopeFace(n)
    xLine2 = xSlopeFace(n+1)
    yLine1 = ySlopeFace(n)
    yLine2 = ySlopeFace(n+1)

    distFromLine
    if dfl < dfsf
      dfsf = dfl
    end_if
  end_loop
end
;-------------------------------------------------------------------------------
define distFromLine
  dxLine = xLine1 - xLine2
  dyLine = yLine1 - yLine2

  distNumerator = abs(dyLine*xObject - dxLine*yObject + xLine1*yLine2 - xLine2*yLine1
      )
  distDenominator = sqrt(dxLine^2 + dyLine^2)

  dfl = distNumerator/distDenominator
end
;-------------------------------------------------------------------------------
define colorWeatheredZone
  bp = ball_head
  loop while bp # null
    xObject = b_x(bp)
    yObject = b_y(bp)
    weatheringFactor
    if wFactor < 1
      b_color(bp) = b_color(bp) + WeatherBallColor
    end_if
    bp = b_next(bp)
  end_loop
end
;-------------------------------------------------------------------------------
```

```
;PropertyCalculator.fis
;-------------------------------------------------------------------------------
define WaveSpeedsFromKn
  ; These factors and exponents were determined empirically with a series of tests
  ; The exponent should, in theory, be 0.5 for all cases. The factor is a function of
  ; Several model parameters and especially the kn/ks ratio and density (1.75 for
      this first case).
  vpFactor = 0.0167
  vsFactor = 0.011

  vpExp = 0.5
  vsExp = 0.5
```

```
12
13    VpFromKn = vpFactor*((2800*KnToVs/p_density)^vpExp)
14    VsFromKn = vsFactor*((2800*KnToVs/p_density)^vsExp)
15  end
16  ;--------------------------------------------------------------------------------
17  define KnFromWaveSpeeds
18    vsFactor = 0.011
19    vsExp = 0.5
20    KnFromVs = (VsToKn/vsFactor)^(1/vsExp)
21  end
22  ;--------------------------------------------------------------------------------
23  define BondStrengthFromUCS
24    NbFromUCS = 0.01*UCSToNb
25  end
26  ;--------------------------------------------------------------------------------
27  define stiffnessCalculator
28    k_n = KnFromVs
29    n_k1       = k_n*th
30    s_k1       = n_k1/kn_ks
31    n_k2       = k_n*th*c_mult
32    s_k2       = n_k2/kn_ks
33    pbn_stiff      = k_n/(r_mult_pb*r_avg*2)*pb_mult
34    pbs_stiff      = k_n/(r_mult_pb*r_avg*2)/kn_ks*pb_mult
35  end
36  ;--------------------------------------------------------------------------------
37  define strengthCalculator
38    ; knowing some strength parameter, set all other strength parameters for the layer
39    Nb = NbFromUCS
40    nb_sb      = 1.0
41    Sb         = Nb/nb_sb
42    pbn_strength   = Nb/r_mult_pb/r_avg/2
43    pbs_strength   = Sb/r_mult_pb/r_avg/2
44  end
45  ;--------------------------------------------------------------------------------
```

```
1   ; fname make_vessel.fis
2   ;--------------------------------------------------------------------------------
3   define slopeFaceArray
4     array xSlopeFace(10)
5     array ySlopeFace(10)
6   end
7   ;--------------------------------------------------------------------------------
8   define SLOPE_vessel; 900
9     glevel_ = 600/temp_fac
10    height = 0.25*temp_fac
11    width = 3.0*height
12
13    AdjustDims
14
15    seat_depth = -rhi*3
16    alpha_a = 80*degrad
17    alpha_b = 30*degrad
18    dx_a = height/1.75
19    dx_d = height/4
20    dx_e = height/3
21    dy_a = height/2
22    dy_b = 5*height/6/2
23    dy_c = 1*height/6/2
24
25    beta_a  = 25*degrad
26
27    x_1 = 0
28    x_9 = 0
29    x_8 = x_9 + dx_a
30    x_7 = x_8 + dy_b/tan(alpha_a)
31    x_6 = x_7 + dy_c/tan(alpha_b)
32    x_5 = x_6 + dx_d
33    x_4 = width - dx_e
34    x_3 = width
```

```
  x_2 = width

  y_1 = 0
  y_9 = dy_a
  y_8 = y_9 + 0
  y_7 = y_8 + dy_b
  y_6 = y_7 + dy_c
  y_5 = y_6 + 0
  y_4 = dy_a
  y_3 = y_4 + 0
  y_2 = 0

  xSlopeFace(1) = x_8
  xSlopeFace(2) = x_7
  xSlopeFace(3) = x_6

  ySlopeFace(1) = y_8
  ySlopeFace(2) = y_7
  ySlopeFace(3) = y_6

end
;-------------------------------------------------------------------------------
```

```
;BoundaryFunctions.fis
;-------------------------------------------------------------------------------
define CreateDashpots
  cFactor = r_avg*2*th*p_density/(1+porosity)
  VsToKn = vsBase
  KnFromWaveSpeeds
  KnToVs = KnFromVs
  WaveSpeedsFromKn
  V_p = VpFromKn
  V_s = VsFromKn
  bp = bound_bph
  loop while bp # null
    ptype = type(b_extra(bp,b_input_next_mem))
    if ptype = 1  ; The boundary particle is not on the base
      xDampC = V_p*cFactor
      yDampC = V_s*cFactor
    else      ; The boundary particle is on the base
      xDampC = V_s*cFactor
      yDampC = V_p*cFactor
    end_if
    b_extra(bp,b_x_damp_mem) = xDampC
    b_extra(bp,b_y_damp_mem) = yDampC

    bp = b_extra(bp,b_bound_next_mem)
  end_loop
end
;-------------------------------------------------------------------------------
define SideStaticXForce
  bp = ff_bph
  loop while bp # null
    xForceOnSide = -b_xfob(bp)
    b_extra(bp,b_xfst_mem) = xForceOnSide
    b_xfap(bp) = xForceOnSide
    bp = b_extra(bp,b_ff_next_mem)
  end_loop
end
;-------------------------------------------------------------------------------
define BaseStaticYForce
  bp = input_bph
  loop while bp # null
    yForceOnBase = -b_yfob(bp)
    b_extra(bp,b_yfst_mem) = yForceOnBase
    b_yfap(bp) = yForceOnBase
    bp = b_extra(bp,b_input_next_mem)
  end_loop
end
```

```
;-------------------------------------------------------------------------------
define FreeFieldVelocity
  bp = ff_bph
  loop while bp # null
    clp = b_extra(bp,b_ref_clump_mem)
    b_extra(bp,b_x_refvel_mem) = cl_xvel(clp)
    b_extra(bp,b_y_refvel_mem) = cl_yvel(clp);***
    bp = b_extra(bp,b_ff_next_mem)
  end_loop
end
;-------------------------------------------------------------------------------
define BoundControl
  bp = bound_bph
  loop while bp # null
    xStaticForce = b_extra(bp,b_xfst_mem)
    xInputForce = b_extra(bp,b_xfin_mem)
    xRelVel = -(b_xvel(bp) - b_extra(bp,b_x_refvel_mem))
    yRelVel = -(b_yvel(bp) - b_extra(bp,b_y_refvel_mem));***
    xViscousForce = xRelVel*b_extra(bp,b_x_damp_mem)
    yViscousForce = yRelVel*b_extra(bp,b_y_damp_mem);***
      b_xfap(bp) = xStaticForce + xInputForce + xViscousForce
      b_yfap(bp) = yStaticForce + yInputForce + yViscousForce;***
      bp = b_extra(bp,b_bound_next_mem)
  end_loop
end
;-------------------------------------------------------------------------------
define boundaryStrength
  cp = contact_head
  loop while cp # null
    xObject = c_x(cp)
    yObject = c_y(cp)
    baseStrength
    sideStrength
    cp = c_next(cp)
  end_loop
end
;-------------------------------------------------------------------------------
define baseStrength
  ; yObject
  if yObject < ffWidth
    bFactor = 1 + 10*(1 - 2*yObject/height)
    pbp = c_pb(cp)
    if pbp # null
      pb_nstrength(pbp) = pb_nstrength(pbp)*bFactor
      pb_sstrength(pbp) = pb_sstrength(pbp)*bFactor
    end_if
  end_if
end
;-------------------------------------------------------------------------------
define sideStrength
  ; xObject
  if xObject < ffWidth
    bFactor = 1 + 10*(1 - xObject/ffWidth)
    pbp = c_pb(cp)
    if pbp # null
      pb_nstrength(pbp) = pb_nstrength(pbp)*bFactor
      pb_sstrength(pbp) = pb_sstrength(pbp)*bFactor
    end_if
  else
    if xObject > width - ffWidth
      bFactor = 1 + 10*(xObject/(width - ffWidth) - 1)
      pbp = c_pb(cp)
      if pbp # null
        pb_nstrength(pbp) = pb_nstrength(pbp)*bFactor
        pb_sstrength(pbp) = pb_sstrength(pbp)*bFactor
      end_if
    end_if
  end_if
end
;-------------------------------------------------------------------------------
```

```
define make_boundaries_clump
  clmp = null
  bp = bound_bph
  loop while bp # null
    clmp = cl_add(clmp,bp)
    bp = b_extra(bp,b_bound_next_mem)
  end_loop
end
;------------------------------------------------------------------------------
```

```
;List Preservation
;------------------------------------------------------------------------------
define ListPreservation
; This function should be attached to a particle deletion fishcall
  section
  bDelete = fc_arg(0)
  asdf = b_type(bDelete)
  if asdf = 1
    exit section
  end_if
  bNextSlot = b_extra(bDelete,b_bound_next_mem)
  ptype = type(bNextSlot)
  if ptype = 4
    if bDelete = ff_bph
      ff_bph = bNextSlot
    end_if
    bPrevious = bound_bph
    bCheck = b_extra(bPrevious,b_bound_next_mem)
    loop while bCheck # bDelete
      bPrevious = bCheck
      bCheck = b_extra(bPrevious,b_bound_next_mem)
    end_loop
    b_extra(bPrevious,b_bound_next_mem) = bNextSlot
    b_extra(bPrevious,b_ff_next_mem)  = b_extra(bDelete,b_ff_next_mem)
  end_if
  end_section
end
;------------------------------------------------------------------------------
```

E.3 Loading the Model

The following outlines the sets of functions and commands used to load the PFC slope model.

```
; fname SLP_test.pfc
call dirs.fis
dirs
set cwdir fis_dir
call BoundaryFunctions.fis
call BuildModel.fis
call cleanup_BPM.fis
call Elastic.fis
call FishcallMaster.fis
call fnames_BPM.fis
call history_from_python.fis
call LoadCase.fis
call video_BPM.fis

name_set
dirs
fnames
set log off
set logfile lgfile
set log on overwrite
```

```
instrument
history reset
define historyStep
  historyStep = int(1/(1200*glevel_*tsp_0))
end
resetdisp
set dt tsp_0
set time 0
set hist_rep historyStep
start_history
set fishcall FC_CYC_MOT FishcallMaster01
set fishcall FC_PB_DEL updateContactStiff
buildFractureDomain
;makeSimulationElastic
vid_record
input_SLP
load_SLP
set log on
save finfile
vid_close
write_history
history reset
delete ball
print fish
set log off
set cwdir bat_dir
```

```
; example load batch file
new
;-------------------------------------------------------------------------------
define setFile
modelFile = modelDirectory + 'SLP_j800_ini_587_15.sav'
end
setFile
restore modelFile
define name_set
  motion = '_Northridge'
  CreateVideoFlag = 1
end
call SLP_test.pfc
new
;-------------------------------------------------------------------------------
```

The following functions are used to load the slope model.

```
; LoadCase.fis

; Reads input text file and produces custom loading
;-------------------------------------------------------------------------------
define input_SLP
  checkForTable
; frequency sweep ----------------------------
  if motion = '_swp'
    makeSimulationElastic
    cycNum = 500
    vFactor = 1.0
    inpFile = inp_dir + 'swp_1_to_30Hz_1g.txt'
    command
    table 1 read inpFile
    end_command
  end_if
; Harmonic loading
; 0.5 Hz ---------------------------------------
  if motion = '_ramp0.5v'
    tMaxlimit = 0.2
    cycNum = 1000
    vFactor = 0.0
    inpFile = inp_dir + 'sine_0.5Hz_0.25g.txt'
```

```
    command
    set fishcall 0 rampFactor
      table 1 read inpFile
    end_command
  end_if
; 1 Hz ----------------------------------------
  if motion = '_ramp1v'
    tMaxlimit = 0.2
    cycNum = 500
    vFactor = 0.0
    inpFile = inp_dir + 'sine_1Hz_0.5g.txt'
    command
    set fishcall 0 rampFactor
      table 1 read inpFile
    end_command
  end_if
; 2 Hz ----------------------------------------
  if motion = '_ramp2v'
    tMaxlimit = 0.2
    cycNum = 250
    vFactor = 0.0
    inpFile = inp_dir + 'sine_2Hz_1g.txt'
    command
    set fishcall 0 rampFactor
      table 1 read inpFile
    end_command
  end_if
; 3 Hz ----------------------------------------
  if motion = '_ramp3v'
    tMaxlimit = 0.2
    cycNum = 167
    vFactor = 0.0
    inpFile = inp_dir + 'sine_3Hz_1.5g.txt'
    command
    set fishcall 0 rampFactor
      table 1 read inpFile
    end_command
  end_if
; 5 Hz ----------------------------------------
  if motion = '_ramp5v'
    tMaxlimit = 0.2
    cycNum = 100
    vFactor = 0.0
    inpFile = inp_dir + 'sine_5Hz_2.5g.txt'
    command
    set fishcall 0 rampFactor
      table 1 read inpFile
    end_command
  end_if
;-----------------------------------------------
  if motion = '_Northridge'
    cycNum = 500
    vFactor = 1.6304
    inpFile = inp_dir + 'northridge.txt'
    command
    table 1 read inpFile
    end_command
  end_if
;-----------------------------------------------
; Non-dynamic loading
  if motion = '_pseudo'
    pseudoDamping = 0.7
    vFactor = 1.0
    inpFile = inp_dir + 'zero_shaking.txt'
    command
    table 1 read inpFile
    set fishcall 0 remove FishcallMaster01
    end_command
    FreeFieldXFixOff
    FreeFieldYFixOn
```

```
    InputXFixOn
    pseudostaticFractureDomain
    pseudostaticFailure
    staticRunout
  end_if

  if motion = '_static'
    crk_init
    vFactor = 1.0
    inpFile = inp_dir + 'zero_shaking.txt'
    command
    table 1 read inpFile
    set fishcall 0 remove FishcallMaster01
    end_command
    FreeFieldXFixOn
    FreeFieldYFixOn
    InputXFixOn
    staticFailure2
    oo = out('dropCount = ' + string(dropCount))
    staticRunout
  end_if


  L = table_size(1)
  tStep = xtable(1,2) - xtable(1,1)
    findMaxVelocity
    tMax = tStep*L
    tMaxInv = 1/tMax
  percent_complete = 0.0

  porosityInv = 1/(1+porosity)
end
;-------------------------------------------------------------------------------
define findMaxVelocity
  vMax = 0
  loop index (1,L)
    vv = ytable(1,index)
    if vv > vMax
      vMax = vv
    end_if
  end_loop
end
;-------------------------------------------------------------------------------
define checkForTable
  if L > 0
    ii = del_table(1)
  end_if
end
;-------------------------------------------------------------------------------
define ForceInput
  ; fishcall 0
  vx_in = table(1,ProbTime)*vFactor
  bp = input_bph
  loop while bp # null
    fx_in = 4.0*b_rad(bp)*th*p_density*(V_s)*vx_in*porosityInv
    fy_in = 0.0
    b_extra(bp,b_xfin_mem) = fx_in
    b_extra(bp,b_yfin_mem) = fy_in
    bp = b_extra(bp,b_input_next_mem)
  end_loop
end
;-------------------------------------------------------------------------------
define rampControl
  if vFactor >= redclPGA
    command
      set fishcall 0 remove rampFactor
    end_command
  end_if
end
;-------------------------------------------------------------------------------
```

```
define rampFactor
  ; fishcall 0
  redclPGA = 8/9.81
    maxFactor = tMax
  vFactor = maxFactor*ProbTime*tMaxInv
end
;-------------------------------------------------------------------------------
define load_SLP
  ;snapshot
  loop while ProbTime < tMax*tMaxLimit
    command
      print lgfile
      print percent_complete
      cycle cycNum
      ;snapshot
    end_command
    rampControl
    percent_complete = 100*ProbTime*tMaxInv
  end_loop
  ;snapshot
end
;-------------------------------------------------------------------------------
define xTableAdjust
  deltaT = tStep/glevel_
  tTable = 0
  loop index (1,L)
    xtable(1,index) = tTable
    tTable = tTable + deltaT
  end_loop
end
;-------------------------------------------------------------------------------
define staticFailure2
  crack_0 = crk_num
  dropCount = 0
  loop while crk_num < (crack_0 + 5)
    dropStrength2
    oo = out('-----------------------------------------------' + string(newStrength))
    dropCount = dropCount + 1
  end_loop
end
;-------------------------------------------------------------------------------
define staticRunout
  section
  loop while crack_0 # crk_num
    crack_0 = crk_num
    cyc_num = cyc_num + 1
    command
      print cyc_num
      cycle 5000
    end_command
    if cyc_num > 10
      exit section
    end_if
  end_loop
  end_section
end
;-------------------------------------------------------------------------------
define dropStrength2
  fricDrop = 0.001*p_friction
  cp = contact_head
  loop while cp # null
    if c_y(cp) > (height-gap)/2
    if c_x(cp) > dx_a
      pbp = c_pb(cp)
      if pbp # null
        xObject = c_x(cp)
        yObject = c_y(cp)
        objectLayerNumber
        findStrengthDrop
        pb_nstrength(pbp) = pb_nstrength(pbp) - ndrop
```

```
        pb_sstrength(pbp) = pb_sstrength(pbp) - sdrop
        newStrength = pb_nstrength(pbp)
      end_if
      c_fric(cp) = c_fric(cp) - fricDrop
    end_if
    end_if
    cp = c_next(cp)
  end_loop
  command
    cycle 1
  end_command
end
;-------------------------------------------------------------------------------
define findStrengthDrop
  originalUCS = ucsLayers(LayerID,1)
  UCSToNb = originalUCS
  BondStrengthFromUCS
  strengthCalculator
  originalBondStrength = pbn_strength
  ndrop = 0.001*originalBondStrength
  sdrop = ndrop/nb_sb
end
;-------------------------------------------------------------------------------
define hAcc2
  glevX = kh*glevY
  command
    print crk_num
    print kh
    set grav glevX glevY
    solve average 2e-5 maximum 2e-5 fishhalt halt
    snapshot
  end_command
end
;-------------------------------------------------------------------------------
define pseudoStaticFailure
  command
    damp local pseudoDamping
    set fishcall FC_CYC_MOT remove FishcallMaster01
  end_command
  vMax = 1
  dkh = 0.05
  khMax = 2
  kh = khMin
  haltLIM = 5
  crack_0 = crk_num
  section
    loop while crk_num < (crack_0 + 5)
      kh = kh + dkh
      InputAcc = kh
      if kh > khMax
        exit section
      end_if
      hAcc2
    end_loop
  end_section

  if kh <= khMax
    layerDamping
  end_if
end
;-------------------------------------------------------------------------------
```

```
;-------------------------------------------------------------------------------
define ClumpXFixOn
  clp = clump_head
  loop while clp # null
    cl_xvel(clp) = 0
    cl_xfix(clp) = 1
    clp = cl_next(clp)
```

```
  end_loop
end
;-------------------------------------------------------------------------------
define ClumpYFixOn
  clp = clump_head
  loop while clp # null
    cl_yvel(clp) = 0
    cl_yfix(clp) = 1
    clp = cl_next(clp)
  end_loop
end
;-------------------------------------------------------------------------------
define ClumpRFixOn
  clp = clump_head
  loop while clp # null
    cl_rvel(clp) = 0
    cl_rfix(clp) = 1
    clp = cl_next(clp)
  end_loop
end
;-------------------------------------------------------------------------------
define ClumpXFixOff
  clp = clump_head
  loop while clp # null
    cl_xfix(clp) = 0
    clp = cl_next(clp)
  end_loop
end
;-------------------------------------------------------------------------------
define ClumpYFixOff
  clp = clump_head
  loop while clp # null
    cl_yfix(clp) = 0
    clp = cl_next(clp)
  end_loop
end
;-------------------------------------------------------------------------------
define ClumpRFixOff
  clp = clump_head
  loop while clp # null
    cl_rfix(clp) = 0
    clp = cl_next(clp)
  end_loop
end
;-------------------------------------------------------------------------------
define FreeFieldXFixOn
  bp = ff_bph
  loop while bp # null
    b_xvel(bp) = 0
    b_xfix(bp) = 1
    bp = b_extra(bp,b_ff_next_mem)
  end_loop
end
;-------------------------------------------------------------------------------
define FreeFieldYFixOn
  bp = ff_bph
  loop while bp # null
    b_yvel(bp) = 0
    b_yfix(bp) = 1
    bp = b_extra(bp,b_ff_next_mem)
  end_loop
end
;-------------------------------------------------------------------------------
define FreeFieldRFixOn
  bp = ff_bph
  loop while bp # null
    b_rvel(bp) = 0
    b_rfix(bp) = 1
    bp = b_extra(bp,b_ff_next_mem)
  end_loop
```

```
78  end
79  ;-------------------------------------------------------------------------------
80  define FreeFieldXFixOff
81    bp = ff_bph
82    loop while bp # null
83      b_xfix(bp) = 0
84      bp = b_extra(bp,b_ff_next_mem)
85    end_loop
86  end
87  ;-------------------------------------------------------------------------------
88  define FreeFieldYFixOff
89    bp = ff_bph
90    loop while bp # null
91      b_yfix(bp) = 0
92      bp = b_extra(bp,b_ff_next_mem)
93    end_loop
94  end
95  ;-------------------------------------------------------------------------------
96  define FreeFieldRFixOff
97    bp = ff_bph
98    loop while bp # null
99      b_rfix(bp) = 0
100     bp = b_extra(bp,b_ff_next_mem)
101   end_loop
102 end
103 ;-------------------------------------------------------------------------------
104 define InputXFixOn
105   bp = input_bph
106   loop while bp # null
107     b_xvel(bp) = 0
108     b_xfix(bp) = 1
109     bp = b_extra(bp,b_input_next_mem)
110   end_loop
111 end
112 ;-------------------------------------------------------------------------------
113 define InputYFixOn
114   bp = input_bph
115   loop while bp # null
116     b_yvel(bp) = 0
117     b_yfix(bp) = 1
118     bp = b_extra(bp,b_input_next_mem)
119   end_loop
120 end
121 ;-------------------------------------------------------------------------------
122 define InputRFixOn
123   bp = input_bph
124   loop while bp # null
125     b_rvel(bp) = 0
126     b_rfix(bp) = 1
127     bp = b_extra(bp,b_input_next_mem)
128   end_loop
129 end
130 ;-------------------------------------------------------------------------------
131 define InputXFixOff
132   bp = input_bph
133   loop while bp # null
134     b_xfix(bp) = 0
135     bp = b_extra(bp,b_input_next_mem)
136   end_loop
137 end
138 ;-------------------------------------------------------------------------------
139 define InputYFixOff
140   bp = input_bph
141   loop while bp # null
142     b_yfix(bp) = 0
143     bp = b_extra(bp,b_input_next_mem)
144   end_loop
145 end
146 ;-------------------------------------------------------------------------------
147 define InputRFixOff
```

```
  bp = input_bph
  loop while bp # null
    b_rfix(bp) = 0
    bp = b_extra(bp,b_input_next_mem)
  end_loop
end
;-------------------------------------------------------------------------------
```

```
; FishcallMaster.fis
;-------------------------------------------------------------------------------
define FishcallMaster01
  ;Place (in order) all the fishcalls that need to be run
  ForceInput
  FreeFieldVelocity
  BoundControl


end
;-------------------------------------------------------------------------------
define updateContactStiff
  cp = fc_arg(0)
  c_kn(cp) = n_k1*nFac
  c_ks(cp) = s_k1*sFac
  c_fric(cp) = c_fric(cp)*1.0
end
;-------------------------------------------------------------------------------
```

E.4 Model Output

The histories that can be saved from PFC are limited in scope. In many cases, these histories are sufficient, however, it may be desired at times to export a more complete picture of the state of the model for post-processing. The functions used to define PFC histories truncated for presentation in this appendix. For these cases, 'Model State' functions were developed which wrote the state of the entire model at any given time to ASCII files that could be read and interpreted by external programs. The two model states exported were the particle state and the contact state. Each of these functions resulted in output files containing the entire list of particles or contacts in the model and their respective parameters at the time of execution.

The primary advantage of the 'Model State' outputs is the ability to use tools such as Python or Paraview to visualize and perform calculations on the model in a way that PFC is not designed for. The primary disadvantages of the 'Model State' outputs are the time it takes to generate and write them and the amount of disk space they require. The particle and contact state files for a typical slope model (100,000 particles) require about 75 MB of hard disk space in the format they are written in. Even for fairly short duration simulation, the resulting files can be several gigabytes.

E.4.1 History Functions

The following function is used to define the histories saved during the PFC simulation. It is truncated for the sake of brevity.

```
; These files are truncated for brevity. The trucnacions eliminate the naming of
; variables of monitoring points throuhgout the model. Trucnations are denoted by
    "..."
;-------------------------------------------------------------------------------
define instrument
  A1 = ball_near2(width*0.1,height*0.0)
  A2 = ball_near2(width*0.25,height*0.0)
  ...
  E5 = ball_near2(width*0.9,height*1.0)

  xA1_0 = b_x(A1)
  xA2_0 = b_x(A2)
  ...
  xE5_0 = b_x(E5)

end
;-------------------------------------------------------------------------------
define ProbTime
  ProbTime = time*glevel_
  maxRatio = max_unbal/max_cforce
  avgRatio = av_unbal/av_cforce
  inpXVel = vx_in
  inpYVel = vy_in
  count_particles
  count_contacts
  coord_num = float(c_count)/float(p_count)

  xA1 = (b_x(A1) - xA1_0)*glevel_
  xA2 = (b_x(A2) - xA2_0)*glevel_
  ...
  xE5 = (b_x(E5) - xE5_0)*glevel_

  yA1 = (b_y(A1) - yA1_0)*glevel_
  yA2 = (b_y(A2) - yA2_0)*glevel_
  ...
  yE5 = (b_y(E5) - yE5_0)*glevel_

  xvelA2 = b_xvel(A2)
  ...
  xvelE5 = b_xvel(E5)

  yvelA1 = b_yvel(A1)
  yvelA2 = b_yvel(A2)
  ...
  yvelE5 = b_yvel(E5)

end
;-------------------------------------------------------------------------------
define start_history
   command
    history ProbTime
    history inpXVel
    history inpYVel
    history crk_num

    history xA1
    history xA2
    ...
    history xE5

    history yA1
    history yA2
```

```
    ...
    history yE5

    history xvelA1
    history xvelA2
    ...
    history xvelE5

    history yvelA1
    history yvelA2
    ...
    history yvelE5

  end_command
end
;-------------------------------------------------------------------------------
define write_history
  command
    history write 1 2 3 4 5 6 7 8 9 10 11 12 13 14 15 16 17 18 19 20 21 22 23 24 25
        26 27 28 29 30 31 32 33 34 35 36 37 38 39 40 41 42 43 44 45 46 47 48 49 50 51
         52 53 54 55 56 57 58 59 60 61 62 63 64 65 66 67 68 69 70 71 72 73 74 75 76
        77 78 79 80 81 82 83 84 85 86 87 88 89 90 91 92 93 94 95 96 97 file histfile
        overwrite
  end_command
end
;-------------------------------------------------------------------------------
```

E.4.2 Model State Functions

The following functions are used to create the model state output files for each particle, contact, or measurement cell within the model.

```
; snapshot.fis
; note: various states are commented out depending on the desired output
;-------------------------------------------------------------------------------
define snapshot
  b_sigma
  state_code = string(10000 + ss_num)
; particle_state
; contact_state
  cell_state
  ss_num = ss_num+1
end
;-------------------------------------------------------------------------------

define snapshot_ini
command
;    call count_contacts.fis
;    call count_particles.fis
; call particle_state.fis
  call contact_state.fis
; call cell_state.fis
end_command
ssn = 1
ss_num = 1
;array wra_p(1)
;array wra_c(1)
array wra_cell(1)
end
snapshot_ini
```

```
; extra_ball_mem.fis

```

```
define extra_ball_mem
  slots = 21
  b_xx_mem       = 1    ;sigma xx
  b_yy_mem       = 2    ;sigma yy
  b_xy_mem       = 3    ;sigma xy
  b_yx_mem       = 4    ;sigma yx
  b_cell_bnext_mem  = 5    ;next ball pointer in measurement cell
  b_sj_mem       = 6    ;part of a smooth joint (1/0)
  b_input_next_mem  = 7    ;next ball pointer in input list
  b_bound_next_mem  = 8    ;next ball pointer in boundary particles list
  b_ff_next_mem     = 9    ;next ball pointer in free field boundary list
  b_ref_clump_mem   = 10   ;address of the free field reference clump
  b_x_refvel_mem    = 11   ;x-velocity of the reference clump (0 if no reference clump
       exists)
  b_y_refvel_mem    = 12   ;y-velocity of the reference clump (0 if no reference clump
       exists)
  b_main_flag_mem   = 13   ;flag for if the ball is part of the main model: 0 for no;
      1 for yes
  b_side_flag_mem   = 14   ;left or right side flag: 0 for left; 1 for right
  b_x_damp_mem    = 15   ;x-direction damping coefficent
  b_y_damp_mem    = 16   ;y-direction damping coefficent
  b_xfin_mem      = 17     ;x-direction applied force
  b_yfin_mem      = 18   ;y-direction applied force
  b_xfst_mem      = 19   ;x-direction static force
  b_yfst_mem      = 20   ;y-direction static force
  b_layer_mem     = 21   ;particle layer ID number

  command
    set extra ball slots
  end_command

end
```

```
; particle_state.pfc
;-------------------------------------------------------------------------------
define particle_state
  p_fname = statefile + '_particles_' + state_code + '.dat'
  oo = open(p_fname,1,1)

  wra_p(1) = 'time = ' + string(time)
  oo = write(wra_p,1)

  column_1 = 'ball pointer'
  column_2 = 'x position'
  column_3 = 'y position'
  column_4 = 'radius'
  column_5 = 'x vel'
  column_6 = 'y vel'
  column_7 = 'r vel'
  column_8 = 'x fob'
  column_9 = 'y fob'
  column_10 = 'moment'
  column_11 = 'rotation'
  column_12 = 'x disp'
  column_13 = 'y disp'
  column_14 = 'sigma_xx'
  column_15 = 'sigma_yy'
  column_16 = 'sigma_xy'
  column_17 = 'sigma_yx'

  wra_p(1) = column_1 + ','
  wra_p(1) = wra_p(1) + column_2 + ','
  wra_p(1) = wra_p(1) + column_3 + ','
  wra_p(1) = wra_p(1) + column_4 + ','
  wra_p(1) = wra_p(1) + column_5 + ','
  wra_p(1) = wra_p(1) + column_6 + ','
  wra_p(1) = wra_p(1) + column_7 + ','
  wra_p(1) = wra_p(1) + column_8 + ','
  wra_p(1) = wra_p(1) + column_9 + ','
```

```
  wra_p(1) = wra_p(1) + column_10 + ','
  wra_p(1) = wra_p(1) + column_11 + ','
  wra_p(1) = wra_p(1) + column_12 + ','
  wra_p(1) = wra_p(1) + column_13 + ','
  wra_p(1) = wra_p(1) + column_14 + ','
  wra_p(1) = wra_p(1) + column_15 + ','
  wra_p(1) = wra_p(1) + column_16 + ','
  wra_p(1) = wra_p(1) + column_17

  oo = write(wra_p,1)

  ii=1
  bp = ball_head
  loop while bp # null
  if b_rad(bp)> 2*rhi
  else
    ii_1 = string(bp)
    ii_2 = string(b_x(bp))
    ii_3 = string(b_y(bp))
    ii_4 = string(b_rad(bp))
    ii_5 = string(b_xvel(bp))
    ii_6 = string(b_yvel(bp))
    ii_7 = string(b_rvel(bp))
    ii_8 = string(b_xfob(bp))
    ii_9 = string(b_yfob(bp))
    ii_10 = string(b_mom(bp))
    ii_11 = string(b_rot(bp))
    ii_12 = string(b_xdisp(bp))
    ii_13 = string(b_ydisp(bp))
    ii_14 = string(b_extra(bp,b_xx_mem))
    ii_15 = string(b_extra(bp,b_yy_mem))
    ii_16 = string(b_extra(bp,b_xy_mem))
    ii_17 = string(b_extra(bp,b_yx_mem))

    wra_p(1) = ii_1 + ','
    wra_p(1) = wra_p(1) + ii_2 + ','
    wra_p(1) = wra_p(1) + ii_3 + ','
    wra_p(1) = wra_p(1) + ii_4 + ','
    wra_p(1) = wra_p(1) + ii_5 + ','
    wra_p(1) = wra_p(1) + ii_6 + ','
    wra_p(1) = wra_p(1) + ii_7 + ','
    wra_p(1) = wra_p(1) + ii_8 + ','
    wra_p(1) = wra_p(1) + ii_9 + ','
    wra_p(1) = wra_p(1) + ii_10 + ','
    wra_p(1) = wra_p(1) + ii_11 + ','
    wra_p(1) = wra_p(1) + ii_12 + ','
    wra_p(1) = wra_p(1) + ii_13 + ','
    wra_p(1) = wra_p(1) + ii_14 + ','
    wra_p(1) = wra_p(1) + ii_15 + ','
    wra_p(1) = wra_p(1) + ii_16 + ','
    wra_p(1) = wra_p(1) + ii_17

    oo = write(wra_p,1)
  end_if
    bp = b_next(bp)
    ii = ii +1
  end_loop
  oo = close(p_fname)
end
;-------------------------------------------------------------------------------
```

```
; particle_state.pfc
;-------------------------------------------------------------------------------
define contact_state
  c_fname = statefile + '_contacts_' + state_code + '.dat'
  oo = open(c_fname,1,1)

  wra_c(1) = 'time = ' + string(time)
  oo = write(wra_c,1)
```

```
9
10    column_1 = 'contact pointer'
11    column_2 = 'ball 1'
12    column_3 = 'ball 2'
13    column_4 = 'active flag'
14    column_5 = 'x position'
15    column_6 = 'y position'
16    column_7 = 'x unit normal'
17    column_8 = 'y unit normal'
18    column_9 = 'normal force'
19    column_10 = 'viscous normal force'
20    column_11 = 'shear force'
21    column_12 = 'viscous shear force'
22    column_13 = 'bond flag'
23    column_14 = 'broken flag'
24    column_15 = 'failure mode'
25    column_16 = 'bond normal force'
26    column_17 = 'bond shear force'
27    column_18 = 'bond max n_stress'
28    column_19 = 'bond max s_stress'
29    column_20 = 'bond moment'
30
31    wra_c(1) = column_1 + ','
32    wra_c(1) = wra_c(1) + column_2 + ','
33    wra_c(1) = wra_c(1) + column_3 + ','
34    wra_c(1) = wra_c(1) + column_4 + ','
35    wra_c(1) = wra_c(1) + column_5 + ','
36    wra_c(1) = wra_c(1) + column_6 + ','
37    wra_c(1) = wra_c(1) + column_7 + ','
38    wra_c(1) = wra_c(1) + column_8 + ','
39    wra_c(1) = wra_c(1) + column_9 + ','
40    wra_c(1) = wra_c(1) + column_10 + ','
41    wra_c(1) = wra_c(1) + column_11 + ','
42    wra_c(1) = wra_c(1) + column_12 + ','
43    wra_c(1) = wra_c(1) + column_13 + ','
44    wra_c(1) = wra_c(1) + column_14 + ','
45    wra_c(1) = wra_c(1) + column_15 + ','
46    wra_c(1) = wra_c(1) + column_16 + ','
47    wra_c(1) = wra_c(1) + column_17 + ','
48    wra_c(1) = wra_c(1) + column_18 + ','
49    wra_c(1) = wra_c(1) + column_19 + ','
50    wra_c(1) = wra_c(1) + column_20
51
52    oo = write(wra_c,1)
53
54    ii=1
55    cp = contact_head
56    loop while cp # null
57      gather_c_info
58      oo = write(wra_c,1)
59      cp = c_next(cp)
60      ii = ii +1
61    end_loop
62    cp = broken_head
63    oo = close(c_fname)
64  end
65  ;-------------------------------------------------------------------------------
66  define gather_c_info
67    ii_1 = string(cp)
68    ii_2 = string(c_ball1(cp))
69    ii_3 = string(c_ball2(cp))
70    ii_4 = string(c_active(cp))
71    ii_5 = string(c_x(cp))
72    ii_6 = string(c_y(cp))
73    ii_7 = string(c_xun(cp))
74    ii_8 = string(c_yun(cp))
75    ii_9 = string(c_nforce(cp))
76    ii_10 = string(c_nvforce(cp))
77    ii_11 = string(c_sforce(cp))
78    ii_12 = string(c_svforce(cp))
```

```
79
80    if c_pb(cp) # null
81      pbp = c_pb(cp)
82      ii_13 = string(1)
83      ii_14 = string(c_broken(cp))
84      ii_15 = string(c_slipwork(cp))
85      ii_16 = string(pb_nforce(pbp))
86      ii_17 = string(pb_sforce(pbp))
87      ii_18 = string(pb_nstress(pbp))
88      ii_19 = string(pb_sstress(pbp))
89      ii_20 = string(pb_mom(pbp))
90    else
91      ii_11 = string(0)
92      ii_12 = string(0)
93      ii_13 = string(0)
94      ii_14 = string(0)
95      ii_15 = string(0)
96      ii_16 = string(0)
97      ii_17 = string(0)
98      ii_18 = string(0)
99      ii_19 = string(0)
100     ii_20 = string(0)
101   end_if
102
103   wra_c(1) = ii_1 + ','
104   wra_c(1) = wra_c(1) + ii_2 + ','
105   wra_c(1) = wra_c(1) + ii_3 + ','
106   wra_c(1) = wra_c(1) + ii_4 + ','
107   wra_c(1) = wra_c(1) + ii_5 + ','
108   wra_c(1) = wra_c(1) + ii_6 + ','
109   wra_c(1) = wra_c(1) + ii_7 + ','
110   wra_c(1) = wra_c(1) + ii_8 + ','
111   wra_c(1) = wra_c(1) + ii_9 + ','
112   wra_c(1) = wra_c(1) + ii_10 + ','
113   wra_c(1) = wra_c(1) + ii_11 + ','
114   wra_c(1) = wra_c(1) + ii_12 + ','
115   wra_c(1) = wra_c(1) + ii_13 + ','
116   wra_c(1) = wra_c(1) + ii_14 + ','
117   wra_c(1) = wra_c(1) + ii_15 + ','
118   wra_c(1) = wra_c(1) + ii_16 + ','
119   wra_c(1) = wra_c(1) + ii_17 + ','
120   wra_c(1) = wra_c(1) + ii_18 + ','
121   wra_c(1) = wra_c(1) + ii_19 + ','
122   wra_c(1) = wra_c(1) + ii_20
123
124 end
125 ;-------------------------------------------------------------------------------
```

```
1  ; m_cells.fis
2  define m_cells
3    ; creates an array of measurement cells (m_cells)
4    cell_mem
5    cell_head = null
6    total = 0
7    x_spacing = ffWidth
8    y_spacing = x_spacing
9    x_i = xMinBound
10   y_i = yMinbound
11   x_num = round((xMaxBound - xMinBound)/x_spacing) + 1
12   y_num = round((yMaxBound - yMinBound)/y_spacing) + 1
13   loop n (1,y_num)
14     y_cell = y_i
15     loop m (1,x_num)
16       x_cell = x_i
17       eval_cell
18       x_i = x_i + x_spacing
19     end_loop
20     x_i = xMinBound
21     y_i = y_i + y_spacing
```

```
22    end_loop
23
24  end
25  ;------------------------------------------------------------------------------
26  define eval_cell
27    ; evaluates a cell to determine if it contains any particles and adds it to
28    ; a linked list of measurement cells if it does (via the 'link_cell' function).
29    ; all particles in each linked cell is also added to a new linked list specific
30    ; to the measurement cell it's in (via the 'link_particle' function).
31    num_ = 0
32    cell_bph = null
33    cell_stress_xx = 0
34    cell_stress_yy = 0
35    cell_stress_xy = 0
36    cell_stress_yx = 0
37    x_end = x_cell + x_spacing
38    y_end = y_cell + y_spacing
39    bp = ball_head
40    loop while bp # null
41      extraType = type(b_extra(bp,b_bound_next_mem))
42      if extraType = 1
43      if b_clump(bp) = null
44        if b_x(bp) > x_cell
45        if b_x(bp) < x_end
46        if b_y(bp) > y_cell
47        if b_y(bp) < y_end
48          num_ = num_ + 1
49          b_mem_slot = b_cell_bnext_mem
50          link_particle
51        end_if
52        end_if
53        end_if
54        end_if
55      end_if
56      end_if
57      bp = b_next(bp)
58    end_loop
59    if num_ # 0
60      link_cell
61    end_if
62    total = total + num_
63  end
64  ;------------------------------------------------------------------------------
65  define link_cell
66    ; adds a cell to a linked list of cells.
67    ; requires that cell_head be initialized outside of m_cells
68    cell_ad = cell_head
69    cell_head = get_mem(11)
70    mem(cell_head) = cell_ad
71    mem(cell_head + _cell_x) = x_cell
72    mem(cell_head + _cell_y) = y_cell
73    mem(cell_head + _cell_pnum) = num_
74    mem(cell_head + _cell_bph) = cell_bph
75    mem(cell_head + _cell_sxx) = null
76    mem(cell_head + _cell_syy) = null
77    mem(cell_head + _cell_sxy) = null
78    mem(cell_head + _cell_syx) = null
79    mem(cell_head + _cell_sdiff) = null
80    mem(cell_head + _cell_rmult) = null
81
82  end
83  ;------------------------------------------------------------------------------
84  define cell_mem
85    ; provides descriptors for the memory addresses for measurement cell information
86    _cell_next  = 0 ; next cell in the cell linked list
87    _cell_x   = 1 ; x position of the lower left corner of the cell
88    _cell_y   = 2 ; y position of the lower left corner of the cell
89    _cell_pnum  = 3 ; number of particles within the cell
90    _cell_bph = 4 ; memory address of the particle head of the linked list of particles
          in the cell
```

```
  _cell_sxx   = 5 ; the average xx component of the stress tensor for the cell
  _cell_syy   = 6 ; the average yy component of the stress tensor for the cell
  _cell_sxy   = 7 ; the average xy component of the stress tensor for the cell
  _cell_syx = 8 ; the average yx component of the stress tensor for the cell
  _cell_sdiff = 9 ;
  _cell_rmult = 10;

end
;-------------------------------------------------------------------------------
define link_particle
  ; links a set of particles to form an additional linked list
  b_extra(bp,b_mem_slot) = cell_bph
  cell_bph = bp
end
;-------------------------------------------------------------------------------
define color_cells
cell_p = cell_head
  cid = 0
  loop while cell_p # null
    cid = cid + 1
    b_cell = mem(cell_p + _cell_bph)
    if cid = 2
      loop while b_cell # null
        b_color(b_cell) = CellBallColor
        b_cell = b_extra(b_cell,b_cell_bnext_mem)
      end_loop
      cid = 0
    end_if

    cell_p = mem(cell_p + _cell_next)
  end_loop
end
```

Appendix F

FREQUENCY SWEEP RESULTS FOR MODELS WITH VARYING JOINT SETS

This appendix contains figures of the frequency sweep (1 to 30 Hz) results for slope models presented in Chapter 6. Refer to that chapter for details on the structures of the slope models.

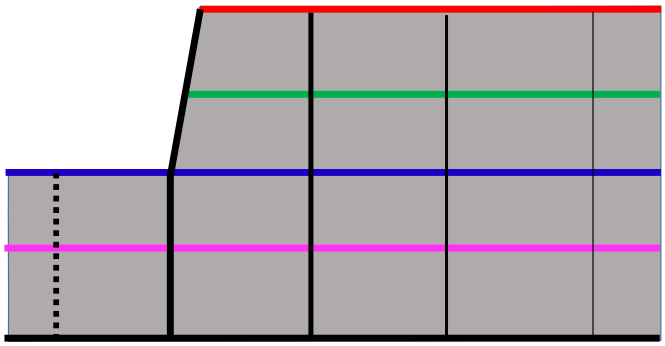

Figure F.1: Graphical legend for monitored particles in BPM slopes. Line colors correspond to elevations and line widths and types correspond to position from the slope face.

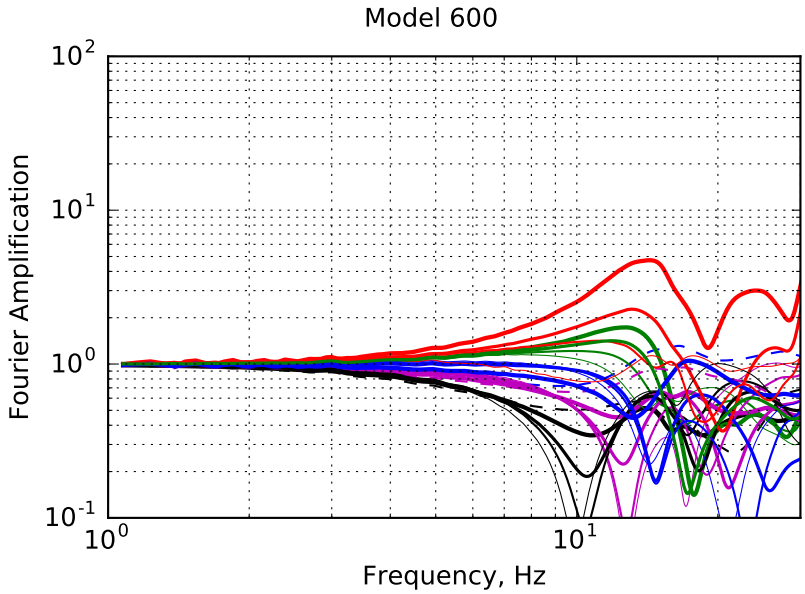

Figure F.2: Fourier amplitude amplification of acceleration in Model 600. The first mode of the slope is at about 14.2 Hz. Refer to Chapter 6 for model details.

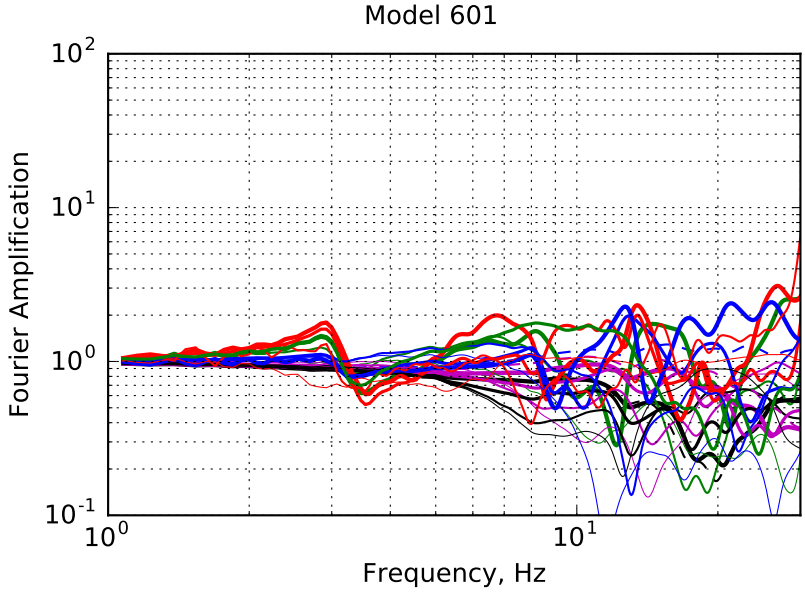

Figure F.3: Fourier amplitude amplification of acceleration in Model 601. The first mode of the slope is at about 2.9 Hz. Refer to Chapter 6 for model details.

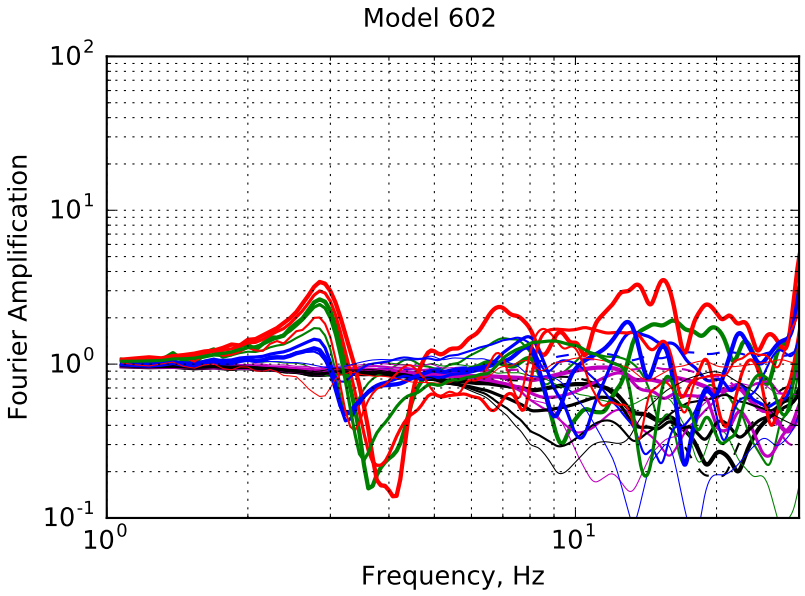

Figure F.4: Fourier amplitude amplification of acceleration in Model 602. The first mode of the slope is at about 2.85 Hz. Refer to Chapter 6 for model details.

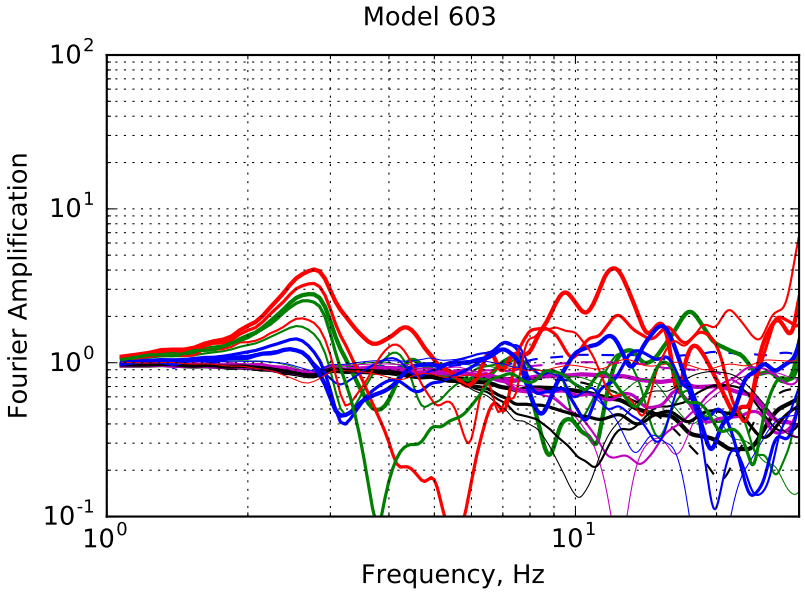

Figure F.5: Fourier amplitude amplification of acceleration in Model 603. The first mode of the slope is at about 2.7 Hz. Refer to Chapter 6 for model details.

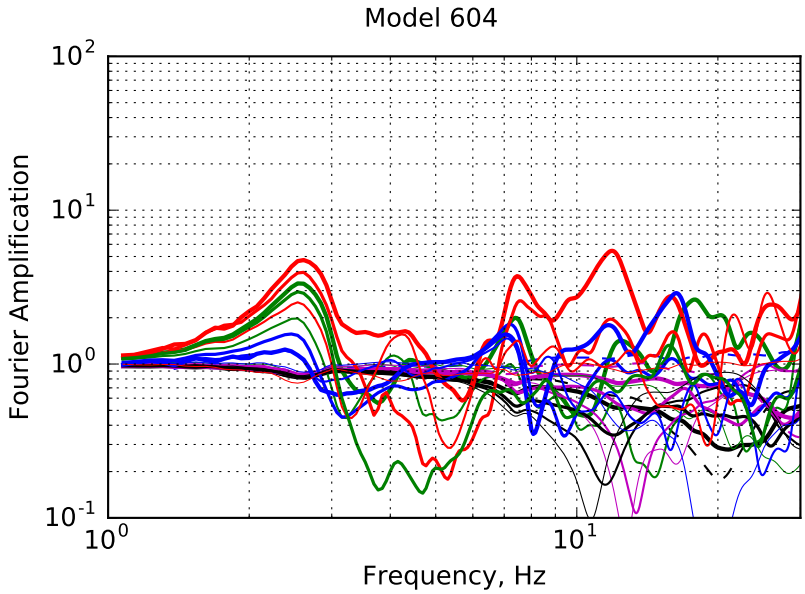

Figure F.6: Fourier amplitude amplification of acceleration in Model 604. The first mode of the slope is at about 2.6 Hz. Refer to Chapter 6 for model details.

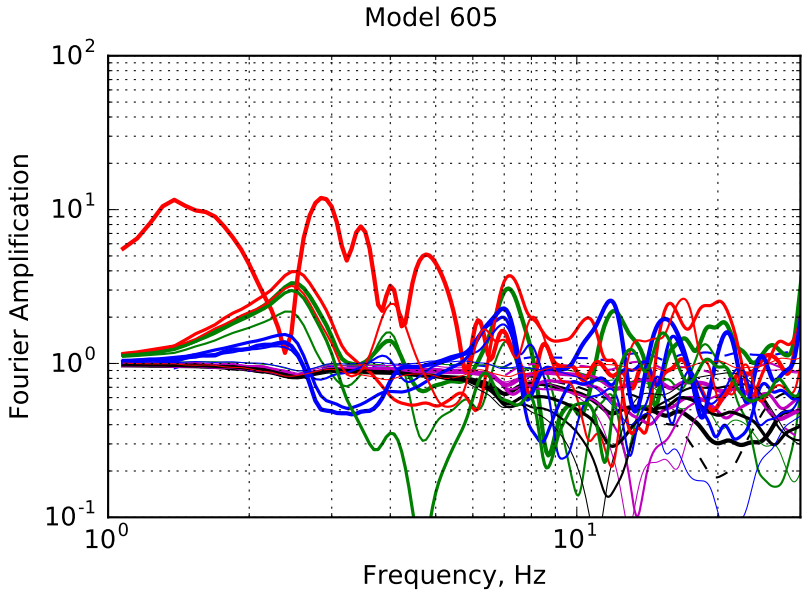

Figure F.7: Fourier amplitude amplification of acceleration in Model 605. The first mode of the slope is at about 2.5 Hz. Refer to Chapter 6 for model details.

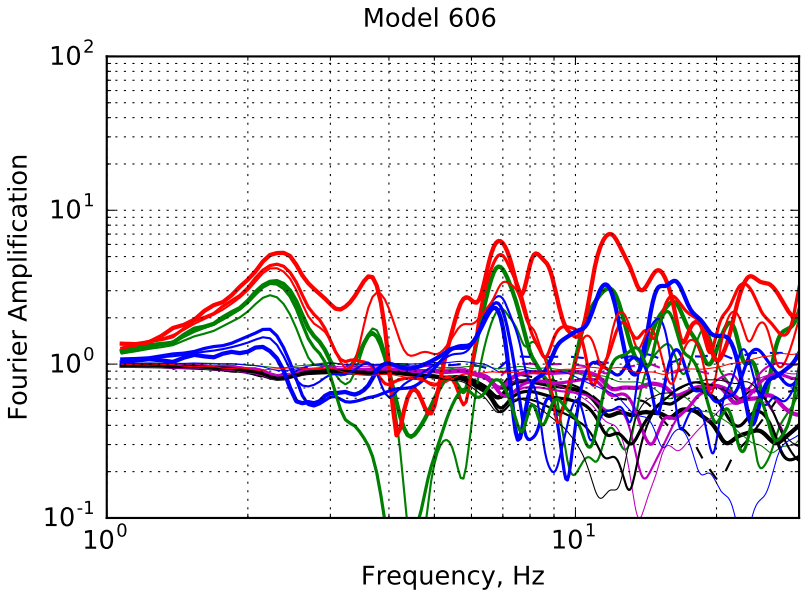

Figure F.8: Fourier amplitude amplification of acceleration in Model 606. The first mode of the slope is at about 2.3 Hz. Refer to Chapter 6 for model details.

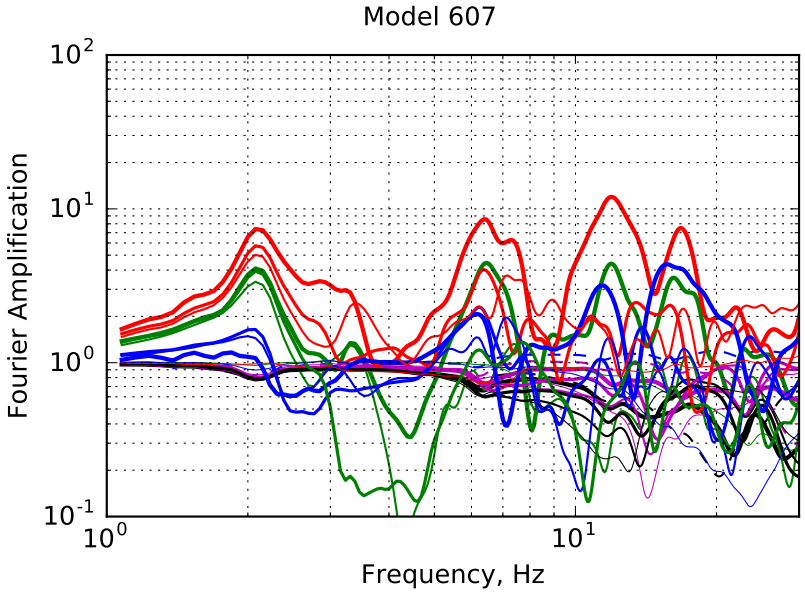

Figure F.9: Fourier amplitude amplification of acceleration in Model 607. The first mode of the slope is at about 2.1 Hz. Refer to Chapter 6 for model details.

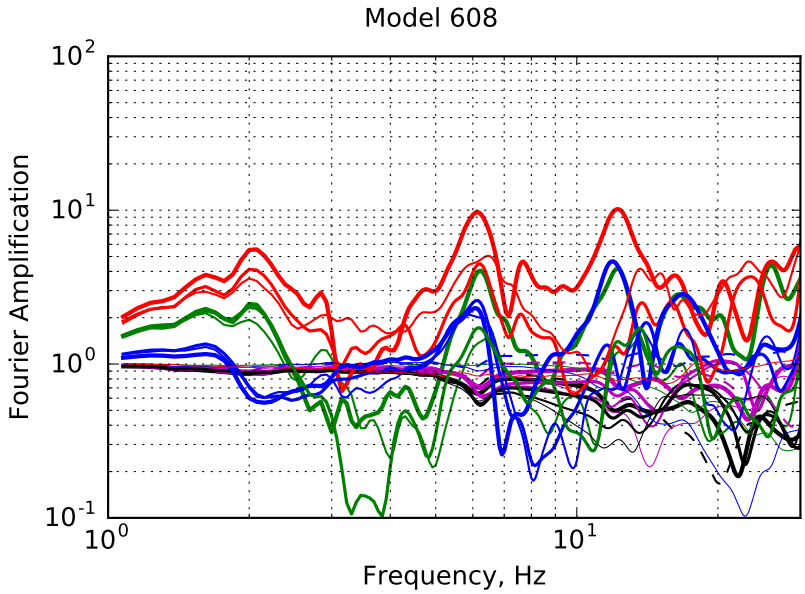

Figure F.10: Fourier amplitude amplification of acceleration in Model 608. The first mode of the slope is at about 2.0 Hz. Refer to Chapter 6 for model details.

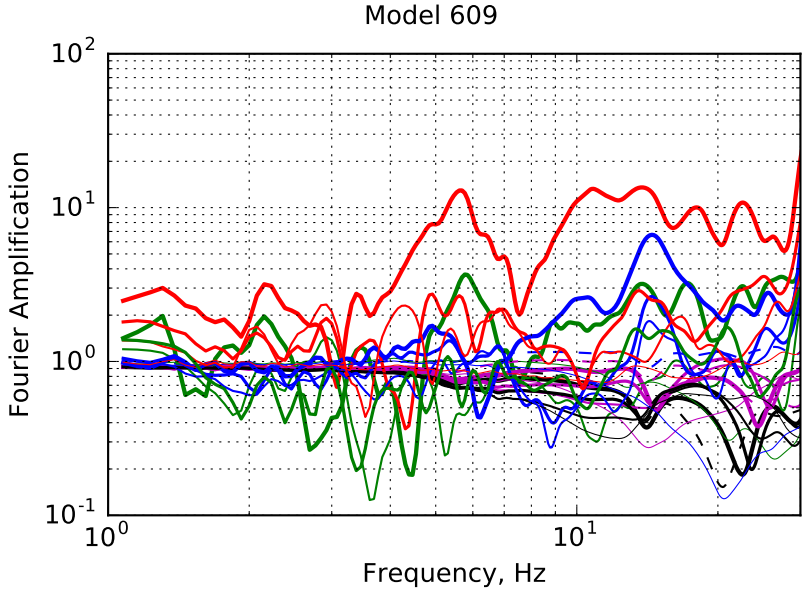

Figure F.11: Fourier amplitude amplification of acceleration in Model 609. The first mode of the slope is at about 2.1 Hz. Refer to Chapter 6 for model details.

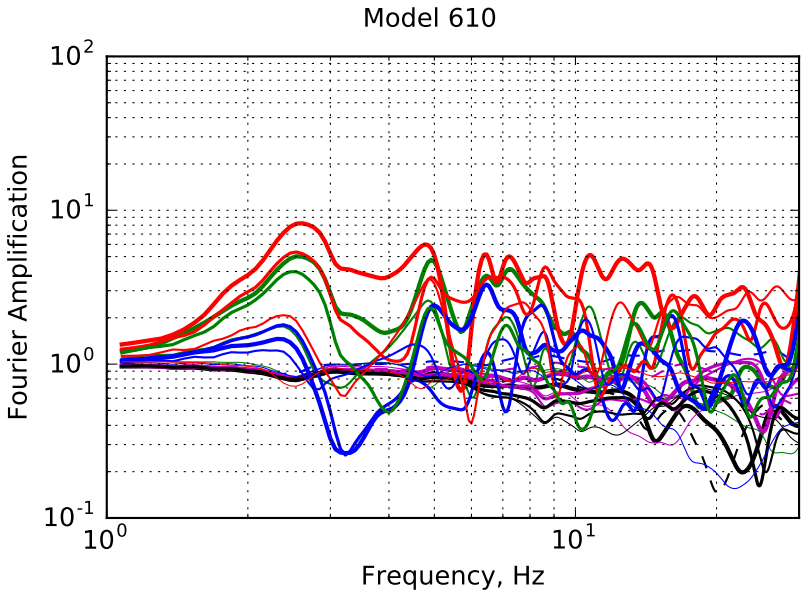

Figure F.12: Fourier amplitude amplification of acceleration in Model 610. The first mode of the slope is at about 2.6 Hz. Refer to Chapter 6 for model details.

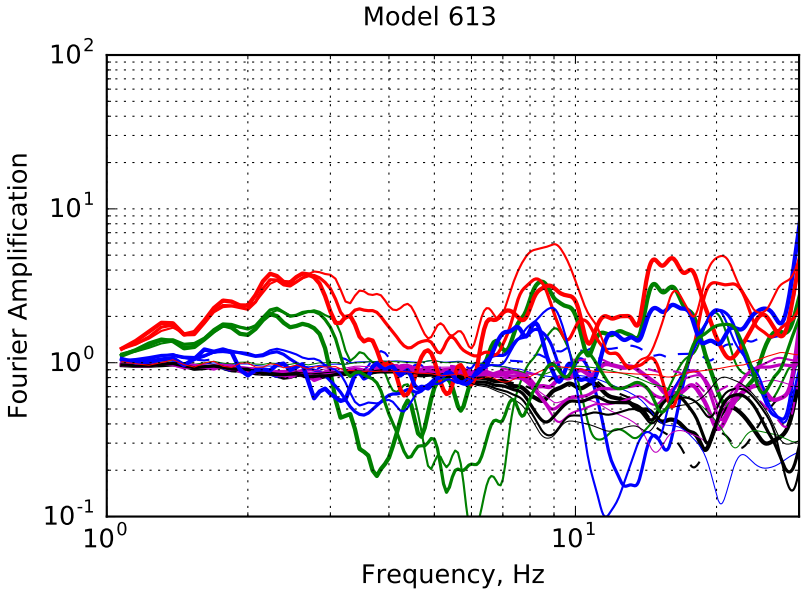

Figure F.13: Fourier amplitude amplification of acceleration in Model 613. The first mode of the slope is at about 2.7 Hz. Refer to Chapter 6 for model details.

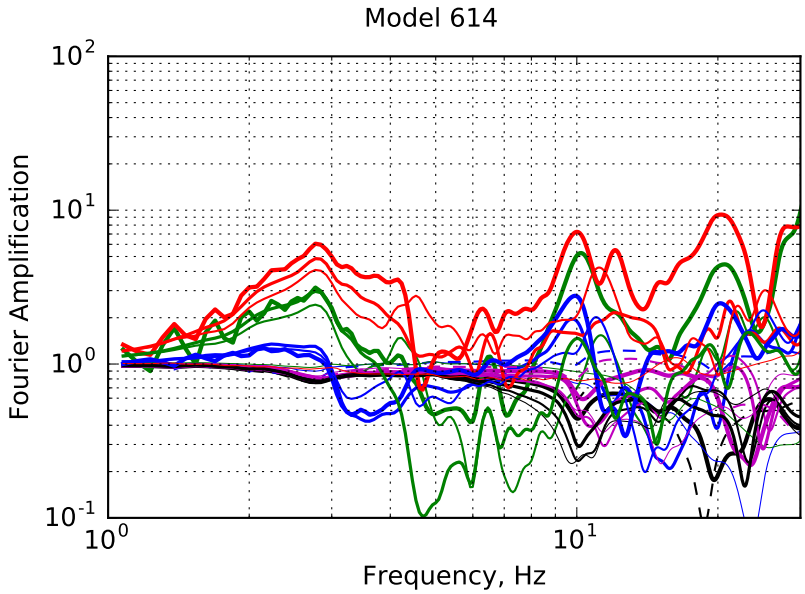

Figure F.14: Fourier amplitude amplification of acceleration in Model 614. The first mode of the slope is at about 2.8 Hz. Refer to Chapter 6 for model details.

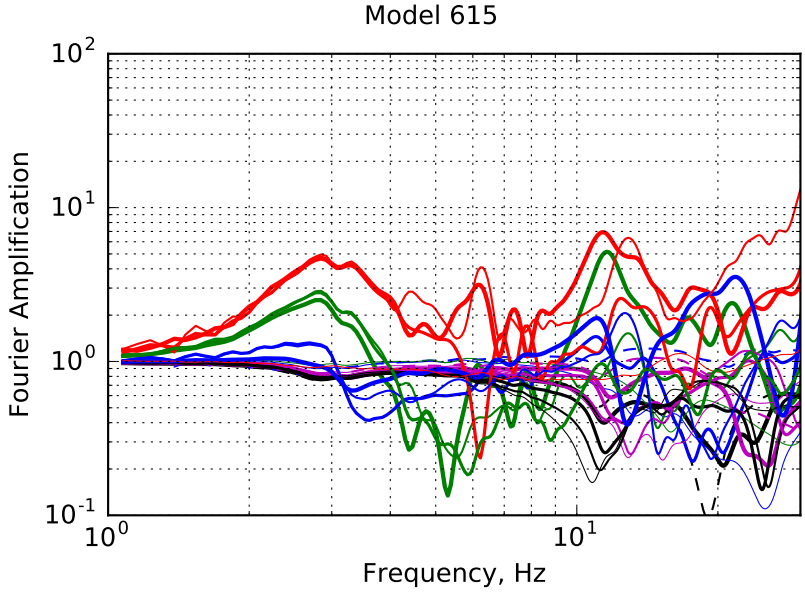

Figure F.15: Fourier amplitude amplification of acceleration in Model 615. The first mode of the slope is at about 3.0 Hz. Refer to Chapter 6 for model details.

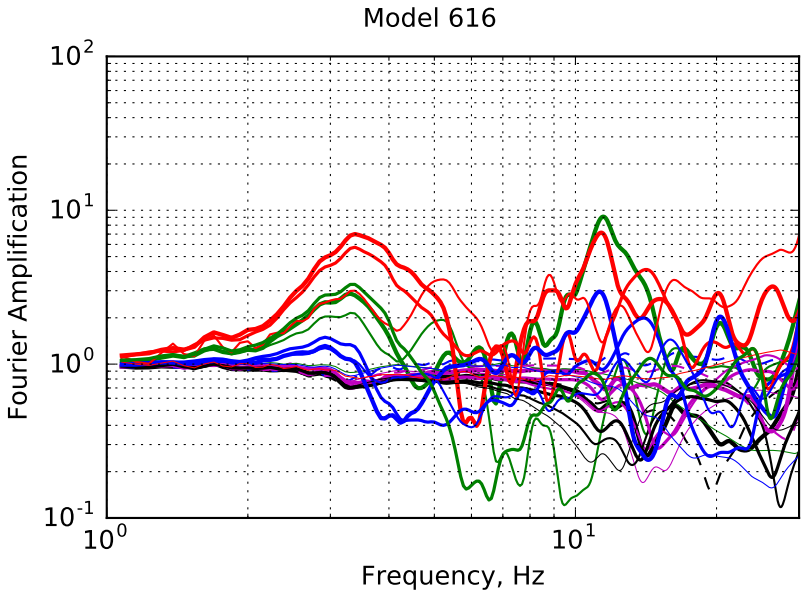

Figure F.16: Fourier amplitude amplification of acceleration in Model 616. The first mode of the slope is at about 3.4 Hz. Refer to Chapter 6 for model details.

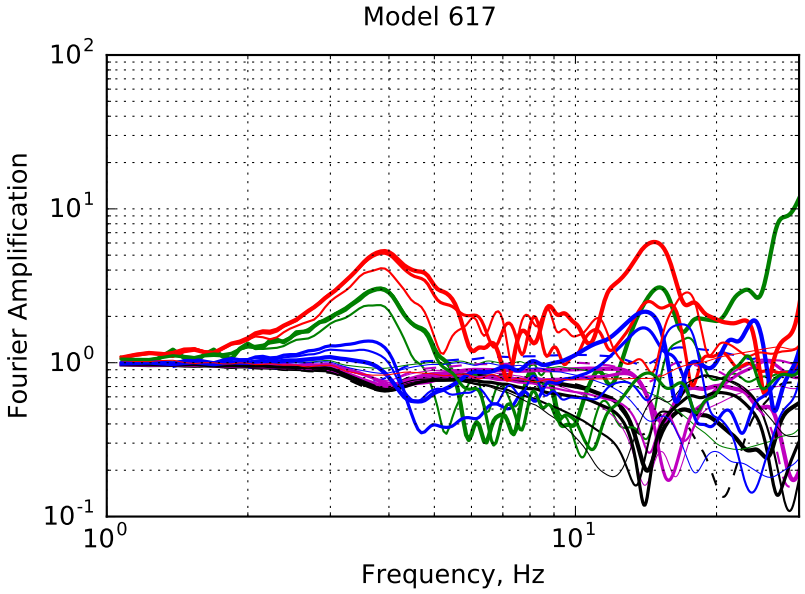

Figure F.17: Fourier amplitude amplification of acceleration in Model 617. The first mode of the slope is at about 4.0 Hz. Refer to Chapter 6 for model details.

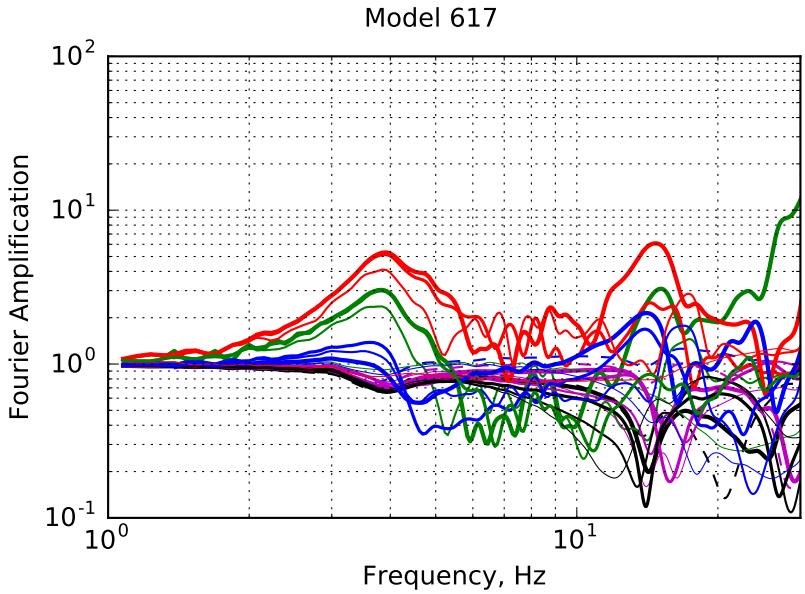

Figure F.18: Fourier amplitude amplification of acceleration in Model 617. The first mode of the slope is at about 4.4 Hz. Refer to Chapter 6 for model details.

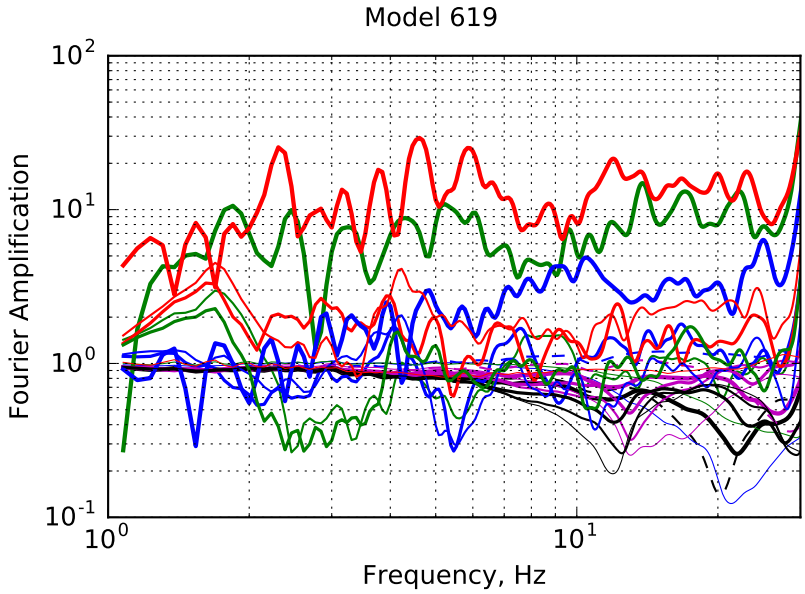

Figure F.19: Fourier amplitude amplification of acceleration in Model 619. 1.7 Hz. Refer to Chapter 6 for model details.

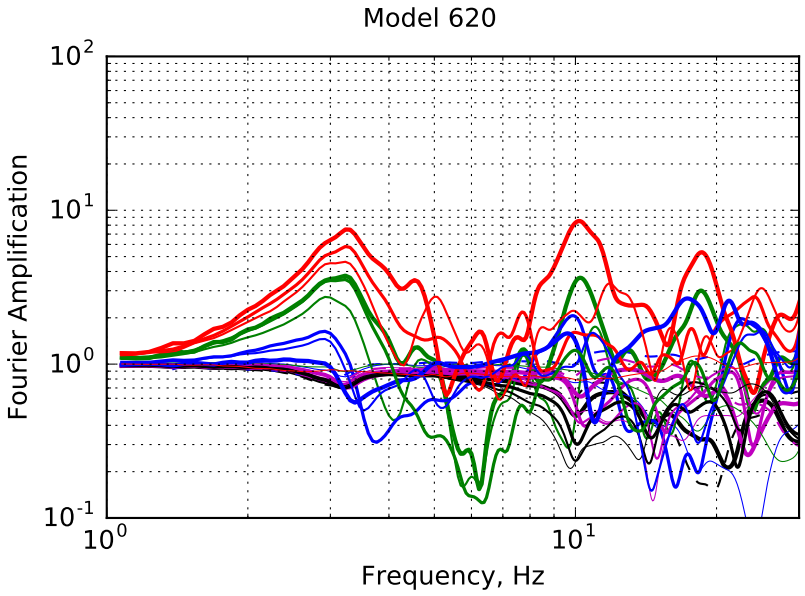

Figure F.20: Fourier amplitude amplification of acceleration in Model 620. The first mode of the slope is at about 3.2 Hz. Refer to Chapter 6 for model details.

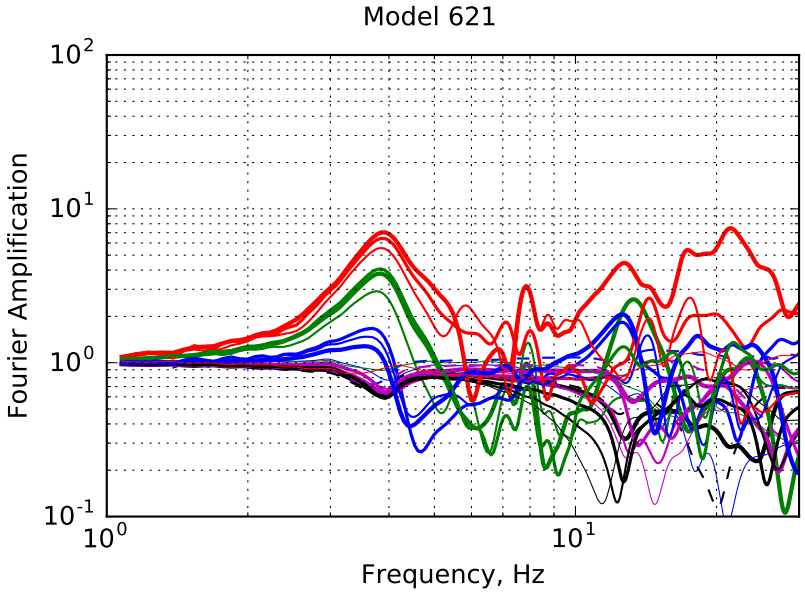

Figure F.21: Fourier amplitude amplification of acceleration in Model 621. The first mode of the slope is at about 3.9 Hz. Refer to Chapter 6 for model details.

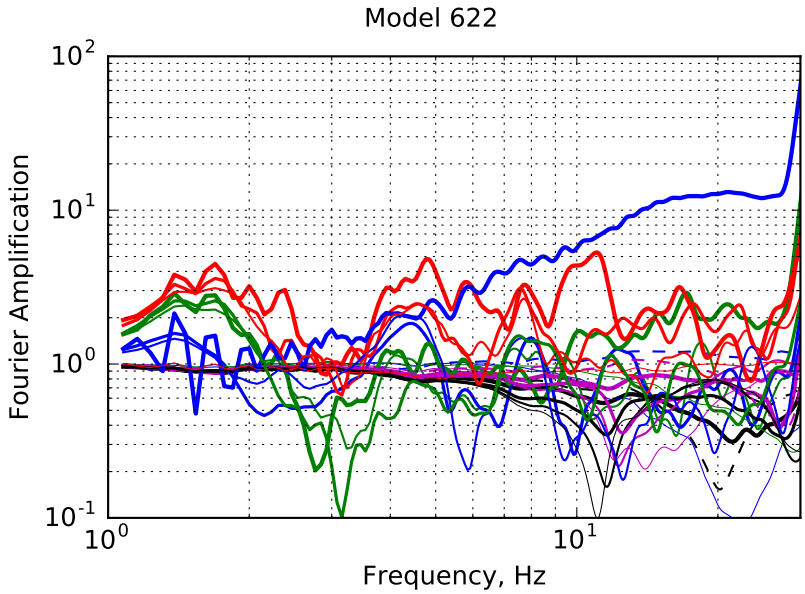

Figure F.22: Fourier amplitude amplification of acceleration in Model 622. The first mode of the slope is at about 1.7 Hz. Refer to Chapter 6 for model details.

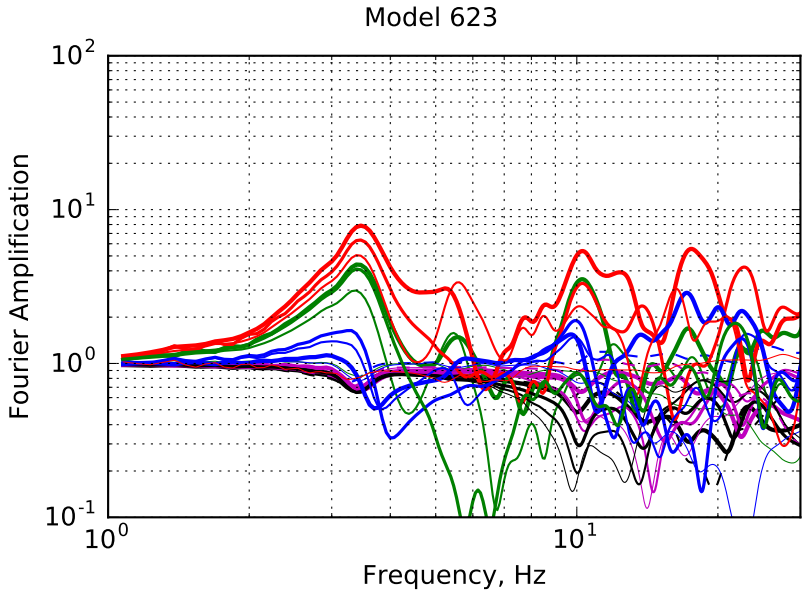

Figure F.23: Fourier amplitude amplification of acceleration in Model 623. The first mode of the slope is at about 3.4 Hz. Refer to Chapter 6 for model details.

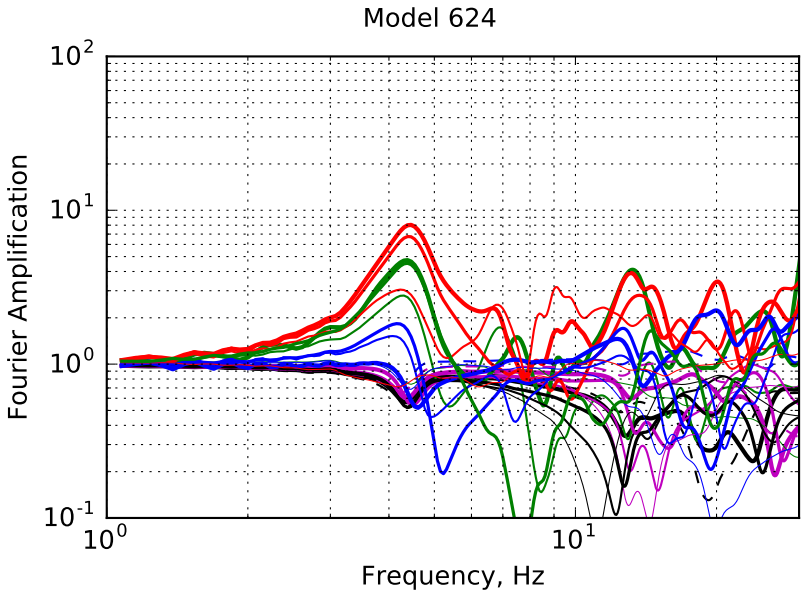

Figure F.24: Fourier amplitude amplification of acceleration in Model 624. The first mode of the slope is at about 4.4 Hz. Refer to Chapter 6 for model details.

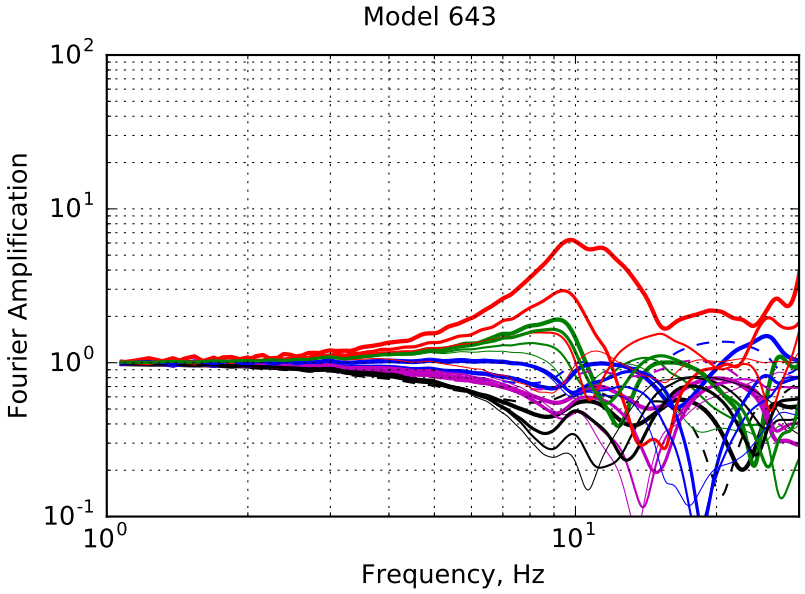

Figure F.25: Fourier amplitude amplification of acceleration in Model 643. The first mode of the slope is at about 9.8 Hz. Refer to Chapter 6 for model details.

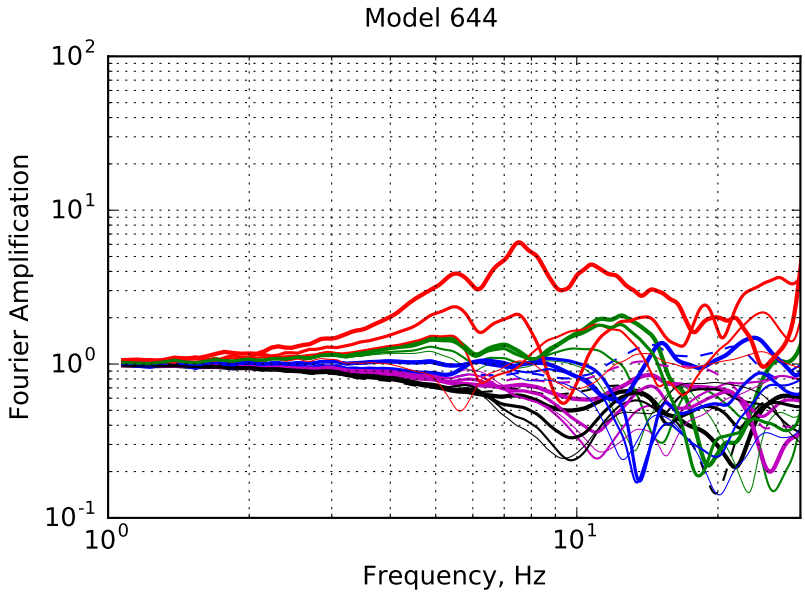

Figure F.26: Fourier amplitude amplification of acceleration in Model 644. The first mode of the slope is at about 7.5 Hz. Refer to Chapter 6 for model details.

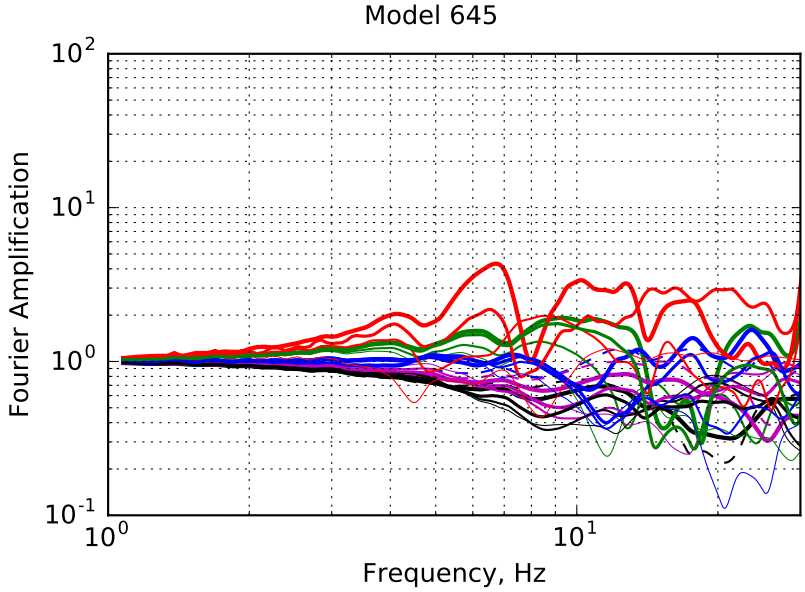

Figure F.27: Fourier amplitude amplification of acceleration in Model 645. The first mode of the slope is at about 6.7 Hz. Refer to Chapter 6 for model details.

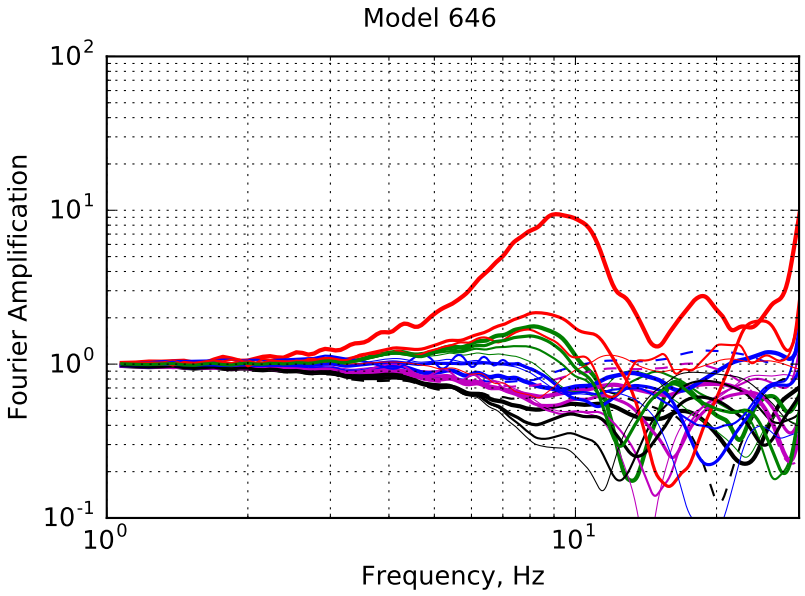

Figure F.28: Fourier amplitude amplification of acceleration in Model 646. The first mode of the slope is at about 9.1 Hz. Refer to Chapter 6 for model details.

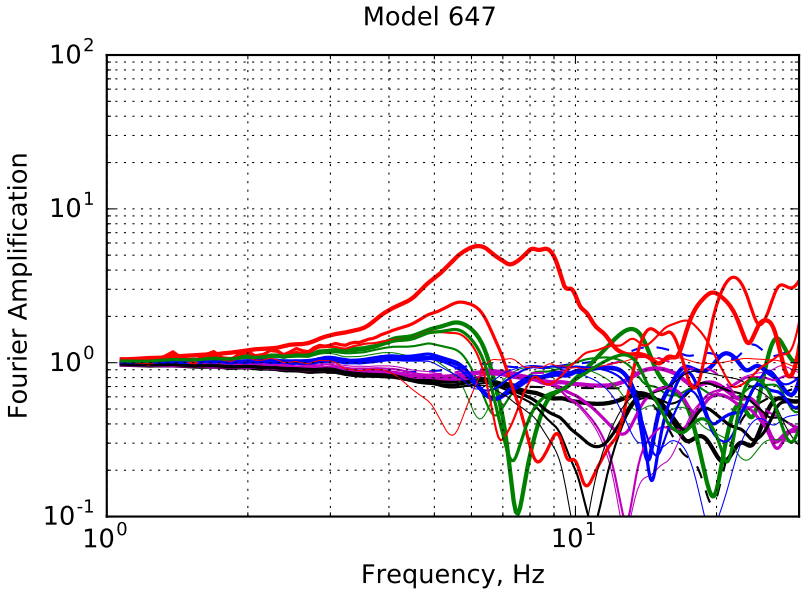

Figure F.29: Fourier amplitude amplification of acceleration in Model 647. The first mode of the slope is at about 6.2 Hz. Refer to Chapter 6 for model details.

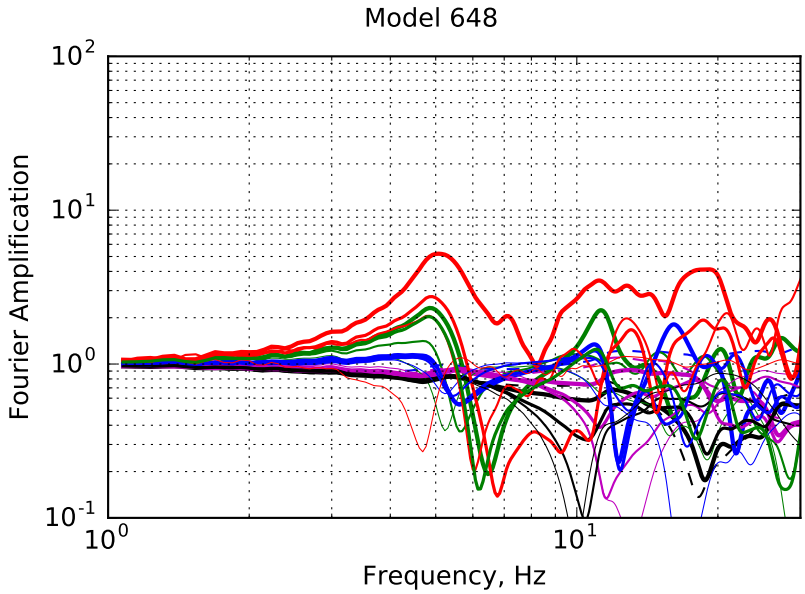

Figure F.30: Fourier amplitude amplification of acceleration in Model 648. The first mode of the slope is at about 5.1 Hz. Refer to Chapter 6 for model details.

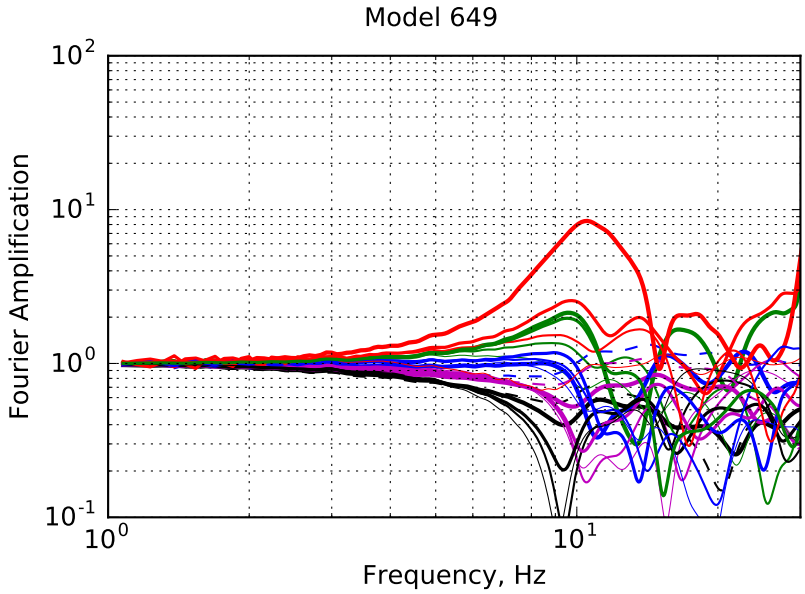

Figure F.31: Fourier amplitude amplification of acceleration in Model 649. The first mode of the slope is at about 10.5 Hz. Refer to Chapter 6 for model details.

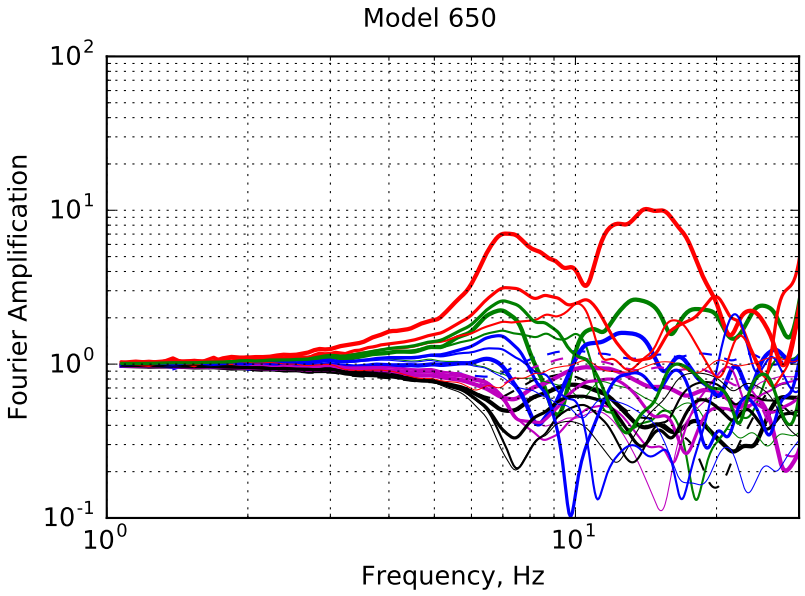

Figure F.32: Fourier amplitude amplification of acceleration in Model 650. The first mode of the slope is at about 7.2 Hz. Refer to Chapter 6 for model details.

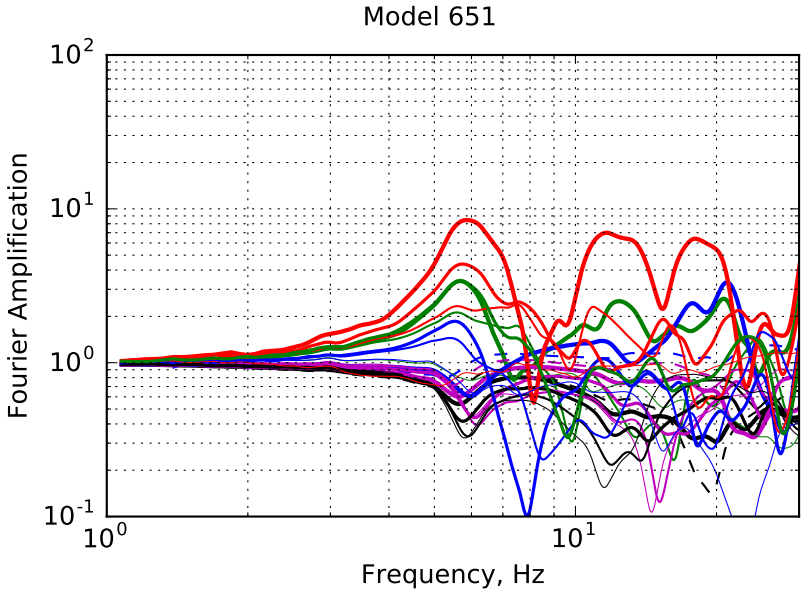

Figure F.33: Fourier amplitude amplification of acceleration in Model 651. The first mode of the slope is at about 7.2 Hz. Refer to Chapter 6 for model details.

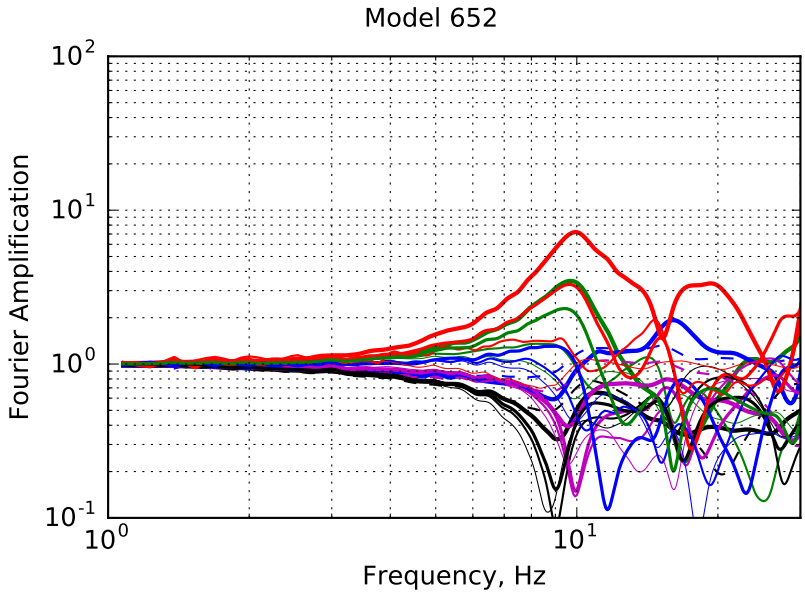

Figure F.34: Fourier amplitude amplification of acceleration in Model 652. The first mode of the slope is at about 9.9 Hz. Refer to Chapter 6 for model details.

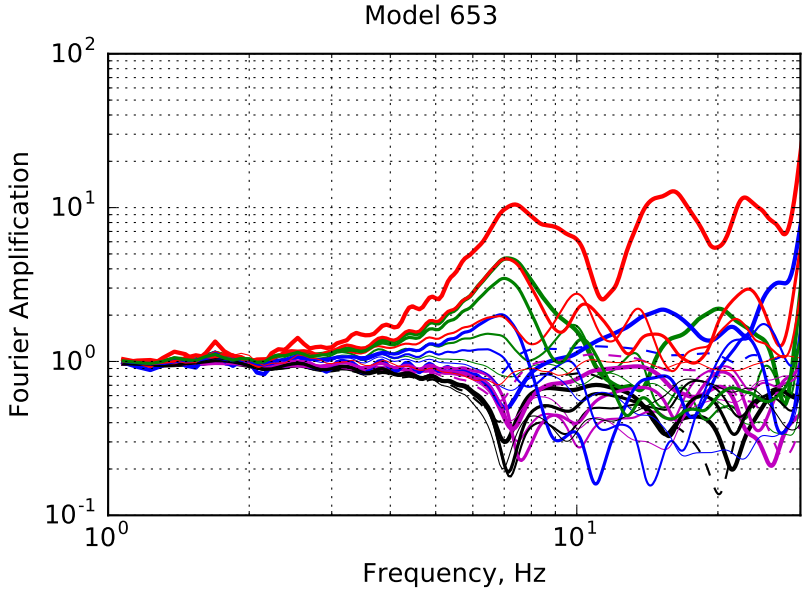

Figure F.35: Fourier amplitude amplification of acceleration in Model 653. The first mode of the slope is at about 7.4 Hz. Refer to Chapter 6 for model details.

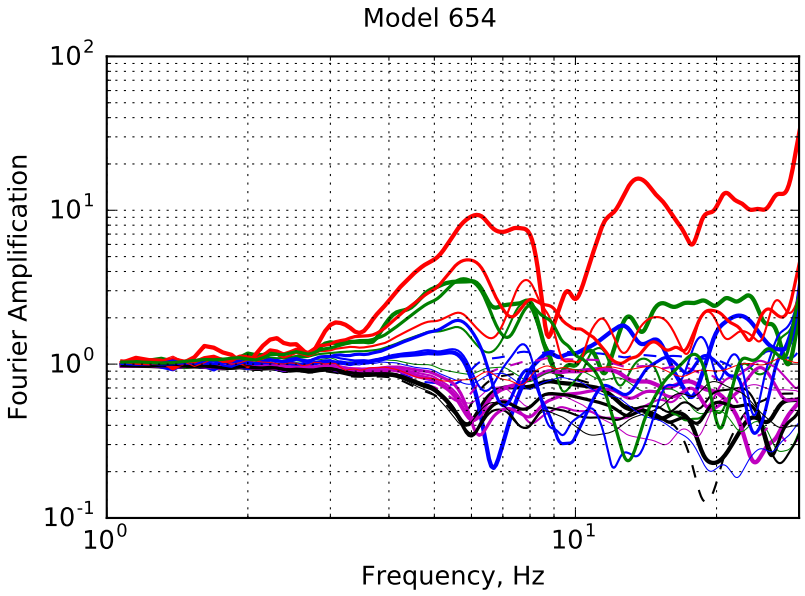

Figure F.36: Fourier amplitude amplification of acceleration in Model 654. The first mode of the slope is at about 6.2 Hz. Refer to Chapter 6 for model details.

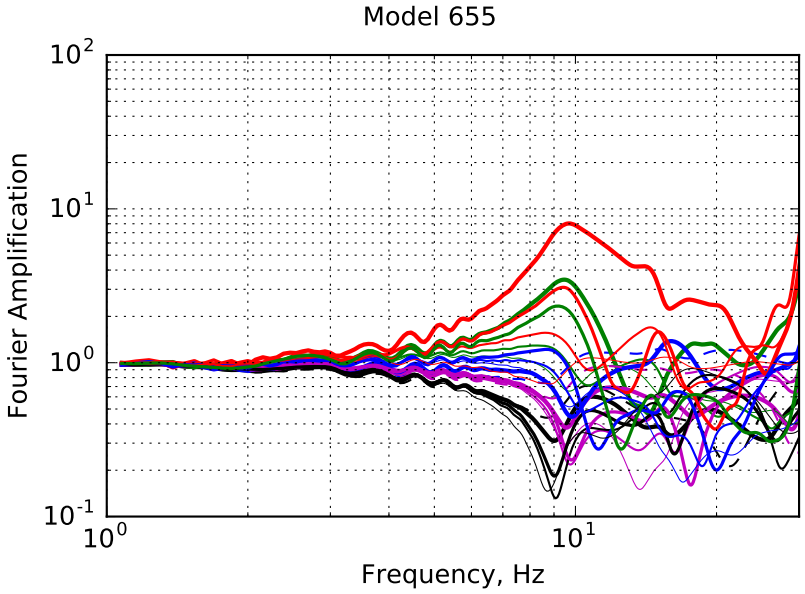

Figure F.37: Fourier amplitude amplification of acceleration in Model 655. The first mode of the slope is at about 9.7 Hz. Refer to Chapter 6 for model details.

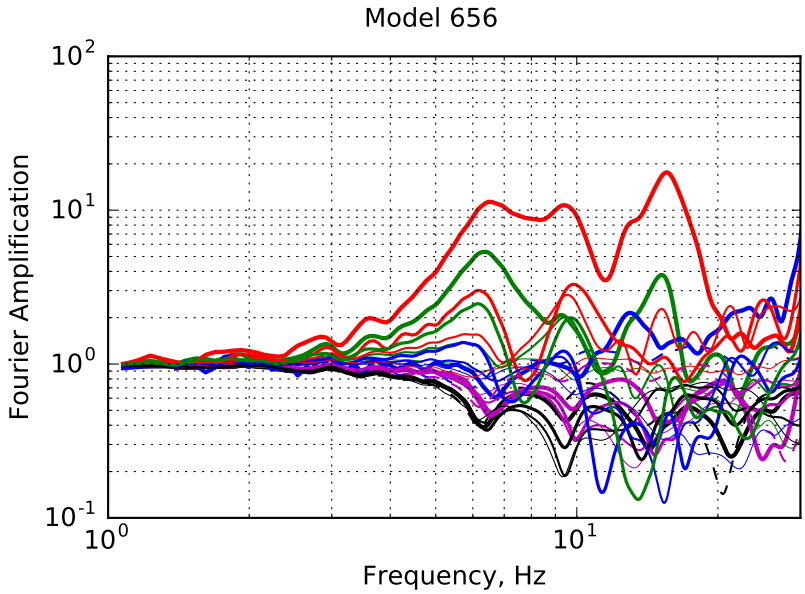

Figure F.38: Fourier amplitude amplification of acceleration in Model 656. The first mode of the slope is at about 6.4 Hz. Refer to Chapter 6 for model details.

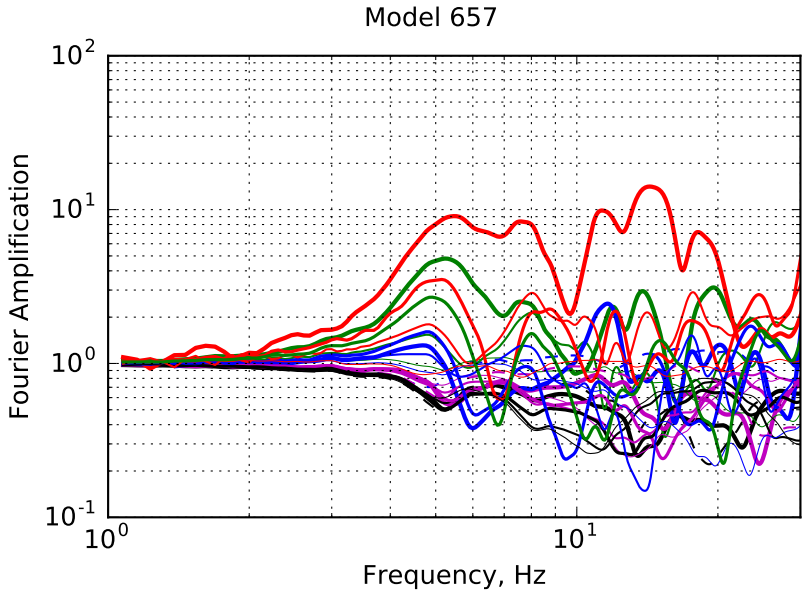

Figure F.39: Fourier amplitude amplification of acceleration in Model 657. The first mode of the slope is at about 5.5 Hz. Refer to Chapter 6 for model details.

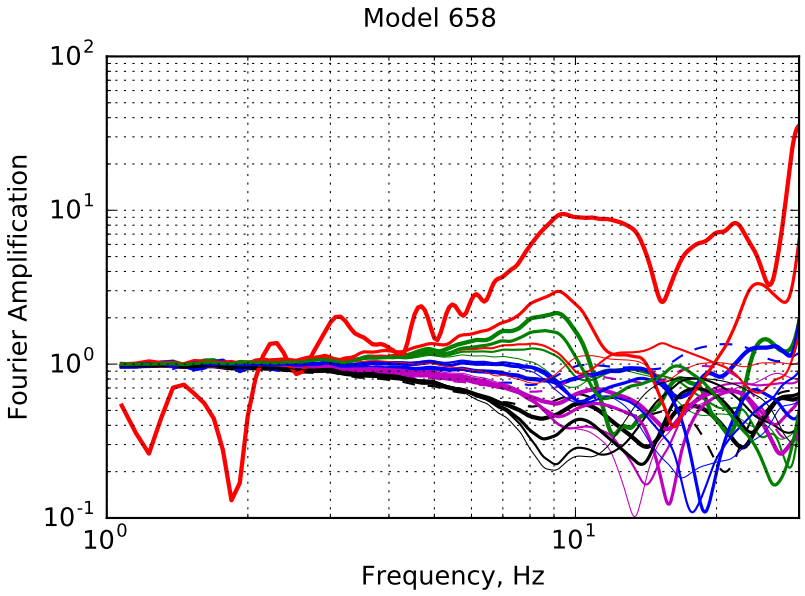

Figure F.40: Fourier amplitude amplification of acceleration in Model 658. The first mode of the slope is at about 9.4 Hz. Refer to Chapter 6 for model details.

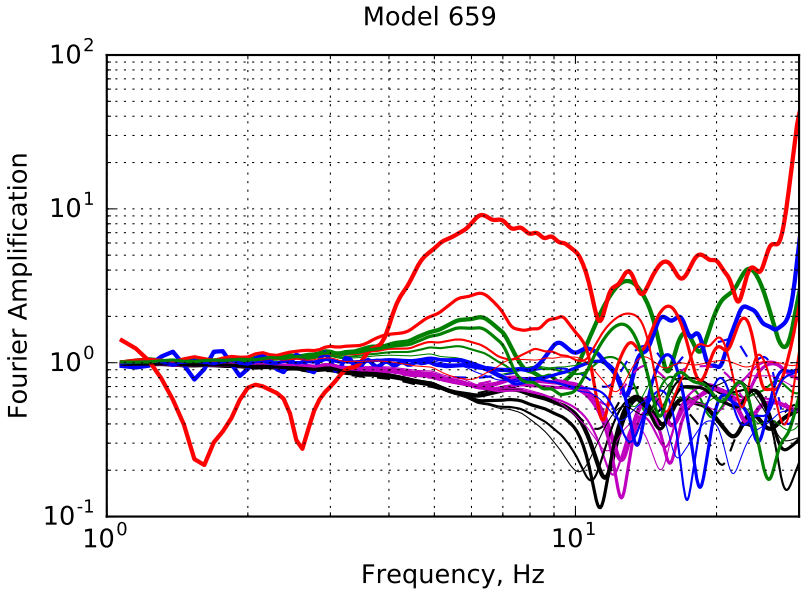

Figure F.41: Fourier amplitude amplification of acceleration in Model 659. The first mode of the slope is at about 6.3 Hz. Refer to Chapter 6 for model details.

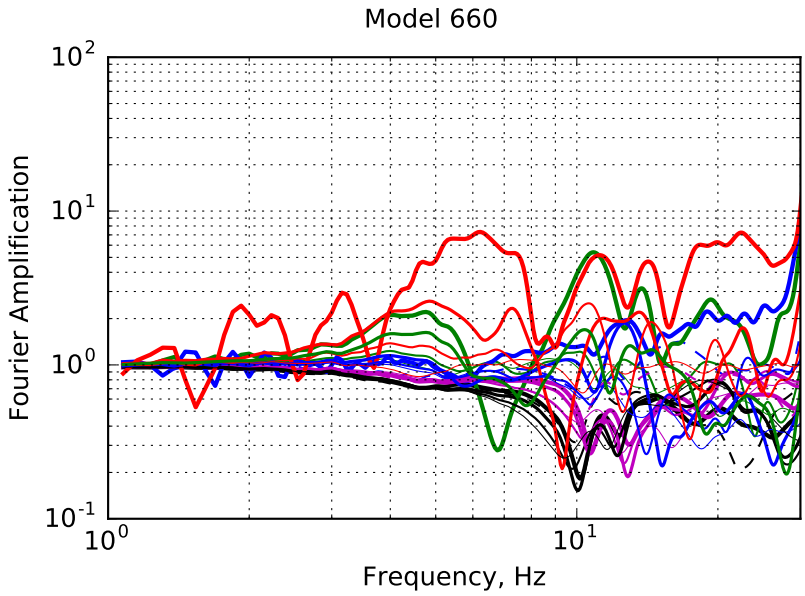

Figure F.42: Fourier amplitude amplification of acceleration in Model 660. The first mode of the slope is at about 5.1 Hz. Refer to Chapter 6 for model details.